

DISTRIBUTION STATEMENT A

Approved for Public Release

Distribution Unlimited

Properties of Complex Inorganic Solids 2

Edited by

Annemarie Meike

Antonios Gonis

Patrice E. A. Turchi

*Lawrence Livermore National Laboratory
Livermore, California*

and

Krishna Rajan

*Rensselaer Polytechnic Institute
Troy, New York*

20020124 412

Kluwer Academic/Plenum Publishers
New York, Boston, Dordrecht, London, Moscow

Library of Congress Cataloging-in-Publication Data

International Alloy Conference (2nd: 1999: Davos, Switzerland)

Properties of complex inorganic solids 2/edited by Annemarie Meike ... [et al].

p. cm.

"Proceedings of the Second International Alloy Conference, held August 8-13, 1999, in Davos, Switzerland"—T.p. verso.

Includes bibliographical references and index.

ISBN 0-306-46498-5

I. Alloys—Congresses. 2. Inorganic compounds—Congresses. I. Meike, Annemarie. II. Title.

TA483 .I59 1999

620.1'6—dc21

00-048741



Proceedings of Second International Alloy Conference,
held August 8-13, 1999, in Davos, Switzerland

ISBN 0-306-46498-5

©2000 Kluwer Academic/Plenum Publishers, New York
233 Spring Street, New York, N.Y. 10013

<http://www.wkap.nl/>

10 9 8 7 6 5 4 3 2 1

A C.I.P. record for this book is available from the Library of Congress

All rights reserved

No part of this book may be reproduced, stored in a retrieval system, or transmitted
in any form or by any means, electronic, mechanical, photocopying, microfilming, recording,
or otherwise, without written permission from the Publisher

Printed in the United States of America

Properties of Complex Inorganic Solids 2

ACKNOWLEDGEMENT

We are grateful to the following organizations for their financial support:

- **United Engineering Foundation**
- **Materials, Metals and Minerals Society Electronic, Magnetic, and Photonic**

Materials Division

- **U.S. Office of Naval Research Materials Division**
- **U.S. Army Research Office Physics Division**
- **Lawrence Livermore National Laboratory Chemistry and Materials Science, and Earth and Environmental Sciences Directorates**

PREFACE

The triennial International Alloy Conferences (IACs) aim at the identification and promotion of the common elements developed in the study, either experimental, phenomenological, or theoretical and computational, of materials properties across materials types, from metals to minerals. To accomplish this goal, the IACs bring together scientists from a wide spectrum of materials science including experiment, theory, modeling, and computation, incorporating a broad range of materials properties. The first IAC, IAC-1, took place in Athens, Greece, June 16-21, 1996. The present volume of proceedings contains the papers presented at IAC-2, that took place in Davos, Switzerland, August 8-13, 1999.

The topics in this book fall into several themes, which suggest a number of different classification schemes. We have chosen a scheme that classifies the papers in the volume into the categories Microstructural Properties; Ordering, Kinetics and Diffusion; Magnetic Properties and Elastic Properties. We have juxtaposed apparently disparate approaches to similar physical processes, in the hope of revealing the dynamic character of the processes under consideration. We hope this will invigorate new kinds of discussion and reveal challenges and new avenues to the description and prediction of properties of materials in the solid state and the conditions that produce them.

Microstructural characteristics provide access to both the design of materials and their physical history. Microstructure can determine the physical properties of a material, can speak volumes of the conditions that formed it and can contribute to its future evolution. Thus microstructure can be of as much interest to those who would like to reconstruct conditions (archeologists, forensic engineers and geologists) that caused certain microstructures as to those who wish to fabricate materials with new properties or predict their failure. The Microstructural Considerations Section contains contributions that discuss the potential contribution of microstructure to the future development and properties of a material, including works on phase transformations, diffusion, phase instabilities, grain and twist boundaries, and the effects of electronic structure on properties.

The section on Ordering presents contributions to the characterization and modeling of ordering phenomena. The section includes studies oriented toward discovering comprehensive principles of solids, as well as more focused studies that discuss the relative applicability of modeling approaches to explain experimentally observed perturbations of a system and their effects on ordering. Articles on ordering are also found elsewhere in this volume within the Kinetics and Diffusion Section and the Elastic Considerations Section.

Papers in the Kinetics and Diffusion Section address processes that are timed in spans of minutes to potentially thousands of years. Applications range from the development of more efficient materials to understanding the history of the earth. Although the application, scale and heterogeneity of the systems studied in this section vary markedly, the fundamental mechanisms that govern the processes of interest are essentially the same.

The ability to predict and understand phase transitions is at the heart of predicting material properties in inaccessible conditions, whether due to scale, temperature, pressure or time. Properties of the phase transitions themselves are keys to engineering design. Experimental and modeling papers represented in the Phase Stability and Transformations section push the limits of understanding these phenomena in all those directions and at a number of scales. The experimental design required to understand crystal configurations (symmetry and lattice parameters) under extreme conditions can be a challenge in itself. As for the other topics in this book there is synergy between model construction and experiment. The experimental results at times pose questions that may be addressed through models, and the models drive new possibilities that can be verified through experiment.

The understanding of magnetic properties in alloys clearly requires the need for connecting length scales. From electronic structure to microstructure, the papers in this section deal with both theoretical and experimental challenges of describing magnetic behavior over a wide range of length scales. The issues addressed in the Magnetic Properties Section explore a variety of microstructures ranging from thin films to bulk materials. Experiment and theory/computation are well represented in this domain. Giant magnetoresistance effects, ballistic transport, Fermi-surface and charge transfer effects are discussed, along with the relative merits of different computational techniques used in these studies.

The last section, entitled Elastic Properties, contains contributions related to elastic effects. The themes that are explored relate to the accommodation of an imposed pressure, various relaxation effects, the loss of elastic response, and phase stability considerations as they relate to elastic constraints. The work represented in this section is diverse and appears to only scratch the surface of a wide range of dynamic effects caused by elastic response that range from subtle interatomic relationships to property-determinant processes, all of which may provide the basis for future materials design.

As the editors of this second IAC, we are grateful to a number of organizations for their generous financial support. We express our gratitude to the United Engineering Foundation, especially Norm Stoloff and Barbara Hickernell; the Materials, Metals and Minerals Society, through its Electronic, Magnetic, and Photonic Materials Division; the U.S. Office of Naval Research Materials Division, the U.S. Army Research Office Physics Division, and to Lawrence Livermore National Laboratory Chemistry and Materials Science, and Earth and Environmental Sciences Divisions for their timely approval of our proposals for financial assistance and their generosity. We are also deeply thankful to the United Engineering Foundation that agreed to make the IAC part of their regularly sponsored conferences, and for providing an outstanding administrative assistance in the execution of IAC-2. Finally, we thank Kluwer/Plenum for publishing the proceedings of the conference and for their patience while they were being assembled.

A. Meike
A. Gonis
P. E. A. Turchi
K. Rajan

March 2000

CONTENTS

MICROSTRUCTURAL PROPERTIES

Fast ionic transport along twin walls in ferroelastic minerals	3
E. K. H. Salje*	
Dependence of carbide precipitation on grain boundary structure in sensitized austenitic stainless steel.	17
Hiroyuki Kokawa, Takashi Koyanagawa, Masayuki Shimada, Yukata S. Sato, and Takeshi Kuwana	
Grain boundary engineering for the control of oxygen embrittlement	27
S. Yamaura, Y. Igarashi, S. Tsurekawa, and T. Watanabe	
Self-assembly in epitaxial semiconductor alloys	39
K. Rajan, Y.-C. Chen, V. Bucklen, C. A. Wang, G. W. Charache, G. Nichols, M. Freeman, and P. Sanders	
Electromigration and electronic structure	49
A. Lodder* and J. P. Dekker	

ORDERING

<i>Ab initio</i> study of vacancies in metals and compounds.	63
P. A. Khorzhavyi, I. A. Abrikosov, and B. Johansson	
Order and disorder phenomena at surfaces of binary alloys	77
F. F. Haas, F. Schmid*, and K. Binder	
Analytical description of the short-range order in alloys with many-body atomic interactions	89
R. V. Chepulskii	
Changes in the atomic coordinates and state of anion and cation order induced by alloying and temperature change in $Y_2[M(2)_yM(1)_{1-y}]_2O_7$ pyrochlore solid solutions	101
Bernhardt J. Wuensch and Kevin W. Eberman	
Ordering kinetics in B2-FeAl	115
H. Lang, K. Rohrhofer, W. Pfeiler, H. Schweiger, and R. Podloucky	
Theoretical study of spinodal disordering and disordering relaxation	123
T. Mohri	

KINETICS AND DIFFUSION

Using arrested solid-solid multiphase reactions in geological materials to deduce the rate of crustal uplift	141
William E. Glassley* and Annemarie Meike	
Kinetic features of non-simplest alloy orderings: DO ₃ , L1 ₂ , and L1 ₀ orderings	155
K. D. Belashenko, V. Yu. Dobretsov, I. R. Pankratov, G. D. Samolyuk, and V. G. Vaks	
Kinetics of phase separation in a binary alloy: Influence of the atomic mobilities	175
M. Athenes, P. Bellon, and G. Martin	
Point defect energies in L1 ₂ -ordered Ni ₃ Al.	187
H. Schweiger, R. Podlousky, W. Püschl, M. Spanl, and W. Pfeiler	
Tests of the polymorphous coherent potential approximation	199
J. S. Faulkner*, B. Ujfalussy, Nassrin Moghadam, G. M. Stocks, and Yang Wang	

PHASE STABILITY AND TRANSFORMATION

Iron phase diagram and high pressures and temperatures	221
S. K. Saxena* and L. S. Dubrovinsky	
Effects of continuous atomic displacement on the phase stability of metallic alloys	235
K. Masuda-Jindo, R. Kikuchi, and Vu Van Hung	
Maximization of cluster entropies via an irreversible algorithm: Application to the cluster variation method	249
Victor L. Vinograd, Udo Becker, and Andrew Putnis	
CVM Calculations of the solid-state equilibria in the Fe-Co phase diagram	261
C. Colinet and A. Antoni-Zdziobek	
The Onsager cavity field in FCC alloys	267
S. Shallcross and B. L. Györfy	
<i>In-situ</i> chemical dynamics and phase mapping under steep thermal gradients using time-resolved and spatially resolved x-ray diffraction	285
J. Wong*, E. M. Larson, J. B. Holt, T. Ressler, and J. W. Elmer	
Development and properties of ϵ -martensite in Co-Cr-Mo alloys for biomaterials Applications	301
Hugo F. Lopez, Armando Aldivar, and P. Huang	

MAGNETIC PROPERTIES

Diffuse scattering of Cu ₃ Au displacements and Fermi surface effects	329
W. Schweika*, G. E. Ice, J. L. Robertson, C. J. Sparks, and J. Bai	
<i>Ab initio</i> theory of perpendicular transport in metallic magnetic multilayers	343
Josef Kudrnovsky*, Vaclav Drchal, Claudia Blaas, Peter Weinberger, Ilja Turek, and Patrick Bruno	

The Fermi surfaces of metallic alloys and the oscillatory magnetic coupling between magnetic layers separated by such alloy spacers	365
B. L. Györfy * and N. N. Lathiotakis	

On element-specific magnetometry with linear dichroism in photoemission	381
F.O. Schumann, R. F. Willis, K. W. Goodman, and J. G. Tobin*	

ELASTIC PROPERTIES

Deformation and fracture of TiC/Mo(Nb) in-situ composites.	393
S. Hanada, N. Nomura, and K. Yoshimi	

Doubled fatigued strength of box welds by using low transformation temperature welding material	401
Akihiko Ohta, Naoyuki Suzuki, and Yoshio Maeda	

The evaluation of the fracture strain of ITO films on polymeric substrates	409
Z. Chen, W. Wang, and B. Cotterell	

<i>Ab initio</i> study of structure and compressibility of garnets	417
V. Milman, R. H. Nobes, E. V. Akhmatkaya, B. Winkler, C. J. Pickard, and J. A. White	

Short-range ordering kinetics and microstructural development during post-deformation annealing.	429
M. Spanl, P. Rosenkranz, A. Korner, W. Püschl, W. Pfeiler	

Point defects in NiAl alloys under pressure.	439
A. Y. Lozovoi*, Ali Alavi, Pavel A. Korzhavyi, and Michael W. Finnis	

Microstructural characteristics of mixed III-V layers	455
S. Mahajan*	

Dynamical lattice instabilities in alloy phase diagrams	473
Göran Grimvall	

Bond-order potentials for transition metals based binary alloys: Ti-Al and Mo-Si alloys	479
S. Znam, D. Nguyen-Manh, D.G. Pettifor, and V. Vitek	

The magnetite (001) surface: Insights from molecular dynamics calculations	499
James R. Rustad*, Evgeny Wasserman, and Andrew R. Felmy	

Chairpersons/Organizers of IAC-2	511
--	-----

Participants' Photos	512
--------------------------------	-----

List of Participants	515
--------------------------------	-----

Index	521
-----------------	-----

*Invited Speaker

MICROSTRUCTURAL PROPERTIES

FAST IONIC TRANSPORT ALONG TWIN WALLS IN FERROELASTIC MINERALS

E.K.H. Salje

Department of Earth Sciences
University of Cambridge
Downing Street
Cambridge, CB2 0EQ, UK

INTRODUCTION

Ionic mobility is often enhanced for transport along grain boundaries when compared with bulk transport. Fine grained ceramics may show much faster transport than single crystals and, thus, observation of fast transport in the natural environment (e.g. mineral assemblies) could be conjectured to be intrinsically linked to grain boundary effects.^(1,2) This conjecture may not be correct for ferroelastic minerals, however. Such minerals undergo ferroelastic phase transitions which generate characteristic microstructures.⁽³⁾ Simple elements of ferroelastic microstructures are twin boundaries which often combine in order to form more complex patterns such as needles, combs, junctions and forks. In each case the local structural modification inside a twin wall is rather subtle because there are no topological defects present as in grain boundaries. The only changes are small variations of atomic bond distances and/or local changes of atomic ordering schemes. Despite the relative weakness of the structural perturbations, it was found that transport along ferroelastic twin boundaries can be strongly enhanced.

The key experiment which proved enhanced transport of oxygen along twin boundaries was performed by Aird and Salje.⁽⁴⁾ In this experiment, the incipient phase transition between insulating WO_3 and metallic electron conductor WO_{3-x} was used to probe the transport along twin walls. A twinned WO_3 crystal was heated at 730 K in a sodium vapour. In a gas transport reaction, oxygen from the surface of the crystal was removed. These oxygen positions were then replenished by diffusion of oxygen from the inside of the crystal, leaving behind oxygen vacancies in form of WO_{3-x} . Optical inspection of the sample showed that metallic WO_{3-x} was formed near the surface of the crystal and along connected twin boundaries while the bulk of the material remained insulating. The interconnectivity of the metallic phase was then measured at low temperatures at which WO_{3-x} becomes superconducting. Indeed, fully connected superconducting pathways were observed along twin boundaries. This experiment clearly demonstrates that preferential transport of oxygen along ferroelastic twin walls exists in materials with perovskite

structures. Later work confirmed this observation and showed that also Na-ions can be transported preferentially along twin boundaries.

Similar effects are expected to occur in other minerals with Ar in feldspars as a typical example. It is the purpose of this chapter to illustrate the geometric and energetic properties of twin boundaries in minerals and non-metallic materials. Emphasis is put on the observation that boundaries between two twins are not atomistically narrow but are typically 1nm–7nm wide which is sufficient for some localised transport paths.^(5,6,7)

FERROELASTIC TWIN WALLS

The most simple description of the internal structure of a ferroelastic twin wall follows from the minimisation of the energy density of the ferroelastic phase transition:

$$\delta \int G \, d\mathbf{r}^3 = 0$$

and a Landau potential of the form

$$G = \frac{1}{2} A \theta_s \left[\coth \frac{\theta_s}{T} - \coth \frac{\theta_s}{T_c} \right] Q^2 + \frac{1}{4} B Q^4 + \frac{1}{2} g (\nabla Q)^2$$

where θ_s is the quantum mechanical saturation temperature, Q is the order parameter, g is the Ginzburg (or dispersion) parameter and A , B are parameters related to interatomic interactions.⁽⁸⁾ The minimum condition leads in differential form to an Euler-Lagrange equation with the appropriate boundary conditions. The solution is

$$Q = Q_0 \tanh \frac{x}{W}$$

$$W^2 = 2g / \left[A \theta_s \left(\coth \frac{\theta_s}{T} - \coth \frac{\theta_s}{T_c} \right) \right]$$

and shows the classic divergence of the equivalent correlation length at $T \rightarrow T_c$.⁽⁹⁾ Experimental observations determined the Ginzburg parameter leading to a wall thickness at $T \rightarrow 0K$ between $2W_0/a=2$ and $2W_0/a=12$. The parameter a indicates the lattice parameter of the material. The wall energy at $T \rightarrow 0K$ is in this approximation for a second order phase transition

$$E_{\text{wall}} = W_0 (AT_c^2 / B)$$

with numerical values of some 10^{-2} J / m^2 . This energy is of a similar order of magnitude as surface energies.

Once a single twin is generated inside a large crystal at $T \ll T_c$, its lifetime is virtually unlimited. There is no mechanism in a stress-free crystal by which the crystal could get rid of the twin wall. The only possible decay channel is the lateral movement of the wall until it disappears through the surface. This lateral movement is prevented, however, by lattice pinning and the fact that atomic fluctuations around a twin wall will not lead to its macroscopic movement even on a geological timescale.^(10,11)

Several twin walls can combine to form a hierarchical structure which may represent equilibrium configurations under suitable boundary conditions or they are the result of kinetic processes. The latter case is most important in ferroelastics of the order/disorder type in which the strain is generated by atomic ordering processes rather than atomic displacements. It has been shown that strain coupling between the ordering atoms is the dominant interaction mechanism in most materials. In this case, the relevant energy expression for the whole system can be expressed as ⁽¹²⁾

$$E = \frac{1}{2} u^T \phi u - u^T F \tilde{Q}$$

where u is a column matrix of arbitrary atomic displacements, superscript T denotes a transpose, and ϕ is the matrix of interatomic force constants as frequently used in lattice dynamics. Also \tilde{Q} is the column matrix of $\tilde{Q}(R_i)$ of the occupancies at the position R_i . $\tilde{Q}(R_i)$ is related with the scalar order parameter Q via

$$Q = \frac{1}{N} \sum \tilde{Q}(R_i)$$

where the summation is carried over the whole sample. F is a matrix which contains a set of force constants describing the structural deformation as a function of the ordering process. This energy expression can now be minimised with respect to the displacements u leading to new displacements u' and an Ising-type energy:

$$E = \frac{1}{2} u'^T \phi u' - \frac{1}{2} \tilde{Q}^T (F^T \phi^{-1} F) \tilde{Q}$$

The displacement u' and the local order parameters \tilde{Q} are now completely decoupled. The first term represents the energy of a harmonic crystal in which the effective exchange energy $J(R)$ becomes

$$J(R) = F^T \phi^{-1} F$$

The actual form of $J(R)$ is quite complicated owing to the large range of the elastic forces and their strong anisotropy. At large distances one obtains the following asymptotic forms in ferroelastic systems:

$$J(R) \sim \frac{A_4 Y_{4m}(\theta, \phi) + A_2 Y_{2m}(\theta, \phi)}{R^3} + \frac{Z}{N}$$

where Y_{lm} represents the spherical harmonic order l . The first term decays with the third power of the interatomic distance which leads to the long range interaction between domain structures. The last term is the Zener-Eshelby interaction and relates to the assumption of free boundaries of the crystal with N atoms and its change of shape on undergoing the ferroelastic phase transition.⁽¹³⁾ It is this term which determines the transition temperature while the first term governs the spontaneous formation of microstructures.

The phase transition is governed by the long-ranged anisotropic forces resulting from the elastic response of the lattice. This behaviour effectively suppresses critical fluctuations in the ferroelastic systems, making their mean-field description almost exact with zero or

very small Ginzburg intervals. The thermodynamics of the system can be formulated in terms of Landau-Ginzburg functionals which are capable of describing an inhomogeneous state with domain walls, including their energy and equilibrium shape. Bending of domain walls then require non-local theories which introduces extra analytical complications.

The evolution of microstructures can now be explored by numerical simulation. For this purpose, the crystal structure is divided into an elastic matrix and the active atoms which are involved in the ordering process. The jump of atoms between different sites in the crystal structure is then simulated by Monte Carlo methods. The relaxation of the elastic matrix is calculated by direct energy minimisation or molecular dynamics techniques. A typical time sequence of microstructures is shown in Fig. 1.^(14,15,16,17)

A snapshot of a ferroelastic fluctuation at $T \gg T_c$ is shown in Fig. 1a. The crystal has the characteristic tweed pattern of interwoven boundaries between the two ferroelastic states (red and green) with undistorted regions (yellow) reminiscent of domain walls. Once this sample is quenched to $T < T_c$ the fluctuations coarsen rapidly to a tartan pattern with better defined wall segments. Further time evolution relates to the formation of straight domain walls and needle domains. Needle domains combine to form comb patterns. Such patterns then transform into stripe patterns via the retraction of individual needle domains.

While some domain wall orientations are fully determined by crystallographic symmetry operations, others are not.⁽³⁾ In the first case the walls are called W-walls while in the latter case they are indexed W'-walls. The W'-walls depend sensitively on local strain fluctuations. A typical example for the time evolution of W' walls in feldspar is shown in Fig. 2. The phase transition relates to the ordering of the Al and Si in alkali feldspar with Al on either in one of the two positions of the two ordered domains (blue or yellow) or in another position which is fully occupied by Si in the ordered state (white).⁽¹⁶⁾ For the $t = 0$ initial configuration the random, high-temperature distribution of Al is shown. Cooling the sample increasingly eliminates the energetically unfavourable white positions and leads to cluster formation of the predominantly blue and yellow patches. The walls between the domains are ill defined and wiggle around their equilibrium position. Wall-like features are only recovered after very long annealing times. This tumbling of W' walls at early stages of atomic ordering is also observed in the mineral cordierite (Al, Si ordering in $Mg_2Al_4Si_5O_{18}$) while the kinetic processes in displacive systems are often too rapid in order to allow the observation of such wiggly W' walls.

While these microstructures are transient (although sometimes with lifetime on a geological time scale) similar structures can be observed as true equilibrium structures if suitable boundary conditions are applied. A typical example is the formation of stripe pattern in films of $YBa_2Cu_3O_{7-8}$ (YBCO) on $SrTiO_3$ substrates.⁽¹⁸⁾ The main reason for such differences is the presence of elastic stresses near the contact between the thin film and the substrate which do not exist in single crystals. The difference between lattice parameters of the film and the substrate (the "lattice misfit") causes deformations in both materials. The deformation of the thin film directly affects the process of oxygen ordering. Another possible reason for the appearance of the substrate-generated stresses in the film is the formation of mismatch dislocations near the interface. The dislocations are expected when the lattice misfit between the film and the substrate is relatively large and coherence of the film-substrate interface cannot be preserved.

INTERNAL WALL STRUCTURES

Transport in twin walls is related to the local structural environment. Even small structural modifications of the wall structure are expected to show significant changes of the transport coefficients. We now consider the example of the mineral cordierite, $Mg_2Al_2Si_5O_{18}$ to demonstrate a possible mechanism by which wall structures can be modified. Al and Si atoms in cordierite are disordered in a hexagonal structure at high temperatures and order at low temperatures.

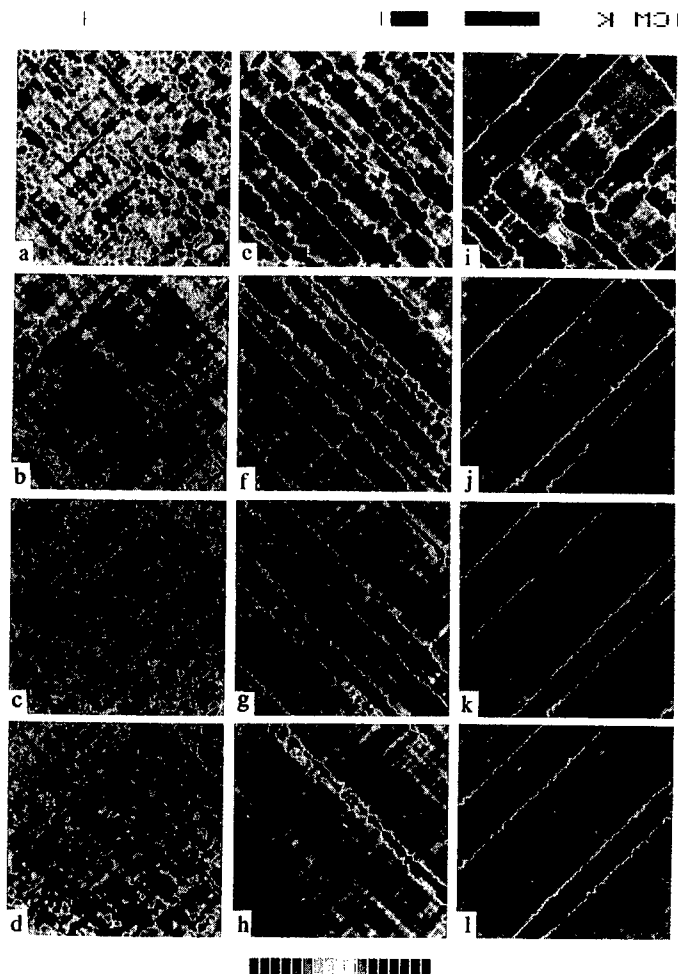


Figure 1. Microstructures and twin formation as simulated by molecular dynamics calculations (for details see Saljee& Parlinski, 1911). The system has been equilibrated at $T = 1.75 T_c$ and subsequently quenched below T_c and annealed. The annealing temperatures are $0.93 T_c$ (a–d), $0.83 T_c$ (e–h) and $0.73 T_c$ (i–l). The patterns occur after different annealing times. The time steps are: (a – e – i) directly after quench (0.4 time units) (b, f, j): 6 time units, (c, g, k): 13.6 time units and (d, h, l): 26 time units. The series a–d shows local fluctuations in a matrix which coarsens with increasing annealing time. The series e–h shows rough twin walls a coarsening of the twin structure, i–l shows sharper twin walls with intersection only in (i) after the quench.

The symmetry reduction from hexagonal to orthorhombic cordierite relates to the point groups $6/mmm$ and mmm , the active representation is E_{2g} . In such a case, the expected form of the Landau potential (truncated to three terms) is given by⁽¹⁹⁾

$$G = \frac{1}{2}A(q_1^2 + q_2^2) + \frac{1}{3}B(q_1^2 + q_2^2)^{3/2} \cos\left(3 \tan^{-1} \frac{q_1}{q_2}\right) + \frac{1}{4}C(q_1^2 + q_2^2)^2$$

It depends on two components of the order parameter, q_1 and q_2 . In the simulation of Blackburn⁽²⁰⁾, Blackburn and Salje⁽²¹⁾, we only allow orthorhombic cordierite to form. This constraint corresponds to setting B very high in the above equation. Thus, the free energy of the system is minimised when the second (angular) term is minimised. This happens when the cosine is equal to -1 which occurs when q_1 / q_2 is given by $\pm \sqrt{3}$ or 0 . This gives three possible values of the (normalised) vector order parameter q :

$$q = (q_1, q_2) = (0, 1), (\pm \sqrt{3}/2, -1/2)$$

which correspond to the three domains. The three strains for such domains with respect to the crystallographic axes are:

$$e_1 = e \begin{pmatrix} -1/2 & -\sqrt{3}/2 & 0 \\ -\sqrt{3}/2 & 1/2 & 0 \\ 0 & 0 & 0 \end{pmatrix} e_2 = e \begin{pmatrix} -1/2 & -\sqrt{3}/2 & 0 \\ -\sqrt{3}/2 & 1/2 & 0 \\ 0 & 0 & 0 \end{pmatrix} e_3 = e \begin{pmatrix} 1 & 0 & 0 \\ 0 & -1 & 0 \\ 0 & 0 & 0 \end{pmatrix}$$

We see that the order parameters are simply the reduced spontaneous strain components, e_{11}/e and e_{12}/e with:

$$\begin{aligned} e_{11}/e &= q_2 = \sin(\pi/2 + 2\pi/3s) \\ e_{12}/e &= q_1 = \cos(\pi/2 + 2\pi/3s) \end{aligned}$$

where s is a ring spin value. Thus, the order parameters can be calculated from its spin value. As we go through the wall in the y direction we see a stepwise variation of the order parameters. In a real wall it is expected that gradient energies will smooth off the order parameter profiles. Also shown are the normalised order parameters, Q_1 and Q_2 which are given by

$$Q_1 = 2/\sqrt{3}q_1 \quad Q_2 = 2/3(q_2 + 1/2)$$

which give values of $Q = (Q_1, Q_2) = (\pm 1, 0), (0, 1)$ for the three stable bulk configurations expected.

Since the coefficient of B in the Gibbs free energy can always be set to -1 , we can define $G' = G + B$ and write this out as:

$$G' = \frac{1}{2}Aq_1^2 + \frac{1}{4}Cq_1^4 + \frac{1}{2}Aq_2^2 + \frac{1}{4}Cq_2^4 + \frac{1}{2}Cq_1^2q_2^2$$

which is a standard 2-4 potential in q_1 and q_2 with a biquadratic coupling term. There are only two coefficients, A and C because of symmetry constraints. In addition, we now add

Ginzburg terms to provide a gradient energy and integrate the free energy density to give the total free energy:

$$G' = \int \left[\frac{1}{2} A q_1^2 + \frac{1}{4} C q_1^4 + \gamma_1 \left(\frac{\partial q_1}{\partial y} \right)^2 + \frac{1}{2} A q_2^2 + \frac{1}{4} C q_2^4 + \gamma_2 \left(\frac{\partial q_2}{\partial y} \right)^2 + \frac{1}{2} C q_1^2 q_2^2 \right] dy$$

where y is a coordinate perpendicular to the wall. In writing the Ginzburg term in this simple way (as a scalar field) we assume that the wall is flat with no twisting.

It is necessary to find the set of parameters A , C etc., which give rise to the bulk values of q_1 and q_2 at $T = 0$, these values are $\sqrt{3}/2$ and $-1/2$ respectively. To explore phase space more thoroughly, we generalise the Gibbs free energy to

$$G' = \frac{1}{2} A_1 q_1^2 + \frac{1}{4} C_1 q_1^4 + \frac{1}{2} A_2 q_2^2 + \frac{1}{4} C_2 q_2^4 + \frac{1}{2} C_3 q_1^2 q_2^2$$

Minimising this equation gives four solutions for q , ($q_1 = 0, q_2 = 0$) ($q_1 \neq 0, q_2 = 0$), ($q_1 = 0, q_2 \neq 0$), ($q_1 \neq 0, q_2 \neq 0$). Clearly the latter is the one which corresponds to the required ground state. It turns out that the required value of q , $=(\sqrt{3}/2, 1/2)$, is obtained when

$$\begin{aligned} A_1 &= -1/4 (C_2 + 3C_1) \\ A_2 &= -1/4 (3C_2 + 3C_1) \end{aligned}$$

These parameters give rise to $q_1 = \sqrt{3}/2, q_2 = -1/2$ as one minimum. However, the energy of this minimum will only be less than those of the other minima if $C_2 < C_1$ as can be shown by calculating the energies of the four minima of equation 4.8. If $C_2 < C_1$ then the $q_1 = 0, q_2 \neq 0$ phase has a lower energy. At the critical point where $C_2 = C_1 = C$, we see that $A_1 = A_2 = A = -C$ gives the required minimum. However, this critical point is a borderline case and in practice it is necessary to perturb A_1 and A_2 slightly away from A and C_1 and C_2 away from C :

$$\begin{aligned} A_1 &= A + \delta A_1 \\ A_2 &= A + \delta A_2 \\ C_1 &= C + \delta C_1 \\ C_2 &= C + \delta C_2 \end{aligned}$$

in order to be able to realise the correct ground state. This perturbation implies that the system is somewhat less than hexagonal in its high symmetry form. In experimental cordierite, this could be due to external stresses, defects, finite size effects and edge effects in the sample. In the computer simulation, edge and finite size effects will cause the symmetry reduction. The free energy expression for a nonuniform distribution is therefore given by:

$$G' = \int \left[\frac{1}{2} A_1 q_1^2 + \frac{1}{4} C_1 q_1^4 + \gamma_1 \left(\frac{\partial q_1}{\partial y} \right)^2 + \frac{1}{2} A_2 q_2^2 + \frac{1}{4} C_2 q_2^4 + \gamma_2 \left(\frac{\partial q_2}{\partial y} \right)^2 + \frac{1}{2} C_3 q_1^2 q_2^2 \right] dy$$

We may now use the calculus of variations to write PDEs for the order parameters as the system approaches its minimum free energy:

$$\begin{aligned}\frac{\partial q_1}{\partial t} &= -\frac{\delta G'}{\delta q_1} = \gamma_1 \frac{\partial^2 q_1}{\partial y^2} A_1 q_1 - C_1 q_1^3 - C_2 q_1 q_2^2 \\ \frac{\partial q_2}{\partial t} &= -\frac{\delta G'}{\delta q_2} = \gamma_2 \frac{\partial^2 q_2}{\partial y^2} A_2 q_2 - C_1 q_2^3 - C_2 q_1^2 q_2\end{aligned}$$

with the boundary condition:

$$\begin{aligned}\left[\frac{\partial q_1}{\partial y} \right]_{y=\pm\infty} &= 0 \\ \left[\frac{\partial q_2}{\partial y} \right]_{y=\pm\infty} &= \pm 1\end{aligned}$$

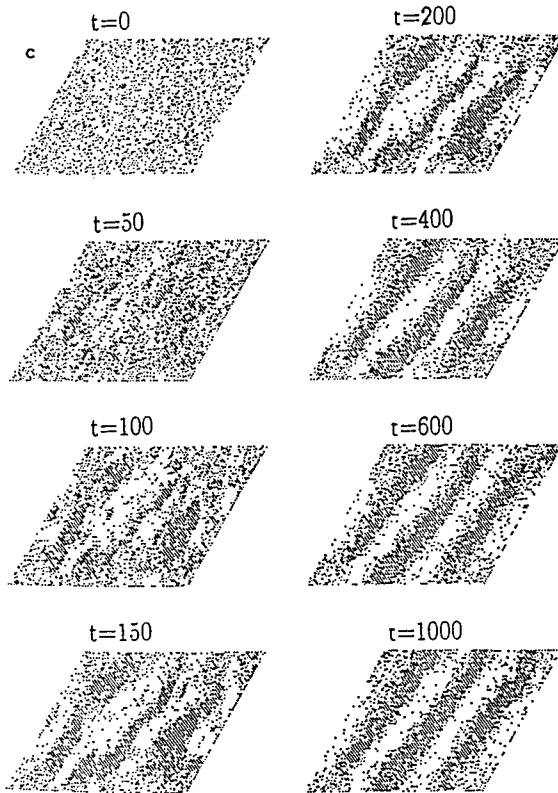


Figure 2: Sequences of snapshots of the simulated twin microstructure corresponding to different annealing times, t (indicated in Monte Carlo steps per ordering atom). Only Al atoms distributed over Tl positions of a single crankshaft are shown. Different symbols (heavy and lights dots) are used to distinguish between Tlo and Tlm sites. The first snapshot in each sequence corresponds to the initial, totally disordered Al-Si distribution. The annealing temperature is approximately $0.7T_c$.

We now proceed to solve these equations numerically using an Euler method. The sample is divided into grid points and the derivatives are written using finite differences. C_1 is taken to be 1 and C_2 is 0.9 (so that C_2 is less than but close to C_1 as required). This gives $A_1^0 = -0.975$ and $A_2^0 = -0.925$ at $T = 0$. Both A_1 and A_2 vary with temperature as:

$$A_1 = A_1'(T - T_c) = A_1^0 \left(1 - \frac{T}{T_c}\right)$$

$$A_2 = A_2'(T - T_c) = A_2^0 \left(1 - \frac{T}{T_c}\right)$$

so that the ratio $A_1 / A_2 = A_1^0 / A_2^0$ is constantly equal to 39/37. In a computer simulation by Blackburn and Salje (1999) the following values of A_1 and A_2 were used

A_1	-0.975	-0.800	-0.600	-0.400	-0.200	-0.100
A_2	-0.925	-0.759	-0.569	-0.379	-0.190	-0.095

Finally, one must choose values of the Ginzburg coefficients γ_1 and γ_2 . The parameter which varies as a result of the formation of a sandwich wall but which is fixed in a strain wall is q_2 . Therefore in order to encourage the formation of a sandwich wall we must set $\gamma_2 < \gamma_1$. Physically this means that topological walls form more readily than strain walls which is indeed observed to be the case in the computer simulations of the atomistic model. We therefore set $\gamma_1 = 1$ and $\gamma_2 = 0.2$. At higher values of γ_2 the sandwich wall does not form.

The initial configuration used in the simulation was a tanh function for q_1 and Gaussian peak for q_2 inside the wall. Fig. 3 shows the final, converged distributions of the order parameters for the different A coefficients listed above. In each case, the program was run until the free energy had reached its minimum to five decimal places and the order parameter plots had converged to those shown in the figure.

We see that the choice of parameters does indeed give $Q = (\pm, 0)$ in the bulk at $T = 0$, $A_1 = -0.975$ and there is a peak in Q_2 at the sandwich wall. If Q_2 were set at zero then there would be no coupling and the Q_1 curve would be a tanh function with width $\propto 1/(T_c - T)$. In the $T = 0$ solution, however, Q_1 is considerably distorted away from such a curve by the high value of Q_2 in the wall. In fact Q_2 almost reaches its saturated value of 1. Rather than being Gaussian shaped, the Q_2 peak has a rounded tip and there is a dip in Q_2 at its base.

As temperature is increased, both order parameter maximum values decrease but their widths remain approximately constant. The value of Q_2 in the bulk (away from the wall) increases somewhat. Bearing in mind that $Q_2 = 1/2(3Q_2 - 1)$, it can be seen that the strain component $e_{11} \propto q_2$ continues to change sign inside the wall as expected. However, between $A_1 = -0.4$ and -0.2 , a phase transition occurs above which the sandwich wall takes on a new profile. In this latter configuration, Q_1 is much closer to the expected tanh profile and its width does change with temperature. Q_2 is much flatter and less sharp and resembles a Gaussian distribution.

Returning to fig. 3 we observe that, at $A_1 = -0.2, -0.1$, Q_2 is above 1/3 both inside and outside the wall indicating that q_2 and hence e_{11} do not change sign as we move across the wall. Certainly a configuration whereby 3 domains are placed together without interacting with each other should have e_{11} changing sign like this: $-1/2, 1, -1/2$. Although such a strain configuration is observed at low temperatures, it appears that the more rapid thermal

fluctuation at high temperatures cause the system to escape from such a configuration and adopt a new state with e_{11} positive in the bulk and becoming more positive in the wall. So the strain component is not even attempting to change its sign but doing the opposite. This configuration still has $e_{12} = 0$ inside the wall however: it is just that the direction of the stretching and contraction in the wall have now reversed.

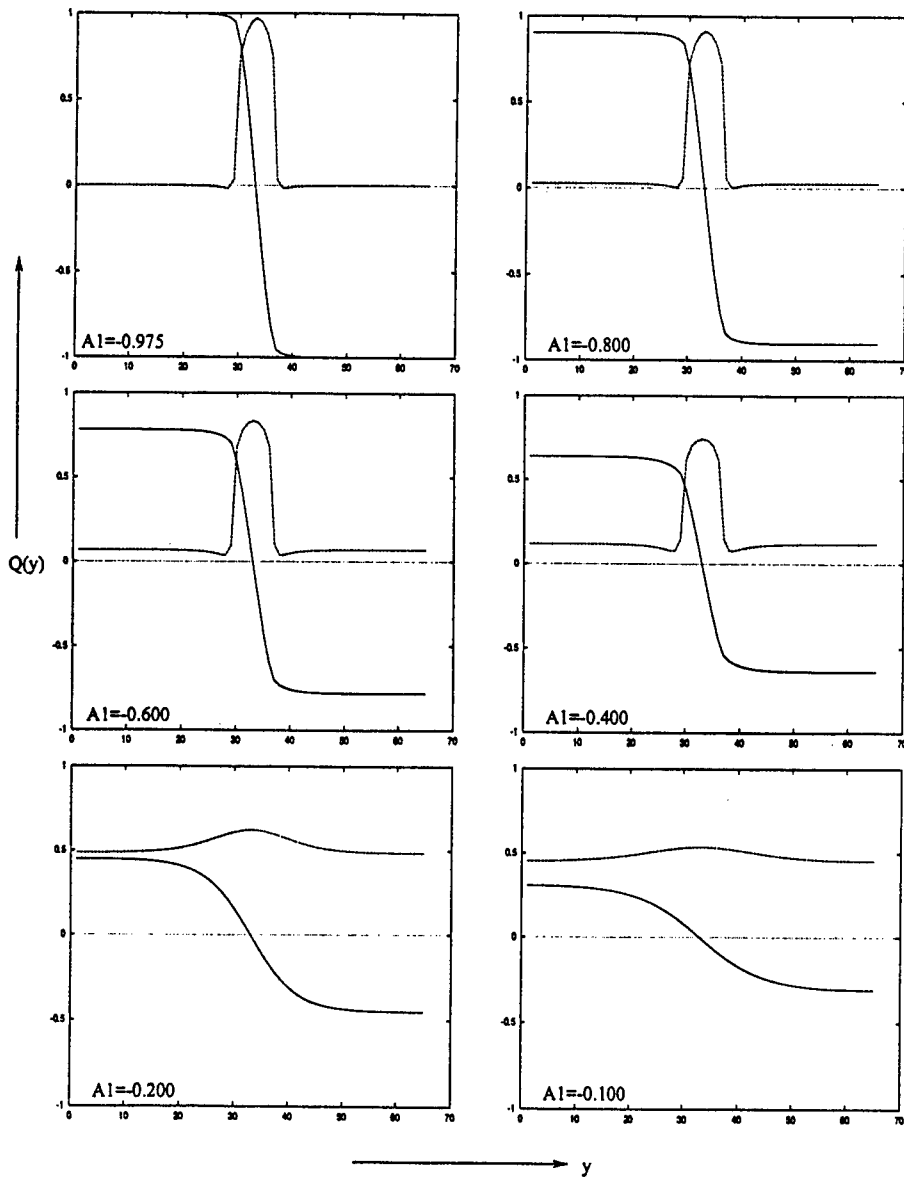


Figure 3a. Final (converged) order parameter plots at different temperatures. The expected sandwich wall is stable until $A_1 = 0.4$ but then changes into another form at higher temperatures (see text)

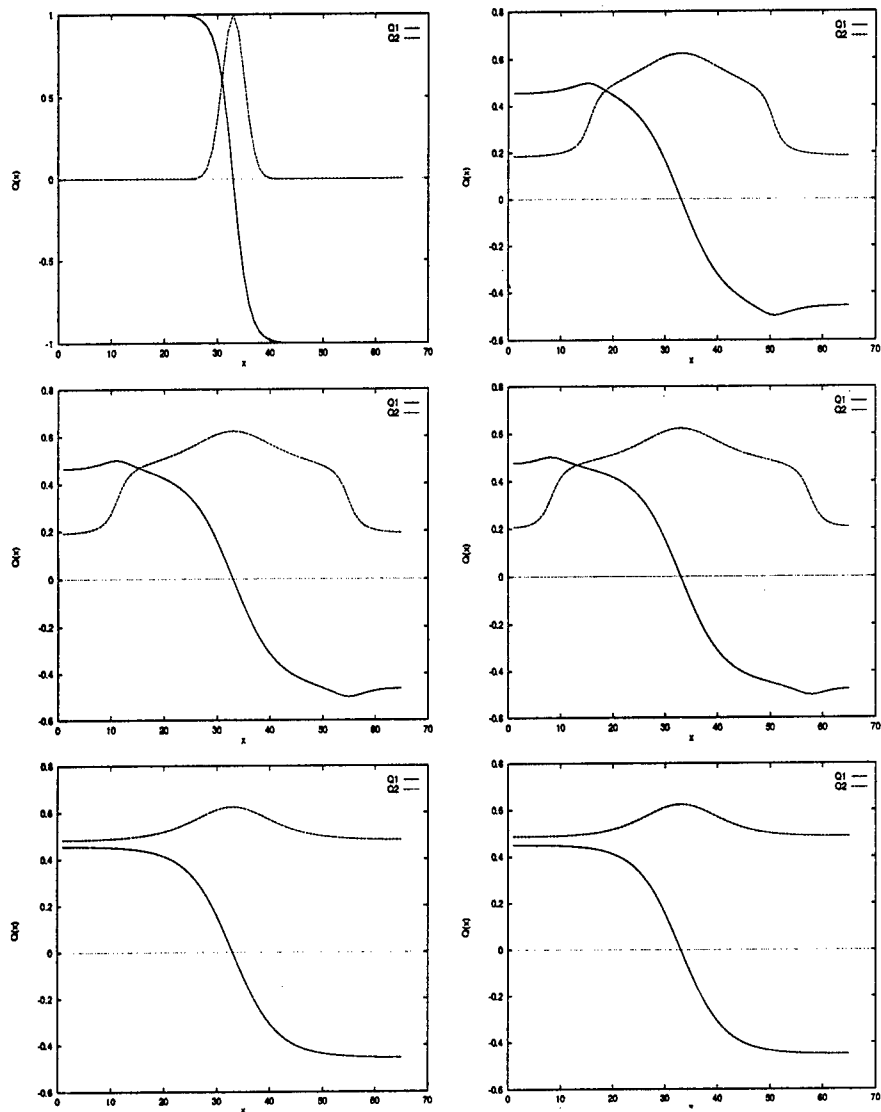


Figure 3b: Time evolution of order parameters at $A_1 = -0.2$. At this temperature the system moves away from the expected strain configuration and adopts a different strain inside the wall (see text). The sequence is from left to right and top to bottom.

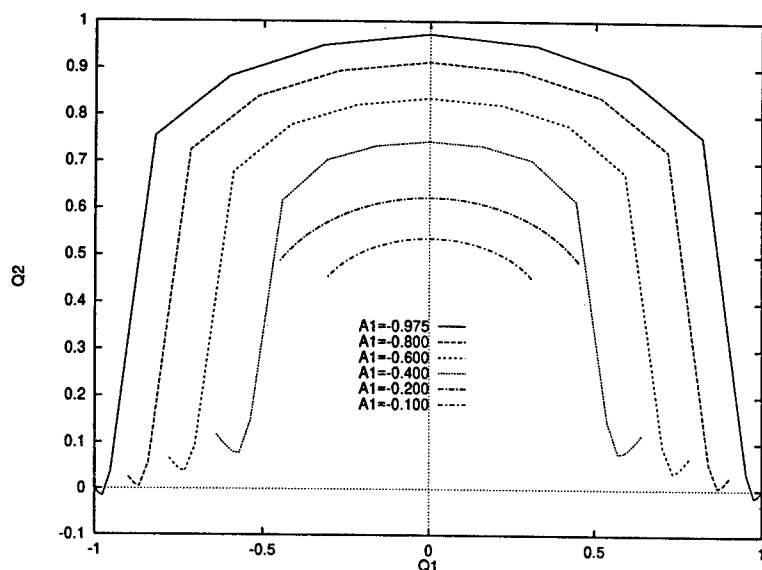


Figure 3c: Q_1, Q_2 trajectories for a variety of temperatures (i.e. values of A_1 and A_2). The parameter Q goes from right to left in each case.

Bulk values of Q_1 simply decrease with temperature to zero at $T = T_c$ while the bulk value of Q_2 first increases towards its infinite temperature limit of $1/3$, then jumps above $1/3$ as the transition point inherent in fig. 3 is passed then decreases to $1/3$ with further increases of temperature.

These sandwich walls are examples of chiral walls so called because the order parameter Q rotates as we move through the wall. The direction of rotation indicates the chirality of the wall. The free energy depends only on the squares of the order parameters q_1 and q_2 so that the sign of the order parameters is irrelevant. Houchmandzadeh et al⁽²²⁾ described how this would lead to degeneracy between positive and negative chiral walls. However, in our system the order parameters are linked to the strain components so that the signs of q_1 and q_2 are significant. For example if (at $T = 0$) we again allowed q_1 to go from $\sqrt{3}/2$ to $-\sqrt{3}/2$ along y but had q_2 going as $+1/2$, in the bulk (outside the sandwich wall). However only the strains are energy-allowed in the bulk and the value of e is fixed by the interaction strengths between atoms. Therefore the two types of chirality are not degenerate in our system and the chirality gives the energy minimum. The fact that the G-L equations shows the chiralities to be degenerate is due to the approximations involved in formulating these equations.

These arguments clearly demonstrate that structural states which may not be stable in the bulk can still appear inside the domain wall and significantly modify transport properties. Sandwich walls will generally enhance the wall thickness and it may be speculated that they enhance rather than reduce ionic transport. Further experimental studies are needed to clarify this hypothesis.

REFERENCES

1. J. Maier, Electrochemical investigation methods of ionic transport properties in solids, *Solid State Phenomena* 35, 39-40 (1994).
2. L. Eyring, In *Nonstoichiometric Oxides*, O.T. Sorensen ed. Acad. Press New York (1981).
3. E. K. H. Salje, *Phase transitions in ferroelastic and co-elastic crystals, student edition*. Cambridge University Press, Cambridge, England, (1993).

4. A. Aird, and E. K. H. Salje, Sheet superconductivity in twin walls: experimental evidence of WO_{3-x} , *J. Phys.: Condens. Matter* 10 L377-L380, (1998).
5. J. Chrosch, and E. K.H. Salje, The temperature dependence of the domain wall width in LaAlO_3 , *J. Apply Phys.* 85, No. 2, 722-727, (1999).
6. Stuart A. Hayward, et al., Thickness of pericline twin walls in anorthoclase: an X- ray diffraction study, *Euro J Mineral* 8, 130-1310 (1996).
7. K R Locherer, J. Chrosch & E K H Salje "Diffuse X-ray Scattering in WO_3 ", *Phase Transitions* Vol. 67 (1998) 51-63.
8. E. Salje, B. Wruck and H. Thomas, Order parameter saturation and a low-temperature extension of Landau theory, *Z. Phys B. Condensed Matter* 82, (1991), 399-404.
9. K. Locherer et al., X-ray analysis of mesoscopic twin structures, *Phil. Trans. R. Soc. Lond. A*, 2815-2845, (1996).
10. E.K.H. Salje and Y Ishibashi, Mesoscopic structures in ferroelastic crystals: needle twins and right-angled domains, *J. Phys.: Condens. Matter* 8: 44, 8477-8495 (1996).
11. E. K.H. Salje et al., Needle twins and right-angled twins in minerals: comparison between experiment and theory, *American Mineralogist* vol. 83, 811-822 (1998).
12. A.M. Bratkovsky, V. Heine and E.K.H. Salje. Strain effects, particularly in phase transitions, *Phil. Trans. R. Soc. Lond. A*, 354, 2875-2896 (1996).
13. J. D. Eshelby, Continuum theory of defects, *Solid State Phys.*, 3, 79 (1956).
14. A.M. Bratkovsky et al., Strain coupling as the dominant interaction in structural phase transitions, *Phase Transitions*, vol 55, 79-126 (1995).
15. A.M. Bratkovsky, et al., The theory of fluctuations and texture embryos in structural phase transitions mediated by strain, *J. Phys.: Condens. Matter* 6, 3679-3696 (1994).
16. I. Tsatskis and E.K.H. Salje, Time evolution of pericline twin domains in alkali feldspars: A computer-simulation study, *American Mineralogist*, vol. 81, 800-810 (1996).
17. K. Parlinski, E.K.H. Salje, and V. Heine, Annealing of Tweed Microstructure in High T_c Superconductors studied by a Computer Simulation, *Acta metall. mater.* 41, no. 3, 839-847 (1993).
18. D.A. Vul, and E.K.H. Salje, Periodic twin microstructures in $\text{YBa}_2\text{Cu}_3\text{O}_7$ thin films: a computer simulation study, *Physica C* 253, 231-242 (1995).
19. E.K.H. Salje, Structural states of Mg cordierite II: Landau theory, *Phys. Chem. Min.* 14, 455 (1987).
20. J. Blackburn, thesis. Time evolution of microstructure in complex systems: a computer simulation study, Cambridge University (1999)
21. J.F. Blackburn, and E.K.H. Salje, Time evolution of twin domains in cordierite: a computer simulation study, *Phys. Chem. Minerals* 26, 275-296 (1999).
22. B. Houchmanzadeh, J. Lajzerowicz and E. Salje, "Relaxations near Surfaces and Interfaces for First, Second and Third Neighbour Interactions: Theory and applications to polytypism *J. Phys. Condensed Matter* 4, 9779-9794 (1992) .

DEPENDENCE OF CARBIDE PRECIPITATION ON GRAIN BOUNDARY STRUCTURE IN SENSITIZED AUSTENITIC STAINLESS STEEL

Hiroyuki Kokawa, Takashi Koyanagawa*, Masayuki Shimada,
Yutaka S. Sato, and Takeshi Kuwana
Department of Materials Processing, Graduate School of Engineering
Tohoku University, Aoba-yama 02, Sendai 980-8579, Japan
* Now with Toshiba Corporation

ABSTRACT

Grain boundary carbide precipitation and intergranular corrosion in sensitized austenite stainless steel were examined by transmission electron microscopy (TEM) to clarify the effect of grain boundary structure on precipitation and corrosion. A type 304 steel, which had been solutionized at 1350 K was heat-treated at temperatures of 800-1300 K. Oxalic acid etch and Strauss tests showed that the frequency of grain boundaries with $M_{23}C_6$ carbide precipitation and corroded boundaries increased with holding time at sensitizing temperatures. The grain boundary carbide precipitation was observed during heat treatment at 1000 K by TEM. Grain boundaries were characterized on the basis of the Coincidence Site Lattice (CSL) theory using electron diffraction Kikuchi patterns. The observations revealed that the propensity to intergranular precipitation depends strongly on the grain boundary structure. Carbide precipitates tend to be detected at grain boundaries with higher Σ -values or larger deviation angles ($\Delta\theta$) from low- Σ CSL misorientations. The border lines between precipitation and no precipitation can be drawn by a deviation parameter of $\Delta\theta/\Delta\theta_c$, where $\Delta\theta_c$ is the maximum deviation angle by Brandon's criterion. The border line of $\Delta\theta/\Delta\theta_c$ decreased with the increase in the holding time at 1000 K. This means that the more ordered boundary needs the longer time for intergranular carbide precipitation and corrosion than less ordered or random boundaries.

INTRODUCTION

One of the major reasons for intergranular corrosion in austenitic stainless steel is chromium depletion due to chromium carbide precipitation at grain boundaries. Several techniques have been suggested to avoid the intergranular corrosion, such as reduction of carbon content in the material, stabilization treatment by the addition of titanium, niobium or zirconium. Recent grain boundary structure studies have shown that grain boundary phenomena (grain boundary diffusion (1), precipitation (2,3), corrosion (4,5), etc.) strongly depend on the grain boundary crystallographic nature and atomic structure (1). Time-temperature-transformation and -precipitation curves reported for austenitic stainless steels indicated that twin boundaries are not susceptible to both carbide precipitation and corrosion

because atomic structure is highly regular and coherent as compared to other high angle boundaries (6,7). Trillo and Murr (8,9) have shown remarkable resistance of coherent twin boundary to carbide precipitation because of extreme low boundary energy. After a short time exposure to a sensitizing temperature, such as in welding, an austenitic stainless steel has a mixed structure of sensitized and unsensitized boundaries (10). This suggests that each grain boundary has its own sensitivity to sensitization depending on the grain boundary nature and structure (atomic regularity at the boundary), and that short-time sensitization, such as weld decay(11), can be inhibited by controlling grain boundary nature and structure in the material. The purpose of the present study is to make clear the relationship between grain boundary sensitization and structure in an austenitic stainless steel according to the Coincidence Site Lattice (CSL) theory (1), and to suggest that a suitable grain boundary design and control (12-15) can prevent the weld decay in stainless steels, such as by a proprietary thermomechanical process (16).

EXPERIMENTAL PROCEDURES

Table 1 shows the chemical composition of type 304 austenitic stainless steel used in this study. The 304 steel sheets of 0.75x5x20 mm in size were solution-treated at 1350 K for 600 s, and then they were heat-treated at temperatures of 800-1300 K for 10-10^{4.5} s. Both treatments accompanied water-quenching. These specimens were examined by 10% oxalic acid etch and Strauss tests, and were observed by optical and transmission electron microscopy. The crystallographic orientation in each grain was determined by electron diffraction Kikuchi patterns. The grain boundaries were characterized on the basis of CSL theory (17) using misorientation matrices (18-23), i.e. the deviation angle $\Delta\theta$ from the nearest- Σ CSL orientation relationship was given as the rotation angle of deviation matrix M_d from the misorientation matrix at a grain boundary (24). The maximum deviation angle, $\Delta\theta_c$, which can be accommodated in a Σ -boundary by introducing grain boundary structural dislocations, is given by Brandon's criterion (25), $\Delta\theta_c = 15\Sigma^{-1/2}$ in degrees. A parameter $\Delta\theta/\Delta\theta_c$ was used to evaluate the grain boundary regularity (26-28). The regularity of grain boundary structure is considered to decrease with the increase of Σ -value, because the density of CSL points in the two crystal lattices decreases (1). CSL boundaries with $\Sigma \leq 29$ were regarded as ordered boundaries in this study.

Table 1. Chemical composition of 304 stainless steel used in this study (wt%)

C	Si	Mn	P	S	Ni	Cr
0.055	0.60	1.00	0.029	0.005	8.48	18.28

RESULTS AND DISCUSSION

Figure 1 shows optical microstructures of heat-treated specimens at 1000 K after 10% oxalic acid etching. The frequency of grooved boundaries increases with the holding time at 1000 K. The time-temperature-intergranular carbide precipitation diagram given by 10% oxalic acid etching is shown in Fig.2. Solid circle indicates that grooved boundaries were observed in the specimen. The number beside solid circle corresponds to the number ratio in percentage of grooved boundaries to all boundaries in the specimen excluding twin boundaries, and + sign means discontinuous grooves at boundaries as seen in Fig.1(b). The frequency of intergranular carbide precipitation increases with the holding time at every temperature.

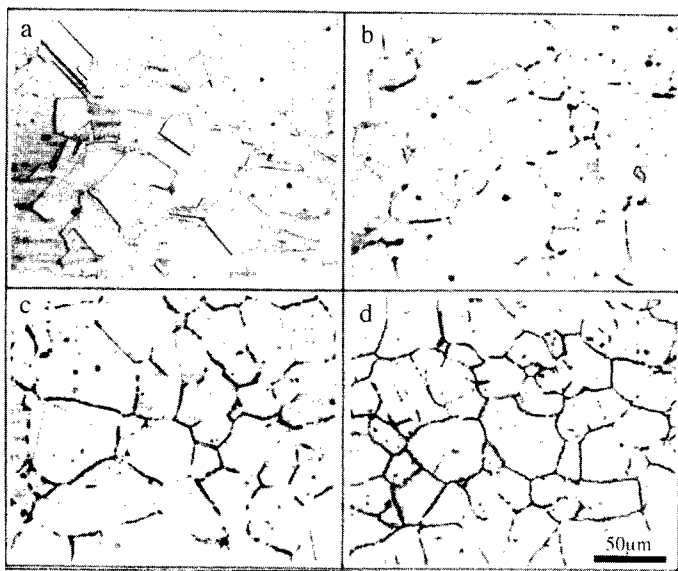


Figure 1. Optical microstructures of 304 steel heat-treated at 1000 K for 0 s (a), 100 s (b), 1000 s (c) and 10000 s (d).

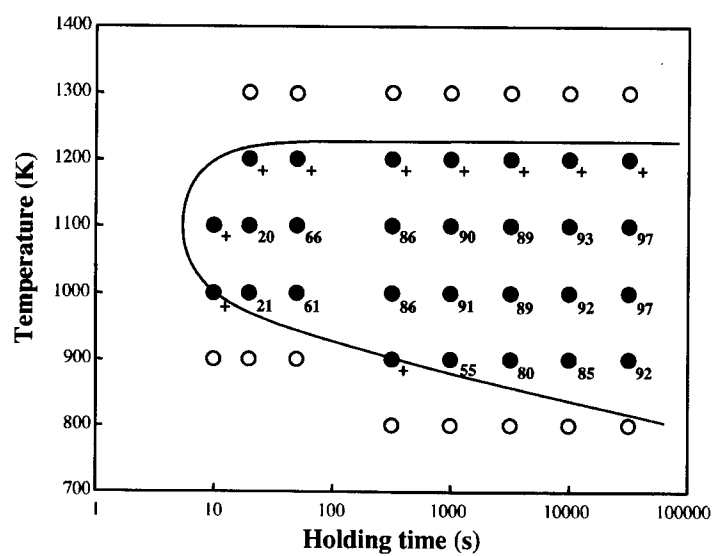


Figure 2. Time-Temperature-Precipitation diagram for intergranular carbide in 304 steel by oxalic acid etch test.

Figure 3 shows optical microstructures of a Strauss-tested specimen which had been heat-treated at 1000 K for 1000 s. The specimen was oxalic acid-etched before Strauss test. Figures 3(a) and (b) were obtained from the same area before and after bend test, respectively. Some of the grain boundaries are cracked by bend test, as shown by arrows in Fig.3(b). Figure 4 is the time-temperature-corrosion diagram given by the Strauss test of the heat-treated specimens. Solid symbols indicate that cracked boundaries were detected after bend test. The frequency of cracked boundaries is shown in percentage beside solid circle (excluding twin boundaries). Solid square means that the specimen was fractured during bend test. The frequency of cracked boundaries also increases with the holding time at every temperature. These diagrams suggest that the time required for carbide precipitation and corrosion depends on the grain boundary character at sensitizing temperatures. Stickler et al. (6) and Cihal et al. (7) reported that general high angle (random) grain boundaries need shorter time for carbide precipitation and corrosion than twin boundaries. However, Figs.2 and 4 indicate that the time is different even among general high angle boundaries, and suggest that the time may depend on the grain boundary structure.

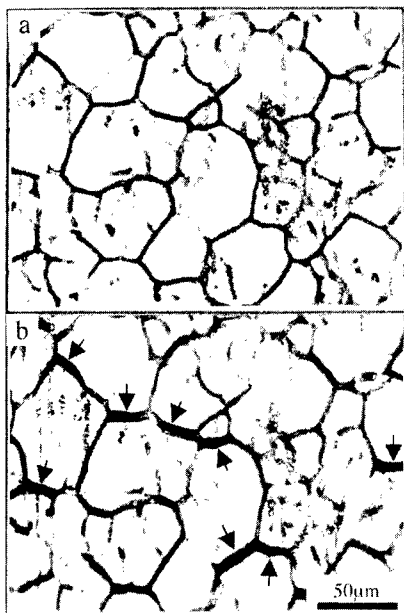


Figure 3. Oxalic acid-etched and Strauss-tested specimen which had been heat-treated at 1000 K for 1000 s: (a) before and (b) after bend test.

Figures 5 and 6 show grain boundary structures as revealed by TEM in a specimen heat-treated at 1000 K for 100 s. Intergranular carbide precipitation is detected at the grain boundary in Fig.6, but not at the grain boundary in Fig.5. Grain boundary characterization with Kikuchi patterns revealed that the nearest CSL relationship is $\Sigma 9$ for both grain boundaries, but the values of $\Delta\theta/\Delta\theta_c$ are 1.45 and 2.54 for the grain boundaries in Figs.5 and 6, respectively. The grain boundary with smaller $\Delta\theta/\Delta\theta_c$ has no carbide. Figure 7 shows the relationships between grain boundary precipitation and regularity obtained from TEM observations of heat-treated specimens at 1000 K for 10^2 – $10^{4.5}$ s. In the figures, the Σ -value of the nearest CSL is taken as abscissa, and the deviation angle $\Delta\theta$ from the CSL is the vertical

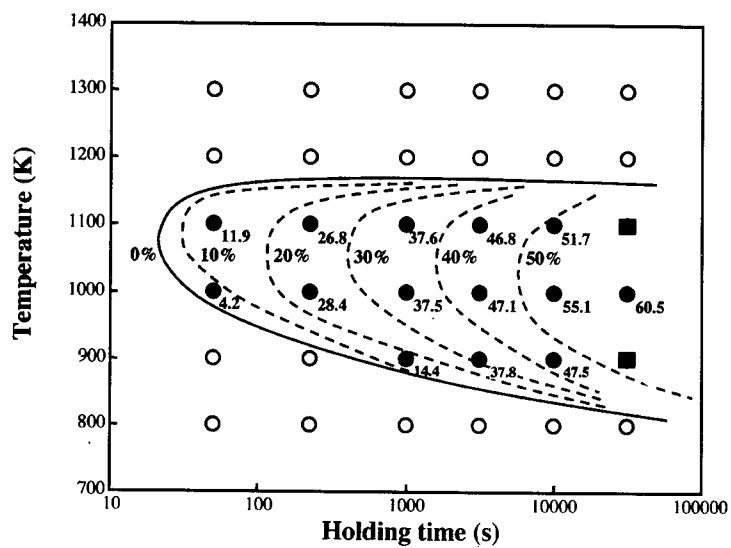


Figure 4. Time-Temperature-Intergranular corrosion diagram for 304 steel by Strauss test.

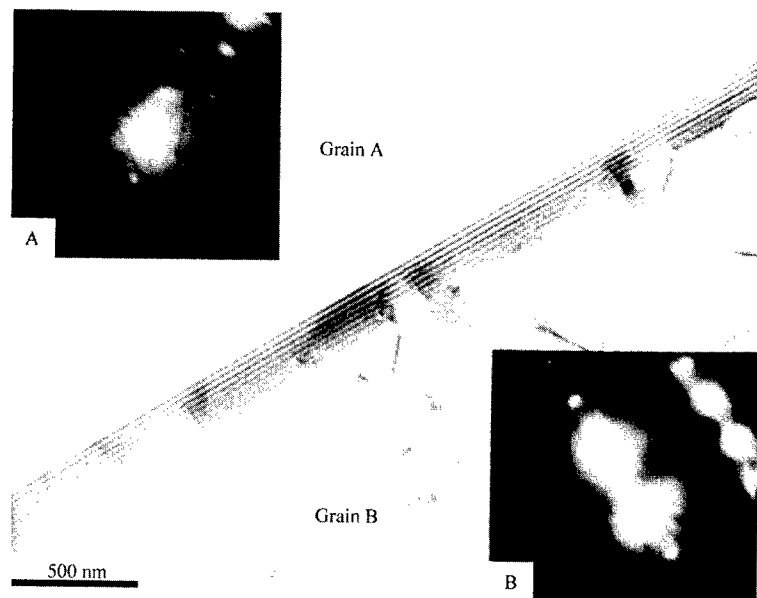


Figure 5. A grain boundary TEM structure deviated 7.25 degrees from $\Sigma 9$ CSL orientation relationship in 304 steel heat-treated for 100 s at 1000 K.

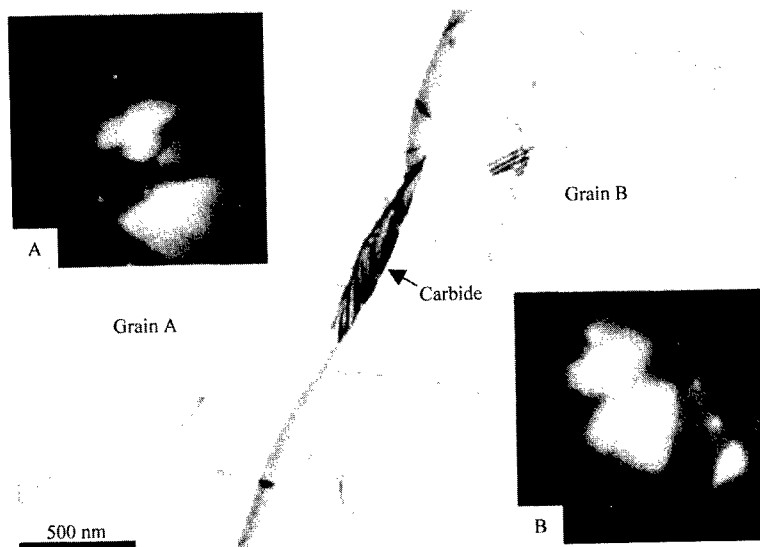


Figure 6. A grain boundary TEM structure deviated 12.72 degrees from $\Sigma 9$ CSL orientation relationship in 304 steel heat-treated for 100 s at 1000 K.

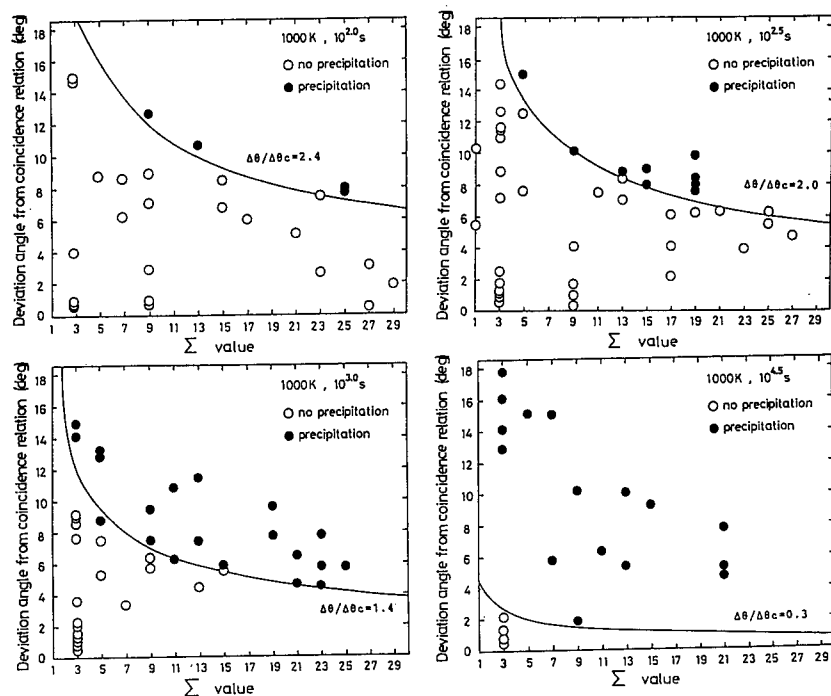


Figure 7. Relationships between intergranular carbide precipitation and deviation angle from CSL relationship in 304 steel heat-treated for 100 s at 1000 K for 10^2 s, $10^{2.5}$ s, 10^3 s and $10^{4.5}$ s.

axis. Solid and open circles indicate precipitation and no precipitation at grain boundaries, respectively. Increases in $\Delta\theta$ and Σ -value mean decrease in the regularity of grain boundary structure¹⁾.

In the specimen heat-treated at 1000 K for 100 s, as seen in Fig. 7(a), only the boundaries with lower regularity (high Σ and/or $\Delta\theta$) have precipitates, and the borderline between precipitation and no precipitation corresponds to the line of $\Delta\theta/\Delta\theta_c = 2.4$. Figures 7(b)-(d) indicate that the $\Delta\theta/\Delta\theta_c$ values of borderlines are 2.0, 1.4 and 0.3 in specimens heat-treated at 1000 K for $10^{2.5}$, 10^3 and $10^{4.5}$ s, respectively.

Figures 8 and 9 show grain boundary TEM structures in the specimen heat-treated at 1000 K for $10^{4.5}$ s. The long-time aging at 1000 K led to precipitation even at a $\Sigma 9$ CSL boundary in Fig. 8 ($\Delta\theta/\Delta\theta_c = 0.34$), while the $\Sigma 3$ boundary in Fig. 9 ($\Delta\theta/\Delta\theta_c = 0.16$) was still free from precipitation. Figure 7 reveals that a more ordered boundary needs longer time for carbide precipitation and corrosion than a less ordered boundary. This tendency may be resulted from more difficult nucleation and lower growth rate of carbide at a more ordered boundary because of lower grain boundary energy. Figure 10 summarizes the relationship between the $\Delta\theta/\Delta\theta_c$ of the borderline and the holding time at 1000 K. The $\Delta\theta/\Delta\theta_c$ decreases with the increase of holding time. If the grain boundary structure could be kept smaller than the $\Delta\theta/\Delta\theta_c$ in Fig. 10 by grain boundary engineering (15,16), intergranular precipitation and corrosion would not occur. The $\Delta\theta/\Delta\theta_c$ is much larger than 1 at a short holding time as shown in Fig. 10. This fact suggests that the conditions to prevent intergranular carbide precipitation by controlling grain boundary character is not very severe for a short time exposure to a sensitizing temperature, such as in welding thermal cycles. Grain Boundary Engineering (15) could inhibit the weld decay of austenitic materials.

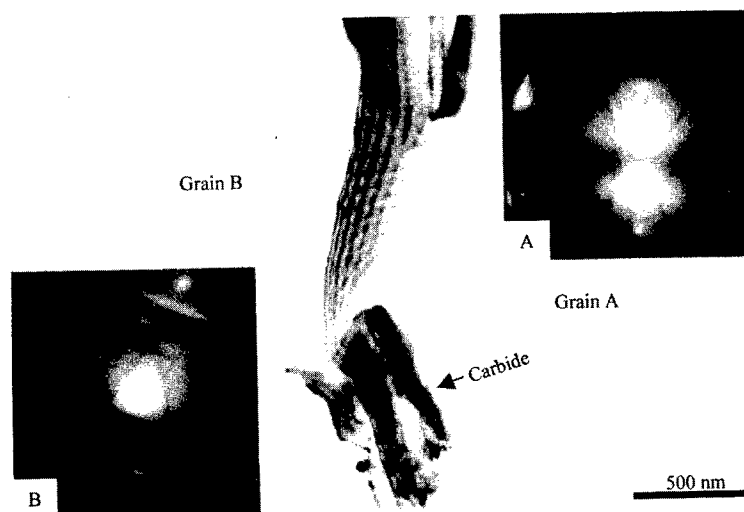


Figure 8. A grain boundary TEM structure deviated 1.72 degrees from $\Sigma 9$ CSL orientation relationship in 304 steel heat-treated for $10^{4.5}$ s at 1000 K.

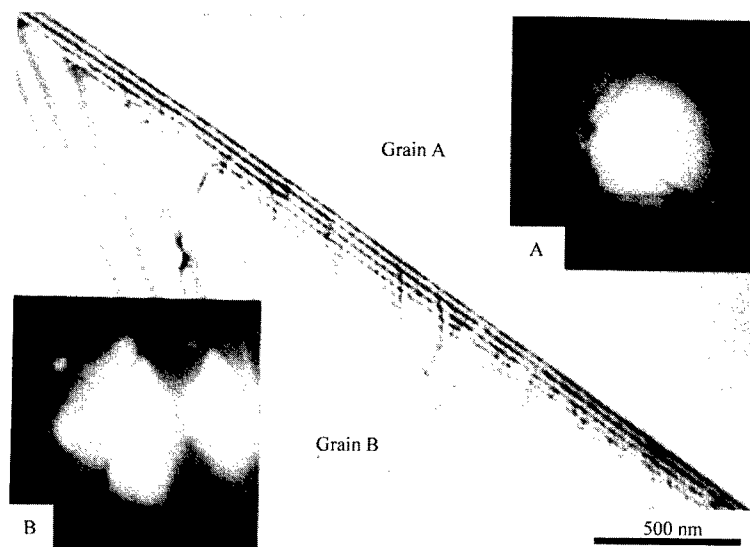


Figure 9. A grain boundary TEM structure deviated 1.38 degrees from $\Sigma 3$ CSL orientation relationship in 304 steel heat-treated for $10^{4.5}$ s at 1000 K.

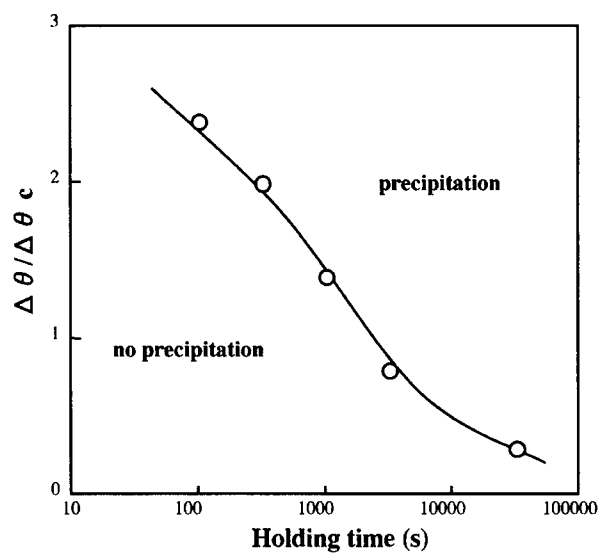


Figure 10. Effect of the deviation parameter $\Delta\theta/\Delta\theta_c$ from CSL relationship and the holding time on intergranular carbide precipitation in 304 steel heat-treated at 1000 K.

CONCLUSION

The effect of crystallographic character of grain boundary on intergranular carbide precipitation and corrosion was examined in a 304 austenitic stainless. The 304 steel was heat-treated at high temperatures and observed by TEM. At sensitizing temperatures, the frequency of grain boundaries with carbide precipitation and corroded boundaries increased with the holding time. Grain boundary characterization revealed that the propensity to intergranular carbide precipitation and corrosion depends sensitively on the grain boundary structure. Carbide precipitates tend to be detected at grain boundaries with higher Σ -values or larger deviation angles ($\Delta\theta$) from low- Σ CSL misorientations. The border lines between precipitation and no precipitation can be drawn by a deviation parameter of $\Delta\theta/\Delta\theta_c$, where $\Delta\theta_c$ is the maximum deviation angle by Brandon's criterion. The border line of $\Delta\theta/\Delta\theta_c$ decreased with the increase in the holding time at 1000 K. This means that the more ordered boundary needs the longer time for intergranular carbide precipitation and corrosion than less ordered or random boundaries.

ACKNOWLEDGMENTS

The present work was supported by the Grant-in-Aid for COE Research (No.11CE2003), The Ministry of Education, Science, Sports and Culture, and by the Japan Atomic Energy Research Institute (JAERI) Nuclear Research Promotion Program. The authors wish to thank to Professor T. Watanabe for his useful advice, and Mr. A. Honda for his technical assistance. Financial support from Kawasaki Steel 21st Century Foundation is gratefully acknowledged.

REFERENCES

1. P. H. Pumphrey, Special High Angle Boundaries. "Grain Boundary Structure and Properties", ed. by G. A. Chadwick and D. A. Smith, p. 139, Academic Press, London, (1976).
2. J. Le Coze, M. Biscondi, J. Levy, C. Goux, Precipitation intergranulaire dans des bicristaux orientes d'aluminium-cuivre. *Mem. Sci. Rev. Met.*, 70(1973), 397.
3. J. Le Coze, M. Biscondi, Intergranular Precipitation in Aluminum-Copper Bicrystals. *Can. Metall. Quart.*, 13(1974), 59.
4. M. Froment, Sur le mecanisme de la corrosion intergranulaire des materiaux metalliques. *J. de Phys.*, 36(1975), c4-371.
5. X. R. Qian, Y. T. Chou, Correlation Between Grain-Boundary Corrosion and Grain-Boundary Energy in Niobium Bicrystals. *Phil. Mag. A*, 45(1982), 1075.
6. R. Stickler, A. Vinckier, La morphologie des carbures (Cr,Fe)₂₃C₆ et son influence sur la corrosion intergranulaire d'un acier inoxydable 18/8. *Mem. Sci. Rev. Met.*, 60(1963), 489.
7. V. Cihal, I. Kasová, Relation between carbide precipitation and Intercrystalline Corrosion of stainless steels. *Corrosion Sci.*, 10(1970), 875.
8. E. A. Trillo, L. E. Murr, A TEM investigation of M₂₃C₆ carbide precipitation behaviour on varying grain boundary misorientations in 304 stainless steels. *J. Mater. Sci.*, 33(1998), 1263.
9. E. A. Trillo, L. E. Murr, Effects of carbon content, deformation, and interfacial energetics on carbide precipitation and corrosion sensitization in 304 stainless steel. *Acta Mater.*, 47(1999), 235.
10. T. Kuwana, H. Kokawa, Transmission electron microscope observations of SUS304L austenitic stainless steel welds. *Trans. JWS*, 16(1985), 99.
11. H. Kokawa, T. Kuwana, Relationship between grain boundary structure and intergranular corrosion in heat-affected zone of type 304 stainless steel weldments. *Trans. JWS*, 23(1992), 73.
12. T. Watanabe, Approach to grain boundary design for strong and ductile polycrystals. *Res. Mechanica.*,

- 11(1984), 47.
13. T. Watanabe, The potential for grain boundary design in materials development Mater. Forum, 11(1988), 284.
14. T. Watanabe, The importance of grain boundary character distribution (GBCD) to recrystallization grain growth and texture Scripta Metall. Mater., 27(1992), 1497.
15. G. Palumbo, E. M. Lehockey, and P. Lin, Applications for grain boundary engineered materials. JOM, 50-2(1998), 40.
16. P. Lin, G. Palumbo, U. Erb, K. T. Aust, Influence of grain-boundary-character-distribution on sensitization and intergranular corrosion of Alloy-600. Scripta Metall. Mater., 33-9(1995), 1387.
17. W. Bollmann, Crystal defects and crystalline interfaces, Springer-Verlag, Berlin, (1970).
18. D. H. Warrington, P. Bufalini, The coincidence site lattice and grain boundaries. Scripta Met., 5(1971), 771.
19. W. Bollmann, B. Michaut, G. Sainfort, Pseudo-subgrain-boundaries in stainless steel. Phys. Stat. Sol. (a), 13(1972), 637.
20. H. Grimmer, W. Bollmann, D.H. Warrington, coincidence-site lattices and complete pattern-shift lattices in cubic crystals. Acta Cryst. A, 30(1974), 197.
21. P. H. Pumphrey, The use of transmission electron microscopy in the study of special high-angle grain boundaries in polycrystals. Phys. Stat. Sol. (a), 28(1975), 545.
22. W. A. Clark, D. A. Smith, the dislocation structure of a $E\infty=9$ related coincidence boundary in stainless steel. Phil. Mag. A, 38(1978), 367.
23. H. Kokawa, T. Watanabe, S. Karashima, Reexamination of deviation angles from exact csl misorientations in early work on grain boundary characterization. Scripta Metall., 21(1987), 839.
24. V. Randle, B. Ralph, A practical approach to the determination of the crystallography of grain boundaries. J. Mater. Sci., 21(1986), 3823.
25. D. G. Brandon, The Structure of High-Angle Grain Boundaries. Acta Metall., 14(1966), 1479.
26. H. Kokawa, T. Watanabe, S. Karashima, Sliding behaviour and dislocation structures in aluminium grain boundaries. Phil. Mag. A, 44(1981), 1239.
27. H. Kokawa, T. Watanabe, Dissociation of lattice dislocations in coincidence boundaries. J. Mater. Sci., 18(1983), 1183.
28. H. Kokawa, T. Watanabe, S. Karashima, Structural changes during sliding of aluminium grain boundaries with different initial structures. Scripta Metall., 17(1983), 1155.

GRAIN BOUNDARY ENGINEERING FOR THE CONTROL OF OXIDATION EMBRITTLEMENT

S. Yamaura, Y. Igarashi, S. Tsurekawa, and T. Watanabe

Laboratory of Materials Design and Interface Engineering,
Department of Machine Intelligence and Systems Engineering,
Graduate School of Engineering, Tohoku University, Sendai, Japan

ABSTRACT

The effect of grain boundary type on intergranular oxidation was studied in a nickel-40at%iron alloy. It has been found that intergranular oxidation takes place preferentially at random boundaries while low- Σ coincidence boundaries, particularly $\Sigma 3$, $\Sigma 11$, $\Sigma 19$ and $\Sigma 27$ coincidence boundaries have excellent oxidation resistance. The grain boundary engineering for the control of oxidation-assisted intergranular brittleness has been attempted by taking account important roles of the grain size, the grain boundary character distribution (GBCD) and the grain boundary connectivity. The presence of an optimal grain boundary microstructure for this purpose has been predicted.

INTRODUCTION

High temperature oxidation is the most typical type of dry corrosion occurring in metals and alloys during their heat treatment, hot working and service exposed to air at high temperatures. This type of environment-induced metallurgical phenomenon degrades the strength of materials and damages their surfaces^{1,2}. Preferential oxidation at grain boundaries is often observed which is known as intergranular oxidation. Intergranular oxidation can be particularly detrimental because it enhances intergranular fracture, resulting in premature failure and severe brittleness. So far, intergranular oxidation at high temperature has been extensively studied³⁻⁶. Several workers have pointed out that intergranular oxidation can occur only at certain grain boundaries in alloy and intermetallics^{5,6}. From recent knowledge of grain boundary structure and properties⁷, it is very likely that the extent of intergranular oxidation depends on the character and structure of grain boundary. In recent years, the grain boundary character distribution (GBCD), which was first introduced by one of the present authors as a new microstructural factor⁸, has been demonstrated to control boundary-related bulk properties of polycrystalline materials^{9,10}. Moreover a new approach to grain boundary engineering has been successfully attempted by controlling GBCD in development of high temperature materials¹⁰ and stress corrosion-resistant materials¹¹. This investigation has been made to study the effect of grain boundary type on intergranular oxidation and to establish grain bound-

ary engineering for the control of oxidation-assisted intergranular brittleness in polycrystalline materials by manipulating the grain size, GBCD and the grain boundary connectivity.

EXPERIMENTAL PROCEDURE

Specimen Preparation

In order to study structure-dependent intergranular oxidation at individual boundaries, stable- and coarse-grained specimens with the grain size of about 5 mm were prepared thermomechanically from a vacuum melted Ni-40at%Fe alloy ingot by 50% cold rolling and vacuum annealing (10^{-5} Pa) at 1473K for 4h. Table 1 shows the detailed chemical composition of the alloy. The surface of the specimens with the dimension of 5mm \times 8mm \times 3 mm was mechanically polished with abrasive papers and Al_2O_3 paste. For a study of grain boundary engineering for fracture control, ribbon specimens of 100 μ m in thickness were prepared by rapid solidification at roller speeds of 28.3 m/s and 14.1m/s and subsequent annealing at temperatures ranging from 1073K to 1473K, resulting in different grain sizes and GBCDs.

Table 1 Chemical composition (wt%) of the alloy used in this study

Ni	Fe	Co	Mn	Cu	Mg	Al	C	P	S	Si
61.1	39.0	0.009	<0.001	<0.001	<0.001	<0.004	1ppm	7.8ppm	7ppm	7ppm

Oxidation Test

Oxidation tests were carried out in a resistance heating furnace under both dilute oxygen atmosphere (25.9ppm O_2 +Ar, slightly flowing) and atmospheric oxygen pressure (99.999% in purity 101.3kPa O_2 , slightly flowing) at 1273K for 5h. After oxidation treatment, as schematically shown in Fig. 1, the external scale was removed down to internal oxidation zone in order to observe intergranular oxidation at individual grain boundaries. Optical micrographs in Fig. 2 (a) and (b) clearly show that there is the difference of the propensity to intergranular oxidation between grain boundaries. The oxide penetration depth can be used as a measure of the propensity to intergranular oxidation. After observations of intergranular oxidation the specimens were etched by nital to remove strained surface layer for orientation analysis of individual grains and the characterization of grain boundaries by the SEM-ECP technique operating 40kV¹².

Characterization of Grain Boundaries

Grain boundaries were characterized on the basis of the determination of the orientation of grains and of the orientation relationship between grains by using the SEM-ECP technique.

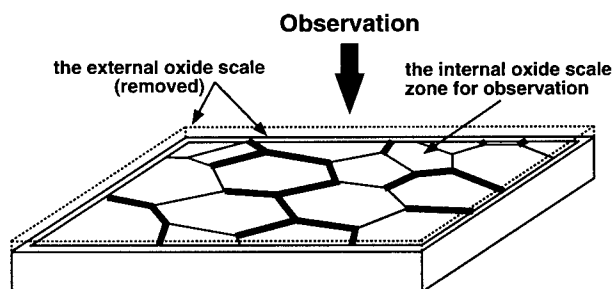


Figure 1 A schematic illustration of the observation of intergranular oxidation in a specimen. Thick solid lines and thin solid lines indicate "heavily oxidized" grain boundaries and "non-oxidized" ones, respectively.

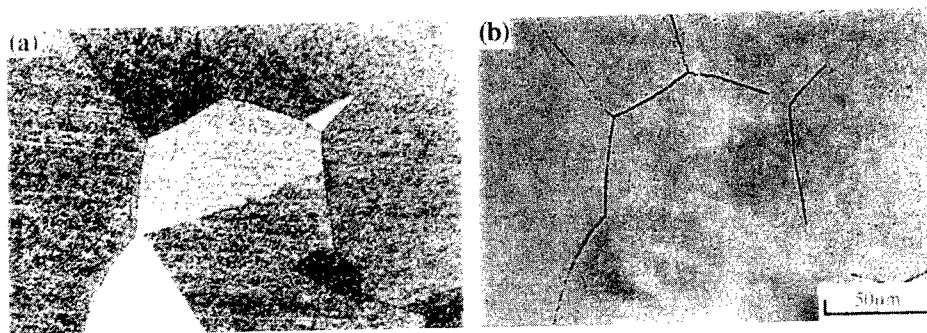


Figure 2 Optical micrographs of the surface of specimen oxidized at 1273K for 5h; (a) the surface of a specimen oxidized in dilute oxygen atmosphere, (b) internal oxidation zone observed after polishing the surface.

Grain boundaries are classified into three categories based on the misorientation angle and coincidence orientation relationship; the first one is low-angle boundary with the misorientation angle smaller than 15° . High angle boundaries are classified into two groups by the Brandon criterion for coincidence site lattice (CSL) boundary, $\Delta\theta_c = 15^\circ/\Sigma^{1/2}$. When $\Delta\theta \leq \Delta\theta_c$, the boundary is defined as CSL boundary while $\Delta\theta > \Delta\theta_c$ non-CSL or random boundary (R), where $\Delta\theta$ is the deviation angle from the exact coincidence site lattice orientation angle. The value of Σ is considered as a measure of grain boundary structural order. CSL boundary with a smaller Σ value like $\Sigma 3$ is taken as a special low-energy boundary. The grain boundary character distribution (GBCD) in the ribbon specimens with fine grain size or conventional grain size was also determined in this work by using a HITACHI FE-SEM-EBSP on-line-analyzing equipment, called "Orientation Imaging Microscope (OIM)" operating at 30kV.

Fracture Test

The relative fracture strength was determined at room temperature by three point bending test for ribbon specimens, with the dimension of 5mm width and 8-12mm gauge length, which were oxidized in air under tensile stress of 10-14MPa at 1073K.

STRUCTURE-DEPENDENT INTERGRANULAR OXIDATION

Coincidence-Site-Lattice (CSL) Approach to Intergranular Oxidation

Figure 3 shows structure-dependent intergranular oxidation. There is a significant difference of the propensity to oxide formation between different types of grain boundary. Random boundaries are preferential sites for oxidation, but low-angle $\Sigma 1$ boundary and high angle low Σ (such as $\Sigma 3$) CSL boundaries (hereafter called coincidence boundaries) are immune from oxidation. A systematic analysis of structure-dependent intergranular oxidation can be made by plotting the data points which show heavily oxidized boundary (filled circle), slightly oxidized boundary (filled triangle) and non-oxidized boundary (open circle) as function of Σ value and the deviation angle from the exact coincidence orientation given by the Brandon criterion mentioned above, as shown in Figs. 4 (a) and (b), for different oxygen pressures. It has been found that the propensity to intergranular oxidation can be reasonably related to the grain boundary type depending on whether the grain boundary is of random type ranging above the upper region separated by the dotted line given by the Brandon criterion, or coincidence boundaries in the region below the line.

Effect of Oxygen Pressure

Structure-dependent intergranular oxidation has been found to be more significant in dilute oxygen atmosphere (Fig. 4 (a)) than in pure oxygen gas (Fig. 4 (b)). This may suggest

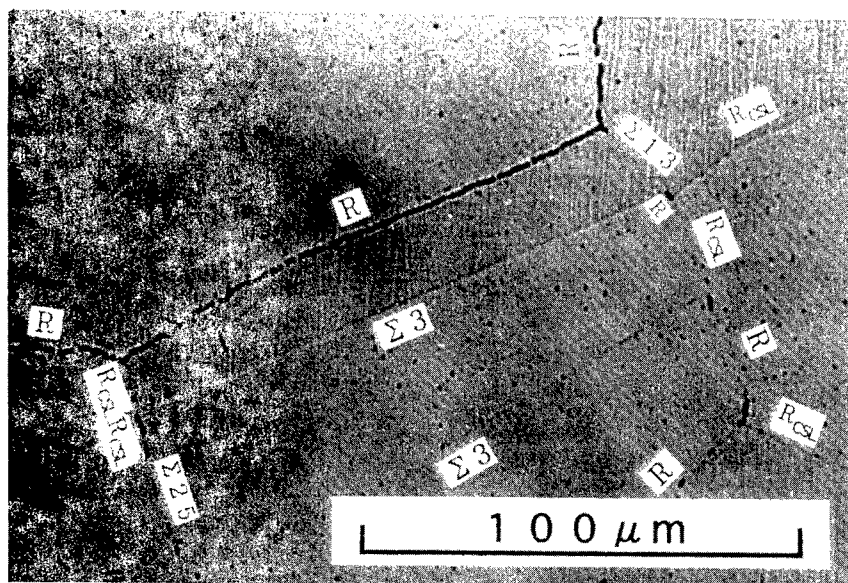


Figure 3 An example of the observation of an internal oxidation zone in the specimen oxidized in dilute O_2 atmosphere. The difference in intergranular oxidation between random boundaries (R) and coincidence ones (Σ) is closely shown. Random boundaries which are close to a near- Σ relationship are indicated as R_{cs} .

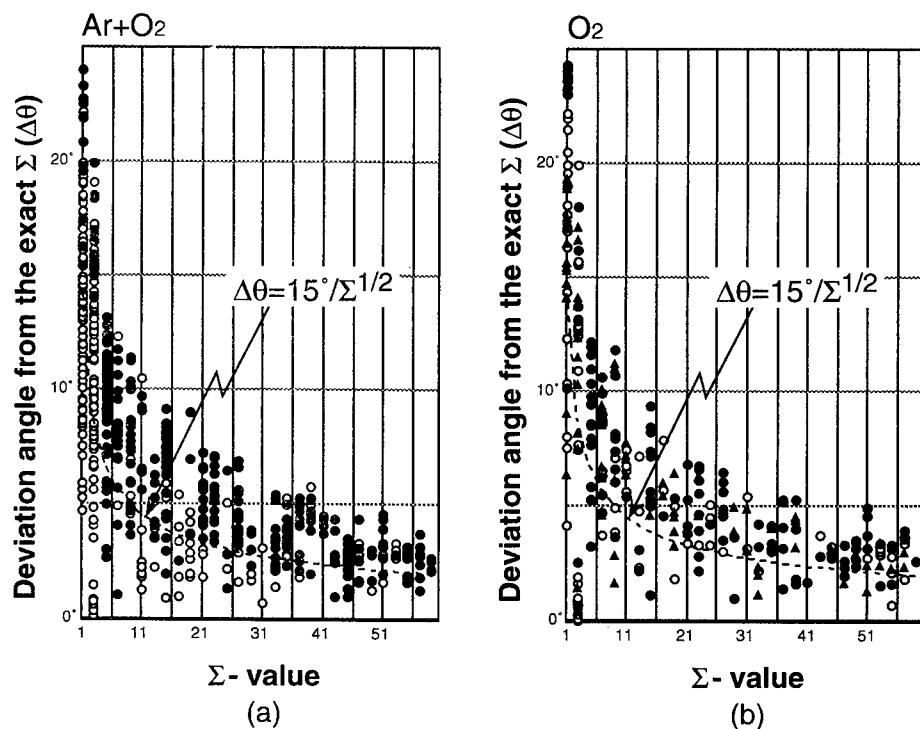


Figure 4 Dependence of intergranular oxidation morphology on Σ value and the deviation angle, $\Delta\theta$ in dilute oxygen gas (a) and in pure oxygen gas (b) (● heavily oxidized boundary, ▲ slightly oxidized boundary and ○ non-oxidized boundary).

that intergranular diffusion which is well known to depend strongly on the grain boundary type¹³, can play more important role in internal oxidation when utmost oxide scale is not formed under low oxygen pressure. Moreover it is worth noting that $\Sigma 3$, $\Sigma 11$ and $\Sigma 19$ coincidence boundaries are particularly resistant to oxidation. The reason for this will be discussed below, in detail.

Σ Dependence of Oxidation at Coincidence Boundaries

It has been shown that there is a distinctive difference of oxidation resistance between coincidence boundary and random boundary. Now let us look at the relationship between oxidation resistance and Σ value which defines specific coincidence boundaries. Fig. 5 (a) is a plot of coincidence boundaries with Σ larger than 3, including the results obtained from all

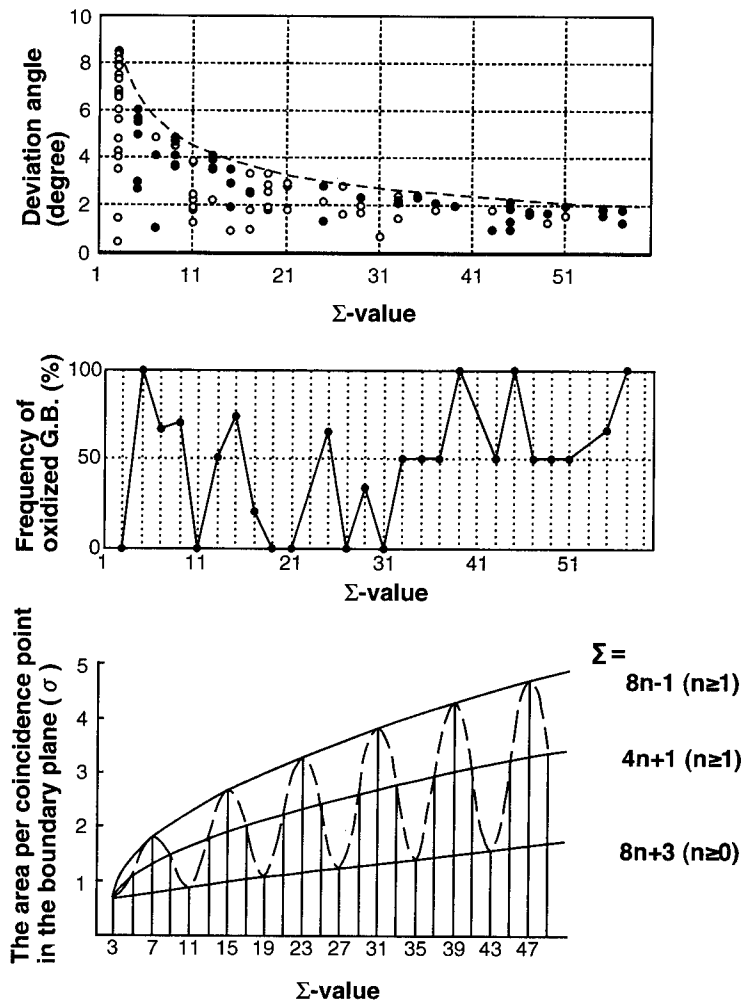


Figure 5 (a) Dependence of intergranular oxidation morphology on Σ value and the deviation angle, $\Delta\theta$, (b) the fraction of oxidized grain boundaries are plotted as a function of Σ value, (c) the feature of the grain boundary energy of fcc metals calculated by Smith¹⁴.

the specimens oxidized in a dilute O_2 atmosphere. The fraction of "heavily oxidized" boundaries (filled circles) is plotted as a function of Σ value in Fig. 5 (b). It is clear that $\Sigma 3$, $\Sigma 11$, $\Sigma 19$ and $\Sigma 27$ coincidence boundaries have excellent resistance to intergranular oxidation. The reason for this is explained as follows. Fig. 5 (c) shows the relationship between the area per coincidence point in the boundary plane (σ), which probably corresponds to grain boundary energy and the Σ value for fcc crystal structure. This figure was originally presented by D. A. Smith and the lowest σ value for any given Σ was used¹⁴. The Σ dependence of the fraction distribution in Fig. 5 (b) is quite similar to the σ value indicated in Fig. 5 (c). As clearly seen the value of σ for fcc coincidence boundaries does not increase monotonously like that of bcc coincidence boundaries. There exist three groups with specific Σ values given by the following series: $\Sigma = 8n-1$ ($n \geq 1$), $\Sigma = 4n+1$ ($n \geq 1$) and $\Sigma = 8n+3$ ($n \geq 0$) which has lower energies, includes $\Sigma 3$, $\Sigma 11$, $\Sigma 19$ and $\Sigma 27$. This likely explains that intergranular oxidation depends on the grain boundary energy in the Ni-40at%Fe alloy with fcc structure. The present investigation has revealed that intergranular oxidation depends on the grain boundary character (Σ , $\Delta\theta/\Delta\theta_c$) and the grain boundary energy. The detail has been discussed elsewhere¹⁵.

Observation of Intergranular Oxides by EPMA

EPMA across the oxidized boundaries was carried out to confirm the presence of grain boundary oxides. Grain boundaries in Figs. 6 (a) and (b) were observed in the specimen oxidized in a dilute oxygen atmosphere, corresponding to random boundary heavily oxidized and low-angle boundary having fewer oxides, respectively. The precipitate in Fig. 6 (a) is regarded as Fe-based oxide from the enrichment of iron at the boundary although oxygen could not be detected by our EPMA. The present observation is consistent with conventional studies of selective oxidation of Fe^+ cation along grain boundaries^{3,7}.

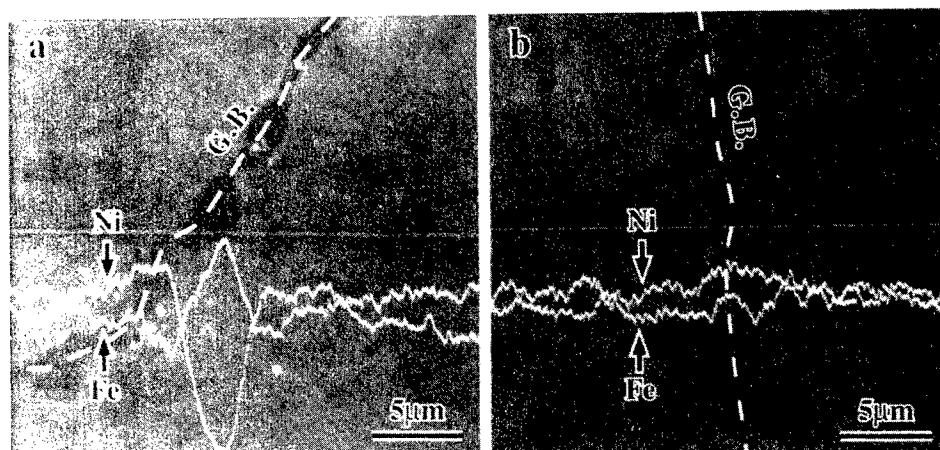


Figure 6 Electron probe micro analysis (EPMA) scanned across the boundaries. The concentration profiles of Fe and Ni are shown for different types of boundaries; (a) random boundary heavily oxidized, (b) low-angle boundary having fewer oxides.

OXIDATION-ASSISTED INTERGRANULAR FRACTURE

In order to study the effect of intergranular oxidation on fracture characteristics, ribbon specimens of the nickel-iron alloy with systematically controlled grain size and grain boundary character distribution (GBCD) were used for fracture tests. Figures 7 (a) and (b) show OIM micrographs with GBCD for as-solidified ribbons produced at roller speeds of 28.3m/s

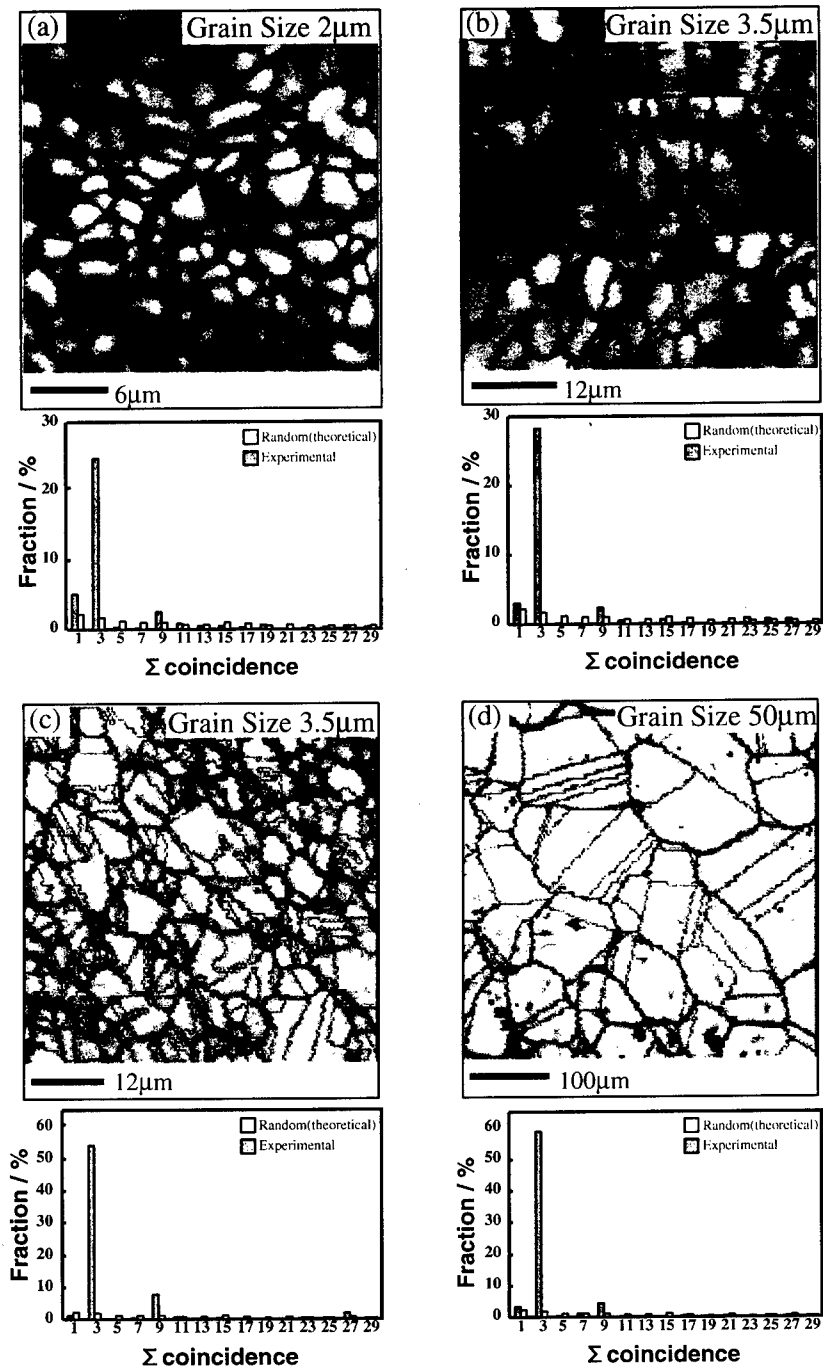


Figure 7 Grain boundary microstructures observed by OIM; (a) as-solidified at roller speed of 28.3m/s, (b) as-solidified at roller speed of 14.1m/s, (c) solidified at 28.3m/s and annealed at 1073K for 1h, (d) solidified at 28.3m/s and annealed at 1473K for 1h.

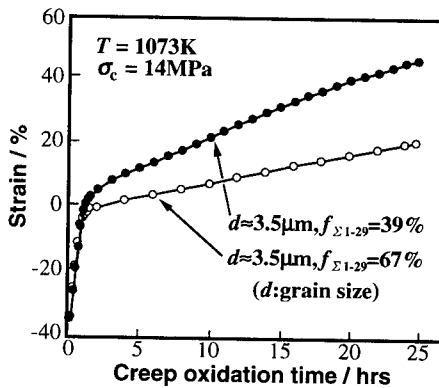
Table 2 Details of grain boundary microstructure in ribbon specimens

Processing Designation	Rapid Solidification Roll Speed (m/s)	Subsequent Annealing		Grain Boundary Microstructure				
				Grain Size (μm)	Grain Boundary Character Distribution			
					Low Angle	Twin	$\Sigma 5 - \Sigma 29$	Random
RS-1	28.3 (3600 r.p.m.)	—	—	2	5.1	24.7	7.4	62.8
RSA-1	28.3	1073	1	3.5	1.1	53.8	12.1	33.0
RSA-2	28.3	1273	1	30	2.3	60.7	8.5	28.5
RSA-3	28.3	1473	1	50	3.1	58.9	7.6	30.4
RS-2	14.1 (1800 r.p.m.)	—	—	3.7	4	28	7	61

and 14.1m/s, respectively. The average grain size increases with decreasing roller speed, but the GBCD did not change significantly, showing the presence of a high frequency of $\Sigma 3$ coincidence boundaries around 25%-28%. However the frequency of $\Sigma 3$ boundaries can be drastically increased by annealing after rapid solidification, as shown in Figs. 7 (c) and (d). Grain growth took place during annealing, resulting in a great increase of the average grain size up to 50 μm depending on the annealing temperature, as given by Table 2. Moreover the frequency of $\Sigma 3$ boundaries was drastically increased by annealing, up to 60% being almost double of that for as-solidified ribbons. Now let us look at fracture characteristic of oxidized specimens of the alloy.

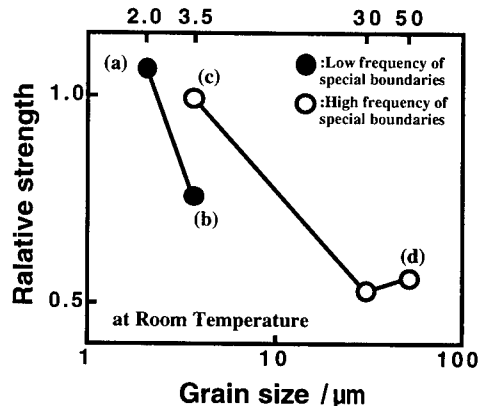
Effect of GBCD

Figure 8 shows creep curves obtained from the specimens with different values of the total frequency of coincidence with $\Sigma 1 - \Sigma 29$ boundaries (67% and 39%) and almost the same grain size ($d \approx 3.5 \mu\text{m}$). Creep tests were conducted in air at 1073K under a tensile stress of 14MPa. It is evident that the specimen with a higher frequency of low Σ coincidence boundaries has higher resistance to creep deformation, as reported recently on a nickel-iron alloy (Inconel 600)¹⁶. Moreover we can expect that intergranular oxidation occurred during creep deformation.

**Figure 8** Creep curves for ribbon specimens with different frequencies of coincidence boundaries and the same grain size ($d \approx 3.5 \mu\text{m}$).

Effect of Grain Size

Figure 9 shows the relative fracture strength obtained by three point bending test at room temperature from the specimens received creep test. We can easily recognize that the fracture strength decreases with increasing the grain size for both as-solidified specimens (filled circles) and subsequently annealed ones (open circles). This result demonstrates that the fracture strength is a function of the grain size and the grain boundary character distribution (GBCD). Figures 10 (a) - (d) are optical micrographs which show fracture paths observed at the sectioned plane in the

**Figure 9** Relative fracture strength as a function of grain size for as-solidified specimens (filled circles) and solidified-annealed specimens (open circles).

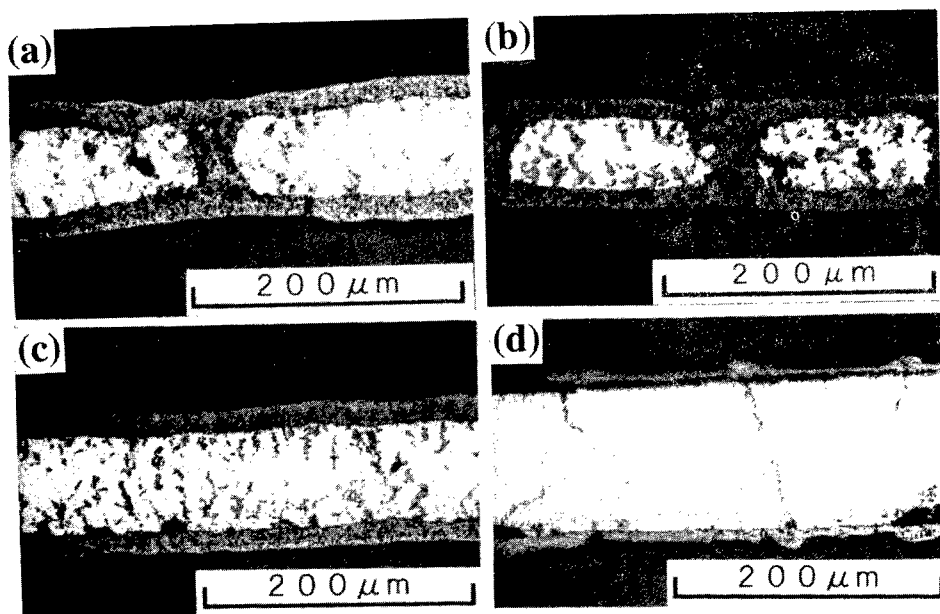


Figure 10 Optical micrographs of the sectioned planes after fracture test in differently processed specimens;
 (a) as-solidified at 28.3m/s, $d=2\mu\text{m}$,
 (b) as-solidified at 14.1m/s, $d=3.7\mu\text{m}$,
 (c) solidified-annealed at 1073K, 1h, $d=3.5\mu\text{m}$,
 (d) solidified-annealed at 1473K, 1h, $d=50\mu\text{m}$.

specimens after fracture test. Figures 10 (a) and (b) are from the as-solidified specimens and Figs. 10 (c) and (d) are from the annealed specimens. It was confirmed that fracture took place along grain boundaries for the both type of the specimens. Many short cracks were observed when the grain size was small while a few long cracks were observed as seen in Figs. 10 (b) and (d).

GRAIN BOUNDARY ENGINEERING FOR THE CONTROL OF OXIDATION-ASSISTED BRITTLENESS

On the basis of the observations of structure-dependent intergranular oxidation and oxidation-assisted intergranular fracture in a Ni-40at%Fe alloy, a new approach to grain boundary engineering is proposed for the control of oxidation-assisted intergranular brittleness in polycrystalline materials by manipulating the grain size, grain boundary character distribution (GBCD) and the grain boundary connectivity, as schematically shown in Fig. 11.

Since intergranular oxidation takes place preferentially at random boundaries, a decrease of the fraction of random boundaries is essential to the control of oxidation-assisted intergranular fracture. However the total length of intergranular crack is controlled by the grain size and the grain boundary connectivity, particularly of random boundaries which are heavily oxidized. One of the present authors pointed out that fracture mode can change depending on the GBCD and the grain boundary connectivity and that a typical intergranular brittleness is observed when more random boundaries are connected to each other in a polycrystal⁹. When a propagating crack meets strong low-energy boundaries like low Σ coincidence boundaries at a triple junction, it will not be able to proceed in intergranular fracture mode and the fracture mode changes to transgranular fracture mode which needs more energy for fracture resulting in an increase of ductility of a polycrystal. Now we may conclude that there must be an optimal grain boundary microstructure defined by the grain size, GBCD and the grain boundary connectivity.

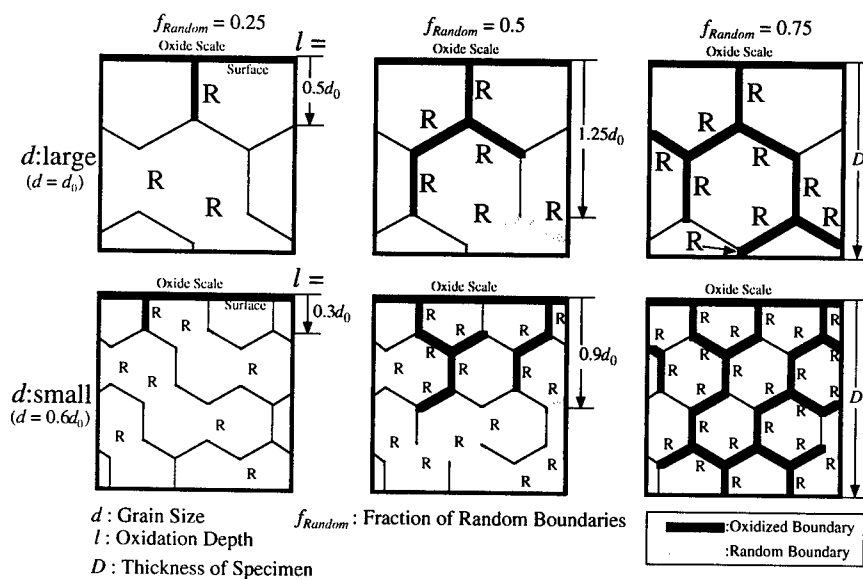


Figure 11 A schematic illustration of oxidation-assisted intergranular fracture controlled by the grain size, the grain boundary character distribution and the grain boundary connectivity.

CONCLUSIONS

It has been found that intergranular oxidation can take place preferentially at random boundaries and that low- Σ coincidence boundaries, particularly $\Sigma 3$, $\Sigma 11$, $\Sigma 19$ and $\Sigma 27$ coincidence boundaries are resistant to intergranular oxidation in a nickel-40at% iron alloy. The observations of structure-dependent intergranular oxidation has been utilized to establish the grain boundary engineering for the control of oxidation-assisted intergranular brittleness. A new approach to this objective has been proposed, paying particular attention to the importance of the grain size, the grain boundary character distribution (GBCD) and the grain boundary connectivity. The presence of an optimal grain boundary microstructure is predicted.

ACKNOWLEDGEMENTS

This work was supported by a Grant-in-Aid for Scientific Research (B) (2) from the Ministry of Education, Science, Sports and Culture of Japan. The authors thank Dr. K. Kawahara for his help in preparation for the manuscript.

REFERENCES

1. Birks, N. and Meier, G. H., *Introduction of High Temperature Oxidation of Metals*, Edward Arnold, (1983).
2. Rapp, R. A., The high temperature oxidation of metals forming cation-diffusing scales, *Met. Trans.*, **15(b)**: 195, (1984).
3. Matsuno, F., Nishikida, S. and Harada, T., Oxidation of Fe-Ni alloys at high temperatures, *Tetsu to Hagane*, **67**: 2029, (1981).
4. Bricknell, R. H. and Woodford, D. A., Grain boundary embrittlement of the iron-based superalloy IN903A, *Met. Trans.*, **12A**: 1673, (1981).
5. Katsman, A., Grabke, H. J. and Levin, L., Penetration of oxygen along grain boundaries during oxidation of alloys and intermetallics, *Oxidation of Metals*, **46**: 313, (1996).

6. Czerwinski, F. and Szpunar, J. A., The effect of reactive element on texture and grain boundary character distribution in nickel oxide, *Corrosion Science*, **39**: 1459, (1997).
7. Kusabiraki, K., Ikegami, J., Nishimoto, T. and Ooka, T., High-temperature oxidation of Fe-38Ni-13Co-4.7Nb-1.5Ti-0.4Si superalloy in Ar-H₂O atmosphere, *Tetsu to Hagane*, **80**: 574, (1994).
8. Kusabiraki, K., Sakuradani, K., and Saji, S., Effect of tensile stress on grain boundary selective oxidation in an Fe-36%Ni alloy, *Tetsu to Hagane*, **84**: 291, (1998).
9. Watanabe, T., An approach to grain boundary design for strong and ductile polycrystals, *Res Mechanica*, **11**: 47, (1984).
10. Watanabe, T., Grain boundary design and control for high temperature materials, *Mater. Sci. Eng.*, **A166**: 11, (1993).
11. Palumbo, G., Lehigh, E. M. and Lin, P., Applications for grain boundary engineered materials, *J. Metals*, **50**, 40, (1998).
12. Watanabe, T., Observation of plane-matching grain boundaries by electron channelling patterns, *Phil. Mag.*, **A47**: 141, (1983).
13. Kaur, I. and Gust, W., *Fundamentals of Grain and Interphase Boundary Diffusion*, Ziegler Press, Stuttgart, (1988).
14. Smith, D. A., On the density of coincidence sites in grain boundaries, *Scripta Met.*, **8**: 1197, (1974).
15. Yamaura, S., Igarashi, Y., Tsunekawa, S. and Watanabe, T., Structure-dependent intergranular oxidation in Ni-Fe polycrystalline alloy, *Acta Mater.*, **47**: 1163, (1999).
16. Was, G. S., Thaveepungsriporn, V. and Crawford, D. C., Grain boundary misorientation effect on creep and cracking in Ni-Based Alloys, *J. Metals*, **50**: 44, (1998).

SELF-ASSEMBLY IN EPITAXIAL SEMICONDUCTOR ALLOYS

K. Rajan¹, Y-C. Chen¹, V. Bucklen¹, C.A. Wang²,
G.W. Charache³, G. Nichols³, M. Freeman³, and P. Sander³

¹Department of Materials Science & Engineering
Rensselaer Polytechnic Institute Troy NY USA

²Lincoln Laboratory, Massachusetts Institute of Technology
Lexington MA USA

³Lockheed-Martin, Schenectady NY USA

ABSTRACT

With the development of new optoelectronic device architectures and applications, there has been extensive interest in the fundamental issues governing phase stability in chemically complex epitaxial compound semiconductors. We review some of the recent experimental findings in this field, point out the importance of different microstructural length scales associated with the different types of phase instabilities, and introduce three-dimensional natural superlattices found in $\text{Ga}_{1-x}\text{In}_x\text{As}_y\text{Sb}_{1-y}/\text{GaSb}$ epitaxial heterostructures.

INTRODUCTION

A fundamental property of semiconductors is the energy bandgap, E_g , between the maximum in the filled valence band and the minimum in the conduction band. This bandgap determines the energy (or wavelength) at which the material absorbs or emits light. The application of III-V semiconductor alloys in device structures is of importance for high-speed microelectronics and optoelectronics. Figure 1 shows the variation of lattice constant as a function of bandgap for the family of III-V ternary compound semiconductors. These alloys have allowed optoelectronic device engineers to tailor the bandgap to the need of the device by altering the alloy composition. The one-to-one relationship between bandgap and lattice constant is a major obstacle for high-quality device crystal growth because only a few alloy compositions can be grown nearly lattice-matched on commercially available substrates.

The most advanced semiconductor devices currently being developed depend on the ability to grow single-crystal materials with the variation of E_g in the growth direction with no changes in lattice constant (i.e., E_g and lattice constant must be independently specified). This restriction

can be relaxed by incorporating a fourth component, thus adding an extra degree of freedom so that both the energy bandgap and lattice constant can be adjusted independently. For instance, there is no III-V ternary compound semiconductor suitable for the thermophotovoltaic (TPV) device applications, $E_g \sim 0.5\text{--}0.7\text{ eV}$, lattice-matched to a GaSb substrate. However, by choosing a quaternary system, such as $\text{Ga}_{1-x}\text{In}_x\text{As}_y\text{Sb}_{1-y}$, a range of x, y combinations can be chosen, as indicated by the two-end-arrow line, to achieve both the E_g and the lattice parameter required [Fig. 1].

When using ternary or quaternary materials, the device designer usually presumes that the alloy is completely random-distributed. However the thermodynamics of an alloy system and the kinetics regarding the processing conditions often produce material that has some degree of macroscopic or microscopic ordering. Short-range ordering occurs when atoms adopt correlated neighboring positions over distances of the order of a few lattice spacings. This can be manifested as the preferential association of like atoms, as in clustering, or of unlike atoms, as in chemical ordering. Long range ordering occurs over many tens of lattice spacings. Both short range ordering and long range ordering are actually results of phase separation in very small length scales and have been widely reported, (see for example, Zunger and Mahajan [1], Suzuki [2], Rajan [3], Lockwood et al. [4]). Mahajan [5], McDevitt et al. [6], and Millunchick et al. [7] found that larger length scales of phase separation can also occur such as spinodal decomposition, and composition modulation. Stringfellow [8] also pointed out that most III-V quaternary alloys have miscibility gaps. It is interesting to note that experiments have shown that the presence of phase separation leads to significant alteration of the band structure and the crystal symmetry [1]. Therefore, it is very important to understand the phase stability of a compound semiconductor alloy.

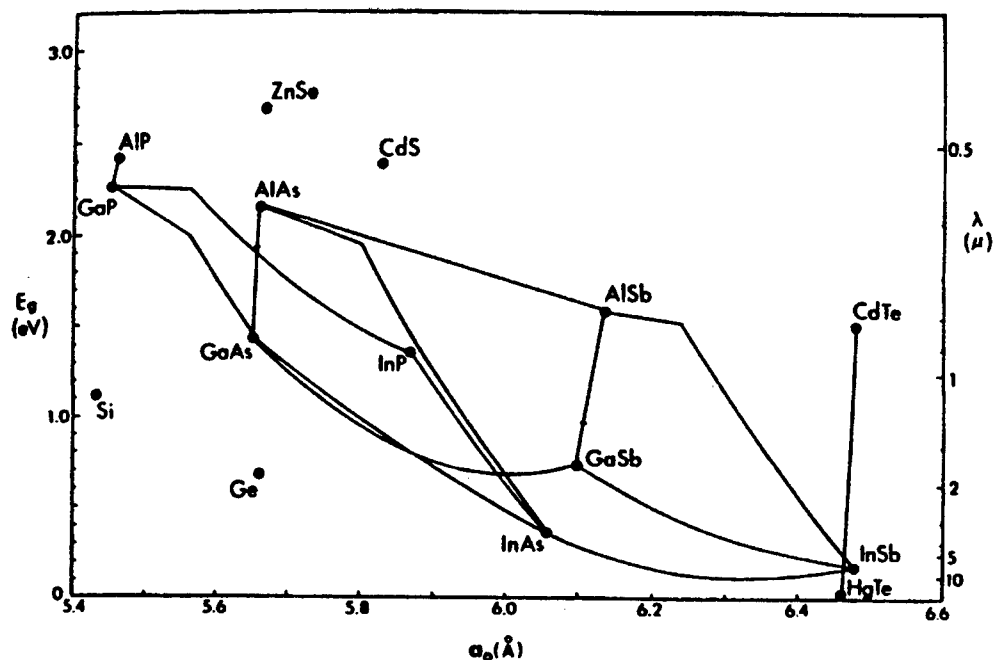


Figure 1. Theoretical relationship between the energy bandgap and lattice parameter of III-V compound semiconductors.

This paper reviews some of the recent experimental findings in this field and points out the importance of different microstructural length scales associated with the different types of phase instabilities associated with ternary and quaternary compounds. Of particular focus is the ability to take advantage of intrinsic thermodynamic and kinetic behavior of these complex semiconductor alloys in epitaxial structures to potentially "engineer" compositional modulations of varying length scales, which would not normally appear in bulk alloy systems. Hence, new "self-assembled" microstructures can be generated. This paper outlines some of the crystallographic and structural characteristics of such self-assembled alloy systems and discusses the possible mechanisms governing their formation and stability.

EXPERIMENTAL DETAILS AND RESULTS

The microstructure of $\text{Ga}_{1-x}\text{In}_x\text{As}_y\text{Sb}_{1-y}$ epitaxial heterostructures was investigated on samples grown by organometallic vapor phase epitaxy (OMVPE). Samples were grown with different alloy compositions while still maintaining lattice-matching of the epilayer to the GaSb substrate (refer to Figure 2 for the relative position in the quasi-binary phase diagram). The $\text{Ga}_{1-x}\text{In}_x\text{As}_y\text{Sb}_{1-y}$ epilayers were grown, lattice matched, on (100), Te-doped, 6° misoriented toward (111)_B GaSb substrates. A vertical rotating-disk reactor with H_2 carrier gas at a flow rate of 10 slpm (standard liter per minute) and reactor pressure of 150 Torr was used. All organometallic sources were used, including: solution trimethylindium, triethylgallium, tertiarybutylarsine, and trimethylantimony. The total group III mole fraction was typically 7×10^{-4} which resulted in a growth rate of $\sim 5 \mu\text{m/h}$. The V/III ratio was typically 1.5 – 1.6 and the growth temperature was

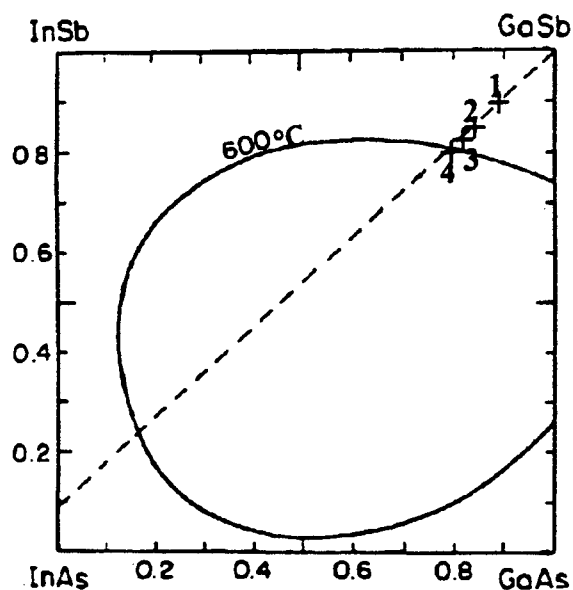


Figure 2. Phase diagram shows the relative positions of specimen #1, #2, #3 and #4. The solid curve is the calculated spinodal isotherm for $\text{Ga}_{1-x}\text{In}_x\text{As}_y\text{Sb}_{1-y}$ at temperature of 600 °C [9]. Dashed line represents compositions lattice-matched to GaSb.

525°C. Photoluminescence (PL) measurements were made at 4 K and 300 K. Typical PL results of layers reported in an earlier study are shown in Figure 3. From the phase diagram, it is expected that as the composition gets more InAs-rich, the homogeneity of the epitaxial layer would diminish. The increase of the PL full-width-half-max (FWHM), as the composition gets InAs-rich, is consistent to the prediction from the phase diagram.

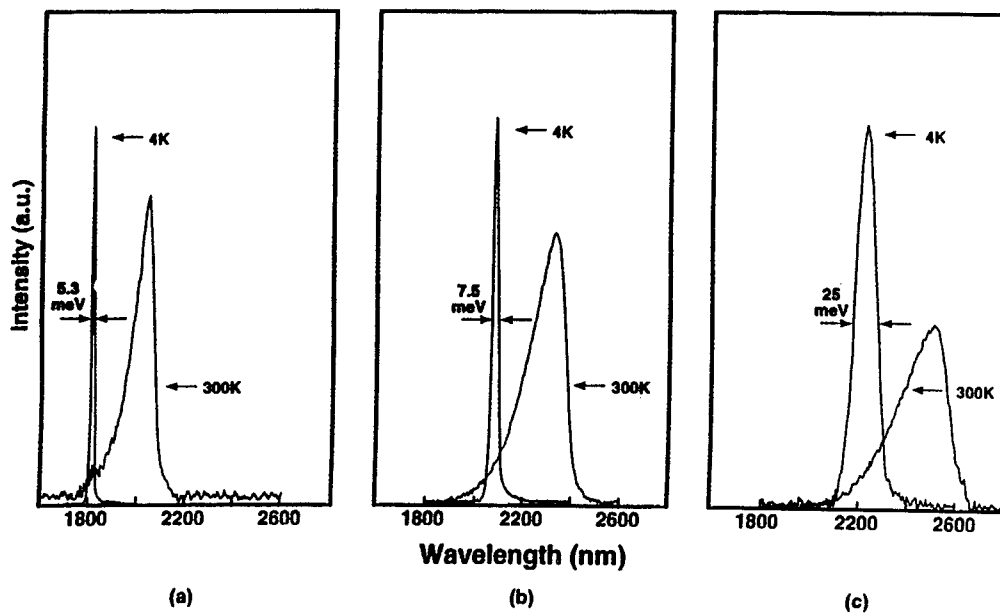


Figure 3. Photoluminescence spectra measured at 4 and 300 K of $\text{Ga}_{1-x}\text{In}_x\text{As}_y\text{Sb}_{1-y}$ grown on $(100) 6^\circ$ toward $(111)_B$ GaSb substrates. (a) $x = 0.09$, $y = 0.08$, (b) $x = 0.16$, $y = 0.15$, (c) $x = 0.20$, $y = 0.18$. TEM specimens #1, #3, and #4 of similar alloy composition of (a), (b), and (c), respectively.

Transmission electron microscope (TEM) thin foils were prepared in both a traditional mechanical thinning (for plan-view samples) and a wedge thinning (for cross-section samples) followed by Ar^+ ion milling, using a liquid N_2 cold rotating stage to exclude the preparation effects. For each specimen, a plane-view and two cross-section TEM thin foils were prepared for observation. Figure 4 (a) is a $(2\bar{2}2)$ reflection, (011) cross-section dark-field (DF) image of sample #4. Speckle-like structure was visible and modulated in the $[01\bar{1}]$ direction.

In Figure 4 (a), one other interesting long period (or what one may term “self organized”) microstructure was observed and it modulated in the direction approximately 10 degrees off surface orientation. It should be noted that as we are studying cross sectional samples, double diffraction effects associated with transmission through multi-layers is not an issue. Hence, one is able to discriminate between image contrast due to modulations from that observed from Moire fringes. The fact that it was shown in some (400) and $(02\bar{2})$ reflection images, and the observation of side-bands at the major reflection spots, strongly suggested that the observed microstructure was associated with composition variation. This microstructure is usually called self-assembled or self-organized composition modulation (SOCM). Figure 4 (b) is a

magnification micrograph showing this SOCM microstructure. The periodicity of this SOCM is $\sim 20\text{nm}$. Figure 4 (c) is the transmission electron diffraction (TED) pattern of this thin foil, in (011) cross-section. The elongation of the diffraction spot in $\sim [100]$ direction can be seen and is consistent with the image observation.

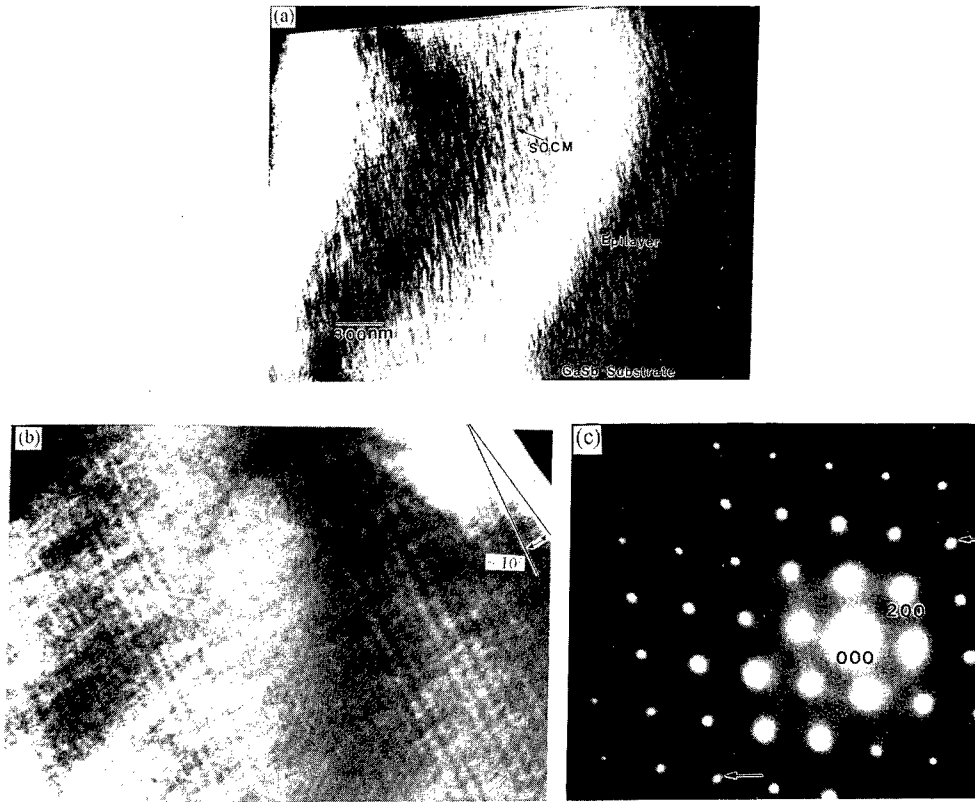


Figure 4. (a) TEM (011) cross-section (222) reflection DF image of sample #4, $x = 0.20$, $y = 0.18$. Speckle-like structure was visible and modulated in $[01\bar{1}]$ direction and SOCM was found modulated $\sim 10^\circ$ off surface orientation (b) magnification micrograph showing the SOCM microstructure (c) electron diffraction pattern showing the side-band at the major reflection spots

Image interference that presents itself as a regular pattern across and image can be especially difficult to remove using a spatial approach. The best way to eliminate such periodic or coherent noise is by converting the image to a set of frequencies, and editing out the frequencies causing the problem [10]. The image's frequency domain can be presented as a symmetrically centered cloud of points, where brightness represents amplitude of the waveform, and the position represents the frequency of the waveform. In a normal image, the spectrum will appear as a roughly circular cloud that is brighter and denser near at its center. Images containing a regular pattern will reflect pattern-like effects in their spectra. It is this characteristic that can be manipulated to remove coherent noise. Coherent noise usually manifests itself as bright points outside of the central cloud. Removing these points eliminates the frequency causing the noise. In order to validate which frequencies should be removed, we used inverse Fourier transforms to reproduce the fine structure in the diffraction patterns. Figure 5 (a) is a (222) reflection (011) DF image of sample #4. Image filtering results are shown in Figure 5 (b) and (c). By using this

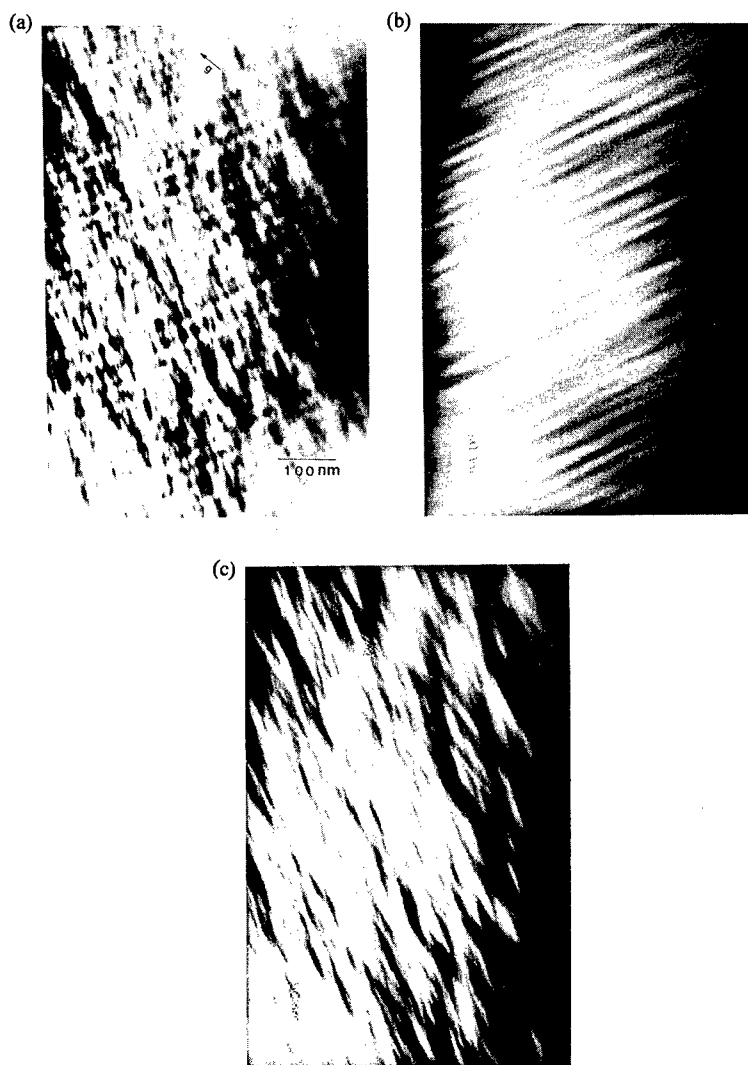


Figure 5. (a)TEM (011̄) cross-section (222) reflection DF image of sample #4, $x = 0.20$, $y = 0.18$. Image-processing deconvolution results show details of the SOCM microstructure (b), and the speckle-like structure (c).

technique, deconvolution of the two different length scales of phase separation, speckle-like and SOCM microstructure, was accomplished. From the imaging results, a three-dimensional microstructure model was proposed for the SOCM microstructure found in this study and is shown in Figure 6.

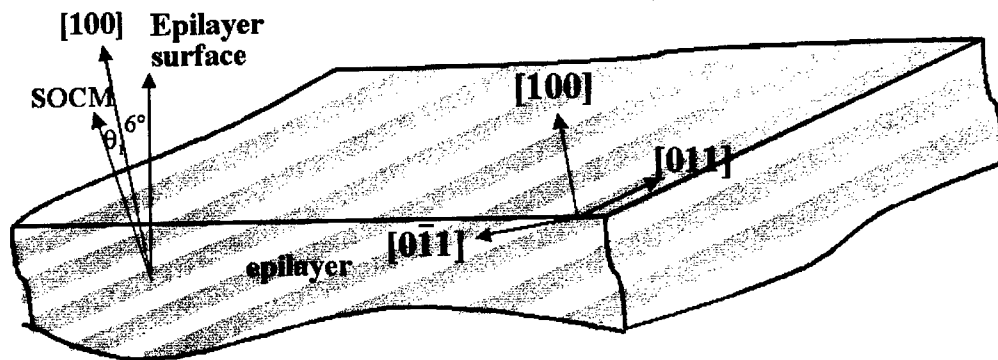


Figure 6. Schematic diagram showing the crystallography and microstructure of the SOCM.

DISCUSSION

The formation of lateral composition modulation has been extensively discussed (see for example, Zunger and Mahajan [1], and Millunchick et al. [7]) and has been exploited to obtain high densities of nanometer-sized quantum wires (QWR), without the processing limitations of other fabrication methods. Application of this technique to the InAlAs system can lead to novel polarization-sensitive devices, (Abraham et al. [11]). In a laser structure, cladding layers consisting of AlAs/InAs SPS can produce QWR behavior in active layers of InGaAs due to composition modulation induced strain fields (Peiro et al. [12]).

It was not until recent years that the vertical composition modulation started to draw the attention of device engineers. This type of composition modulation has a very regular periodicity which makes fabricating the natural superlattices in the scales of nanometers in a single epitaxial layer "by-itself" possible. However, many questions regarding vertical composition modulation still remain unanswered. In the GaAlAs system, Petroff et al. [13] suggested that changes in Gibbs free energy introduced by an exchange reaction could result in a miscibility gap in the $\text{Ga}_x\text{Al}_{1-x}\text{As}$ phase diagram and thus cause these plate-like structures (i.e. lateral composition modulation). Madhukar et al. [14] suggested that the formation of plate-like structures is a result of a kinetic effect driven by the geometry of sites on the $\{110\}$ surface. The concept of kinetic segregation employed by Madhukar and Van Vechten [15] indicated that the plates observed in $\text{Ga}_{0.75}\text{Al}_{0.25}\text{As}$ layers are not associated with the thermodynamic intrinsic properties of the epitaxial layers, but could be related to instabilities in growth conditions. Ipatova et al. [16] predicted that the formation of a modulated two-phase structure with a macroscopic period could occur in quaternary alloys by a process of spontaneous coherent phase separation. They considered such phase separation occurs in the bulk layer starting at an inclusion and develops to give a series of coherent phase separated plates in the form of a superlattice. These mechanisms outlined above, however, do not explain the growth behavior found in MBE-grown InAsSb by Seong et al. [17] or in OMVPE-grown GaInAsSb found in this study. The fact that this SOCM was not found in our previous liquid phase epitaxy (LPE) study, Chen et al. [18], suggests it is a surface mediated microstructure.

The growth model proposed by Barabasi [19] was based on the step-flow mode of growth associated with the preferred atomic sites relative to the steps introduced by the substrate miscut. Thus, Te (Se) diffuses on the surface, seeking a step rich in like atoms, (i.e., Se wants to attach to the edge of a terrace made up of mostly Se atoms and likewise for Te). He also proposed a critical miscut angle concept [19] (below which no natural superlattice (NS) is formed) which is in agreement with the results in the ZnSeTe system [20]. However, the plate-like structure found in InAsSb system by Seong et al. [17] on non-miscut (001) substrates does not fit this critical miscut criteria. Seong et al. proposed a growth model for plate-like structures found in InAsSb system and argued that the first-grown material consisted of plates of the Sb-rich phase and between these there were smaller islands of the As-rich phase. The growth continued by the plates of the Sb-rich phase spreading laterally and overgrowing the islands of the As-rich phase. Tersoff [21] suggested that stress-driven alloy decomposition during step-flow growth can occur according to his calculations and proposed a possible superlattice structure. These models all explain the formation of lateral composition modulation, however, no crystallography related structure model has been proposed to explain the inclined SOCM microstructure found in this study.

Combining our experimental results with the growth models, which have been proposed, a growth model that explains the unique crystallographic feature found in this study is proposed. In the SOCM microstructure found here, the phase instability and the surface steps were attributed to the initial phase separation and modulation in composition in the early stage of the epitaxial growth to form the thermodynamically stable GaAs-rich and InSb-rich bands, similar to that suggested by Barabasi [19]. However, the way the adatoms accommodated themselves onto the film surface is strongly affected by the underlying layers of atoms [22, 23]. If there is an extension of the GaAs-rich (or InSb-rich) band, of approximately 10 atomic positions along $[01\bar{1}]$ direction, before the InSb-rich (or GaAs-rich) band started to grow on the surface layer, the subsequent growth will result in a SOCM with ~ 10 degrees of misorientation from the surface orientation. Figures 7 (a) and (b) are schematic diagrams showing the proposed mechanism.

CONCLUSIONS

A number of other studies have reported the presence of self-organized superlattices (although the term of 'self-assembly' is more recent). The results shown here demonstrate the presence of two distinct microstructures: the speckle-like structure for a range of compositions and long-period microstructures, the SOCM, as a function of composition. These research results, those from other researchers, and the fact that we didn't observe this type of microstructure in our previous LPE studies strongly suggest that the long-period microstructure is influenced by surface mediated processes. Recently, numerous models have been proposed in the literature, each designed to rationalize specific microstructural observations; however they all have in common the theme of step mobility and surface reconstruction.

This paper reviews these concepts and models, and presents the observations of the three-dimensional SOCM found in $\text{Ga}_{1-x}\text{In}_x\text{As}_y\text{Sb}_{1-y}/\text{GaSb}$ epitaxial heterostructures. This is also the first report of the concurrency of the speckle-like structure and the SOCM microstructure in this system. In summary:

- ♦ Self-assembled layers are similar to the long period microstructures that were first experimentally observed over two decades ago in compound epitaxial systems.
- ♦ The formation of self-assembled layers is intrinsically associated with phase separation. In fact, in the case of the quaternary antimonides, the speckle-like structure co-exists with the SOCM microstructure and not long range ordering, as is well known for many other epitaxial compound semiconductors.

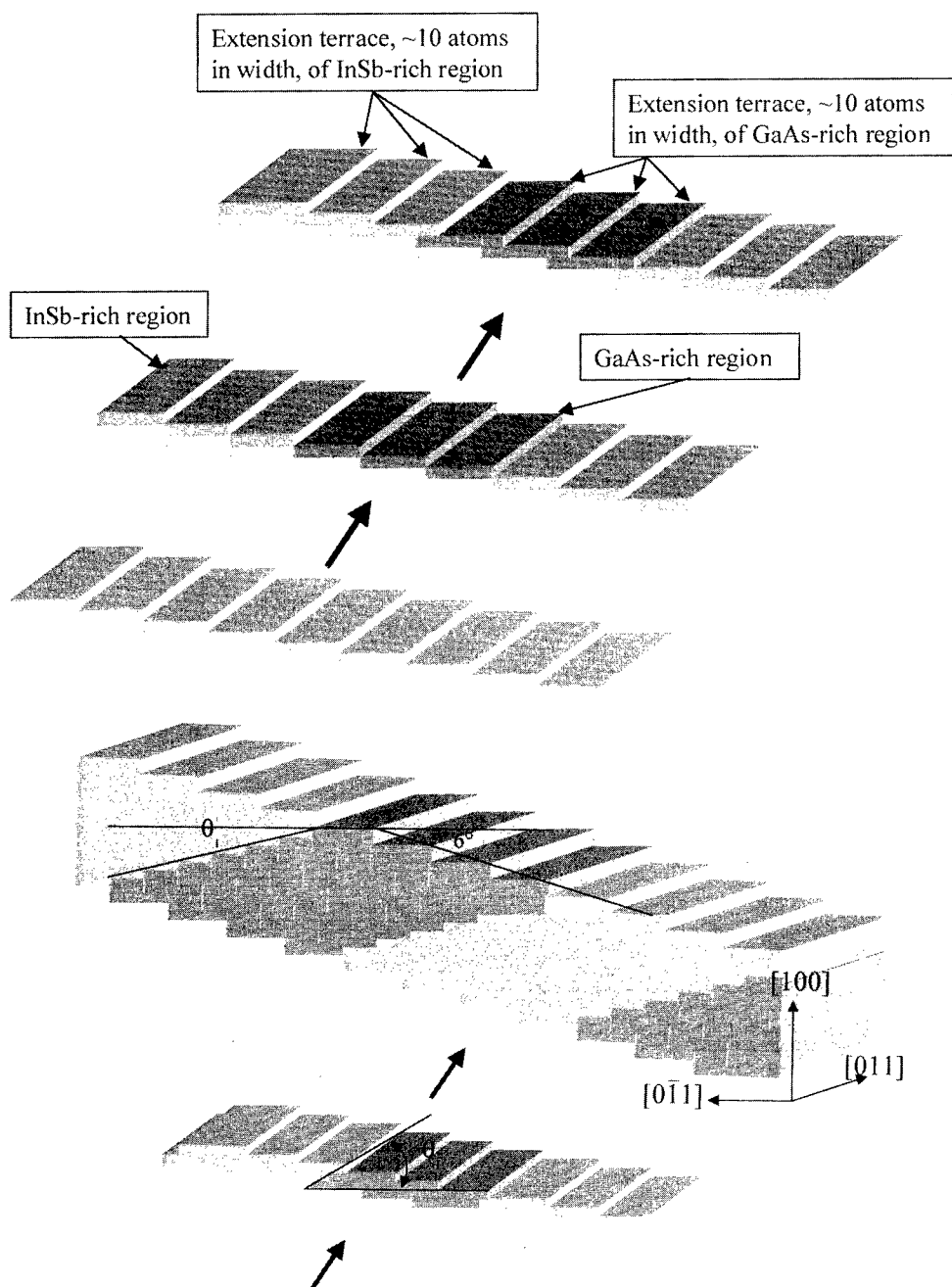


Figure 7. Schematic diagrams (a) showing the initial stage of the formation of the tilt of the SOCM; the extended terraces can be seen as the areas pointed by arrows, (b) the subsequent growth results in the tilted SOCM.

- ◆ Our studies are consistent with the literature in suggesting that a complex relationship between surface structure and the associated chemical functionality of surface steps may govern the mechanisms controlling the SOCM formation.
- ◆ While there has been much focus on structural models of the interface to rationalize the crystallographic evolution of the self assembled layers, the subsequent growth of these self-assembled layers microstructurally resembles lamellar growth of two phase systems.

REFERENCES

1. A. Zunger and S. Mahajan, Handbook on Semiconductors, completely revised edition, edited by T. S. Moss, V3, edited by S. Mahajan, 1399 (1994)
2. T. Suzuki, MRS Bulletin, 33, July (1997)
3. K. Rajan, Precious and Rare Metal Technologies, p. 589, edited by A. E. Torma and I. H. Gundler Elsevier, Published by Amsterdam (1989)
4. D. Lockwood, K. Rajan, E. W. Fenton, J-M. Baribeau and M. Denhoff, Solid State Comm., Vol. 61, 465 (1987)
5. S. Mahajan, B. V. Dutt, H. Temkin, R. J. Cava and W. A. Bonner, J. Cryst. Growth 68, 589 (1984)
6. T. L. McDevitt, S. Mahajan, and D. E. Laughlin Phys. Rev. B, 45, 6614 (1992)
7. J. Mirecki Millunchick, R. D. Twisten, S. R. Lee, D. M. Follstaedt, and E. D. Jones, S. P. Ahrenkie, Y. Zhang, H. M. Cheong, and A. Mascarenhas; MRS Bulletin, 38, July (1997)
8. G. B. Stringfellow, Journal of Crystal Growth 65, 454 (1983)
9. K. Onabe, Japanese Journal of Applied Physics 21, 964 (1982)
10. *Image Pro Plus: The Proven Solution for Image Analysis*, Media Cybernetis, L. P., MD (1997)
11. P. Abraham, M. A. Garcia Perez, T. Benyattou, G. Guilot, M. Sacilotti, and X. Letartre, Semicond. Sci. Technol. 10, 1585 (1995)
12. F. Peiro, A. Cornet, J. C. Ferrer, J. Merante, R. G. Halkias, and A. Georgakilas; Materials Research Society Symposium Proceedings, edited by E. D. Jones, A. Mascarenhas, and P. Petroff (MRS, Pittsburgh, 1996) p265
13. P. M. Petroff, J. Vac. Sci. Technol. 14, 473 (1977)
14. A. Madhukar, Surf. Sci. 132, 344 (1983)
15. J. A. Ven Vechten, J. Cryst. Growth 71, 326 (1985)
16. I. P. Ipatova, V. A. Shchukin, V. G. Malyshkin, A. Yu. Maslov, and E. Anastassakis, Solid State Commun. 78, 19 (1991)
17. T-Y. Seong, A. G. Norman, I. T. Ferguson and G. R. Booker, J. Appl. Phys. 73, 8227 (1993)
18. Y-C. Chen, V. Bucklen, M. Freeman, R. P. Cardines Jr, G. Nichols, P. Sanders, G. Charache, and K. Rajan, Fourth NREL Conf. CP 460, 535 (1999)
19. A.-L. Baragasi, Appl. Phys. Lett. 70, 764 (1997)
20. S. P. Ahrenkiel, S. H. Xin, P. M. Reimer, J. J. Berry, H. Luo, S. Short, M. Bode, M. Al-Jassim, J. R. Buschert, and J. K. Furdyna, Phys. Rev. Lett. 75, 1586 (1995)
21. J. Tersoff, Phys. Rev. Lett. 77 (10), 2017 (1996)
22. M. Ishimaru, S. Matsumura, N. Kuwano and K. Oki, J. Cryst. Growth 128, 499 (1993)
23. M. Ishimaru, S. Matsumura, N. Kuwano and K. Oki, J. Appl. Phys. 77, 2370 (1995)

ELECTROMIGRATION AND ELECTRONIC STRUCTURE

A. Lodder

Faculty of Sciences, Division Physics and Astronomy, Free University, De Boelelaan 1081, 1081 HV Amsterdam, The Netherlands

alod@nat.vu.nl

J. P. Dekker

Max-Planck-Institut für Metallforschung, Seestrasse 92, D-70174 Stuttgart, Germany

present address: Boterbloem 85, 1689 RH Zwaag, The Netherlands

hdek@fibonacci.nl

ABSTRACT

Regarding the two different contributions to the driving force, the direct force and the wind force, the rôle of the electronic structure has been quite different for the two. For the wind force increasingly sophisticated descriptions have been used, namely pseudopotential models, finite cluster models and, at the end, an *ab initio* Korringa-Kohn-Rostoker (KKR) Green's function description. We will illustrate this by showing for which systems by now the wind force has been calculated, which include almost all FCC and BCC metals, while both self-electromigration and impurity migration have been treated. Some new results will be presented as well, which simulate electromigration along a grain boundary and over a surface.

The direct force, on the other hand, has mainly been discussed in terms of the simple free electron, or jellium model. However, it will be shown that we have arrived at a point, at which more sophisticated descriptions of the electronic structure involved are becoming important. A recent analysis of new experimental results leads to the conclusion that a migrating hydrogen atom effectively can have a direct valence

smaller than unity, depending on the metal studied. By this it becomes challenging to perform calculations of the electronic structure of an interstitial, not only at its equilibrium position, but also at positions lying along the jump path.

INTRODUCTION

The process of the drift of atoms due to an applied voltage, called electromigration, is known both in materials science and in fundamental physics. The development of voids at the cathode side of an aluminum film, and the growth of hillocks at the anode,[1] which is due to self-electromigration, shorten the lifetime of an integrated circuit. In electronic industry a great deal of effort is made in slowing down this process. In fundamental physics the efforts have been directed towards the understanding and calculation of the driving force, which is commonly written as a sum of two components, a direct force $\mathbf{F}_{\text{direct}}$ and a wind force \mathbf{F}_{wind} . The direct force is due to a net charge of the migrating atom, while the wind force is due to scattering of the current-carrying electrons off the atom. Both forces are proportional to the electric field and can be characterized by a valence [2]

$$\mathbf{F} = (Z_{\text{direct}} + Z_{\text{wind}}) e\mathbf{E} = Z^* e\mathbf{E}. \quad (1)$$

The effective valence Z^* is the measurable quantity. Although consensus consists about the form of Eq. (1), the present understanding of the two contributions is quite different. The wind force, being proportional to the current density, is found to be inversely proportional to the sample resistivity ρ , independently of the complexity of the theoretical formulation used in the description of the total force. So, Z^* can be written as

$$Z^* = Z_{\text{direct}} + \frac{K}{\rho}, \quad (2)$$

in which the temperature independent proportionality constant K is determined by the scattering of the electrons by the migrating atom. In addition, a microscopic quantum-mechanical expression for the wind force is available. This expression has been applied recently for *ab initio* calculations of the wind valence of interstitial atoms such as hydrogen [3], and of substitutionally migrating atoms [4, 5], in numerous FCC and BCC metals.

In contrast to the consensus concerning the wind force, and its computational accessibility, the magnitude of the direct force has been the subject of a long-standing controversy. Either one is in favour of complete screening, so that only the wind force remains, or one defends that the direct force is effectively unscreened. The controversy started in 1962, being induced by the screening prediction of Bosvieux and Friedel

[6], and has not come to an end completely yet.[7, 8] Unfortunately, an attempt to decide in this issue by measuring the driving force on hydrogen in the transition metals V, Nb, and Ta turned out to be not conclusive.[9, 10] Sorbello [7] even expresses the possibility that the conventional distinction of two contributions to the driving force, Eq. (1), eventually may turn out to be less meaningful than it has been assumed to be up to now.

The purpose of this contribution is twofold. First, under the section headings *Some characteristic results for the wind valence* and *Preliminary results for migration along a grain boundary*, the advanced character of present-day calculations of the wind force will be illustrated by reviewing a few characteristic published results and by presenting some preliminary results. The latter pertain to migration along a line of vacancies modeling a grain boundary, and over the inner side of a void, modeling migration over a surface. Secondly, under the section heading *Electromigration of hydrogen and the direct valence*, it will be shown, that recent experimental results for electromigration of hydrogen in Pd and some PdAg alloys imply values of Z_{direct} for hydrogen, which are significantly smaller than unity, the bare hydrogen valence. It will be concluded, that this makes it interesting to undertake advanced electronic structure calculations for interstitial hydrogen at its interstitial position, and at intermediate positions, lying along the electromigration jump path.

But first we give a brief description of the theory.

THEORY

The wind force on an atom at some position \mathbf{R}_1 in a metallic system is described by the quantum-mechanical expression [11]

$$\mathbf{F}_{\text{wind}} = \sum_k f(k) \langle \psi_k | -\nabla_{\mathbf{R}_1} v_1 | \psi_k \rangle, \quad (3)$$

which traces back to the pioneering work of Bosvieux and Friedel.[6] In this equation v_1 is the potential of the atom feeling the force, k combines the band index n and the crystal momentum \mathbf{k} of the electron, and $f(k)$ is the electron distribution function given by

$$f(k) = f_{FD}(k) - e\tau \mathbf{E} \cdot \mathbf{v}_k \delta(\epsilon_{\text{Fermi}} - \epsilon_k), \quad (4)$$

which differs from the Fermi-Dirac distribution $f_{FD}(k)$ due to the presence of the electric field \mathbf{E} , and in which τ is the transport relaxation time and \mathbf{v}_k is the velocity of the electron in the state k . In order to calculate ψ_k , which is the true locally perturbed electron wave function,

a Green's function formalism is used.[4] The wave function is calculated for a dilute-alloy-type configuration, *i.e.* a cluster containing the locally perturbed atoms at and around the migrating atom, possibly including a vacancy in the case of substitutional electromigration, embedded in an infinite lattice of unperturbed metallic host atoms. The advanced character of this treatment becomes clear, if one compares it with the jellium [12], model-pseudopotential [13, 14] and finite-cluster-in-free-space [15] treatments used in the past. The first treatment can at most bring out some trends. The second treatment applies to simple metals only, so that the intensively investigated transition metals are beyond its scope. The finite-cluster method, although treating all local multiple scattering exactly, is essentially a free electron treatment, so that no band structure effects are represented by it.

Just one more remark about the theory, in particular about Eq. (3). Due to its simply looking form people are inclined to think that it is just the Hellmann-Feynman force, which is given by the expectation value of the force operator $-\nabla_{\mathbf{R}_1} v_1$ for a system in the ground state. [16, 17, 18, 19] However, the Hellmann-Feynman theorem was derived for a finite system such as a molecule, and cannot be applied to a current-carrying solid. This requires a derivation in the framework of non-equilibrium quantum statistical mechanics, such as the one made by Kumar and Sorbello, which also ends up with the expectation value of the force operator.[20] Therefore, referring to the Hellmann-Feynman force in the context of electromigration, can be regarded merely as confusing.

SOME CHARACTERISTIC RESULTS FOR THE WIND VALENCE

In this section we give an account of four results obtained by the method described above, which have led to a better understanding of the physical nature of the driving force and which show that some intuitive ideas are not generally applicable.

First, in measuring the driving force on hydrogen in the dilute hydrides V(H), Nb(H) and Ta(H), it was found that $Z_{\text{Ta}}^* < Z_{\text{V}}^* < Z_{\text{Nb}}^*$, and that the wind valence in V and Nb was positive, while in Ta it was negative. [9, 21] Neither the ordering in magnitude, nor the difference in the wind valences are obvious regarding the position of the elements in the Periodic System. The electronic structure of the three elements is very similar, and the densities of states of Nb and Ta are almost identical. However, a straightforward calculation of the wind valence lead to agreement with experiment.[3] Analysis of the results brought about, that the electronic charge density for H in Ta was markedly different

from the density distribution in V and Nb, which must be attributed to relativistic contributions in the much heavier Ta. So, a close similarity of the electronic properties of two metals in reciprocal space, does not exclude marked differences in direct space. Further, apparently, the wind force is very sensitive to the local charge distribution, which, up to now, has only been shown for transition metals in such a dramatic way by the means of the KKR-Green's function formalism.

Secondly, results of the same set of calculations implied, that an old simplification broke down. It was generally assumed, that electron conduction, such as in simple and noble metals, would evidently lead to a negative wind valence, and that a positive wind valence was bound to be due to hole conduction. However, it became clear, that the obtained positive wind valences obtained for hydrogen in V and Nb, could not be attributed to hole conduction. Interestingly, it was already the earlier applied finite-cluster-in-free-space treatment [15] that lead to a similar conclusion. Although in that treatment the environment of the cluster was free space, positive wind valences were found for hydrogen in V and Nb. This could not at all be due to hole effects, because in such a model there are not even electron bands. It had to be attributed to multiple scattering effects inside the cluster.

A third revealing result was undermining for another generally used notion, namely that the sign of the wind valence is typical for a given metal. From a systematic calculation of the wind valence for substitutional impurities in V, Nb, and Ta, it was found, that Mn in V, and Mn and Tc in both Nb and Ta, formed an exception. These impurities experience a wind force against the current direction of the electrons, contrary what was found for all other impurities.[22] In a separate study it was already made explicit, that local multiple scattering effects in the defect, containing the migrating impurity and a vacancy, can be strong. [5] Now it can be concluded, that such effects can even lead to surprising effects.

Finally, it was found that for self-electromigration the sign of the wind valence in some metals could depend on the crystal structure.[22] In the low-temperature close-packed structure the wind valence for Ca, Sr and Zr is negative, while it is positive for the BCC structure. Results are given in Table 1, in which the constant K , as it occurs in Eq. (2), is given as well. In order to clear up this result local charge distribution studies have to be carried out, which has not been done yet, as far as the authors know. As a guide one could investigate implications of the fact, that in a close-packed structure the crystal atoms overlap more than in a BCC structure. More overlap generally implies wider bands and more electronlike behaviour, leading to a negative wind valence.

For a recent application of the method to a study of the electromigration in Al, which metal is of technological interest, we refer to Dekker et al. [23]

Table 1 Self-electromigration in Ca, Sr and Zr for different crystal structures. Zr in the HCP structure is treated as an FCC metal with the same density.

Metal	K^{FCC}	Z_{wind}^{FCC} (473 K)	K^{BCC}	Z_{wind}^{BCC} (0.9 T_m)	T_m	Remarks
Ca	-1.4	-0.25	70	5.4	1112	FCC for $T < 720$ K
Sr	-8.3	-0.38	28	0.5	1041	FCC for $T < 718$ K
Zr	-52	-0.71	14	0.1	2125	HCP, but BCC for $T > 1135$ K

PRELIMINARY RESULTS FOR MIGRATION ALONG A GRAIN BOUNDARY

As an illustration of the possibilities of the available KKR-Green's function method, we show some results for simulations of migration along a grain boundary and over a surface. The local electromigration defect in a FCC structure is depicted in Figure 1. The migration path runs from position 1 to the vacancy at the position 2. We model a grain boundary to be a line of vacancies, so we omit atoms at the positions 19 and 20. Similarly, omitting the atoms at the positions 3 and 5 creates a high barrier on one side of the path, which is enough to simulate vacuum, or, equivalently, migration over a surface.

In Figure 2 the bold line shows the variation of the quantity K along the path for a jumping Al atom. It varies from $-25 \mu\Omega\text{cm}$ at the initial position to $-63 \mu\Omega\text{cm}$ halfway along the path, called the saddle point position. The average over the path is $K = -39 \mu\Omega\text{cm}$.

The other curves in the figure correspond to configurations with additional vacancies at some of the positions in the cluster displayed in Figure 1. It is clear that the wind force depends on the positions of the vacancies. When the vacancy occupies position 19 the path averaged $K = -42 \mu\Omega\text{cm}$, whereas a vacancy at position 3 leads to $K = -21 \mu\Omega\text{cm}$. For two additional vacancies one finds for vacancies at the positions 19 and 20, that $K = -46 \mu\Omega\text{cm}$. For vacancies at the positions 3 and 5 $K = -1 \mu\Omega\text{cm}$. All curves in the figure are symmetric with respect to the saddle point position, at 0.5, apart from the curve corresponding to one additional missing atom at the position 19. By adding a vacancy at the position 20, represented by the dashed curve, the symmetry is restored.

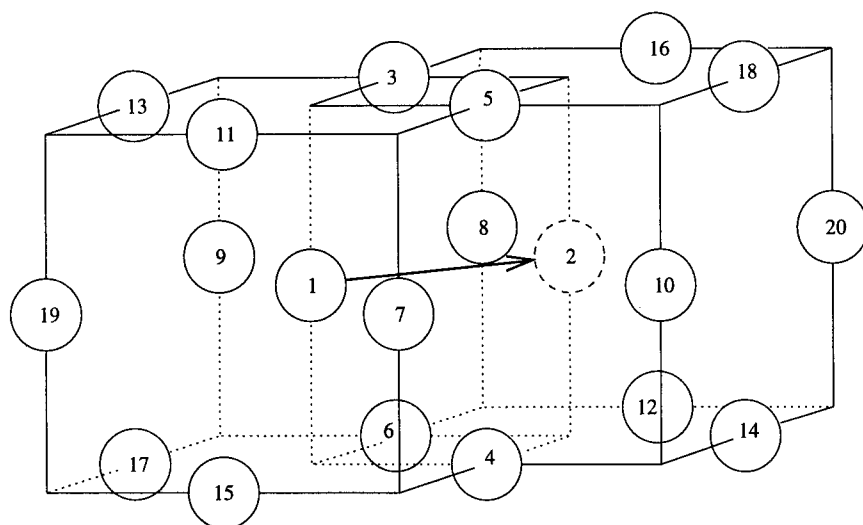


Figure 1 The cluster of perturbed atoms in the FCC structure. The labels of the positions are used in the text. The wind force on the atom labeled by 1 is calculated at several positions along its jump path to the vacant position labeled by 2. The atoms at all other positions are assumed to occupy exact lattice positions.

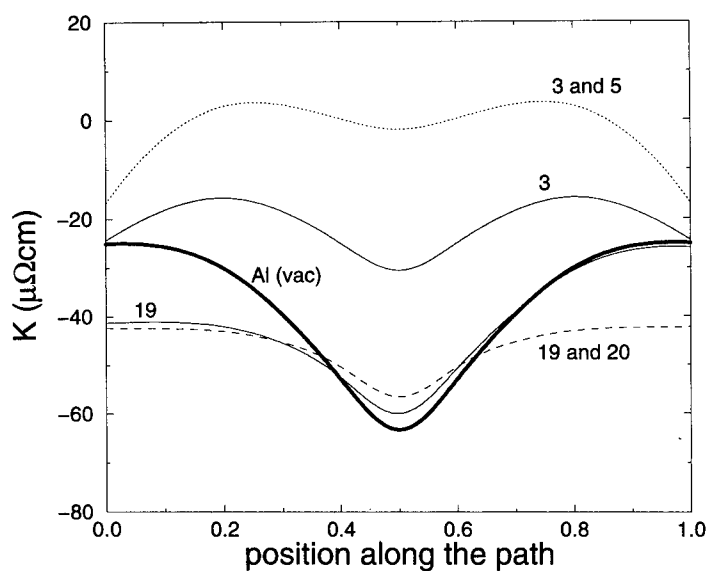


Figure 2 Variation of K for a host Al atom with one vacancy next to it, at the final position 2 (bold line), and with additional vacancies at one or two positions in the perturbed cluster, as indicated along the lines. The labels of the positions correspond to those in Figure 1.

The effects are really impressive. From these simulations one would conclude, that electromigration along a grain boundary involves a significant increase of the wind force, while migration over a surface would involve a reduction. The latter trend is in agreement with results obtained by Bly and Rous. [24]

ELECTROMIGRATION OF HYDROGEN AND THE DIRECT VALENCE

Compared with the sophistication involved in the calculation of the wind force, the theoretical status of the direct force is rather poor. Till now the extreme view points of no screening and complete screening are based on impurity-in-a-jellium model treatments only.[8] The same holds for a recent proposal, in which Z_{direct} is not a constant, but given by the following resistivity-dependent expression[10]

$$Z_{\text{direct}} = \frac{Z_i}{1 + (b/\rho)^2}. \quad (5)$$

In this expression Z_i and ρ are the unscreened ionic valence and the contribution to the sample resistivity due to electron-phonon scattering respectively, and b is an adjustable parameter. It is clear that Eq. (5) bridges the gap between the two extremes in the controversy, because in the high-resistivity limit $Z_{\text{direct}} \rightarrow Z_i$, while for low temperatures, when $\rho \rightarrow 0$, complete screening, so $Z_{\text{direct}} \rightarrow 0$, is found. Since actual electromigration experiments are done at relatively high temperatures, in general way above room temperature, the complete-screening limit can be considered as being of academic interest only. On the other hand, experimentally determined Z_{direct} -values are rarely equal to the bare protonic charge of unity. Verbruggen and Griessen found the values 1.11, 0.44 and 1.22 for Z_{direct} in V(H), Nb(H) and Ta(H), respectively.[9] These values were obtained from a fit of the measured Z^* , by a $1/\rho$ plot, according to Eq. (2). In a first attempt to describe the measured results using Eq. (5), a value $Z_i = 1$ could be used, but in retrospection the fitted b -values were rather unrealistic. A more realistic plot, describing recently obtained data for hydrogen in Pd and two alloys with Ag,[25] is reproduced in Figure 3.[26] The bold lines show the constant- Z_{direct} fit according to Eq. (2). One nicely sees an increasing negative slope on adding silver to palladium. For pure silver, having large negative Z^* -values, a very steep slope is expected. The thinner lines follow from a fit, using Eq. (5) in Eq. (2), and taking $Z_i = 1$. These three lines obviously end at the value $Z^* = 1$ in the origin. The fit for Pd(H) would be acceptable, but for the two alloys the fit is not good at all. One has to conclude that taking $Z_i = 1$ beforehand does no justice to experimental findings. So either one has to abandon Eq. (5), and to look for a new theory, or one could try to interpret Eq. (5) more

flexibly. It is tempting to exploit the latter approach first, on the one hand, because of the obvious merits of Eq. (5), on the other hand, because no new theory is available, and it is not clear at all how to come to something usable. The new use of Eq. (5) is inspired by the

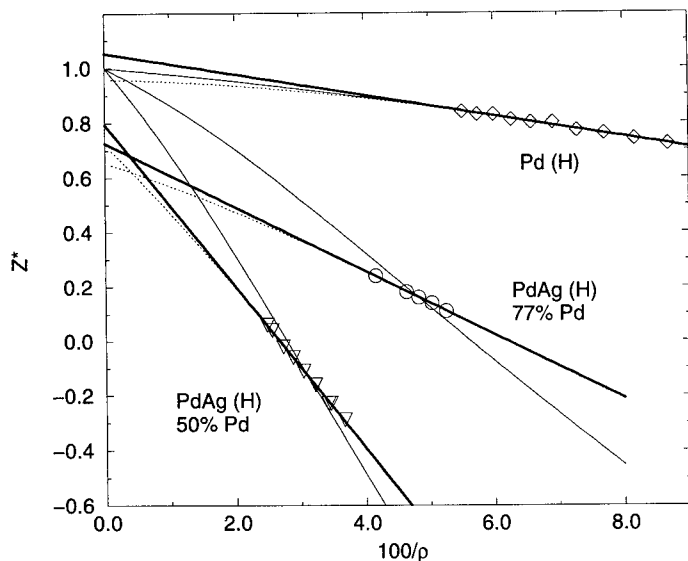


Figure 3 The effective valence Z^* of hydrogen in pure Pd and two alloys with Ag, plotted as a function of $100/\rho$.

results obtained so far. It is possible to make a reasonable choice for the parameter b , such that not too much screening is left in the range of the measured points. The choice made is such, that $b/\rho_{\min} = \frac{1}{2}$, in which ρ_{\min} is the smallest resistivity of the experimental set. For $b/\rho = \frac{1}{2}$, Eq. (5) gives a direct valence equal to $\frac{4}{5}Z_i$, where the unscreened valence Z_i now has to be determined by a fit. It must be admitted, that this choice implies some dependence on the actual sets of measuring points. However, the possible range of experimentally accessible points is rather limited, and, regarding that, the overall sensitivity to the precise choice is rather small.

For the choice made, the result of the fit for the three systems is shown by the dotted lines in Figure 3. It is seen that this new fit is as good as the constant- Z_{direct} fit is. The only difference is that the unscreened valence Z_i obtained this way is necessarily somewhat smaller than Z_{direct} obtained by means of a constant- Z_{direct} fit. However, more importantly, this analysis of the experimental results demonstrates evidently, that the valence of hydrogen in a metal can deviate significantly from the protonic valence of 1, which comes out according to the jellium model of

a metal. So, metallic effects have to be considered in explaining such a deviation. It is the first time, that this conclusion can be drawn without restriction.[26] The small Z_i -values found from hydrogen in Nb, lying between 0.4 and 0.7, are particularly intriguing in this respect.

Metallic effects can be studied only by doing selfconsistent charge density calculations. Such calculations are possible, and have been carried out extensively for substitutional impurities in metallic hosts in the past fifteen years. However, the description of dilute interstitial alloys has not shown any development at all since some first preliminary activity.[28] The barriers encountered at the time have been razed in the meantime.[29] This activity should not be carried out for the impurity at its initial position only, but at all positions along its jump path, similarly as it now is done routinely for the wind force.[4, 5, 23]

REFERENCES

- [1] I. A. Blech and C. Herring, "Stress generation by electromigration". *Appl. Phys. Lett.* **29** (1976) 131.
- [2] P. S. Ho and T. Kwok, "Electromigration in metals". *Rep. Progr. Phys.* **52** (1989) 301.
- [3] J. van Ek and A. Lodder, "Electromigration in transition metals: II. Light interstitials in Cu, Ag, Ni, Pd, Al, V, Nb and Ta". *J. Phys.: Cond. Mat.* **3** (1991) 7331.
- [4] J. P. Dekker, A. Lodder, and J. van Ek, "Theory for the electromigration wind force in dilute alloys". *Phys. Rev. B* **56** (1997) 12167.
- [5] J. P. Dekker and A. Lodder, "Electromigration in dilute body-centred cubic alloys". *J. Phys.: Cond. Mat.* **10** (1998) 6687.
- [6] C. Bosvieux and J. Friedel, "Sur l'électrolyse des alliages métalliques". *J. Phys. Chem. Solids* **23** (1962) 123.
- [7] R. S. Sorbello, "Theory of Electromigration", in *Solid State Physics*, Vol. 51, Eds. H. Ehrenreich and F. Spaepen (Academic Press, San Diego, 1998), page 159.
- [8] For a review see J. van Ek and A. Lodder, "Electromigration of Hydrogen in Metals: Theory and Experiment". *Defect and Diff. Forum* **115-116** (1994) 1.
- [9] A. H. Verbruggen, and R. Griessen, "Experimental evidence for nonintegral direct-force valence in electromigration". *Phys. Rev. B* **32** (1985) 1426.
- [10] A. Lodder, "Electromigration of hydrogen in V, Nb and Ta: a new description of the measured sample-resistivity-dependent effective valence". *J. Phys.: Cond. Matter* **3** (1991) 399.

- [11] R. S. Sorbello, A. Lodder, and S. J. Hoving, "Finite-cluster description of electromigration". Phys. Rev. B **25**(1982) 6178.
- [12] R. S. Sorbello, "Basic Concepts in Electromigration". Mat. Res. Soc. Symp. Proc. **225** (1991) 3.
- [13] R. S. Sorbello, "A pseudopotential based theory of the driving forces for electromigration in metals". J. Phys. Chem. Solids **34** (1973) 937.
- [14] R. S. Sorbello, "Atomic configuration effects in electromigration", J. Phys. Chem. Solids **42** (1981) 309.
- [15] A. Lodder, and M. G. E. Brand, "Electromigration in transition-metal hydrides: a finite-cluster-model study" J. Phys. F: Metal Phys. **14** (1984) 2955.
- [16] Hellmann, H., *Einführung in die Quantenchemie*, Deuticke, Leipzig and Vienna, 1937.
- [17] Feynman, R. P., "Forces in Molecules". Phys. Rev. **56** (1939) 340.
- [18] Sorbello, R. S., and Dasgupta, B. B., "Force on an atom in an electrostatic field: Feynman-Hellmann theorem and oscillator strengths". Phys. Rev. B **21**(1980) 2196.
- [19] A. Lodder and J. P. Dekker, "The Electromigration Force in Metallic Bulk", in *Stress Induced Phenomena in Metallization*, Fourth Int. Workshop (Tokyo, Japan, 1997), Eds. H. Okabayashi, S. Shingubara, and P. S. Ho, (Am. Inst. Phys, Woodbury, N.Y., 1998), 315.
- [20] Kumar, P., and Sorbello, R. S., "Linear Response Theory of the Driving Forces for Electromigration". Thin Solid Films **25**(1975) 25.
- [21] Erckmann and H. Wipf, "Electrotransport of Interstitial H and D in V, Nb, and Ta as Experimental Evidence for the Direct Field Force". Phys. Rev. Lett. **37** (1976) 341.
- [22] J. P. Dekker and A. Lodder, "Calculated electromigration wind force in face-centered-cubic and body-centered-cubic metals". J. Appl. Phys. **84** (1998) 1958.
- [23] J. P. Dekker, P. Gumbsch, E. Arzt, and A. Lodder, "Calculation of the electromigration wind force in Al alloys". Phys. Rev. B **59** (1999) 7451.
- [24] D. N. Bly and P. J. Rous "Theoretical study of the electromigration wind force for adatom migration at metal surfaces". Phys. Rev. B **53** (1996) 13909.

-
- [25] R. Pietrzak, R. Szatanik, and M. Szuszkiewicz, "Investigation of diffusion and electromigration of hydrogen in palladium and PdAg alloy". *J. Alloys Comp.* **282** (1999) 130.
 - [26] A. Lodder and K. Hashizume, "The direct force on electromigrating hydrogen isotopes". *J. Alloys Comp.* **288** (1999).
 - [27] K. Hashizume, K. Fujii, and M. Sugisaki, "Effective valence of tritium in the alpha phase of niobium". *Fusion Techn.* **28** (1995) 1179.
 - [28] S. Ellialtioglu, H. Akai, R. Zeller, and P. H. Dederichs, "Ab-initio calculations of interstitial impurities in Cu" *Ann. Int. Symp. Electr. Str. Met. All.* **15** (1985) 99.
 - [29] J. P. Dekker, A. Lodder, R. Zeller and A. F. Tatarchenko, "Accurate evaluation of the interstitial KKR Green function" *Phys. Rev. B* **54** (1996) 4531.

ORDERING

AB INITIO STUDY OF VACANCIES IN METALS AND COMPOUNDS

P. A. Korzhavyi

I. A. Abrikosov

B. Johansson

Condensed Matter Theory Group, Physics Department

Uppsala University, SE-751 21 Uppsala, Sweden

ABSTRACT

The results of ab initio calculations of the vacancy formation energies in all the transition and noble metals are presented. We also report on the formation energies of native point defects in the NiAl intermetallic compound. The calculations are performed within the locally self-consistent Green's function method and include multipole electrostatic corrections to the atomic sphere approximation. The results are in excellent agreement with experiment and existing full-potential calculations. We also perform a qualitative analysis of constitutional and thermal defects in NiAl within the Wagner-Schottky model of a lattice gas of non-interacting defects.

INTRODUCTION

The existence of vacancies in metals and intermetallic compounds plays an important role for the kinetic and thermodynamic properties of materials. In this connection the vacancy formation energy is a key concept in the understanding of the processes which occur in alloys during mechanical deformation or heat treatment. The number of vacancies in an elemental metal at equilibrium conditions is usually small. Even close to the melting point it is much less than one atomic percent. However,

the equilibrium vacancy concentration may be of order of ten percent in compounds where vacancies are constitutional (structural) defects.

The formation energies of point defects in metals [1, 2] and compounds [3, 4, 5] can nowadays be obtained from *ab initio* electronic structure calculations based on density functional theory [6]. These energies may be used to evaluate the equilibrium concentrations of point defects as a function of temperature and composition within the framework of statistical mechanical approaches among which the Wagner-Schottky model [7] of a lattice gas of non-interacting point defects is the simplest and most commonly used one. In the present work we perform a complete analysis of possible solutions of the Wagner-Schottky model. We discuss how to characterize the type of constitutional and thermal disorder in different compositional regions of a binary compound using the point defect energies obtained from *ab initio* calculations.

METHODOLOGY

NOTATIONS AND DEFINITIONS

Let us consider a bulk crystal of an elemental metal containing N_{at} atoms and N_V vacancies at zero temperature. The number of vacancies in the system is allowed to change while the number of atoms is kept constant.

The vacancy formation energy (in the dilute limit and at $T=0$) is defined as follows:

$$E_V = \left. \frac{\partial E}{\partial N_V} \right|_{N_V \rightarrow 0} = \left. \frac{\partial \varepsilon}{\partial x_V} \right|_{x_V \rightarrow 0}, \quad (1)$$

where E is the total energy of the system, ε is the energy per atom, and $x_V = N_V/N_{at}$ is the *atomic* concentration of vacancies.

Let us now consider a single-phase, off-stoichiometric alloy having a fixed atomic composition, $A_{1-x}B_x$. We assume two inequivalent sublattices A and B with the multiplicity factors m_A and m_B , respectively, so the ideal stoichiometric composition is $A_{m_A}B_{m_B}$. The alloy components (A atoms and B atoms) and vacancies, $i = \{A, B, V\}$ may occupy N lattice sites on the two sublattices $\alpha = \{A, B\}$. The sublattices have a balanced number of lattice sites, $N_\alpha = (m_\alpha/m)N$, where $m = m_A + m_B$.

Let us denote the number of lattice sites on sublattice α occupied by component i as $N_{i\alpha}$. To describe the distribution of the alloy components between the sublattices, one can use either atomic ($x_{i\alpha} = N_{i\alpha}/N_{at}$) or site ($c_{i\alpha} = n_{i\alpha}/N_{\alpha}$) concentrations. One can easily transform between these two kinds of concentrations using the relationship $c_{i\alpha} = (m/m_{\alpha})x_{i\alpha}/(1+x_V)$, where $x_V = x_{V_A} + x_{V_B}$ is the net concentration of vacancies.

The formation energies, E_d , of the four types of point defects, $d = \{B_A, V_A, A_B, V_B\}$, may be defined similar to Eq. (1):

$$E_d = \left. \frac{\partial \Delta \varepsilon}{\partial x_d} \right|_{x_d \rightarrow 0}, \quad (2)$$

where $\Delta \varepsilon = \varepsilon(A_{1-x}B_x) - (1-x)\varepsilon(A) - x\varepsilon(B)$ is the alloy formation energy (per atom).

Among the four *total defect concentrations*, x_d , only three are linearly independent:

$$x_{B_A} - x_{A_B} + \frac{m_B}{m}x_{V_A} - \frac{m_A}{m}x_{V_B} = \delta. \quad (3)$$

Here $\delta = x - (m_B/m)$ is the deviation from stoichiometry. Those defects which are present in the *maximally ordered state* (i.e. at $T \rightarrow 0$) of an off-stoichiometric alloy are called *constitutional defects*. The defects which appear at finite temperatures are called *thermal defects*, and their concentrations, $x_d^t = x_d - x_d^c$, must obey the following constraint

$$x_{B_A}^t - x_{A_B}^t + \frac{m_B}{m}x_{V_A}^t - \frac{m_A}{m}x_{V_B}^t = 0. \quad (4)$$

That is, thermal defects in ordered compounds always appear in the form of composition-conserving combinations of point defects. A composition-conserving defect (CD) may be specified by a quasichemical reaction:

$$\sum_d n_d d = 0, \quad (5)$$

where the coefficients n_d obey the balance equation similar to Eq. (4). The energy of the reaction,

$$E_{CD} = \sum_d n_d E_d, \quad (6)$$

can be understood as the formation energy of the corresponding CD.

DETAILS OF CALCULATIONS

The defect formation energies were calculated using a supercell approach. Total energy calculations were performed for $2 \times 2 \times 2$ supercells (32 lattice sites) in the case of the fcc structure and $3 \times 3 \times 3$ supercells (54 sites) in the case of the bcc or B2 crystal structures, each supercell containing one point defect.

The present calculations were performed within the framework of an order- N , locally self-consistent Green's function (LSGF) method introduced by Abrikosov *et al.* [8, 9]. The atomic sphere approximation (ASA) was used for the one-electron potential, however, the electrostatic potential and energy contributions due to the non-spherical (multipole) components of the electron density were taken into account. This so-called ASA+M technique allows one to obtain the surface energies [10, 11] and the vacancy formation energies [2] for transition and noble metals with an accuracy typical for the most precise full-potential methods.

The vacancies were modeled by empty spheres. Equal radii were used for all the atomic and empty spheres. Our calculations were performed using the angular momentum cutoff $l_{max} = 3$. The multipole components of the charge density up to $l = 6$ were taken into account. The total energy was calculated in the framework of the local density approximation (LDA). In the case of B2 NiAl, non-local corrections in the form of the generalized gradient approximation [12] (GGA) were taken into account. The core states were recalculated at each self-consistency loop. The volume of each supercell was relaxed to its calculated equilibrium value. The effect of local distortions around point defects was not considered.

VACANCIES IN TRANSITION AND NOBLE METALS

The calculated zero temperature vacancy formation energies for the $3d$, $4d$, and $5d$ transition and noble metals are presented in Fig. 1 together with the recommended experimental values. In our calculations all the metals have been treated in the fcc and bcc crystal structures. We also compare in Fig. 3 the present vacancy formation energies with those obtained in previous full-potential KKR Green's function calculations of vacancies in all the *fcc* $4d$ metals [1]. From this comparison we find that the agreement with the experimental and full-potential results is excellent. We conclude that the ASA+M calculations yield very reasonable vacancy formation energies, in contrast to the standard ASA calculations which typically overestimate the vacancy formation energy by a factor of 2.

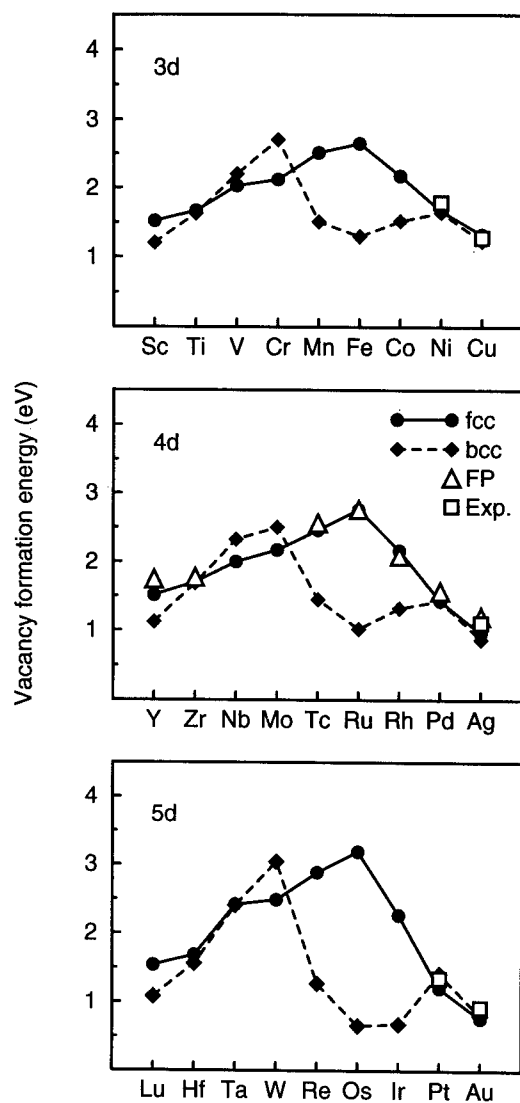


Figure 1 Vacancy formation energies for the 3d, 4d, and 5d transition and noble metals calculated in the fcc and bcc structures and compared with the recommended experimental values [13] (squares) and full-potential calculations [1] (triangles). All calculations were non spin-polarized.

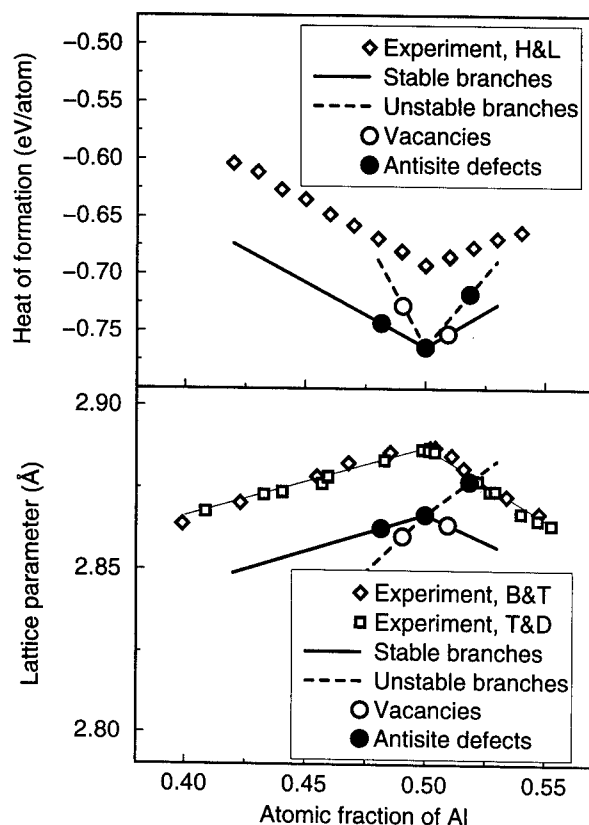


Figure 2 Heat of formation (a) and lattice parameter (b) of NiAl alloys as a function of alloy composition. Experimental data by Henig & Lukas [14] (H&L) (corrected for the standard state of Al), Bradley & Taylor [15] (B&T), and Taylor & Doyle [16] (T&D) are shown for comparison.

POINT DEFECTS IN NIAL

DEFECT FORMATION ENERGIES

In Fig. 2 we compare the calculated and experimental formation energies and the lattice parameters for the B2 NiAl alloys. On either side away from the exact stoichiometric composition the calculated results are reported for two possible branches of the alloys: one corresponds to alloys with constitutional antisite defects (antisite branch), and the other corresponds to alloys with constitutional vacancies (vacancy branch). Our calculations correctly predict the relative stability of the antisite and vacancy branches for the Ni-rich and Al-rich NiAl, respectively. A nice agreement for the slopes of the concentration dependence is seen between the results of our calculations for the stable branches and experimental data.

Table 1 Calculated defect formation energies (eV) in NiAl

Ni_{Al}	V_{Al}	Al_{Ni}	V_{Ni}
1.13	1.91	2.51	0.62

The calculated defect formation energies in NiAl are given in Table 1. By definition, Eq. (2), these energies depend on standard states of the pure elements and therefore do not have an absolute physical meaning. This also makes problematic a direct comparison of the defect formation energies calculated in this work with the results of previous calculations [3, 17, 4] in which different standard states have been used. However, the formation energies of composition-conserving defects are independent of the standard states and can be compared directly. A careful analysis of the theoretical defect formation energies in NiAl shows that all they are in good agreement with each other [18]. The question of how these energies can be used to analyze the equilibrium defect concentrations will be addressed in the following subsections.

WAGNER-SCHOTTKY MODEL

For a highly-ordered $A_{1-x}B_x$ compound containing small concentrations of constitutional and thermal defects, the Wagner-Schottky model (lattice gas of non-interacting point defects) may be applied, which is formulated as follows:

(i) The alloy formation energy (per atom) depends linearly on defect concentrations,

$$\Delta\varepsilon = \Delta\varepsilon_0 + \sum_d E_d x_d \quad , \quad (7)$$

where $\Delta\varepsilon_0$ is the formation energy of the defect-free, stoichiometric $A_{m_A}B_{m_B}$. The parameters E_d are the defect formation energies defined by Eq. (2).

(ii) Only the mean-field configurational entropy is taken into account:

$$s = \sum_{\alpha} \frac{m_{\alpha}}{m} (1 + x_V) \ln \left[\frac{m_{\alpha}}{m} (1 + x_V) \right] - \sum_{\alpha} \sum_i x_{i_{\alpha}} \ln x_{i_{\alpha}} \quad . \quad (8)$$

The minimization of the free energy leads to the following set of Bragg-Williams-type equations for equilibrium defect concentrations:

$$c_{V_A}^{m_A} c_{V_B}^{m_B} = \exp[-E_{MV}/T] \quad , \quad E_{MV} = m_A E_{V_A} + m_B E_{V_B} \quad ;$$

$$\frac{c_{A_B} c_{V_A}}{c_{A_A} c_{V_B}} = \exp[-E_{JA}/T] \quad , \quad E_{JA} = E_{A_B} + E_{V_A} - E_{V_B} \quad ;$$

$$\frac{c_{B_A} c_{V_B}}{c_{B_B} c_{V_A}} = \exp[-E_{JB}/T] \quad , \quad E_{JB} = E_{B_A} + E_{V_B} - E_{V_A} \quad . \quad (9)$$

This set of equations together with Eq. (3) can be solved numerically [5] or analytically [19] in order to obtain the equilibrium defect concentrations.

Let us note that the equilibrium defect concentrations are fully determined by the energies of the three following defect reactions:

(MV): Multivacancy or Schottky defect, $0 \rightarrow m_A V_A + m_B V_B$;

(JA): Vacancy jump to sublattice A, $V_B \rightarrow V_A + A_B$;

(JB): Vacancy jump to sublattice B, $V_A \rightarrow V_B + B_A$.

TYPES OF CONSTITUTIONAL AND THERMAL DISORDER

Possible types of solutions to the Wagner-Schottky model in the low-temperature limit (i.e. types of constitutional and primary thermal defects) may be qualitatively classified in terms of two following dimensionless parameters:

$$z_A = E_{JA}/E_{MV} \quad \text{and} \quad z_B = E_{JB}/E_{MV} \quad . \quad (10)$$

Formally, the set of defect concentrations in a binary alloy of a fixed atomic composition forms a domain belonging to a 3-dimensional hyperplane given by Eq. (3) in the 4-dimensional space of the defect concentrations x_d . Natural boundaries of this domain are given by the inequalities $x_{i_a} \geq 0$. The Wagner-Schottky model is valid at small defect concentrations, i.e. in the vicinity of the boundary of the domain.

Let us first consider the case of $T = 0$. The equilibrium is determined by the global minimum of the alloy formation energy, Eq. (7). As a linear function of the defect concentrations, the latter must have the global minimum at the boundary of the domain (the opposite case corresponds to a compound which is unstable against a spontaneous generation of defects). In a non-degenerate case, the minimum will be at a *vortex* of the domain where all the defect concentrations but one are equal to zero. Which defect type is the constitutional one, i.e. remains in the maximally ordered state of a non-stoichiometric alloy, may be determined from the map shown in Fig. 3a.

For example, our calculations of point defect energies in NiAl give $z_A = z_{Ni} = -0.06$ and $z_B = z_{Al} = 1.50$. From Fig. 3a one easily finds that in an off-stoichiometric $Ni_{0.5-\delta}Al_{0.5+\delta}$ alloy the constitutional defects must be either antisite atoms Ni_{Al} ($\delta < 0$), or vacancies V_{Ni} ($\delta > 0$). The corresponding concentrations are $x_{Ni_{Al}}^c = -\delta$ and $x_{V_{Ni}}^c = 2\delta$.

Thermal disorder appears in the form of composition-conserving reactions, Eq. (5). Any of these reactions can be associated with a certain direction in the domain of possible defect concentrations. Thus, with increasing temperature, the equilibrium state of the alloy will follow a certain trajectory. At low temperatures the trajectory goes in the easiest compliance direction along which the *effective* formation energy

$$E_{CD}^{eff} = -\frac{d \ln x_d^t}{dT^{-1}} \quad , \quad (d \in CD) \quad (11)$$

of the corresponding CD (primary thermal defect) is minimal. Note, however, that at high temperatures the trajectory may deviate from its initial direction.

It is the exact result for non-interacting defects, that the easiest compliance direction coincides with an *edge* of the domain where one has two non-zero concentrations of thermal point defects. Therefore, the primary thermal defect involves only *two* types of point defects.

There are four composition-conserving defects consisting of two types of point defects which may become primary thermal defects in a binary alloy of any composition including the defect-free stoichiometric alloy:

(X): Exchange-antisite defect, $0 \rightarrow B_A + A_B$;

(MV): Multivacancy or Schottky defect, $0 \rightarrow m_A V_A + m_B V_B$;

(MA): Multiple defect of type A, $0 \rightarrow m V_A + m_B A_B$;

(MB): Multiple defect of type B, $0 \rightarrow m V_B + m_A B_A$.

The presence of the constitutional defects in the A-rich or B-rich off-stoichiometric alloys gives an additional possibility to satisfy Eq. (4) by replacing the constitutional antisites by vacancies and vice versa. Since the formation of such a defect may be viewed as a transition of the alloy from the stable to the unstable branch, we will call it an *interbranch* defect:

(IA \pm): Interbranch A, $m_A A_B \rightleftharpoons m V_B$;

(IB \pm): Interbranch B, $m_B B_A \rightleftharpoons m V_A$.

Here we consider two limiting cases: nearly stoichiometric alloy, $x_d^c \ll x_d^t \ll 1$, and concentrated off-stoichiometric (A-rich or B-rich) alloy, $x_d^t \ll x_d^c \ll 1$. The effective formation energy may be evaluated as follows:

$$E_{CD}^{eff} = E_{CD} / (\sum_d' n_d) \quad , \quad (12)$$

where the primed sum does not include the constitutional defects in the case of concentrated off-stoichiometric alloys.

The results for the stoichiometric, A-rich, and B-rich alloys are plotted in Fig. 3b-d. Each field in the corresponding map denotes the range of the z_A and z_B parameters for which the given composition-conserving defect dominates at low temperatures.

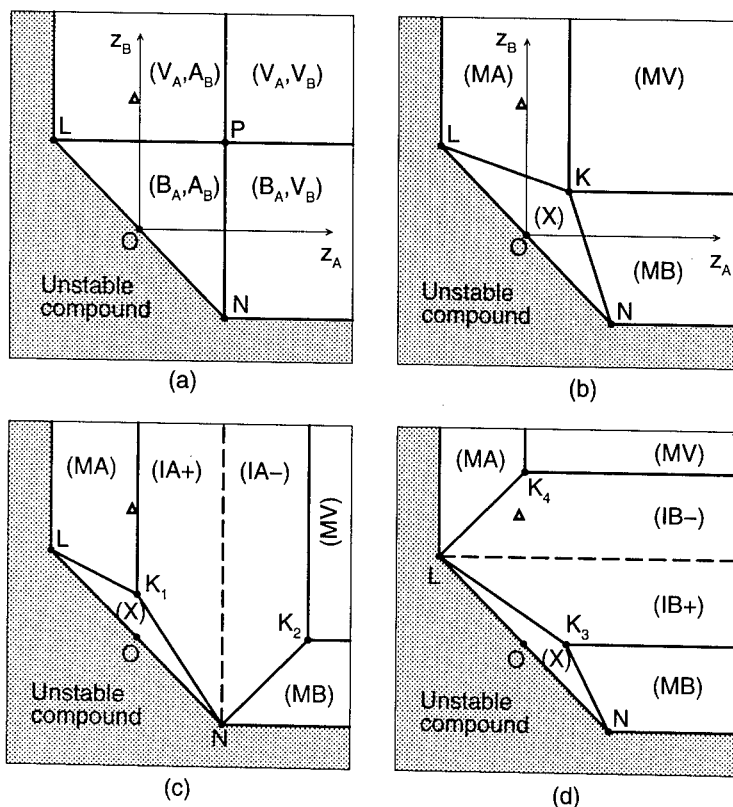


Figure 3 (a) Two-dimensional map of constitutional defects. Each field is labeled by the pair of the constitutional defects (in parentheses) corresponding to B-rich and A-rich regions, respectively. Maps of primary thermal defects in the stoichiometric (b), A-rich (c), and B-rich (d) alloys. Each field is labeled by the name of the composition-conserving defect which dominates at low temperatures. The point coordinates (z_A, z_B) are as follows: O(0,0); L($-m_B^{-1}, m_B^{-1}$); N($m_A^{-1}, -m_A^{-1}$); P(m_A^{-1}, m_B^{-1}); K(m^{-1}, m^{-1}); K₁(0, m^{-1}); K₂(1,0); K₃(m^{-1} , 0); and K₄(0,1). The triangle corresponds to B2 NiAl (A=Ni, B=Al).

In the case of NiAl, we find that the MA (triple) defect, $0 \rightarrow 2V_{Ni} + Ni_{Al}$, dominates in the stoichiometric and Ni-rich NiAl, whereas the IB- (interbranch Al) defect, $2V_{Ni} \rightarrow Al_{Ni}$ is the primary thermal defect in Al-rich NiAl. At high temperatures, however, the triple defect becomes dominant also in Al-rich NiAl [5].

While a triple defect produces three point defects thereby increasing the vacancy concentration, an interbranch defect brings totally -1 point defect into the system and decreases the concentration of vacancies. Due to the competition between the triple and interbranch Al defects in the Al-rich NiAl, the equilibrium vacancy concentration decreases with increasing temperature up to a certain limit, but at higher temperatures the vacancy concentration starts to increase because the triple defect becomes dominant. As a result, a minimum appears in the temperature dependence of the equilibrium vacancy concentration [20, 5, 18].

SUMMARY

We have used the order- N LSGF method in conjunction with an electrostatic multipole correction to the atomic sphere approximation, ASA+M, to calculate the vacancy formation energies in the $3d$, $4d$, and $5d$ transition and noble metals. The results are in excellent agreement with the available full-potential calculations and with experiment. The method has also been applied to calculate the formation energies of native point defects in B2 NiAl.

By means of geometrical analysis of the Wagner-Schottky model, we have shown that the type of constitutional and thermal disorder in a binary compound is completely determined by two parameters that are certain dimensionless combinations of the point defect energies. These parameters are used to construct two-dimensional maps of possible types of disorder for different compositional regions of the compound. The types of thermal disorder in NiAl are characterized.

Acknowledgments

The work of PK is sponsored by SKB AB, the Swedish Nuclear Fuel and Waste Management Company. IA and BJ acknowledge financial support from the Swedish Natural Science Research Council.

REFERENCES

- [1] P. H. Dederichs, B. Drittler, R. Zeller, in *Application of Multiple Scattering theory to Materials Science*, edited by W. H. Butler *et al.* MRS Symposia Proceedings No. 253 (Mater. Res. Soc. Proc.

253, Pittsburgh, 1992) p. 185.

- [2] P. A. Korzhavyi, I. A. Abrikosov, B. Johansson, A. V. Ruban, and H. L. Skriver, *First-principles calculations of the vacancy formation energy in transition and noble metals*. Phys. Rev. B **59**, 11693 (1999).
- [3] C. L. Fu, Y.-Y. Ye, M. H. Yoo, and K. M. Ho, *Equilibrium-Point Defects in Intermetallics with the B2 Structure - NiAl And FeAl*. Phys. Rev. B **48**, 6712 (1993).
- [4] B. Meyer and M Fähnle, *Atomic defects in the ordered compound B2-NiAl: A combination of ab initio electron theory and statistical mechanics* Phys. Rev. B **59**, 6072 (1999).
- [5] P. A. Korzhavyi, I. A. Abrikosov, and B. Johansson, in *High-Temperature Ordered Intermetallic Alloys VIII*, edited by E. P. George, M. Yamaguchi, and M. J. Mills (Mater. Res. Soc. Proc. **552**, Pittsburgh, 1999), in press.
- [6] R. O. Jones, O. Gunnarsson, *The Density Functional Formalism, its Applications And Prospects*. Rev. Mod. Phys. **61**, 689 (1989).
- [7] C. Wagner and W. Schottky, Z. Physik. Chem. B **11**, 163 (1930).
- [8] I. A. Abrikosov, A. M. N. Niklasson, S. I. Simak, B. Johansson, A. V. Ruban, and H. L. Skriver, *Order-N Green's function technique for local environment effects in alloys*. Phys. Rev. Lett. **76**, 4203 (1996).
- [9] I. A. Abrikosov, S. I. Simak, B. Johansson, A. V. Ruban, and H. L. Skriver, *Locally self-consistent Green's function approach to the electronic structure problem*. Phys. Rev. B **56**, 9319 (1997).
- [10] H. L. Skriver and N. M. Rosengaard, *Abinitio Work Function of Elemental Metals*. Phys. Rev. B **46**, 7157 (1992).
- [11] A. V. Ruban, H. L. Skriver, and J. Nørskov, *Surface segregation energies in transition-metal alloys*. Phys. Rev. B **59**, 15990 (1999).
- [12] J. P. Perdew, K. Burke, and M. Ernzerhof, *Generalized gradient approximation made simple*. Phys. Rev. Lett. **77**, 3865 (1996).
- [13] P. Ehrhart, P. Jung, H. Schultz, and H. Ullmaier, in *Atomic Defects in Metals*, edited by H. Ullmaier, Landolt-Börnstein, New Series, Group III, Vol. 25 (Springer-Verlag, Berlin, 1991).
- [14] E.-T. Henig and H. L. Lukas, *Calorimetric Determination of Enthalpy of Formation and Description of Defect Structure of Ordered Beta-Phase (Ni, Cu)_{1-X}Al_X*. Z. Metallkd. **66**, 98 (1975).
- [15] A. J. Bradley and A. Taylor, Proc. R. Soc. A **159**, 56 (1937).
- [16] A. Taylor and N. J. Doyle, J. Appl. Crystallogr. **5**, 201 (1972).

- [17] Y. Mishin and D. Farkas, *Atomistic simulation of point defects and diffusion in B2 NiAl .1. Point defect energetics*. Philos. Mag. A **75**, 169 (1997).
- [18] P. A. Korzhavyi, A. V. Ruban, A. Y. Lozovoi, Yu. Kh. Vekilov, I. A. Abrikosov, and B. Johansson, (to be published).
- [19] M. Hagen and M. W. Finnis, *Point defects and chemical potentials in ordered alloys*. Philos. Mag. A **77**, 447 (1998).
- [20] A. A. Smirnov, Soviet Physics - Doklady **36**, 479 (1991); Phys. Metals **12**, 377 (1993).

ORDER AND DISORDER PHENOMENA AT SURFACES OF BINARY ALLOYS

F. F. Haas

*Institut für Physik, Johannes Gutenberg Universität Mainz
D55099 Mainz*

F. Schmid

*Max-Planck Institut für Polymerforschung, Ackermannweg 10
D55021 Mainz
schmid@mpip-mainz.mpg.de*

K. Binder

*Institut für Physik, Johannes Gutenberg Universität Mainz
D55099 Mainz
binder@chaplin.physik.uni-mainz.de*

ABSTRACT

We present recent Monte Carlo results on surfaces of bcc-structured binary alloys which undergo an order-disorder phase transformation in the bulk. In particular, we discuss surface order and surface induced disorder at the bulk transition between the ordered (DO_3) phase and the disordered (A2) phase. An intricate interplay between different ordering and segregation phenomena leads to a complex surface behavior, which depends on the orientation of the surface under consideration.

INTRODUCTION

The structure and composition of alloys at external surfaces and internal interfaces often differs significantly from that in the bulk. In most cases, this refers only to very few top layers at the surface, over a thickness of order 1 nm. In the vicinity of a bulk phase transition, however, the thickness of the altered surface region can grow to reach mesoscopic dimensions, of order 10-100 nm. If the bulk transition is second order, for example, the thickness of the surface region is controlled by the bulk correlation length, which diverges close to the critical point[1]. Close to first order bulk transitions, mesoscopic wetting layers may form[2].

While these various surface phenomena are fairly well understood in simple systems, such as surfaces of liquid mixtures against the wall of a container, the situation in alloys is complicated due to the interplay between the local structure, the order and the composition profiles. In alloys which undergo an order/disorder transition, for example, the surface segregation of one alloy component can induce surface order[3, 4, 5] or partial surface order[6, 7] at surfaces which are less symmetric than the bulk lattice with respect to the ordered phase. Even more subtle effects can lead to surface order at fully symmetric surfaces[8, 9, 10, 11]. Furthermore, different types of order may be present in such alloys[12], which can interact in a way to affect the wetting behavior significantly [14, 15].

In this contribution, we discuss a situation where such an interplay of segregation and different types of ordering leads to a rather intriguing surface behavior: Surface induced disorder in a binary (AB) alloy on a body centered cubic (bcc) lattice close to the first order bulk transition between the ordered DO_3 phase and the disordered bulk phase. Surface induced disorder is a wetting phenomenon, which can be observed when the bulk is ordered and the surface reduces the degree of ordering – usually due to the reduced number of interacting neighbors [13, 16, 17]. A disordered layer may then nucleate at the surface, which grows logarithmically as the bulk transition is approached. According to the theoretical picture, the surface behavior is driven by the depinning of the interface between the disordered surface layer and the ordered bulk.

MONTE CARLO SIMULATIONS

In order to study the validity of this picture, we consider a very idealized minimal model of a bcc alloy with a DO_3 phase: The alloy is

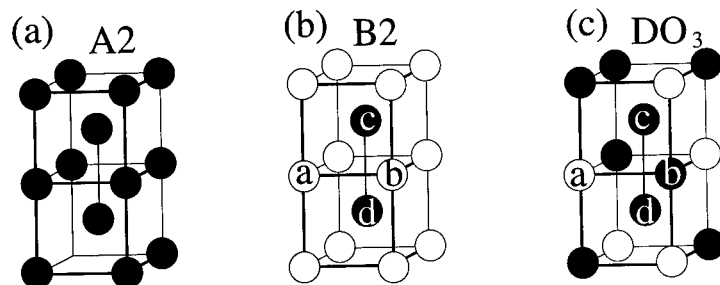


Figure 1 Ordered phases on the bcc lattice: (a) disordered A2 structure, (b) ordered B2 and (c) DO₃ structure. Also shown is assignment of sublattices *a*, *b*, *c* and *d*.

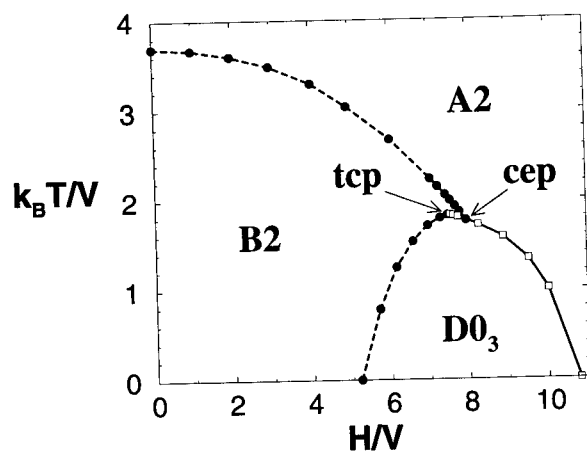


Figure 2 Phase diagram in the $T - H$ plane. First order transitions are solid lines, second order transitions dashed lines. Arrows indicate positions of a critical end point (cep) and a tricritical point (tcp).

mapped on an Ising model on the bcc lattice with negative nearest and next nearest neighbor interactions. The Hamiltonian of the system then reads

$$\mathcal{H} = V \sum_{\langle ij \rangle} S_i S_j + \alpha V \sum_{\langle\langle ij \rangle\rangle} S_i S_j - H \sum_i S_i, \quad (1)$$

where Ising variables $S = 1$ represent A atoms, $S = -1$ B atoms, the sum $\langle ij \rangle$ runs over nearest neighbor pairs, $\langle\langle ij \rangle\rangle$ over next nearest neighbor pairs, and the field H is the appropriate combination of chemical potentials μ_A and μ_B driving the total concentration c of A in the alloy, ($c = (\langle S \rangle + 1)/2$).

The phases exhibited by this model are shown in Figure 1. In the disordered (A2) phase, the A and B particles are distributed evenly among all lattice sites. In the ordered B2 and DO₃ phases, they arrange themselves as to form a superlattice on the bcc lattice. The parameter α was chosen $\alpha = 0.457$, such that the highest temperature at which a DO₃ phase can still exist is roughly half the highest temperature of the B2 phase, like in the experimental case of FeAl. The resulting phase diagram is shown in Figure 2.

In order to characterize the ordered phases, it is useful to divide the bcc lattice into four face centered cubic (fcc) sublattices as indicated on Figure 1, and to define the order parameters

$$\begin{aligned} \psi_1 &= (\langle S \rangle_a + \langle S \rangle_b - \langle S \rangle_c - \langle S \rangle_d)/2 \\ \psi_2 &= (\langle S \rangle_a - \langle S \rangle_b + \langle S \rangle_c - \langle S \rangle_d)/2 \\ \psi_3 &= (\langle S \rangle_a - \langle S \rangle_b - \langle S \rangle_c + \langle S \rangle_d)/2, \end{aligned} \quad (2)$$

where $\langle S \rangle_\alpha$ is the average spin on the sublattice α . In the disordered phase, all sublattice compositions are equal and all order parameters vanish as a consequence. The B2 phase is characterized by $\psi_1 \neq 0$ and the DO₃ phase by $\psi_1 \neq 0$ and $\psi_2 = \pm\psi_3 \neq 0$. The two dimensional vector (ψ_2, ψ_3) is thus an order parameter for DO₃ ordering, and the latter can be characterized conveniently in terms of its absolute value.

$$\psi_{23} = \sqrt{(\psi_2^2 + \psi_3^2)/2}. \quad (3)$$

We have studied free (110) and (100) surfaces of this model at the temperature $T = 1k_B T/V$ in the DO₃ phase close to the transition to the disordered phase. To this end, we have first located the transition point very accurately by thermodynamic integration[18], $H_0/V = 10.00771$ [1]. We have then performed extensive Monte Carlo simulations of slabs each 100-200 layers thick, with free boundary conditions at the two confining

(110) or (100) planes, and periodic boundary conditions in the remaining directions.

In all of our simulations, the average value of the Ising variable in the top layer was one, *i.e.*, the top layer was completely filled with A atoms. Having stated this, we shall disregard this layer in the following and discuss the structure starting from the next layer underneath the surface. The layer order parameters $\psi_i(n)$ and the layer compositions $c(n)$ can be determined in a straightforward manner for (110) layers, since they contain sites from all sublattices. In the case of the (100) layers, it is useful to define c and the ψ_i based on the sublattice occupancies on two subsequent layers.

Fig. 3 shows the calculated profiles for two choices of H close to the transition. One clearly observes the formation of a disordered film at the surface, which increases in thickness as the transition point is approached. The film is characterized by low order parameters ψ_1 and ψ_{23} , and by a slightly increased concentration c of A sites. The structure very close to the surface depends on its orientation: The composition profiles display some characteristic oscillations at a (110) surface, and grow monotonously at a (100) surface. The order ψ_{23} drops to zero. The order ψ_1 drops to zero at the (110) surface, and at the (100) surface, it changes sign and increases again in the outmost two layers. The latter is precisely an example of the segregation induced ordering mentioned earlier[3, 4, 5].

We can thus distinguish between two interesting regions in these profiles: The near-surface region, where the properties of the profiles still reflect the peculiarities of the surface, and the interfacial region, where the profiles are determined from the properties of the interface separating the disordered surface film from the ordered bulk.

The structure of the profiles in the interfacial region is basically determined by the fluctuations of the interface, which are characterized by a transverse correlation length $\xi_{||}$. The latter is in turn driven by the thickness of the film and the interfacial tension σ or, more precisely, by a rescaled dimensionless interfacial tension

$$1/\omega = 4\pi\xi_b^2\sigma/k_BT, \quad (4)$$

with the bulk correlation length ξ_b . The renormalization group theory of critical wetting[2], which should apply here[16], predicts that the transverse correlation length diverges according to a power law

$$\xi_{||} \propto \frac{1}{\sqrt{\omega}}(H_0 - H)^{-\nu_{||}} \quad (5)$$

as H_0 is approached, with the exponent $\nu_{\parallel} = 1/2$. With this knowledge, one can calculate the effective width of the order parameter profiles, $\xi_{\perp} \propto \sqrt{-\omega \ln(H_0 - H)}$, the profiles of layer susceptibilities etc. We have examined these carefully at the (110) interface and the (100) interface, both for the order parameters ψ_1 and ψ_{23} , and we could fit everything nicely into the theoretical picture. Our further discussion here shall focus on the near-surface region.

Assuming that the order in the near-surface region is still determined by the fluctuations of the interface, the theory of critical wetting predicts a power law behavior

$$\psi_{\alpha,1} \propto (H_0 - H)^{\beta_1} \quad (6)$$

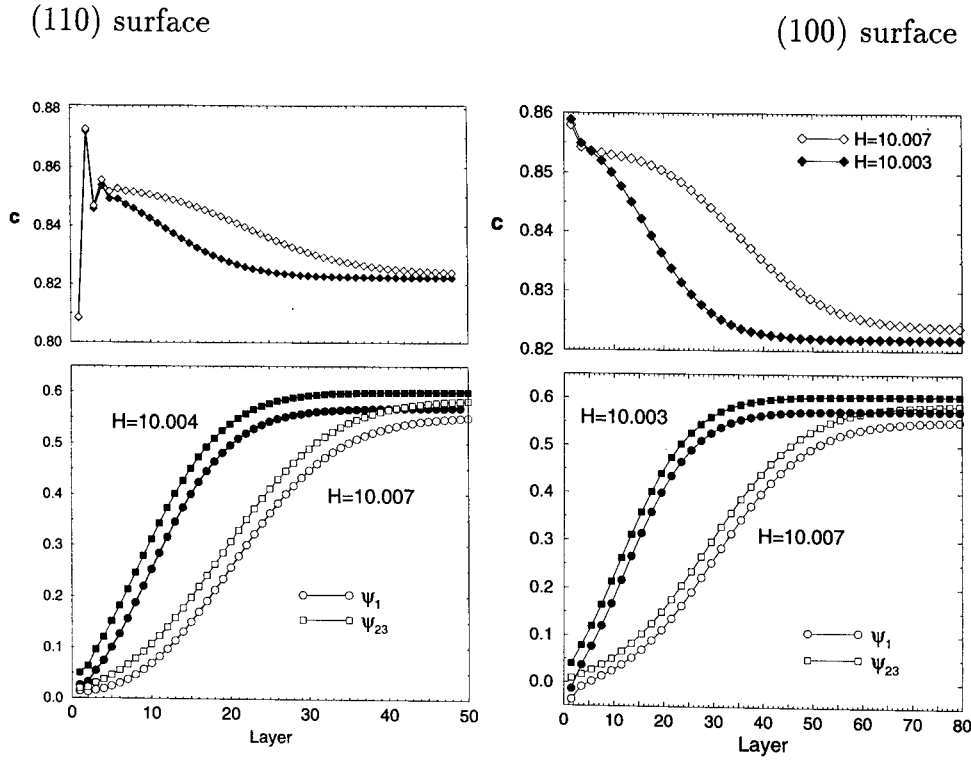
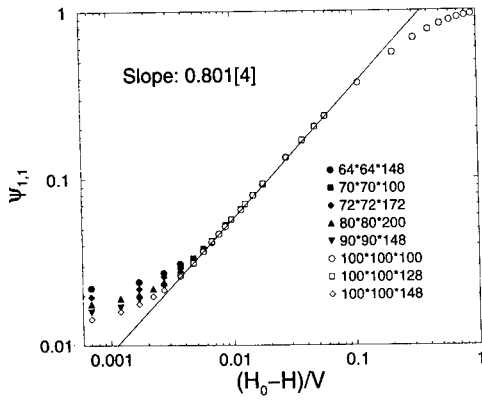


Figure 3 Profiles of the total concentration (top) and order parameters ψ_1 (bottom, circles) and ψ_{23} (bottom, squares) at the (110) surface (left) and at the (100) surface (right) for different fields H in units of V as indicated.

for value $\psi_{\alpha,1}$ of the order parameter ψ_{α} directly at the surface, regardless of the structure of the surface. Figure 4 shows that, indeed,

the surface order parameter $\psi_{23,1}$ decays according to a power law at both the (110) and the (100) surface, with the same exponent and the exponent is in both cases identical within the error, $\beta_1 = 0.618$. Furthermore, we notice strong finite size effects close to the H_0 . Since these are asymptotically driven by the ratio $(L/\xi_{||})$, they can be exploited to determine the behavior of $\xi_{||}$ as the phase transition is approached, *i.e.*, the exponent $\nu_{||}$. The finite size scaling analysis yields $\nu_{||} = 1/2$ [19], in agreement with the theory.

(110) surface



(100) surface

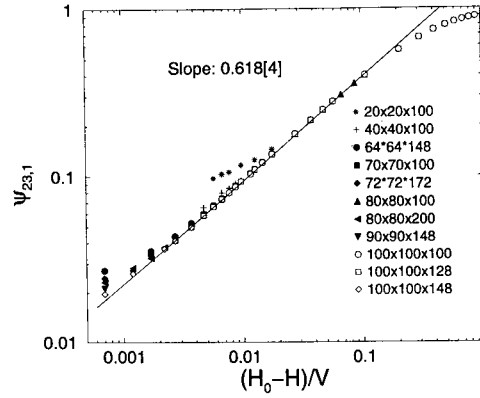


Figure 4 Order parameter ψ_{23} at the surface at the (110) surface (left) and the (100) surface (right) vs. $(H_0 - H)/V$ for different system sizes $L \times L \times D$ as indicated. Solid line shows power law with exponent $\beta_1 = 0.618$.

The profiles of ψ_{23} thus seem entirely determined by the depinning of the interface, in agreement with the standard theory of critical wetting. The situation is however different when one looks at the other order parameter, ψ_1 . This is not particularly surprising in the case of the (100) surface. We have already noted that this surface breaks the symmetry with respect to the ψ_1 ordering, hence the segregation of A particles to the top layer induces additional ψ_1 order at the surface (Figure 5). The (110) surface, on the other hand, is not symmetry breaking. The order ψ_1 decays at the surface, yet with an exponent $\beta_1 = 0.801$ which differs from that observed for ψ_{23} (Figure 6). Even more unexpected, the finite size effects cannot be analyzed consistently with the assumption that the transverse correlation length diverges with the exponent $\nu_{||} = 1/2$, but rather suggest $\nu_{||} = 0.7 \pm 0.05$. The order parameter fluctuations

of ψ_1 at the surface seem to be driven by a length scale which diverges at H_0 with an exponent different from that given by the capillary wave fluctuations of the depinning interface.

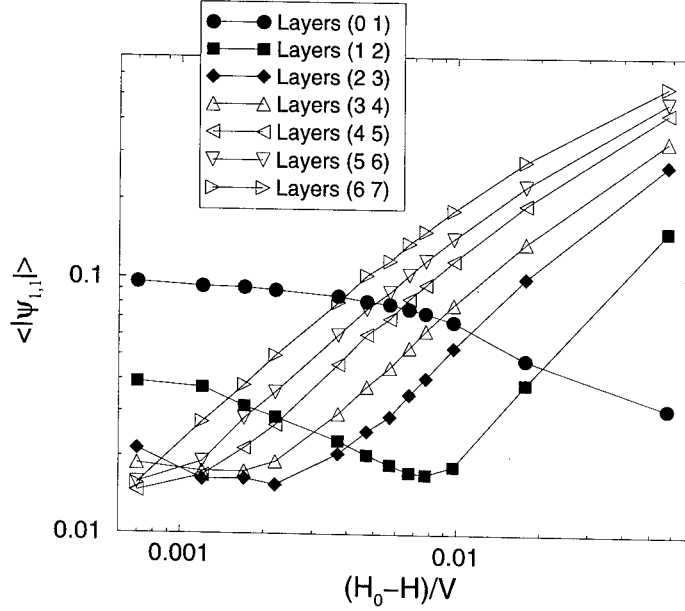


Figure 5 Order parameter ψ_1 in the first layers underneath the (100) surface vs. $(H_0 - H)/V$.

SUMMARY

To summarize, we have seen that the phenomenology of surface induced disorder in a relatively simple bcc alloy with just two coupled types of ordering is much more complex than predicted by the standard theory of surface induced disorder and critical wetting. Looking at our profiles, we were able to distinguish between two regions, the near-surface region and the interfacial regions. In the situations studied in our simulations, it seemed that these regions could be well separated from each other. Some rapid variations of the profiles in the near-surface region, are followed by smooth changes in the interfacial region. The local surface structure affects the total composition profile relatively strongly, and has practically no influence on the profile of the DO_3 order, ψ_{23} . In the case of the B2 order, ψ_1 , the situation is more intriguing. The symmetry breaking (100) surface induces local order in the near-surface region

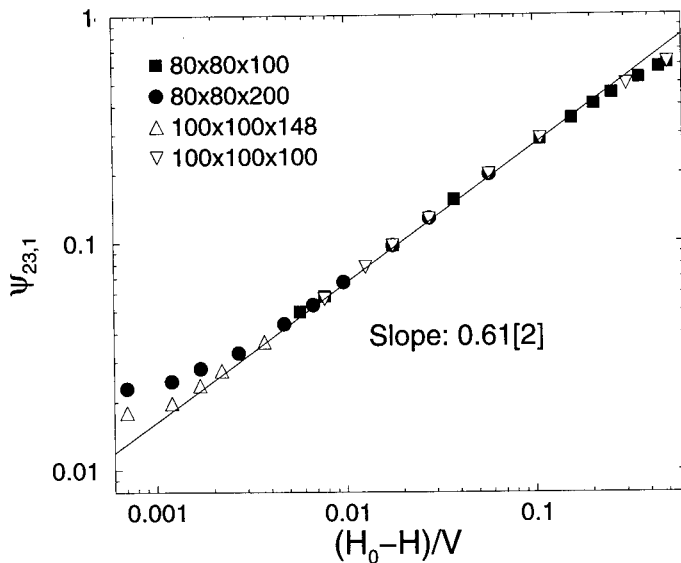


Figure 6 Order parameter ψ_1 at the (110) surface vs. $(H_0 - H)/V$ for different system sizes $L \times L \times D$ as indicated. Solid line shows power law with exponent $\beta_1 = 0.801$.

which apparently does not couple to the interface. At the non-symmetry breaking (110) surface, ψ_1 was found to exhibit qualitatively new and unexpected power law behavior as the wetting transition is approached.

The last observation clearly requires further exploration in the future. The picture will be even more complex in situations where the near-surface profiles and the interfacial profiles cannot be separated any more. We expect that this could be the case, *e.g.*, at (111) surfaces, which break the symmetry with respect to both B2 and DO₃ ordering.

F.F. Haas was supported by the Graduiertenförderung of the Land Rheinland-Pfalz.

REFERENCES

- [1] For reviews on surface critical phenomena see K. Binder in *Phase Transitions and Critical Phenomena*, Vol. 8, p. 1 (1983), C. Domb and J.L. Lebowitz eds., Academic Press, London; S. Diehl, *ibid*, Vol. 8, p. 1 (1983).
- [2] For reviews on wetting see, *e.g.*, P. G. de Gennes, *Rev. Mod. Phys.* **57**, 827 (1985); S. Dietrich in *Phase Transitions and Critical Phenomena*, C. Domb and J.L. Lebowitz eds (Academic Press, New York, 1988), Vol. 12; M. Schick in *Les Houches, Session XLVIII - Liquids at Interfaces*, J. Charvolin, J. F. Joanny, and J. Zinn-Justin eds. (Elsevier Science Publishers B.V., 1990).

-
- [3] F. Schmid, *Surface order in body centered cubic alloys*. Zeitschr. f. Phys. **B 91**, 77 (1993).
 - [4] S. Krimmel, W. Donner, B. Nickel, and H. Dosch, *Surface segregation induced critical phenomena at FeCo(001) surfaces* Phys. Rev. Lett. **78**, 3880 (1997).
 - [5] A. Drewitz, R. Leidl, T. W. Burkhardt, and H. W. Diehl, *Surface critical behavior of binary alloys and antiferromagnets: Dependence of the universality class on surface orientation*. Phys. Rev. Lett. **78**, 1090 (1997); R. Leidl and H. W. Diehl, *Surface critical behavior of bcc binary alloys*. Phys. Rev. B **57**, 1908 (1998); R. Leidl, A. Drewitz, and H. W. Diehl, *Wetting phenomena in bcc binary alloys*. Int. Journal of Thermophysics **19**, 1219 (1998).
 - [6] H. Reichert, P.J. Eng, H. Dosch, I.K. Robinson, *Thermodynamics of surface segregation profiles in Cu₃Au (100) resolved by X ray scattering*. Phys. Rev. Lett. **74**, 2006 (1995).
 - [7] F. Schmid, *Surface ordering and surface segregation in binary alloys*, in *Stability of Materials*, p 173, A. Gonis *et al* eds., (Plenum Press, New York, 1996).
 - [8] L. Mailänder, H. Dosch, J. Peisl, R.L. Johnson, *Near surface critical X-ray scattering in Fe₃Al*. Phys. Rev. Lett. **64**, 2527 (1990).
 - [9] W. Schweika, K. Binder, and D. P. Landau, *Surface induced ordering in models for frustrated face-centered cubic alloys*. Phys. Rev. Lett. **65**, 3321 (1990).
 - [10] W. Schweika, D.P. Landau, and K. Binder, *Surface induced ordering and disordering in face centered cubic alloys: A Monte Carlo study* Phys. Rev. B **53**, 8937 (1996).
 - [11] W. Schweika, D.P. Landau, *Monte Carlo studies of surface induced ordering in Cu₃Au alloy models*, in *Computer Simulation Studies in Condensed-Matter Physics X*, P. 186 (1997).
 - [12] for reviews see D. De Fontaine in *Solid State Physics* **34**, p 73 H. Ehrenreich, F. Seitz and D. Turnbull eds., Academic Press, New York 1979; K. Binder in *Festkörperprobleme (Advances in Solid State Physics)* **26**, p 133, P. Grosse ed., Vieweg, Braunschweig 1986.
 - [13] R. Lipowsky, J. Appl. Phys. **55**, 2485 (1984).
 - [14] E. H. Hauge, *Landau theory of wetting in systems with a two component order parameter* Phys. Rev. B **33**, 3323 (1985).
 - [15] D. M. Kroll, G. Gompper, *Wetting in fcc Ising antiferromagnets and binary alloys*. Phys. Rev. B **36**, 7078 (1987); G. Gompper, D. M. Kroll, *Wetting in fcc Ising antiferromagnets and binary alloys II: Monte Carlo study and renormalization group study*. Phys. Rev. B **38**, 459 (1988).
 - [16] D. M. Kroll and R. Lipowsky, *Interface delocalization transitions in semi-infinite systems*. Phys. Rev. B **28**, 6435 (1983).

-
- [17] H. Dosch, *Critical Phenomena at Surfaces and Interfaces (Evanescent X-ray and Neutron Scattering)*, Springer Tracts in Modern Physics Vol 126 (Springer, Berlin, 1992).
 - [18] K. Binder, *Monte Carlo study of entropy for face-centered cubic Ising antiferromagnets* . Z. Phys. B **45**, 61 (1981).
 - [19] F. F. Haas, Dissertation Universität Mainz (1998); F. F. Haas, F. Schmid, and K. Binder, *Surface induced disorder in body centered cubic alloys, to appear in Phys. Rev. B (June 2000)*, in preparation.

ANALYTICAL DESCRIPTION OF THE SHORT-RANGE ORDER IN ALLOYS WITH MANY-BODY ATOMIC INTERACTIONS

R. V. Chepulsii

Department of Solid State Theory, Institute for Metal Physics, N. A. S. U., UA-03680

Kyiv-142, Ukraine

chep@imp.kiev.ua

ABSTRACT

The high-accuracy ring approximation elaborated in [R. V. Chepulsii and V. N. Bugaev, *J. Phys. Condens. Matter* **10**, 7309; 7327 (1998)] by use of the thermodynamic fluctuation method in the context of the modified thermodynamic perturbation theory as applied to the lattice gas model is generalized for calculation of the short-range order (SRO) parameters and their Fourier transform in disordered binary alloys with many-body atomic interactions of arbitrary order and effective radius of action. On the basis of the comparison with the Monte Carlo simulation data, the numerical accuracy of the derived approximation is studied. It is demonstrated that the temperature dependence of a position in reciprocal space of the SRO Fourier transform's maximums is correctly described within this approximation.

INTRODUCTION

In [1], a number of analytical approximations were elaborated for calculation of the short-range order (SRO) parameters and their Fourier transform in disordered (i.e. without a long-range order) binary alloys with a Bravais crystal lattice and with many-body atomic interactions

of arbitrary orders and effective radius of action. To achieve this aim, the Krivoglaz approach [2] based on application of the thermodynamic fluctuation method within the mean-field approximation was used. From the all obtained approximations, the generalized spherical model one yielded the highest numerical accuracy of results.

However, within the spherical model approximation it is impossible to describe the phenomenon of temperature dependence of a position in reciprocal space of the SRO Fourier transform's maximum in case of temperature independent atomic interactions. The presence of nonpair atomic interactions has no effect on this conclusion [1]. Thus, the use of this approximation is not adequate when the denoted phenomenon takes place, as, e.g., in Pd-V [3, 4], Cu-Au, Cu-Pd [5]-[9] as well as Pt-V [10]-[12] alloys and in a binary Madelung lattice [4, 13].

In case of *absence* of nonpair atomic interactions in alloy, the denoted temperature dependence can be correctly (see [4]) described using the ring approximation, derived by use of the thermodynamic fluctuation method within the first order of a modified thermodynamic perturbation theory under the choice of the inverse effective number of atoms interacting with one fixed atom as a small parameter of expansion [14, 15]. For such description to be correct also in case of alloys with nonpair atomic interactions (such as Cu-Au and Cu-Pd ones [5]-[7]), it seems to be useful to generalize the ring approximation to this case. The present paper is devoted to the performance of such generalization.

THEORY

In general, in the framework of the lattice gas model, the Hamiltonian H of a two-component A-B alloy with a Bravais crystal lattice and with many-body atomic interactions of arbitrary orders and radius of action can be written in the following form [1]

$$\begin{aligned} H &= Nv_0 + \sum_{n=1}^N \frac{1}{n!} \sum_{\mathbf{R}_1, \mathbf{R}_2, \dots, \mathbf{R}_n} V_{\mathbf{R}_1, \mathbf{R}_2, \dots, \mathbf{R}_n}^{(n)} C_{\mathbf{R}_1} C_{\mathbf{R}_2} \dots C_{\mathbf{R}_n} = \\ &= Nv_0 + \sum_{\mathbf{R}} V_{\mathbf{R}}^{(1)} C_{\mathbf{R}} + \frac{1}{2} \sum_{\mathbf{R}_1, \mathbf{R}_2} V_{\mathbf{R}_1, \mathbf{R}_2}^{(2)} C_{\mathbf{R}_1} C_{\mathbf{R}_2} + \\ &\quad + \frac{1}{6} \sum_{\mathbf{R}_1, \mathbf{R}_2, \mathbf{R}_3} V_{\mathbf{R}_1, \mathbf{R}_2, \mathbf{R}_3}^{(3)} C_{\mathbf{R}_1} C_{\mathbf{R}_2} C_{\mathbf{R}_3} + \dots \end{aligned} \quad (1)$$

In Eq. (1): v_0 is the energy per site of "alloy" in which all N sites are occupied by B-type atoms, $V_{\mathbf{R}_1, \mathbf{R}_2, \dots, \mathbf{R}_n}^{(n)}$ is the mixing potential of n -th order ($n=1, 2, \dots, N$), $C_{\mathbf{R}}$ takes the values 1 or 0 depending on whether the site \mathbf{R} is occupied by an A- or B-type atom, the summations on the vectors $\mathbf{R}, \mathbf{R}_1, \mathbf{R}_2, \dots, \mathbf{R}_N$ are carried over all crystal lattice sites. The expression for the grand thermodynamic potential Ω of the system in

question may be presented in the following form [16]:

$$\Omega = \Omega_0 - k_B T \ln \Delta \Gamma + \Delta \Omega, \quad (2)$$

where

$$\Omega_0 = N (v_0 - \mu_B), \quad (3)$$

$$\Delta \Omega = -k_B T \ln \left\langle \exp \left[-\frac{1}{k_B T} \sum_{n=2}^N \frac{1}{n!} \sum_{1, 2, \dots, n} W_{1, 2, \dots, n}^{(n)} C_1 C_2 \dots C_n \right] \right\rangle, \quad (4)$$

$$W_{\mathbf{R}_1, \mathbf{R}_2, \dots, \mathbf{R}_n}^{(n)} = \begin{cases} V_{\mathbf{R}_1, \mathbf{R}_2}^{(2)} + \mu \delta_{\mathbf{R}_1, \mathbf{R}_2} & , \text{ if } n=2 \\ V_{\mathbf{R}_1, \mathbf{R}_2, \dots, \mathbf{R}_n}^{(n)} & , \text{ if } n > 2 \end{cases}, \quad (5)$$

$$\mu = 2 \left(V_{\mathbf{R}}^{(1)} - \mu_A + \mu_B \right), \quad (6)$$

μ_A and μ_B are the chemical potentials of A- and B-type atoms, respectively, T is the absolute temperature, k_B is the Boltzmann constant, the sign $\langle \dots \rangle$ means the statistical average over all states with given values of the long-range order parameters, $\delta_{\mathbf{R}_1, \mathbf{R}_2}$ is the Kronecker's delta,

$$\ln \Delta \Gamma = - \sum_{\mathbf{R}} [P_{\mathbf{R}} \ln P_{\mathbf{R}} + (1 - P_{\mathbf{R}}) \ln (1 - P_{\mathbf{R}})], \quad (7)$$

$$P_{\mathbf{R}} = \langle C_{\mathbf{R}} \rangle \quad (8)$$

and is equal to the probability of finding an A-type atom at the site \mathbf{R} . Notice that the values of the chemical potentials μ_A and μ_B and, therefore [see (6)], the value of μ must satisfy the general thermodynamic relationships

$$P_{\mathbf{R}} = \langle C_{\mathbf{R}} \rangle \quad (9)$$

and is equal to the probability of finding an A-type atom at the site \mathbf{R} . Notice that the values of the chemical potentials μ_A and μ_B and, therefore [see (6)], the value of μ must satisfy the general thermodynamic relationships

$$\langle N_A \rangle = - (\partial \Omega / \partial \mu_A)_T, \quad \langle N_B \rangle = - (\partial \Omega / \partial \mu_B)_T. \quad (10)$$

According to the general approach of the thermodynamic perturbation theory [14]-[19], the expression (4) for $\Delta \Omega$ can be expanded in a cumulant series in powers of the inverse temperature. Following to the

generalized Brout's approach [17, 16], let us select the contributions Ω_{zero} and Ω_{ring} to the cumulant expansion from the summands proportional, respectively, to zeroth and first powers of the quantity z^{-1} with z being equal to the effective number of atoms interacting with one fixed atom:

$$\Omega_{\text{zero}} = \Omega_0 + \sum_{n=1}^N \frac{1}{n!} \sum_{\mathbf{R}_1, \mathbf{R}_2, \dots, \mathbf{R}_n} W_{\mathbf{R}_1, \mathbf{R}_2, \dots, \mathbf{R}_n}^{(n)} P_{\mathbf{R}_1} P_{\mathbf{R}_2} \dots P_{\mathbf{R}_n} - k_B T \ln \Delta \Gamma, \quad (11)$$

$$\Omega_{\text{ring}} = -\frac{k_B T}{2} \sum_{n=1}^{\infty} \frac{1}{n (-k_B T)^n} \sum_{\mathbf{R}_1, \mathbf{R}_2, \dots, \mathbf{R}_n} f_{\mathbf{R}_1 - \mathbf{R}_2} f_{\mathbf{R}_2 - \mathbf{R}_3} \dots f_{\mathbf{R}_n - \mathbf{R}_1}, \quad (12)$$

where

$$f_{\mathbf{R}_i - \mathbf{R}_j} = P_{\mathbf{R}_i} (1 - P_{\mathbf{R}_i}) \sum_{l=0}^{N-2} \sum_{\mathbf{R}'_1, \mathbf{R}'_2, \dots, \mathbf{R}'_l} \frac{P_{\mathbf{R}'_1} P_{\mathbf{R}'_2} \dots P_{\mathbf{R}'_l}}{l!} W_{\mathbf{R}_i, \mathbf{R}_j, \mathbf{R}'_1, \mathbf{R}'_2, \dots, \mathbf{R}'_l}^{(2+l)}. \quad (13)$$

In the case of the disordered state of alloy, when $P_{\mathbf{R}} = c = N_A/N$ for any \mathbf{R} , we have

$$\begin{aligned} \Omega_{\text{zero}} |_{P=c} &= \Omega_0 + N \left\{ \frac{\mu c^2}{2} + \sum_{l=2}^N \frac{c^l}{l!} \tilde{V}_{0,0,\dots,0}^{(l)} + k_B T [c \ln c + (1-c) \ln (1-c)] \right\}, \\ & \quad (14) \end{aligned}$$

$$\Omega_{\text{ring}} |_{P=c} = \frac{k_B T}{2} \sum_{\mathbf{q}} \ln \left[1 + \frac{c(1-c)}{k_B T} (\mu + \tilde{V}_{\mathbf{q}}^{\text{eff}}) \right], \quad (15)$$

where

$$\tilde{V}_{\mathbf{k}}^{\text{eff}} = \sum_{n=0}^{N-2} \frac{c^n}{n!} \tilde{V}_{\mathbf{k},0,0,\dots,0}^{(2+n)} = \tilde{V}_{\mathbf{k}}^{(2)} + c \tilde{V}_{\mathbf{k},0}^{(3)} + \frac{c^2}{2} \tilde{V}_{\mathbf{k},0,0}^{(4)} + \dots, \quad (16)$$

$$\tilde{V}_{1,2,\dots,n-1}^{(n)} = \sum_{1,2,\dots,n-1} V_{1,2,\dots,n-1,0}^{(n)} \exp \left(-i \sum_{i=1}^{n-1} \mathbf{k}_i \mathbf{R}_i \right) \quad (17)$$

is the Fourier transform of the n -th order mixing potential and each

summation on wave vector is carried over all the points specified by the cyclic boundary conditions in the corresponding first Brillouin zone.

Applying the thermodynamic fluctuation method [1, 2],[14]-[19] to the expressions for Ω_{zero} and $\Omega_{\text{zero}} + \Omega_{\text{ring}}$ and using (10), we obtain, respectively, the two following approximate expressions

$$\alpha_{\mathbf{k}}^{\text{SM}} = \left[1 + \frac{c(1-c)}{k_{\text{B}}T} (\mu + \tilde{V}_{\mathbf{k}}^{\text{eff}}) \right]^{-1}, \quad (18)$$

$$\alpha_{\mathbf{k}}^{\text{ring}} = \left[1 + \frac{c(1-c)}{k_{\text{B}}T} (\mu + \tilde{V}_{\mathbf{k}}^{\text{eff}} + \tilde{V}_{\mathbf{k}}^{\text{ring}}) \right]^{-1} \quad (19)$$

for the Fourier transform $\alpha_{\mathbf{k}}$ of the SRO Warren-Cowley parameters $\alpha_{\mathbf{R}}$

$$\alpha_{\mathbf{k}} = \sum_{\mathbf{R}} \alpha_{\mathbf{R}} \exp(-i\mathbf{k}\mathbf{R}), \quad (20)$$

$$\alpha_{\mathbf{R}_1 - \mathbf{R}_2} = \left(\langle C_{\mathbf{R}_1} C_{\mathbf{R}_2} \rangle - c^2 \right) [c(1-c)]^{-1}. \quad (21)$$

In (19)

$$\tilde{V}_{\mathbf{k}}^{\text{ring}} = N^{-1} \sum_{\mathbf{q}} \left\{ \frac{c(1-c)\varphi_{\mathbf{q}}^{(4)} - /2 + (1-2c)\varphi_{\mathbf{q}}^{(3)} - \varphi_{\mathbf{q}}^{(2)}}{1 + \varphi_{\mathbf{q}}^{(2)} c(1-c)/(k_{\text{B}}T)} - \right. \\ \left. - \frac{\left[c(1-c)\varphi_{\mathbf{q}}^{(3)} - \right]^2 + 2c(1-c)(1-2c)\varphi_{\mathbf{q}}^{(2)}\varphi_{\mathbf{q}}^{(3)} - + (1-2c)^2\varphi_{\mathbf{q}}^{(2)}\varphi_{\mathbf{q}}^{(2)}}{2k_{\text{B}}T \left[1 + \varphi_{\mathbf{q}}^{(2)} c(1-c)/(k_{\text{B}}T) \right] \left[1 + \varphi_{\mathbf{q}}^{(2)} - c(1-c)/(k_{\text{B}}T) \right]} \right\} \quad (22)$$

and, taking into account only pair, triplet and quadruple atomic interactions,

$$\begin{aligned} \varphi_{\mathbf{k}}^{(2)} &= \mu + \tilde{V}_{\mathbf{k}}^{\text{eff}} = \mu + \tilde{V}_{\mathbf{k}}^{(2)} + c\tilde{V}_{\mathbf{k},0}^{(3)} + \frac{c^2}{2}\tilde{V}_{\mathbf{k},0,0}^{(4)}, \\ \varphi_{\mathbf{k}_1,\mathbf{k}_2}^{(3)} &= \tilde{V}_{\mathbf{k}_1,\mathbf{k}_2}^{(3)} + c\tilde{V}_{\mathbf{k}_1,\mathbf{k}_2,0}^{(4)}, \\ \varphi_{\mathbf{k}_1,\mathbf{k}_2,\mathbf{k}_3}^{(4)} &= \tilde{V}_{\mathbf{k}_1,\mathbf{k}_2,\mathbf{k}_3}^{(4)}. \end{aligned} \quad (23)$$

In both expressions (18) and (19), μ is the quantity to be found from the equation

$$N^{-1} \sum_{\mathbf{q}} \alpha_{\mathbf{q}} = 1 \quad (24)$$

at substitution of the corresponding function $\alpha_{\mathbf{k}}$.

The expression (18) corresponds to the generalized spherical model approximation derived in [1]. The expression (19) is a generalization of the ring approximation [14] to this case of alloys with nonpair atomic interactions. In analogy, we shall call this approximation the generalized ring one. Note that such name of the approximation is in accordance with the topology of the diagrams corresponding to Ω_{ring} within the diagram technique developed in [16].

INSTABILITY WAVE VECTORS

Within the mean-field approximation, as it follows from the corresponding expression for the critical temperature T_c of the order-disorder phase transition in alloy with only pair atomic interactions:

$$k_B T_c = -c(1-c) \min_{\mathbf{k}} \tilde{V}_{\mathbf{k}}^{(2)} = -c(1-c) \tilde{V}_{\mathbf{k}_0}^{(2)}, \quad (25)$$

one should investigate the minima of the Fourier transform $\tilde{V}_{\mathbf{k}}^{(2)}$ of the pair mixing potential, if one wants to find the instability wave vector \mathbf{k}_0 [18]-[20]. Because the positions of the maxima of the Fourier transform $\alpha_{\mathbf{k}}$ of the SRO parameters correspond to the instability wave vectors when the temperature approaches its critical value, the above conclusion may be achieved from the following mean-field like Krivoglaz-Clapp-Moss formula [2, 21]

$$\alpha_{\mathbf{k}} = A \left[1 + \frac{c(1-c)}{k_B T} \tilde{V}_{\mathbf{k}}^{(2)} \right]^{-1} \quad (26)$$

(A is a normalization factor), which is characterized by the coincidence of the positions of the maxima of $\alpha_{\mathbf{k}}$ with the positions of the minima of $\tilde{V}_{\mathbf{k}}^{(2)}$ in the reciprocal space at arbitrary values of the concentration and temperature.

In case of presence of nonpair atomic interactions in an alloy, the expressions

$$k_B T_c = -c(1-c) \min_{\mathbf{k}} \tilde{V}_{\mathbf{k}}^{\text{eff}} = -c(1-c) \tilde{V}_{\mathbf{k}_0}^{\text{eff}} \quad (27)$$

(see [1]) and (18) are the analogies of (25) and (26), respectively. Therefore, in this case, the function $\tilde{V}_{\mathbf{k}}^{\text{eff}}$ plays the role of $\tilde{V}_{\mathbf{k}}^{(2)}$, and the minima of $\tilde{V}_{\mathbf{k}}^{\text{eff}}$ rather than of $\tilde{V}_{\mathbf{k}}^{(2)}$ should be investigated if one wants to find the instability wave vectors within the mean-field approximation. Note that the information concerning the topology of the function $\tilde{V}_{\mathbf{k}}^{\text{eff}}$ is also useful for prediction of a high temperature behavior of the SRO Fourier transform, because, at high temperatures, the generalized spherical model approximation (18) demonstrates the high numerical accuracy of results [14].

From the corresponding expressions (19)-(24), it follows that, within the generalized ring approximation, the positions of the maxima of $\alpha_{\mathbf{k}}$ may not coincide with the positions of the minima of $\tilde{V}_{\mathbf{k}}^{\text{eff}}$ in the reciprocal space. Thus, within this approximation, even in case of temperature independent atomic interactions, the description of the temperature dependence of a position in reciprocal space of the SRO Fourier transform's

maximum in principle is possible, in contrast to the generalized spherical model approximation. To verify such possibility, we consider the case of Ni-V alloy in the next section.

CASE OF NI-V ALLOY

The parameters of atomic interactions for this alloy were calculated within the Connolly-Williams method in [22]. By use of these parameters, we investigated the behavior of the Fourier transform of the SRO parameters in cases of Ni_3V ($c=0.25$) and NiV ($c=0.50$) disordered alloys within the generalized spherical model (18) and ring (19) approximations. The obtained results are presented in Fig. 1.

From Fig. 1, it follows that, in the case of Ni_3V ($c=0.25$) alloy, the SRO Fourier transforms $\alpha_{\mathbf{k}}$ as calculated within both the generalized spherical model and ring approximations have the absolute maxima in $W(1, \frac{1}{2}, 0)$ point. (We present the decart coordinates of points in a reciprocal space in units of $\frac{2\pi}{a}$, where a is the lattice parameter).

In the case of NiV ($c=0.50$) alloy, the SRO Fourier transforms $\alpha_{\mathbf{k}}$ as calculated within the generalized spherical model and ring approximations have the absolute maxima in different points: in $X(1, 0, 0)$ and in a non-high symmetry point belonging to the high-symmetry line $\Sigma(\frac{h}{\sqrt{2}}, \frac{h}{\sqrt{2}}, 0)$, respectively. Note that the results presented in Fig. 1 obtained within the generalized ring approximation in the case of NiV ($c=0.50$) alloy correspond to comparatively low temperatures. At sufficiently high temperatures, the results obtained within both the generalized spherical model and ring approximations are identical in accordance with the high numerical accuracy of the generalized spherical model approximation at high temperatures [1].

CONCLUSIONS

From a comparison of the data presented in Fig. 1 and those obtained in [23], it follows that the results obtained within the generalized ring approximation is in agreement with that of the Monte Carlo simulation in both considered cases, in contrast to those obtained within the generalized spherical model approximation. Thus, within the generalized ring approximation, the description of the temperature dependence of a position in reciprocal space of the SRO Fourier transform's maximum for temperature independent atomic interactions is really possible and correct. Note that the knowledge of the correct position of such maximum when the temperature approaches its critical value is helpful for determination of the long-range order superstructure appearing as a result of

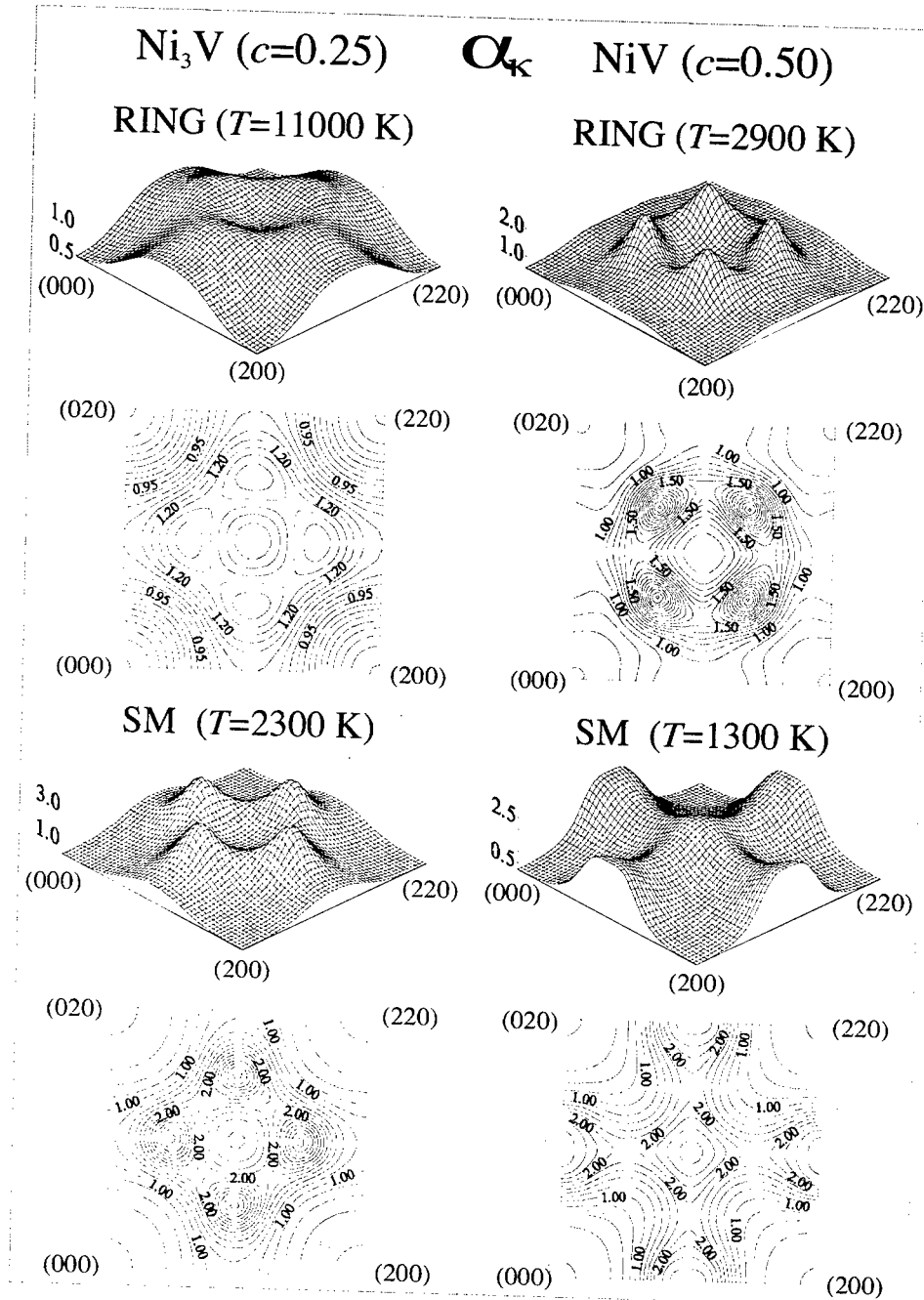


Figure 1. The dependencies of the Fourier transform of the SRO parameters with respect to the wave vector within the plane $(h,k,0)$ in the corresponding first Brillouin zone as calculated within the generalized spherical model (17) (SM) and ring (18) (RING) approximations in the cases of Ni_3V and NiV alloys.

order-disorder phase transition, because the position of this maximum characterizes one of such superstructure wave vectors [18]-[20].

It should be noted that, within both the generalized spherical model and ring approximations, the effective radius of atomic interactions in alloy is not limited *a priori* (in contrast to the widely used Monte Carlo and cluster-variation methods), because only the Fourier transforms of the mixing potentials appear in the corresponding expressions (18)-(24). Moreover, it is revealed [1, 16] that the numerical accuracies of these approximations turn higher with increasing such effective radius. Thus, the generalized spherical model and ring approximations may be recommended for a description of actual alloys with a long-range character of atomic interactions caused, for example, by the strain-induced (elastic) effects. Note that, within the high-accuracy Tokar-Masanskii-Grishchenko approximation [24, 25] based on application of the γ -expansion method [26], it is possible to take into account long-range contributions of only the pair interatomic potentials, whereas the nonpair atomic interactions are not taken into account within this approximation at all. As shown in [16], the generalized spherical model and ring approximations can be readily applied in combination with such widely used approaches for calculation of interatomic potentials in alloys as the generalized perturbation [27]-[30] and Connolly-Williams [31]-[32] methods as well as the mean-field concentration functional theory [33]-[35].

The other important advantage of the generalized spherical model and ring approximations is the ability to calculate the Fourier-transform of the SRO parameters directly, without neglecting the values of these parameters for coordination shells with large radius, as is done within the Monte Carlo and cluster-variation methods. It is especially important in the case of alloys with long-range atomic interactions and/or of alloys whose temperature is close to the order-disorder phase transition temperature (due to the corresponding increase of the effective radius of interatomic correlations). In [16], it is revealed that the above-mentioned neglect may result in a wrong description of the SRO Fourier transform in the vicinity of the origin of the reciprocal space. Within the generalized spherical model and ring approximations, through the integration of the SRO Fourier-transform over the first Brillouin zone, it is possible to calculate the SRO parameter for an arbitrary given coordination shell as well.

ACKNOWLEDGMENTS

The author thanks Dr. V. N. Bugaev, Dr. V. I. Tokar and Dr. I. Tsatskis for helpful discussions. He is also grateful to Prof. V. B. Molodkin and Dr. A. N. Timoshevskii for constant support during this

research. The support from the Foundation of the Fundamental Investigations of Ukraine through Grants No. 2.4/965 and No. 2.4/993 and from STCU through Grant No. 120 is gratefully acknowledged.

REFERENCES

- [1] R. V. Chepul'skii, *Analytical description of the short-range order in alloys with many-body atomic interactions*, J. Phys.: Condens. Matter **10**, 1505 (1998).
- [2] M. A. Krivoglaz, *Diffuse Scattering of X-rays and Thermal Neutrons by Fluctuational Inhomogeneities of Imperfect Crystals* (Springer-Verlag, Berlin-Heidelberg, 1996).
- [3] F. Solal, R. Caudron, F. Ducastelle, A. Finel and A. Loiseau, *In situ Diffuse Neutron-Scattering On Disordered Pd₃V and Ni₃V*, Phys. Rev. Lett. **58**, 2245 (1987).
- [4] R. V. Chepul'skii and V. N. Bugaev, *Analytical description of temperature dependence of a position in reciprocal space of the short-range order Fourier transform's maximum in alloys*, J. Phys. Chem. Solids **59**, 1469 (1998).
- [5] V. V. Ozoliņš, C. Wolverton and A. Zunger, *Anomalous temperature dependence of the X-ray diffuse scattering intensity of Cu₃Au*, Phys. Rev. Lett. **79**, 955 (1997).
- [6] C. Wolverton, V. V. Ozoliņš and A. Zunger, *First-principles theory of short-range order in size-mismatched metal alloys: Cu-Au, Cu-Ag, and Ni-Au*, Phys. Rev. B **57**, 4332 (1998).
- [7] V. V. Ozoliņš, C. Wolverton and A. Zunger, *Cu-Au, Ag-Au, Cu-Ag, and Ni-Au intermetallics: First-principles study of temperature-composition phase diagrams and structures*, Phys. Rev. B **57**, 6427 (1998).
- [8] I. Tsatskis, *Quadratic short-range order corrections to the mean-field free energy*, J. Phys.: Condens. Matter **10**, L145 (1998).
- [9] I. Tsatskis and E. K. H. Salje, *Short-range order in a steady state of irradiated Cu-Pd alloys: comparison with fluctuations at thermal equilibrium*, J. Phys.: Condens. Matter **10**, 3791 (1998).
- [10] D. Le Bolloc'h, R. Caudron and A. Finel, *Experimental and theoretical study of the temperature and concentration dependence of the short-range order in Pt-V alloys*, Phys. Rev. B **57**, 2801 (1998).
- [11] I. Tsatskis, *Origin of the anomaly in diffuse scattering from disordered Pt-V alloys*, Phys. Lett. A **241**, 110 (1998).

- [12] I. Tsatskis, *Coalescence of the Fermi surface related diffuse intensity peaks in disordered alloys*, Phil. Mag. Lett. **78**, 403 (1998).
- [13] C. Wolverton and A. Zunger, *Short-Range and Long-Range Order of the Binary Madelung Lattice*, Phys. Rev. B **51**, 6876 (1995).
- [14] R. V. Chepulskii and V. N. Bugaev, *Analytical methods for calculation of the short-range order in alloys: I. General theory*, J. Phys.: Condens. Matter **10**, 7309; 7327 (1998).
- [15] R. V. Chepulskii, *Analytical methods for calculation of the short-range order in alloys: I. General theory*, J. Phys. Chem. Solids **59**, 1473 (1998).
- [16] R. V. Chepulskii, *The effect of nonpair atomic interactions on the short-range order in disordered alloys*, J. Phys.: Condens. Matter **11**, 8645; 8661 (1999).
- [17] R. Brout, *Phase Transitions* (Benjamin, New York, 1965).
- [18] A. G. Khachaturyan, , J. Prog. Mat. Sci. **22**, 1 (1978).
- [19] D. de Fontaine, , Solid State Physics **34**, 73 (1979).
- [20] A. G. Khachaturyan, *Theory of Structural Transformations in Solids* (John Wiley & Sons, New York, 1983).
- [21] P. C. Clapp and S. C. Moss, *Correlation Functions of Disordered Binary Alloys. I-*, Phys. Rev. **142**, 418 (1966); *ibid.* **171**, 754 (1968).
- [22] Z. W. Lu and A. Zunger, *Unequal Wave Vectors in Short-Range Versus Long-Range Ordering in Intermetallic Compounds*, Phys. Rev. B **50**, 6626 (1994).
- [23] C. Wolverton and A. Zunger, *First-Principles Theory of Short-Range Order, Electronic Excitations and Spin Polarization in Ni-V and Pd-V Alloys*, Phys. Rev. B **52**, 8813 (1995).
- [24] V. I. Tokar, I. V. Masanskii and T. A. Grishchenko, *A Simple and Accurate Theory of Short-Range Order in Alloys*, J. Phys.: Condens. Matter **2**, 10199 (1990).
- [25] I. V. Masanskii, V. I. Tokar and T. A. Grishchenko, *Pair Interactions in Alloys Evaluated From Diffuse-Scattering Data*, Phys. Rev. B **44**, 4647 (1991).
- [26] V. I. Tokar, *New Ward-Takahashi Identities in Statistical Mechanics of Many- Fermion Systems*, Phys. Lett. A **110**, 453 (1985).
- [27] F. Ducastelle and F. Gautier, *Generalized Perturbation-Theory in Disordered Transitional Alloys*, J. Phys. F: Metal Phys. **6**, 2039 (1976).
- [28] F. Ducastelle, *Order and Phase Stability in Alloys* (Elsevier, New York, 1991).

-
- [29] A. Gonis, X. G. Zhang, A. J. Freeman, P.E.A Turchi, G.M. Stocks, and D. M. Nicholson *Configurational Energies and Effective Cluster Interactions in Substitutionally Disordered Binary-Alloys*, Phys. Rev. B **36**, 4630 (1987).
- [30] P. E. A. Turchi, G. M. Stocks, W. H. Butler, D. M. Nicholson, and A. Gonis *1st-Principles Study of Ordering Properties of Substitutional Alloys Using the Generalized Perturbation Method*, Phys. Rev. B **37**, 5982 (1988).
- [31] J. W. D. Connolly and A. R. Williams, *Density-Functional Theory Applied to Phase-Transformations in Transition-Metal Alloys*, Phys. Rev. B **27**, 5169 (1983).
- [32] A. Zunger, in *Statics and Dynamics of Alloy Phase Transformations*, ed. P. E. A. Turchi and A. Gonis, NATO ASI Series (Plenum, New York, 1994) p. 361.
- [33] B. L. Gyorffy and G. M. Stocks, *Concentration Waves and Fermi Surfaces in Random Metallic Alloys*, Phys. Rev. Lett. **50**, 374 (1983).
- [34] G. M. Stocks et al., in *Statics and Dynamics of Alloy Phase Transformations*, ed P. E. A. Turchi and A. Gonis, NATO ASI Series (Plenum, New York, 1994) p. 305.
- [35] J. B. Staunton, D. D. Johnson and F. J. Pinski, *Compositional Short-Range Ordering in Metallic Alloys - Band- Filling, Charge-Transfer, and Size Effects From a 1st- Principles All-Electron Landau-Type Theory*, Phys. Rev. B **50**, 1450 (1994).

CHANGES IN THE ATOMIC COORDINATES AND STATE OF ANION AND CATION ORDER INDUCED BY ALLOYING AND TEMPERATURE CHANGE IN $Y_2[M(2)_yM(1)_{1-y}]_2O_7$ PYROCHLORE SOLID SOLUTIONS

Bernhardt J. Wuensch¹ and Kevin W. Eberman²

¹ Department of Materials Science and Engineering
Massachusetts Institute of Technology
Cambridge, Massachusetts 02139-4307

² 3M Center, Building 204-C-26, St. Paul, Minnesota 55144-1000

ABSTRACT

Pyrochlore oxides, $A_2B_2O_7$, are superstructures based upon a fluorite-type (C1) arrangement of ions. Usually the B cation is tetravalent, and A is a larger trivalent ion. These species are ordered among the 8-coordinated interstices in the simple cubic anion array. To achieve charge balance, one-eighth of the anions in the parent fluorite array are omitted in an ordered fashion such that only six anions coordinate B. The nearest-neighbor oxygen ion to the vacant anion site is displaced from its ideal location and relaxes toward the vacancy. The driving force for the ordering that creates the pyrochlore superstructure is believed to be the size difference between the A and B cations. Some, but not all, pyrochlores disorder when heated to very high temperature (usually above 2000° C). It has recently been observed that substitution of a larger tetravalent cation in solid solution in the B site, $A_2(B'_yB_{1-y})_2O_7$, will progressively drive the system toward disorder to a non-stoichiometric fluorite structure which lacks long-range order.

Details of the atomic arrangements that accompany chemically-driven disorder in a number of pyrochlore solid solutions were determined through Rietveld analyses of neutron and X-ray powder diffraction patterns. Results have been obtained for solid solutions with $A = Y$ and pair-wise substitution of Zr, Sn or Ti in the B site. One would anticipate the rates of disorder in the cation and anion arrays to be coupled through Coulombic interactions. Remarkably, anion and cation arrays disorder at independent rates in all systems. The (Sn-Ti) solid solutions displayed little disorder despite appreciable overlap in the range of radius ratio R_A/R_B with that of other systems. Thermally-induced disorder was examined with in-situ diffraction measurements at temperatures up to 1500° C and revealed behavior similar to the effects induced by solid solution.

INTRODUCTION

The pyrochlores, $A_2B_2O_7$, constitute a large family of ceramic oxides with a remarkable range of physical properties: catalytic activity, electro-optic and piezoelectric behavior, ferro and ferrimagnetism, and giant magnetoresistance. Our interest in the materials is based in part on their electrical behavior. This can be metallic, semiconducting or ionic, depending on composition and doping. It has been suggested¹ that a monolithic fuel cell might be fabricated from a single pyrochlore composition appropriately doped to have electronically-conducting electrode regions separated by an electrolyte region that is an oxygen fast ion conductor. Mechanical and chemical compatibility of cathode, electrolyte, and anode would be assured as a consequence of their consisting of same oxide.

A second and more fundamental reason for our interest in the pyrochlore oxides is the fact that some materials with this structure type undergo disorder transformations that involve *both* the cation and anion arrays. We are aware of no other structure type for an oxide that displays such behavior. It has recently been found that the disordering process may be driven chemically through alloying with a cation species that reduces the difference in average size of the cations that constitute the A and B atoms in the generalized formula. We describe in the present paper the results of some recent studies of the structural nature of this disorder process. Remarkably, it is found that in an ionic system the disorder process proceeds independently in the anion and cation arrays in spite of the fact that one might intuitively expect coupling of the state of disorder in the oppositely-charged arrays.

Some pyrochlore oxides, but not all, have been shown to disorder at elevated temperatures. In the present work we also provide a brief description of the first in situ studies of the changes in atomic arrangement as a function of temperature up to 1500° C. The disorder processes in the cation and anion arrays are, again, found to take place at independent rates.

THE PYROCHLORE STRUCTURE TYPE

A discussion of the disorder processes in the present systems requires familiarity with the nature of the pyrochlore structure. The prototype phase that gives its name to the structure type is a mineral² with idealized composition $(Ca,Na)_2(Nb,Ta)_2O_6$ (O,OH,F). A much greater variety of cations is commonly found to be incorporated in solid solution in specimens that occur in nature. The prototype mineral is a II-V compound; phases may be synthesized in which A^{2+} is a species such as Ca, Ag or Cd, and B^{5+} is Nb, Ta, or Sb. The majority of known pyrochlore oxides, however, and those that are examined in the present study, are III-IV phases in which A is a trivalent ion, usually the larger of the two cation species, and B is a smaller tetravalent species.

The pyrochlore structure is a superstructure with a lattice constant equal to twice that of a parent MO_2 arrangement of ions. The latter configuration of ions, known as the fluorite structure type (also referred to, for alloys, as the C1 structure), is a face-centered cubic array of M^{4+} within which anions are situated in all of the available tetrahedral interstices, Fig. 1a. Each cation is coordinated by a regular cube of anions; the cubes are linked by the sharing of edges. The anion arrangement may be viewed as a primitive cubic array within which cations occupy alternate cubes.

The pyrochlore superstructure, space group $Fd\bar{3}m$, is derived from the fluorite arrangement. The A^{3+} and B^{4+} ions order among the cation sites in the fluorite arrangement such that rows of each cation species alternate along $\langle 110 \rangle$ directions, Fig. 1b. If the origin of the cell is placed at an A^{3+} , this cation occupies position $16c \bar{3}m 000$ in the space group; B^{4+} occupies position $16d \bar{3}m 1/2 1/2 1/2$. Charge compensation is achieved by ordered omission of anions from 1/8 of the sites that would be occupied in an ideal

fluorite-type structure. The A^{3+} cation remains coordinated by eight O^{2-} ions, but only six anions surround B^{4+} , Fig. 1c. Two crystallographically-independent anions are present in the structure. A first, designated O(1), occupies position $48f \text{ } \bar{m} \bar{x} \frac{1}{8} \frac{1}{8}$ of the space group. A second ion, designated O(2), is situated in position $8a \text{ } \bar{4} 3m \frac{3}{8} \frac{3}{8} \frac{3}{8}$. The oxygen ion missing from an ideal fluorite-like structure would occur at position $8b \text{ } \bar{4} 3m \frac{1}{8} \frac{1}{8} \frac{1}{8}$. This anion site is indicated in Fig. 1 by a small cross. If the variable coordinate, x , of O(1) was precisely equal to $\frac{3}{8}$ the oxygen ions in the pyrochlore structure would constitute the regular cubic array that occurs in the fluorite structure-type. Instead, x is usually greater than 0.375. This represents a distortion whereby O(1) relaxes towards the "vacant" O(3) position. The relaxation undoubtedly occurs, at least in part, as a consequence of the absence of a repulsive interaction with the oxygen ion that would occupy the O(3) position in an ideal fluorite-like arrangement of anions. It should be noted, however, that the smaller B^{4+} cations are located between O(1) and the vacant site. The larger bond distance between A^{3+} and O(1) relative to the interionic separation of B^{4+} and O(1) will also contribute to displacement of O(1) towards the unoccupied anion position.

STABILITY FIELD OF THE PYROCHLORE STRUCTURE TYPE

In the early 1970's a number of workers³⁻⁵ synthesized series of pseudo-binary pyrochlores in which a specific B^{4+} ion, (such as Sn^{4+} , Ti^{4+} , or Hf^{4+}) was combined with a series of trivalent cation species of different radii. The latter included the lanthanide elements and other trivalent ions such as Y^{3+} , Tl^{3+} , or Bi^{3+} . These studies provided insight into the driving forces for ordering in the pyrochlore structure type. When the existence of a pyrochlore phase was plotted in a field defined by the radius of the A^{3+} ion along a

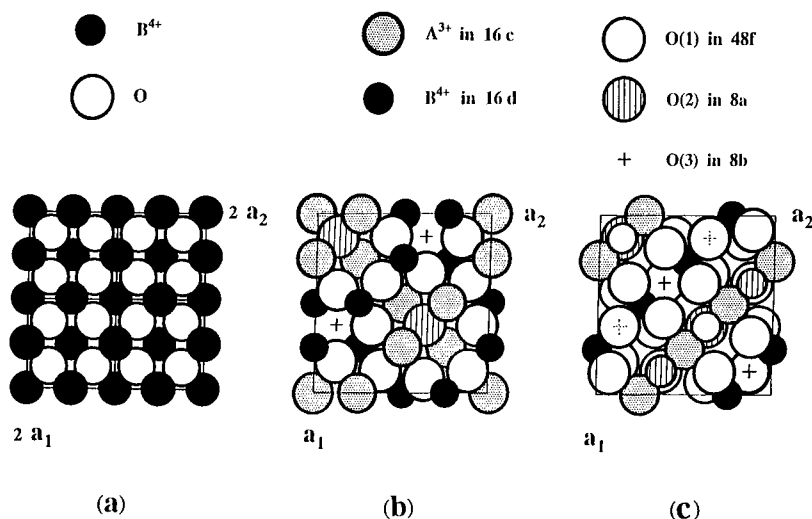


Figure 1. Projections along a_3 of the cell contents of the fluorite structure type and the ordered pyrochlore superstructure. (a) Projection of the cell contents for $0 \leq z \leq 1/4$ for the fluorite (C1) structure type. Cations in a fcc arrangement are coordinated by a regular tetrahedron of anions. (b) Projection of the contents of the pyrochlore cell for $0 \leq z \leq 1/8$ showing the ordering scheme for the tetrahedrally-coordinated cations. Note the displacement of O(1) in direction of the unoccupied O(3) site (marked with a cross). The distortion depicted $\Delta = x - 3/8 = 0.4207$, is the value found for $Y_2Sn_2O_7$. (c) Projection of the pyrochlore structure for $1/8 - \Delta \leq z \leq 3/8 + \Delta$ showing the distorted 8-fold coordination of A^{3+} by four O(1) and two O(2) anions, and 6-fold coordination of B^{4+} by six O(1) ions and two O(3) sites. Two O(1)-O(2) pairs superpose in projection about A^{3+} . The anion "on top" (larger z) is depicted as a circle of slightly reduced diameter.

vertical axis and the radius of B^{4+} horizontally, it was found that formation of an ordered pyrochlore occurred for $R_A > 0.98 \text{ \AA}$ when $0.58 < R_B < 0.68 \text{ \AA}$ and only when R_A/R_B was above a lower limit⁵ when $R_B > 0.68$. For values of R_A/R_B below this phase boundary a disordered, non-stoichiometric fluorite structure was formed in which cations were distributed at random in a face-centered cubic array. Oxygen ions occupied all tetrahedral interstices in the array with a probability of 7/8. It seems likely that the assessment of formation of a pyrochlore structure as opposed to a defect fluorite structure may often have been done in a rather binary fashion: the phase was assumed to be an ordered pyrochlore structure if superstructure peaks were observed in X-ray diffraction patterns, and to be a defect fluorite structure if such maxima could not be detected. States of intermediate order seem not to have been considered.

A number of $A_2B_2O_7$ pyrochlores, but by no means all, have been observed to disorder into a nonstoichiometric fluorite structure $(A, B)O_{7/4}$ at elevated temperature. The order/disorder transition usually occurs at very high temperatures—for example: 2300° C for $\text{Nd}_2\text{Zr}_2\text{O}_7$, 2200° C for $\text{Sm}_2\text{Zr}_2\text{O}_7$ and 1530° C for $\text{Gd}_2\text{Zr}_2\text{O}_7$.^{6,7} The transition temperature decreases as phases approach the pyrochlore/defect fluorite phase boundary. To our knowledge, no study has examined the atomic rearrangement at temperatures near those at which the phase transition takes place. The presence or absence of superstructure diffraction peaks has been the main tool employed to determine the disappearance of the pyrochlore ordering.

If formation of the pyrochlore structure (as opposed to a non-stoichiometric fluorite state) is controlled by ionic size and the radius ratio R_A/R_B , then substitution of a larger B^{4+} cation in a solid solution $A_2(B_yB_{1-y})_2O_7$ or of a smaller ion A' in $(A'_zA_{1-z})_2B_2O_7$ might be expected to drive the system toward disorder.⁸ Samples in solid solution systems $\text{Gd}_2(\text{Zr}_y\text{Ti}_{1-y})_2\text{O}_7$ and $\text{Y}_2(\text{Zr}_y\text{Ti}_{1-y})_2\text{O}_7$ were examined by Moon.⁹⁻¹¹ X-ray diffraction patterns showed that the intensity of the pyrochlore superstructure peaks diminished continuously with increasing y and became undetectable for $y > 0.90$ for the Zr-Ti system. The onset of disorder and the presumed partial occupancy of anion sites in the structure caused the oxygen-ion conductivity to increase by three orders of magnitude. The present work was directed toward determination of the atomic nature of the disorder process and testing of the assumption that the state of order is solely a function of the average ionic radii of the species occupying the A and B sites in the structure. Another objective was to determine whether the structural changes accompanying disorder were the same for thermally-driven as for compositionally-created disorder.

EXPERIMENTAL

Preparation of Samples

Powder samples of multi-component refractory oxides are commonly prepared by solid state reaction. The usual strategy is to prepare a highly-homogeneous mixture of precursor compounds in order to reduce the diffusion distance for reaction, homogenization, and equilibration. The specimens used in the present studies were prepared by the Pechini liquid-mix procedure.¹² Metal-organic compounds of the cations were dissolved in solutions of citric acid and ethylene glycol and gradually heated to $150 - 200^\circ \text{ C}$ to form a polyester in which the homogeneity of the liquid solution was presumably preserved. The sample was then heated to remove excess ethylene glycol and water, resulting in the formation of a hard resin. The resin, in turn, was charred at approximately 500° C to oxidize the organic material and form a powder. X-ray diffraction showed the product to be amorphous. The powder was then calcined at 1000° C for on the order of twelve hours to provide a powder which was found to have the pyrochlore structure type.

A final annealing was performed for periods of 72 hours at temperatures of about 1550° C to equilibrate the distribution of the component anions.

Diffraction Analysis

The site occupancies, the coordinate, x , for O(1) and the coefficients for description of anisotropic thermal vibrations were determined through analysis of powder diffraction patterns obtained from the pyrochlore specimens. Rietveld powder profile analysis was used for this purpose.¹³ No attempt is made in this procedure to separate overlapped diffraction maxima and obtain an integrated intensity for individual peaks corresponding to a specific set of Miller indices. Instead, the structural parameters, as well as instrumental parameters that are necessary to describe the shape of the profile, are adjusted, by least squares procedures, to provide optimum fit of a computed powder diffraction profile to the entire pattern that was measured experimentally. The instrumental parameters include the zero point in diffraction angle, parameters to describe the variation of background intensity as a function of diffraction angle and the shape of the diffraction maxima. A total of 14 structural variables was necessary to describe the partially-ordered structures. Usually 34 instrumental parameters were employed to describe the profile shape.

The fact that the pyrochlore structure is a superstructure makes the analysis of partially-ordered structures extremely difficult. The diffraction pattern of a superstructure consists of two subsets of diffraction maxima. A first set of peaks corresponds in intensity and diffraction angle to those that would be produced by the fluorite structure type. These intensities provide only information on the average structure and contain little information on the perturbations that create the superstructure. The second subset of intensities are superstructure intensities that occur at diffraction angles that are characteristic of the lattice constants of the true supercell. The intensities of these peaks are usually feeble and become zero for a completely disordered structure. The magnitude of the supercell intensities depends on the perturbations of the ideal average structure that result in formation of a superstructure. For pyrochlore these perturbations are the amount of displacement of O(1) from its ideal location at $x = 3/8$, the occupancy of the normally-vacant site O(3)—and thus the scattering power of oxygen—and the contrast in average scattering power between the species occupying the A-site and those in the B-site. The highly-disordered structural states that are of greatest interest are, therefore, those that are most difficult to determine: the perturbations diminish and the superstructure intensities approach zero. For this reason, neutron diffraction rather than X-ray diffraction was employed for the majority of the structure determinations reported below. Neutrons provided several advantages for the present analyses. The scattering power of atoms for X-ray diffraction is proportional to the number of electrons on the atom and, as may be seen in Table 1, the scattering by oxygen is small compared to that by the cations.¹⁴ The contribution of oxygen to the superstructure intensities will consequently be rather small. For neutrons, however, the scattering length of oxygen is more comparable to the cation species. The unique feature provided by neutrons for the present work, however, is that the scattering length of Ti is *negative*. The physical significance of a "negative" atom is that the scattered neutron beam experiences a phase shift of π relative to most elements. This provides unusually high contrast between the A-site and a B-site that primarily contains Ti^{4+} . Indeed, for highly ordered titanates the intensity of some superstructure diffraction peaks is several times larger than those of the fundamental peaks. This fortunate situation permits the analysis of even highly-disordered states of titanate pyrochlores with high precision.

One additional limitation of the present diffraction analyses requires mention. Although it is not immediately obvious, it is impossible to determine, from a single set of diffraction data, the distribution of several ionic species over a smaller number of independent structural sites. All that may be determined, even though the bulk

stoichiometry is known, is the average scattering length in each independent site. This information does not specify a unique mode of cation partitioning. For example, for $Y_2(Zr_yTi_{1-y})_2O_7$ if both the A and B site have full occupancy:

$$[Y]_A + [Y]_B = 1 \quad (1)$$

$$[Zr]_A + [Zr]_B = y \quad (2)$$

$$[Ti]_A + [Ti]_B = 1 - y \quad (3)$$

where Kröger-Vink notation has been used to specify the fractional occupancy of each species in the A and B sites. The average scattering length of the A site was adjusted by the least-squares method in refinement of the structures. The result will represent

$$b_A = [Y]_A b_Y + [Zr]_A b_{Zr} + [Ti]_A b_{Ti} \quad (4)$$

The scattering length of the B site is constrained to follow b_A as a dependent variable because of the known stoichiometry of the phase, namely

$$b_A + b_B = b_Y + y b_{Zr} + (1-y) b_{Ti} \quad (5)$$

Although there are six site occupancies for a pseudo ternary pyrochlore, the above equations constitute only five relations between these variables. The ambiguity may be resolved, in principle, through analysis of a second, independent diffraction pattern. This was indeed done for the $Y_2(Zr_ySn_{1-y})_2O_7$ pyrochlore: powder profile analysis was performed for both neutron data and an X-ray diffraction pattern obtained with Cu K α radiation. In general, the refinements were quite successful, yielding residuals for the Bragg peaks (defined as the sum of the difference between observed and calculated intensity divided by the sum of the observed intensity) that ranged from the order of 1.5 to 8.0%. The larger

Table 1. Comparison of neutron scattering lengths, the number of electrons available to scatter x-rays, and the ionic radii plus coordination numbers for the ionic species present in the $A_2^{3+}B_2^{4+}O_7$ pyrochlores of the present studies

Ion	Coordination number	Ionic Radius (Å)	Atomic number	Number of electrons	Neutron scattering length (10^{-12} cm)
O^{2-}	[4]	1.38	8	10	0.5803(4)
Ti^{4+}	[6]	0.605	22	18	-0.3438(2)
	[8]	0.74			
Y^{3+}	[6]	0.900	39	36	0.775(2)
	[8]	1.019			
Zr^{4+}	[6]	0.720	40	36	0.716(3)
	[8]	0.84			
Sn^{4+}	[6]	0.690	50	46	0.6226(2)
	[8]	0.81			

residuals were encountered for highly disordered structures in which the superstructure intensities were extremely weak.

RESULTS OF THE STUDIES OF COMPOSITIONALLY-INDUCED DISORDER

Structures were determined for the end member compositions and three to four intermediate compositions of solid solutions along the pseudo-binary joins in the ternary system $Y_2(Zr,Sn,Ti)_2O_7$. In the present report we will, in the interest of brevity, confine the discussion to the variation in lattice parameters, the positional coordinate of O(1) whose variation with composition will be seen to be a very sensitive measure of the state of disorder, and the change in bond distances as well as anion and cation site occupancies with composition.

The measured lattice parameters, a , are shown as a function of the fractional substitution, y , of the larger B^{4+} ion in Fig. 2a. A linear variation is found for all three solid solution series in accord with Vegard's law. Lattice constants may be very precisely determined by means of Rietveld analysis and the standard deviation in the values that appear in Fig. 2a range from one to three in the fourth figure beyond the decimal point.

The first pyrochlore system to be analyzed¹⁷ was $Y_2(Zr_yTi_{1-y})O_7$. These results have previously been published in detail.¹⁸ The superstructure intensities were found to progressively diminish with increasing zirconium content and were undetectable for a sample with $y = 0.90$. The value of positional parameter, x , for O(1) is plotted as a function of the average radius of the tetravalent cation in Fig. 2b. The parameter decreases steeply in a non-linear fashion that can be very precisely fit by a parabolic dependence. It is interesting to note that a least squares fit to the specimens with y up to 0.60 extrapolates precisely to the value of $3/8$ for an ideal fluorite-type array at $y = 0.90$ which, indeed, was found to have the disordered nonstoichiometric fluorite structure as noted above. It appears, therefore, that our selection of composition increments fortuitously placed a sample composition exactly at the compositional phase boundary between the ordered

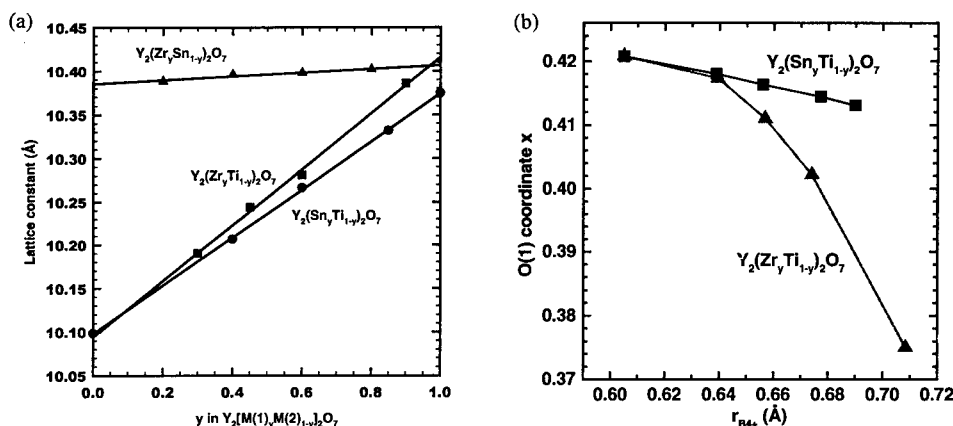


Figure 2. (a) Variation of pyrochlore lattice constants with the atomic fraction, y , of the larger tetravalent ion that has been substituted in the B^{4+} site. Results for the Zr-Ti pyrochlore were obtained by Heremans¹⁸ and the data for Zr-Sn materials by Ku²². (b) Comparison of the change in the x coordinate of O(1) as a function of the mean radius of the tetravalent cations nominally occupying the B site. The linear variation for $Y_2(Sn,Ti)_{1-y}O_7$ suggests that the larger Sn^{4+} ion progressively replaces Ti^{4+} in the B site. The rapidly nonlinear decrease of x for $Y_2(Zr,Ti)_{1-y}O_7$ obtained by Heremans¹⁸ suggests mixing of the contents of B site with the larger Y^{3+} in the A site and/or O^{2-} entering the O(3) interstitial site. This interpretation is confirmed by the refined values for site-occupancy factors.

pyrochlore phases and the nonstoichiometric fluorite structure. The nonlinear dependence suggests that mixing of the cation occupancies of the A and B sites and/or filling of the normally-vacant O(3) site must have occurred. If not, one would expect a more or less linear decrease of y upon substitution of the larger tetravalent ion in the B site as a result of the increase in the average B-O(1) bond length. Examination of the effective scattering length of the A site, Fig. 3a, shows this to indeed be the case. The experimental scattering length for the A site was found to be equal to that of yttrium (within one standard deviation) for the first half of the solid solution series. Beyond that, the scattering length decreased abruptly to that for the random occupancy present in the fluorite-structured composition with $y = 0.90$. The abrupt increase in mixing between the cation sites with composition is reminiscent of the variation in the Bragg-Williams order parameter for a binary alloy as a function of temperature. It is amusing to note in passing that the Bragg-Williams model is based on the assumption that the energy for formation of an anti-site defect decreases as the extent of disorder increases. In the present system it seems reasonable to assume that the coulombic part of the energy for creating an anti-site defect would diminish as the average charge of the cations occupying the two sites approached equality. The anion site occupancies, Fig. 3b, display a remarkably different behavior. Oxygen ions begin to occupy the interstitial O(3) site almost immediately upon substitution of the larger Zr^{4+} ion, and the occupancy increases roughly linearly throughout the range of the solid solution. The two independent, oxygen sites, O(1) and O(2), that are normally fully-occupied, disorder at different rates. The O(1) site tends to lose occupancy first. The initial occupancy of O(3) is therefore entirely by anions derived from the O(1) position, a behavior which is understandable in view of the fact that the O(1) anions are the nearest neighbors to the O(3) position. It is interesting to note that depletion of the O(2) site begins only as mixing between the cation occupancies begins. It is not clear which disordering process is cause and which is effect of the other. This result seemed quite remarkable as one might expect the disorder processes in the cation and anion arrays to be more strongly coupled in an ionic structure.

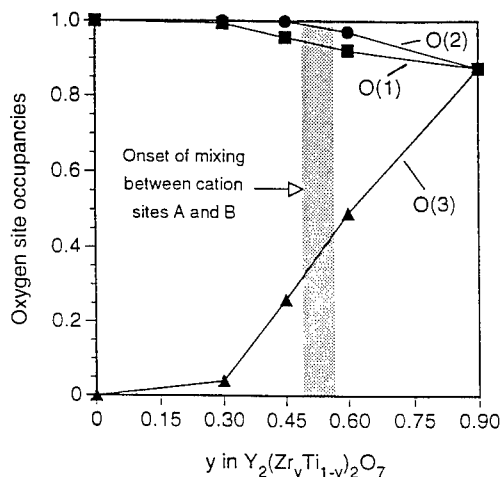


Figure 3. (a) The average scattering length of the cations that occupy the A site normalized by the scattering length of Y^{3+} , the strongest scatterer, as a function of increasing substitution of the larger Zr^{4+} ion for Ti^{4+} in $\text{Y}_2(\text{Zr}_y\text{Ti}_{1-y})_2\text{O}_7$. The rapid decrease in scattering length for $y > 0.50$ signals disordering of the cation species¹⁶ and culminates in a random distribution at $y = 0.90$. (b) Change in the occupancy of the anion sites as a function of increasing Zr^{4+} content in $\text{Y}_2(\text{Zr}_y\text{Ti}_{1-y})_2\text{O}_7$ solid solutions¹⁸. A random distribution of anions is responsible for the average site occupancy of 7/8 that is present in the non-stoichiometric fluorite-type structure that forms at $y = 0.90$.

The second system to be examined¹⁹ was $Y_2(Sn_yTi_{1-y})_2O_7$. The ionic radius of Sn^{4+} is intermediate to that of Zr^{4+} and Ti^{4+} (Table 1) and has a radius that corresponds to an average occupancy of the B site by $(Zr_{0.74}Ti_{0.26})$. The average radius of the B site for the Sn-Ti solid solutions thus overlaps that of the Zr-Ti series to a considerable degree. The system was examined to test the hypothesis that the state of order of a pyrochlore depends primarily on the radius ratio R_A/R_B . The variation of lattice constant with y was, again, found to very closely follow a linear relation in accord with Vegard's law, Fig. 2a. The variation of the x coordinate for O(1) with tin content, y , is shown in Fig. 2b where it may be compared with the behavior observed for $Y_2(Zr_yTi_{1-y})_2O_7$. The dependence of the oxygen position is quite different for the two solid-solution series. The Sn-Ti solid solutions show a more or less linear variation with tin content rather than the rapid, parabolic decrease of the Zr-Ti solid solutions that proved to be indicative of the onset of disorder. The linear variation for the Sn^{4+} - Ti^{4+} phases, in contrast, suggest simple substitution of the larger Sn^{4+} ion for Ti^{4+} in the B site, with little or no cation mixing or disorder of the anion array. The values obtained for site occupancies confirm this interpretation. Departure from full occupation of the O(1) site was insignificant and was therefore fixed at unity at all compositions. The normally-vacant O(3) site displayed occupancies that were zero within one standard deviation except for an occupancy value of 0.013 (2.4 standard deviations above zero) at $y = 0.60$. Mixing of the trivalent and tetravalent cations was found to be insignificant for low concentrations of the larger Sn^{4+} ion ($0 < y < 0.60$). For compositions rich in tin ($y = 0.85$ and 1.0) the Y^{3+} occupancy of the A site decreased to 0.99 and 0.88 respectively, Fig 4a. It is clear that the state of disorder in $Y_2(Sn, Ti)_2O_7$ pyrochlores is not strongly determined by the average radius of the tetravalent ion that occupies the B site. The difference in behavior, as discussed below, must lie in the characteristics of the bonding between tin and oxygen and is likely due to a pronounced covalent character to the interaction. As with the Zr^{4+} - Ti^{4+} solid solution

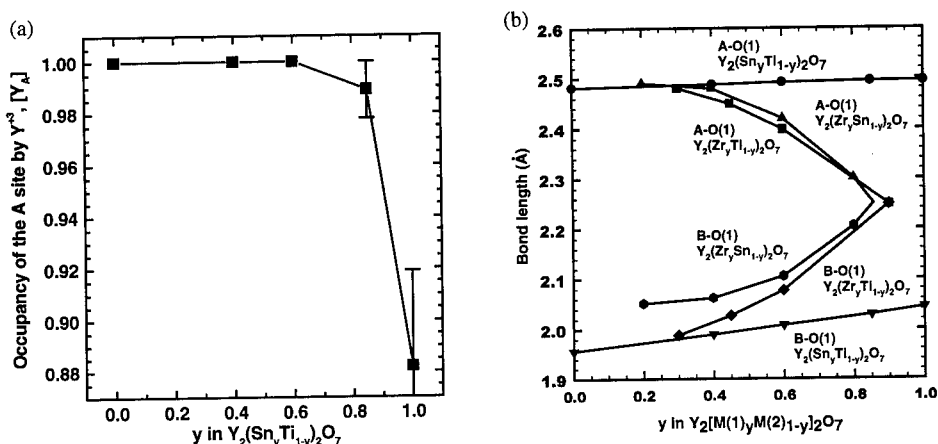


Figure 4. (a) The change in the fractional occupancy of the 8-coordinated A site in $Y_2(Sn_yTi_{1-y})_2O_7$ as a function of the fractional replacement of Ti^{4+} by the larger Sn^{4+} ion. The decrease for $y > 0.60$ signifies the onset of a slight amount of cation disorder over the A and B sites. (b) Change in bond distances between the 8-coordinated A site and O(1) and the 6-coordinated B site to O(1) with increasing substitution of a larger tetravalent cation. The merging of A-O(1) and B-O(1) distances to a common value equal to $a\sqrt{3}/8$ occurs at the composition at which formation of a non-stoichiometric fluorite structure that lacks long-range order occurs.

series, independent rates of disorder are seen in the cation and anion arrays, although the amount of disorder for the Sn-Ti system is small in comparison. Moreover, in contrast to the Zr-Ti series, the disorder is more pronounced in the cation array; the anion arrangement essentially remains completely ordered. The suggestion that the nature of the $\text{Sn}^{4+}\text{-O}(1)$ bonding accounts for the different behavior of the system is supported by the results of an analysis of the structural changes in the $\text{Gd}_2(\text{Sn}_y\text{Ti}_{1-y})_2\text{O}_7$ system.¹⁹ The Gd^{3+} pyrochlores showed a disordering behavior that was qualitatively similar to the Y^{3+} pyrochlores: A very small degree of cation mixing at high Sn contents and very little occupancy of the normally-vacant O(3) site. Maximum occupancy once more occurred at an intermediate composition on the order of $y = 0.6$.

Despite overlap in their ranges of the ratio R_A/R_B , the Zr-Ti solid solutions rush to full disorder at compositions with $y < 1$, whereas structures in the Sn-Ti series display persistent, nearly-complete order at all compositions. An investigation of the third leg of the pseudo-ternary $\text{Y}_2(\text{Zr},\text{Sn},\text{Ti})_2\text{O}_7$ system was thus anticipated to shed light on the factors that determine the state of disorder of the pyrochlores in this system. The $\text{Y}_2(\text{Zr}_y\text{Sn}_{1-y})_2\text{O}_7$ solid solution series was the system least amenable to analysis, however, because of the absence of the large contrast in scattering between the A site and B sites that was created by the negative scattering length of Ti. Tin has the smallest scattering length in the case of neutron diffraction (Table 1) but there is little contrast between the scattering length of the three cation species. In the case of X-rays, Y^{3+} and Zr^{4+} are isoelectronic, Table 1, and cannot be distinguished in an X-ray diffraction study. Tin is a stronger scatterer. The nearly identical scattering of Y^{3+} and Zr^{4+} in X-ray diffraction, however, reduces the problem of the cation distribution to a two atom/two site problem, and the partitioning of Sn^{4+} between the A and B sites can, in principle, be established. Neither X-ray diffraction or neutron diffraction provides a distinct advantage in maximizing the intensity of the superstructure reflections. Consequently, two independent sets of X-ray powder diffraction data were collected using $\text{Cu K}\alpha$ X-radiation.²⁰⁻²² A powder diffraction profile was also collected with neutron scattering. Measurements were performed at the Center for Neutron Research at the National Institute of Standards and Technology in Gaithersburg, MD.^{21,22} Both types of radiation, as expected, provided superstructure intensities that were exceedingly weak. In spite of the very high standard deviations in the refined parameters, the results obtained from the analysis of the three independent data sets are in very good accord. The behavior of $\text{Y}_2(\text{Zr}_y\text{Sn}_{1-y})_2\text{O}_7$ solid solutions was virtually the same as that found for the Zr^{4+} - Ti^{4+} phases. The positional coordinate for O(1) decreased in a parabolic fashion to the undistorted value of $3/8$ at a value of y in the neighborhood of 0.85. The occupancy of the normally-vacant O(3) site increased linearly with y up to the average occupancy of $7/8$ for a disordered nonstoichiometric state. The occupancies of O(1) and O(2) change relatively little, decreasing from full occupancy to 0.875 for the fully disordered state that is near $y = 0.85$. The standard deviations in the site occupancies of O(1) and O(2) are very large because of the extreme weakness of the superstructure reflections in the Zr - Sn system. The relative depletion in the O(1) and O(2) occupancies as disorder progresses cannot be specified.

Values for the anion and cation site occupancies carry large standard deviations because of correlations with other parameters—notably the parameters that describe thermal vibration of the ions. However, most interatomic distances in the structure depend only on the value of the lattice constant, a , which may be determined very precisely. Distances that involve O(1) are exceptions as they depend, as well, on the positional coordinate, x , for this ion, but the value of x may also be precisely established. Figure 4b presents the A-O(1) and B-O(1) interionic distances as a function of y for all three solid solution systems. The A-O(1) and B-O(1) separations change slowly for the Zr-Ti and Zr-Sn systems at small values of y before much disorder has occurred. As y increases

beyond 0.5 the A-O(1) bond distance decreases and B-O(1) rises with increasing rapidity as mixing between cations occurs and interstitial oxygen continues to fill the normally-vacant O(3) site. The two branches join upon complete disorder to a non-stoichiometric fluorite structure for which both bond distances are equal to $a\sqrt{3}/8$. The system that contains the largest pair of cations, Zr-Sn, reaches complete disorder at a slightly smaller fraction of Zr ($y=0.85$, by extrapolation) than the Zr-Ti system.

The bond distances for $Y_2(Sn_yTi_{1-y})_2O_7$ display a strikingly different variation with y that is consistent with the lack of anion order and little mixing between the cations in the A and B sites: the A-O(1) separation remains constant and the B-O(1) distance increases linearly with y as the larger Sn replaces Ti. It is interesting to note that there is a slight non-linear up turn to B-O(1) bond length for $y>0.7$ that corresponds to the small amount of the larger Y^{3+} that enters the B site as is indicated in Fig. 4a.

RESULTS OF STUDIES OF THERMALLY-INDUCED DISORDER

Structural changes induced as two pyrochlores were slowly heated to 1500° C were examined with pulsed-neutron diffraction data obtained on the Special Environment Powder Diffractometer at IPNS, Argonne National Laboratory. One objective of the investigation was to examine whether the independent rates of cation and anion disorder that were observed during compositionally-driven disorder would also occur during thermally-driven disorder. The second objective was to determine if the structures examined at ambient temperature represented equilibrium distributions of the ions or whether the different state of disorder found for anions and cations resulted from rearrangement during cooling. These pyrochlores are, after all, oxygen fast-ion conductors. However, it would be hard to understand how cooling could result in an *increased* degree of disorder for the mobile anions! As previously noted, pyrochlores tend to disorder at extremely high temperatures that are difficult to achieve in a diffraction experiment. One specimen that was selected for examination, therefore, was $Y_2(Zr_{0.60}Ti_{0.40})_2O_7$ for which the A site found to have *ca.* 1% of the scattering power of Y^{3+} replaced by some combination of Zr^{4+} and Ti^{4+} (about 10% of the way to complete disorder), Fig. 3a, and an interstitial O(3) site that had 0.488 occupancy, Fig. 3b. It was reasoned that further disorder might proceed at an accessible temperature if the sample were initially in a highly disordered state. The second specimen was $Y_2Sn_2O_7$, a pyrochlore found to be fully ordered, and one which contained a tetravalent ion that did not create disorder when substituted for Ti^{4+} .

The lattice constants were found to increase linearly with increasing temperature with linear expansion coefficients of 8.90 and $10.9 \times 10^{-6} K^{-1}$ for the stannate and zirconium titanate, respectively. The stannate is the more tightly bonded of the two phases as a consequence of lack of disorder, strong Sn-O bonding or both. The x coordinate for both phases was found to increase with temperature, corresponding to *increased* distortion of the anion array as opposed to the more symmetric arrangement that one might anticipate at elevated temperature. The origin of this effect is apparent when bond distances are examined, Fig. 5b. The thermal expansion coefficients for the A^{3+} -O(1) bonds are comparable values of 13.01 and $12.66 \times 10^{-6} K^{-1}$ for the stannate and zirconium titanate, respectively, while those for the B^{4+} -O(1) bonds are 5.79 and $8.33 \times 10^{-6} K^{-1}$. The Y^{3+} O(1) bond is, as might be expected, weaker than the B^{4+} -O(1) interaction and, accordingly, expands more rapidly with increasing temperature. This results in additional displacement of O(1) toward the vacant O(3) interstice. The linear thermal expansion coefficient for Sn-O(1) is considerably smaller than that for the (Zr,Ti) - O(1) interaction, suggesting a stronger bond with a covalent component.

Figure 5 shows that the O(1) coordinate and the bond distances for $Y_2Sn_2O_7$ increase linearly over the temperature range 20° -1400° C. No significant change in anion

or cation site occupancy was found in the refinements performed at individual temperatures. The phase $\text{Y}_2\text{Sn}_2\text{O}_7$, remains steadfastly ordered at all temperatures. Partially-disordered $\text{Y}_2(\text{Zr}_{0.6}\text{Ti}_{0.4})_2\text{O}_7$ behaves quite differently! The O(1) coordinate increases linearly up to a temperature of 1000° C, upon which the temperature dependence levels out and then rapidly decreases to a value that is smaller than the coordinate found under ambient conditions. This behavior, as has been seen, is characteristic of the onset of cation and anion disorder. This interpretation is supported by the behavior of bond distances as a function of temperature, Fig. 5b. The Y^{3+} -O(1) bond in the (Zr-Ti) phase increases linearly until a temperature of 1000° C is attained, then leveling and beginning a decline. Conversely, the B-O(1) separation begins to rapidly increase as Y^{3+} enters the B site. This provides additional evidence for mixing of the occupancies of the cation sites. The average scattering length of the A site shows little variation, however. Therefore, the tetravalent cation that exchanges with Y^{3+} in the A site must be primarily Zr^{4+} rather than the negatively-scattering Ti^{4+} . The occupancy of O(1) and O(2) changed little with temperature. Surprisingly, the occupancy of the interstitial O(3) site *decreased*. The total oxygen content of the cell therefore decreased with increasing temperature as a result of reduction of the sample and exchange of oxygen with the atmosphere. No comparable effect was observed for the stannate in which the O(3) interstitial site is unoccupied. The exchange of oxygen with the environment thus appears to involve primarily the O(3) site whose occupancy represents a structural defect. Data were recorded both as the samples were heated and as they were cooled. The structural changes in both the cation and anion arrangements were reversible. The structure analyses performed at ambient temperature thus would appear to provide results that represent equilibrium structures.

CONCLUDING REMARKS

The present diffraction analyses have shown that cation and anion disorder proceed quite independently as an ordered pyrochlore structure approaches a non-stoichiometric

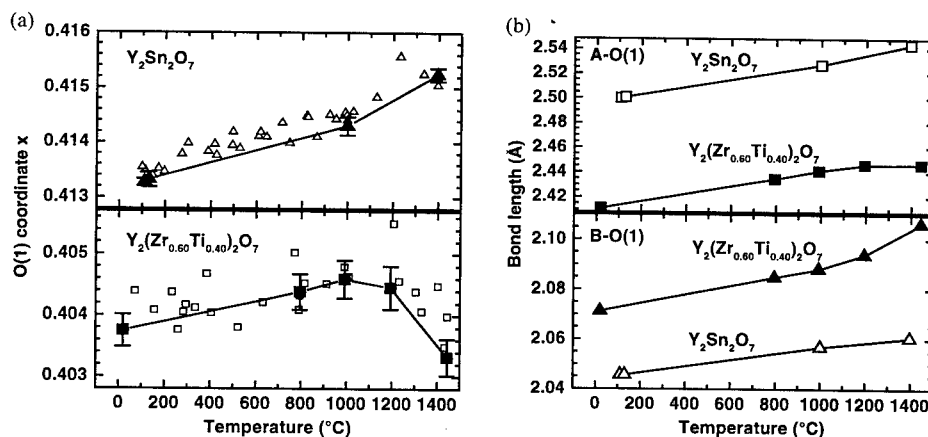


Figure 5. (a) Change in the x coordinate of O(1) as a function of increasing temperature for fully-ordered $\text{Y}_2\text{Sn}_2\text{O}_7$ and partially-disordered $\text{Y}_2(\text{Zr}_{0.6}\text{Ti}_{0.4})_2\text{O}_7$. Open symbols are values derived from neutron powder profiles collected over relatively short periods of time as the sample was heated or cooled. The results were the same. Filled symbols represent results obtained when the specimen was equilibrated at temperature for several hours. The sharp decrease in x beginning at 1000° C for the titanate represents the onset of additional disorder. (b) Interionic bond distances A-O(1) and B-O(1) as a function of temperature. The downturn in the A-O distance and the corresponding upturn in the B-O separation represents the onset of additional disorder as the larger Y^{3+} occupying the A site and the smaller tetravalent cations in the B site begin to mix.

fluorite state. This is true whether the disorder is induced by increase in temperature or by compositional change through substitution of a species that lowers the average difference in size between the A^{3+} and B^{4+} cations.

The radius-ratio criterion does not hold for $Y_2(Sn_yTi_{1-y})_2O_7$ solid solution as all samples in this system remained completely ordered. The behavior is attributed to a strong Sn-O interaction, perhaps arising from a significant covalent contribution to the bond. This view is supported by the low thermal expansion coefficient observed for this bond distance. In addition, other workers have found bridging electron density in the Sn-O bond in Fourier maps of the scattering density in $Y_2Sn_2O_7$ ²³ and bond-valence sums in a series of $Ln_2Sn_2O_7$ phases that show increasing covalency as the radius of Ln increases.²⁴ All of these stannates were found to be fully-ordered pyrochlores.

Covalency notwithstanding, the reason for the similar disordering behavior of $Y_2(Zr_yTi_{1-y})_2O_7$ and $Y_2(Zr_ySn_{1-y})_2O_7$ seems to be a strong preference of Zr for an 8-coordinated site. The mixing of the B^{4+} and Y^{3+} in the zirconates seems to preferentially involve exchange of Y^{3+} and Zr^{4+} in the initial states of disorder. This conclusion is based on the average scattering length found for the A-site after the onset of thermally-induced disorder in $Y_2(Zr_{0.6}Ti_{0.4})_2O_7$, and on the combined X-ray and neutron analyses²¹ of $Y_2(Zr_ySn_{1-y})_2O_7$. The structural data obtained in these studies provides a satisfactory qualitative explanation²⁵ for the very different enhancements of oxygen-ion conductivity as a function of composition that have been measured, the behavior that supplied the initial motivation for these studies. In work that is currently in progress, we have found that the solid solutions, $(Sc_zYb_{1-z})_2Ti_2O_7$, in which a smaller cation species is substituted in the A site, display order/disorder changes as a function of composition and temperature that are analogous to those described in the present work.

REFERENCES

1. M. A. Subramanian, G. Aravamudan, and G. V. Subba Rao, Oxide pyrochlores - A review, *Prog. Solid State Chem.* 15: 55-143 (1983).
2. H. L. Tuller, Ionic and mixed conductors: Materials design and optimization, in *High Temperature Electrochemistry: Ceramics and Metals*, Proceedings 17th Risø International Symposium on Materials Science, F. W. Poulsen, N. Bonanos, S. Linderth, M. Mogensen, and B. Zachau-Christiansen, eds. Risø National Laboratory, Roskilde, Denmark (1996).
3. F. Brisse and O. Knop, Pyrochlores. III. X-ray, neutron, infrared, and dielectric studies of $A_2Sn_2O_7$ stannates, *Canad. J. Chem.* 46: 859-873 (1968).
4. O. Knop, F. Brisse, and L. Castelliz, Pyrochlores. V. Thermoanalytic, X-ray, neutron, infrared and dielectric studies of $A_2Ti_2O_7$ titanates, *Canad. J. Chem.* 47: 971-990 (1969).
5. W. E. Klee and G. Weitz, Infrared spectra of ordered and disordered pyrochlore-type compounds in the series $RE_2Ti_2O_7$, $RE_2Zr_2O_7$ and $RE_2Hf_2O_7$, *J. Inorg. Nucl. Chem.* 31: 2367-2372 (1969).
6. D. Michel, M. Perez y Jorba, and R. Collongues, Etude de la transformation ordre-désordre de la structure fluorite à la structure pyrochlore pour des phases $(1-x)ZrO_2 - xLn_2O_3$, *Mater. Res. Bull.* 9: 1457-1468 (1974).
7. S. Meilicke and S. Haile, Order-disorder transitions in gadolinium zirconate: a potential electrolyte material in solid oxide fuel cells, *Mater. Res. Soc. Sympos. Proc.* 135: 55-60 (1995).
8. As the variable x has been pre-empted for use in indicating the variable positional coordinate for O(1), we employ the variable y to represent the fractional substitution of a larger species in the B^{4+} site, and z to designate fractional substitution of a smaller species in the A^{3+} site. Increase of either y or z should, therefore, drive the structure toward disorder.
9. P. K. Moon, *Electrical Conductivity and Structural Disorder in $Gd_2Ti_2O_7$ - $Gd_2Zr_2O_7$ and $Y_2Ti_2O_7$ - $Y_2Zr_2O_7$ Solid Solutions*, Ph.D. Thesis, Department of Materials Science and Engineering, Massachusetts Institute of Technology, Cambridge, MA, February 1988.
10. P. K. Moon and H. L. Tuller, Ionic conduction in the $Gd_2Ti_2O_7$ - $Gd_2Zr_2O_7$ system, *Solid State Ionics* 28-30: 470-474 (1988).
11. P. K. Moon and H. L. Tuller, Intrinsic fast oxygen ionic conductivity in the $Gd_2(Zr_xTi_{1-x})_2O_7$ and $Y_2(Zr_xTi_{1-x})_2O_7$ pyrochlore systems, *Mat. Res. Soc. Sympos. Proc.* 135: 149-163 (1989).

12. M. P. Pechini, Method of preparing lead and alkaline earth titanates and niobates and coating method using the same to form a capacitor, U.S. Patent 3, 330, 697 (1967).
13. H. M. Reitveld, A profile refinement method for nuclear and magnetic structures, *J. Appl. Cryst.* 2:65-71 (1971).
14. The ionic radii in Table 1 were determined by Shannon¹³, the neutron scattering lengths are those tabulated by Sears¹⁶.
15. R. D. Shannon, Revised effective ionic radii and systematic studies of interatomic distances in halides and chalcogenides, *Acta Crystallogr.* A32: 751-767 (1976).
16. V. F. Sears, Scattering lengths for neutrons, in *International Tables for Crystallography, Vol. C, Mathematical, Physical and Chemical Tables*, A. J. C. Wilson, ed., Kluwer Academic Publishers, Dordrecht, Boston, London (1995).
17. C. Heremans, *Fast-Ion Conductors: Single Crystal Growth of Copper and Silver Halides and Structural Determination of $Y_2(Zr_yTi_{1-y})_2O_7$ Pyrochlores*, Ph.D. Thesis, Massachusetts Institute of Technology, Cambridge, MA, June 1993.
18. C. Heremans, B. J. Wuensch, J. K. Stalick, and E. Prince, Fast-ion conducting $Y_2(Zr_yTi_{1-y})_2O_7$ pyrochlores: Neutron Rietveld analysis of disorder induced by Zr substitution, *J. Solid State Chem.* 117: 108-121 (1995).
19. K. W. Eberman, *Crystallographic Origins of Fast-Ion Conduction in Pyrochlore*, Ph.D. Thesis, Department of Materials Science and Engineering, Massachusetts Institute of Technology, Cambridge, MA, June 1998.
20. E. M. E. Yeo, *Synthesis and Rietveld X-ray Analysis of $Y_2(Sn_{1-y}Zr_y)_2O_7$ Pyrochlore Powders: Disorder with Zr Substitution*, S.B. Thesis, Department of Materials Science and Engineering, Massachusetts Institute of Technology, Cambridge, MA, June 1998.
21. E. M. Ku, *Synthesis, Cation Distribution, and Disorder of Fast-Ion Conducting Pyrochlore Oxides: A Combined Neutron and X-ray Rietveld Analysis*, S.M. Thesis, Department of Materials Science and Engineering, Massachusetts Institute of Technology, Cambridge, MA, February 1999.
22. E. M. Ku, E. M. E. Yeo, and B. J. Wuensch, Crystal chemistry of $Y_2(Zr_ySn_{1-y})_2O_7$ pyrochlore solid solutions and its relations to fast-ion conduction, *Mater. Res. Soc. Sympos. Proc.* 547: 327-332 (1999).
23. C. J. Howard, D. J. Cookson, B. J. Kennedy, T. Ikeda, M. Takata, and M. Sakata, Charge and nuclear density distribution of the pyrochlore $Y_2Sn_2O_7$ by MEM, (abstract), *Acta Crystallogr.* A52: C349 (1996).
24. B. J. Kennedy, B. A. Hunter, and C. J. Howard, Structural and bonding trends in tin pyrochlore oxides, *J. Solid State Chem.* 130: 58-65 (1997).
25. B. J. Wuensch, K. W. Eberman, C. Heremans, E. M. Ku, P. Önnnerud, E. M. E. Yeo, S. M. Haile, J. K. Stalick, and J. D. Jorgensen, Connection between oxygen-ion conductivity of pyrochlore fuel-cell materials and structural change with composition and temperature, *Solid State Ionics*, in press.

ORDERING KINETICS IN B2-FeAl

H. LANG, K. ROHRHOFER, AND W. PFEILER

Institut für Materialphysik, University of Vienna, Strudlhofgasse 4, A-1090, Vi

H. SCHWEIGER AND R. PODLOUCKY

*Center of Computational Materials Science and Department for Physical Che
Vienna, Liechtensteinstrasse 22a/1/3, A-1090 Vienna, Austria*

ABSTRACT

Changes in the degree of long-range order (LRO) have been investigated in B2-ordered intermetallic Fe-44.8at%Al by residual resistometry. Order variations were observed during isochronal and isothermal small-step annealing after different thermal pre-treatment. It is observed that atomic mobility in this alloy starts at about 500K. Between 500K and 700K reversible changes of resistivity are interpreted as arising from local changes of order only. Above 710K changes of LRO are observed which lead to the reversible adjustment of equilibrium plateau values above 870K. Two individual processes are found for both ordering regimes, which concern only local sample areas and the total sample volume, respectively.

INTRODUCTION

Because of their extraordinary high-temperature mechanical and corrosion properties intermetallic compounds are of great interest for technical applications. As these attractive characteristics are linked to long-range ordering (LRO), knowledge of ordering kinetics is necessary.

Whereas ordering kinetics has been investigated recently by various groups for L1₀- and L1₂-ordered alloys [1-5] there is still a lack of investigations on B2-ordered alloys. Problems have been encountered in studying B2 beta brass [6] because of a too high atomic mobility in this alloy system. High temperature intermetallics of the B2-type like FeAl on the other hand remain highly ordered right up to the melting temperature. This keeps the variation with temperature of the LRO-parameter very small limiting the possibility to study LRO-kinetics by most experimental methods.

Very recently it was tried to study LRO-kinetics in B2 FeAl by using *residual resistometry*. Due to the extreme sensitivity for structural changes this method is a very powerful tool for investigating ordering effects in highly ordered

materials as already been shown for L1₂-ordered Ni₃Al [4]. In the present paper we report an investigation of ordering kinetics by residual resistometry on B2-ordered FeAl.

EXPERIMENTAL PROCEDURE

Sample material of the composition Fe-44.8at%Al was alloyed by the Swiss Federal Institute of Technology from 4N Fe and 5N Al by high frequency melting under purified Argon atmosphere (grain size about 300 μ m). A thin slice of about 0.2mm thickness was cut. Subsequently, S-shape resistivity samples were punched out by spark erosion. For electrical conductivity glasswool isolated wires (annealings up to 923K possible) were contacted to strips of pure copper which were carefully spot-welded to the sample. All annealings were carried out in a quartz tube furnace under argon atmosphere (temperature stability ± 2 K). Resistivity measurement was done by the potentiometric method in liquid N₂ on water quenched samples relative to a dummy specimen (accuracy $\pm 3 \times 10^{-4}$).

The present results of isothermal measurements were obtained subsequent to several earlier isochronal measurements [7]. To adjust a well defined initial state, the sample was annealed for 3h at 1223K, slowly cooled to 773K and water quenched. As-measured resistivity values were corrected for a continuous drift (see [8]).

RESULTS AND DISCUSSION

Resistivity measurements during isochronal annealing treatment [7] give evidence that the atomic mobility in this intermetallic alloy starts at about 500K (fig.1). Between 540 and 710K the electrical resistivity shows a slight increase, although the LRO-equilibrium corresponding to these temperatures should result in a tendency to much lower resistivity values. Above 710K a drastic decrease in resistivity is found which obviously can be attributed to a marked change in the degree of LRO. For temperatures higher than 840K reversible changes of resistivity are observed reflecting that the sample now has obtained a degree of LRO which is in equilibrium with the actual annealing temperatures.

In addition, residual electrical resistivity was measured during isothermal small-step annealing between 473 and 933K [8]. Two different regimes of ordering can be distinguished with respect to the ordering relaxation rate. For short annealing times *small* reversible changes of resistivity result which vary linearly with temperature. For long annealing times a tendency towards *bigger* changes of resistivity is obtained. This is in good correspondence with model calculation in Bragg-Williams approximation (virtual transition temperature $T_{O/D}=1573$ K) using the Rossiter formalism [9] with fit parameter $A=0.943$. In

figure 2 the relative change of resistivity during isothermal long-time annealings (■) and the final plateau values corresponding to LRO-equilibrium as calculated in Bragg-Williams approximation (thick horizontal lines) are given. In addition, plots of the separated slower LRO effect (overall LRO, see below) and the much faster second process (local ordering, see below) are shown.

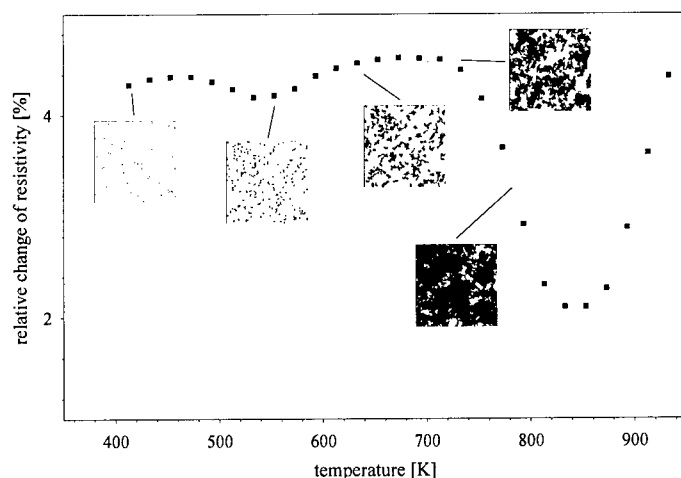


Figure 1. Relative change of electrical resistivity during isochronal annealing. The small inserts for some given temperatures show schematically the regions which have been visited by vacancies during isochronal annealing time (black).

Our interpretation of the presence of two different ordering regimes is as follows. As known from the literature the formation enthalpy of vacancies of about 0.7eV in Fe-44.8at%Al is relatively low [10,11]. In contrast, the migration enthalpy of about 1.6eV is rather high [12]. Therefore, having once annealed the sample at high temperatures a high number of vacancies is retained, which due to the high migration enthalpy are more or less immobile during subsequent annealings at low temperature. Because of this restricted mobility the annihilation of vacancies is rather small resulting in a practically constant number of vacancies in the observed temperature range [13].

At temperatures below about 650K, only atom jumps over a few lattice distances are possible during short observation periods (e.g. isochronal time interval of 20min.). These jumps therefore will result in restricted areas around each vacancy with a degree of order which locally corresponds to the actual annealing temperature ('local ordering'). The size of these regions increases with temperature and/or annealing time. For high enough annealing temperatures (starting at about 710K for isochronal annealing) or long enough annealing times the regions begin to overlap (impingement) and only then an overall LRO-equilibrium can be adjusted within the total sample volume.

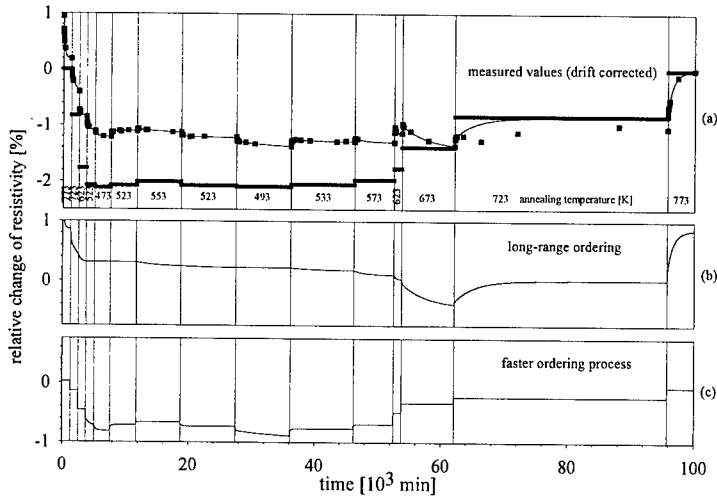


Figure 2. (a) Relative changes of resistivity versus annealing time during isothermal small-step annealing (■). In addition LRO-equilibrium values as calculated in Bragg-Williams approximation (thick horizontal lines) are shown. (b) Slow overall adjustment of LRO within total sample volume. (c) Fast (local) ordering.

A fit of the experimental data of isothermal annealings within the frame of the above model yielded two exponential processes for each of both ordering regimes. In figure 3 an Arrhenius plot of the relaxation times obtained is given. For the regime of local ordering equal activation enthalpies of $1.3 \pm 0.1 \text{ eV}$ each and frequency factors of $\tau_0 = 6 \times 10^{-11} \text{ s}$ for the fast and $\tau_0 = 6 \times 10^{-9} \text{ s}$ for the slow process are obtained. The activation enthalpies of the overall LRO adjustment were found to be $0.8 \pm 0.1 \text{ eV}$ ($\tau_0 = 4 \times 10^{-3} \text{ s}$) for the fast and $1.5 \pm 0.1 \text{ eV}$ ($\tau_0 = 6 \times 10^{-6} \text{ s}$) for the slow process.

The two processes found for local ordering are interpreted as jumps between vacancies and atoms in nearest neighbour position. As discussed above the vacancy concentration can be assumed as being practically constant. In this case the measured activation enthalpy of 1.3 eV is due to vacancy migration only. The difference in relaxation times for these two processes may be caused by the different concentration of vacancies on the two sublattices. The frequency factors of both local ordering processes are in correspondence with typical Debye frequencies, which supports the assumption that only single vacancy jumps are involved. Both processes contribute to a similar amount to the corresponding resistivity changes.

The activation enthalpy of ordering for the slow overall LRO-process is found to be very close to the enthalpies of local ordering. Therefore it is assumed that the obtained energy corresponds to the migration energy of atom jumps to nearest neighbour vacancies. The origin of the very low activation enthalpy of 0.8 eV of the fast process has not been clarified yet, although there are hints to such a second LRO-process by Schaefer et al. [14]. In contrast to local ordering

the frequency factors of the overall ordering processes are much higher and may be connected with correlated atom jumps. A comparison of the contributions of the two overall LRO-processes shows that the slower process dominates contributing to about 90% to this ordering regime. For an illustration of the model of 'local ordering' we simulated the random walk of vacancies over a square lattice containing 10^8 atoms. The inserts in figure 1 show snapshots of the lattice after times of isochronal annealing up to the respective temperatures. The black areas represent the regions which had been visited by the vacancies. For low annealing.

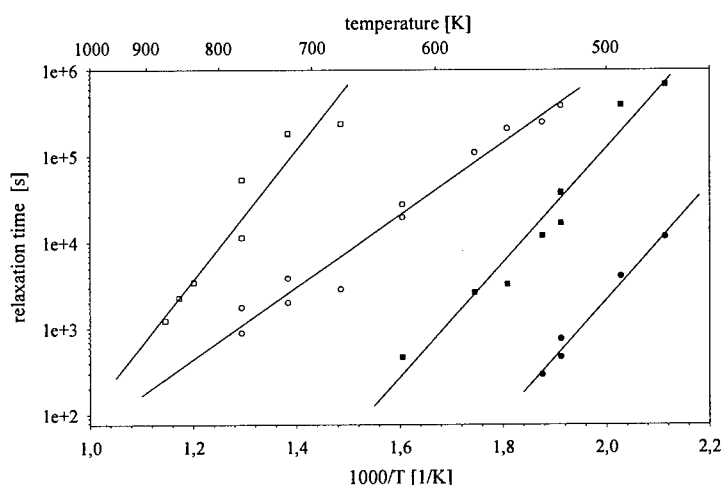


Figure 3. Arrhenius plot of all relaxation processes involved in changes of LRO. Local ordering process: fast (●) and slow (■); overall long-range ordering: fast (○) and slow (□).

temperatures and/or short annealing times these regions are well separated, whereas for temperatures above 710K and/or very long annealing times at lower temperatures they become interconnected (impingement).

As a test for the above interpretation of two regimes of ordering, local and overall, it was tried to fit the change of resistivity during isochronal annealing using the activation enthalpies and pre-factors as analysed from isothermal measurements under the assumption of constant vacancy concentration. The LRO-equilibrium values for each annealing temperature were determined by a model calculation in Bragg-Williams approximation ($T_0/D=1573K$) and applying the Rossiter formalism with $A=0.943$. The equilibrium values of local ordering were taken from isothermal measurements. In figure 4 the measured change in resistivity during isochronal annealing (■) and the calculated behaviour of resistivity (thin line) are shown. In addition, fitted equilibrium values of local ordering (●) and of LRO (▲) as well as a linear regression function for local ordering (dotted line) and a LRO-equilibrium line as calculated in Bragg-Williams approximation (thick line) are given. A very good

correspondence between the calculated and the measured values can be observed. Further, above 850K an excellent fit between the measured isochrone and the values as calculated in Bragg-Williams approximation is found. Therefore it can be concluded that above 850K LRO-equilibrium is reached within the isochronal annealing time (20min).

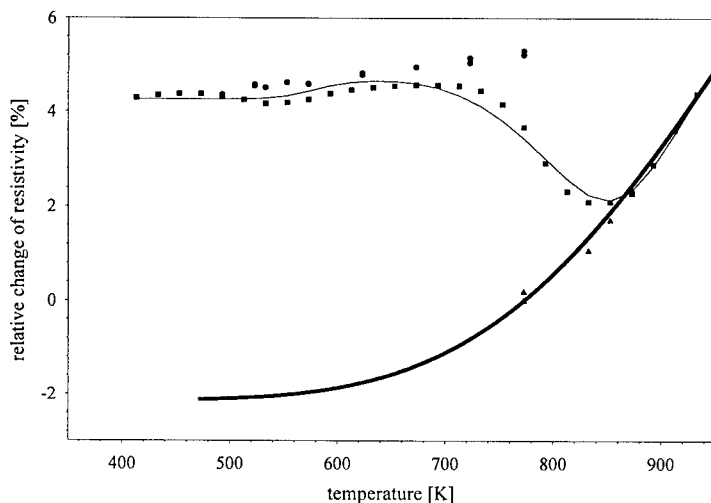


Figure 4. Relative change of resistivity during isochronal annealing as measured (■) and as calculated (thin line). In addition, equilibrium values of local ordering (●) and LRO equilibrium values (▲) as obtained by isothermal measurements are given. Dotted line: local ordering, linear approximation of equilibrium values; thick line: overall LRO-equilibrium as calculated in Bragg-Williams approximation.

CONCLUSIONS

The conclusions drawn from the present study by residual resistometry can be summarised as follows:

- 1) Atomic mobility in Fe-44.8 at%Al starts at about 500K.
- 2) Isothermal small-step annealing suggests two ordering regimes: local ordering due to the limited range of vacancy motion at low temperatures and/or short annealing times; a second regime of overall long-range ordering for high temperatures and/or very long annealing times when the whole sample volume is reached by vacancies. Two 'equilibrium lines' of order are obtained, a metastable one for local ordering and a stable one for the overall process.
- 3) The ordering kinetics of both regimes is composed of two sub-processes each. Vacancy parameters are obtained from a corresponding Arrhenius analysis under the assumption of a constant vacancy concentration within the investigated temperature range.
- 4) Using these values the resistivity change during isochronal annealing can be fitted very well, supporting the two-regime model of ordering kinetics developed in the present paper.

ACKNOWLEDGEMENT

Financial support by the Austrian 'Fonds zur Förderung der wissenschaftlichen Forschung' contract no. P12420-Phy.

REFERENCES

1. A. Sattonnay and O. Dimitrov, *Long-range order relaxation and phase transformation in gamma-TiAl alloys*, Acta Mat. **47**, 2077 (1999).
2. H. Lang and W. Pfeiler, in: *Solid-Solid Phase Transformations*, W.C. Johnson, J.M. Howe, D.E. Laughlin and W.A. Soffa, eds., The Minerals, Metals & Materials Society, Warrendale (1994), p. 479.
3. W. Pfeiler, R. Kozubski, H.P. Karnthaler and C. Rentenberger, *Kinetics of defect recovery and long-range ordering in Ni3Al+B. 1. Simultaneous recovery and ordering in cold-rolled materia*. Acta Mater. **44**, 1563 (1996)
4. R. Kozubski and W. Pfeiler, *Kinetics of defect recovery and long-range ordering in Ni3Al+B .2. Atomic jump processes studied by "order-order" relaxation experiments*. Acta Mater. **44**, 1573 (1996)
5. C. Dimitrov, X. Zhang and O. Dimitrov, *Kinetics of long-range order relaxation in Ni3Al: The effect of stoichiometry*. Acta Mater. **44**, 1691 (1999).
6. J.S. Clark and N. Brown, *A study of a dilute concentration of disorder in the beta-CuZn superlattice*. J. Phys. Chem. Solids **19**, 291 (1961).
7. K. Rohrhofer, H. Lang, P. Rosenkranz, R. Kozubski, W. Püschl and W. Pfeiler, *Changes in the degree of LRO in B2-ordered intermetallic FeAl*. Mat. Res. Soc. Symp. Proc. 552, KK8.23.1 (1999).
8. K. Rohrhofer, H. Lang, W. Püschl and W. Pfeiler, *B2-ordered intermetallic FeAl: Changes in the degree of LRO*. in: Proceedings of the International Conference on Solid-Solid Phase Transformations '99, Ed. M. Koiwa, K. Otsuka and T. Miyazaki. The Japan Institute of Metals, 1999, p. 53.
9. P.L. Rossiter, *The Electrical Resistivity of Metals and Alloys*, Cambridge University Press, Cambridge 1987.
10. M. Kogachi and T. Haraguchi, *Quenched-in vacancies in B2-structured intermetallic compound FeAl*. Mat. Sci. Eng. A230, **124** (1997).
11. R. Würschum and H.-E. Schaefer, Mat. Sci. Forum **255-257**, 81 (1997).
12. J.P. Rivière and J. Grilhe, Acta Met. **20**, 1275 (1972).
13. G.S. Collins, J. Fan and B. Bai, in: *Structural Intermetallics 1997*, Ed. M.V. Nathal et al., The Minerals, Metals & Materials Society, 1997.
14. H.-E. Schaefer, K. Frenner, R. Würschum, *High-temperature atomic defect properties and diffusion processes in intermetallic compounds*. Intermetallics **7**, 277 (1999). A. Sattonnay and O. Dimitrov, Acta Mat. **47**, 2077 (1999).

THEORETICAL STUDY OF SPINODAL DISORDERING AND DISORDERING RELAXATION

Tetsuo MOHRI

Division of Materials Science and Engineering
Graduate School of Engineering
Hokkaido University, Sapporo, 060-8628, JAPAN

ABSTRACT

By employing Cluster Variation and Path Probability Methods, disordering relaxation kinetics of $L1_0$ ordered phase at 1:1 stoichiometric composition is studied. The instability temperature above the order-disorder transition temperature is termed *spinodal disordering* temperature at which the susceptibility is confirmed to diverge. The temperature dependence of the relaxation time behaves not monotonically but increases towards the spinodal disordering temperature. This is believed to be the pseudo-critical slowing down phenomenon reported for the first-order transition.

INTRODUCTION

Destabilization of a disordered system quenched in an ordered phase field due to the excitation and amplification of an ordering wave has been termed spinodal ordering (de Fontaine, 1975). The loss of the stability is well analyzed within the framework of thermodynamics (Sanchez, 1981; Mohri et al., 1985a), and the mathematical condition of the spinodal ordering has been described as the vanishing condition of the second order derivative of the free energy functional with respect to correlation functions (Sanchez et al., 1978; Mohri et al., 1985b) which constitute a set of independent configurational variables of a given system. The evidence of the spinodal ordering has been examined by diffraction experiments (Banerjee et al., 1984; Takeda et al., 1987). As opposed to the Nucleation-Growth mechanism (hereafter abbreviated as NG) which is characterized as the appearance of sharp superlattice spots, a continuous transfer of the diffuse intensities towards superlattice spots features the spinodal ordering.

It is natural to extend the notion of the spinodal ordering to an ordered phase up-quenched in the disordered phase field. In this case, spontaneous disordering reaction of the metastable ordered phase is expected. One may call this phenomenon *spinodal*

disordering. As will be demonstrated latter, this can be examined by the free energy-Long range order parameter (hereafter abbreviated as LRO) curve. The vanishing of the free energy hump between the stable disordered phase and a metastable ordered phase characterizes the spinodal disordering.

The Cluster Variation Method (hereafter abbreviated as CVM) (Kikuchi,1951) has been recognized as one of the most powerful and reliable theoretical tools for describing the thermodynamic behavior of a given system. The key to the success of the CVM is due to the fact that CVM is capable of incorporating wide range of atomic correlations, which assures the accuracy of the calculated free energy. The first aim of the present study is to provide a thermodynamic evidence of the spinodal disordering based on free energy-LRO curve derived by the CVM. A particular emphasis throughout this study is placed on the $L1_0$ - *disorder* transition at a fixed 1:1 stoichiometric composition.

Besides such a thermodynamic point of view, it is desirable to discuss the kinetic evidence of the spinodal disordering reaction. Starting with the metastable ordered phase, the trace of time evolution of the LRO provides the insight of the reaction process. The spontaneous reaction characterized by the non-existence of the free energy hump could be reflected as the absence of configurational fluctuations at the initiation of the disordering transition. A critical examination of this point is attempted with an appropriate kinetics model.

Path Probability Method (hereafter abbreviated as PPM) (Kikuchi,1966) is the natural extension of the CVM to the time domain and, therefore, inherits various excellent features of the CVM. It has been amply demonstrated (Mohri,1990; Mohri,1994a,b; Mohri,1996) that the steady state values calculated for the long-time limit coincides with the equilibrium ones derived by the CVM. The combination of PPM and CVM, therefore, provides a unique tool to study the time-evolution behaviour from non-equilibrium towards final equilibrium state in a consistent manner. The second aim of the present study is to examine the kinetic evidence of the spinodal disordering reaction based on PPM calculations.

According to the earlier investigation (Bolton and Leng,1975) based on the linearized Fokker-Planck equation within the Bragg-Williams free energy Model (Bragg and Williams, 1934), a slowing-down behavior of the relaxation time is predicted for the first-order transition. This is expected not in the vicinity of the transition temperature but near the spinodal disordering temperature defined above. Although their unified analysis with thermodynamics and kinetics reveals an essential feature of the slowing-down phenomenon, the Bragg-Williams free energy model has been criticized for the lack of reliability to describe the thermodynamic behavior of a given system. In particular, the first order nature of the $L1_0$ - *disorder* transition is not fully reproduced with the Bragg-Williams model. Also, the applicability of the linearized kinetic equation to the *far-from-equilibrium* regime is not rationalized. Such short comings are expected to be overcome by the present calculations based on CVM and PPM.

As approaching transition temperature, a dynamic feature of the transition is manifested and various pre-transition phenomena including the slowing-down phenomenon begin to appear. A key theoretical quantity to analyze such phenomena is the generalized susceptibility. Calculations of the susceptibility within the CVM have been one of the main focal points in the series of our investigations (Mohri,1999; Mohri,2000a,b) on pre-transition behavior. Even by combining CVM with electronic structure total energy calculations, the first-principles study of the susceptibility was attempted for Cu-Au system. The main results are reproduced from the previous study (Mohri,2000a). The discussions on the calculated susceptibility constitute the third subject of the present paper.

Finally, the temperature dependence of the relaxation time during the isothermal aging process following up-quenching operation of the $L1_0$ ordered phase is calculated by PPM (Mohri,2000a,b). In contrast to the susceptibility which provides thermodynamic

information on the intrinsic stability of a given system, the present calculations are expected to yield a direct evidence comparable with experimental measurements. The organization of the present paper is as follows. For the sake of completeness, in the next section we summarize the theoretical aspects of CVM and PPM. The main results and discussion are presented in the third section.

THEORETICAL BACKGROUND

Cluster Variation Method

Theoretical aspects of the CVM have been amply demonstrated in already published papers. Therefore, in this section, essential aspects necessary for the present study are recalled.

The key of the CVM is the wide range of atomic correlations explicitly incorporated in the free energy formula through the entropy term. The range of the atomic correlations is equivalently expressed as the size of the cluster and, therefore, the largest cluster involved in the entropy term determines the level of the approximation. Within the Tetrahedron approximation (Kikuchi, 1974), for instance, for which the tetrahedron cluster is the largest cluster, the entropy term is given as

$$S = k_B \cdot \ln \frac{\left(\prod_{ij} (N \cdot y_{ij})! \right)^6 \cdot (N!)}{\left(\prod_i (N \cdot x_i)! \right)^5 \cdot \left(\prod_{ijkl} (N \cdot w_{ijkl})! \right)^2}, \quad (1)$$

where k_B is the Boltzmann constant, N the total number of lattice points and x_i, y_{ij}, w_{ijkl} are probabilities for point, pair and tetrahedron clusters, respectively, of which atomic configuration is specified by subscript(s). It is noted that +1 and -1 are assigned to subscript depending on A and B atoms, respectively. Throughout the present study, body of the calculations are carried out with the Tetrahedron approximation.

A common practice of formulating the internal energy is to employ the nearest neighbor pair interaction energy model given as

$$E = \frac{1}{2} \cdot N \cdot Z \cdot \sum_{i,j} e_{ij} \cdot y_{ij} \quad (2)$$

where Z is the coordination number and e_{ij} is the atomic pair interaction energy between the nearest neighbor i - j pair.

Since, for most metallic alloy systems, a central force is responsible for cohesion, the neglect of the multi-body interaction forces may be rationalized as a first approximation. On the other hand, the effects of the distant pair interaction energies are not trivial. According to the ground state analysis (Richards and Cahn, 1971; Kaburagi and Kanamori, 1975), however, it is assured that the $L1_0$ ordered phase can be stabilized with merely nearest neighbor pair interactions. In order to avoid numerical complications, the present study is limited to the nearest neighbor pair interaction model. Then, together with the entropy formula given in eq.(1), the free energy is symbolically written as

$$F = E - T \cdot S = F(T, \{e_{ij}\}, x_i, y_{ij}, w_{ijkl}) \quad (3)$$

Equivalent to the cluster probability is the correlation function, ξ_i , where the subscript i indicates the size and the type of an atomic cluster. With a spin variable $\sigma(p)$ which takes either +1 or -1 depending upon A or B atom, respectively, located on the lattice point p , the correlation function, ξ_i , is formally defined as the ensemble average of the spin variables,

$$\xi_i = \langle \sigma(p_1) \cdot \sigma(p_2) \cdots \sigma(p_i) \rangle \quad (4)$$

It is readily shown (Sanchez et al, 1978; Mohri et al, 1985b) that the correlation functions and a cluster probability are related by a linear transformation through,

$$x_{i_1 i_2 \cdots i_n} = \frac{1}{2^n} \left\{ 1 + \sum_{n'} V_{nn'}(i_1 i_2 \cdots i_n) \cdot \xi_{n'} \right\} \quad (n' \in n) \quad (5)$$

where the left-hand side indicates the cluster probability of a n -point cluster and this should not be confused with the point probability x_i , and $V_{nn'}(i_1 i_2 \cdots i_n)$ constitutes the sum of the products of i_1, i_2, \cdots, i_n which are either +1 or -1 depending upon A or B atom, respectively, located on n lattice points. Instead of describing the mathematical derivation of eq.(5), it is rather easy to grasp the insights by exemplifying cluster probabilities written in terms of the correlation functions. Demonstrated below are the three kinds of cluster probabilities appeared in the entropy term in eq.(1),

$$x_i = \frac{1}{2} (1 + i \xi_1) \quad (6)$$

$$y_{ij} = \frac{1}{2^2} \{ 1 + (i + j) \xi_1 + ij \xi_2 \} \quad (7)$$

and

$$w_{ijkl} = \frac{1}{2^4} \{ 1 + (i + j + k + l) \cdot \xi_1 + (ij + ik + il + \cdots + kl) \cdot \xi_2 \\ + (ijk + ij l + \cdots + jkl) \cdot \xi_3 + ijkl \cdot \xi_4 \} \quad (8)$$

Hence the symbolic representation of the free energy given by eq.(3) is rewritten as

$$F = F(T, \{e_{ij}\}, \xi_1, \xi_2, \xi_3, \xi_4) \quad (9)$$

It should be noted that the above expressions are derived for a disordered phase, while the distinction of the sublattices based on the symmetry is indispensable for an ordered phase. One can realize that the breaking of the symmetry lifts the degeneracy of the correlation functions for a disordered phase as $\xi_1 \rightarrow \xi_1^\alpha$ and ξ_1^β ; $\xi_2 \rightarrow \xi_2^{\alpha\alpha}, \xi_2^{\alpha\beta}$ and $\xi_2^{\beta\beta}$; $\xi_3 \rightarrow \xi_3^{\alpha\alpha\beta}$ and $\xi_3^{\alpha\beta\beta}$ and $\xi_4 \rightarrow \xi_4^{\alpha\alpha\beta\beta}$, where α and β constitute sublattices of the $L1_0$ ordered phase. Hence, the free energy expression for $L1_0$ ordered phase corresponding to eq.(9) is written as

$$F^{L1_0} = F(T, \{e_{ij}\}, \xi_1^\alpha, \xi_1^\beta, \xi_2^{\alpha\alpha}, \xi_2^{\alpha\beta}, \xi_2^{\beta\beta}, \xi_3^{\alpha\alpha\beta}, \xi_3^{\alpha\beta\beta}, \xi_4^{\alpha\alpha\beta\beta}) \quad (10)$$

The advantage of the correlation function over the cluster probability is due to the fact that the correlation functions form a set of independent configurational variables. And it has been shown that any configurational quantities can be expanded in the configurational space spanned by the correlation functions (Connolly and Willaims, 1983; Sanchez et al., 1984). In fact, the internal energy given by eq.(2) is expanded as

$$E(\{\xi_k\}) = \sum_k v_k \cdot \xi_k \quad (11)$$

where the coefficient term v_k is the effective cluster interaction energy for the cluster specified by k . The effective interaction energy v_k can be easily related to the atomic pair interaction energies e_{ij} by substituting eq.(7) into eq.(2) and comparing the resulting expression with eq.(11). The effective pair interaction energy v_2 , for instance, is related to the atomic pair interaction energy e_{ij} as

$$v_2 = \frac{3}{2} \cdot (e_{AA} + e_{BB} - 2e_{AB}) \quad , \quad (12)$$

which has been known as the interaction parameter in thermochemistry. Then, by replacing $\{e_{ij}\}$ with $\{v_k\}$, the free energy expression for disordered and $L1_0$ ordered phases given by eqs.(9) and (10) are, respectively, rewritten as

$$F^{dis} = F(T, \{v_k\}, \xi_1, \xi_2, \xi_3, \xi_4) \quad (13)$$

and

$$F^{L1_0} = F(T, \{v_k\}, \xi_1^\alpha, \xi_1^\beta, \xi_2^{\alpha\alpha}, \xi_2^{\alpha\beta}, \xi_2^{\beta\beta}, \xi_3^{\alpha\alpha\beta}, \xi_3^{\alpha\beta\beta}, \xi_4^{\alpha\alpha\beta\beta}) \quad (14)$$

Finally, the equilibrium state is obtained by minimizing the free energy with respect to the correlation functions,

$$\left(\frac{\partial F}{\partial \xi_l^\gamma} \right)_{T, \{v_k\}, \{\xi_{k,k \neq l}\}} = 0 \quad , \quad (15)$$

where γ represents either α or β for the $L1_0$ ordered phase while no specification is necessary for the disordered phase. The comparison of the equilibrium free energies of disordered and $L1_0$ ordered phases yield a phase diagram as will be shown in the next section. Also, the generalized susceptibility which is one of the major interests in the present study is calculated based on eq.(14).

It is pointed out that, in order to achieve higher accuracy, Tetrahedron-Octahedron (hereafter abbreviated as T-O) approximation (Sanchez et al., 1978; Sanchez et al., 1980; Mohri et al., 1985b) is desirable. However, the T-O approximation of the PPM for $L1_0$ ordered phase is not yet at our hand. In order to keep the consistency between CVM and PPM calculations, the Tetrahedron approximation is employed in the present study. We, however, note that Tetrahedron approximation has been recognized as the minimum meaningful approximation for fcc-based systems and various calculations including

first-principles calculations were achieved successfully within the Tetrahedron approximation.

Path Probability Method

Unique to the PPM is the fact that the cluster probabilities or their derivatives are not explicitly dealt with, which is in marked contrast with other kinetic theories. Also, it is noted that most kinetic theories assume that driving force of the time evolution is proportional to the gradient of the free energy, but this is valid only for the *near-equilibrium* transition. On the contrary, being free from the free energy, PPM is able to deal with not only the *near-equilibrium* but also *far-from-equilibrium* transitions.

As was described in the previous section, PPM is the natural extension of the CVM to the time domain. Corresponding to the free energy of the CVM is the *path probability function* P , while the counterpart of the cluster probabilities in the CVM is the *path variable*, $\Xi_{\eta,\zeta}(t; t + \Delta t)$, which relates the cluster probabilities ρ at time t and at time $t + \Delta t$ through

$$\rho_{\phi}(t + \Delta t) = \rho_{\psi}(t) + \sum_{\eta,\zeta} C_{\eta,\zeta} \cdot \Xi_{\eta,\zeta}(t; t + \Delta t) \quad (16)$$

where ψ , ϕ , η and ζ represent an atomic configuration and $C_{\eta,\zeta}$ is a coefficient term which depends on the type of the kinetics adopted in the model. One may grasp the insights by exemplifying the relation between point path variables $\Xi_{\psi,\phi}(t; t + \Delta t) = X_{i,j}$ and point cluster probabilities $\rho_i(t) = x_i(t)$ and $\rho_i(t + \Delta t) = x_i(t + \Delta t)$ given in the following manner,

$$x_i(t) = X_{i,1} + X_{i,\bar{1}} \quad (17)$$

and

$$x_i(t + \Delta t) = X_{i,1} + X_{\bar{1},i} \quad (18)$$

Hence, corresponding to eq.(16), one may obtain

$$x_i(t + \Delta t) = x_i(t) - X_{i,\bar{1}} + X_{\bar{1},i} \quad (19)$$

with $C_{i,\bar{1}} = -1$ and $C_{\bar{1},i} = 1$. In a similar manner, the relationships given by eq.(16) can be confirmed for a bigger cluster.

By employing the path variables, the path probability function is written as the product of three terms,

$$P = P_1 \cdot P_2 \cdot P_3 \quad (20)$$

with

$$P_1 = (\theta \cdot \Delta t)^{N(x_{i,\bar{1}} + x_{\bar{1},i})} (1 - \theta \cdot \Delta t)^{N(x_{i,1} + x_{\bar{1},\bar{1}})} \quad (21)$$

$$P_2 = \exp\left(-\frac{\Delta E}{2k_B \cdot T}\right) \quad (22)$$

and

$$P_3 = \frac{\left(\prod_{ij,kl} (N \cdot Y_{ij,kl})!\right)^6 (N!)}{\left(\prod_{ijkl,mnop} (N \cdot W_{ijkl,mnop})!\right)^2 \left(\prod_{i,j} (N \cdot X_{i,j})!\right)^5} \quad (23)$$

where θ is the spin-flip probability per unit time, $Y_{ij,kl}$ and $W_{ijkl,mnop}$ are the path variables for pair and tetrahedron clusters, respectively, and ΔE is the change of the internal energy during an infinitesimal time period Δt . With the aid of eq.(11), ΔE is further described as

$$\Delta E = \sum_i v_i \cdot \Delta \xi_i - \mu_i \cdot \Delta \xi_i \quad (24)$$

where $\Delta \xi_i$ is the change of correlation function for i -cluster during Δt and μ_i is the effective chemical potential. It is also noted that the spin-flip probability is further described as

$$\theta = \nu \cdot \exp\left(-\frac{\Delta Q}{k_B \cdot T}\right) \quad (25)$$

which incorporates thermal activation process characterized by attempt frequency ν and activation barrier ΔQ .

Two points should be made clear about the path probability function. First, P_1, P_2 and P_3 described above are valid only for the spin kinetics (Glauber dynamics) (Glauber, 1953). When the exchange kinetics (Kawasaki dynamics) (Kawasaki, 1966) is considered, the additional constraints are imposed since the species is strictly preserved, which is in marked contrast with spin kinetics for which the conservation law is not observed. Furthermore, when the vacancy mechanism is taken into account, in addition to the conservation law of exchange kinetics, the microscopic freedom of atomic motion is greatly increased. Although the formal structure of eq.(16) is not altered in both exchange kinetics and vacancy mechanism, the coefficient term $C_{\eta,\zeta}$ is largely modified depending on the type of kinetics. In order to avoid numerical complications accompanied by exchange kinetics or vacancy mechanism, the present study is limited to a simple spin kinetics. Hence, the present study should be viewed as a precursor to a more realistic alloy kinetics for which vacancy mechanism is predominant. Consequently, 1 and $\bar{1}$ which indicated A and B atoms should be read as *up* and *down* spins, respectively.

The second point is that above formulae are developed for a disordered phase and the modification is necessary for the $L1_0$ ordered phase due to the broken symmetry, which is quite analogous to what was discussed for CVM in the previous section. For the point path variables, for instance, the degeneracy is lifted as $X_{i,j} \rightarrow X_{i,j}^\gamma$ where γ specifies the

sublattices, α and β . It should be recalled that one of the well accepted definitions of LRO is the difference of the concentrations of a fixed species between two sublattices. By extending eq.(19) to an $L1_0$ ordered phase, time evolution of the LRO, $S(t)$, is given as

$$\begin{aligned} S(t + \Delta t) &= x_i^\alpha(t + \Delta t) - x_i^\beta(t + \Delta t) \\ &= x_i^\alpha(t) - x_i^\beta(t) - (X_{i,\bar{i}}^\alpha - X_{i,\bar{i}}^\beta) + (X_{i,i}^\alpha - X_{i,i}^\beta) \\ &= S(t) - (X_{i,\bar{i}}^\alpha - X_{i,\bar{i}}^\beta) + (X_{i,i}^\alpha - X_{i,i}^\beta) \end{aligned} \quad (26)$$

For a larger cluster, a similar argument is also applied.

The most probable path of the time evolution is determined by maximizing the path probability function with respect to the path variables,

$$\left(\frac{\partial P}{\partial \{\Xi_{\psi,\phi}^\gamma\}} \right) = 0 \quad (27)$$

This is a counterpart of the minimization condition of the CVM free energy given in eq.(15). Then, by solving simultaneous equations, one can obtain the optimized set of path variables for each time step. With these optimized path variables, time evolution of the cluster probabilities are pursued through eq.(16) with a given set of initial conditions which are pre-determined by the CVM as an equilibrium condition at the initial temperature before the up-quenching operation. In particular, for the LRO which is our main concern, eq.(26) can be directly applicable with $S(t=0)$ as an initial condition to follow the time evolution behavior. Main results are presented in the following section.

RESULTS AND DISCUSSION

Phase diagram and spinodal disordering within CVM

The phase diagram calculated within the Tetrahedron approximation of the CVM for $L1_0$ -disorder in the vicinity of 1:1 stoichiometric composition is shown in Fig. 1. The temperature axis, $k_B \cdot T / v_2$, is normalized with respect to the nearest neighbor effective pair interaction energy v_2 . Note that this convention is held throughout the present study, and in order to simplify the notation, $k_B \cdot T / v_2$ is written as T unless a specific remark is made. A broken line in the figure is the locus of the $\langle 100 \rangle$ spinodal ordering temperature. The transition temperature and spinodal ordering temperature obtained at 1:1 stoichiometry in the present study are 1.89 and 1.63, respectively.

Shown in Figs.2(a)-(g) are the temperature variation of the free energy-LRO curve at 1:1 stoichiometric composition. At a fixed composition of 1:1 stoichiometry, the number of the independent variables is reduced due to the lattice symmetry and the free energy of the $L1_0$ ordered phase given in eq.(14) is rewritten as

$$F^{L1_0} = F(T, \{v_k\}, \xi_1^\alpha, \xi_2^\alpha, \xi_2^\beta, \xi_3^\alpha, \xi_3^\beta, \xi_4^\alpha, \xi_4^\beta) \quad (28)$$

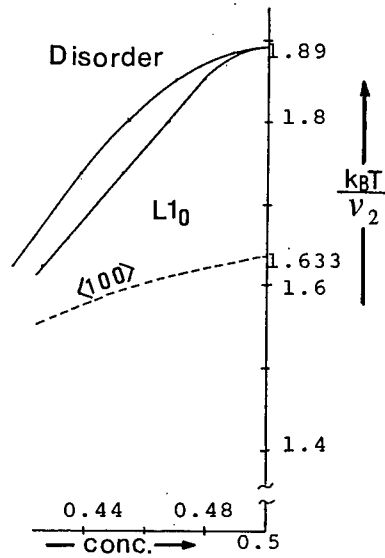


Figure 1. $L1_0$ -disorder phase diagram in the vicinity of 1:1 stoichiometric composition. Temperature axis is normalized with respect to nearest neighbor effective pair interaction energy v_2 . The broken line is the locus of $\langle 100 \rangle$ spinodal ordering.

where the relations, $\xi_1^\alpha = -\xi_1^\beta$, $\xi_2^{\alpha\alpha} = \xi_2^{\beta\beta}$ and $\xi_3^{\alpha\alpha\beta} = -\xi_3^{\alpha\beta\beta}$ are noticed. Among these variables, ξ_1^α serves as the LRO parameter defined as S in the previous section. The equivalence of ξ_1^α and S is readily verified with the following relation

$$x_i^\gamma = \frac{1}{2} (1 + i \cdot \xi_1^\gamma) \quad (29)$$

where γ refers to α or β . This is an extension of eq.(6) defined for a disordered phase to an ordered phase. All other correlation functions in eq.(28) are short-range order parameters. Hence, the series of figures in Fig.2 are obtained by minimizing the free energy with respect to the short range order parameters under a given set of LRO ξ_1^α and temperature T ,

$$\left(\frac{\partial F^{L1_0}}{\partial \xi_n^\gamma} \right)_{T, \{\xi_1^\alpha, \xi_m^\gamma, m \neq n\}} = 0 \quad (30)$$

This is a constrained minimization process.

In each figure, vertical and horizontal axes indicate free energy and LRO, respectively, and null value of the LRO indicates a complete random solid solution while a unity suggests a completely ordered $L1_0$ phase which is realized only at absolute 0 K. A finite value indicates some degree of order. At the transition temperature T_i (Fig. 2d), the free energies of both disordered and ordered phases become equivalent. Above the transition temperature, the free energy of the disordered phase becomes lower than that of the ordered

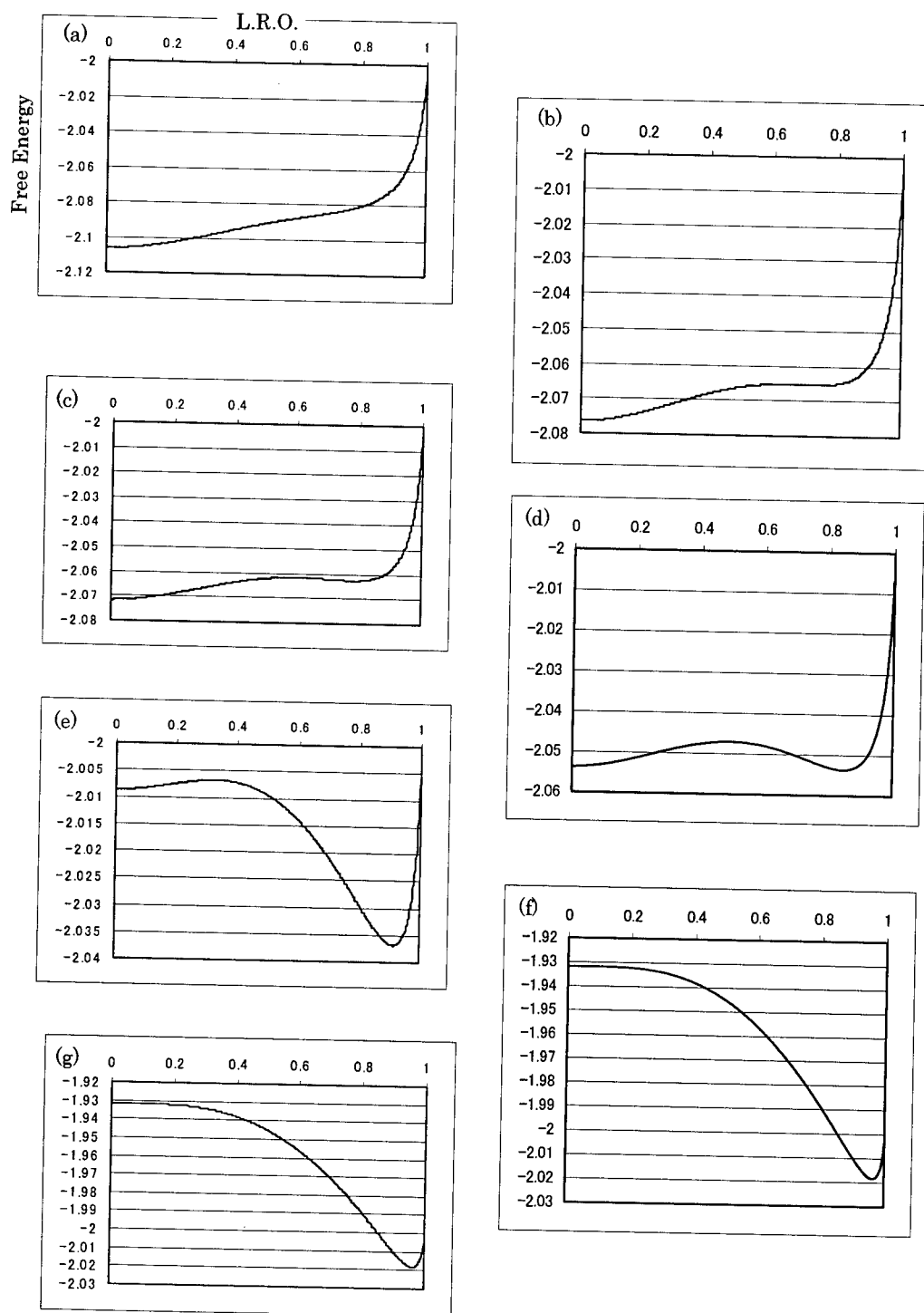


Figure 2. Temperature dependence of Free energy-LRO parameter curves calculated within the Tetrahedron approximation of the CVM. The vertical and horizontal axes indicate free energy and LRO, respectively. (a) $T=2.0$, (b) at spinodal disordering temperature $T^+=1.94$, (c) $T=1.93$, (d) at Transition temperature $T_t=1.893$, (e) $T=1.80$, (f) at spinodal ordering temperature $T^-=1.633$ and (g) $T=1.60$.

phase and the disordered phase is stabilized. One notices there exists two regimes above the transition temperature. One is characterized by an unstable ordered phase (Fig. 2a) and the other is by a metastable ordered phase (Fig. 2c). These are distinguished by the existence or non-existence of the free energy hump, and the temperature at which this free energy hump starts to appear or disappear is the *spinodal disordering* temperature (hereafter denoted by T^+) (Fig. 2b), a central concern of the present paper. In the figures, one easily notices that the analog to the spinodal disordering is the spinodal ordering temperature (hereafter denoted by T^-) (Fig. 2f) below the transition temperature. These two notions are conjugate of each other.

It is noticed that, at the spinodal disordering (ordering) temperature, the free energy curve becomes flat at the metastable ordered (disordered) phase, indicating the loss of stability and spontaneous disordering (ordering) process sets in. This is the thermodynamic significance of the spinodal disordering (ordering) temperature, and is mathematically written as the vanishing condition of the second-order derivative of the free energy with respect to the LRO parameter.

Kinetic evidence of spinodal disordering

So far, the spinodal disordering is discussed based on the free energy, namely the vanishing condition of the second-order derivative of the free energy with respect to LRO at the metastable ordered phase in the disordered phase region. It is desirable to examine the kinetic aspect of the spinodal disordering as was attempted for the spinodal ordering (Mohri, 1994a).

The system at 1:1 stoichiometric composition is maintained initially at $T = 1.20$, then is up-quenched at two temperatures, 1.93 and 2.00, above the transition temperature and the time evolution of LRO is calculated based on eq.(26). The superheated ordered phase is expected to transform to a more stable disordered phase either by NG or spinodal disordering mechanism.

The three curves in Fig. 3 are time evolution behaviour of LRO at $T = 1.93$ for three different initial conditions. Note that the time is normalized with respect to the spin-flip probability throughout the present study. The upper thick curve indicates the *natural* relaxation for which no extra chemical potential is added at the initial time $t = 0$. Hence, the initial value of LRO 0.9965 is exactly the equilibrium LRO at $T = 1.20$. One can see that the LRO relaxes with time towards a steady state value of 0.7831 which is confirmed to be the equilibrium value at $T = 1.93$ for the metastable $L1_0$ ordered phase. This confirms that the first-order transition does not proceed without fluctuation. The other two curves indicate the *biased* relaxation for which extra chemical potential $\Delta\mu_1$ is imposed in eq.(24) right after the up-quenching operation. This is reflected as the deviations from the equilibrium LRO at $T = 1.20$ suggested by the natural relaxation curve at $t = 0$, which simulates the fluctuation to trigger the first-order transition. As one can see by a thin solid line, when the imposed fluctuation is small, the system goes back to the metastable $L1_0$ ordered phase, which is indicated by the merging into the natural relaxation curve. On the contrary, for the bigger initial fluctuation (lower thick curve), the system transforms to the stable equilibrium disordered state as is confirmed by the null value of the LRO in the steady state.

Hence, one realizes that, below the spinodal disordering temperature, there exists a critical amount of ordering fluctuation which is necessary to trigger the transition. This is, in a manner, similar to a NG process. It should be, however, noticed that the actual NG process takes place spatially in a heterogeneous manner and the present free energy expression which assumes the uniformity of a system is not fully appropriate for the description of the NG.

As shown in Fig. 4 at $T = 2.0$ above the spinodal disordering temperature, on the other hand, no appreciable fluctuation is necessary to trigger the transition. The superheated metastable $L1_0$ ordered phase spontaneously transforms to a disordered phase. We claim this is the kinetic evidence of the spinodal disordering process.

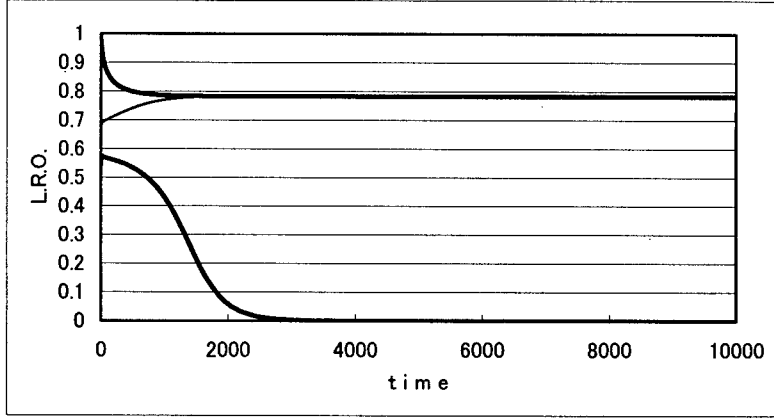


Figure 3. Time evolution behavior of LRO at temperature $T=1.93$ under three kinds of extra chemical potentials imposed at an initial time. Time axis is normalized with respect to the spin-flip probability.

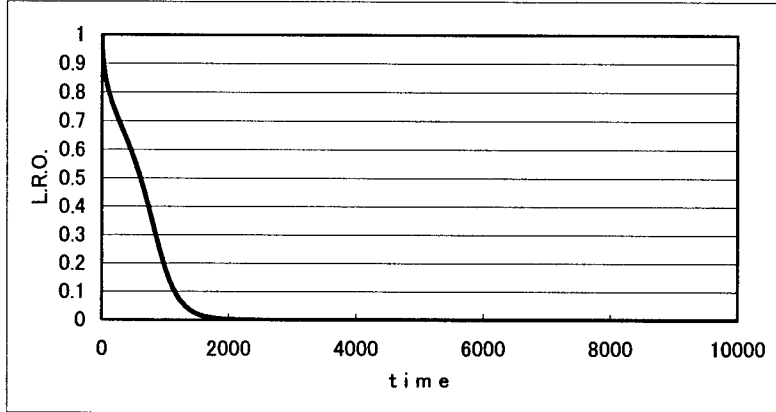


Figure 4. Time evolution of LRO at $T=2.0$. Time axis is normalized with respect to the spin-flip probability.

Generalized susceptibility

Dynamic aspects of the phase transition phenomenon is manifested as approaching the transition temperature. One of the measures of such a behavior is the temperature dependence of the generalized susceptibility, χ , which is defined as the inverse of the second order derivative of the free energy function,

$$\chi^{-1} = \left(\frac{\partial^2 F^{L_0}}{\partial \xi_1^2} \right)_{T, \{\xi_{m, m \neq 1}\}} \quad (31)$$

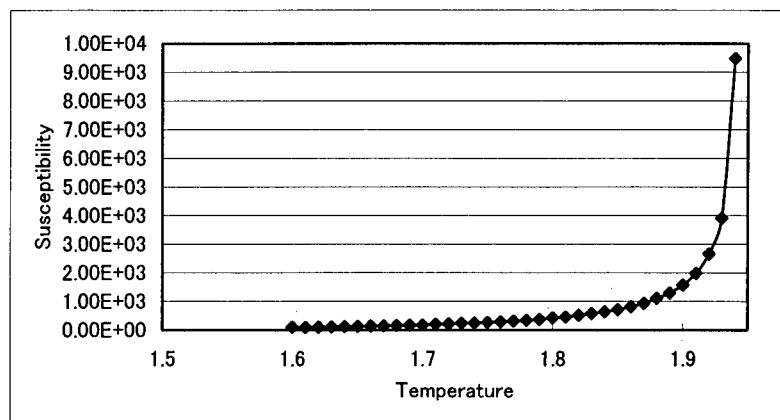


Figure 5. Temperature dependence of the susceptibility at 1:1 stoichiometry calculated within the Tetrahedron approximation of the CVM.

Hence, this provides a measure of the flatness of the free energy surface. In the present study, we calculate the temperature dependence of the generalized susceptibility at a fixed 1:1 stoichiometry for the stable and metastable $L1_0$ ordered states below and above the transition temperature, respectively. The results are shown in Fig. 5. One easily confirms that the susceptibility increases abruptly as approaching the spinodal disordering temperature of $T^+ = 1.94$.

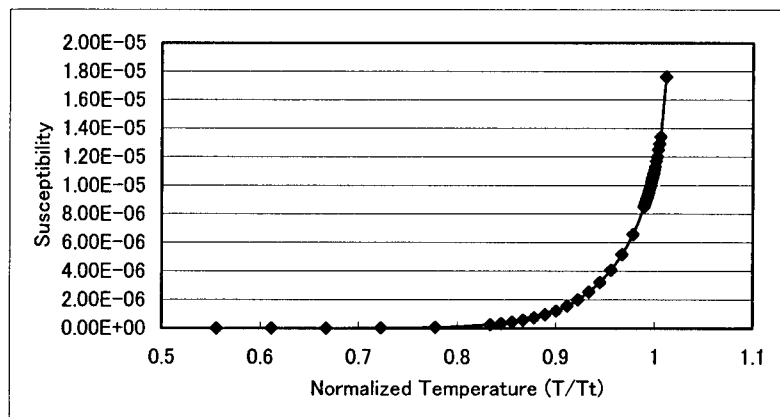


Figure 6. First-principles calculation of the temperature dependence of the susceptibility for Cu-Au system at 1:1 stoichiometric composition. The temperature axis is normalized with respect to the transition temperature, 912 K.

This is in many ways quite similar to the divergence behavior of the susceptibility for a second order transition. In fact, Fig. 2b clearly indicates that the present divergence behavior shares the common origin with that of second order transition, namely the flattening of the free energy surface. In the first order transition, this takes place at the spinodal disordering temperature while, for the second-order transition, transition temperature and spinodal ordering and disordering temperatures coincide $T^+ = T_i = T^-$, which is termed *critical temperature* T_c .

In order to examine a realistic alloy system, the first-principles calculation of susceptibility was attempted for Cu-Au system (Mohri, 2000a). We first performed the electronic structure total energy calculations for a set of selected ordered compounds as well as pure constituents as a function of lattice constant. Then, by performing the Cluster Expansion Method (Connolly and Williams, 1983), we extracted the effective cluster interaction energies up to nearest neighbor tetrahedron cluster. This procedure is originated in eq.(11) and has been amply demonstrated in the previous literatures (Terakura et al., 1987; Mohri et al., 1988; Mohri et al., 1991). For the entropy part, Tetrahedron-Octahedron approximation of the CVM was employed, for which 32 independent configurational variables participate to describe the free energy of the $L1_0$ ordered phase. Once the free energy expression is derived, the minimization is performed to obtain the equilibrium state. Since the free energy is the function of not only the correlation functions but also the lattice constant, an extra minimization procedure with respect to the lattice constant is required in addition to eq.(30). Then, the second order derivative given by eq.(31) is calculated to estimate the susceptibility. More detailed procedure is described in the previous publications and we simply demonstrate the results obtained at fixed 1:1 stoichiometric composition in Fig. 6. The temperature axis is normalized with respect to the transition temperature. The transition temperature determined by the present study is 912 K which is highly overestimated as compared with experimental value. The overestimation has been ascribed to the neglect of the local lattice relaxation process (Mohri et al., 1988; Mohri et al., 1991), but we simply assumed that the overall feature of the resultant temperature dependence may not be seriously affected when the local relaxation is properly incorporated. One sees that the susceptibility steadily increases above the transition temperature up to the spinodal disordering temperature, $T^+ = 1.015(926 \text{ K})$. We note that more elaborate first-principles calculation (Ozolins et al., 1998a,b) incorporating the local lattice relaxation effects will provide correct temperature scale.

Temperature dependence of the relaxation time

As was seen, spinodal disordering was thermodynamically characterized by CVM and kinetics evidence was provided by PPM. In the previous section, CVM calculation of the susceptibility suggested that the slowing-down phenomenon is expected near the spinodal disordering temperature. In the present section, this is directly examined from the stand point of kinetics based on PPM.

The system is again initially maintained at temperature $T=1.2$ and is up-quenched to various temperatures. The relaxation time τ during the isothermal aging process at aging temperature T defined by the following equation is calculated.

$$\xi_i^\alpha(t) = \xi_i^\alpha(t=\infty) - \{\xi_i^\alpha(t=\infty) - \xi_i^\alpha(t=0)\} \cdot \exp\left(-\frac{t}{\tau}\right) \quad (32)$$

In the above eq.(32), $\xi_i^\alpha(t=0)$ and $\xi_i^\alpha(t=\infty)$ are, respectively, the equilibrium values of ξ_i^α at initial temperature 1.20 and at the isothermal aging temperature T , respectively, determined by CVM.

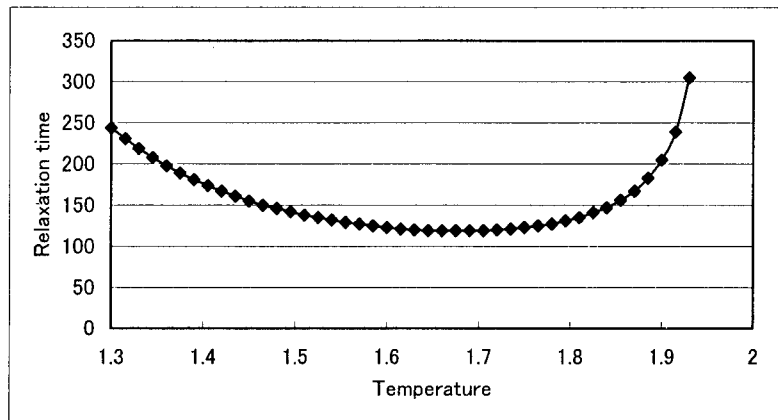


Figure 7. Temperature dependence of the relaxation time. The system is initially at $T=1.20$. In the present calculation, the attempt frequency and activation energy are assumed to be 10 and 13, respectively.

Shown in Fig. 7 is an example of calculated results with $\nu=10$ and $\Delta Q=13$ in eq.(25). One can see that the relaxation time once decreases with increase of temperature, whereas an abrupt rise is observed towards the spinodal disordering temperature through the transition temperature. This is a kinetic evidence of the slowing-down phenomenon for the first-order transition.

In fact, based on electrical resistivity measurements, slowing-down behavior has been reported (Dahmani et al.,1985) for Ni_3Pt -disorder transition. In view of the first-order nature of the transition, the phenomenon was termed *pseudo-critical* slowing down. This finding is most likely an experimental evidence of what we discussed in the present paper. We, however, should carefully clarify the following point before drawing any definite conclusions.

The free energies of two competing phases, *ie.*, disorder and Ll_0 ordered phases, approach together and finally becomes equivalent at T_i . Hence the driving force for the disordering transition itself is gradually lost. In an ordinary experimental situation, this effect is not easily separated from the slowing-down phenomenon due to the flattening of the free energy surface, but they are rather superimposed. Hence, the abrupt increase of the relaxation time experimentally observed near the transition temperature is not ascribed to a single origin without a careful analysis. The rapid up-quenching experiment with efficient heating capability is quite necessary. This is believed to be an important subject to be explored in the future.

REFERENCES

- Banerjee,S, Urban,K. and Wilkens,M.,1984, Order-disorder transformation in Ni_4Mo under electron irradiation in a high-voltage electron microscope, *Acta metall.* **32**;299.
 Bolton, H.C. and Leng, C.A.,1975,Relaxation near a first-order transition in an AB_3 alloy, *Phys. Rev. B***11**;2069.

- Bragg, W.L. and Williams, E.J., 1934, The effect of thermal agitation on atomic arrangement in alloys, *Proc. Roy. Soc. A* **145**; 69.
- Connolly, J.W.D. and Williams, A.R., 1983, Density functional theory applied to phase transformations in transition-metal alloys, *Phys. Rev.* **B27**; 5169.
- Dahmani, C.E., Cadeville, M.C. and Pierron-Bohnes, V., 1985, Temperature dependences of atomic order relaxations in Ni-Pt and Co-Pt alloys, *Acta metall.* **33**; 369.
- de Fontaine, D., 1975, k-space symmetry rules for order-disorder reactions, *Acta metall.* **23**; 553.
- Glauber, R.J., 1953, Time-dependent statistics of the ising model, *J. Math. Phys.* **4**; 294.
- Kaburagi, M. and Kanamori, J., 1975, A method of determining the ground state of the extended-range classical lattice gas model, *Prog. Theoret. Phys.* **54**; 30.
- Kawasaki, K., 1966, Diffusion constants near the critical point for time-dependent ising models. I, *Phys. Rev.* **145**; 224.
- Kikuchi, R., 1951, A theory of cooperative phenomena, *Phys. Rev.* **81**; 998.
- Kikuchi, R., 1966, The path probability method, *Prog. Theoret. Phys. Kyoto, Suppl.* **35**; 1.
- Kikuchi, R., 1974, Superposition approximation and natural iteration calculation in cluster-variation method, *Chem. Phys.* **60**; 1071.
- Mohri, T., Sanchez, J.M. and de Fontaine, D., 1985a, Short range order diffuse intensity calculations in the cluster variation method, *Acta metall.* **33**; 1463.
- Mohri, T., Sanchez, J.M. and de Fontaine, D., 1985b, Binary ordering prototype phase diagrams in the cluster variation approximation, *Acta metall.* **33**; 1171.
- Mohri, T., Terakura, K., Oguchi, T. and Watanabe, K., 1988, First principles calculation of thermodynamic properties of noble-metal alloys, *Acta metall.* **36**; 547.
- Mohri, T., Terakura, K., Takizawa, S. and Sanchez, J.M., 1991, First-principles study of short range order and instabilities in Au-Cu, Au-Ag and Au-Pd alloys, *Acta metall.* **39**; 493.
- Mohri, T., 1990, Kinetic path for a relaxation process of an f.c.c. disordered phase, *Acta metall.* **38**; 2455.
- Mohri, T., 1994a, Spinodal ordering evidenced by PPM, *Statics and Dynamics of Alloy Phase Transformations*, Ed. by P.E.A. Turchi and A. Gonis, Plenum Press, New York; 665.
- Mohri, T., 1994b, Atomic ordering process and a phase diagram, *Solid->Solid Phase Transformations*, Ed. by W.C. Johnson et al., The Minerals, Metals and Materials Society; 53.
- Mohri, T., 1996, Kinetic path and fluctuations calculated by the path probability method, *Theory and Applications of the Cluster Variation and Path Probability Methods*, Ed. by J.L. Moran-Lopez and J.M. Sanchez, Plenum Press, New York; 37.
- Mohri, T., 1999, Configurational thermodynamics and kinetics studied by cluster variation and path probability methods, *Solid-Solid Phase Transformations*, The Japan Institute of Metals Proceedings, Vol. 5 (JIMIC-3), ed. by M. Koiwa, K. Otsuka and T. Miyazaki; 669.
- Mohri, T., 2000a, Pseudo critical slowing down within the CVM and PPM, Modelling and Simulation in Mat. Sci. and Engr., in press.
- Mohri, T., 2000b, in preparation.
- Ozolins, V., Wolverton, C. and Zunger, A., 1998a, Cu-Au, Ag-Au, Cu-Ag and Ni-Au intermetallics: First-principles study of temperature-composition phase diagrams and structures, *Phys. Rev.* **B57**; 6427.
- Ozolins, V., Wolverton, C. and Zunger, A., 1998b, First-principles theory of vibrational effects on the phase stability of Cu-Au compounds and alloys, *Phys. Rev.* **B58**; R5897.
- Richards, M.J. and Cahn, J.W., 1971, Pairwise interactions and the ground state of ordered binary alloys, *Acta metall.* **19**; 1263.
- Sanchez, J.M., 1981, Pair correlations in the cluster variation approximation, *Physica* **111A**; 200.
- Sanchez, J.M. and de Fontaine, D., 1978, The fcc ising model in the cluster variation approximation, *Phys. Rev.* **B17**; 2926.
- Sanchez, J.M. and de Fontaine, D., 1980, Ordering in fcc lattices with first- and second-neighbour interactions, *Phys. Rev.* **B21**; 216.
- Sanchez, J.M., Ducastelle, F. and Gratias, D., 1984, Generalized cluster description of multicomponent systems, *Physica*, **128A**; 334.
- Takeda, S., Kulik, J. and de Fontaine, D., 1987, Spinodal ordering beyond the Lifshitz point in Cu₃Pd observed by high voltage electron microscopy, *Acta metall.* **35**; 2243.
- Terakura, K., Oguchi, T., Mohri, T. and Watanabe, K., 1987, Electronic theory of the alloy phase stability of Cu-Ag, Cu-Au and Ag-Au systems, *Phys. Rev.* **B35**; 2169.

KINETICS AND DIFFUSION

USING ARRESTED SOLID - SOLID MULTIPHASE REACTIONS IN GEOLOGICAL MATERIALS TO DEDUCE THE RATE OF CRUSTAL UPLIFT

William E. Glassley and Annemarie Meike
Earth and Environmental Sciences Directorate
Lawrence Livermore National Laboratory, Livermore
CA 94550 USA

ABSTRACT

The history geological terrains experience can be traced as a series of temperature and pressure changes. Each change drives the system toward a new state of thermodynamic equilibrium. The resultant overprinted rock fabrics, textures and chemical heterogeneities can be difficult to interpret. However, if carefully chosen, features from the scale of kilometers to nanometers can be used to reconstruct the history of mountain systems. Uplift of the Sri Lankan Central Highlands was rapid enough to preserve well-developed symplectite textures, some of which represent arrested solid-state diffusion-controlled reactions of garnet + O_2 to form orthopyroxene + plagioclase + magnetite, as the rocks were exhumed from over 30 km in the earth's crust. Our objective has been to determine the reaction mechanisms responsible for symplectite development, and to establish the time interval over which these reactions occurred, to constrain the rate of mountain uplift. Considering that the most rapid mechanism is solid state grain-boundary diffusion of oxygen, the reaction time can be constrained by bounding the rate of oxygen supply to the reaction site. The solid state grain boundary diffusion rate of oxygen has been inferred to be ca. 10^{-14} m²-sec (Farver and Yund, 1991), but is sensitive to inferred grain boundary width. The range of rates thus determined allows the distinction between rapid uplift similar to that of the Himalayan Mountains, and the slow and progressive erosion of a less dramatic terrain. Further constraints on diffusion control and energetic relationships are determined from crystallographic relationships between the reactant and product phases, and submicron scale microstructures.

INTRODUCTION

The evolution of the Earth's crust is recorded in the chemical and physical characteristics of the mineral phases that make up the crust. This history is preserved as recrystallization events, which can include changes in mineral composition and/or mineral structure, or can be recorded as net transfer reactions in which there is a change in the assemblage of coexisting mineral phases. These changes occur in response to changes in

pressure, temperature and stress conditions, which are the primary variables that affect rock properties.

Generally, the history of large-scale events, such as mountain building and continental collisions, often extend over many millions of years. Often these histories include periods of time during which the rocks being considered experienced high pressures (0.1 to 1 GPa) and high temperatures (300 to 900 °C). The resulting history of pressure and temperature change (P-T history) thus tracks the up and down movement of a portion of the Earth's crust through time. Dating the rocks in such a sequence provides information concerning the time at which the rock sequence attained a particular pressure-temperature state, provided the date can be reliably tied to a specific mineral assemblage, a specific suite of micro-chemical properties, or a particular micro-structural characteristic. If a series of dates can be obtained at well-defined points along the P-T history, then the rate of movement of the crust can be determined.

Rates of change in P-T histories are useful for piecing together crustal history, since such data allow motion vectors to be determined. Plate tectonics is the conceptual framework within which the evolution of the Earth's crust is described. This paradigm relates events recorded in the crust to movements of crustal segments. The magnitude and orientation of movement vectors allow distinction to be made between the different regimes that cause destruction, formation and modification of crust.

Establishing movement rates on anything other than a multi-million year time scale has been difficult because of the lack of good benchmarks for mechanisms that can be used to record such events. Nevertheless, such data are required in order to refine models of plate motion, and to further develop understanding of the underlying mechanisms controlling plate dynamics.

In this report we present the preliminary determination of the rate of a specific diffusion-controlled, arrested net transfer reaction that potentially records a specific point along a P-T trajectory for a sequence of rocks from Sri Lanka. Further application of this approach may allow refinement of highly resolved motion vectors for crustal segments, thus contributing to a better understanding of plate movements and the mechanisms controlling plate tectonics.

DIFFUSION CONTROLLED REACTIONS IN ROCKS

Diffusion controlled processes are responsible for many of the key chemical characteristics that record P-T history. Compositional zoning within crystalline phases, inter-phase ion exchange, and net transfer reactions involving multiple crystalline phases are all diffusion controlled. Each of these diffusion-controlled processes could potentially be used to evaluate the time-resolved motion vectors, if the underlying diffusion controls could be determined. However, a major limitation in deciphering the relevant rates is uncertainty in the applicable diffusion coefficients. Diffusion coefficients derived for geological materials differ by many orders of magnitude, depending upon the relative importance of a fluid phase along grain boundaries. In certain cases, such as the formation of hornblende-spinel-orthopyroxene coronas around olivines (Ashworth, 1993) textures have been described in terms of fluid-absent grain-boundary and intra-crystalline Al diffusion, and have been used to infer that long time periods (>1 million years) were required for corona growth. In contrast, corona growth has also been documented in carbonate-silicate experimental systems in which the total time duration of mineral development was tens of days, and the presence of a fluid phase was documented (Lutge and Metz, 1993).

Symplectites (Figure 1) are similar to corona textures in that a shell of product minerals surrounds a reactant mineral phase. In some cases the shell is complete, in others it is discontinuous. The product minerals develop when the free energy at the grain boundary exceeds that of a different but compositionally equivalent mineral assemblage. This condition has been observed to develop between pairs of minerals, as well as in response to changes in chemical potentials.

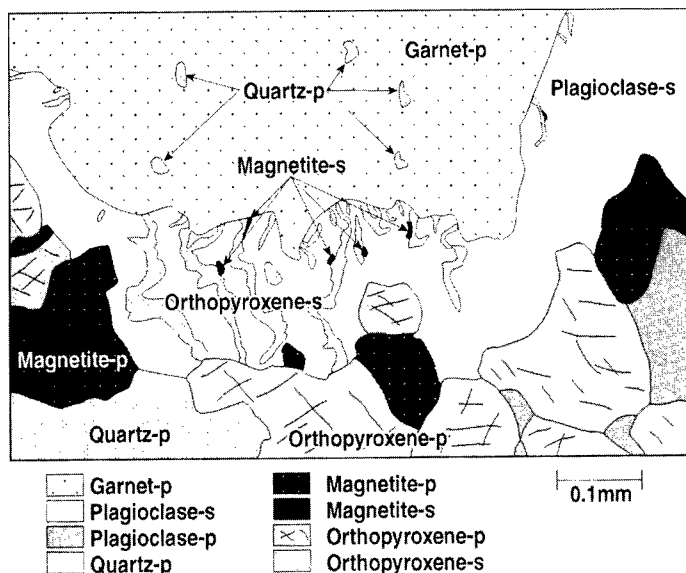


Figure 1. Schematic diagram of symplectite texture and phase relationships.. Note the difference in grain size and grain form between the mineral phases that had formed prior to symplectite development (designated by “-P” for primary) and those minerals that form during symplectite growth (designated by “-S” for secondary). Figure modified from Sandiford et al. (1988).

Symplectites commonly are worm-like intergrowths of two or three minerals. The large length to width ratio of these crystals, and their very small size, suggest that crystal interfacial energy is high and, hence, the duration of time at elevated temperature insufficient to allow grain coarsening. The long axis of the worm-like forms is generally at a high angle to the interface with the reactant mineral phase, thus providing a relatively high number of symplectite mineral grain boundaries per unit area of reactant mineral surface area. As discussed later, this is significant for models of symplectite growth in which grain boundary diffusion is the rate-limiting step. The textures indicate that reaction did not completely consume the garnet, providing a clear example of an arrested reaction relationships

SRI LANKA PYROXENE-FELDSPAR-MAGNETITE SYMPLECTITES

The geology of Sri Lanka (Fig. 2) is dominated by the Highland Series, which runs as a broad band in a NNE – SSW trend through the central part of the island. These rocks are high-grade metamorphic rocks which have experienced a complex metamorphic and structural history. This history includes an early recrystallization event between 1.94 and

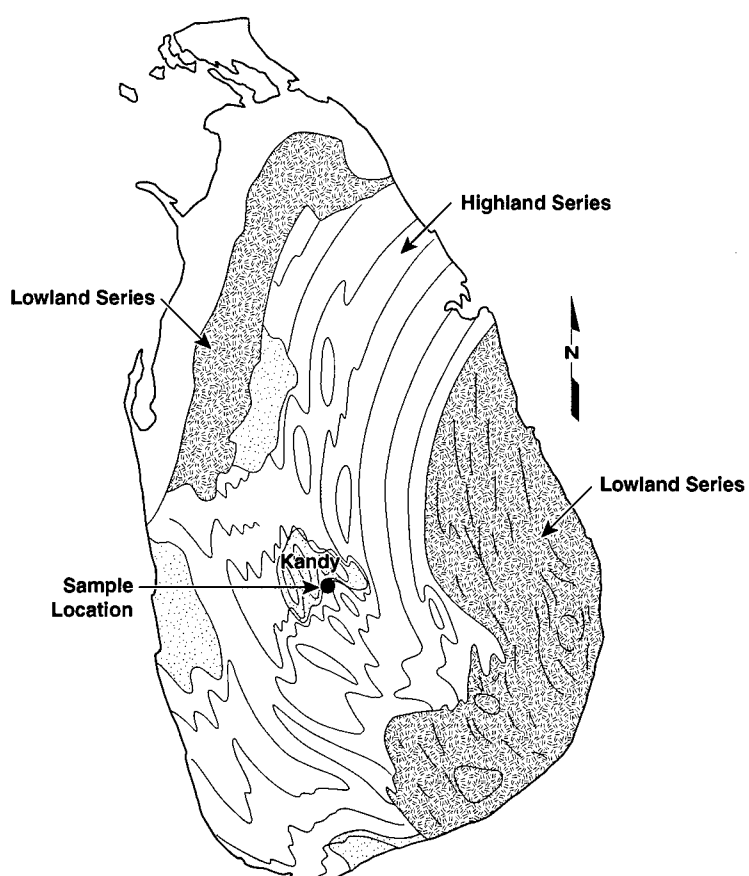


Figure 2. Geology of Sri Lanka. The samples were collected from outcrops near the city of Kandy. Map modified from Sandiford et al. (1988).

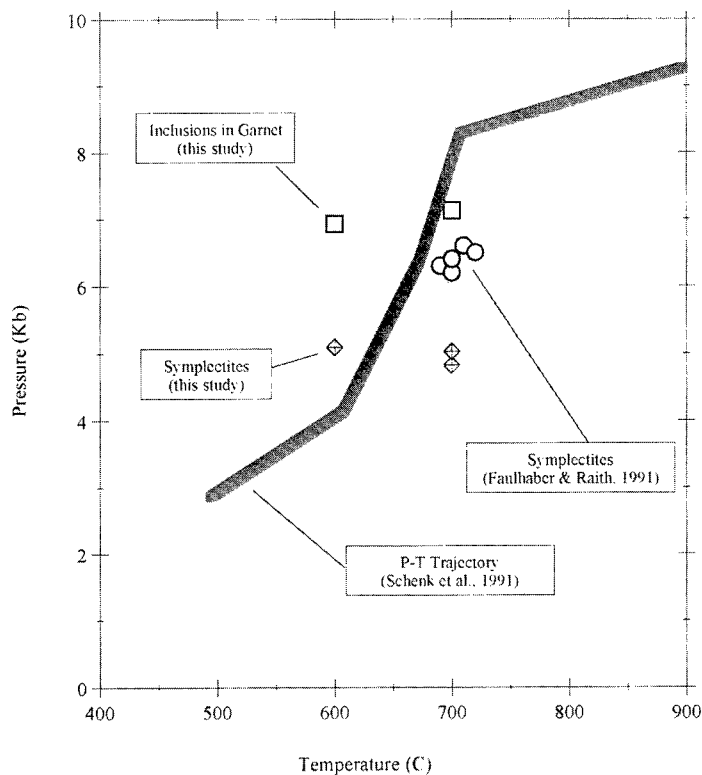


Figure 3. The inferred temperature-pressure pathway followed by the Highland Series rocks. The heavy shaded line, which is derived from the trajectory presented in Schenk et al. (1991), is their generalized interpretation of the conditions of recrystallization during cooling and uplift of the Highland Series rocks. Also shown are the P-T conditions determined by Faulhaber and Raith (1991) for the symplectites they analyzed from the Highland Series rocks. The P-T conditions computed for garnet and coexisting quartz inclusions in our samples are indicated, as are the conditions computed for the symplectites in this study. Because the absolute temperatures are unknown for our samples, we computed pressures, assuming the temperatures were between 600°C and 700°C, based on the coexistence of garnet-orthopyroxene-plagioclase. We infer that the actual conditions of symplectite growth fall close to the inferred P-T trajectory of Schenk et al. (1991).

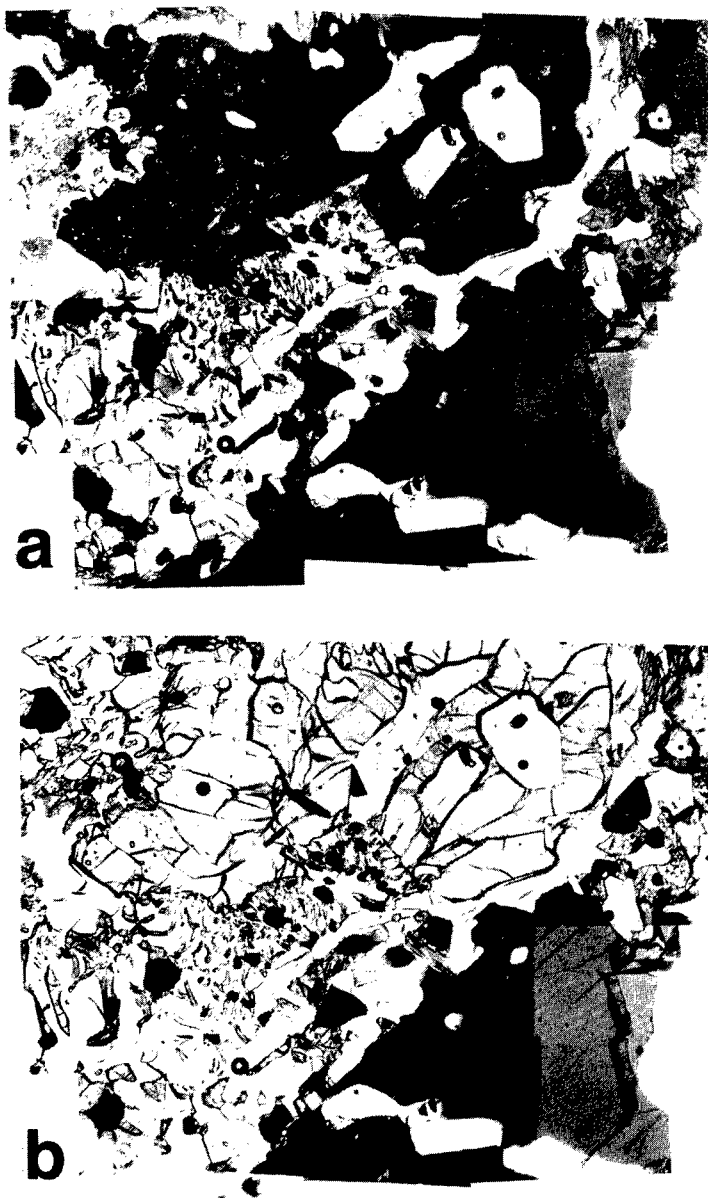


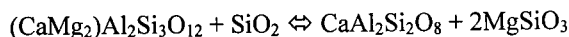
Figure 4. Photomicrographs of Sri Lanka symplectites used in this study. a. with polarizing filter. b. without polarizing filter. Largest figure dimension is 2.3 mm.

1.1 billion years ago, followed by a series of deformations and recrystallizations, culminating in relatively rapid uplift sometime between 0.67 and 0.55 billion years ago (Sandiford et al., 1988; Kriegsman, 1991; Kehelpannala, 1991).

Some interpretations suggest that the Highland Series has been emplaced over lower grade rocks during the last major recrystallization (e.g., Kriegsman, 1991). Nevertheless, there is general agreement that this complex history involves an early stage at very high temperatures (ca. 900°C) at elevated pressures (ca. 0.8-1.0 Gpa). This period was followed by possibly protracted, nearly isobaric cooling, and then a dramatic increase in the rate of change of pressure with temperature, suggesting rapid uplift (Schenk et al., 1991: Fig. 3).

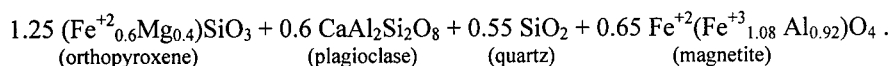
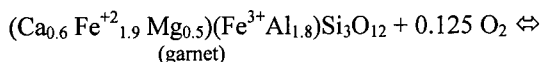
Within the Highland Series, near the city of Kandy, occurs a series of rock outcrops in which symplectites of orthopyroxene, plagioclase, and magnetite have developed around almandine garnets (Fig. 4). The symplectites developed in rocks that originally were composed of plagioclase feldspars, orthopyroxenes, hornblendes, biotites, garnet and quartz. Although plagioclase feldspars, orthopyroxenes, hornblendes, biotites and quartz in the bulk rock show clear evidence of strain, the symplectite grains do not. Hence, the minerals composing the symplectite are generally compatible with conditions suitable for orthopyroxene stability, but they post date the deformation period.

The garnets that have symplectite surrounding them contain inclusions of plagioclase and quartz. Quartz also occurs within the symplectites at the garnet-symplectite interface as a product mineral phase. This stable coexistence of garnet + quartz demonstrates that the symplectites did not form in response to the reaction:



Instead, the reaction relationship represented by the symplectite must represent a change in some chemical condition affecting the external grain surfaces of the garnet, and not a change in intensive parameters such as temperature or pressure.

We propose that the actual reaction responsible for symplectite growth was controlled by oxygen availability:



The stoichiometry of this reaction is based on microprobe analyses of the compositions of the mineral phases occurring at the garnet – symplectite interface, with the exception of the spinel phase (magnetite), the composition of which is based on partial analyses of these phases, and their optical properties in reflected light. This reaction suggests that the change in chemical condition was related to the oxygen fugacity.

The outer edge of the symplectite defines the original location of the garnet grain boundary, prior to reaction. Symplectite development occurs as a volume replacement of garnet by the nearly compositionally equivalent assemblage orthopyroxene-plagioclase-magnetite-quartz. In order to sustain symplectite growth, oxygen diffusion must occur along the symplectite grain boundaries.

Within the symplectite occur domains in which the optical orientation of separate orthopyroxene grains is the same. This suggests that mineral growth during garnet breakdown is controlled by some topotactic relationship with the underlying garnet.

Optical examination suggests that more distant (earlier formed) symplectite grains are more equant than those immediately adjacent to the garnet (Fig. 4). Measurement of the grain dimensions is consistent with this inference (Fig. 5). This suggests grain coarsening has occurred over the lifetime of the reaction process that generated the symplectites. As noted below, this point may play a role in explaining the arrested state of these reactions.

OXYGEN GRAIN BOUNDARY DIFFUSION AND SYMPLECTITE FORMATION

Diffusion in geological materials has been the subject of several recent investigations (Ashworth, 1993; Farver and Yund, 1990, 1991, 1995a,b, 1996 1998; Ashworth et al., 1998 a,b; Obrien, 1999). These results add to a large body of literature that has shown through various means and in a wide range of materials that intercrystalline or volume diffusion is orders of magnitude slower than fluid mitigated grain boundary diffusion. Debate still exists, however, over several key aspects of what is considered to be grain boundary diffusion in the absence of a fluid phase. Some studies (Ashworth, 1993) have suggested that fluid absent grain boundary diffusion is virtually indistinguishable from volume diffusion, and thus the corresponding diffusion coefficients are assigned approximately equivalent values. Others have presented experimental results purporting to demonstrate that fluid-absent grain boundary diffusion coefficients are intermediate between those of volume diffusion and fluid-mitigated grain boundary diffusion (Farver and Yund, 1991). Important in these debates are questions concerning the width of grain boundaries, which may be expected to change with pressure and temperature, and the physics of atomic migration in these regions.

Le Claire (1963) developed a formalism to evaluate analytical data obtained from laboratory experiments that consider grain boundary diffusion, which is expressed as:

$$D^*\delta = [(d\ln c)/(dy^{6/5})]^{-5/3} (4D/t)^{1/2} [(d\ln c)/(d(\eta\beta^{-1/2})^{6/5})]^{5/3} \quad (1)$$

where D^* is grain boundary diffusion coefficient, δ is grain boundary width, c is the concentration at depth y , D is the volume diffusion coefficient, η is a dimensionless number dependent on D , y , δ and time, and β is a parameter dependent on D , D^* , δ and time. This formalism is based on rearrangement and simplification of the equations derived by Whipple (1954). This formalism is valid within limits described by Le Claire, as confirmed by Chung and Wuensch (1996). The fundamental limit is that β be greater than approximately 10. When applied, these limits result in the following simplified version of (1):

$$D^*\delta = [(d\ln c)/(dy^{6/5})]^{-5/3} (4D/t)^{1/2} (0.661) \quad (2)$$

Using the approach proposed by Le Claire, Farver and Yund (1991, 1995a,b, 1996, 1998) have analyzed the results of a series of experiments they have conducted in which they consider grain boundary diffusion of oxygen, potassium and calcium in geological materials. From these analyses they have proposed grain boundary diffusion coefficients for these elements.

We have opted to use their diffusion coefficient for fluid-absent oxygen grain boundary diffusion to evaluate the time duration over which the symplectite developed in the Sri Lanka sample described above. Our interest is in establishing a time limit for the duration of reaction. We believe that using this diffusion coefficient will provide a means for defining a time interval over which it is likely symplectite growth occurred. These results are preliminary for several reasons.

First, the effective grain boundary width remains unknown. Formation of the symplectites occurred at highly elevated temperatures and pressures, and evidently during uplift. There are no experimental data for grain boundary widths under such conditions. We have therefore taken $1e-9$ meters as a first approximation of an average grain boundary width for the present polyminerale assemblage for similar reasons to those discussed by Farver and Yund (1991). They consider estimates for metals and simple oxides as well as

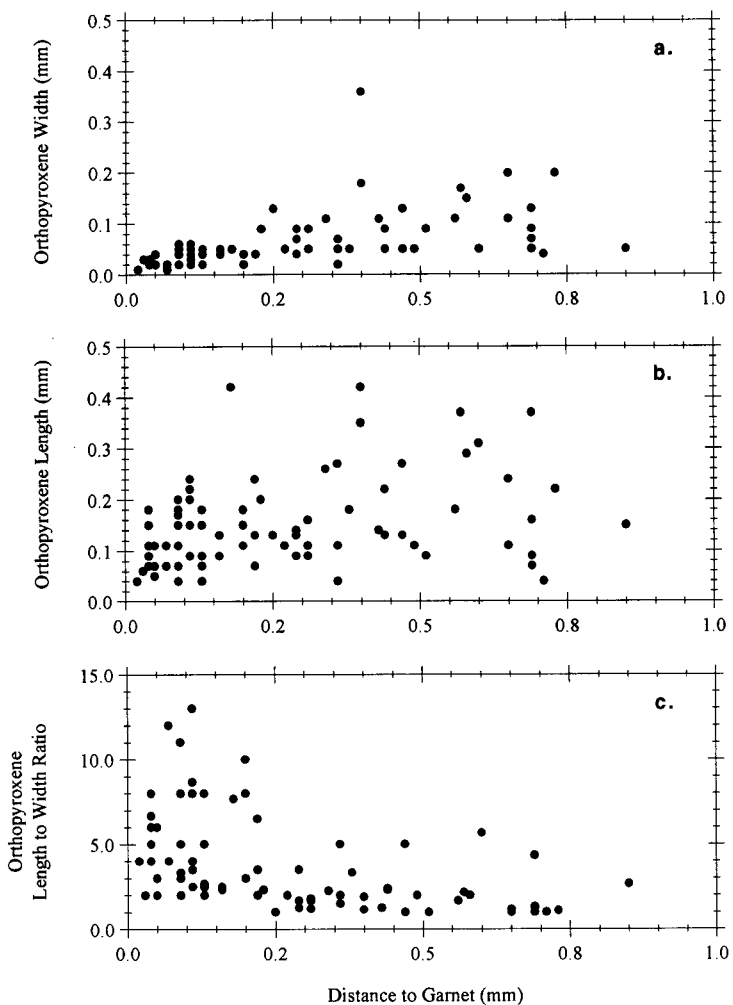


Figure 5. Width (a.) and length (b.) dimensions of seventy-four symplectite orthopyroxene grains, as a function of distance from garnet grain edge. All distances are in millimeters. Also shown is the length to width ratio of the orthopyroxene grains, as a function of distance from the garnet (c.).

ex-post facto transmission electron microscope (TEM) observations (not at pressure or temperature) of more complex silicate structures. The value of $1\text{e-}9$ meters should be near the lower limit of possible values for the polymineralic symplectite assemblage. Grain boundary widths, Farver and Yund (1991) note, must be on the order of a unit dislocation width (Burgers vector of albite and orthoclase is 0.8 nm).

Second, we have assumed that grain boundary properties in these natural rocks are similar to the mineralogically distinct (quartz vs plagioclase-orthopyroxene-magnetite-quartz) and laboratory annealed fine grained quartz samples used in the Farver and Yund (1991) experiments. It is unlikely that the grain boundaries are identical, but the differences, and their significance with respect to the magnitude of the diffusion coefficients are unknown. In the absence of reference data that would allow us to better characterize the natural grain boundaries, we will use the data from the reported experiments and emphasize the inherent uncertainties that must be kept in mind.

Third, in order to apply the Farver and Yund diffusion coefficients it is necessary to assume that the role of a fluid phase was the same. This cannot be assured. It is conceivable that the grain boundaries in the Sri Lanka samples were partially wetted by a fluid phase of unknown composition. For the present, we will simply assume that fluid condition along the grain boundaries in the different sets of materials was similar.

We can constrain the time duration of the reaction by considering two limits. The maximum distance over which diffusion could have occurred is the width of the symplectite zone. Although this width varies from location to location, a value of $1\text{e-}4$ meters is about average. We also assume in this case that the diffusion gradient was linear over this distance, and was constant with time. The minimum distance over which diffusion occurred cannot be established directly, but for calculational purposes we assume that it was approximately equivalent to that achieved in the laboratory experiments of Farver and Yund (1991) ($6\text{e-}6$ meters). Assuming that the rate-limiting step in the reaction progress was oxygen diffusion, we solve for the time duration required for oxygen to diffuse these distances. The results for these calculations are shown in Figure 6.

DISCUSSION

The results in Figure 6 show that the maximum time over which symplectite growth occurred was approximately 500 years, and the minimum time was a few weeks, depending upon the actual diffusion distance. From the physical perspective argued in the paragraph below, the longer time period is unlikely.

Initiation of the symplectite growth at the original garnet surface must have begun when the P-T- $f\text{O}_2$ conditions achieved values outside the garnet stability field. Symplectite growth would then be limited by oxygen diffusion along symplectite grain boundaries. Two possible reaction pathways can be postulated that would reflect the evolution of the symplectite, once its development had been initiated. Either the diffusion gradient at the garnet interface maintained a constant value and migrated inward toward the garnet, or the gradient decreased with time as the symplectite grew (Figure 7). In the case of the former scenario, the gradient would migrate at a rate equivalent to the diffusion rate. In this case, the total time required to achieve a symplectite thickness of 1×10^{-4} meters would be approximately 0.1 years, at 600°C .

Were the diffusion gradient to have decreased with time, oxygen would have been depleted in the region immediately outside the original garnet surface. The decrease in oxygen fugacity would be expected to be recorded in the minerals adjacent to the original garnet surface. However, neither a change in oxide mineralogy nor evidence of reactions involving reduction of iron in mixed Fe^{++} - Fe^{+++} phases is seen in this area. Hence, we

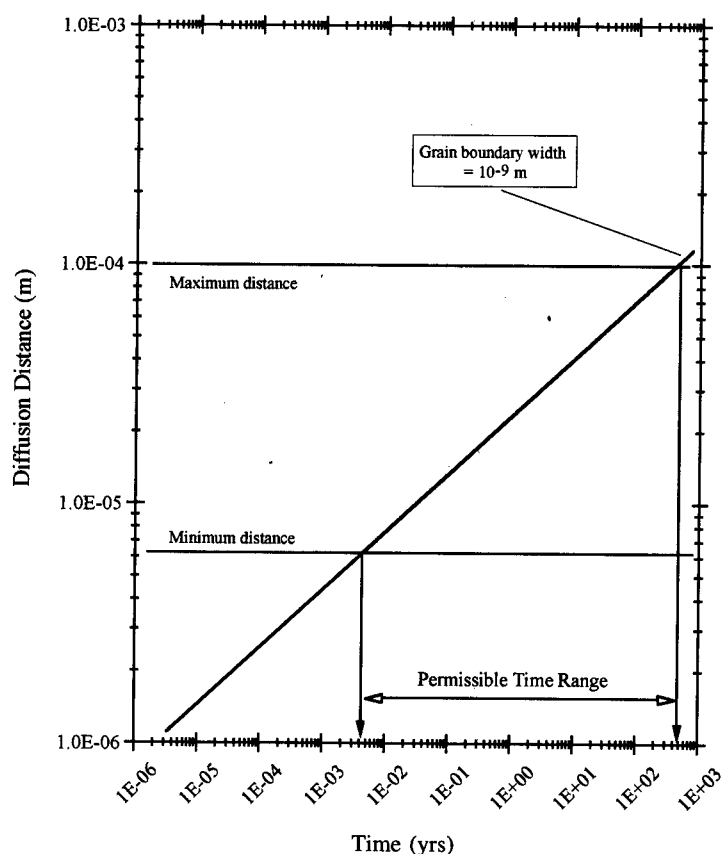


Figure 6. Diffusion distance (in meters) as a function of time (years). The line labeled “Grain boundary width = 10^{-9} m” indicates time-distance correlation for the computed set of conditions described in the text, which assumes a temperature of ca. 600°C. The shaded region encloses the possible range of distances over which diffusion operated during symplectite growth. The maximum distance is the approximate measured width of the symplectite. The minimum distance is that inferred to be operative in the experiments reported by Farver and Yund (1999), which is 6e-6 meters.

Table 1. Values, sources and assumptions for key variables used in calculation of diffusion distances

Variable	Assigned Value	Comment
Grain Boundary Width	1.0 E -9 meters	Assumed from Farver and Yund, 1991
Oxygen Diffusion Coefficient	5.0 E -15	Ibid, assuming 600°C
Concentration Gradient (dlnC)	3.4	Ibid

conclude that oxygen flux along symplectite grain boundaries occurred at a rate approximately equivalent to that at the symplectite-garnet interface.

These results imply that the symplectite textures formed over a few week period during decompression. This short duration reflects the mechanism responsible for this grain growth – grain boundary diffusion of a relatively mobile component. This is in contrast to retrograde corona textures formed around olivines (Ashworth, 1993), for example, in which the rate-limiting step in the corona growth is Al volume diffusion. The mechanism responsible for the symplectite-forming reaction cannot be resolved between changes in pressure, temperature or oxygen fugacity. It is likely that a combination of changes involving these variables was responsible, since these variables are coupled.

Cessation of the reaction could have been the result of changes in oxygen fugacity, or changes in the mobility of oxygen along the grain boundaries. The latter may have been at least partially responsible since, as previously noted, the symplectite grains become less elongate and coarsen with time. This change has the consequence of diminishing the density of grain boundaries that are oriented perpendicular to the garnet surface, making more tortuous the oxygen diffusion pathway. We speculate that a point was eventually reached at which oxygen diffusion was choked off due to this reorganization of grain boundaries.

CONCLUSIONS

The results presented here suggest that symplectite growth around garnets in this environment was controlled by changes in oxygen fugacity. This change was associated with decompression and could result from any combination of changes in P-T and oxygen partial pressure.

Available evidence suggests that the duration of the symplectite growth was on the order of a few weeks. This short duration reflects the mechanism responsible for this grain growth – grain boundary diffusion of a relatively mobile component. Far slower reactions have been estimated for mechanisms such as retrograde corona textures in which the rate-limiting step is Al volume diffusion. The resulting diffusion coefficients are approximately

nine orders of magnitude larger, and the inferred time duration for the corona growth are millions of years.

These results emphasize that trajectories of inferred pressure-temperature pathways in P-T diagrams grossly integrate complex histories, and do not provide any direct information about rate of crustal movement. To fully understand crustal evolution, methods resulting data can then be used to place within a plate tectonics framework the vertical component of motion specific crustal terrains have experienced.

Uncertainties in the calculations we have performed primarily reflect the use of values for variables, such as grain boundary width, that were obtained from measurements on materials (metals and simple oxides) which are not close analogs to complex silicates. Also, the conditions under which the measurements were made do not closely approximate the extreme temperatures and pressures experienced by the geological materials. Obtaining more accurate measurements or calculated values for geologically appropriate mineral phases is a significant challenge but, when accomplished, will greatly enhance our ability to better constrain the evolutionary history of the crust and greatly expand our ability to understand large scale geological processes.

* This work was performed under the auspices of the U.S. Department of Energy by University of California Lawrence Livermore National Laboratory under contract No. W-7405-Eng-48.

REFERENCES

- Ashworth, J.R., 1993, Fluid-absent diffusion kinetics of Al inferred from retrograde metamorphic coronas. *Am. Min.* 78:331.
- Ashworth, J. R., Sheplev, V. S. Bryxina, N. A., Kolobov, V. Y. and Reverdatto V.V. 1998a, Diffusion-controlled corona reaction and overstepping of equilibrium in a garnet granulite, Yenisey Ridge, Siberia. *J. Met. Geol.* 16:231.
- Ashworth, J. R., Sheplev, V. S. Bryxina, N. A., Kolobov, V. Y. and Reverdatto V.V. 1998b, Textures of diffusion-controlled reaction in contact-metamorphosed Mg-rich granulite, Kokchetav area, Kazakhstan. *Mineral. Mag.* 62:213.
- Chung, Y-C. and Wuensch, B. J., 1996, Assessment of the accuracy of Le Claire's equation for determination of grain boundary diffusion coefficients from solute concentration gradients. *Materials Letters.* 28: 47.
- Farver, J.R. and Yund, R.A., 1990, The effect of hydrogen, oxygen, and water fugacity on oxygen diffusion in alkali feldspar. *Geochim Cosmochim Acta* 54:2953.
- Farver, J.R. and Yund, R.A., 1991, Measurement of oxygen grain boundary diffusion in natural, fine-grained, quartz aggregates. *Geochim Cosmochim Acta* 55:1597.
- Farver, J.R. and Yund, R.A., 1995a, Grain boundary diffusion of oxygen, potassium and calcium in natural and hot-pressed feldspar aggregates. *Contrib. Mineral. Petrol.* 118:340.
- Farver, J.R. and Yund, R.A., 1995b, Interphase boundary diffusion of oxygen and potassium in K-feldspar/quartz aggregates. *Geochim Cosmochim Acta* 59:3697.
- Farver, J.R. and Yund, R.A., 1996, Volume and grain boundary diffusion of calcium in natural and hot-pressed calcite aggregates. *Contrib. Mineral. Petrol.* 123:77.
- Farver, J.R. and Yund, R.A., 1998, Oxygen grain boundary diffusion in natural and hot-pressed calcite aggregates. *Earth Planet. Sci. Lett.* 161:189.
- Faulhaber, S. and Raith, M., 1991, Geothermometry and geobarometry of high-grade rocks: a case study on garnet-pyroxene granulites in southern Sri Lanka. *Min. Mag.* 55:33.
- Kehelpannala, K.V. W., 1991, Structural evolution of high-grade terrains in Sri Lanka with special reference to the areas around Dodanaslanda and Kandy, in: *The Crystalline Crust of Sri Lanka, Part I*, A. Kroner, ed., Geological Survey Department, Prof. Paper No. 5, Republic of Sri Lanka, Colombo.
- Kriegsman, L., 1991, Structural geology of the Sri Lanka basement – A preliminary review, in: *The Crystalline Crust of Sri Lanka, Part I*, A. Kroner, ed., Geological Survey Department, Prof. Paper No. 5, Republic of Sri Lanka, Colombo.

-
- Le Claire, A.D. 1963. The analysis of grain boundary diffusion measurements. *Brit. J. Appl. Phys.* 14:351.
- Luttge, A. and Metz, P. 1993. Mechanism and kinetics of the reaction- $\text{1dolomite} + 2\text{quartz} = \text{1diopside} + 2\text{CO}_2$ – a comparison of rock-sample and of powder experiments. *Contr. Min. Pet.* 115:155.
- O'Brien, P. J., 1999, Assymetric zoning profiles in garnet from HP-HT granulite and implications for volume and grain-boundary diffusion. *Mineral. Mag.* 63:227.
- Sandiford, M., Powell, R., Martin, S.F., and Perera, L.R.K., 1988, Thermal and baric evolution of garnet granulites from Sri Lanka. *J. Metamorp. Geol.* 6:351.
- Schenk, V., Raase, P., and Schumacher, R., 1991, Metamorphic zonation and P-T history of the Highland Complex in Sri Lanka, in: *The Crystalline Crust of Sri Lanka, Part I*, A. Kroner, ed., Geological Survey Department, Prof. Paper No. 5, Republic of Sri Lanka, Colombo.
- Whipple, R.T.P., 1954, Concentration contours in grain boundary diffusion. *Philos. Mag.* 45:1225.

KINETIC FEATURES OF NON-SIMPLEST ALLOY ORDERINGS: D0₃, L1₂, AND L1₀ ORDERINGS

K.D. Belashchenko, V.Yu. Dobretsov, I.R. Pankratov, G.D. Samolyuk,
and V.G. Vaks

Russian Research Centre 'Kurchatov Institute', Moscow 123182, Russia

ABSTRACT

The earlier-developed master equation approach is used to study kinetic features of alloy orderings with more than two types of ordered domains. We develop a kinetic cluster field method being a kinetic analogue of the known cluster variation method, and present a microscopical model for deformational interactions in concentrated alloys. The described methods are used for extensive simulations of various phase transformations involving D0₃, L1₂ and L1₀ orderings. The simulations reveal a number of interesting microstructural effects, many of them agreeing well with experimental observations.

INTRODUCTION

Studies of microstructural evolution under phase transitions of alloy ordering attract great attention from both fundamental and applied points of view, see e.g. [1, 2, 3, 4, 5, 6, 7, 8, 9]. There has been much theoretical work on these problems, e.g. [10, 11, 12]. However, most of theoretical papers treat the simplest B2 type orderings with just two types of antiphase ordered domains (APDs) and one type of antiphase boundaries (APBs) between them. Yet ordered structures in real alloys are usually much more complex and include many types of APDs and

APBs. The 'multivariant' character of the ordering results in a number of kinetic features that are absent for the simplest B2 ordering. In this work we discuss these features for the phase transformations involving the most typical multivariant orderings, D0₃, L1₂ and L1₀.

To investigate these problems we employ the microscopical master equation approach to the configurational kinetics of non-equilibrium alloys suggested in Refs. [13, 14, 15, 16, 17]. First we discuss some extensions of this approach necessary to treat the orderings under consideration. Then we describe an application of the developed methods to studies of microstructural evolution and morphological features of such orderings.

THE KINETIC CLUSTER FIELD APPROACH

We consider a binary alloy A-B with the interaction Hamiltonian

$$H = \sum_{i>j} v_{ij} n_i n_j + \sum_{i>j>k} v_{ijk} n_i n_j n_k + \dots \quad (1)$$

where $n_i = n_{iA}$ is unity if the site i is occupied by A atom and $n_i = 0$ otherwise. The general form of the master equation approach was described in Refs. [16] and [17]. Below we present several main equations of this approach. The fundamental master equation for the probability P to find the configuration $\{n_i\} = \alpha$ is:

$$dP(\alpha)/dt = \sum_{\beta} [W(\alpha, \beta)P(\beta) - W(\beta, \alpha)P(\alpha)] \quad (2)$$

where for the transition probability $W(\alpha, \beta)$ we adopt the conventional 'thermally activated atomic exchange' model [13, 14]. The most general expression for $P\{n_i\}$ can be written as

$$P\{n_i\} = \exp[\beta(\Omega + \sum_i \lambda_i n_i - Q)]. \quad (3)$$

Here $\beta = 1/T$, the 'quasi-Hamiltonian' Q is an analogue of the Hamiltonian H in (1):

$$Q = \sum_{i>j} a_{ij} n_i n_j + \sum_{i>j>k} a_{ijk} n_i n_j n_k + \dots, \quad (4)$$

the 'local chemical potentials' λ_i and the 'quasi-interactions' $a_{i\dots j}$ (being, generally, both time and space dependent) are the parameters of the distribution, and the 'generalized grand canonical potential' $\Omega = \Omega\{\lambda_i, a_{i\dots j}\}$ is determined by normalization.

The kinetic cluster field approach (KCFA) corresponds to putting quasi-interactions $a_{i\dots j}$ in Eq. (3) equal to interactions $v_{i\dots j}$ in Eq. (1), i.e. neglecting kinetic renormalizations of the quasi-interactions. Then one can derive from Eqs. (1)–(4) the kinetic equation for the mean occupations $c_i(t) = \langle n_i \rangle$ averaged over the time-dependent distribution $P\{n_i\}$ [16]:

$$\frac{dc_i}{dt} = \sum_j M_{ij} 2 \sinh[\beta(\lambda_j - \lambda_i)/2] \quad (5)$$

where M_{ij} is the generalized mobility the general expression for which is presented in [17]. One can also show that the local chemical potential λ_i in Eqs. (3), (5) is the partial derivative of the generalized free energy $F\{c_i\}$: $\lambda_i = \partial F / \partial c_i$, and in KCFA we have: $F = \Omega - \sum_i \lambda_i c_i$ [16, 17].

The simplest approximation for the solution of Eqs. (5) is the kinetic mean field approximation (KMFA) which is a kinetic analogue of the thermodynamic MFA. KMFA can be sufficient for studies of many problems [12, 13, 14, 15], in particular, phase transformations in BCC-based alloys involving B2 and D0₃ orderings. However, to describe orderings in FCC alloys, in particular, L1₂ and L1₀ orderings, MFA is known to be insufficient and more accurate methods are necessary, such as the cluster variation method (CVM) [18, 19, 20]. Recently we suggested a simplified version of CVM, the tetrahedron cluster field method (TCFM) [21] which combines a high accuracy of CVM in the description of thermodynamics for a number of realistic alloy models with a great simplification in the calculations making it possible to develop its kinetic generalization. In [21] we considered four alloy models: the second-neighbor interaction models 1, 2 and 3 with the ratio v_2/v_1 equal to (-0.125) , (-0.25) and (-0.5) , respectively, and the fourth-neighbor interaction model 4 with v_n estimated by Chassagne *et al* [24] from their experimental data for Ni–Al alloys: $v_1 = 1680$ K, $v_2 = -210$ K, $v_3 = 35$ K, and $v_4 = -207$ K. Phase diagrams for these models have been calculated using both TCFM and a rather accurate version of CVM, the tetrahedron-octahedron CVM for the ordered phase and the double tetrahedron-octahedron CVM for the disordered phase [19, 20]. The results of these two methods are quite close to each other which is illustrated by Figure 1 for models 2 and 4; for models 1 and 3 the agreement between TCFM and CVM is similar.

The thermodynamic TCFM described in [21] can be immediately generalized to its kinetic version, KTCFM, to study the evolution of non-equilibrium alloys. Here we present the KTCFM expression for the local chemical potential λ_i which determines the generalized driving force

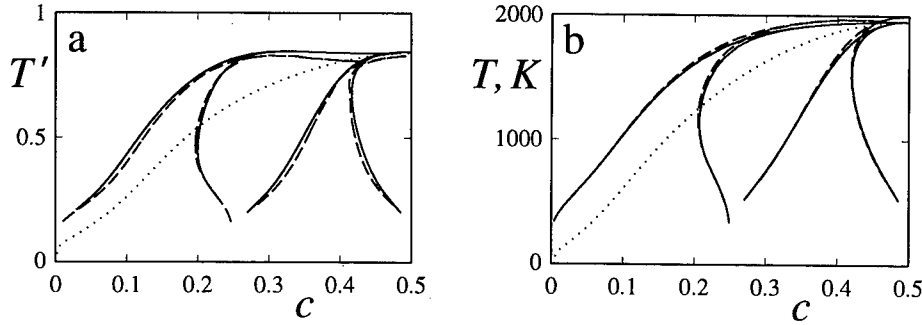


Figure 1 Phase diagram $c - T'$ for the second-neighbor interaction model 2 with $v_2/v_1 = -0.25$ where $T' = T/v_1$ is the reduced temperature (a) and phase diagram $c - T$ for the model 4 with v_n estimated from experiments [24] for Ni-Al alloys (b). The solid and dashed lines are the phase equilibrium curves calculated in [21] by TCFM and CVM, respectively, which separate the following phases or two-phase regions (from left to right): disordered A_1 ; $A_1 + L_{12}$; L_{12} ; $L_{12} + L_{10}$; L_{10} . The dotted line is the ordering spinodal calculated by TCFM.

$\lambda_j - \lambda_i$ in Eq. (5):

$$\lambda_i = \ln \frac{c_i}{1 - c_i} + \sum_{j,n>1} \lambda_i^{ij,n} + \sum_{\{jkl\} \in tY,i} \ln [y_i^{ijkl}(1 - c_i)/c_i] \quad (6)$$

The terms $\lambda_i^{ij,n}$ in the first sum in (6) correspond to the contributions of non-nearest neighbor interactions $v_{ij} = v_n$ being n th neighbors in the lattice which are described in the pair cluster approximation and are written analytically [21]. The last sum describes the contributions of the nearest-neighbor interactions in the approximation of 'non-overlapping tetrahedron clusters' which was suggested by Yang [22] and is illustrated by figure 2.

Each term of this sum corresponds to the Yang's tetrahedron of sites i, j, k, l , while $\{jkl\} \in tY, i$ means that the summation is performed over four Yang's tetrahedrons that contain site i . The quantity $y_i^{ijkl} = y_i^\alpha \{c_s\}$ is determined by a system of equations:

$$c_i = y_i^\alpha \partial \ln Z_\alpha / \partial y_i^\alpha \quad (7)$$

where Z_α is the cluster partition function being a polynomial in y_s^α with s equal to i, j, k or l :

$$Z_\alpha = 1 + \sum_{s=i,j,k,l} y_s^\alpha + \zeta \sum_{s<s'} y_s^\alpha y_{s'}^\alpha + \zeta^3 \sum_{s<s'<s''} y_s^\alpha y_{s'}^\alpha y_{s''}^\alpha + \zeta^6 y_i^\alpha y_j^\alpha y_k^\alpha y_l^\alpha$$

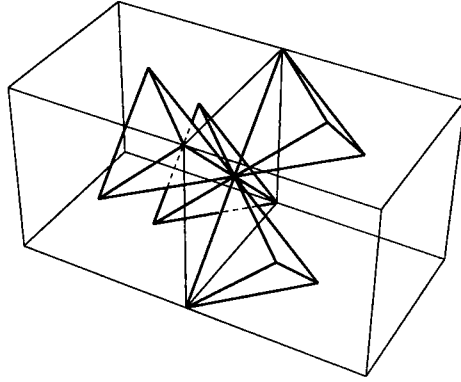


Figure 2 Decomposition of the FCC lattice into tetrahedron clusters suggested by Yang [22] and used in the tetrahedron cluster field method.

and $\zeta = \exp(-\beta v_1)$. Eqs. (7) for y_s^α in each cluster α form a system of four algebraic equations which is easily solved using Newton's method.

MODELS FOR DEFORMATIONAL INTERACTIONS

Effective interactions $v_{i\dots j}$ in the Hamiltonian (1) include the 'chemical' contributions $v_{i\dots j}^c$ which describe the energy changes under substitution of some atoms A by atoms B in the rigid lattice, and the 'deformational' interactions $v_{i\dots j}^d$ related to the difference in the lattice deformation under such a substitution. A microscopical model for v^d in the dilute alloys was suggested by Khachaturyan [23]. The deformational interaction in concentrated alloys can lead to some new effects being absent in the dilute alloys, in particular, to the lattice symmetry changes under phase transformations, such as the tetragonal distortion under L1₀ ordering. Earlier these effects were treated only phenomenologically [10]. Below we describe a microscopical model for calculations of v^d which generalizes the Khachaturyan's approach [23] to the case of concentrated alloys.

Supposing a displacement \mathbf{u}_k of site k relative to its position \mathbf{R}_k in the 'average' crystal A_cB_{1-c} to be small we can write the alloy energy H as

$$H = H_c\{n_i\} - \sum_k u_{\alpha k} F_{\alpha k} + \frac{1}{2} \sum_{\alpha k, \beta l} u_{\alpha k} u_{\beta l} A_{\alpha k, \beta l} \quad (8)$$

where α and β are Cartesian indices and both the Kanzaki force \mathbf{F}_k and the force constant matrix $A_{\alpha k, \beta l}$ are certain functions of occupation numbers n_i . For the force constant matrix we use the conventional average crystal approximation: $A_{\alpha k, \beta l}\{n_i\} \rightarrow A_{\alpha k, \beta l}\{c\} \equiv \bar{A}_{\alpha k, \beta l}$, while

the Kanzaki force can be written as a series in n_i :

$$F_{\alpha k} = \sum_i f_{\alpha k, i}^{(1)} n_i + \sum_{i>j} f_{\alpha k, ij}^{(2)} n_i n_j + \dots \quad (9)$$

Minimizing the energy (8) with respect to displacements \mathbf{u}_k we obtain for the deformational Hamiltonian H^d :

$$H^d = -\frac{1}{2} \sum_{\alpha k, \beta l} F_{\alpha k} (\bar{A}^{-1})_{\alpha k, \beta l} F_{\beta l} \quad (10)$$

where $(\bar{A}^{-1})_{\alpha k, \beta l}$ means the matrix inverse to $\bar{A}_{\alpha k, \beta l}$ which can be written explicitly using the Fourier transformation. For dilute alloys one can retain in Eq. (9) only the first sum which corresponds to a pairwise H^d of Khachaturyan [23]. The next terms in (9) lead to non-pairwise interactions, and the term of (10) bilinear in $f^{(2)}$ describes the above-mentioned effects of possible lattice symmetry changes on microstructural evolution.

To describe these effects in the FCC lattice we retain in Eq. (9) only terms with $f^{(1)}$ and $f^{(2)}$ and suppose that they correspond to just nearest-neighbor interactions. Then the model, for symmetry considerations, includes only two parameters $f^{(2)}$ which can be found from experimental data about the lattice parameter changes under $L1_2$ and $L1_0$ orderings.

LONG-RANGED AND LOCAL ORDER PARAMETERS

The distribution of mean occupations c_i under alloy ordering can be described in terms of both long-ranged and local order parameters. For the homogeneous equilibrium $D0_3$ phase this distribution can be written in terms of two long-ranged order parameters, η and ζ :

$$c_i = c + \eta \exp(i\mathbf{g}_1 \mathbf{R}_i) + \zeta [\exp(i\mathbf{g}_2 \mathbf{R}_i) \text{sgn}(\eta) + \exp(-i\mathbf{g}_2 \mathbf{R}_i)]. \quad (11)$$

Here \mathbf{R}_i is the BCC lattice vector of site i ; $\mathbf{g}_1 = [111]2\pi/a$ and $\mathbf{g}_2 = [111]\pi/a$ are the B2 and $D0_3$ superstructure vectors; η is the B2 type order parameter which is also present in the B2 phase, while the parameter ζ is characteristic of the $D0_3$ phase. Each of the parameters η and ζ in (11) can be both positive and negative, thus there are four types of ordered domains differing in these signs and two types of APBs between these domains. The APB separating two APDs differing in the sign of η will be called an ' η -APB' or a B2 type APB, while that separating two APDs with the same sign of η and different signs of ζ will be called a ' ζ -APB' or a $D0_3$ type APB [8].

The transient partially ordered alloy states, in particular, APBs, can be conveniently described in terms of the local squared order parameters

η_i^2 and ζ_i^2 and the local concentrations \bar{c}_i . A suitable description is provided by 'site-centered' local parameters which correspond to spatial averaging over a nearest neighborhood of each site i :

$$\begin{aligned}\eta_i^2 &= \frac{1}{16} \left[c_i - \frac{2}{z_{nn}} \sum_{j=nn(i)} c_j + \frac{1}{z_{nnn}} \sum_{j=nnn(i)} c_j \right]^2, \\ \zeta_i^2 &= \frac{1}{16} \left\{ \left[c_i - \frac{1}{z_{nnn}} \sum_{j=nnn(i)} c_j \right]^2 + \left[\frac{2}{z_{nn}} \sum_{j=nn(i)} c_j \sin(\mathbf{g}_2 \mathbf{R}_{ji}) \right]^2 \right\}, \\ \bar{c}_i &= \frac{1}{4} \left[c_i + \frac{2}{z_{nn}} \sum_{j=nn(i)} c_j + \frac{1}{z_{nnn}} \sum_{j=nnn(i)} c_j \right].\end{aligned}\quad (12)$$

Here \mathbf{R}_{ji} is $\mathbf{R}_j - \mathbf{R}_i$, $nn(i)$ or $nnn(i)$ means the summation over nearest or next-nearest neighbors of site i , and z_{nn} or z_{nnn} is the total number of such neighbors. The distribution of η_i^2 or ζ_i^2 is similar to that observed in the transmission electron microscopy (TEM) images with the superstructure vector \mathbf{g}_1 or \mathbf{g}_2 , respectively. Therefore, these distributions, to be called η^2 - or ζ^2 -representation, can be compared directly with the experimental TEM images.

For the homogeneous L1₂ or L1₀ ordering the distribution of c_i can be written as [23]:

$$c_i = c + \eta_1 \exp(i\mathbf{k}_1 \mathbf{R}_i) + \eta_2 \exp(i\mathbf{k}_2 \mathbf{R}_i) + \eta_3 \exp(i\mathbf{k}_3 \mathbf{R}_i) \quad (13)$$

where \mathbf{R}_i is the FCC lattice vector, η_1 , η_2 and η_3 are three components of the vector order parameter, and \mathbf{k}_α is the superstructure vector corresponding to η_α :

$$\mathbf{k}_1 = [100]2\pi/a, \quad \mathbf{k}_2 = [010]2\pi/a, \quad \mathbf{k}_3 = [001]2\pi/a. \quad (14)$$

For the cubic L1₂ structure $|\eta_1| = |\eta_2| = |\eta_3|$, $\eta_1 \eta_2 \eta_3 > 0$, and four types of ordered domains are possible. In the tetragonal L1₀ structure only one component η_α is present, being either positive or negative. Therefore, six types of ordered domains are possible with two types of APBs: the 'shift'-type APBs separating two APDs with the same tetragonal axis, and the 'flip'-type APBs separating the APDs with perpendicular tetragonal axes.

The local squared order parameters $\eta_{\alpha i}^2$ and the local concentration \bar{c}_i for the L1₂ and L1₀ orderings can be naturally defined as:

$$\eta_{\alpha i}^2 = \frac{1}{16} \left[c_i + \frac{1}{4} \sum_{j=nn(i)} c_j \exp(i\mathbf{k}_\alpha \mathbf{R}_{ji}) \right]^2,$$

$$\bar{c}_i = \frac{1}{4} \left[c_i + \frac{1}{4} \sum_{j=nn(i)} c_j \right], \quad (15)$$

while the partially ordered alloy states can be conveniently characterized by the distribution of the quantities $\eta_i^2 = \eta_{1i}^2 + \eta_{2i}^2 + \eta_{3i}^2$ to be called η^2 -representation.

KINETICS OF PHASE TRANSFORMATIONS INVOLVING D0₃ ORDERING

Microstructural features of D0₃ ordering distinguishing it from the simplest B2 ordering are related to the presence of four types of different ordered domains and two types of APBs mentioned in section 4. To study these features we made KMFA-based 2D and 3D simulations for two alloy models: the Fe-Al type model with relatively long-range interactions taken from work [25] where the observed Fe-Al phase diagram in the c, T range of our interest was fairly well reproduced by the MFA calculation with the following values of interactions v_n between n -th neighbours: $v_2/v_1 = 0.184$, $v_3/v_1 = -0.844$, $v_{n>3} = 0$, and the Fe-Si type model with relatively short-range interactions taken from the analogous fit for Fe-Si alloys [26] with $v_2/v_1 = 0.5$ and $v_{n>2} = 0$.

We investigated the microscopical structure of different APBs in the D0₃ phase, ζ -APBs and η -APBs, which correspond to vanishing of local order parameters ζ_i or η_i in the APB. We have shown that at a ζ -APB both the local B2 order parameter η_i and the local concentration \bar{c}_i have either a pit (when the c, T point is to the left of the curve $c + \eta_0 = 0.5$ in the c, T plane where η_0 is the equilibrium value of η at the given concentration c and temperature T), or a hump (when the c, T point is to the right of this curve), while for the c, T values near the curve $c + \eta_0 = 0.5$ this pit or hump is small. Experimental observations showing faint [111] contrast on ζ -APBs in the D0₃-ordered Fe₃Al type alloys [5, 8] support this conclusion.

We also simulated phase transformations after a rapid quench of a disordered BCC alloy (A2 phase) into the D0₃, A2+D0₃ or B2+D0₃ region of the phase diagram, as well as the D0₃→B2+D0₃ transition. We observed a number of microstructural features connected with the multivariance of the D0₃ ordering, in particular:

(i) Ordering of the initially disordered alloy quenched to any c, T point below the B2 ordering spinodal, whether it be in the single-phase D0₃, two-phase A2+D0₃ or two-phase B2+D0₃ region, develops through a transient B2 ordering, in accordance with the considerations of Allen and Cahn [1].

(ii) The network of APBs in a single-phase $D0_3$ ordered alloy contains a lot of triple junctions (or triplanar lines in 3D systems) which makes the APDs much more regular-shaped and equiaxial compared to the 'swirl-shaped' APDs arising under orderings with only two types of ordered domains, e.g. under $B2 \rightarrow D0_3$ ordering [8].

(iii) Due to the above-mentioned topological features of $D0_3$ ordering the ordered precipitates formed under the $A2 \rightarrow A2 + D0_3$ phase separation are much more regular-shaped than the 'swirl-shaped' precipitates formed under the $A2 \rightarrow A2 + B2$ transition. This difference is accentuated when significant elastic anisotropy is present which results in the formation of approximately rectangular ordered domains within the disordered matrix under the $A2 \rightarrow A2 + D0_3$ transition, compared to the network of elongated rod-like (or plate-like, in 3D systems) precipitates for the $A2 \rightarrow A2 + D0_3$ or $B2 \rightarrow B2 + D0_3$ transition.

(iv) Under the $A2 \rightarrow A2 + D0_3$ phase transition the disordered A2 phase wets the ζ -APBs, but this process is notably more sluggish compared to the wetting of η -APBs by the A2 phase. However, at later stages of the $A2 \rightarrow A2 + D0_3$ transition and in absence of significant elastic effects the ζ -APBs are mostly wetted by the A2 phase, while the remaining segments of these APBs become short, and the microstructure includes few or no extended ζ -APBs, which agrees with experimental observations [1].

(v) Under the $D0_3 \rightarrow B2 + D0_3$ transition the B2 phase wets ζ -APBs, in agreement with the observations [4] for Fe-Si alloys.

To illustrate points (i)–(iv) in figures 3 and 4 we show some microstructures under $A2 \rightarrow A2 + D0_3$ and $A2 \rightarrow A2 + B2$ transformations obtained in our 2D simulation for two alloy models, I and II. Model I corresponds to the Fe-Al type chemical interaction v^c and the deformational interaction v^d characterized by the reduced elastic anisotropy parameter $B^* = 0.3$ [11]; for the model II v^c corresponds to a similar model used in [12] while v^d is the same as in model I. The reduced time t' here and below is $t\gamma_{nn}^{AB}$ where γ_{nn}^{AB} is the configuration independent factor in the probability of an A \rightarrow B atomic exchange between neighboring sites per unit time defined in works [15, 16, 17].

The first stage of both $A2 \rightarrow A2 + D0_3$ and $A2 \rightarrow A2 + B2$ transformations corresponds to congruent ordering at approximately unchanged initial concentration as discussed in [1, 9] and below. Frame 3a illustrates the transient B2 ordered state mentioned in point (i) in which only η -APDs separated by η -APBs are present. Frame 3b shows the formation of ζ -APDs within initial η -APDs, and these ζ -APDs are much more regular-shaped than the η -APDs in frame 4b. Frames 3b–3d also illustrate the wetting of η - and ζ -APBs by the disordered A2 phase mentioned in point (iv). Later on the deformational interaction tends to align ordered precipitates along elastically soft (100) directions [11], and

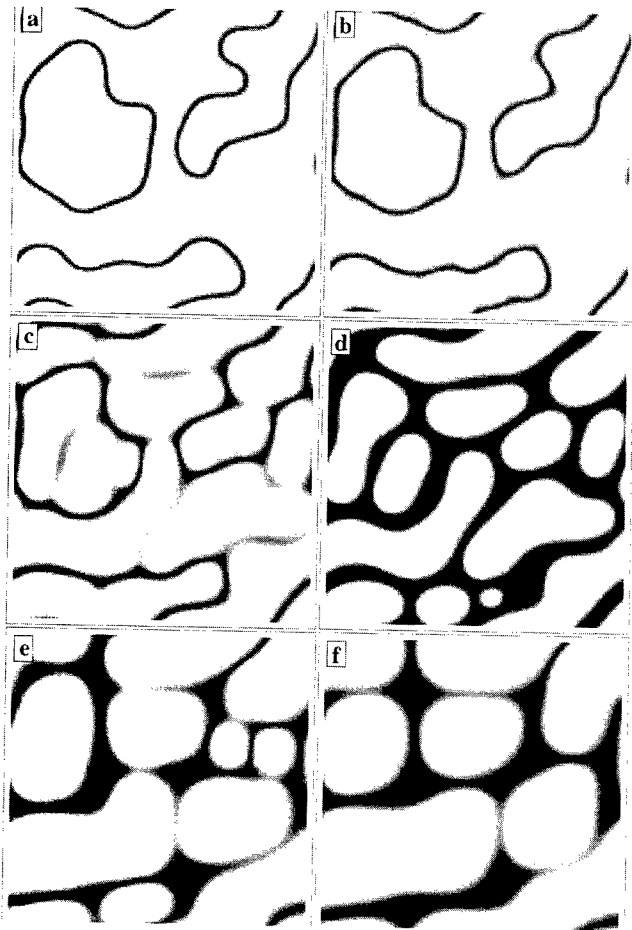


Fig. 3 (left) Temporal evolution of an alloy model I described in the text under $A2 \rightarrow A2 + D0_3$ transformation at $c = 0.187$, $T/T_c = 0.424$ (where T_c is the B2 ordering critical temperature) shown in the η^2 -representation for the following values of reduced time t' : (a) 10, (b) 30, (c) 100, (d) 500, (e) 1000, and (f) 2000. The simulation box contains 128×128 lattice sites. The grey level linearly varies with η_i^2 between its minimum and maximum values from dark to bright.

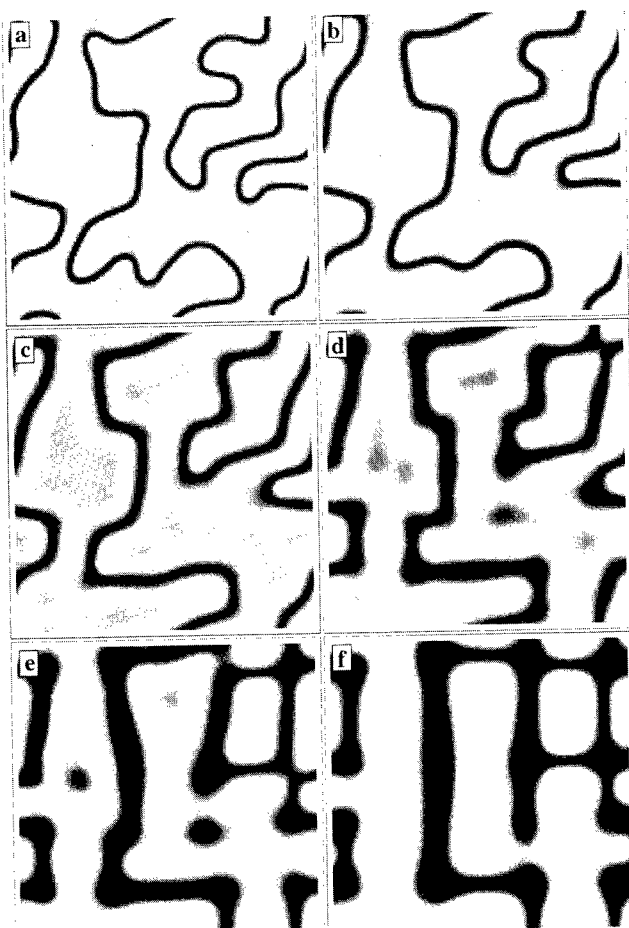


Fig. 4 (right) The same as in figure 3 but for the alloy model II described in the text under $A_2 \rightarrow A_2 + B_2$ transformation at $c = 0.35$ and $T/T_c = 0.424$.

frame 3f shows an array of approximately rectangular $D0_3$ -ordered precipitates, unlike rod-like structures seen in frame 4f. The microstructure in frame 3f is similar to those observed under the $A2 \rightarrow A2 + D0_3$ transition in Fe-Ga alloys [2], while the microstructures seen in Fe-Si alloys under $B2 \rightarrow B2 + D0_3$ transition [4] are similar to those shown in frame 4f; the latter agrees with the topological equivalence of the $A2 \rightarrow A2 + B2$ and $B2 \rightarrow B2 + D0_3$ transitions.

KINETIC FEATURES OF TRANSFORMATIONS INVOLVING $L1_2$ AND $L1_0$ ORDERINGS

We employed the KTCFM-based simulations to investigate the following problems.

1. The dependence of microstructural evolution and transient morphologies after a rapid quench of a disordered FCC alloy (A1 phase) under $A1 \rightarrow L1_2$, $A1 \rightarrow A1 + L1_2$ and $A1 \rightarrow L1_0$ transformations on the type of effective interaction between alloy components, in particular, on the range of the chemical interaction and on the deformational interaction.

2. The microscopical structure and local ordering at various antiphase boundaries in the $L1_2$ and $L1_0$ phases.

3. The occurrence of transient congruent ordering under $A1 \rightarrow A1 + L1_2$ transformation and the microstructural features of this stage.

In our simulations we used five alloy models with different types of interaction: the second-neighbor interaction models 1, 2, 3 and the Ni-Al type model 4 mentioned in section 2, and the 'extended-range' fourth-neighbor interaction model 5 with $v_2/v_1 = -0.5$, $v_3/v_1 = 0.25$, and $v_4/v_1 = -0.125$. To discuss the influence of elastic forces on the $A1 \rightarrow A1 + L1_2$ transition we also consider two more models, 2' and 4', which correspond to the addition to the chemical interactions $v_n = v_n^c$ of models 2 and 4 of the deformational interaction v^d with the parameters corresponding to Ni-Al alloys. The simulations were performed in the FCC simulation boxes of volume $V_b = L^2 \times H$ with periodic boundary conditions. We used both 3D simulations with $H = L$ and quasi-2D simulations with $H = 1$ (in the lattice constant a units), and all significant features of evolution in both types of simulation were found to be similar.

Simulations of the $A1 \rightarrow L1_2$ transformation were made at the stoichiometric concentration $c = 0.25$ for the five above-mentioned alloy models. Our results show that the microstructural evolution sharply depends on the interaction type, particularly on the interaction range R_{int} . For the short-range interaction systems, particularly for model 1 with the smallest R_{int} , transient microstructures include mainly the conservative antiphase boundaries (APBs) with (100) type orientation [18].

The distribution of APBs in such systems reveals a number of peculiar features (most of which can be illustrated by figure 5): characteristic 'step-like' APBs with (100) oriented steps and small ledges normal to them; triple junctions of two conservative APBs normal to each other with a non-conservative APB; analogous 'quadruple' junctions; loop-like configurations of non-conservative APBs adjacent to conservative ones, etc. These features agree well with the experimental observations for Cu_3Au alloy [5, 6]. In the course of the microstructural evolution the conservative APBs remain virtually immobile, and the evolution is realized via motion of non-conservative APBs and their interaction with the conservative APBs. This interaction includes a number of specific kinetic processes which can be followed in figure 5: 'sweeping' of conservative APBs by a moving non-conservative APB (which is seen in the left lower and right upper parts of frames 5b and 5c); wetting of conservative APBs by non-conservative APBs (seen in the left upper corner of frames 5b and 5c); motion of triple junctions of two non-conservative APBs with a conservative APB along the direction of the latter (illustrated by formation of two vertical conservative APBs in the right upper part of frames 5c–5e); and a peculiar process of 'splitting' of a non-conservative APB into a conservative and a non-conservative APB with the formation of triple junction or a new antiphase domain. The latter process can be illustrated by the left upper part of frames 5d–5f. First a non-conservative APB (nc-APB) seen in the left upper corner of frame 5d moves down sweeping two adjacent conservative APBs (c-APBs). When it reaches a triple junction of its adjacent c-APB with two other nc-APBs seen in frame 5d, the resulting junction of three nc-APBs immediately splits into two triple junctions, that of a pair of c-APBs with an nc-APB and that of a c-APB with two nc-APBs, with the formation of a new APD seen in frames 5e and 5f. The splitting effect is related to very small energies of the conservative APBs in short-range interaction systems, and it was observed only in model 1 with the shortest interaction range.

We also studied the influence of non-stoichiometry on the evolution by simulating the $\text{Al} \rightarrow \text{L}_{12}$ transformation for the second-neighbor interaction model 2 at $c = 0.22$ and $c = 0.32$. The APB distribution does not reveal a great sensitivity to the concentration, but the internal structure of APBs shows significant compositional changes. The degree of local disordering of APBs at lower $c = 0.22$ is notably higher than at $c = 0.25$, while at $c = 0.32$ both the non-conservative and conservative APBs show a significant degree of local ordering of the L_{10} type.

The microstructural evolution under $\text{Al} \rightarrow \text{L}_{12}$ transition for the fourth-neighbor interaction models 4 and 5 greatly differs with that for the short-range interaction systems. Transient microstructures for the Ni–Al type model 4 include mainly non-conservative APBs, and the APB

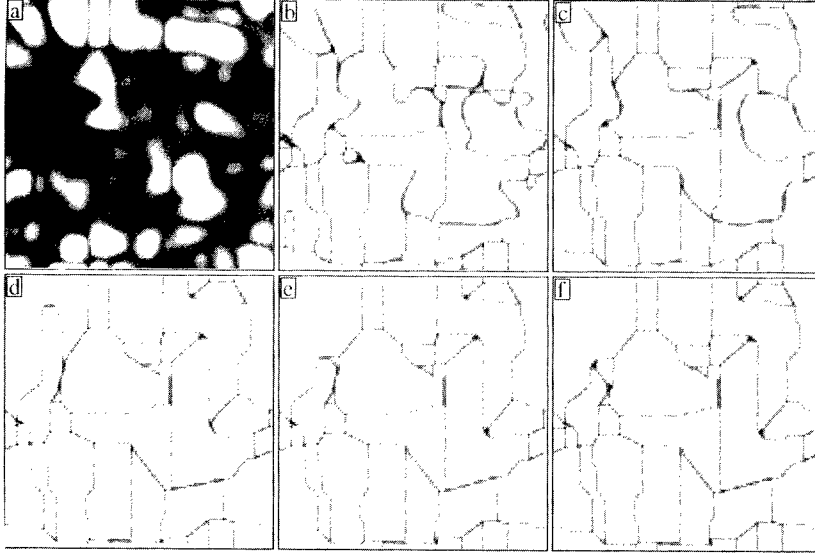


Fig. 5 Temporal evolution of the second-neighbor interaction model 1 with $v_2/v_1 = -0.125$ under $A1 \rightarrow L1_2$ transformation shown in the η^2 -representation for the simulation box size $V_b = 64^2 \times 1$ at $c = 0.25$, $T' = T/v_1 = 0.35$ and the following values of reduced time t' : (a) 2, (b) 3, (c) 20, (d) 100, (e) 177 and (f) 350. The grey level linearly varies with $\eta_i^2 = \eta_{1i}^2 + \eta_{2i}^2 + \eta_{3i}^2$ between its minimum and maximum values from dark to bright.

distribution reveals only a slight anisotropy. However, the conservative APBs are also present and make a noticeable effect on microstructures, which agrees with experimental observations for the Ni_3Al type alloys [3]. At the same time, the microstructures for the extended range interaction model 5 show neither conservative APBs nor anisotropy in the APB distribution while the triple junctions of APBs form approximately equiangle configurations characteristic of isotropic systems. These microstructures are similar to those observed in CuPd alloys [5].

The general features of the evolution under the $A1 \rightarrow L1_0$ transition in the absence of significant deformational effects (in particular, at the first stages of the transformation) are similar to those under the $A1 \rightarrow L1_2$ transition, but the presence of six types of APDs and two different types of APBs results in a number of specific effects. To illustrate that, in figure 6 we show some microstructures under the $A1 \rightarrow L1_0$ transition for the short-range interaction model 2. The comparison with analogous results for the same model under the $A1 \rightarrow L1_2$ transition shows that the tendency to form conservative APBs at stoichiometric $c = 0.5$ (frame 6b) is more pronounced than at $c = 0.25$ under $A1 \rightarrow L1_2$ transition, though at off-stoichiometric $c = 0.44$ (frame 6a) this tendency is notably reduced. Frames 6c and 6d illustrate the structure of APBs and reveal a number of differences between the shift-type and flip-type

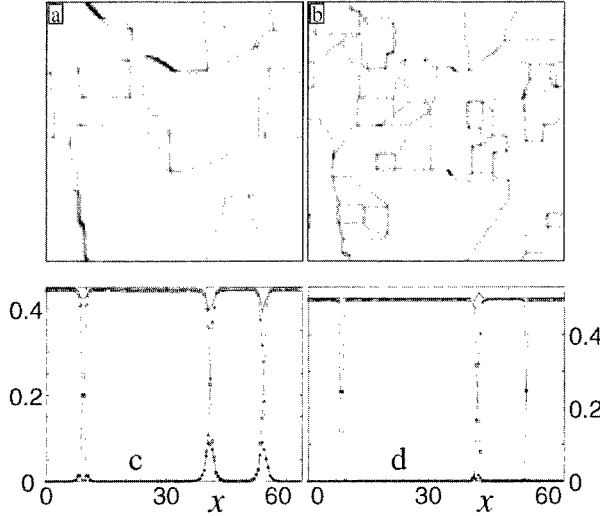


Fig. 6 Upper row: Ordered domains for the alloy model 2 with $v_2/v_1 = -0.25$ under $A1 \rightarrow L1_0$ transformation for $V_b = 64^2 \times 1$ at $T' = 0.5$, $t' = 200$ and the following concentrations: (a) $c = 0.44$, and (b) $c = 0.5$. Lower row: Profiles of local concentration $\bar{c}_i = \bar{c}(x)$ (solid line) and local order parameters $|\eta_1(x)|$, $|\eta_2(x)|$ and $|\eta_3(x)|$ (circles, triangles and squares) at $y = 4$ for the microstructures shown in frames (a) and (b), respectively.

APBs mentioned in section 4, as well as between the conservative and non-conservative APBs for each type. Denoting for brevity the first, second and third APB from the left in frames 6c and 6d as APB-1, APB-2 and APB-3, respectively, we note that APB-1 is the conservative shift-type APB, APB-2 is the non-conservative flip-type APB, and APB-3 is the flip-type APB which is non-conservative in frame 6c and conservative in frame 6d. Therefore, the profiles $\bar{c}(x)$ and $|\eta_\alpha(x)|$ in frames 6c and 6d illustrate the structure of different APBs, in particular, a peculiar local ordering $|\eta_{3i}| = |\eta_{2i}|$ within the conservative shift-type APB-1 separating two η_3 -ordered APDs.

In the presence of deformational interaction the nonlinear in n_i Kanzaki forces discussed in section 3 induce the tetragonal distortion under $L1_0$ ordering, as well as the microstructural effects related to this distortion, in particular, the 'tweed' and 'twin' structures which correspond to the microstructures of (110) oriented stripes of adjacent APDs with alternating (100) and (010) tetragonal axis. The phenomenological theory of these structures was discussed by Khachaturyan *et al* [10]. We simulated the formation of tweed and twin structures under the $A1 \rightarrow L1_0$ transition using the microscopic model of non-pairwise deformational interactions described in section 3. The simulated microstructures are similar to those observed in experiments and provide an information about the microscopical details of tweed and twin formation.

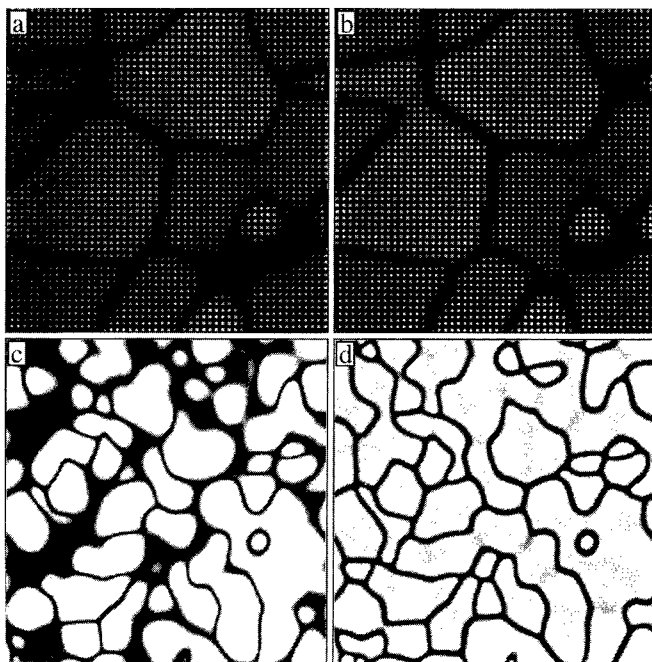


Fig. 7 Temporal evolution of the alloy model 2 with $v_2/v_1 = -0.25$ under $A1 \rightarrow A1+L1_2$ transformation at $c = 0.12$, $T' = 0.3$. Upper frames correspond to 3D simulation with $V_b = 50^3$ shown in the c -representation (grey level linearly varies with c_i between its minimum and maximum from dark to bright) for $t' = 8.6$ (a) and $t' = 10$ (b). Lower frames correspond to 2D simulation with $V_b = 128^2 \times 1$ shown in the η^2 -representation for $t' = 5.6$ (c) and $t' = 10$ (d).

The simulations of the $A1 \rightarrow A1+L1_2$ transition show that in the absence of significant elastic interaction the microstructural evolution depends on the interaction type much weaker than that under the $A1 \rightarrow L1_2$ transition. For both short- and extended-range interaction systems the interphase boundary (IPB) energies are approximately isotropic, in great difference with the APB energies in the $L1_2$ phase which are highly anisotropic in the short-range interaction systems and virtually isotropic in the extended-range interaction systems. Because of that the transient microstructures under the $A1 \rightarrow A1+L1_2$ transition in the systems with short-range interaction can show anisotropy only at the first stages of the evolution, when the APBs formed under congruent ordering are not yet strongly wetted by the disordered phase. Later on this wetting transforms the APBs into IPBs and the initial anisotropy falls off.

The effect of elastic forces on microstructural evolution was studied in the simulations for models 2' and 4' with short-range and extended-range chemical interactions, respectively. The results of these simulations agree with the phenomenological description of elastic effects developed by Khachaturyan *et al* [11, 27], and our simulations illustrate and specify many points noted by these authors. In particular, for model 2' the elas-

tic effects are manifested even at early stages of transformation, shortly after the completion of congruent ordering when the sizes l of ordered precipitates are relatively small: $l10a$, which is related to the short-range character of chemical interactions. On the contrary, for the Ni–Al type model 4' these effects become noticeable only at the advanced stages of coarsening when the precipitate sizes become sufficiently large: $l50a$.

We also consider the problem of transient congruent ordering under alloy decomposition with ordering discussed by a number of authors [1, 7, 9]. The presence of this stage under the $A1 \rightarrow A1 + L1_2$ transition was recently questioned as at the early stages of this transition in Al–Li alloys Haasen *et al* [7] observed microstructures with neighboring in-phase ordered domains separated by a disordered layer which seemed to be incompatible with an occurrence of congruent ordering. To clarify the problem we made simulations of the $A1 \rightarrow A1 + L1_2$ transition under conditions similar to those of experiments by Haasen *et al*. In all our simulations we observed the stage of congruent ordering. At the same time, both before and after this stage we observed many microstructures with neighboring in-phase domains, and some of the simulated microstructures are quite similar to those observed by Haasen *et al* [7]. This is illustrated by microstructures in figure 7 where the neighboring in-phase domains can be seen both in the left upper and the right lower part of frame 7a, as well as in many places of frame 7c. However, these microstructures correspond to the stages before the completion of congruent ordering, and later on the neighboring in-phase domains coalesce with each other which is seen from comparison of frames 7b and 7a or 7d and 7c. Therefore, the experiments [7] can correspond to the other stages of evolution and do not contradict to the occurrence of congruent ordering. We also discuss the temporal evolution of local concentrations and local order parameters in the course of congruent ordering. We show that a depletion of local concentration near APBs begins virtually simultaneously with the appearance of ordered domains, and after a completion of congruent ordering the local concentration within APB is already depleted. Therefore, the commonly used term 'congruent ordering' actually corresponds to the presence of APBs with a locally equilibrated, depleted concentration rather than to a 'strictly congruent' state with an unchanged initial concentration throughout the alloy.

ACKNOWLEDGEMENTS

The authors are much indebted to Georges Martin for numerous stimulating discussions. The work was supported by the Russian Fund of Basic Research, Grant No. 97-02-17842.

REFERENCES

- [1] Allen S M and Cahn J W 1976 *Mechanisms of Phase-Transformations Within Miscibility Gap of Fe-Rich Fe-Al Alloys* Acta Met. **24** 425
- [2] Oki K, Matsumura S and Eguchi T 1987 *Phase Separation and Domain Structure of Iron-based Ordering Alloys* Phase Transitions **10** 257
- [3] Cahn R W, Siemers P A and Hall E L 1987 *The Order-Disorder Transformation in Ni₃Al and Ni₃Al-Fe Alloys .2. Phase-Transformations and Microstructures* Acta Metall. **35** 2753
- [4] Matsumura S, Oyama H and Oki K 1989 *Dynamical Behavior of Ordering With Phase-Separation in Off- Stoichiometric Fe₃Si Alloys* Mater. Trans., JIM **30** 695
- [5] Loiseau A, Ricolleau C, Potez L and Ducastelle F 1994 *Solid-Solid Phase Transformations* ed W C Johnson *et al* (Warrendale: The MMM Society) p 385
- [6] Potez L and Loiseau A 1994 *High-Resolution Electron Microscopy Studies of Antiphase Boundaries in Cu₃Au* J. Interface Sci. **2** 91
- [7] Schmitz G, Hono K and Haasen P 1994 *High-Resolution Electron-Microscopy of the Early Decomposition Stage of Al-Li Alloys* Acta Metall. Mater. **42** 201
- [8] Korner A 1995 *Analysis of the Evolution of Antiphase Boundaries in a Fe-Al Alloy During in-Situ Transmission Electron-Microscopy Heating* Phil. Mag. Lett. **72** 21
- [9] Loiseau A 1996 *Curr. Opin. Solid State Mater. Sci.* **1** 369
- [10] Chen L-Q, Wang Y and Khachaturyan A G 1992 *Kinetics of Tweed and Twin Formation during an Ordering Transition in a Substitutional Solid Solution* Phil. Mag. Lett. **65** 15
- [11] Chen L-Q, Wang Y Z and Khachaturyan A G 1994 *Statics and Dynamics of Alloy Phase Transformations (NATO Advanced Study Institute, Series B: Physics 319)* ed A Gonis and P E A Turchi (New York: Plenum) p 587
- [12] Dobretsov V Yu, Vaks V G and Martin G 1996 *Kinetic features of phase separation under alloy ordering* Phys. Rev. B **54** 3227
- [13] Martin G 1990 *Atomic Mobility in Cahn Diffusion-Model* Phys. Rev. B **41** 2279
- [14] Gouyet J F 1993 *Atomic Mobility and Spinodal-Decomposition Dynamics in Lattice Gases - Simple Discrete Models* Europhys. Lett. **21** 335

- [15] Vaks V G, Beiden S V and Dobretsov V Yu 1995 *Mean-Field Equations For Configurational Kinetics of Alloys At Arbitrary Degree of Nonequilibrium* Pis. Zh. Eksp. Teor. Fiz. **61** 65 (Engl. Transl. JETP Lett. **61** 68)
- [16] Vaks V G 1996 *Master equation approach to the configurational kinetics of nonequilibrium alloys: Exact relations, H-theorem, and cluster approximations* Pis. Zh. Eksp. Teor. Fiz. **63** 447 (Engl. Transl. JETP Lett. **63** 471)
- [17] Belashchenko K D and Vaks V G 1998 *The master equation approach to configurational kinetics of alloys via the vacancy exchange mechanism: general relations and features of microstructural evolution* J. Phys.: Condens. Matter **10** 1965
- [18] Kikuchi R and Cahn J W 1979 *Theory of Interphase and Antiphase Boundaries in Fcc Alloys* Acta Met. **27** 1337
- [19] Mohri T, Sanchez J M and de Fontaine D 1985 *Short-Range Order Diffuse Intensity Calculations in the Cluster Variation Method* Acta Met. **33** 1171
- [20] Finel A 1994 *Statics and Dynamics of Alloy Phase Transformations (NATO Advanced Study Institute, Series B: Physics 319)* ed A Gonis and P E A Turchi (New York: Plenum) p 495
- [21] Vaks V G and Samolyuk G D 1999 *On accuracy of different cluster models used in describing ordering phase transitions in fcc alloys* Zh. Eksp. Teor. Fiz. **115** 158 (Engl. Transl. Sov. Phys.-JETP **88** 89)
- [22] Yang C N 1945 *Generalization of the Quasi-Chemical Method in the Statistical Theory of Superlattices* J. Chem. Phys. **13** 66
- [23] Khachaturyan A G 1983 *Theory of Structural Phase Transformations in Solids* (New York: Wiley)
- [24] Chassagne F, Bessiere M, Calvayrac Y, Cenedese P and Lefebvre S 1989 *X-Ray Diffuse-Scattering Investigation of Different States of Local Order in Ni-Al Solid-Solutions* Acta Met. **37** 2329
- [25] Hasaka M 1980 *Ordering and Phase Separation in the Fe-Al Alloy* Trans. JIM **21** 660
- [26] Inden G 1974 *Ordering and Segregation Reactions in Bcc Binary-Alloys* Acta Metall. **22** 945
- [27] Wang Y, Banerjee D, Su C C and Khachaturyan A G 1998 *Acta mater.* **46** 2983

KINETICS OF PHASE SEPARATION IN A BINARY ALLOY: INFLUENCE OF THE ATOMIC MOBILITIES

M. Athenes¹, P. Bellon² and G. Martin¹

¹CEA Saclay, Section de Recherche de Metallurgie Physique, 91191 Gif-sur-Yvette, France
mathenes@cea.fr

²Department of Materials Science and Engineering, University of Illinois
1304 W. Green St. Urbana Illinois 61801, USA

ABSTRACT

An atomistic kinetic model with a vacancy mediated diffusion mechanism is used to study the precipitation kinetics from a supersaturated solution. We show that, for a given alloy thermodynamics, varying the vacancy-solute binding energy affects the contribution of the coagulation process to coarsening both for low and high solute supersaturation. We also observe that varying the temperature affects the phase separation kinetic pathway in agreement with experimental observations, but at variance with kinetic simulations carried out with the standard direct exchange dynamics.

INTRODUCTION

When a supersaturated solid solution is quenched below the binodal line, a solute rich phase precipitates out of a solvent. The kinetics of phase separation are well described by the theories of nucleation, growth and coarsening [1] in the metastability region, or by the theory of spinodal decomposition in the instability region [2]. However, these mean field type theories rest on simplifications which make it difficult to take into account practical features such as the details of the alloy thermodynamics or of the diffusion process. Ising-like or Potts-like models can well reproduce the alloy thermodynamics, as far as coherent precipitation is concerned. They consider that atoms are located on a three dimensional rigid lattice and assume that the alloy internal energy is given by the sum of atomic pairwise interaction energies. Kinetic Monte Carlo simulations with the direct exchange dynamics, (i.e the Kawasaki dynamics [3]) have mainly focused on scaling properties [4, 5].

If we realise that the physical evolution of the alloy configuration is nothing but the result of vacancy jumps on the lattice, the kinetic pathway can be generated provided that the jump frequencies correctly depend on the alloy configuration. Monte Carlo simulations with a vacancy diffusion mechanism [6, 7] show that for concentrated alloys, the Lifshitz-Slyozov-Wagner regime [8] is reached much faster than with the direct exchange dynamic, as a result of enhanced interfacial diffusion by the vacancies. Soisson *et al* [9] showed that the vacancy interfacial diffusion enables neighbouring precipitates to migrate. Neighbouring precipitates were then observed to encounter each other, leading to a coagulation mechanism competing with the classical evaporation-condensation coarsening mechanism.

In this paper, we examine the influence of varying the ratio of solute to solvent mobilities on the phase separation kinetics on a b.c.c. lattice by considering an atomistic kinetic model treated by a Monte Carlo technique. We follow the approach of a recent Monte Carlo study of precipitation of the B2 ordered phase for which the effect of varying the solute and solvent mobilities was investigated [10]. It was shown, among other things, that individual vacancies could yield to localized or delocalized ordering depending on the asymmetry of the solute and solvent mobilities. We put special emphasis on the early stages when solute atoms are nucleating into small clusters. We also discuss the results obtained with a direct exchange dynamics, so as to better understand the specific effects of the vacancy diffusion mechanism.

ATOMISTIC KINETIC MODEL

A rigid lattice with body centered cubic (BCC) structure and periodic boundary conditions is considered. For computer efficiency atomic positions are given in a rhombohedral frame with one atom per unit cell and $N = L^3$ lattice sites ($L = 64$, unless specifically noted). The alloy consists of N_A A atoms, N_B B atoms and one vacancy V , with $N = N_A + N_B + 1$. Interaction energies are taken as pair interactions ϵ_{XY} between nearest neighbour sites, where X, Y equals A or B. We consider a $A - B$ binary system which exhibits a miscibility gap below which the solid solution decomposes into A-rich and B-rich phases. The unmixing transition is of first order and with nearest neighbour interactions only, the critical temperature is $T_c \approx \frac{-\epsilon}{k} \times 0.62$ at $A_{0.5}B_{0.5}$ composition for a negative ordering energy $\epsilon = \epsilon_{AA} + \epsilon_{BB} - 2\epsilon_{AB}$. The equilibrium phase diagram is constructed by Monte-Carlo in the semi-grand canonical ensemble.

The thermodynamic properties of the $A - V$ and $B - V$ binaries are determined by their respective ordering energies ϵ_{AA} and ϵ_{BB} (no ghost interactions between atoms and vacancies are considered here: $\epsilon_{AV} = \epsilon_{BV} = 0$). From a practical point of view, our system is so highly diluted with respect to vacancies, that, in simulations with a constant vacancy concentration, the only effect of the asymmetry parameter $u = \epsilon_{AA} - \epsilon_{BB}$ on equilibrium properties is to affect the degree of occupation of the vacancy inside A-rich or B-rich phase domains. For convenience, we define $a^* = u/\epsilon$ as the degree of asymmetry.

With nearest neighbour interactions only, the parameter a^* also determines the binding energy between a vacancy and a B solute atom in the A-rich matrix. It is defined as the energy difference between the associated (nearest neighbour) vacancy-solute pair and the dissociated pair embedded in a perfect solvent matrix. The binding energy between V and B is $E_{VB} = \frac{\epsilon}{2}(1 + a^*)$.

The activation energy E_{XV}^{act} for an $X - V$ exchange is derived from a broken bond model [11, 12, 13] for which $E_{XV}^{\text{act}} = E_{sp} - E_i$ and where E_{sp} and E_i are the internal energies at saddle point and in the initial stable configuration. We have simplified the saddle point contribution by introducing a parameter c^* to account for the nature of the jumping atom. The activation barrier then writes as the sum of two contributions. The first one is configuration independent and yields a scaling factor for the jump frequency, the second one depends on the configuration as given by eq. 1:

$$E_{XV}^{\text{act}} = \frac{\epsilon}{2} \begin{cases} n_B - a^*n_A + c^* & \text{if } X = A \\ n_A + a^*n_B & \text{if } X = B \end{cases} \quad (1)$$

where n_A and n_B are the number of A and B nearest neighbours of the atom to be exchanged with the vacancy. Using the rate theory, the frequency of the $X - V$ exchanges is $w_X = \nu \exp\{-\frac{E_{XV}^{\text{act}}}{kT}\}$, where ν is the attempt frequency. The time unit is chosen as ν^{-1} .

RESIDENCE TIME ALGORITHMS

The vacancy jumps form a Markovian process which can be well simulated by a "residence time algorithm" (RTA) whose general concepts were discussed by Lanore [15]. Here, we use the simpler version introduced by Young and Elcock [14], for which a transition (here a vacancy jump) is performed at each step and the time is incremented by the average time the system stays in its configuration. The advantage of the RTA is to eliminate the numerous unsuccessful attempts that are present at low temperatures in the conventional Metropolis algorithm. This technique has been extended to design higher order residence time algorithms which similarly eliminate reversal jumps along the correlated vacancy pathways and perform an efficient vacancy move at each step [16]. The second order algorithm (2RTA) was eventually used for the low temperature simulations, for which the problem of vacancy reversal jumps on solute atoms is crucial.

TRACER DIFFUSION MEASUREMENTS

Prior to studying the kinetics of phase separation, let us first examine the diffusion properties given by the present atomistic model for a dilute solid solution. A and B tracer diffusion coefficients are computed

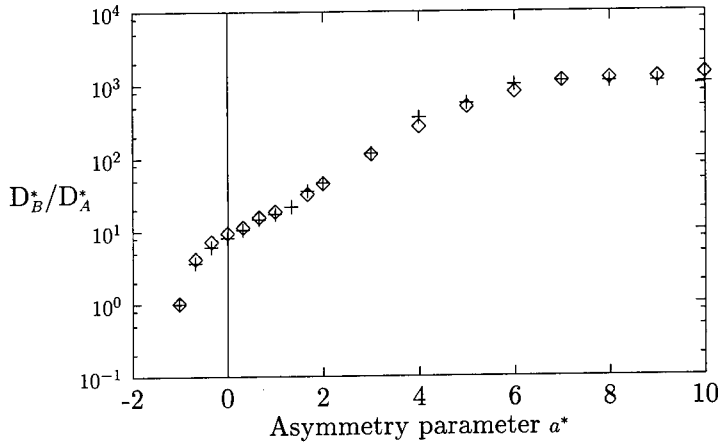


Figure 1. Evolution of the diffusivity ratio as a function of the degree of asymmetry a^* : \diamond , one solute atom in the computational box, $+$, two solute atoms, with $T=0.32 T_c$.

with the second order residence time algorithm as a function of the vacancy-solute binding energy. The simulation box contains 16^3 sites. The temperature is $T=0.32T_c$ and the solubility limit is 2.5×10^{-4} at.% which corresponds to one B atom in the box.

We introduce one or two B atoms in the box and we investigate the effect of varying the vacancy-solute binding energy (a^* varies, c^* is set to zero). In figure 1, the ratio D_B^*/D_A^* is plotted as a function of the a^* parameter. For $a^* = -1$, the vacancy-solute binding energy is zero and we observe that the solute and the solvent diffuse at the same speed. This is due to the fact that when no solute-solute bounds are present, all vacancy jump frequencies are equal. When the a^* parameter increases, the D_B^*/D_A^* ratio increases. This results from two facts: the vacancy concentration around the solute atoms increases, and the vacancy-solute exchange occurs more frequently due to the higher activation barrier involving A atoms ($-\frac{7\epsilon a^*}{2}$). However, since a vacancy-solute exchange is very probably followed by the equivalent reverse jump, its contribution to solute diffusivity saturates. For the simulations with two solute atoms, we observe a transient interval $a^* \in [4, 6]$ for which the diffusivity ratio is larger (B diffuses faster) than as obtained with one solute atom. If no interaction between the two B atoms takes place, the diffusivity ratio should be equal or lower than the diffusivity ratio obtained with one solute atom. This effect therefore results from the existence of diffusion sequences involving the two solute atoms simultaneously. Such sequences have been identified and are depicted in figure 2. The vacancy jump sequences for the migration of the monomer is also given. The corresponding migration barriers are given in Table 1, and consider, as the reference state, the vacancy associated to the monomer or to the dimer. Moreover, the fact that in figure 1, D_B^*/D_A^* stabilizes at a value larger than half the value obtained with one solute atom for $a^* > 6$ is a further proof of the manifestation of a specific correlated sequences involving the vacancy and the two solute atoms.

Let us stress that the diffusion models for dilute alloys [18, 19], first developed by Lidiard for the FCC lattice [20], consider that solute atoms do not interact together and can not account for the diffusion mechanisms involving more than one solute atom simultaneously. However, these diffusion models show that the solute diffusivity not only depends on the concentration of the vacancy-monomer first neighbour pairs (via the binding energy E_{VB}) but also on the mobility of the vacancy-solute pairs (via the vacancy-monomer exchange frequency w_2). Although these jumps, necessary for the monomer to migrate, have a very low activation barrier ($\frac{7\epsilon}{2}$) in our model, their effect on the solute diffusivity was observed to be limited. This results from the strong correlations between these vacancy-monomer exchanges and the fact that two such consecutive jumps leave the alloy configuration unchanged. The diffusion theory for the dilute BCC alloy [18, 19] shows that the contribution of the vacancy-monomer exchanges (of frequency

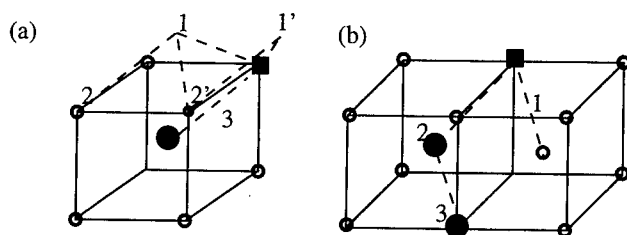


Figure 2. (a) Diffusion of a monomer. When the vacancy-solute binding energy is attractive enough, the pair can migrate without dissociating by performing the schematized sequences (1-2, 1-2' or 1'-2') together with vacancy-solute exchanges (jump 3). Activation energies are given in Table 1; (b) Diffusion of a dimer. When the vacancy-solute binding energy is attractive enough, a complex formed by two solute atoms and a vacancy can migrate without dissociating. When $\epsilon - u < 0$, the most stable position of the complex is the position schematized in (b). Combination of sequence 1 and sequence 2-3 allows the complex to migrate. Activation energies are given in Table 1.

Table 1. Various activation energies for the migration of a monomer or a dimer. The activation barrier corresponding to a vacancy jump depicted in figure 2 is given by equation 1. The cumulated barrier is the energy difference between the saddle position of the corresponding jump and the configuration as depicted in figure 2. ΔE is the energy difference between the configuration after the corresponding jump and the initial configuration of figure 2. The parameter c^* is set to zero.

Jump number	Activation barrier	Cumulated barrier	ΔE
Monomer			
1	$\frac{1}{2}(-7u)$	$\frac{1}{2}(-7u)$	$\frac{1}{2}(-\epsilon - u)$
2	$\frac{1}{2}(\epsilon - 6u)$	$\frac{1}{2}(-7u)$	0
3	$\frac{1}{2}\epsilon$	$\frac{1}{2}\epsilon$	0
Dimer			
1	$\frac{1}{2}(\epsilon - 6u)$	$\frac{1}{2}(\epsilon - 6u)$	0
2	$\frac{1}{2}(6\epsilon + u)$	$\frac{1}{2}(6\epsilon + u)$	$\frac{1}{2}(-\epsilon + u)$
3	$\frac{1}{2}\epsilon$	$\frac{1}{2}(6\epsilon + u)$	0

w_2) to B tracer diffusion is proportional to $w_2 f_B$ where the solute correlation factor f_B depends on the dissociative jump frequency w_3 (from the monomer) according to the following expression:

$$f_B = \frac{7Fw_3}{w_2 + 7Fw_3} \quad (2)$$

where w_3 is the vacancy-solute dissociative jump frequency and the numerical factor $7F$, calculated in [21] as a function of the frequency ratio w_4/w_0 between a vacancy-solute associative jump and the vacancy jump in the pure matrix. The numerical factor $7F$ slightly varies with this frequency ratio and decreases from 7 to 3 when w_4/w_0 increases from 0 to $+\infty$. With the $a^* = 0$ parametrization, we also have $w_2 = \nu \exp \frac{-7\epsilon}{2kT}$ and $w_2 = \nu$ for the two remaining frequencies. The contribution of the vacancy-monomer exchanges to the solute diffusivity thus saturates when w_2 is great compared to the dissociative vacancy jump frequency w_3 as observed in the simulations when $a^*=0$. Since in these simulations, the solute diffusivity is mainly controlled by the association-dissociation of the vacancy from the monomers, we have introduced the c^* parameter in the activation energy for the B atoms in equation 1 so as to decouple the contribution arising from the vacancy-solute exchanges to the one arising from the vacancy-solute binding energy.

PHASE SEPARATION KINETIC SIMULATIONS

Since varying the asymmetry parameter a^* affects the diffusion properties of solute atoms without modifying the thermodynamics of the binary A-B, we examine the effect of a^* on the clustering mechanism. We consider a supersaturated solid solution with 8 at.% of solute and at $T/T_c=0.12$. Two parametrizations are considered. For the first parametrization, the vacancy-solute binding energy is set to zero ($a^* = -1$). For the second parametrization, the system exhibits an "attractive" vacancy-solute binding energy: we set $a^* = 0$. In figure 3, one observes that the decrease of the number of monomers precedes ($a^* = -1$) or accompanies ($a^* = 0$) that of dimers. At this low temperature, we have observed that the dimers are very stable so we can neglect the influence of their dissociation on the clustering process. Thus, the two opposite behaviours observed result from the different mobilities of the monomers and dimers. The activation barrier controlling the migration of monomers is $\frac{\epsilon-6u}{2}$ while the one for the dimer is $\frac{2\epsilon-5u}{2}$. When $a^* = 0$, the dimers are more mobile than the monomers and they both cluster simultaneously. When $a^* = -1$, the dimers are less mobile relatively to the monomers. The latter thus precipitates first and the number of dimers increases transiently. Then the dimers precipitate after sufficient depletion of the matrix in monomers.

Since varying the a^* parameter modifies the clustering mechanism, it is interesting to investigate the influence of this parameter on the degree of advancement of the precipitation as given by the Warren-Cowley nearest neighbour short range order parameter α_1 . In figure 4, we have plotted the number of various n -mers ($n < 5$) and the α_1 parameter as a function of time, and we have examined the slope (n) of $\log \alpha_1$ versus $\log t$ in the range $0.1 < \alpha_1 < 0.5$. When $a^* = 0$, the various n -mers are clustering concomitantly leading to a high $\alpha_1(t)$ value of n . When $a^* = -1$, phase separation proceeds via the successive depletion of the n -mers, leading to a lower value for the $\alpha_1(t)$ slope.

We now show that the two types of clustering mechanism of the n -mer (i.e concomitant or successive clustering of the n -mers) may explain the features of experimental resistivity response observed in Fe1.34at.%Cu alloy. The degree of advancement ξ of the precipitation kinetics in Fe1.34at.%Cu system has been studied using the electrical resistivity measurements of Barbu *et al.* [22], which give access to the amount of solute atoms remaining in solid solution. These experiments show that the first stages of the resistivity responses can be properly reproduced using the Kolmogorov-Johnson-Mehl-Avrami law (KJMA) for which the degree of advancement ξ is function of the time:

$$\xi(t) = 1 - \exp \left(- \left(\frac{t}{\tau} \right)^n \right). \quad (3)$$

where the relaxation time τ depends on the diffusion coefficient of the system, and the exponent n depends on the phase transformation mechanism. The KJMA exponents measured experimentally were found to be

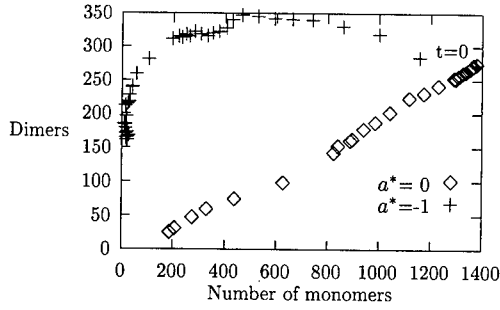


Figure 3. Depletion of monomers and dimers starting from a solid solution with $C_B=8\text{at}\%$ and $T=0.13T_c$ for various a^* values with the vacancy diffusion mechanism, the decrease of the number of monomers precedes ($a^*=-1$ +) or accompanies ($a^*=0$ \diamond) that of dimers.

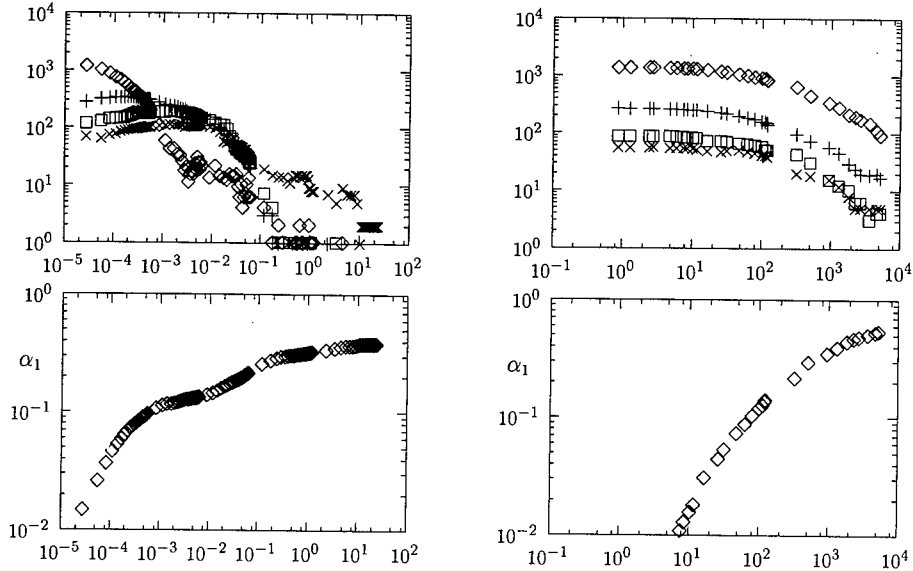


Figure 4. Time evolution of the number of n -mers ($n < 5$) (upper row) and the Warren-Cowley nearest neighbour order parameter (lower row) for two distinct asymmetries: $a^*=-1$ (left column) and $a^*=0$ (right column) ($C_B=8\text{at}\%$ and $T=0.32T_c$).

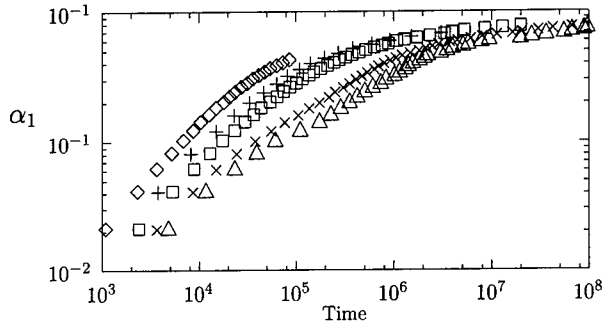


Figure 5. Time evolution of the short range order parameter α_1 for the vacancy dynamics with $C_B=3\text{at}\%$ and $a^*=0$ and at different reduced temperatures $\frac{T}{T_c}$: \diamond 0.18, $+$ 0.23, \square 0.27, \times 0.34, \triangle 0.38.

lower than the values predicted by classical theories [23] and were decreasing from 0.8 to 0.4 with increasing temperature from 670K to 770K.

Assuming that the degree of advancement ξ is described by the Warren-Cowley parameter α_1 , Soisson, Barbu and Martin [9] showed that the time evolution of α_1 can be reproduced by the KJMA law and that the exponent n varies with temperature in the same range [0.4, 0.8] exhibiting the same tendency as observed experimentally. Since the exponent n derived by these authors corresponds, to the slope of $\log \alpha_1$ versus $\log t$ curves for α_1 ranging from 0.1 to 0.5, we believe that increasing the a^* parameter or decreasing the temperature results in the same effect. When the vacancy-solute binding energy is negative, i.e. “attractive”, decreasing the temperature increases the vacancy segregation on solute clusters, making them more mobile relatively to monomers. Figure 5 clearly shows the cluster mobility effect when temperatures is varied while $a^* = 0$ and $C_B=3\%$: we observe that the slope of the curve $\log \alpha_1$ versus $\log t$ in the range $0.1 < \alpha_1 < 0.5$, increases from 0.46 at $0.38T_c$, to 0.73 at $0.18T_c$.

DIRECT EXCHANGE MODEL

Simulations with the direct exchange dynamics are carried out to better identify the specificity of the vacancy diffusion mechanism. Dobretsov *et al.* [24, 25] studied the effect of varying the asymmetry of the pairwise interaction energies with a direct exchange mechanism and the mean field description introduced in [13]. It was shown that the asymmetry can affect the mobility of antiphase boundaries for the ordering alloy [24] and coagulation process by the bridge coarsening mechanism for the phase separating alloy [25]. This last study shows that when the asymmetry is varied, a coagulation mechanism occurs and becomes predominant over the evaporation-condensation mechanism. We now vary the asymmetry parameter in the Monte Carlo simulations, so as to understand if the coagulation effect observed with the vacancy dynamics can be recovered with the direct exchange dynamics when the ratio of the solute to solvent mobility varies. The direct exchange dynamics is implemented as follows: two nearest neighbour atoms are randomly selected. The activation barrier $E_{AB}^{\text{act}} = E_{sp} - E_{\text{initial}}$, is computed, where E_{sp} is the energy of the system at the saddle position. The activation energy, then, is written :

$$E_{AB}^{\text{act}} = \frac{\epsilon}{2} [(m_B - n_B) + a^* (m_B + n_B) + C(a^*)]. \quad (4)$$

where m_B and n_B are the numbers of B nearest neighbours of the A and B atoms, respectively, and $C(a^*) = \frac{\epsilon}{2} [Z - 1 - Za^*] + E_{sp}$ is a a^* -dependant constant and includes the constant contribution to the saddle position E_{sp} . The frequency of the $A - B$ exchange is given by rate theory : $w = \nu \exp\{-\frac{E_{AB}^{\text{act}}}{kT}\}$ and the specific residence time algorithm introduced by Börtz *et al.* [26] is used.

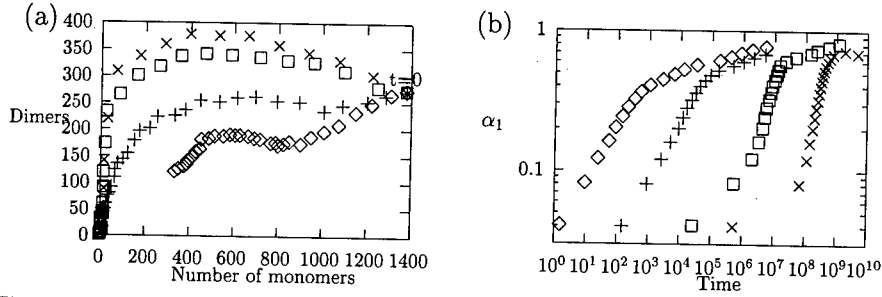


Figure 6. Simulations carried out with the direct exchange dynamics: (a) Depletion of monomers and dimers starting from a solid solution with $C_B=8\text{at}\%$ and $T=0.13T_c$ for various a^* values ($a^*=-2$ \times , $a^*=-1$ \square , $a^*=0$ $+$ and $a^*=1$ \diamond) (b): Time evolution of the short range order parameter at different reduced temperatures for $C_B=1\text{at}\%$ and $a^*=0$ ($\frac{T}{T_c} \times 0.39$, \square 0.31, $+$ 0.21, \diamond 0.16).

Let us stress that the present activation model accounts for the difference of strength of AA and BB bonds. At variance, the kinetic Ising model correlates the activation barrier to the energy of the final configuration, and the activation energy is $\Delta E_{AB}^{\text{Ising}} = \frac{1}{2} (E_{\text{final}} - E_{\text{initial}}) + Q$ where Q is a constant and E_{final} and E_{initial} are respectively the energy after and before the jump. It can be easily checked that the asymmetry parameter cancels out from the activation energy which reduces to :

$$\Delta E_{AB}^{\text{Ising}} = \frac{\epsilon}{2} (n_B - m_B) + Q' \quad (5)$$

where Q' is a constant. With such a model, the mobilities of A and B monomers in the B- and A-rich phase, respectively, are identical: A and B atoms thus play a symmetrical role with respect to the activation energy.

Simulations with varying a^*

We investigate the effect of varying the asymmetry parameter on the kinetic pathway in the monomer-dimer plane. The same simulations as with the vacancy dynamics were carried out at $T=0.12T_c$ and with $C_B=8\text{at}\%$. We observe in figure 6.a that varying the parameter of asymmetry also induces a change in the kinetic pathway. Since the decrease of the number of dimers starts to accompany that of monomers for $a^* > 1$ instead of $a^* > -1$ for the vacancy dynamics, the effect appears delayed with respect to a^* . So as to explain this trend, we consider the activation energies for the migration of a monomer and a dimer. A dimer can migrate by combining dissociation and association moves. The AB exchange leading to the dissociation has an activation energy of $\frac{\epsilon}{2}(7 - 6a^*)$ and costs more than the associative move $\frac{\epsilon}{2}(9 - 6a^*)$. Compared to the activation energy for the exchange of a monomer $\frac{\epsilon}{2}(8 - 7a^*)$, dimers start to migrate faster than monomers when $a^* > 1$. This explains the delay of the a^* -effect when we compare simulations with the atom exchange and the vacancy dynamics: with a vacancy diffusion mechanism, the dimers become more mobile than the monomers when $a^* > -1$.

Complementary simulations were carried out to examine the effect of the asymmetry on the time evolution of the α_1 parameter. A similar delay was observed for the effect of varying the asymmetry. This delay is attributed to the weaker interfacial diffusion with the direct exchange dynamics.

Simulations with varying the temperature

We examine for a given parametrization ($a^* = 0$), the effect of varying the temperature. Simulations were carried out with $C_B=1\%$. In figure 6.b, the α_1 curves are represented for various temperatures: we observe

that the slope of the α_1 values ranging from 0.1 to 0.5, decreases from 1.36 at $0.38T_c$ to 0.44 at $0.16T_c$. This tendency is opposite to the one obtained with the vacancy dynamics and to the trend observed experimentally in FeCu [22]. These simulations show that the increasing effect of vacancy interfacial diffusion when temperature decreases can not be recovered with the direct exchange dynamics.

CLUSTER DISTRIBUTION AND DYNAMICAL PERCOLATION LIMIT

Here we report additional effects of varying the mobilities, which were observed with both the vacancy and the direct exchange diffusion mechanism. We have represented the mean cluster size $L^{(2)}$ as a function of the short range order parameter. We define the mean cluster size as $L^{(2)} = \frac{\sum l^2 n(l)}{\sum l n(l)}$, where $n(l)$ is the number of clusters containing l solutes following [27].

For dilute alloys, we observe in figure 7.a ($C_B=1\text{at}\%$) that when a^* increases from -1 to 1, the mean cluster size is enhanced for any given value of α_1 . This means that there are fewer but larger clusters in the computational box which results from the activation of the coagulation mechanism. Coagulation therefore broadens the cluster size distributions for both vacancy and direct exchange dynamics. With the latter dynamics, increasing a^* , increases the diffusion in B-rich phase and thus the random motion of whole solute clusters which is responsible for the coagulation mechanism. In contrast, in the mean field simulations of Dobretsov *et al* [25], droplets coagulation was observed for negative values of the a^* parameter. This opposite effect of a^* results from the fact that this coagulation mechanism results from the solute accumulation in solute-enriched and slow-diffusing regions which form bridges between droplets. Such an effect was not identified in our Monte Carlo simulations at low solute concentration. However, for greater solute concentrations, a somewhat equivalent behaviour has been identified.

For more concentrated alloys, the a^* -effect on the mean cluster size previously described can be reversed. This results from the displacement of the dynamical percolation limit: as shown by Müller-Krumbhaar [27], the site percolation limit can be generalized to take into account the site correlation resulting from the appearance of short range order at finite temperature above the miscibility gap. Below the miscibility gap, the concept of dynamical percolation limit was introduced [28, 29] to account for the formation of a transient infinite cluster during the phase separation in the kinetic Ising model.

The influence of a^* on the dynamical percolation limit is seen in figure 7.b: the mean cluster size $L^{(2)}$ increases with the short range parameter, i.e. as phase separation proceeds, then reaches a steady transient value (up to $\alpha_1 \approx 0.6$); for $a^* = -1$, the cluster size saturates at a value very close to the total number of solute atoms in the computational cell; as phase separation proceeds, this latter very large percolated cluster splits into smaller ones ($L^{(2)}$ decreases for $\alpha_1 > 0.6$); on the contrary, for $a^* = 1/2$ with the vacancy dynamics and for $a^* = 1$ with the direct exchange dynamics, the transient steady value of the mean cluster size is approximately 1/200 the total number of B atoms, for the same range as above. Clearly, the dynamical percolation limit is below 18at.% for $a = -1$ and above for $a = +1$ ($a = +1/2$ for the vacancy dynamics). The dynamical percolation limit thus increases when a^* is increased. Notice that the observed behaviour seems to be independent of the diffusion mechanism (direct exchange or vacancy) although a more detailed study is necessary to check whether or not the dynamical percolation limit depends or not on the latter.

Increasing a^* activates interface diffusion and the coagulation mechanism, and relatively slows down the migration and depletion of monomers (which remains isolated from other solute atoms). This results in building of isolated and compact clusters instead of further depleting the matrix in monomers. At variance, decreasing a^* increases the relative mobility of the solute atoms as long as they remain isolated from other solute atoms. Since n -mers ($n > 2$) are less mobile, a ramified structure is built from the successive absorption of the monomers. This behaviour favours the occurrence of a single percolated cluster.

CONCLUSION

Kinetic Monte Carlo simulations based on vacancy or direct exchange diffusion mechanism were carried out to study the precipitation process from a supersaturated solid solution in a binary alloy on a b.c.c lattice.

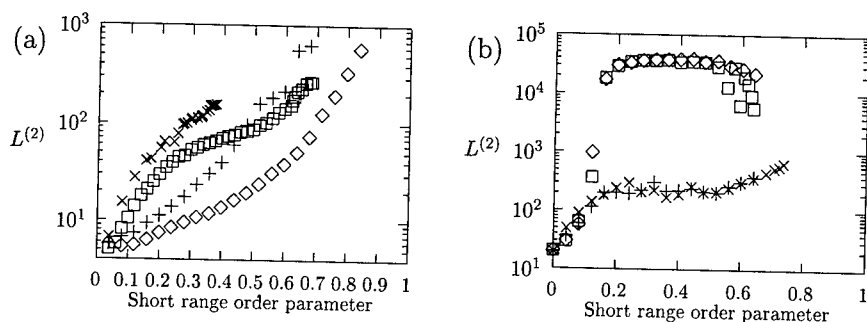


Figure 7. Evolution of the mean cluster size $L^{(2)}$ as a function of the α_1 short range order parameter, for the vacancy dynamics (\square $a^*=-1$ and \times $a^*=1/2$) and for the direct exchange dynamics (\diamond $a^*=-1$ and $+$ $a^*=1$) (a) $C_B=1\text{at}\%$ and at $T=0.32T_c$ for the vacancy dynamics and at $T=0.16T_c$ for the direct exchange dynamics, (b) $C_B=18\text{at}\%$ and at $T=0.32T_c$.

Atomic interactions are represented by constant pairwise interaction energies, and once the equilibrium phase properties of the binary system are set, varying the asymmetry of the pairwise interaction energies affects the ratio of solute to solvent tracer diffusion as well as the mobility of the n -mers ($n > 2$) relative to the monomers. The relative mobility of n -mers ($n > 2$) affects:

- (i) the precipitation kinetics. When n -mers diffuse at similar velocities in a dilute alloy, they cluster at the same time, which results in a high value of the KJMA exponent. In contrast, when n -mers ($n > 2$) diffuse slower than monomers, precipitation proceeds via the progressive depletion of the matrix with n -mers of increasing size n ;
- (ii) the cluster size distribution. When the mobility of n -mers increases relative to that of monomers, one observes a broadening of the cluster size distribution. This effect is attributed to the coagulation mechanism, the effect of which increases with the degree of asymmetry;
- (iii) the dynamical percolation transition. The solute composition at the transition decreases as the n -mers are less mobile. Activating interface diffusion and the coagulation mechanism results in building isolated and compact clusters. At variance, when n -mers are less mobile, the faster monomers are quenched as they collide ramified clusters and thus build a percolating structure. The dynamical percolation limit is therefore decreased.

The main differences between the direct exchange and the vacancy diffusion mechanism lie in the effect of temperature. With the direct exchange kinetics, the various n -mers must transiently create some additional heteroatomic bonds in order to migrate. Since these bonds are energetically unfavorable, decreasing the temperature results in slowing down the relative mobilities of the various n -mers with respect to the mobility of the monomers. When atomic diffusion proceeds by vacancy jumps, vacancies tend to segregate at interfaces to suppress the unfavorable heteroatomic bonds, and enables the n -mers to migrate without creating additional wrong bonds. Therefore, the weight of the n -mers to the diffusion process increases when the temperature is lowered. This results in increasing the KJMA exponent in agreement with experimental observations in FeCu alloy. Since this tendency can not be recovered with the direct exchange dynamics, it is a signature of the vacancy mediated diffusion mechanism on the kinetics of phase separation.

REFERENCES

- [1] R. Wagner and R. Kampmann (1991), in *Phase Transformation in Materials* (edited by P. Haasen). VCH, Weinheim.
- [2] K. Binder (1991), in *Phase Transformation in Materials* (edited by P. Haasen). VCH, Weinheim.
- [3] K. Kawasaki (1984), *Phys. Rev.* **145**, 224 and **148**, 375.

- [4] J. G. Amar, F. E. Sullivan and R. D. Mountain (1988), Phys. Rev. B **37**, 196.
- [5] D. A. Huse (1986), Phys. Rev. B, **34**, 7845.
- [6] P. Fratzl and O. Penrose (1994), Phys. Rev. B **50**, 3477.
- [7] C. Frontera, E. Vives, T. Castan, A. Planes (1996), Phys. Rev. B **53**, 2886.
- [8] M. Lifshitz, and V. V. Slyozov (1961), J. Phys. Chem. Solids **19**, 35.
- [9] F. Soisson, A. Barbu, and G. Martin (1996), Acta Mater. **44** 3789-3800.
- [10] M. Athènes, P. Bellon, G. Martin, F. Haider (1996), Acta Mat. **44**, 4739.
- [11] Girifalco (1964), J. Phys. Chem. Solids, **24**, 323.
- [12] R. Kikuchi and H. Sato (1969), J. Chem. Phys., **51**, 161.
- [13] G. Martin (1990), Phys. Rev. B **41** 2279.
- [14] M. Young and E. W. Elcock (1966), Proc. Phys. Soc. **89** 735.
- [15] J.-M. Lanore (1974), Rad. Effects, **22** 153.
- [16] M. Athènes, P. Bellon and G. Martin (1997), Phil. Mag. A, **76**, 527.
- [17] J. Hoshen, R. Kopelman (1976), Phys. Rev. B **14** 3438.
- [18] A. R. Allnatt and A. B. Lidiard (1993), *Atomic transport in solids*, Cambridge University Press.
- [19] J.-L. Bocquet, Y. Limoge and G. Brebec (1996), *Physical metallurgy*, edited by R. W. Cahn and P. Haasen Amsterdam Elsevier 535.
- [20] A. B. Lidiard (1955), Phil. Mag. **46** 1218.
- [21] A. D. LeClaire (1970), Phil. Mag. **21** 819.
- [22] T. N. Lê, A. Barbu, and F. Maury (1992), Scripta Met. Mater. **26** 771.
- [23] J. W. Christian, (1975) *The theory of transformations in alloys and metals*. p. 525. Pergamon Press, Oxford.
- [24] V. G. Vaks, S. V. Beiden and V. Yu. Dobretsov (1995), Pis'ma v ZhETF **61**, 65.
- [25] V. Yu. Dobretsov, G. Martin, F. Soisson and V. G., Vaks (1995), Europhys. Lett. **31**, 417.
- [26] A. B. Börtz, M. H. Kalos and J. Lebowitz (1975), J. Comp. Phys., **17** 10.
- [27] H. Müller-Krumbhaar (1974), Phys. Lett. **50A** 27.
- [28] S. Hayward, D. W. Heermann, D. W. and K. Binder (1987), J. Stat. Physics **49**, 1053-1081.
- [29] G. Lironis, D. W. Heermann, D. W. and K. Binder (1989), J. of Phys. A: Math. Gen. **23** L329-L334.

POINT DEFECT ENERGIES IN L₁₂-ORDERED Ni₃Al

H. SCHWEIGER AND R. PODLOUCKY

Center for Computational Materials Science and Department for Physical Chemistry, University of Vienna, Liechtensteinstrasse 22a/1/3, A-1090 Vienna, Austria

W. PÜSCHL, M. SPANL, AND W. PFEILER

Institut für Materialphysik, University of Vienna, Strudlhofgasse 4, A-1090 Vienna, Austria

ABSTRACT

Experimental investigation of order-order relaxations in Ni₃Al by residual resistometry yielded a very high ordering activation energy of about 4.6eV being in correspondence with tracer experiments, where the tracer atom substitutes the Al-atom. Qualitatively, this might be interpreted by breaking of bonds to the 12 surrounding Ni nearest neighbour atoms of the ordered L₁₂-lattice. For the purpose of a more fundamental understanding the properties of vacancies and antisites in Ni₃Al were studied by means of *ab-initio* calculations for supercells. Formation energies for Ni- and Al-vacancies were derived using a grandcanonical ensemble. Further, vacancy migration energies were determined successively displacing atoms from their equilibrium position to a vacant nearest neighbour position. Correlated jumps during a jump cycle were also taken into account.

Key words: L₁₂-intermetallics, point defects, defect energies, *ab-initio* calculations

INTRODUCTION

In binary alloys of the L₁₂-type like in all long-range ordered alloys the degree of order for thermodynamic reasons depends on temperature. At 0 K A and B atoms in a stoichiometric alloy sit on their respective sublattices only, that is, the majority A atoms (Ni) on the face centres of the cubic unit cell (α sublattice) and the minority B atoms (Al) on the cube corners (β sublattice). With rising temperature an ever increasing number of antisites (A on β , B on α) will be found in thermodynamical equilibrium, reducing the

(A on β , B on α) will be found in thermodynamical equilibrium, reducing the degree of order which can be expressed by a long-range order (LRO) parameter as a function of the number of antisites. Changing the temperature by a small amount ΔT after LRO equilibrium has been established a new antisite distribution, equivalent to a new state of order, must be adjusted as an equilibrium state at the new temperature.

In a number of experiments this kind of 'order-order' relaxation has been measured in $\text{Ni}_{76}\text{Al}_{24}$ by the very sensitive method of residual resistometry [1]. Closer inspection of the electrical resistivity curves as a function of time reveals that equilibrium is not reached by a single exponential but by two processes with distinctly different rates. From an Arrhenius analysis an identical activation energy of 4.6eV follows for both processes, the pre-factors accounting for the difference in the rates. Interestingly, in a similar investigation of another group on stoichiometric Ni_3Al a much lower activation energy was determined [2]. The origin for this differences is still under discussion and the present investigation shall help to clarify this problem.

Atoms must move for the degree of order to change. It is therefore natural to look up diffusion data for comparison. But Ni^* tracer diffusion experiments [3,4] yield a much lower activation energy of only 3eV. On the other hand diffusion experiments with Ti^* where the tracer atom substitutes Al yield a much higher activation energy of 4.6eV [5] which is in correspondence with the above results from resistometry. That is, we must keep in mind that the situation in usual diffusion experiments in ordered alloys is essentially different from order relaxation experiments. In the first case, a specified kind of atom is transported through the lattice, keeping the average distribution of atoms over the sublattices and therefore the state of order constant. In order-order relaxation there is, however, a *net flow of atoms between the sublattices*.

ATOM JUMPS AND STATISTICS

In close-packed lattices like L1_2 exchange with nearest neighbour vacancies is the only plausible mechanism for atom migration, comprising diffusion as well as order relaxation. The topology of the ordered L1_2 lattice leads to the following considerations for elementary atom jumps (fig. 1). A vacancy on an α (majority) sublattice site (at the centre in fig. 1) is surrounded by 8 α sites (shown schematically in the same column) and 4 β sites (columns to the left and right) as nearest neighbours. Exchange with an A atom on α or an antisite B atom on α (shown in the vertical direction in fig. 1) does not change the antisite distribution and the degree of order but amounts to diffusion of A or B atoms via the majority sublattice [6]. Exchange with a B atom on β creates an antisite (indicated by the + sign), whereas exchange with an A atom on β removes an antisite (- sign). A vacancy on a β site is surrounded only by 12 α sites as nearest neighbours. It

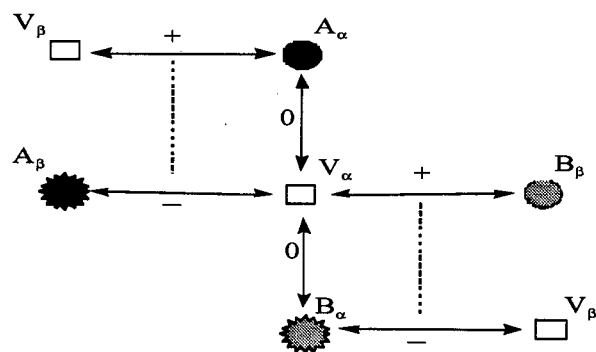
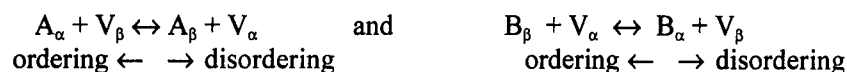


Figure 1. Schematic plot of possible atomic jumps between α - and β -sublattice being either connected with the creation and annihilation of antisite atoms (horizontal jumps) or not (vertical jumps).

can move only by the creation or destruction of antisites (horizontal jumps). There can be no diffusion by nearest neighbour jumps within the β sublattice.

Changes of the degree of order proceed therefore by the following reactions:



An ideal statistical description of an ordering alloy would be an ensemble of systems with occupation numbers for each lattice site specified for each system. In order to be able to calculate anything clearly some approximation must be made. One method would be to do a number of numerical experiments on a particular system with reduced size, that is, a Monte Carlo (MC) simulation [7,8]. You could also keep track of the development of cluster occupation probabilities by the Path Probability Method (PPM, [9]). The most simple way would be to average over the sites within a sublattice and to subject them to averaged surroundings. Within this (mean-field) approximation the occupancy of the A atoms on β sites changes according to a master equation:

$$\frac{d}{dt}(p_{A\beta}) = 12p_{V\beta}p_{A\alpha}v_1 - 12p_{V\alpha}p_{A\beta}v_2 \quad (1)$$

with $p_{A\beta}$ the probability of finding an A atom on a β site, $p_{V\alpha}$ the probability of finding a vacancy on an α site etc. The jump rates can be taken as $v_i = v_0 \exp(-\Delta G_i / kT)$, ΔG_1 being in this case the Gibbs free energy barrier for an exchange of an A atom on α with a vacancy on β , ΔG_2 the barrier for the reverse jump [10]. Although in this approximation you do not get information about the probability of pairs or higher clusters of any structure

element and cannot describe inhomogeneities at a larger scale it reflects the fundamental ingredients of any kinetics: The concentration of reaction partners and the probability of the single reaction. In equilibrium the forward and reverse reaction must balance out to zero and all concentrations must correspond to those resulting from equilibrium statistical mechanics.

Whatever kinetic description we choose, we need to know defect (mainly vacancy) formation energies and the energy profiles of migration paths where we are interested not only in single jumps but also in correlated jump sequences which have been proposed repeatedly for diffusion in ordered alloys [11]. Since we cannot derive these details of the jump processes unequivocally by analysis of the experimental data which are even controversial we decided to do a quantum-mechanical *ab-initio* calculation.

CALCULATION OF DEFECT FORMATION AND MIGRATION ENERGIES

The Vienna *ab-initio* simulation package (VASP) [12] based on ultrasoft pseudopotentials was used after carefully checking its reliability against an all-electron method (FLAPW [13,14]).

Generalised gradient approximation (GGA) is the best choice for exchange and correlation, since ground state properties of Ni_3Al are then in excellent agreement to experimental data (e.g. lattice constant $a^{\text{exp}} = 3.572 \text{ \AA}$, $a^{\text{GGA}} = 3.576 \text{ \AA}$; bulk modulus $B_0^{\text{exp}} = 1.75 \text{ Mbar}$ and $B_0^{\text{GGA}} = 1.77 \text{ Mbar}$). More details can be found in a forthcoming publication.

Point defects and their migration are modelled with supercells of 32 atoms for which calculation of structural relaxation and total energies are tractable by *ab-initio* methods. Ionic relaxations around a point defect are derived by force minimisation; embedding the defect in an ordered lattice corresponds to constant unit cell volume and cell shape which is taken from the calculated equilibrium of pure Ni_3Al ordered lattice.

Assuming the defects to be sufficiently dilute and therefore non-interacting and taking a grandcanonical ensemble within a mean field approach [15-17] point defect formation energies and defect concentrations including configurational entropy are calculated for an off-stoichiometric cell which closer resembles the actual specimens of $\text{Ni}_{76}\text{Al}_{24}$. Small changes in concentration are realised by constitutional defects, in our case antisites for Ni-rich and Al-rich compounds. Adding thermal defects for $T > 0\text{K}$ defect concentrations are gained by full point defect thermodynamic treatment. This way, defect energies and defect concentrations are obtained as a function of temperature and composition.

For a comparison with experiment realistic simulation of kinetic processes involves knowledge of migration barriers, a quantity which is difficult to determine experimentally. We studied two different migration processes for the L1_2 structure:

a) direct jumps:

an atom neighbouring a vacancy just jumps to the vacant site of the other sublattice leaving behind a vacancy now on its own sublattice;

b) a sequence of jumps:

within a six-jump cycle different atom-vacancy exchange processes occur in order to move an atom (e.g. Ni) from its original place to a nearest neighbour position of its own sublattice, combined with a similar movement of the neighbouring (e.g. Al) vacancy.

Figure 2 illustrates in row 1 and 2 two possible 6-jump cycle mechanisms for an original Ni-vacancy within the (001) plane (Ni-1) and leaving the (001) plane (Ni-2), the rows 3 and 4 show the corresponding processes for Al-vacancies. The vacancy position is denoted by a hexagon. In-plane movement: Al-1, Ni-1; out-of-plane movement: Al-2, Ni-2.

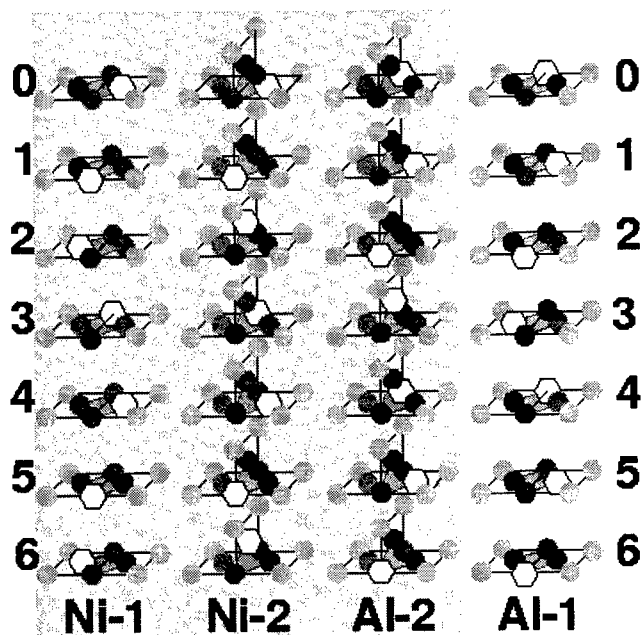


Figure 2. 6 jump cycle mechanisms for an original Ni-vacancy within the (001) plane (Ni-1) and leaving the (001) plane (Ni-2); the right side shows the corresponding processes for Al-vacancies. Vacancy position denoted with a hexagon. In-plane movement: Al-1, Ni-1; out-of-plane movement: Al-2, Ni-2.

Figures 3 and 4 show the corresponding paths for the Al-atom moving to a Ni-vacancy and Ni moving to an Al-vacancy, respectively. The calculated values were obtained when all positions of atoms surrounding the moving Al were relaxed by minimising the atomic forces derived from the *ab-initio* machinery. We first want to concentrate on the jumps to nearest neighbours only (process of type a, jumps 0→1, back jumps 5→6). For jumps of the Al-atom the strong asymmetry is rather striking, illustrating that Al does not like to have other Al atoms as its nearest neighbours. The rather large size of the Al-atom would be a very plausible argument. However, within an *ab-*

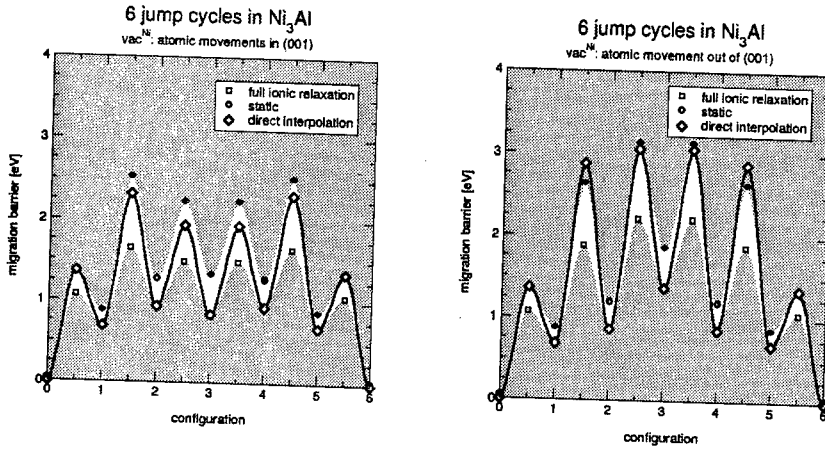


Figure 3. Calculated migration energies for Al-vacancies during six-jump-cycles in Ni_3Al . Direct jump: 0-1, six-jump-cycle: 0-6. Left: in (001) plane. Right: out of (001) plane.

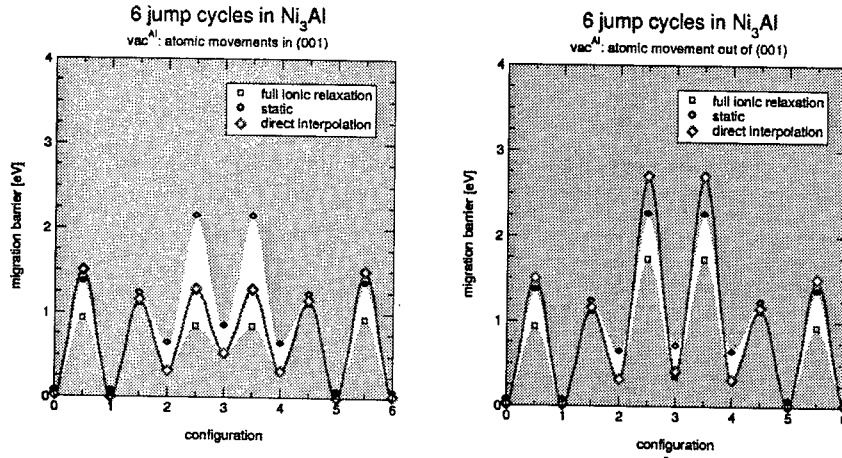


Figure 4. Calculated migration energies for Ni-vacancies during six-jump-cycles in Ni_3Al . Direct jump: 0-1, six-jump-cycle: 0-6. Left: in (001) plane. Right: out of (001) plane.

initio approach there are no model parameters such as atomic size but just quantum mechanical interactions reflecting the extension of wave functions.

The relative minimum at the right side (close to a Ni-site) is not at a lattice site position indicating the repulsion of nearest neighbour Al atoms. This minimum is rather flat leaving a barrier of only 0.3 eV for the jump back to the Al sublattice compared to 1eV for the forward jump.

Migration of a Ni-atom to an Al-vacancy results in a rather symmetric barrier; Ni sitting then on the wrong sublattice is even slightly more stable compared to its original position. Again referring to a simple size argument Ni is small enough to be accommodated on any sublattice rather independent of its neighbours. Both barrier heights (forward and backward jump) amount to 0.9 eV when atoms are relaxed during Ni movement. If no relaxation is allowed (static case) barriers increase to 1.5 eV.

NUMERICAL RESULTS

The results for defect formation energies for vacancies on the Ni and Al sublattices and for both types of antisites are presented in Table I. The values are derived for stoichiometric Ni_3Al and $\text{Ni}_{76}\text{Al}_{24}$ at $T=1000$ K.

The most striking result is, that the formation energy of Al-vacancies is very high. Furthermore, both types of vacancy formation energies are considerably larger than the corresponding energies required to create antisite defects. The more appropriate GGA-calculation shows that for formation energies of defects a reduction of 0.1 to 0.5 eV is observed compared the older LDA results [16].

Another important contribution to the defect formation energies arises from relaxation of ionic positions in the vicinity of the defects. The change of ionic positions due to relaxation is small. Largest relaxation is found for Al atoms on Ni sites, with 5.8% outward relaxation of the Al nearest neighbours and a 1.7% inward relaxation of the Ni nearest neighbours. Around the Ni vacancy an inward relaxation occurs amounting to -3.4% and -0.8% for the Al and Ni nearest neighbour shells, respectively.

Table I. Defect formation energies E_f for Ni_3Al and $\text{Ni}_{76}\text{Al}_{24}$ at 1000 K. Ionic positions: frozen and relaxed. Values as derived from GGA calculations

1000 K	E_f [eV]	V_{Ni}	V_{Al}	Al_{Ni}	Ni_{Al}
Ni_3Al	frozen	1.38	2.35	1.01	1.01
	relaxed	1.50	2.01	0.51	0.51
$\text{Ni}_{76}\text{Al}_{24}$	frozen	1.54	1.88	1.63	0.40
	relaxed	1.54	1.91	0.63	0.39

Astonishingly, the relaxed values for vacancy formation energy in the stoichiometric case turns out to be considerably increased. However, the calculation of vacancy formation energies is coupled to those of antisite defects by occupation of the same sublattice. In our case the strongest relaxation effects were found for Al_{Ni} leading even to an increase of the

formation energy of V_{Ni} compared to its unrelaxed value for the stoichiometric case.

The assumption that cell shape relaxations are not relevant due to embedding in an ordered system was checked for the actual supercell size (32 atoms). Cell shape relaxations were calculated: The Ni antisite and both vacancy supercells show a slight decrease in volume by 1%. The supercell containing the Al antisite expands by 0.5% and is tetragonally distorted ($c/a < 1.01$).

The migration energies for the different jump processes are shown in Table II for the frozen (unrelaxed) and the relaxed state.

Table II. Migration energies E_m for Ni_3Al . Ionic positions: frozen and relaxed. Values as derived from GGA calculations

jump process	E_m [eV]	
	frozen	relaxed
$Ni \rightarrow V_{Al}$	1.50	0.90
$Al \rightarrow V_{Ni}$	1.35	1.00
$Ni \rightarrow V_{Ni}$	1.80	1.00
$Ni \rightarrow^1 V_{Ni}$	2.50	1.65
$Ni \rightarrow^2 V_{Ni}$	3.70	2.20
$Al \rightarrow^1 V_{Al}$	2.15	1.10
$Al \rightarrow^2 V_{Al}$	2.70	1.70

A process also shown here is the jump of a Ni atom to a nearest neighbour Ni-vacancy leading to a symmetric barrier of height 1.0 eV (relaxed) and 1.8 eV (not relaxed). However, this type of migration has no influence on residual resistivity because there is no change of order connected with this process.

Processes of type b) refer to the six-jump model as described in detail by Debiaggi et al. [11]. For original Al-vacancies the mechanism is similar (Al-1 in-plane and Al-2 out-of-plane movements). For the jumps 6, 5, 4 the migration energy curves are symmetric with respect to jumps 1, 2, 3. Each cycle starts and ends with a jump of Al (or Ni) to a nearest neighbour Ni-vacancy (or Al-vacancy). Between the lattice site configurations only half-way positions of the moving atom were calculated.

A range of migration energies is given for static calculations (upper boundary of white area) and fully relaxed calculations (lower boundary of white area). In that case, after the moving atom is in half position all atomic positions are relaxed which in some cases lowers the barrier substantially (e.g. Al-1 jumps 2, 3, 4). The line in the white areas is the result for semi-relaxed calculations: for the migrating atom at lattice sites the atomic geometry is fully relaxed, at half-way positions the ionic relaxation is derived by linear interpolation of the previously relaxed configurations.

For three of the six-jump cases (Ni-1, Ni-2, Al-2) rather high barriers occur (even for semi- and fully-relaxed calculations) compared to the Al-1 case. We therefore conclude, if any six-jump mechanism is realistic it can only be the in-plane mechanism starting with an Al-vacancy as illustrated in the right panel of figure 2 (white background).

DISCUSSION

Various kinds of atom jumps with different activation energies work together in changing the distribution of atoms in an ordered alloy. It is important to understand how the single-event parameters calculated by *ab-initio* methods show up in the LRO measurements, e.g. electrical resistivity. Making the plausible assumption that resistivity values are proportional to the number of antisites of either kind we may as a first approximation start from the simple master equation ansatz (eq. 1), in this case describing the development of β antisite density. The probability of finding a β vacancy in the first term on the right-hand side of eq. (1) follows from thermodynamics as

$$p_{V\beta} = e^{-\frac{E_{f\beta}}{kT}} \quad (2)$$

with $E_{f\beta}$ being the energy of formation of a β vacancy. The rate v_1 is associated with the energy of exchange $\Delta E_{V\beta, A\alpha}$ of a β vacancy with an adjacent A atom on the α sublattice:

$$v_1 = v_{eff} e^{-\frac{\Delta E_{V\beta, A\alpha}}{kT}} \quad (3)$$

Here we have taken entropy effects into the pre-factor and neglected the associated volume change. Analogous considerations apply to the second term in eq. (1) representing the back jumps. We further note that due to atom conservation in a stoichiometric alloy (neglecting the number of vacancies which is assumed to be small)

$$p_{A\alpha} + \frac{1}{3}p_{A\beta} = 1 \quad (4)$$

In equilibrium the net flow is zero. Taking a small departure from the equilibrium number of antisites as an initial value – which corresponds to the situation in small-step annealing – so that

$$p_{A\beta} = p_{A\beta}^{\infty} + \Delta p_{A\beta} \quad (5)$$

and inserting eqns (2-5) into (1) and making use of the equilibrium condition we get

$$\begin{aligned} \frac{d}{dt}(p_{A\beta}) &= -\lambda_{A\beta} \Delta p_{A\beta} \\ \lambda_{A\beta} &= \left[\frac{1}{3} v_{eff} e^{-\frac{(E_{f\beta} + \Delta E_{V\beta, A\alpha})}{kT}} + v'_{eff} e^{-\frac{(E_{f\alpha} + \Delta E_{V\alpha, A\beta})}{kT}} \right] \end{aligned} \quad (6)$$

$\Delta p_{A\beta}$ will thus decay exponentially with a rate that is a linear combination of two Boltzmann factors associated with the jump creating the antisite and the back-jump annihilating the antisite. The development of the number of the other type of antisites can be described by an analogous set of equations. With the activation barriers and vacancy formation energies from the *ab-initio* calculation we get the following pairs of effective activation energies (appearing in the exponent of eq. (6) and its corresponding counterpart: $E_i = (2.96 \text{ eV}, 2.55 \text{ eV})$ for $\lambda_{A\beta}$ and $E_i = (2.58 \text{ eV}, 2.37 \text{ eV})$ for $\lambda_{B\alpha}$. Since two quite similar energies are paired in each case there is no significant curvature of the Arrhenius plot to be expected. Though in the present model we have not allowed for the change in vacancy density it is obvious that the activation energy is well below the 4.6 eV observed in the experiments.

The high activation energy observed by the present investigators is in correspondence with diffusion experiments where the tracer substitutes the Al atoms [5]. Further, a systematic investigation of quasi-binaries where the ternary component occupies the Al sublattice showed an increase of the ordering activation energy with increasing order-disorder transition temperature hinting at a very high energy for pure Ni_3Al [7]. The simple mean-field model therefore appears to be insufficient to render the true kinetics of this system if the high ordering activation energy should hold.

Correlations of jumps in space and time could play an important role. One correlated jump mechanism can be envisioned as follows: An Al atom on its normal sublattice (β) exchanges with an adjacent α vacancy, creating thus a β vacancy. The concentration of β vacancies normally is much lower than that of α vacancies owing to the higher energy of formation. A Ni atom can immediately jump into the β vacancy, blocking effectively the back jump of the Al atom. As a result of this jump sequence two antisites have been generated.

Such effects have in fact been observed by MC simulations of 'order-order' relaxations in A_3B system with L1_2 superstructure [8]. It turned out that a main contribution to the process kinetics experimentally observed is due to highly correlated pairs of A-atom and B-atom jumps which occur when the majority A-atoms are sufficiently mobile [18]. As obtained from the above *ab-initio* calculations considerably higher migration energies are estimated for these correlated atom jumps, which seem to be necessary for a correspondence between experimental and theoretical results.

We are planning for the near future to do MC simulations with the parameters as obtained from *ab-initio* calculations to get more information on this very interesting problems of atomic jumps during changes in the degree of LRO.

ACKNOWLEDGEMENT

Work supported by Austrian Ministry of Science (Project Nr.49.975), Austrian Science Foundation (Project P12538-CHE). Computing facilities provided by the Center for Computational Materials Science in Vienna.

REFERENCES

1. R. Kozubski and W. Pfeiler, *Kinetics of defect recovery and long-range ordering in Ni₃Al+B .2. Atomic jump processes studied by "order-order" relaxation experiments*. Acta Mater. **44**, 1573 (1996).
2. C. Dimitrov, X. Zhang and O. Dimitrov, *Kinetics of long-range order relaxation in Ni₃Al: The effect of stoichiometry*. Acta Mater. **44**, 1691 (1999).
3. G.F. Hancock, Phys.Stat.Sol. (a) **7**, 535 (1971).
4. K. Hoshino, S.J. Rothman and R.S. Averbach, *Tracer diffusion in pure and boron-doped Ni₃Al*. Acta Metall. **36**, 1271 (1988).
5. Y. Minamino, S.B. Jung, T. Yamane and K. Hirao, *Diffusion of cobalt, chromium, and titanium in Ni₃Al*. Metall. Trans. **23A**, 2783 (1992).
6. H. Numakura, T. Ikeda, M. Koiwa and A. Alamazouzi, *Self-diffusion mechanism in Ni-based L1(2) type intermetallic compounds*. Phil. Mag. **77**, 887 (1998).
7. Kozubski, R., *Long-range order kinetics in Ni₃Al-based intermetallic compounds with L1(2)-type superstructure*. Progress Mater. Sci. **41**, 1 (1997).
8. P. Oramus, R. Kozubski, M.C. Cadeville, V. Pierron-Bohnes and W. Pfeiler, *Computer simulation of 'order-order' kinetics in L1(2) superstructure*. Mat. Sci. Eng. **A239-240**, 777 (1997).
9. Mohri, in: Solid-Solid Phase Transformations, W.C. Johnson, J.M. Howe, D.E. Laughlin and W.A. Soffa, eds., The Minerals, Metals & Materials Society, Warrendale (1994), p. 53.
10. G.H. Vineyard, J. Phys. Chem. Solids **3**, 121 (1957).
11. S.B. Debiaggi, P.M. Decorte, and A.M. Monti, *Diffusion by vacancy mechanism in Ni, Al, and Ni₃Al: Calculation based on many-body potentials*. Phys.Stat.Sol. (B) **195**, 37 (1996).
12. G. Kresse and J. Furthmüller, *Efficient iterative schemes for ab initio total-energy calculations using a plane-wave basis set*. Phys. Rev **B 54**, 11196 (1996), and *Efficiency of ab-initio total energy calculations for metals and semiconductors using a plane-wave basis set*. Comput. Mat. Science **6**, 15 (1996).
13. H.J.F. Jansen and A.J. Freeman, *Total-energy full-potential linearized augmented-plane-wave method for bulk solids - electronic and structural-properties of tungsten*. Phys. Rev. **B 30**, 561 (1984).
14. E. Wimmer, H. Krakauer, M. Weinert and A.J. Freeman, *Full-potential self-consistent linearized-augmented-plane-wave method for calculating the electronic-structure of molecules and surfaces - O₂ molecule*. Phys. Rev. **B24**, 864 (1981).
15. S.M. Foiles and M.S. Daw, *Calculation of the defect properties of Ni₃Al using the embedded atom method*. J. Mat. Res. **2**, 5 (1987).
16. C.L. Fu and G.S. Painter, *Point defects and the binding energies of boron near defect sites in Ni₃Al: A first-principles investigation*. Acta Mater. **45**, 481 (1997).
17. J. Mayer, B. Meyer, J.S. Oehrens, G. Bester, N. Börnsen and M. Fähnle, *Effective formation energies of atomic defects in DO₃-Fe₃Al: an ab-initio study*. Intermetallics **5**, 597 (1997).
18. P. Oramus, R. Kozubski, M.C. Cadeville, V. Pierron-Bohnes and W. Pfeiler, in: Y. Mishin, N.E.B. Cowern, C.R.A. Catlow, D. Farkas, G. Vogl eds. *Diffusion Mechanisms in Crystalline Materials*, Mat. Res. Soc. Symp. Proc. **527**, 185 (1998).

TESTS OF THE POLYMORPHOUS COHERENT POTENTIAL APPROXIMATION

J. S. Faulkner,¹ B. Ujfalussy,² Nassrin Moghadam,²
G. M. Stocks,² and Yang Wang³

¹*Alloy Research Center and Dept. of Physics, Florida Atlantic University, Boca Raton, FL 33431*

²*Metals and Ceramics Div., Oak Ridge National Laboratory, Oak Ridge, TN 37831*

³*Pittsburgh Supercomputer Center, Pittsburgh, PA 15213*

ABSTRACT

The coherent potential approximation (CPA) is a powerful mathematical technique for approximating the electronic structure of substitutional solid solution alloys. Most applications of the CPA to date have assumed an isomorphous model of the alloy in which all of the A atoms are assumed to be the same, as are all of the B atoms. The derivation of self-consistent potentials for the alloys within the framework of the CPA and the isomorphous model leads inevitably to the conclusion that the Madelung potential at each site must be zero. The approximate theory resulting from this derivation is called the KKR-CPA. The polymorphous CPA (PCPA) makes use of supercells that contain many atoms, and the Madelung potentials at all of the sites are calculated exactly. PCPA calculations produce a polymorphous alloy model in which every atom in the supercell is different. Tests will be shown that demonstrate the advantages of the PCPA over the KKR-CPA in explaining experiments that depend critically on the charge transfer in an alloy.

Key words: alloy theory, coherent potential approximation, electronic states

INTRODUCTION

The belief that the coherent potential approximation (CPA) gives the most accurate picture of the electronic states in substitutional alloys that is produced by any analytical model is based on numerical tests with simple one-dimensional and three-dimensional models and on the agreement with experiment of calculated properties.¹ The ideal substitutional alloy is one in which A and B atoms are placed randomly on the sites of a Bravais lattice. The theoretical treatments² of the CPA and the model calculations assumed an

isomorphous model of the alloy in which the A atoms all have the same one-electron potential $v_A(\mathbf{r})$, and the B atoms all have the potential $v_B(\mathbf{r})$.

When the theory was extended to include charge self-consistency within the framework of the density functional theory and the local density approximation (DFT-LDA),³ difficulties were encountered. Because all of the work with the CPA made use of an isomorphous model, it was assumed that the self-consistent theory should have that feature. The resulting formalism leads to the result that all of the A atoms have the same electronic charge density $\rho_A(\mathbf{r})$, and the B atoms have $\rho_B(\mathbf{r})$. It predicts a net charge on the A and B atoms,

$$\begin{aligned} q_A &= \int_{\Omega} \rho_A(\mathbf{r}) d\mathbf{r} - Z_A \\ q_B &= \int_{\Omega} \rho_B(\mathbf{r}) d\mathbf{r} - Z_B \end{aligned} \quad (1)$$

where the integral is over the volume of the unit cell Ω and Z is the atomic number. The fact that the atoms are charged means that there must be a Madelung contribution to the one electron potentials $v_A(\mathbf{r})$ and $v_B(\mathbf{r})$. The derivation of the self-consistent potentials within the framework of the CPA and with the restriction that the model must be isomorphous leads inevitably to the conclusion that the Madelung potentials at all of the sites in the alloy must be zero. In addition to the arguments in the original papers,⁴ this result can be deduced from the fact that the only way to have the same potential on all of the A sites and all of the B sites is for the Madelung potential to be assumed to have the value zero. The resulting self-consistent theory is called the Korringa-Kohn-Rostoker CPA (KKR-CPA).

The environment for developing theories for disordered alloys changed dramatically with the advent of order-N DFT-LDA methods and the availability of massively parallel supercomputers. The amount of computer time required for conventional DFT-LDA calculations scales as the cube of the number of atoms in the sample, N^3 , but innovations in computational methods have lead to programs that scale linearly with N . Calculations have been carried out on models of alloys with supercells containing as many as a thousand atoms using an order-N method called the locally self-consistent multiple scattering method (LSMS).^{5,6} Surface effects are eliminated by periodically reproducing the supercells to fill all space. The charges on the Cu atoms in a model of a 50% CuZn disordered alloy calculated with a 1024 atom supercell are shown in Fig. 1.⁷ These charges are positive because Cu atoms take on charge in a CuZn alloy, and the unit of charge is the charge on an electron, which is negative. The full width at half maximum of the distribution is approximately the same as the mean net charge, 0.09978 electron charges. The distribution of charges on the Zn atoms is similar.

It should be emphasised at this point that these LSMS calculations can be considered as essentially exact DFT-LDA calculations on this model, with no built in bias toward any particular charge distribution $\rho(\mathbf{r})$. The atoms in the CuZn model described here are placed on the sites of an ideal bcc Bravais

lattice. There is no reason to expect that there would be significant displacements from the ideal sites due to atomic size effects because the atomic numbers of the atoms differ by one, and experiments have confirmed this expectation.⁸ The muffin-tin approximation is used in the calculations, but there is ample evidence in the literature⁹ that this approximation will not introduce errors for Cu and Zn in this structure. The primary advantage to this approach is that the multiple scattering equations are exact for muffin-tin potentials, and questions of convergence that arise when full potentials are used can be avoided. This is not true if, e. g., the atomic sphere approximation is used. The net charge on the atom at site i centred at the position \mathbf{R}_i is defined to be

$$q_i = \int_{\Omega} \rho_i(\mathbf{r}) d\mathbf{r} - Z_i, \quad (2)$$

where Z_i is Z_A if there is an A atom on the site or Z_B otherwise. In these integrals, the unit cell volumes Ω are the standard Wigner-Seitz cells for the bcc Bravais lattice, all of which have the same size. The charge distribution $\rho_i(\mathbf{r})$ is just the portion $\rho(\mathbf{r})$ of that falls within the i^{th} Wigner-Seitz cell. The values of q_i could be altered arbitrarily, and indeed they could all be made zero, by dividing space in other ways.¹⁰ We choose not to get into such manipulations because they cannot change the underlying physics. The q_i defined in Eq. (2) are the ones that most people have in mind when they consider atomic charges. The Madelung potentials that these q_i lead to are actually used in the self-consistent DFT-LDA calculations and have physical significance. If they are mapped away by some transformation, some other equally complicated expressions will have to be introduced into the calculation to take their place.

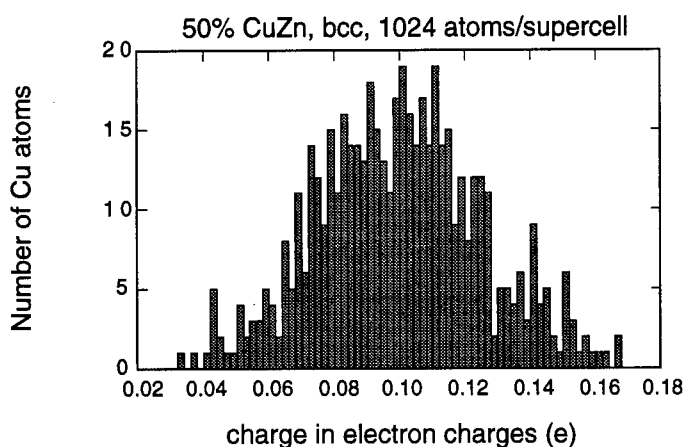


Figure 1. The charges on the Cu atoms in a model of a 50% CuZn disordered alloy calculated with the LSMS using a 1024 atom supercell. The unit of charge is the charge on an electron, which is negative.

The first-principles LSMS calculations lead to a polymorphous model of the alloy in which every atom has a different charge distribution $\rho_i(\mathbf{r})$. The simplest measure of this is the distribution of the q_i shown in Fig. 1. The underlying reason that real alloys are described by the polymorphous model is that the contributions to the Madelung potentials are infinitely long-range in a disordered alloy, just as they are in an ordered intermetallic compound. This can best be seen from the following computational study.

Since all of the net charges are available from a LSMS calculation, it is easy to calculate the contributions to the Madelung potential at site i from all the atoms on nearest-neighbour shells within any distance r_n of the site

$$V^i(r_n) = \sum_{|\mathbf{R}_j - \mathbf{R}_i| \leq r_n} \frac{2q_j}{|\mathbf{R}_j - \mathbf{R}_i|}, \quad (3)$$

where the 2 comes from the use of dimensionless charges and distances. The results of this calculation using charges from the 50% CuZn alloy with 1024 atoms in the supercell is shown in Fig. 2.⁷ The particular site chosen is number 513, which happens to have a Cu atom on it. The dotted line in that figure shows the Madelung potential at site 513 resulting from an Ewald calculation which sums over the infinity of atoms in the periodically reproduced supercells, $V^{513}(\infty)$. The values of the potential $V^{513}(r_n)$ shown include contributions from the first 51 nearest-neighbour shells with values of r_n that stretch out over 7 times the radius of the first nearest-neighbour shell. There is no sign of convergence within this range. This is a simple demonstration of the fact that the only way that the Madelung potential at a site can be calculated correctly is to include the infinity of sites in the model.

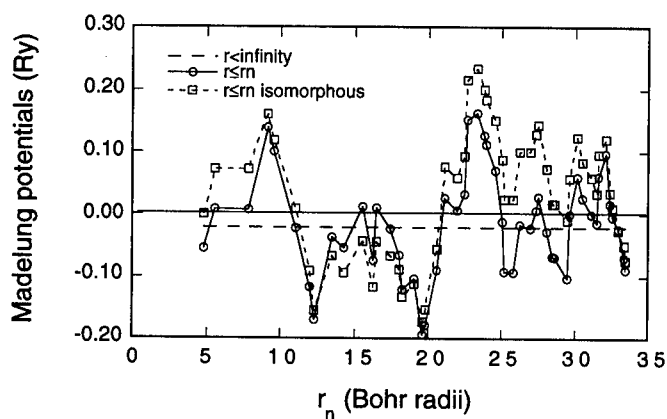


Figure 2. The squares connected by the solid line show the Madelung potentials $V^i(r_n)$ due to the charges from the nearest-neighbor shells within the radius r_n using charges from a 50% CuZn alloy calculated with the LSMS with a 1024 atom supercell. The particular site chosen is number 513, which has a Cu atom on it. The dotted line shows the Madelung potential at site 513 resulting from an Ewald calculation which sums over the infinity of atoms in the periodically reproduced supercells, $V^{513}(\infty)$. The circles connected with a dotted line show the potentials $V_{iso}^i(r_n)$ calculated with average charges on every site.

Efforts to develop an isomorphous model of an alloy with non-zero values of the Madelung potential led to two very similar methods, the screened impurity model CPA (SIM-CPA)¹¹ and the screened CPA (S-CPA).¹² They assume that the charge on an atom in the alloy is screened completely by a shell of charge located at a specific radius r_{eff} . Using calculations on single impurities in an otherwise perfect crystal as a guide,¹³ the effective radius is usually chosen to be equal to the radius of the first nearest-neighbour shell, r_1 . It can be seen from Fig. 2 that the contributions to the Madelung potential in a disordered alloy are not at all like those in a pure metal. Another approach to calculating Coulomb effects within the isomorphous model is based on the use of spheres of different sizes to force the atomic charges to be zero and hence eliminate the problem.¹⁰ This approach has not been studied as much as the SIM-CPA and the S-CPA, and we choose not to go into that area for the reasons given above.

Because of the preconceived notions described above, the results shown in Fig. 2 have caused some consternation. It is useful to study the reason for the long-range nature of $V'(r_n)$ with the help of a calculation on a hypothetical isomorphous model. Consider the potential $V'_{iso}(r_n)$ that is defined as in Eq. (3) except that the charge q_i takes the value of the average charge $q_{Cu} = 0.09978$ e when there is a Cu atom on site i , or $q_{Zn} = -0.09978$ e when a Zn atom is on that site. The results of this calculation are also shown in Fig. 2. It can be seen that the differences between $V^{513}(r_n)$ and $V'_{iso}(r_n)$ are subtle but significant. Clearly, the reason for the long-range nature of $V'(r_n)$ is that the fluctuations in the distribution of A and B atoms is such that the net charge on a shell is of the order of the average charge on an atom $|q|$. This would lead to a contribution from the n^{th} shell that is of order $\pm|q|/r_n$. Because the number of atoms in a nearest-neighbour shell increases with n , the contributions fall off more slowly than that.

One could imagine a DFT-LDA calculation with a starting charge density given by the isomorphous model. As the calculation is iterated to self-consistency, the partial Madelung potentials would evolve from the $V'_{iso}(r_n)$ to $V'(r_n)$ illustrated in Fig. 2. This would be accompanied by the development of a linear relationship between the q_i and the $V'(\infty)$ as described in ref. 7, which is equivalent to the observation that the DFT-LDA produces a Coulomb energy that is described by the quadratic form in the q_i given in Eq. (32) of that reference.

Another result of the subtle differences between $V'_{iso}(r_n)$ and $V'(r_n)$ is seen when they are averaged over all the sites that have a Cu atom on them,

$$V^{Cu}(r_n) = \sum_{i \in Cu} V^i(r_n). \quad (4)$$

The argument is unchanged if they are averaged over all Zn sites. The exact Madelung potentials can also be averaged over the sites

$$V^{Cu}(\infty) = \sum_{i \in Cu} V^i(\infty). \quad (5)$$

It can be seen from Fig. 3 that $V^{Cu}(r_n)$ takes on the value $V^{Cu}(\infty)$ at the second nearest-neighbour shell. Starting with the fourth nearest-neighbour shell, the calculated values for $V^{Cu}(r_n)$ show some scatter about $V^{Cu}(\infty)$, but that can be attributed to the fact that the number of atoms in the supercell, 1024, is still not infinity. It is easy to see either algebraically or computationally that $V_{iso}^{Cu}(r_n)$, defined by

$$V_{iso}^{Cu}(r_n) = \sum_{i \in Cu} V_{iso}^i(r_n), \quad (6)$$

is zero for all values of r_n . This is also illustrated in Fig. 3.

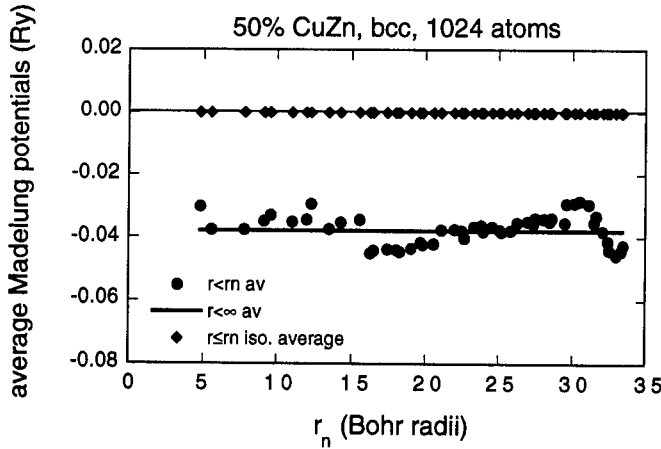


Figure 3. The potentials shown in Fig. 2 averaged over all sites containing Cu atoms. The round dots show the $V^{Cu}(r_n)$ from Eq. (4). The solid line shows $V^{Cu}(\infty)$. The diamond shaped dots show the averages $V_{iso}^{Cu}(r_n)$.

It might appear that the computational results in Fig. 3 provide support for the SIM-CPA and S-CPA approximations, even though they show that r_l would not be a good choice for the effective radius r_{eff} . From a mathematical point of view, this is not the case because one has to mix models in order to make the argument. The isomorphous averages $V_{iso}^{Cu}(r_n)$ are zero, as was anticipated in the derivations of the KKR-CPA. It does hold out the hope that the SIM-CPA and S-CPA could be made more compatible with the realistic picture of the Coulomb energy described in ref. 7, but the arguments given in the original papers will have to be revised. In their present form, there are serious problems with the SIM-CPA and S-CPA. It has been shown that the form for the total Coulomb energy that arises naturally from the model cannot be used. The expression must be multiplied by an adjustable parameter β that cannot be obtained from within the theory.¹⁴ The parameter β multiplies the Coulomb energy, but it does not occur in the one-electron potential. This violates one of the basic tenets of the DFT-LDA. The explanation for these difficulties that comes from the present discussion is that in a rigorously

derived isomorphous CPA the Madelung shifts should be zero, and the effort to introduce non-zero shifts will lead to difficulties.

The LSMS method is based on the multiple scattering equations of Rayleigh¹⁵ that are also the basis for the Korringa-Kohn-Rostoker band theory method.¹⁶ It follows that the method is well-adapted to treat transition metals. When solving the multiple-scattering problem, the interaction of an atom with all neighbours in a local interaction zone that includes four or more nearest-neighbour shells is treated exactly. The Coulomb interactions with the remaining infinity of atoms are also treated exactly, but the multiple scattering part is approximated by setting the t-matrices on those sites equal to zero. This process is repeated for each of the N atoms in the cell, and the entire process is iterated until self-consistency is attained.

It was suggested that the size of the interaction zone in the LSMS could be reduced considerably by placing an approximate t-matrix on the other sites, rather than the LSMS choice of zero. The resulting formalism is called the locally self-consistent Green's function (LSGF) method.^{17,18} It was argued that one good choice for the approximate t-matrix would be the one obtained by applying the CPA condition to the atoms at the centres of the local interaction zones. The Coulomb interactions between all of the atoms are treated exactly in the LSGF, as they are in the LSMS. In the applications of the LSGF to date, the multiple-scattering equations are approximated by using a tight-binding linear muffin-tin orbital basis and the atomic sphere approximation.

It might be said that the LSMS and LSGF are order- N in the calculation of wave functions, but the Madelung potentials are not order- N . This does not matter because techniques for calculating Madelung potentials for periodically reproduced supercells using the method due to Ewald¹⁹ are well developed and require very little computer time. The LSGF gives results that are qualitatively the same as the LSMS. In particular, it predicts a polymorphous picture for a substitutional alloy.

The facts outlined above provide a compelling argument for the position that the only proper way to include Coulomb effects in a CPA formalism is to construct a polymorphous CPA (PCPA) which takes into account the uniqueness of all the atoms from the start. Supercells must be used in the implementation of the PCPA because the Madelung potentials will be calculated exactly using the Ewald method, just as they are in the LSMS and LSGF. In fact, such a theory has already been tested because it is just a special case of the LSGF in which the LIZ is chosen to contain just one atom and the approximate t-matrix placed on all the other sites is the CPA t-matrix. Calculations have been successfully carried out with this version of the LSGF,¹⁴ although the method referred to as the CPA in that reference is the SIM-CPA.

Isomorphous CPA's have been quite successful in interpreting the properties of alloys, and formulas have been derived for calculating the useful quantities within that formalism. It is reasonable to be concerned that all of this progress will be lost if the isomorphous model is deserted. In the following section, formulas will be derived for site-diagonal average Green's

functions and non-site-diagonal average Green's functions within the PCPA. It will be shown that they are simply related to the formulas that were derived earlier for the KKR-CPA.²⁰ In Section III, the utility of the method will be demonstrated with calculations. The results will be discussed in the final section.

CALCULATING PROPERTIES WITH THE PCPA

The formulas that are used to calculate properties in the multiple-scattering versions of the CPA were derived in ref. 20, which will be referred to as FS in the following. The exact Green's function for a substitutional alloy is written in FS as

$$G(E, \mathbf{r}, \mathbf{r}') = \sum_{L, L'} Z_L^n(E, \mathbf{r}_n) \tau_{LL'}^{nm} Z_{L'}^n(E, \mathbf{r}_n') - \sum_L Z_L^n(E, \mathbf{r}_n) J_L^n(E, \mathbf{r}_n'). \quad (7)$$

This form of the Green's function is valid when \mathbf{r} and \mathbf{r}' are inside the n^{th} muffin-tin sphere or in the interstitial region between the muffin-tin spheres, where the potential is zero. As a practical matter, it can be considered the Green's function for \mathbf{r} and \mathbf{r}' inside the n^{th} Wigner-Seitz cell. The same Green's function can be written in a different way when \mathbf{r} is in the n^{th} muffin-tin sphere and \mathbf{r}' is in the m^{th} sphere, or they are in the interstitial region. For this case, the Green's function is

$$G(E, \mathbf{r}, \mathbf{r}') = \sum_{L, L'} Z_L^n(E, \mathbf{r}_n) \tau_{LL'}^{nm} Z_{L'}^m(E, \mathbf{r}_m'). \quad (8)$$

In these equations, $Z_L^n(E, \mathbf{r})$ is the solution of

$$[-\nabla^2 + v_n(\mathbf{r}) - E] Z_L^n(\mathbf{r}) = 0, \quad (9)$$

that is regular at the origin and equals

$$Z_L^n(E, \mathbf{r}) = Y_L(\mathbf{r}) j_L(\kappa r) m_L^n(E) - i \kappa Y_L(\mathbf{r}) h_L(\kappa r), \quad (10)$$

when r is greater than the radius of the n^{th} muffin-tin sphere. It is assumed in Eq. (7) that $|\mathbf{r}_n'| \geq |\mathbf{r}_n|$. The matrix $\mathbf{m}^n(E)$ is the inverse of the t -matrix \mathbf{t}^n that describes the scattering from the potential $v_n(\mathbf{r})$. Since \mathbf{t}^n is diagonal for muffin-tin potentials, its inverse is as well, and m_L^n is a diagonal element of that matrix. The functions $j_L(\kappa r)$ and $h_L(\kappa r)$ are Bessel functions, and κ is the square root of the energy. Following FS, the spherical harmonics $Y_L(\mathbf{r})$ are chosen to be real. The function $J_L^n(E, \mathbf{r})$ is the solution of Eq. (9) that is not regular at the origin and approaches $Y_L(\mathbf{r}) j_L(\kappa r)$ when r is greater than the radius of the n^{th} muffin-tin sphere. The coefficients $\tau_{LL'}^{nm}$ are elements of the scattering-path matrix defined below. The Green's is not periodic, $G(E, \mathbf{r}, \mathbf{r}') \neq G(E, \mathbf{r} + \mathbf{R}_n, \mathbf{r}' + \mathbf{R}_n)$ since the alloy is not.

The elements of the scattering-path matrix, $\tau_{LL'}^{nm}(E)$, are most easily obtained by taking the inverse of the matrix

$$M_{LL'}^{nm} = m_l^n \delta_{LL'} \delta_{nm} - g_{LL'}^{nm} \quad (11)$$

That is to say,

$$\tau_{LL'}^{nm} = [M^{-1}]_{LL'}^{nm} \quad (12)$$

The functions $g_{LL'}^{nm}$ are components of the free-electron Green's functions that describe propagation from lattice sites \mathbf{R}_n to \mathbf{R}_m , and are zero when $n=m$. The elements of the inverse of the t-matrix on site \mathbf{R}_n , m_l^n , were defined above.

It was shown in FS that all of the quantities that the CPA is capable of predicting must be obtained from a site-diagonal average Green's function starting from Eq. (7) or a non-site-diagonal average Green's function starting from Eq. (8). The reasons for focusing on the averaged Green's functions are given there.

A major difference between the isomorphous CPA and the PCPA is the nature of the averaging process used. It was natural in FS to use an ensemble-averaging process, the ensemble being the set of $(N_A+N_B)!/N_A!N_B!$ alloys that can be formed by distributing N_A A atoms and N_B B atoms on the lattice sites. In the PCPA, the average is over the sites of one infinitely large sample. The reason is that the only reliable way to calculate the Madelung potential at a site is to include the contributions from the charges on all the other sites. This lesson has been learned from the LSMS, the LSGF, and other order-N techniques. The differences between the various A and B atoms is due to their spatial correlation with all of the other atoms, and information about this spatial correlation is lost in the ensemble-averaging process. The site-averaged Green's function will be periodic.

Using the site-averaging process, the average of the Green's function from Eq. (7) corresponding to the central site ($\mathbf{R}_n=0$) is

$$\begin{aligned} \langle G(E, \mathbf{r}, \mathbf{r}') \rangle &= \frac{1}{N} \sum_{i=1}^N \sum_{L, L'} Z_L^i(E, \mathbf{r}) \tau_{LL'}^{ii} Z_{L'}^i(E, \mathbf{r}') \\ &\quad - \frac{1}{N} \sum_{i=1}^N \sum_L Z_L^i(E, \mathbf{r}) J_L^i(E, \mathbf{r}') \end{aligned} \quad (13)$$

This average is obtained by summing the contributions from the N atoms in the volume V . When adding the contribution from a given atom, the whole lattice is shifted so that the atom appears in the central cell. Another way of describing this process is that, in each term in the sum over i , the origin of the coordinate system is moved to the lattice position \mathbf{R}_i . The limit of this process is reached as N and hence V increase without bound. This is called the site-diagonal average Green's function because the arguments \mathbf{r} and \mathbf{r}' are associated with the same site. It should be clear that the sum is independent of

the site that is chosen to be the central cell, so the averaged Green's function is periodic, $\langle G(E, \mathbf{r}, \mathbf{r}') \rangle = \langle G(E, \mathbf{r} + \mathbf{R}_n, \mathbf{r}' + \mathbf{R}_n) \rangle$.

The first step toward applying the coherent potential approximation to the average Green's function in Eq. (13) is to use the single-site approximation to simplify the scattering-path matrix elements. As was discussed in FS, the single-site approximation to the matrix elements $\tau_{LL'}^{ii}$ is obtained from the inverse of a matrix \mathbf{M}_c^i whose elements are given by

$$\begin{aligned} \mathbf{M}_c^{i,ii} &= \mathbf{m}^i & \text{for } n = i, m = i \\ \mathbf{M}_c^{i,nm} &= \mathbf{m}^c \delta_{nm} - \mathbf{g}^{nm} & \text{for } n \neq i, \text{ or } m \neq i \end{aligned} \quad (14)$$

in a block-matrix notation that eliminates the angular momentum indices. The matrix \mathbf{m}^i is the inverse of the t-matrix that defines scattering from the potential $v_i(\mathbf{r})$, and the matrix \mathbf{m}^c is the inverse of the effective scattering matrix \mathbf{t}_c . Another way to write this scattering-path operator is

$$\tau^{ii} \rightarrow \tau_c^{i,00} = \mathbf{D}^i \tau_c^{00} = \tau_c^{00} \tilde{\mathbf{D}}^i, \quad (15)$$

where

$$\mathbf{D}^i = [\mathbf{I} + \tau_c^{00}(\mathbf{m}^n - \mathbf{m}^c)]^{-1}. \quad (16)$$

The average Green's function in the CPA describes a periodic system with the scattering matrix \mathbf{t}_c on every site. The matrix τ_c^{nm} is the scattering-path matrix for this system, and is obtained from the inverse of the matrix \mathbf{M}_c with elements

$$\mathbf{M}_c^{nm} = \mathbf{m}^c \delta_{nm} - \mathbf{g}^{nm} \quad \text{for all } n \text{ and } m. \quad (17)$$

Since this system is periodic, $\tau_c^{ii} = \tau_c^{jj} = \tau_c^{00}$. It follows that the site-diagonal average Green's function in the single-site approximation is

$$\begin{aligned} G^{SD}(E, \mathbf{r}, \mathbf{r}') &= \frac{1}{N} \sum_{i=1}^N \sum_{L, L'} Z_L^i(E, \mathbf{r}) \tau_{c, LL'}^{i,00} Z_{L'}^i(E, \mathbf{r}') \\ &\quad - \frac{1}{N} \sum_{i=1}^N \sum_L Z_L^i(E, \mathbf{r}) J_L^i(E, \mathbf{r}') \end{aligned} \quad (18)$$

As stated above, Eq. (18) should become identical with the corresponding KKR-CPA equation when it is applied to an isomorphous model. For that case, the functions of position $Z_L^i(E, \mathbf{r})$ and $J_L^i(E, \mathbf{r})$ are all $Z_L^A(E, \mathbf{r})$ and $J_L^A(E, \mathbf{r})$ when there is an A atom on the i^{th} site or $Z_L^B(E, \mathbf{r})$ and $J_L^B(E, \mathbf{r})$ when a B atom is there. This is equivalent to the assumption that the potentials on all the A or B sites are $v_A(\mathbf{r})$ or $v_B(\mathbf{r})$, and hence the t-matrices are \mathbf{t}^A or \mathbf{t}^B . The resulting equation is

$$\begin{aligned}
G_{iso}^{SD}(E, \mathbf{r}, \mathbf{r}') = & \sum_{L, L'} c_A Z_L^A(E, \mathbf{r}) \tau_{LL'}^{A,00} Z_{L'}^A(E, \mathbf{r}') \\
& + \sum_{L, L'} c_B Z_L^B(E, \mathbf{r}) \tau_{LL'}^{B,00} Z_{L'}^B(E, \mathbf{r}') \\
& - \sum_L [c_A Z_L^A(E, \mathbf{r}) J_L^A(E, \mathbf{r}') + c_B Z_L^B(E, \mathbf{r}) J_L^B(E, \mathbf{r}')]
\end{aligned} \quad , \quad (19)$$

which is identical with Eq. (2.33) of FS. The most obvious difference between the Eqs. (18) and (19) is that in the PCPA all the atoms are assumed to be unique, and hence their concentrations are just $1/N$.

To this point, the single-site approximation has been used, but nothing has been said about the definition of the effective scattering matrix τ_c . The relation that defines τ_c in the isomorphous CPA appears in Eq. (5.24) of FS as

$$c_A \tau_c^{A,00} + c_B \tau_c^{B,00} = \tau_c^{00} \quad (20)$$

where $\tau^{A,00}$ is obtained from Eqs. (14) by putting the inverse of the scattering matrix for the potential $v_A(\mathbf{r})$ on the central site and $\tau^{B,00}$ is obtained similarly. This is just the conversion of the original definition of the CPA² into the language of the multiple scattering theory.²¹ The extension of this relation that defines the effective scattering matrix in the PCPA is

$$\frac{1}{N} \sum_{i=1}^N \tau_c^{i,00} = \tau_c^{00}, \quad (21)$$

where the scattering-path matrices are defined in Eq. (15).

The information necessary for calculating self-consistent potentials and total energies in the PCPA is contained in the site-diagonal Green's functions in Eq. (18). As in any other system, the local part of the DFT-LDA potential $v_i(\mathbf{r})$ is calculated from the charge density $\rho_i(\mathbf{r})$. The Madelung contribution is obtained from the net charges q_i in the same way that it is in the LSMS or the LSGF.

The average charge density on a site in the effective crystal is obtained from

$$\langle \rho(\mathbf{r}) \rangle = -\frac{1}{\pi} \text{Im} \int_{-\infty}^{E_F} G^{SD}(E, \mathbf{r}, \mathbf{r}) dE. \quad (22)$$

It may be written

$$\langle \rho(\mathbf{r}) \rangle = \frac{1}{N} \sum_{i=1}^N \rho_i(\mathbf{r}), \quad (23)$$

where

$$\rho_i(\mathbf{r}) = -\frac{1}{\pi} \int_{-\infty}^{E_F} \text{Im} \left[\sum_{L,L'} Z_L^i(E, \mathbf{r}) Z_{L'}^i(E, \mathbf{r}) \tau_{LL'}^{i,00}(E) \right] dE. \quad (24)$$

The term in Eq. (18) that includes the singular solution $J_L^i(E, \mathbf{r})$ normally does not appear in formulae for properties because it is real. The average density of states per site for the alloy can be found from the Green's function by

$$\langle n(E) \rangle = -\frac{1}{\pi} \text{Im} \int_{\Omega} G^{SD}(E, \mathbf{r}, \mathbf{r}) dv, \quad (25)$$

where Ω is the volume of the central unit cell. Clearly, the density of states associated with any site in the effective crystal is the average of that quantity for the individual atoms in V

$$\langle n(E) \rangle = \frac{1}{N} \sum_{i=1}^N n^i(E). \quad (26)$$

where

$$n^i(E) = -\frac{1}{\pi} \text{Im} \left[\sum_{L,L'} \int_{\Omega} Z_L^i(E, \mathbf{r}) Z_{L'}^i(E, \mathbf{r}) d\mathbf{r} \tau_{LL'}^{i,00} \right]. \quad (27)$$

It may seem contradictory to talk about an effective crystal and that is periodic, and at the same time talk about net charges on the sites. A similar apparent contradiction occurs in the isomorphous CPA, because one uses $\rho_A(\mathbf{r})$ and $\rho_B(\mathbf{r})$ to calculate the DFT-LDA potentials in spite of the fact that the effective scatterers on all the sites are the same. Ensuring this does not lead to a real contradiction is the purpose of the CPA condition. The major point of FS is that this is a necessary part of the formalism. A quantity like the total density of states does not require knowledge of the wave functions and can be calculated from the periodic effective crystal with t_c on every site using Lloyd's formula.²² Information about individual sites must be used in the calculation of a property that requires wave functions, such as the potentials, because there is no average wave function in an alloy, only an average Green's function.

In the CPA, the Bloch vector \mathbf{k} is not a good quantum number. In spite of this, the periodicity of the CPA effective crystal has the consequence that \mathbf{k} plays a role in the theory. The number of electronic states with energies between E and $E+dE$ and \mathbf{k} -vector in the element $d\mathbf{k}$ is proportional to the Bloch spectral density function, $A^B(E, \mathbf{k})$. For periodic crystals, $A^B(E, \mathbf{k})$ is a series of δ -functions in E or \mathbf{k} , while in the CPA the peaks are smeared out. The Bloch spectral density function has been used over the years to elucidate

the connection between Fermi surfaces in alloys and their properties. The concentration functional theory of Gyorffy and Stocks²³ has been used to predict alloy structures and the x-ray diffuse scattering intensity map for alloys, which can be compared directly with experiment. The Bloch spectral density is also used to calculate conductivity in alloys.²⁴

The formulae for the Bloch spectral density function derived in FS and displayed in Eqs. (4.8) and (4.9) of that paper are

$$A^B(E, \mathbf{k}) = -(1/\pi) \text{Im} G(E, \mathbf{k}, \mathbf{k}), \quad (28)$$

where

$$G(E, \mathbf{k}, \mathbf{k}) = \sum_n e^{i\mathbf{k} \cdot \mathbf{R}_n} \int_{\Omega} G(E, \mathbf{r}, \mathbf{r} + \mathbf{R}_n) d\mathbf{r}. \quad (29)$$

In Eq. (29), the sum is over all reciprocal lattice vectors, and the integral is over the central unit cell. It should be noted that $G(E, \mathbf{k}, \mathbf{k})$ is not the Fourier Transform of the Green's function, as is used, e. g., in the analysis of positron annihilation experiments.

The Green's function that must be used in $A^B(E, \mathbf{k})$ is obtained from Eq. (8) by means of the site-averaging process

$$\langle G(E, \mathbf{r}, \mathbf{r} + \mathbf{R}_n) \rangle = \frac{1}{N} \sum_{i=1}^N \sum_{L, L'} Z_L^i(\mathbf{r}) \tau_{LL'}^{ij} Z_{L'}^j(\mathbf{r}). \quad (30)$$

The sum is only over site i , because the site j is related to site i by $\mathbf{R}_j = \mathbf{R}_i + \mathbf{R}_n$. This is called the non-site-diagonal average Green's function because the \mathbf{r} and $\mathbf{r} + \mathbf{R}_n$ are in two different Wigner-Seitz cells. As before, the origin of the coordinate system has been shifted to the lattice vector \mathbf{R}_i for each term in the sum over i . The arguments in this equation may be a little confusing. From Eq. (8), the second function may be written $Z_L^j(\mathbf{r} + \mathbf{R}_n - \mathbf{R}_n)$.

It is shown in Eq. (2.43) in FS that the single-site approximation to the scattering-path matrix in this equation is

$$\tau^{ij} = \mathbf{D}^i \tau_c^{ij} \tilde{\mathbf{D}}^j, \quad (31)$$

where τ_c^{ij} is the scattering path matrix for a periodic lattice that has the PCPA scattering matrix \mathbf{t}_c on every site. This matrix is found from the inverse of the matrix \mathbf{M}_c defined in Eq. (17), and depends only on the separation between sites i and j

$$\tau_c^{ij} = \tau_c(\mathbf{R}_{ij}) = [\mathbf{M}_c^{-1}]^{ij}. \quad (32)$$

The matrix D^i is given in Eq. (16). Thus, the non-site-diagonal averaged Green's function is

$$G^{NSD}(E, \mathbf{r}, \mathbf{r} + \mathbf{R}_n) = \frac{1}{N} \sum_{i=1}^N \sum_{L_1, L_2} \sum_{L, L'} Z_{L_1}^i(\mathbf{r}) D_{L_1 L}^i \tau_{c, LL'}^{ij} \tilde{D}_{L' L_2}^j Z_{L_2}^j(\mathbf{r}). \quad (33)$$

Inserting this in Eq. (29) leads to the expression for the averaged Green's function in the k-representation

$$G(E, \mathbf{k}, \mathbf{k}) = \int_{\Omega} G^{SD}(E, \mathbf{r}, \mathbf{r}) d\mathbf{r} + \sum_{\substack{n \\ \mathbf{R}_n \neq 0}} e^{i\mathbf{k} \cdot \mathbf{R}_n} \sum_{LL'} F_{LL'}(\mathbf{R}_n) \tau_{c, LL'}(\mathbf{R}_n), \quad (34)$$

where $G^{SD}(E, \mathbf{r}, \mathbf{r}')$ is defined in Eq. (18). In Eq. (34),

$$F_{LL'}(\mathbf{R}_n) = \frac{1}{N} \sum_{i=1}^N \sum_{L_1, L_2} \int_{\Omega} Z_{L_1}^i(\mathbf{r}) Z_{L_2}^j(\mathbf{r}) d\mathbf{r} D_{L_1 L}^i D_{L_2 L'}^j, \quad (35)$$

which depends on \mathbf{R}_n because $\mathbf{R}_j = \mathbf{R}_i + \mathbf{R}_n$. The integral is less complex than it seems because the matrix $\mathbf{F}(\mathbf{R}_n)$ has weight one in the sense that it is the sum of N integrals, but divided by N .

Specialising to the isomorphous case, for which $Z_L^i(\mathbf{r}) = Z_L^A(\mathbf{r})$ with probability c_A and $Z_L^i(\mathbf{r}) = Z_L^B(\mathbf{r})$ with probability c_B , $F_{LL'}(\mathbf{R}_n)$ becomes

$$\begin{aligned} F_{LL'}^{cc} = & c_A^2 \sum_{L_1, L_2} \int_{\Omega} Z_{L_1}^A(\mathbf{r}) Z_{L_2}^A(\mathbf{r}) d\mathbf{r} D_{L_1 L}^A D_{L_2 L'}^A \\ & + c_A c_B \sum_{L_1, L_2} \int_{\Omega} Z_{L_1}^A(\mathbf{r}) Z_{L_2}^B(\mathbf{r}) d\mathbf{r} D_{L_1 L}^A D_{L_2 L'}^B \\ & + c_B c_A \sum_{L_1, L_2} \int_{\Omega} Z_{L_1}^B(\mathbf{r}) Z_{L_2}^A(\mathbf{r}) d\mathbf{r} D_{L_1 L}^B D_{L_2 L'}^A, \\ & + c_B^2 \sum_{L_1, L_2} \int_{\Omega} Z_{L_1}^B(\mathbf{r}) Z_{L_2}^B(\mathbf{r}) d\mathbf{r} D_{L_1 L}^B D_{L_2 L'}^B, \end{aligned} \quad (36)$$

which does not depend on \mathbf{R}_n . The resulting formula for $G(E, \mathbf{k}, \mathbf{k})$ is identical to Eq. (4.10) of FS, which means that the Bloch spectral densities will be the same.

It is reassuring that the formulas for $F_{LL'}^{cc}$ and $A^B(E, \mathbf{k})$ obtained with the site-averaging process are identical with the ones obtained with the ensemble-averaging process when the former are applied to an isomorphous model. When ensemble averaging is used, the sum in Eq. (33) is over sites i and j independently. Since the function $F_{LL'}^{cc}$ in Eq. (36) does not depend on \mathbf{R}_n , it can be factored out of the sum in Eq. (33). This makes the expression for the Bloch spectral density for the isomorphous case, Eq. (4.15) of FS, considerably easier to deal with computationally.

COMPUTATIONS

It was assumed in the theoretical discussion in the preceding section that the size of the sample and the number of atoms would increase without bound, but, in practical applications of the PCPA, it is necessary to make a supercell approximation as in the LSMS and LSGF. The use of supercells does not interfere with the periodicity of the Green's functions. The calculation of the Madelung potential for all the sites in the supercell takes very little time when the Ewald¹⁹ method is used. Calculations of interesting properties using supercells of various sizes have shown that the supercell approximation is not serious as long as the cells contain some hundreds of atoms. One reason for this is that the Madelung sums are not seriously effected if the actual contents of the adjoining supercells in the large sample are replaced with replicas of the central cell. Another is that the properties of interest in the calculations are self-averaging.

The computer codes used for the PCPA calculations described in this paper are based on the ones that were developed for the implementation of the LSMS method.⁶ The supercell is first generated for the underlying face centered cubic (fcc) or body centered cubic (bcc) Bravais lattice. For bcc alloys, the dimensions of the supercell are normally chosen to be 5X5X5 lattice spacings, and it contains 250 atoms. For fcc alloys, the supercell dimensions are typically 4X4X4, and contain 256 atoms. The next step is to assign atoms to the lattice sites using a random number generator, with the constraint that the alloy model must have the chosen concentration. The computer code can build in short range order as measured by the Warren-Cowley coefficients, but that capability was not used in the present work.

Initial guesses are made for the atomic potentials, and the t -matrices are calculated. Eq. (21) is solved iteratively for the effective scattering matrix t_e , using a generalization of the programs that were originally developed for use in KKR-CPA calculations. The new charge densities for each site are found from Eq. (24), and the potentials $v_i(\mathbf{r})$ are calculated from them and the Madelung sums that have been discussed so much. The whole process is repeated until the total energy and potentials have converged. The advantage in using the muffin-tin approximation were outlined in the discussion of the LSMS given above. Questions of convergence that must be addressed when full-potential methods are used are avoided in the present report, although such methods will be incorporated in later calculations when they are deemed necessary.

All the calculations reported here were performed with the Cray T3E-900 512-processor supercomputer operated by the National Energy Research Scientific Computing Center located at the Lawrence Berkely National Laboratory. It is, of course, always desirable to use the most powerful computing facilities that are available. However, one of the major thrusts of future program development is to simplify the PCPA calculations so that they can be carried out on small workstations or microcomputers.

Table 1. Average charges on the atomic sites measured in electronic charges

alloy	a alloy Bohr radii		LSMS charge e	PCPA charge e	KKR-CPA charge e
50% CuPd	7.1000	Cu	0.17609	0.16084	0.04334
		Pd	-0.17609	-0.16084	-0.04334
80% CuPd	6.9000	Cu	0.07721	0.07453	0.02162
		Pd	-0.31037	-0.29959	-0.08648
50% CuZn	5.5000	Cu	0.10086	0.10143	0.07578
		Zn	-0.10086	-0.10143	-0.07578
50% AgPd	7.6100	Ag	-0.04956	-0.04863	-0.05724
		Pd	0.04956	0.04863	0.05724

LSMS, PCPA, and KKR-CPA calculations of charge transfers in some disordered substitutional alloys are shown in Table I. The LSMS and PCPA calculations for the CuPd alloys use supercells containing 256 atoms based on fcc Bravais lattices, the lattice constant for the 50% alloy being 6.9 atomic units (AU) and for the 80% alloy being 7.1 AU. The disordered 50% CuZn alloy is in the β phase (bcc) with a lattice constant of 5.5 AU. The supercell used with the LSMS calculations contains 432 atoms, while the one for the PCPA calculations contains 256. The 50% AgPd alloy is modeled with a supercell containing 256 atoms and a fcc Bravais lattice with a lattice constant of 7.61 AU in both the LSMS and PCPA calculations. The same lattice constants are used in the KKR-CPA calculations on all these alloy systems, but supercells are not used. The results in Table I demonstrate that the PCPA gives charge transfers that are remarkably close to the ones predicted by the LSMS, which we take to be the exact DFT-LDA answers. The predictions of the KKR-CPA are clearly flawed.

Of course, charge transfers are not experimentally measurable quantities. It is of interest to see if there is a correlation between the ability of a theory to predict charge transfer and a more important property of the alloy, the energy of mixing. The energies of mixing of a series of CuZn alloys were calculated with the LSMS and KKR-CPA, and reported in a previous publication.²⁵ First, a series of total energy calculations were carried out with the LSMS using supercells containing 256 atoms. Calculations were carried out on alloys containing 25%, 50%, 75%, Cu as well as the pure metals for several values of the lattice parameter. The LSMS energies should be taken as the DFT-LDA values because the DFT-LDA is the only approximation in them. From a fit of the energies as a function of the lattice constants, the DFT-LDA prediction for the lattice constants as well as the total energies at the predicted lattice constants was found. KKR-CPA total energy calculations were carried out for the same systems at the DFT-LDA lattice constants. Finally, a PCPA total energy calculation was carried out at the DFT-LDA lattice constant for the 50% CuZn alloy. It was necessary to recalculate the pure Cu and Zn systems with the PCPA codes to make them consistent.

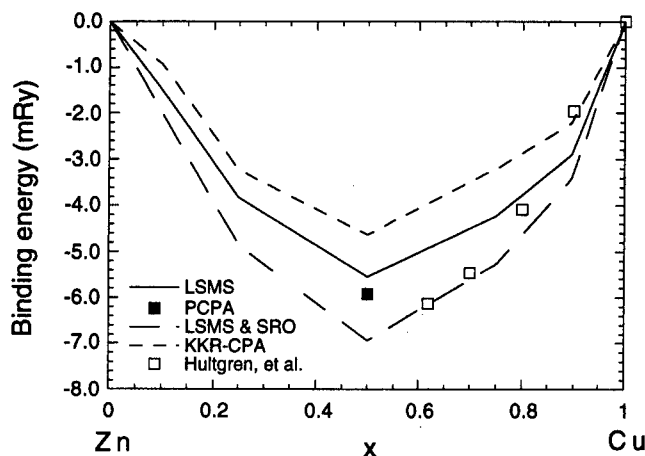


Figure 4. The heats of mixing for the alloys $U(c)$. The solid line shows the results of the LSMS calculations. The short dashes show the KKR-CPA heats of mixing. The solid square shows the heat of mixing calculated from the PCPA. The experimental results are indicated by the open squares, and the LSMS plus short-range order by the line with long dashes.

The heats of mixing for the alloys are found from the total energies $U(c)$ for the different concentrations c using the formula

$$U_{mix}(c) = U(c) - (1-c)U(0) - cU(1), \quad (37)$$

and are plotted in Fig. 4. There are clearly errors in the $U_{mix}(c)$ calculated with either the KKR-CPA or the PCPA, but the errors are not as big as might have been expected considering the highly simplified nature of these calculations in comparison with the LSMS. As pointed out several places,^{6,25} the DFT-LDA predictions for the lattice constants are systematically smaller than the experimental values, and the binding energy is also smaller than experiment. A possible correction to the binding energies is to include short-range order.⁶ This brings the DFT-LDA predictions into alignment with experiment as seen in Fig. 4.

DISCUSSION

The primary conclusion of this research is that averaging the exact Green's function for the alloy and then making the single-site approximation within the philosophy of CPA leads to the PCPA. Applying the additional restriction that the alloy must be isomorphous then leads to the standard KKR-CPA.⁴ The reason that the SIM-CPA and S-CPA run into difficulties is that they are trying to achieve a goal that is mathematically forbidden, which is to include non-zero Madelung potentials in an isomorphous alloy model. Of course, the SIM-CPA and S-CPA may still be useful approximations.

The PCPA is expected to be very helpful in explaining experiments that depend critically on charge transfer. A study of core level shifts in alloys based on LSMS calculations has been published.²⁶ The alloys treated are the ones in Table I. LSMS calculations give predictions for the core level shifts that agree with experiments to within experimental accuracy. Calculations using the PCPA are almost as good as the LSMS, while those done with the KKR-CPA are less good. These results will be published in detail in another journal.

If it is accepted that the best CPA formulation leads to a polymorphous model, it is reasonable to ask why the isomorphous CPA calculations were so useful in explaining properties of alloys. Part of the answer can be seen from Fig. 4, which illustrates that an error in the treatment of the Coulomb effects that appears quite sizable may not lead to such a large error in the binding energies. The KKR-CPA gives about 83% of the DFT-LDA binding energy, even though it predicts only 75% of the correct charge transfer and 0% of the correct Madelung potentials. The error in the PCPA heat of mixing compared to the DFT-LDA value is 0.4 of the KKR-CPA error, and of a different sign. In addition, it can be seen from Figs. 5 and 6 in ref. 25 that differences between the densities of states calculated with the KKR-CPA and the LSMS are not large enough to be seen in most experiments. Many of the early experiments on alloys were measures of the densities of states.

There are a number of extensions to the present work that must be achieved. As mentioned above, it would be useful to develop dedicated PCPA computer codes that could be run on small computers. With the codes that are presently available, the authors of this paper are able to extend the calculations to treat local interaction zones that contain more than one atom, which is the LSGF. Such extensions go beyond the philosophy of the CPA, and they require much more computational power.

Some studies have been published on the effect of increasing the size of the LIZ's in the LSGF,¹⁴ but it would be interesting to check these with calculations that do not employ the tight-binding linear muffin-tin orbital basis and the atomic sphere approximation. From the mathematical point of view, it would be interesting to study LSGF calculations in which the effective scatter t_c is given by Eq. (21). To be precise, the LIZ's contain more than one atom, and the scatters in Eq. (21) describe the central atom of the LIZ embedded in a matrix in which all the other atoms are represented by t_c . Similar calculations were done in the early days of the CPA development, and the Green's functions for the periodic system with a t_c on every site were not analytic.²⁷

REFERENCES

1. J. S. Faulkner, in *Progress in Materials Science*, Vol. 27, edited J. W. Christian, P. Haasen, and T. B. Massalski, (Pergamon Press, Oxford, England, 1982).
2. P. Soven, Phys. Rev. **156**, 809 (1967).
3. Hohenberg and W. Kohn, Phys. Rev. **136**, B864 (1964); W. Kohn and L. J. Sham, Phys. Rev. **140**, A1133 (1965).

4. H. Winter and G. M. Stocks, *Calculation of Self-Consistent Potentials For Substitutionally Disordered-Systems With Application to the Agx-Pd1-X Alloy Series*. Phys. Rev. B **27**, 882 (1983); D. D. Johnson, D. M. Nicholson, F. J. Pinski, B. L. Gyorffy, and G. M. Stocks, *Density-Functional Theory For Random Alloys - Total Energy Within the Coherent-Potential Approximation*. Phys. Rev. Lett. **56**, 2088 (1986); D. D. Johnson, D. M. Nicholson, F. J. Pinski, B. L. Gyorffy, and G. M. Stocks, *Total-Energy and Pressure Calculations For Random Substitutional Alloys*. Phys. Rev. B **41**, 9701 (1990).
5. G. M. Stocks, D. M. C. Nicholson, Y. Wang, W. A. Shelton, Z. Szotek, and W. M. Temmermann, in *High Performance Computing Symposium; Grand Challenges in Computer Simulation, Proceedings of the 1994 Simulation Multiconference*, edited by A. M. Tentner, (The Society for Computer Simulation, San Diego, Ca., 1994); D. M. C. Nicholson, G. M. Stocks, Y. Wang, W. A. Shelton, Z. Szotek, and W. M. Temmermann, *Stationary Nature of the Density-Functional Free-Energy - Application to Accelerated Multiple-Scattering Calculations*. Phys. Rev. B **50**, 14686 (1994).
6. Yang Wang, G. M. Stocks, W. A. Shelton, D. M. C. Nicholson, Z. Szotek, and W. M. Temmerman, *Order-N Multiple-Scattering Approach to Electronic-Structure Calculations*. Phys. Rev. Lett. **75**, 2867 (1995).
7. J. S. Faulkner, Yang Wang, and G. M. Stocks, *Coulomb energies in alloys*. Phys. Rev. B **55**, 7492 (1997).
8. L. Reinhard, B. Schönfeld, and G. Kostorz, *Short-Range Order in Alpha-Brass*, Phys. Rev. B **41**, 1727 (1990).
9. S. G. Louie, K. Ho, and M. L. Cohen, *Self-Consistent Mixed-Basis Approach to the Electronic-Structure of Solids*, Phys. Rev. B **19**, 1774 (1979); J. Neve, B. Sundqvist, and O. Rapp, *Electron Band-Structure, Resistivity, and the Electron-Phonon Interaction for Niobium Under Pressure*, Phys. Rev. B **28**, 629 (1983); A. R. Jani, N. E. Brenner, and J. Callaway, *Band-Structure and Related Properties of BCC Niobium*, Phys. Rev. B **38**, 9425 (1988); D. M. Nicholson and J. S. Faulkner, *Applications of the Quadratic Korringa-Kohn-Rostoker Band-Theory Method*, Phys. Rev. B **39**, 8187 (1989).
10. P. P. Singh and A. Gonis, *Electronic-Structure of Metallic Alloys Using Charge-Neutral Atomic Spheres*, Phys. Rev. B **49**, 1642 (1994).
11. I. A. Abrikosov, Yu. H. Vekilov, A. V. Ruban, *Fast LMTO-CPA Method for Electronic-Structure Calculations of Disordered Alloys - Application to Cu-Ni and Cu-Au Systems*, Phys. Letters A **154**, 407 (1991); I. A. Abrikosov, Yu. H. Vekilov, P. A. Korzhavyi, A. V. Ruban, and L. E. Shilkrot, *Ab-Initio Calculations of the Electronic Topological Transition in Li-Mg Alloys*, Solid State Comm. **83**, 867 (1992).
12. D. D. Johnson and F. J. Pinski, *Inclusion of Charge Correlations in Calculations of the Energetics and Electronic-Structure for Random Substitutional Alloys*, Phys. Rev. B **48**, 11553 (1993).
13. N. Papanikolaou, R. Zeller, P. H. Dederichs, and N. Stefanou, Phys. Rev. B **55**, 4157 (1997).
14. I. A. Abrikosov and B. Johansson, *Applicability of the coherent-potential approximation in the theory of random alloys*, Phys. Rev. B **57**, 14164 (1998).
15. Lord Rayleigh, Philos. Mag. **34**, 481 (1892).
16. J. Korringa, Physica **13**, 392 (1947); W. Kohn and N. Rostoker, Phys. Rev. **94**, 111 (1954).
17. I. A. Abrikosov, A. M. N. Niklasson, S. I. Simak, B. Johansson, A. V. Ruban, and H. L. Skriver, *Order-N Green's function technique for local environment effects in alloys*, Phys. Rev. Lett. **76**, 4203 (1996).

18. I. A. Abrikosov, S. I. Simak, B. Johansson, A. V. Ruban, and H. L. Skriver, *Locally self-consistent Green's function approach to the electronic structure problem*, Phys. Rev. B **56**, 9319 (1997).
19. P. P. Ewald, Ann. Physik **64**, 253 (1921).
20. J. S. Faulkner, and G. M. Stocks, *Calculating Properties With the Coherent-Potential Approximation*. Phys. Rev. B **21**, 3222 (1980).
21. B. L. Gyorffy, Phys. Rev. B **5**, 2382 (1972).
22. P. Lloyd, Proc. Phys. Soc., London **90**, 207 (1967).
23. B. L. Gyorffy and G. M. Stocks, *Concentration Waves and Fermi Surfaces in Random Metallic Alloys*. Phys. Rev. Lett. **50**, 374 (1983).
24. G. M. Stocks and W. H. Butler, *Mass and Lifetime Enhancement Due to Disorder On $\text{Ag}_x\text{Pd}_{1-x}$ Alloys*. Phys. Rev. Letters **48**, 55 (1982); W. H. Butler and G. M. Stocks, *Calculated Electrical-Conductivity and Thermopower of Silver- Palladium Alloys*. Phys. Rev. B **8**, 4217 (1984); J. C. Swihart, W. H. Butler, G. M. Stocks, D. M. Nicholson, and R. C. Ward, *1st-Principles Calculation of the Residual Electrical- Resistivity of Random Alloys*. Phys. Rev. B **57**, 1181 (1986).
25. J. S. Faulkner, Nassrin Moghadam, Yang Wang, and G. M. Stocks, *Comparison of the electronic states of alloys from the coherent potential approximation and an order- N calculation*. Phys. Rev. B **57**, 7653 (1998).
26. J. S. Faulkner, Yang Wang, and G. M. Stocks, *Core level chemical shifts in metallic alloys*. Phys. Rev. Lett. **81**, 1905 (1998).
27. B. G. Nickel and W. H. Butler, Phys. Rev. Lett. **30**, 373 (1973).

PHASE STABILITY AND TRANSFORMATION

IRON PHASE DIAGRAM AT HIGH PRESSURES AND TEMPERATURES

S. K. Saxena¹ and L. S. Dubrovinsky²

¹Center for Study of Matter at Extreme Conditions, VH-150
Florida International University, University Park, Miami, FL 33199

²Institute of Earth Sciences, Uppsala University, S-752 36 Uppsala, Sweden

ABSTRACT

Diamond-anvil cell (DAC) high-pressure technique with *in situ* laser heating of a sample permits the determination of iron phase diagram to pressures reaching planetary cores. The DAC technique in combination with *in situ* x-ray study of iron has revealed the presence of at least one additional state of iron with possibly a double hexagonal closest packed (DHCP) structure given the name β . A review of the available data, indicates that in addition to the previously known triple points, the BCC (body-centered cubic)-HCP (hexagonal closest packed)-FCC (face centered cubic) and the β -BCC-FCC-melt, the following triple-points may exist in the iron phase diagram: the HCP-FCC- β : pressure (P) = 40 (4) GPa at temperature (T) = 1550 (100) K, the β -FCC-melt: P = 60 (10) GPa at T = 2600 (100) K. We define the stability of β -phase between pressures of 37 to 300 GPa at high temperatures. The HCP- β phase boundary has a small negative dP/dT indicating the similarity of physical properties (molar volume, thermal expansion and bulk modulus) between the two but a higher entropy and enthalpy for the β -phase. The melting curve of iron has been determined quite reliably with the laser heated sample in the DAC to a pressure of about 80 gigapascal (GPa). The pressure range of melting has been extended to as high as 200 GPa but is not supported by shock-wave data and requires further studies for confirmation.

INTRODUCTION

Since iron is one of the most abundant elements in Earth forming the major part of the core, it has always been a subject of high interest to geoscientists. There is intensified interest in studying iron at physical conditions of the core because of new developments in high pressure-temperature techniques. Iron occurs in four distinct polymorphs. Three (BCC body centered cubic, δ -BCC and FCC) are stable at one atmosphere and the fourth (HCP) phase at high pressures. Fernandez-Guillermot and Gustafsson (1985) assessed the thermochemical data on BCC, δ -BCC, FCC and melt at 1 bar and calculated a phase diagram to 20 GPa. Saxena et al. (1993) noticed a change in the laser absorption properties of iron at high pressures and temperatures and suggested the occurrence of a fifth phase which they called β . During the last six years, we have conducted a series of experiments on establishing the identity and stability field of this phase (e.g. Saxena et al., 1995, Dubrovinsky et al., 1998).

This paper describes the techniques of studying iron at high pressures and temperatures and summarizes the available data fixing the β -FCC and β -HCP phase boundaries, and the triple points β -FCC-HCP and β -FCC-melt.

EXPERIMENTAL TOOLS

Diamond-anvil cell

The diamond-anvil cell is a device where two opposing diamond-anvils are pressed against each other to squeeze a sample placed in between to reach ultra-high pressures (Fig. 1). The sample is usually contained in a micro-hole created in a metal gasket. The advantage of the diamond-anvil cell as containers for high-temperature, high-pressure research is the ease with which samples can be prepared and squeezed to desired pressures and heated, while simultaneously studying them optically or by x-ray and a variety of spectroscopic techniques. This is due to the transparency of diamonds as well as their hardness and high thermal conductivity. The disadvantages are that the sample size is small and the pressure is uniaxial which may result in large pressure gradients at very high pressures. Both these disadvantages are largely overcome by using high intensity sources such as synchrotron x-ray and releasing the stress by using heated cells. Pressure at room temperature can be measured from the ruby fluorescence technique or by determining the cell constants of an internal standard if x-ray is used.

Laser

One may use scientific grade lasers (CO_2 - and Nd-YLF) in continuous wave (CW) mode to heat a sample to several thousand degrees. The sample is sandwiched between insulating layers of a material that does not absorb the laser energy. For CO_2 -laser (10.600 nm), the insulation can be provided by liquid argon which solidifies as pressure is increased. For Nd-YAG (1064 nm), an oxide such as MgO or any liquid gas that does not react with the sample may be used. The lasers are power stabilized by the manufacturers and one may add further stability by using feed back loops monitoring either the power fluctuation or the thermal radiation. We use a liquid-crystal-based stabilizer (Cambridge Research Inc.) with feedback, which results in intensity stabilization within 0.05% peak-to-peak (RMS). For iron the Nd-YLF (1064 nm) laser is best. To maintain a homogeneous temperature, the sample should be heated from two sides (see later).

X-ray

The use of synchrotron facilities at the Advanced Photon Source (APS) at Argonne National Laboratory may be used for all studies requiring a small size beam and double-side laser heating. Local x-ray diffraction (XRD) facilities may be used for all samples at moderate to low pressures. The National Synchrotron Light Source (NSLS) at Brookhaven National Laboratory (BNL) facilities are used for externally heated cells requiring a small beam size. Because of the use of polychromatic light, the high pressure XRD BNL facility is not particularly useful for structural state studies (e.g. obtaining super lattice reflections requiring the distinction between a double HCP vs. HCP).

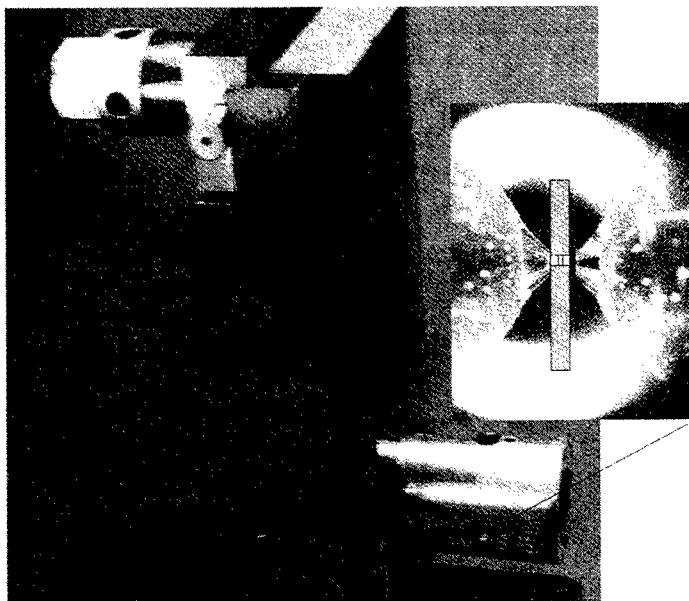


Figure 1. Mao-Bell design diamond-anvil cell. The length of the cell is approximately 6 inches. The piston-cylinder design is used with a diamond glued on WC seats and lodged in position as shown in the insert. Pressure is increased by hand using the screw shown. A gasket between the diamonds contains the sample.

EXPERIMENTAL TECHNIQUES

Laser-heating

Pressurized sample in a DAC may be heated by stabilized Nd-YLF laser (Photonics, 50 Watts CW at 1064 nm, TEM₀₀ mode). Temperatures are determined from the thermal radiation of a hot sample using spectroradiometry as described below. The use of 2-dimensional CCD detector and imaging spectrograph with entrance slit makes it possible to measure temperatures along a narrow vertical strip in one single measurement with spatial resolution of about 3 microns (Fig.2). A detailed description of the laser heating system is given in Shen et al. (1998). In laser heating from one side of the sample, there is a large temperature gradient from the front to back. While this is not a problem for some studies e.g. melting where only surface reaction is involved, it is a definite drawback for determining physical properties of solids where the x-ray samples the whole thickness. Therefore, one should use the technique of heating the sample from both sides (Fig. 3) as developed by Shen et al. (1998).

External heating

One may use a flexible graphite foil for external electric heating (Fig. 4). In such a design, both the diamonds and gasket can be heated homogeneously to temperatures in excess of 1200°C. We use two rectangular flexible graphite slabs (~23*10mm²) of 1mm thickness. Small pieces (~8*10mm²) of the graphite foil of 0.5 mm thickness are glued to the edges of these slabs along their lengths using high temperature graphite glue. These small pieces at the edge of the slabs make the furnace stable and direct the heat to the

sample and the diamond tips. The slabs are indented simultaneously and the Re-gasket is placed between them. The whole furnace is then isolated from the cell using thin sheets of mica (~50 micron) above and below the slabs and screwed together using a thin molybdenum sheet. Two molybdenum electrodes (thickness 4mm) are inserted between the two slabs of graphite foils and finally glued using high temperature ceramic glue. The sample is heated using a DC power supply, with an operating range between 13A/10V-150A/26V. For measuring the temperature, a Pt/Pt13%Rh precision thin micro-thermocouple with a junction diameter around 25 micron is used. The junction of thermocouple is inserted close to the diamond anvil shown in Fig.4, such that it can touch the gasket sitting between the foils. The reproducibility of temperature with such thermocouple attachments near the diamond-gasket interface is within 10 K. All experiments are carried out with flowing argon, which creates an inert ambient condition and acts as a coolant to the cell.

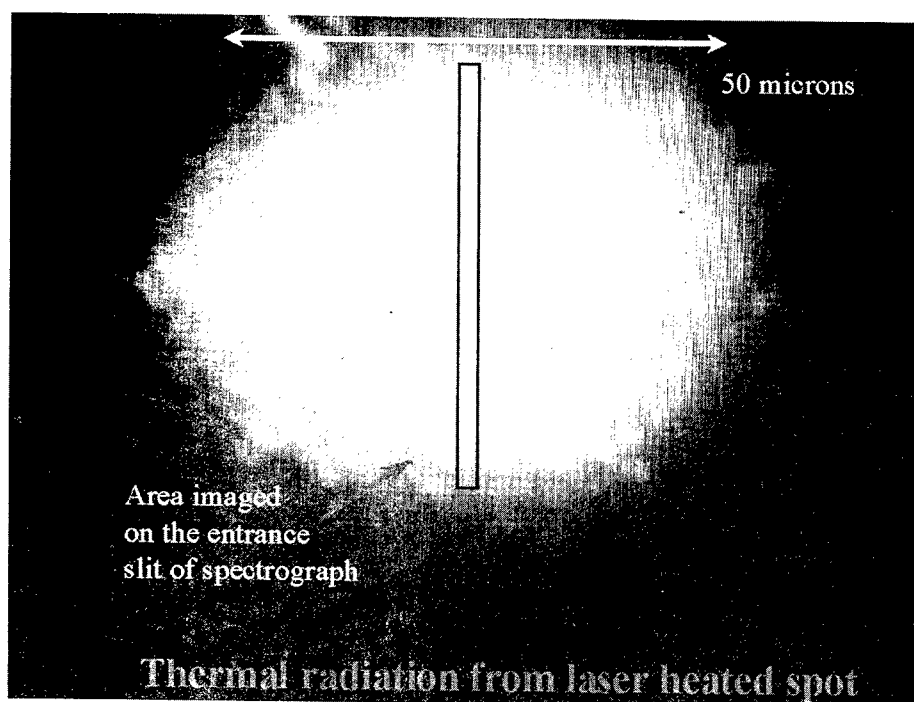


Figure 2. The laser spot. Thermal radiation is collected along the 3 micron size slit in segments of 4 or 8 out of 128 or 256 channels. Since the laser power has a gaussian distribution, the temperature is measured at the top of the profile giving errors of only a few degrees, which is dependant on the thermal gradient.

Multiwavelength Spectral Radiometry

The temperature is measured using the method of spectroradiometry (Jeanloz and Kavner, 1996, Lazor and Saxena, 1996) for heated metals and silicates. For correct temperature determination wavelength dependent emissivity has to be considered when fitting the spectra to the Planck radiation function. After major advances in instrumentation

during the last decade, a poor knowledge of high pressure and temperature emissivity became the main source of systematic errors in temperature measurements in high pressure studies. These errors may range from few tens to several hundreds of degrees depending on the actual emissivity variation with wavelength and the temperature range of a study. Thermal radiation is collected over a range of wavelengths and the resulting spectrum is fitted with Planck's function. The accuracy of measured temperature requires data on emissivity of a sample as a function of pressure, temperature and wavelength (Coates, 1981). In multiwavelength thermometry the spectral radiance of the target at several wavelengths is curve fitted to Planck's or Wien's equation.

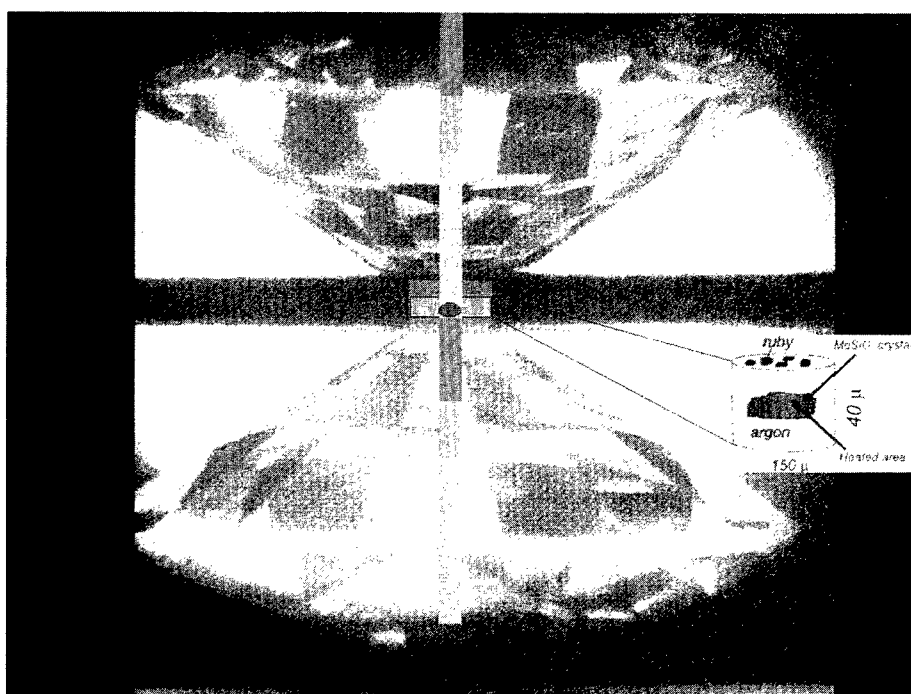


Figure 3. Double-side laser heating. This is accomplished in a DAC designed to reach the sample from both sides. Unlike in the Mao-Bell cell, the pressure here is increased directly with the help of 4 or 6 screws.

Sample preparation and x-ray data collection

The very high-pressure experiments require fine incident X-ray beam ($8 \times 9 \mu^2$ or less) of 0.4 \AA wavelength or less, preferably with an imaging plate performed on a synchrotron radiation facility (e.g. APS, Argonne). Powdered samples (iron of 99.999% purity) are loaded into the $30\text{--}35 \mu$ initial diameter hole in a Re-gasket, which is confined between diamond culets (beveled to 40 or 50μ outer diameter, if pressure is to reach 300 GPa). Pressure is determined with powdered platinum (99.999% purity) as an *in situ* x-ray standard mixed in small proportion with the iron sample. We obtain powder X-ray diffraction data with a Siemens X-ray system consisting of a Smart CCD Area Detector and a direct-drive rotating anode as x-ray generator (18 kW). MoK_α radiation is monochromatized using an incident beam graphite monochromator and passed through a

collimator of diameter 30 to 40 μm to the sample. The diffracted X-ray is collected on a 512x512 pixel area detector. We heat the samples externally in a Mao-Bell type DAC (Dubrovinsky et al., 2000). In our analysis of the integrated x-ray spectra, we use the program GSAS (Larson and Von Dreele, 1994) and Peak Fit 4.0. At Argonne National Lab, we use the double-side laser heating system as established by Shen (see Shen et al. 1998).

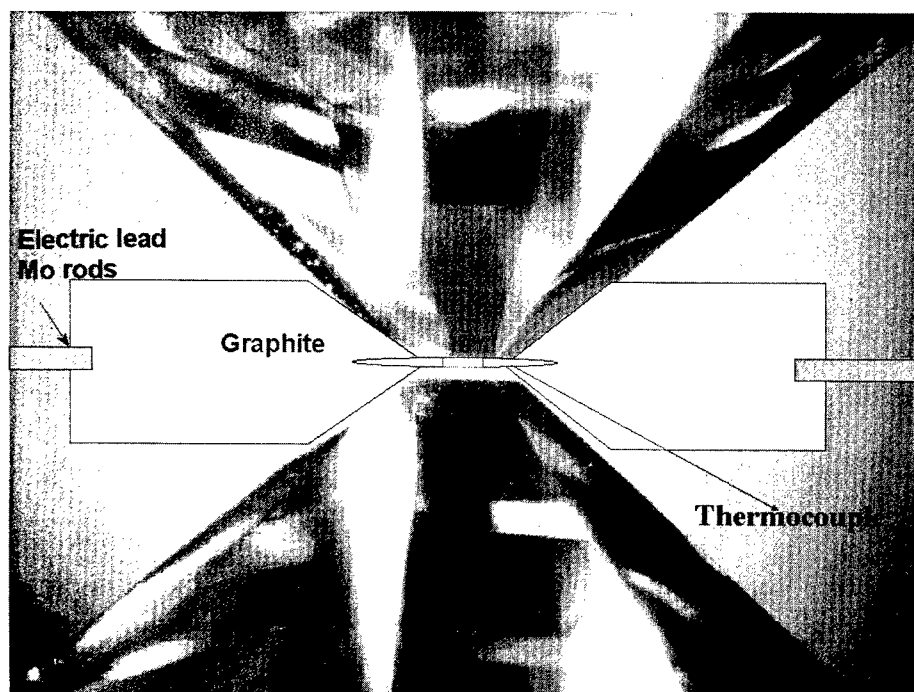


Figure 4. External heating of the sample in a DAC. In this design, the heat is provided through electrical heating of the graphite slabs with a low voltage and high ampere current (up to 150 A). Four mm thick molybdenum electrodes are connected to the two slabs. The metal gasket containing the sample as well as the diamond anvils are thoroughly heated (at least one third to half of the diamonds are within the graphite slabs: this is not represented correctly in the figure).

IRON PHASE DIAGRAM

The new phase β

The distinction between the DHCP and HCP structures is based on the former showing additional super-lattice reflections, which are not as strong as the HCP equivalents. One of the difficulties of experiments in establishing the structure of the β phase is that the Nd-YAG laser heating of a sample requires that the diamonds be thermally insulated from the sample requiring the use of an oxide or an inert gas. The presence of an additional material in the sample complicates the x-ray pattern. Corundum has numerous reflections; silica undergoes several phase transitions and MgO masks the important super-lattice reflections of the DHCP structure. There is also the possibility of a reaction between

iron and the pressure medium. In spite of such difficulties, we were able to use MgO as a pressure medium and by using the 2-dimensional CCD detector were able to discern the super-lattice reflections of the DHCP phase (Dubrovinsky et al., 1999) (Fig. 5). The structure has now been confirmed to pressures as high as 300 GPa (Dubrovinsky et al., 2000). Andrault et al., (1997) report an orthorhombic structure at somewhat higher temperatures but this needs confirmation.

Iron phase relations

Figure 6 shows the existing data for the phase diagram of iron. All x-ray data quenched or in situ have been plotted for the solid phases. From the figures, it is clear that we need several data to bracket (i.e. obtain an assessment of equilibrium pressure or temperature by reversing the direction of reaction) the phase transformations in the pressure and temperature field. The experiments conducted thus far have not been designed to bracket the reversals for β but just to show the existence of the phase over a field of pressure-temperature stability. Based on the data shown in the figures, it is difficult to define the pressure and temperature of the triple points with any precision. The triple point FCC-HCP- β -phase in the figure is in part based on the in situ x-ray data on phase transformation of the FCC phase to HCP and β . The slope of the FCC-HCP boundary based on the data of Funamori et al. (1997) is slightly less steep than those based on the data of Mao et al. (1987) and Boehler et al. (1987). The large scatter in the data on the appearance and disappearance of the FCC or β -phase is due to kinetic difficulties. If one increases temperature rapidly, the phase transition is not recognized until the transition temperature has been exceeded substantially. Similarly rapid cooling leads to underestimation of transition temperatures.

The β -HCP phase boundary

The available data shows a slightly negative slope of the phase transition P-T curve. It is important that several experiments are conducted to establish both the DHCP structure and the phase boundary. Since the temperature range is within the limits of our external heating equipment, this task can be accomplished with no difficulty. We can use argon to moderate pressures and then switch to solid pressure medium such as MgO, checking carefully that no reaction takes place during prolonged heating. In a recent study (Dubrovinsky et al., 2000), we determined the HCP to β -phase transformation between pressures of 135 and 300 GPa. At a pressure of 301 (20) GPa, HCP iron was transformed to β -phase at a temperature of 1350 K; the transition was reversed on cooling below 1250 K, which indicates that transition boundary has a very small negative slope in the pressure-temperature field.

The β -FCC phase boundary

This is a more difficult task because it must be done with double-side-laser heating. However the pressure is limited to a maximum of 70 GPa and argon could be used as a pressure medium. As yet, for the FCC- β -phase boundary, we have little data to go on. One may assume that the FCC-HCP boundary as proposed by Shen et al. (1998) may be considered as the FCC- β -phase boundary. It is difficult to distinguish the DHCP (β -phase) from the HCP phase without the use of a monochromatic beam and angle dispersive measurement; these are essential to recognition of the super-lattice reflections. It is now possible to accomplish this at APS.

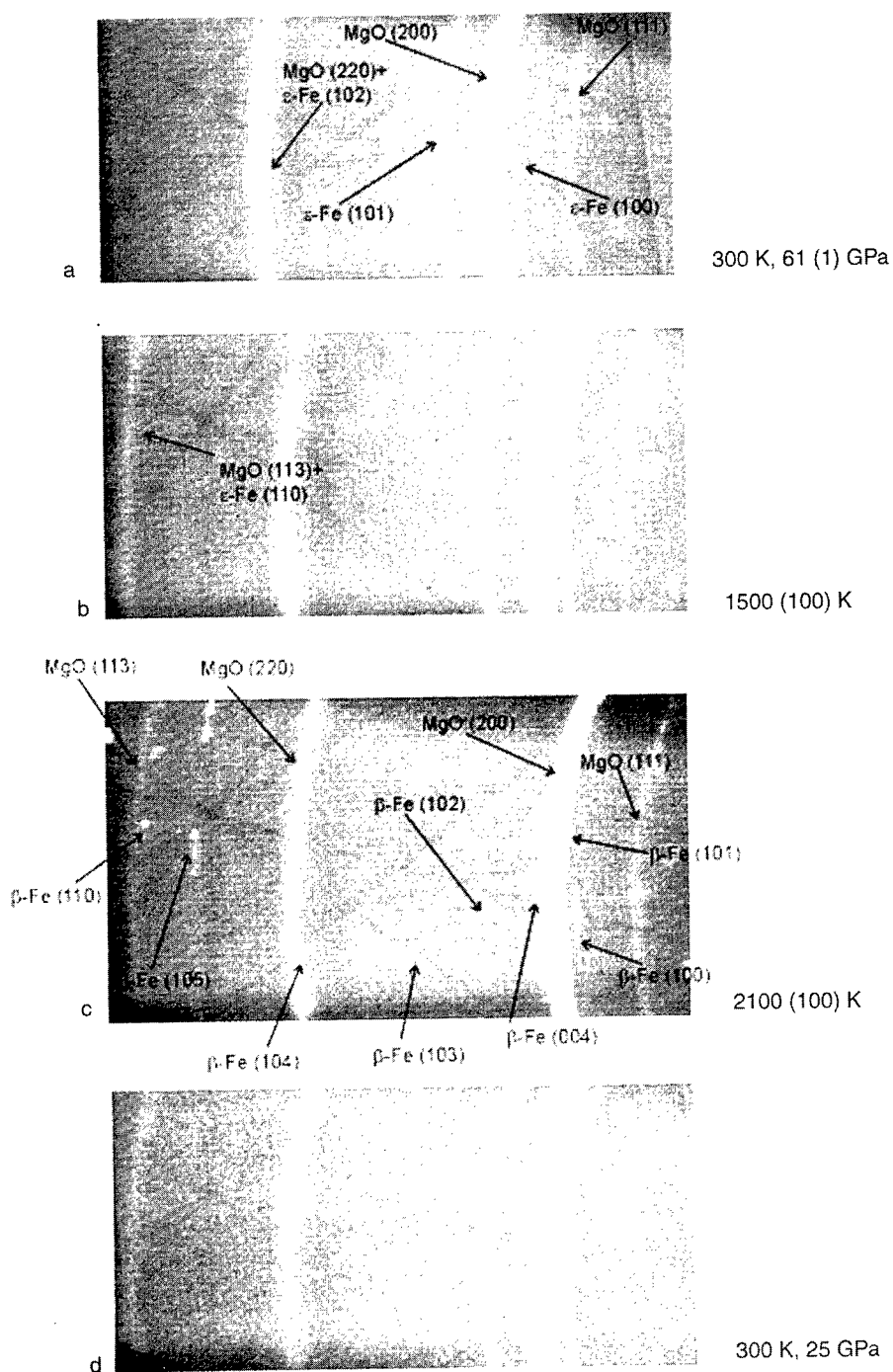


Figure 5. 2-dimensional CCD x-ray data on heated iron (diffraction data from Dubrovinsky et al., 1999). The calculated \pm error is shown in parentheses. a. Reference sample of MgO and HCP iron at 61 GPa at 300 K. b. The same sample at 1500 K and up to 61 GPa; remains untransformed as the HCP structure. c. The same sample at 2100 K. Spots corresponding to super lattice reflections of the b-phase appear as marked. d. The new reflections disappear on cooling.

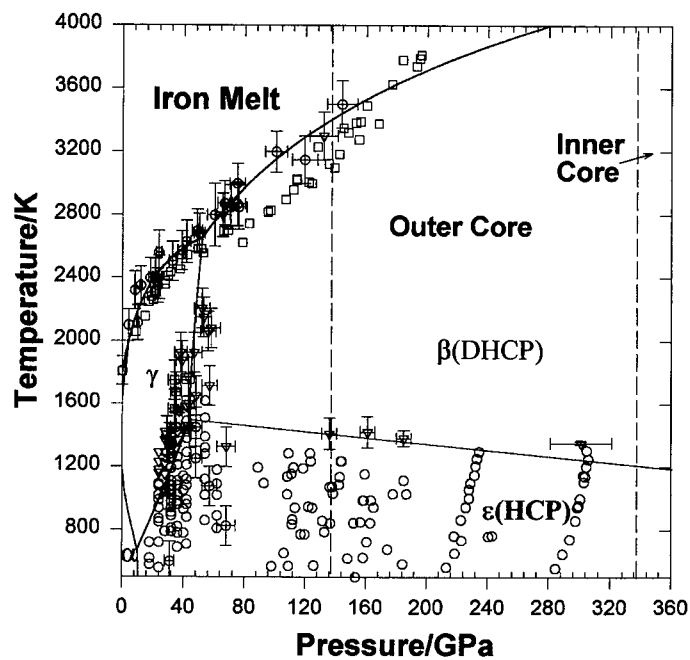


Figure 6. Phase diagram of iron where α and γ represent bcc and fcc lattice types. The vertical dashed lines represent the boundaries between the mantle and outer core (at roughly 135 GPa) and between the inner and outer core (at roughly 340 GPa). All x-ray data, quenched or in situ, have been plotted for the solid phases. Open circles and triangles (no error bars shown): below 80 GPa from Dubrovinsky et al. (1998a) all data above 80 GPa from Dubrovinsky et al. (2000). Triangles with error bars represent β , below 80 GPa from Dubrovinsky et al. (1998b) and above from Dubrovinsky et al. (2000). Melt data: open squares from Boehler (1993); circles with error bars are from Saxena et al. (1994). X-ray data from Shen et al. (1998) are plotted as circles without error bars.

Location of the triple points β -FCC-HCP and β -FCC-melt

Some data on the triple point is presented in the figure above. The task is complicated by the need to combine the laser heating data for the β -FCC boundary with the β -HCP boundary determined from external heating. The FCC-DHCP (or HCP) - melt triple-point was located by Boehler (1993) at ~ 100 GPa. This was based on the argument that there is the depression of the melting curve around 80 - 100 GPa (Boehler et al. 1990). Boehler et al. (1990) did state that this depression may be an artifact. Indeed in our melting experiments we were unable to confirm this depression. Yoo et al. (1995) did not find the HCP-FCC phase transition all the way to melting at 50 GPa. Based on the data of Shen et al., (1998), the triple point DHCP-FCC-melt could be close to 60 GPa possibly at 2640 K. We need to confirm these data.

The melting curve of iron at pressures between 80 and 300 GPa

Melting of iron at pressures above several GPa has been accomplished both by heating iron with a laser in DAC (e.g. Boehler, 1993) and by the shock wave method (Bass et al., 1990, Gallagher and Ahrens, 1994, Yoo et al., 1993) (Fig. 7). The static pressure data supports that iron melts at temperatures that are several hundred degrees lower than those obtained in shock-wave experiments. Recently Ahrens and coworkers (Chen and Ahrens, 1995, 1996) found that it may be possible to reconcile the differences between the iron melting temperatures determined by the two techniques; the differences may not be as large as previously thought. A significant development in this regard is the recent study of Ahrens et al. (1997) who reported the sound speed data along the Hugoniot (the curve

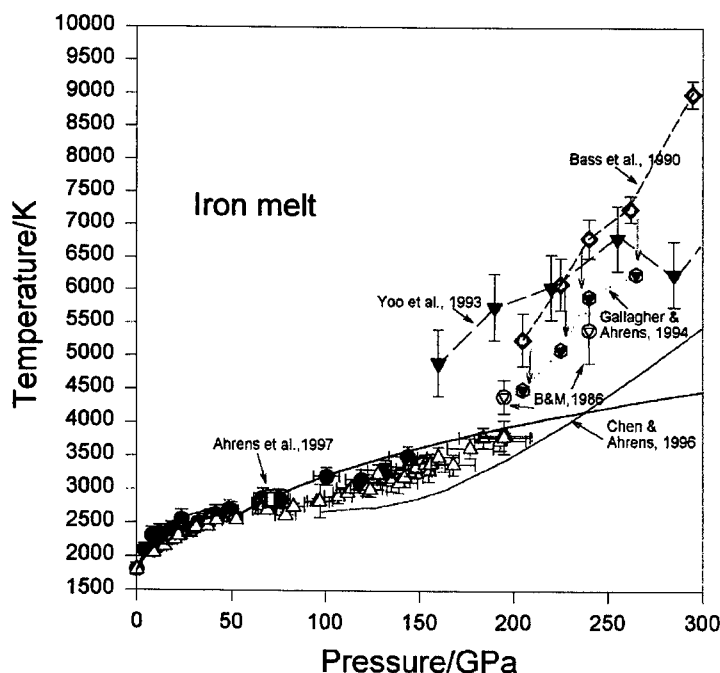


Figure 7. Iron melting at high pressure. Triangles: Boehler (1993), Circles: Saxena et al. (1994). Shock-wave data from various authors as marked. B&M : Brown and McQueen (1986).

representing the velocity of a single shock wave and the pressure, temperature and total heat of that material, before and after the shock passes). They determined that the FCC phase melts at a temperature of 2800 K at a pressure of 70 GPa. This lends strong support to the static pressure measurement of melting temperatures fitting quite well with the x-ray data of Shen et al. (1998).

The melting temperatures determined at ultra-high pressures (Boehler, 1993, Saxena et al., 1994) are not totally without problems. At such pressures, the detection of melting becomes a definite problem. The *in situ* x-ray data are necessary (Shen et al., 1998) but these yield only an upper limit of temperature when iron is totally melted. We cannot ignore the possibility of some reaction between the pressure medium and the sample. The effect of stress on melting in DAC appears to be small to pressures as high as 60 GPa. The differences in the technique of iron melting detection and temperature measurements in DAC technique have led to significant uncertainties in measured temperatures but most data do lie in a band within a range of 250 degrees. The temperature of melting changes continuously decreasing with increasing pressure. According to these data, melting of iron should occur below 4000 K at a pressure of 200 GPa. As discussed by Anderson and Duba (1997), the question of melting at pressures above 200 GPa hinges around the data of Brown and McQueen (1986) who proposed a solid-solid phase transition at ~200 GPa and melting at 243 GPa at temperatures of 4400 and 5500 K respectively. Currently some work is in progress which tends not to support the existence of the solid-solid reaction but this may be due to a number of factors as discussed by N. Holmes and J. Brown at the AGU Fall meeting, 1998. We note from the figure that the DAC data, which extends to a pressure of 200 GPa does not permit a value greater than 4000 K for melting at that pressure. We must treat the data on melting of iron at pressures greater than about 100 GPa with caution and plan new experiments with *in situ* x-ray study. We need to confirm a) that no reaction takes place between the solid pressure medium and iron and b) the visual observation of melting was reliable. The common criterion in determining melting is the visual observation of motion on the sample surface. In our experiments, we combine this method with the recording of a laser-power/sample-temperature dependence. We believe this represents a significant improvement in reliability and objectivity of melting determination. At ultrahigh pressures of several hundreds of GPa, melting detection by visual observation may become problematic due to the very small size of a sample; therefore we conduct several melting experiments with *in situ* x-ray. The melting criterion by the laser-power/sample-temperature function requires very stable intensity of a laser beam.

CONCLUSIONS

New techniques using diamond-anvil cells with laser heating and heating the cell externally have made it possible to explore the behavior of iron to pressures and temperatures as high as those existing in terrestrial planetary cores. An important result of the new studies is the possibility that iron may occur in more than the four structural states (d-BCC, BCC, FCC and HCP) already known. It appears that at least one structural polymorph, the DHCP, may be present. Based on the review of the available data, the location of two triple points is discussed. The β phase is deduced to have similar physical properties as the HCP phase.

ACKNOWLEDGMENTS

The Swedish Natural Science Council (NFR) and the CAMPADA consortium of Nutek and the Department of Sponsored Research at FIU have supported us financially. We thank Annemarie Meike for providing us with a strong motivation to publish and for her invaluable help in editing the paper

REFERENCES

- Ahrens, T. J., Holland, K. G. and Chen, G. Q., 1997, in: *Shock temperatures and the melting point of iron. CP429, Shock Compression of Condensed Matter*, Schmidt, Dandekar and Forbes, eds. The American Inst. Phys.
- Andraut, D., Fiquet, G., Kunz, M., Visocekas, F. and Hausermann, D., 1997, The orthorhombic structure of iron: An in-situ high-T/high-P structure solution and refinement. *Science* 278: 831.
- Anderson, O. L. and Duba, A., 1997, Experimental melting of iron revisited. *J. Geophys. Res.* 102: 22659.
- Anderson, O. L. and Isaak, D. G., 2000, Simulated melting curves for phases of iron. American Mineral. (in press).
- Bass, J. D., Ahrens, T. J., Abelson, J. R. and Hua, T., 1990, Shock temperature measurements: New results for an iron alloy. *J. Geophys. Res.* 95:21757.
- Boehler, R., 1986, The phase diagram of iron to 430 kbar, *Geophys. Res. Lett.*, 13: 1153.
- Boehler, R., Nicol, M. and Johnson, M. L., 1987, Internally-heated diamond-anvil cell: Phase diagram and P-V-T of iron in *High-Pressure Research in Mineral Physics*, Geophys.Monogr. Ser., vol. 39, M. H. Manghnani and Y. Syono eds., TERRAPUB, Tokyo/AGU, Washington DC.
- Boehler, R., 1993, Temperatures in the Earth's core from melting-point measurements of iron at high static pressures, *Nature*, 363:534.
- Boehler, R., von Bargen, N. and Chopelas, A., 1990, Melting, thermal expansion, and phase transition of iron at high pressures, *J. Geophys. Res.*, 95: 21731.
- Brown, J. M. and McQueen, R. G., 1986, Phase transitions, Grüneisen parameters and elasticity for shocked iron between 77 GPa, *J. Geophys. Res.*, 91: 7485.
- Chen, G.Q. and Ahrens, T.J. 1995. Equations of state of α , ϵ and liquid iron and iron's melting curve - thermodynamic calculations. *Geophys. Res. Lett.*, 22, 21-24.
- Chen, G.Q. and Ahrens, T. 1996. High-pressure melting of iron: new experiments and calculations. *Phil. Trans. R. Soc. Lond. A*, 354: 1251.
- Coates, P. B. (1981) Multi-valent pyrometry. *Metrologia*. V 17 103-109.
- Dubrovinsky, L. S., Saxena, S. K., Lazor, P., 1997, X-ray study of iron with in-situ heating at ultra high pressures. *Geophys. Res. Lett.* 24:1835.
- Dubrovinsky, L.S., Saxena S. K., Tutti F., Rekhi S. and LeBehan T., 2000, In situ X-ray study of thermal expansion and phase transition of iron at multimegabar pressure. *Phys. Rev. Lett* (In press).
- Dubrovinsky, L. S., Saxena, S. K., Lazor, P., 1998a, High-pressure and high temperature in situ x-ray diffraction study of iron and corundum to 68 GPa using internally heated diamond-anvil cell. *Phys. Chem. Mineral.* 25:434.
- Dubrovinsky, L. S., Saxena, S. K., Lazor, P., 1998b, Stability of β -iron: A new synchrotron x-ray study of heated iron at high pressures. *European J. Mineralogy*, 10: 43.
- Dubrovinsky, L. S., Lazor, P., Saxena, S. K., Haggkvist, P., Weber, H.P., Le Bihan, T. and Hausermann, D., 1999, Study of laser heated iron using third generation synchrotron x-ray radiation facility with imaging plate at high pressures. *Phys. Chem. Mineral.*, 26:539.
- Fernández Guillermot, A. and Gustafson, P., 1985, An assessment of the thermodynamic properties and the (p,T) phase diagram of iron, *High Temp.-High Press.*, 16: 591.
- Funamori, N., Yagi, T. and Uchida, T., 1997, High-pressure and high-temperature *in situ* x-ray diffraction study of iron to above 30 GPa using MA8-type apparatus. *Geophys. Res. Lett.* 23:953.
- Gallagher, K.G. and Ahrens, T.J., 1994, First measurements of thermal conductivity of griseite and corundum at ultra high pressures and the melting point of iron (abstract), *EOS Trans. Am. Geophys. Un.*, 15 (Suppl.), 653.
- Jeanloz, R. and Kavner, A. , 1996, Melting criteria and imaging spectroradiometry in laser-heated diamond-cell experiments. *Phil. Trans. R. Soc. Lond. A*, 354:1307
- Larson, A.C. and Von Dreele, R.B., 1994, Los Alamos National Laboratory, LAUR, 86-748,
- Lazor, P. and Saxena, S.K., 1996 , Discussion comment on melting criteria and imaging spectroradiometry in laser-heated diamond-cell experiments (by R. Jeanloz & A. Kavner), *Phil. Trans. R. Soc. Lond. A*, 354:1307.
- Mao, H.K., Bell, P.M. and Hadidiacos, C., 1987, Experimental phase relations of iron to 360 kbar, 1400°C, determined in an internally heated diamond anvil apparatus, in *High-Pressure Research in Mineral Physics*, Geophys.Monogr. Ser., vol. 39, M. H. Manghnani and Y. Syono, eds., TERRAPUB, Tokyo/AGU, Washington DC, 1987.
- Saxena, S.K., Shen, G., Lazor, P., 1993, Experimental evidence for a new iron phase and implications for Earth's core, *Science*, 260, 1312-1314.

- Saxena, S.K., Shen, G. and Lazor, P., 1994, Temperatures in Earth's core based on melting and phase transformation experiments on iron, *Science*, 264, 405-407.
- Saxena, S.K., Dubrovinsky, L.S., Häggqvist, P., Cerenius, Y., Shen, G. and Mao, H.K., 1995, Synchrotron X-ray study of iron at high pressure and temperature, *Science*, 269: 1703.
- Saxena, S.K., Dubrovinsky, L.S. and Häggqvist, P., 1996, X-ray evidence for the new phase β -iron at high temperature and high pressure, *Geophys. Res. Lett.*, 23:2441.
- Shen, G. Mao, H. K., Hemley, R. J., Duffy, T. S., Rivers, M. L., 1998, Melting and crystal structure of iron at high pressures. *Geophys. Res. Lett.*, 25:373.
- Yoo, C. S., Holmes, N.C. and Ross, M., 1993, Shock temperatures and melting of iron at earth core conditions. *Phys. Rev. Lett.* 70: 3931.
- Yoo, C.S., Akella, J., Campbell, A.J., Mao, H.K. and Hemley, R.J., 1995, Phase diagram of iron by *in situ* X-ray diffraction: Implications for Earth's core, *Science*, 270:1473.

EFFECTS OF CONTINUOUS ATOMIC DISPLACEMENT ON THE PHASE STABILITY OF METALLIC ALLOYS

K. Masuda-Jindo¹, R. Kikuchi², and Vu Van Hung³

¹ Department of Materials Science and Engineering
Tokyo Institute of Technology, Nagatsuta
Midori-ku, Yokohama 226-8503, Japan

² Materials Science and Mineral Engineering
University of California, Berkeley, CA 94720-1760

³ Hanoi National Pedagogic University
km8 Hanoi-Sontay Highway, Hanoi, Vietnam

INTRODUCTION

The cluster variation method (CVM) has been introduced by Kikuchi [1], and successfully applied to various problems of solid state physics and materials science. For instance, it has been used extensively to investigate temperature-composition phase diagrams of alloys. In the CVM calculations, however, the entropy expression was formulated for permutations of atoms among *rigid lattice points*. This type of approach will be referred to as the *conventional* CVM [1,2] in the present paper.

In real alloys, there are problems which need more than permutations of atoms among rigid lattice points. These problems include local lattice distortion caused by the atomic size

differences, thermal vibration and the effect of elastic interactions on phase diagrams [3]. Responding to the need of removing the restriction of the rigid lattice, the continuous displacement (CD) formulation has been recently introduced [3]. Since the CD formulation is an extension of the conventional CVM, we present the basis of the CD by comparing it with the conventional CVM treatment.

In the present study, we also use the moment method in the statistical dynamics[4], which includes the quantum mechanical effects of the lattice vibrations in the low temperature region. This method can be incorporated with the conventional CVM and applied to study the phase equilibrium of alloys, going beyond the harmonic approximation[5-7]. Using the moment method in the statistical dynamics, the Helmholtz free energy $\Psi(\alpha)$ of the alloy system is given by

$$\Psi(\alpha) = \Psi_0 - \int_0^\alpha \langle V \rangle_\alpha d\alpha, \quad (1)$$

where $\langle \dots \rangle_\alpha$ represents the thermal averaging over the equilibrium ensemble with the Hamiltonian $H = H_0 - \alpha V$. Here Ψ_0 is the free energy of a system corresponding to the unperturbed Hamiltonian H_0 , and V denotes the perturbation due to the atomic displacements. The thermal average $\langle V \rangle_\alpha$ can be written in terms of the moments and determined with the aid of moment formulae.

CONTINUOUS DISPLACEMENT TREATMENT OF CVM

Formulation of CD treatment of CVM

In this subsection, we briefly summarize the essence of the continuous displacement treatment of the CVM. We start with a reference lattice, to each lattice point of which we assign an atom. An atom assigned to a lattice point is actually located at \mathbf{r} away from the lattice point. We define the function $f(\mathbf{r})d\mathbf{r}$ as the probability of finding an atom at \mathbf{r} in the volume element $d\mathbf{r}$. We call $f(\mathbf{r})$ the probability distribution function (PDF) for a point. The displacement \mathbf{r} can take continuous values. For a pair of atoms displaced to \mathbf{r} and \mathbf{r}' from nearest-neighboring lattice points, we define a PDF, $g(\mathbf{r}, \mathbf{r}')$ for the pair. The probability distribution functions can also be defined for larger clusters.

In our previous study, the pair interaction energies have been used for the calculation of the free energies. In order to describe the metallic bonding in the alloy more appropriately, we also use the many body potentials derived from the tight-binding electronic theory [9,10], and extend the original treatment of CVM so as to include these potentials. For the illustrative purpose of the CD scheme, we describe the formulation within the Bragg-Williams approximation.

Two species A and B are denoted by the index $j = 1$ and 2 , respectively. We need two point probability functions $f_j(\mathbf{r})$ where \mathbf{r} is the displacement vector. A lattice position of the reference lattice is written as \mathbf{q}_m . The change in the potential energy due to the atomic displacement \mathbf{r} of the j -th atom in the lattice is evaluated by using the atomic configuration around j -th atom, not pair by pair summation. This is the essence of the formalism of the many body potential. Using the many body potential, the energy of the system of N atoms is given by

$$E = \frac{1}{2} N \sum_m \sum_{jk} \int d\mathbf{r} \epsilon_{jk}(|\mathbf{r} - \mathbf{q}_m|) f_j(\mathbf{r}). \quad (2)$$

The sum over the neighbor \mathbf{q}_m includes not only the first neighbors, but also sufficiently far distant neighbours.

The point probability function $f_j(\mathbf{r})$ obeys the same symmetry requirements as those for the system of single component case. The first symmetries of cubic (fcc or bcc) alloys are 4-fold symmetries:

$$\begin{aligned} R_{4x}(x, y, z) &= (x, -z, y) \\ R_{4y}(x, y, z) &= (z, y, -x) \\ R_{4z}(x, y, z) &= (-y, x, z) \end{aligned} \quad (3)$$

and the mirror symmetries are (xy)-mirrors and (-x, -y)-mirrors. The (xy)-mirrors and (-x, -y)-mirrors are

$$\begin{cases} M_{xy}(x, y, z) = (y, x, z) \\ M_{yz}(x, y, z) = (x, z, y) \\ M_{zx}(x, y, z) = (z, y, x) \end{cases} \text{ and } \begin{cases} M_{xy}(x, y, z) = (-y, -x, z) \\ M_{yz}(x, y, z) = (x, -z, -y) \\ M_{zx}(x, y, z) = (-z, y, -x) \end{cases}, \quad (4)$$

respectively. A 4-fold symmetry changes one sign, and can be constructed by combining M_{xy} 's and M_x 's

$$\begin{aligned} M_{xy}M_y(x, y, z) &= M_{xy}(x, -y, z) = (-y, x, z) = R_{4z}(x, y, z) \\ M_{yz}M_z(x, y, z) &= M_{yz}(x, y, -z) = (x, -z, y) = R_{4x}(x, y, z) \\ M_{zx}M_x(x, y, z) &= M_{zx}(-x, y, z) = (z, y, -x) = R_{4y}(x, y, z). \end{aligned} \quad (5)$$

The inversion changes three signs and can be derived by combining three M_x 's

$$M_z M_y M_x(x, y, z) = (-x, -y, -z) = I(x, y, z). \quad (6)$$

The free energy Ω of the alloy system is given in terms of the point probability function as

$$\begin{aligned} \beta\psi(q) \equiv \frac{\Omega(q)}{NkT} = & \frac{1}{2} \beta \sum_m \sum_{jk} \int dr \epsilon_{jk}(|r - q_m|) f_j(r) \\ & + \sum_j \int dr [f_j(r) \ln f_j(r) - f_j(r)] + \sum_j \beta \lambda_j [c_j - \int dr f_j(r)]. \end{aligned} \quad (7)$$

In the above eq.(7) q is the lattice constant of the reference lattice. We denote q explicitly in (7) to indicate that $\Omega(q)$ and $\psi(q)$ are written for a fixed q . The atomic fraction at each reference lattice point is written as c_j , which is given and fixed. It is important to note that the individual $f_j(r)$ is normalized to c_j rather than to unity.

When we minimize $\beta\psi(q)$, we obtain

$$\frac{\partial(\beta\psi(q))}{\partial(f_j(r))} \equiv \frac{1}{2} \beta \sum_m \sum_j \epsilon_{jk}(|r - q_m|) + \ln f_j(r) - \beta \lambda_j = 0, \quad (8)$$

which leads to

$$f_j(r) = \exp \left[\beta \lambda_j - \frac{1}{2} \beta \sum_m \sum_j \epsilon_{ij}(|r - q_m|) \right]. \quad (9)$$

Then, the free energy of the alloy is given by a simplified form

$$\beta\psi(q) = \frac{\Omega(q)}{NkT} = \beta\psi(q) - \sum_j \int dr f_j(r) \frac{\partial(\beta\psi(q))}{\partial(f_j(r))} = \beta[\lambda_1(q)c_1 + \lambda_2(q)c_2]. \quad (10)$$

Using eq. (10) of the free energy, it is straightforward to obtain the $\psi(q)$ of the equilibrium state at a given temperature T by varying the lattice spacing of the reference lattice q : one can find the minimum of $\psi(q)$ as

$$\left(\frac{\partial \psi(T, q)}{\partial q} \right)_T = 0. \quad (11)$$

After $\psi(q)$ of the equilibrium state is obtained, one can calculate the thermal expansion and thermodynamic quantities of the alloys, and also determine the equilibrium phase diagrams. The above mentioned calculational scheme can be applied straightforwardly to the refined CD-treatments going beyond the Bragg-Williams approximation, i.e., within the context of the CVM.

FCC Alloy

The extension of the CD treatment of the previous subsection to the more refined calculations based on the cluster interactions can be done in a following manner. For the pair approximation of the CD treatment of CVM, the grand potential Ψ of the fcc alloy can be given by

$$\begin{aligned} \Psi = & 6\beta \int dr_1 \int dr_2 \sum_{ij} \epsilon_{ij}(r_1, r_2) g_{ij}(r_1, r_2) - \frac{1}{2} \beta \int dr_1 \int dr_2 \sum_{ij} \{ \mu_i + \mu_j \} g_{ij}(r_1, r_2) - \frac{S^*}{kN} \\ & - \frac{11}{2} \left(\int dr_1 \sum_i L[f_{ii}(r_1)] + \int dr_2 \sum_j L[f_{jj}(r_2)] \right) + 6 \int dr_1 \int dr_2 \sum_{ij} L[g_{ij}(r_1, r_2)] \\ & + \beta \lambda \left[1 - \int dr_1 \int dr_2 \sum_{ij} g_{ij}(r_1, r_2) \right] \\ & + 6 \int dr_1 \int dr_2 \sum_{ij} \{ A_{xil}(r_1) + A_{xjr}(r_2) \} g_{ij}(r_1, r_2) \\ & + 6 \int dr_1 \int dr_2 \sum_{ij} \{ A_{zil}(r_1) + A_{zjr}(r_2) \} g_{ij}(r_1, r_2). \end{aligned} \quad (12)$$

When we minimize the grand potential Ψ with respect to $g_{ij}(r_1, r_2)$, we obtain the basic equation of the pair probability function as

$$\begin{aligned} g_{ij}(r_1, r_2) = & \exp \left[\frac{\beta \lambda}{6} - \beta \epsilon_{ij}(r_1, r_2) + \frac{\beta}{12} \{ \mu_i + \mu_j \} \right] \{ f_{ii}(r_1) f_{jj}(r_2) \}^{11/12} \\ & \times \exp \{ A_{xil}(r_1) + A_{xjr}(r_2) + A_{zil}(r_1) + A_{zjr}(r_2) \} \quad i, j = 1, 2 \end{aligned} \quad (13)$$

When these equations are satisfied and the free energy is a minimum, the Lagrangian constant for normalization λ in eq.(12) is simply $\lambda = \Omega/kT$.

For the phase-separating case, we take the interaction parameters of the 12-6 type of Lennard-Jones potential as

$$4\epsilon^*_1 \equiv 2\epsilon_1(1,2) - \epsilon_1(1,1) - \epsilon_1(2,2) > 0, \quad (14)$$

where the individual parameters are defined by

$$\begin{aligned} \epsilon_1(1,1) &= -\epsilon^*_1 - \epsilon_{11} - \epsilon_{10} \\ \epsilon_1(2,2) &= -\epsilon^*_1 + \epsilon_{11} - \epsilon_{10} \\ \epsilon_1(1,2) &= \epsilon_1(2,1) = +\epsilon^*_1 - \epsilon_1. \end{aligned} \quad (15)$$

In the above eq. (5), the unit of energy ϵ is defined as $2e_{12} - \{e_{11} + e_{22}\} \equiv 4\epsilon > 0$.

Firstly, we investigate the phase separating curves of fcc binary alloys by using the pair approximation. In the calculations of the CD scheme of the CVM, the energy is given by the Lennard-Jones potential with the parameter values chosen appropriately for a systematic understanding of phase separation phenomena.

In Fig.1, we present the phase separating curves of fcc binary alloys for input alloy parameters, (a), (b), (e), and (f) presented in Table 1. For parameters of (e), the energy minimum position is the same as that of (a). The boundary temperature is lower for (e) than for (a), because the effective interaction energy ϵ^* is smaller for (a) than for (e). The slight asymmetry in (e) is due to the difference in the occupation probabilities caused by the difference in the energy curves of $e_{22}(r)$ and $e_{11}(r)$. The curve (d) is higher than (e) by the same effect as that makes (b) and (c) in Fig 1 higher than (a). In case of the parameter set (f) both the energy level and the energy bottom positions for B are changed by a larger amount than in (d). The short center curve is the average of the left and right branches and show how we locate $x(B)_c$ at T_c .

The above mentioned phase separating curves of fcc binary alloys can be also calculated by using the quasi-chemical tetrahedron cluster approximation, without enormously increasing the computational time. In applying the quasi-chemical tetrahedron approximation, the Lagrange multipliers α 's must be modified so as to meet the constraint relations of the 2-fold rotations \mathbf{R}_{2x} and \mathbf{R}_{2z} . We have obtained almost identical phase separating curves of binary fcc alloys, by using the quasi-chemical tetrahedron cluster approximation, in agreement with the tendency obtained by the conventional CVM without the continuous atomic displacements.

BCC Alloys

We now discuss the order-disorder phase transition of bcc alloys [10], using the CD treatment of CVM. As one of the typical examples, we consider bcc binary alloys with B2

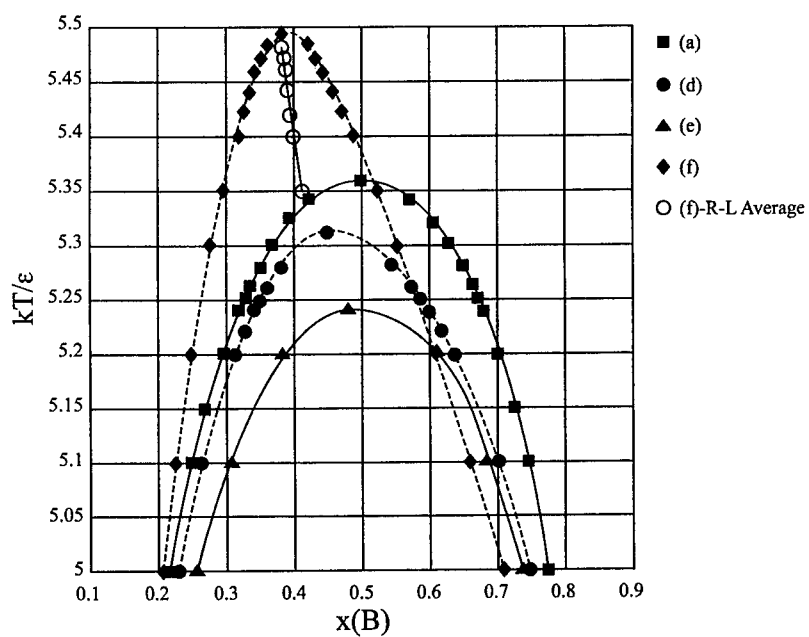


Figure 1. Phase diagrams of size-different fcc binary alloys. The interaction and size parameters are given in Table 1.

Table 1. L.-J. parameters for the phase diagrams of fcc binary alloys

	e_{110}	e_{120}	e_{220}	r_{110}	r_{120}	r_{220}
a	3.00	1.00	3.00	1.00	1.00	1.00
b	3.00	1.00	3.00	1.00	1.005	1.01
c	3.00	1.00	3.00	1.00	1.01	1.02
d	3.00	1.00	2.90	1.00	1.01	1.02
e	3.00	1.00	2.90	1.00	1.00	1.00
f	3.00	1.00	2.739	1.00	1.03	1.06

structure. We take two kinds of sublattices named L and R, and use 1 and 2 for A and B atoms, respectively. The point probability functions are denoted by $f_{iL}(\mathbf{r}_1)$ and $f_{iR}(\mathbf{r}_1)$, and the pair distribution functions by $g_{ij}(\mathbf{r}_1, \mathbf{r}_2)$, in which the first argument \mathbf{r}_1 is on L, and the second one \mathbf{r}_2 on R, respectively. The probabilities of an i-atom on L and a j-atom on R are written as x_{iL} and x_{jR} , respectively. They are written in terms of the point distribution functions and further of the pair functions, as in the treatments of fcc alloys. Then the grand potential for bcc alloys is written as

$$\begin{aligned} \beta\zeta = & 4\beta \int d\mathbf{r}_1 \int d\mathbf{r}_2 \sum_{ij} \varepsilon_{ij}(\mathbf{r}_1, \mathbf{r}_2) g_{ij}(\mathbf{r}_1, \mathbf{r}_2) - \frac{1}{2} \beta \int d\mathbf{r}_1 \int d\mathbf{r}_2 \sum_{ij} \{\mu_i + \mu_j\} g_{ij}(\mathbf{r}_1, \mathbf{r}_2) - \frac{S^*}{kN} \quad (16) \\ & - \frac{7}{2} \left(\int d\mathbf{r}_1 \sum_{i=1}^2 L[f_{iL}(\mathbf{r}_1)] + \sum_{j=1}^2 L[f_{jR}(\mathbf{r}_2)] \right) + 4 \int d\mathbf{r}_1 \int d\mathbf{r}_2 \sum_{i=1}^2 \sum_{j=1}^2 L[g_{ij}(\mathbf{r}_1, \mathbf{r}_2)] \\ & + \beta\lambda \left\{ 1 - \int d\mathbf{r}_1 \int d\mathbf{r}_2 \sum_{ij} g_{ij}(\mathbf{r}_1, \mathbf{r}_2) \right\} - 4 \int d\mathbf{r}_1 \int d\mathbf{r}_2 \sum_{ij} \{A_{x_{iL}}(\mathbf{r}_1) + A_{x_{jR}}(\mathbf{r}_2)\} g_{ij}(\mathbf{r}_1, \mathbf{r}_2) \\ & - 4 \int d\mathbf{r}_1 \int d\mathbf{r}_2 \sum_{ij} \{A_{z_{iL}}(\mathbf{r}_1) + A_{z_{jR}}(\mathbf{r}_2)\} g_{ij}(\mathbf{r}_1, \mathbf{r}_2) . \end{aligned}$$

The subsequent calculations can be done in a similar manner as those for the fcc case.

To investigate the order-disorder phase transition of bcc alloys, we take the following energy parameters:

$$e_{110}=e_{220}=3.0, e_{120}=5.0 \quad r_{110}=r_{120}=r_{220}=1.0 .$$

The energies are chosen to be appropriate for the ordering systems and the conventional pair CVM predicts that T_c is such that $kT_c/\varepsilon'=10.97$. In Fig.2, we present the calculated phase diagram exhibiting the region of ordered and disordered bcc phases. The upper curve is calculated by conventional CVM, while the lower one by the pair approximation of the CD scheme of the CVM. One can see that the critical temperature of order-disorder phase transformation of bcc alloys is reduced drastically, by about 40%, when the atomic displacements arising from the thermal lattice vibrations and the size-misfit between the constituent atoms are taken into account. Therefore, the present calculations using the CD treatment of the CVM clearly suggest that the major discrepancies reported for the cubic alloys [2,11] between the calculated and experimental transition temperatures can be removed quantitatively.

As we see in the above calculations using the CD treatment of the CVM, the critical temperatures both of phase-separating curves and order-disorder transitions of the metallic alloys are reduced significantly compared to those obtained by the conventional CVM. This indicates that the effects of thermal lattice vibrations and local lattice distortions are crucial for the calculations of alloy phase diagrams.

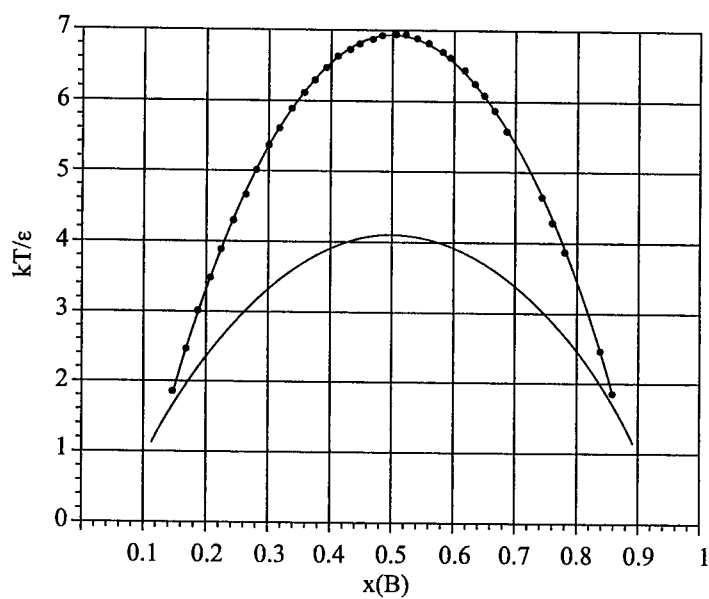


Figure 2. The order-disorder phase diagram of B2 alloys. The upper and lower curves are calculated by conventional CVM and CD scheme of CVM, respectively.

thermal average $\langle\langle I^{\alpha\beta} \rangle\rangle$ is given as [11]

$$\langle\langle I^{\alpha\beta} \rangle\rangle = n_i \frac{P_{AB}}{C_\alpha} \quad (35)$$

where n_i is the number of the nearest-neighbours, and P_{AB} the pair probability function. The pair probability P_{AB} is given by

$$P_{AB} = C_A C_B + S \eta^2 + \varepsilon_{AB}. \quad (36)$$

Here, ε_{AB} is a correlative parameter, and explicit expression of S depends on the ordered structure of the alloys. The probabilities P_i^j are determined by

$$P_A^\alpha = C_A + v_b \eta, P_A^\beta = C_A - v_\alpha \eta, P_B^\alpha = C_B - v_b \eta, P_B^\beta = C_B + v_\alpha \eta \quad (37)$$

From eqs. (14), (16) and (17) one can obtain the free energy of the UAM system as

$$\psi_i^j = 3N \left\{ \frac{u_{0i}^j}{6} + \theta \left[x_i^j + \ln(1 - e^{-2x_i^j}) \right] \right\}, \quad (38)$$

where

$$\left. \begin{aligned} u_{0i}^j &= u_{0i} + n_i \frac{P_{ii}}{2C_i} \Delta\varphi^{(0)}(r_1) - \left(n_1 \frac{P_{ii}}{C_i} \Omega_1 + n_2 P_i^j \Omega_2 \right), \\ k_i^j &= k_i + n_1 \frac{P_{ii}}{4C_i} \Delta\varphi^{(2)}(r_1) + n_2 \frac{P_i^j}{4} \Delta\varphi^{(2)}(r_2), \\ \gamma_i^j &= \gamma_{1i} + n_1 \frac{P_{ii}}{96C_i} \Delta\varphi^{(4)}(r_1) + n_2 \frac{P_i^j}{96} \Delta\varphi^{(4)}(r_2) \\ \zeta_i^j &= \gamma_{2i} + n_1 \frac{P_{ii}}{16C_i} \Delta\varphi^{(4)}(r_1) + n_2 \frac{P_i^j}{96} \Delta\varphi^{(4)}(r_2). \end{aligned} \right\} \quad (39)$$

Then, the full expression for the free energy of the ordered alloy is given by

$$\Psi = \sum_{i,j} v_j P_i^j 3N \left\{ \frac{u_{0i}^j}{6} + \theta \left[x_i^j + \ln(1 - e^{-2x_i^j}) \right] \right\} + k_B N T \sum_{i,j} v_j P_i^j \ln P_i^j. \quad (40)$$

The thermodynamic quantities of the AB alloys can be derived from the free energy of eq.(40). Specifically, for the ordered B2 alloys, the free energy can be written as

$$\begin{aligned} \Psi &= C_A \Psi_A + C_B \Psi_B + \frac{3N\theta}{8} \left(\frac{X_A}{k_{AA}} - \frac{X_B}{k_{BB}} \right) \left[n_1 P_{AB} \Delta\varphi^{(2)}(r_1) + n_2 (C_A C_B - v_\alpha v_\beta \eta^2) \Delta\varphi^{(2)}(r_2) \right] \\ &\quad - \frac{N}{2} \left[n_1 P_{AB} \Omega_1 + 2n_2 (C_A C_B - v_\alpha v_\beta \eta^2) \Omega_2 \right] - TS_c, \end{aligned} \quad (41)$$

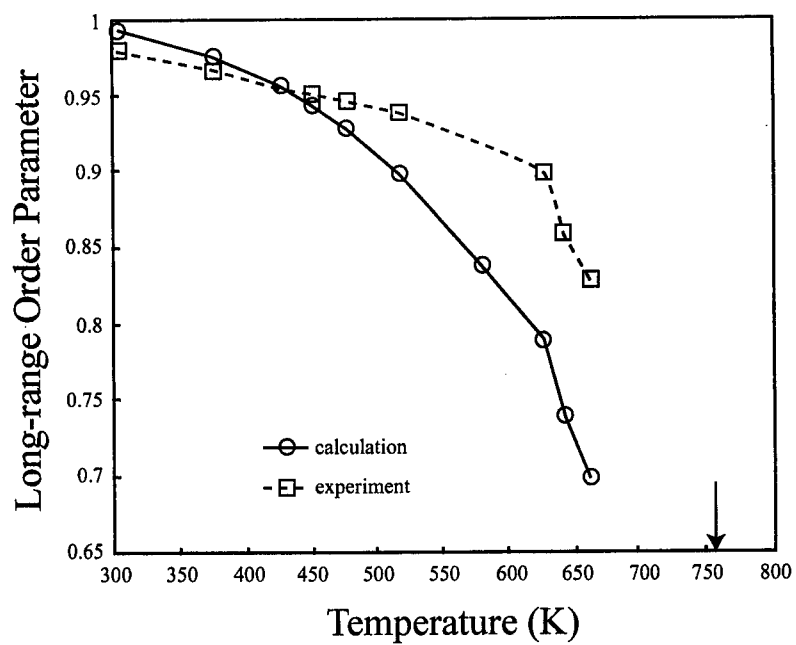


Figure 3. The temperature dependence of the long-range order parameter for Cu_3Au alloy. The arrow indicates the transition temperature obtained by conventional calculation without including the effects of the continuous atomic displacements.

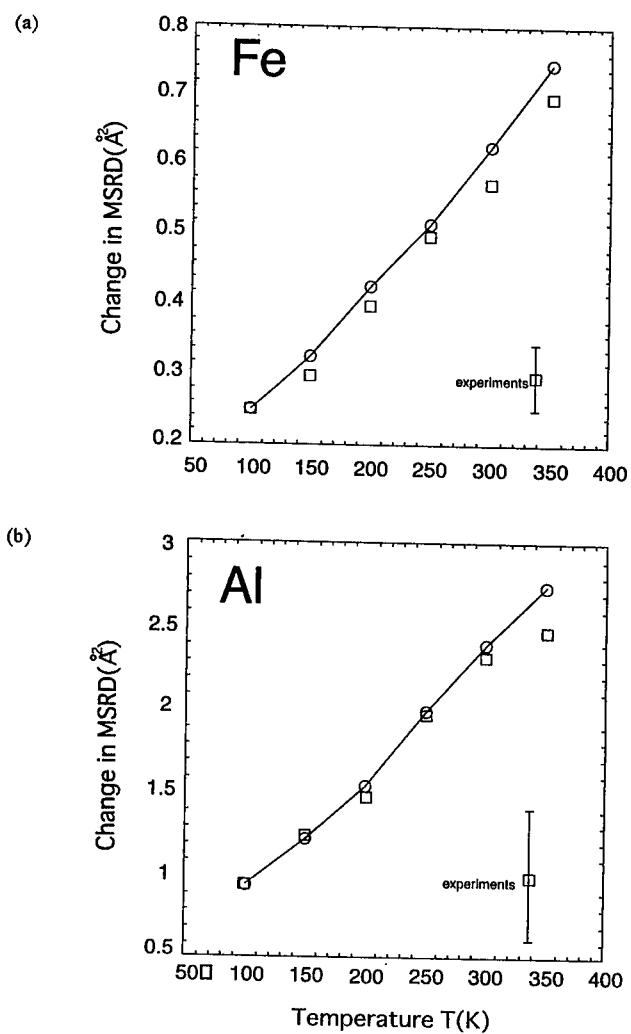


Figure 4. The changes in the MSRD of Fe and Al atoms between the ordered and disordered phases of Fe_3Al , in unit of 10^{-3}\AA^2 .

where Ψ_A and Ψ_B represent the free energies of the metals A and B, respectively, and the remaining terms are added for the description of the alloying effects.

To demonstrate the applicability of the moment method outlined above, we have calculated the critical temperature of the order – disorder phase transition of Cu_3Au alloys. In Fig.3, we present the temperature dependence of the LRO parameter for Cu_3Au alloy, together with the experimental results. The arrow in the figure indicates the critical temperature obtained by the conventional method without continuous atomic displacements. One can see in Fig.3 that the inclusion of continuous atomic displacements lowers the critical temperature quite significantly and play an important role in determining the critical temperature of the order – disorder transitions.

We have also investigated the change in the vibrational properties of the Fe_3Al alloy during the order-disorder transition, using the statistical moment method. In Fig.4, we present the changes in the mean square relative displacement (MSRD) of Fe and Al atoms between the order and disordered states of Fe_3Al alloy. The MSRD is given in unit of 10^{-3}\AA^2 . The MSRD both of Fe and Al atoms in the disordered phase are much larger ($\sim 30\%$) than those of the ordered states. This theoretical finding is related to the anisotropy of the lattice vibrations and of the characteristic thermal lattice expansion in the ordered and disordered states, and the details will be presented elsewhere.

CONCLUSION

The continuous displacement treatment of the CVM has been applied to the calculations of phase equilibria of binary alloy systems. The phase separating diagrams of fcc alloys calculated within the pair and quasi-chemical tetrahedron cluster approximations show that the transition temperatures are drastically reduced compared to those of the conventional CVM. The CD treatment of the CVM has also been applied to investigate the order-disorder phase transition in bcc alloys. In general, it has been shown that the phase transition temperatures are reduced drastically when the continuous atomic displacements are taken into account. We have found that a similar tendency is also obtained by using the moment method in the statistical dynamics which allows us to include the quantum mechanical calculations of the lattice vibrations. The large discrepancy between the experimental and theoretical phase diagrams calculated so far by the conventional CVM and ab initio electronic theory (e.g., CuAu alloy) can be removed by applying the present theoretical scheme.

REFERENCES

1. R. Kikuchi, *A Theory of Cooperative Phenomena*. Phys. Rev. **81**, (1951) 988.
2. T. Horiuchi, S. Takizawa, T. Suzuki, and T. Mohri, *Computer-Simulation Of Local Lattice Distortion In Cu-Au Solid-Solution*, Metall. Trans. **26A**, (1995) 11.
3. R. Kikuchi and K. Masuda-Jindo, *The continuous displacement CVM treatment of alloy systems*, Comp. Mater. Sci. **8**, (1997) 1.

-
4. V.V. Hung and N.T. Hai, *Investigation of the Thermodynamic properties of Anharmonic Crystals with Defects and Influence of Anharmonicity in EXAFs by the Moment Method*, Int. J. Mod. Phys. **B12**, (1998) 191.
 5. J. M. Sanchez, J. P. Stark and V. L. Moruzzi, *1st-Principles Calculation of the Ag-Cu Phase-Diagram*, Phys. Rev. **B44**, (1991) 5411.
 6. M. Asta, R. McCormack and D. de Fontaine, *Theoretical-Study of Alloy Phase-Stability in the Cd-Mg System*, Phys. Rev. **B48**, (1993) 748.
 7. L. Anthony, J. K. Okamoto and B. Fultz, *Vibrational Entropy of Ordered and Disordered Ni₃Al*, Phys. Rev. Lett. **70**, (1993) 1128.
 8. G. D. Garbulsky and G. Ceder, *Effect of lattice-vibrations on the ordering tendencies in substitutional binary-alloys*. Phys. Rev. **B49**, (1994) 6327.
 9. M. W. Finnis and J. E. Sinclair, *A Simple Empirical N-Body Potential for Transition-Metals*, Phil. Mag. **50A**, (1984) 45.
 10. F. Cleri and V. Rosato, *Tight-Binding Potentials For Transition-Metals And Alloys*, Phys. Rev. **B48**, (1993) 22.
 11. R. Kikuchi and K. Masuda-Jindo, *Calculation of alloy phase diagrams by continuous cluster variation method*, Comp. Mater. Sci., **14**, (1999) 295.
 12. A.A. Smirnov, "Molekulyarno-Kineticheskaya Teoriya Metallov (Nauka, Moskva, 1966) (in Russian).

MAXIMIZATION OF CLUSTER ENTROPIES VIA AN IRREVERSIBLE ALGORITHM: APPLICATIONS TO THE CLUSTER VARIATION METHOD

Victor L. Vinograd, Udo Becker, and Andrew Putnis

Institute of Mineralogy, Münster University
D-48149, Münster, Germany

ABSTRACT

The problem of searching for the free energy minimum in cluster-variation models which take account of nearest-neighbor (*nn*) interactions can be reduced to two separate tasks:

- 1) entropy maximization constrained by fixed *nn* pair correlation functions,
- 2) free energy minimization with respect to the *nn* pair correlation functions.

The first task reduces to the maximization of entropy of a basic cluster, with respect to the correlation functions which correspond to all the subclusters larger than the pair. The simplification becomes possible with the use of an irreversible algorithm for the cluster entropy maximization. With the help of the irreversible algorithm the cluster entropy can be found directly as a function of the *nn* pair correlation functions, avoiding explicit introduction of correlation functions of higher-order.

The significant decrease in the number of the cluster variables permits an easy evaluation of CVM approximations based on large basic clusters. The method is discussed in relation to the two-dimensional (square lattice) Ising model for which a series of approximations (up to a 16-point basic cluster) is developed.

INTRODUCTION

Many problems in materials science require modeling of thermodynamic properties of lattice systems with order/disorder. The simplest example of such a system is a binary (A_xB_{1-x}) alloy, where the nearest-neighbor A and B atoms are assumed to interact with a nonzero energy. Depending on the sign and value of the interaction constant J ($J = 2e(AB) - e(AA) - e(BB)$), temperature (T), composition (x) and lattice topology, the system can develop various ordering phenomena such as short-range ordering, long-range ordering, or phase separation. If the lattice geometry is fixed, the equilibrium properties of the system correspond to the global minimum of the Helmholtz free energy function

$$F = E - kT \ln W = E - TS \quad (1)$$

where E is the configurational energy and W is the number of distributions (configurations) of the atoms on lattice sites which have the energy E .

When the interactions are restricted to the nearest neighbor pairs only, the configurational energy E is a simple function of probabilities of the nearest neighbor pairs and J , while W is the number of configurations of A and B that satisfy given values of the pair probabilities. The enumeration of configurations is the most difficult task. W depends not only on the pair probabilities but also on the lattice topology. Exact solution is possible only for one- and two-dimensional lattices¹, therefore an approximate treatment is necessary in the general case. The cluster variation method² (CVM) gives the most reliable way of developing an approximate analytical solution to the problem. It approximates the total entropy as a linear combination of entropy terms related to clusters composed of a reasonably small number of points. The enumeration of atomic configurations of small clusters can be done more easily.

The problem of the enumeration of configurations of equivalent non-interacting clusters reduces to the determination of probabilities of all distinct configurations within a single cluster as a function of given pair probabilities. For example, the entropy of a 4-point square cluster (in fact, the entropy of N equivalent clusters) can be written as follows

$$S_{\text{square}} = -kN \sum_{i,j,k,l} P_{ijkl}^{\text{sq}} \ln P_{ijkl}^{\text{sq}} \quad (2)$$

where P_{ijkl} is a probability of a cluster configuration $ijkl$ where each of the indexes i, j, k, l can be either 1 or -1 value depending on whether atom A or B occupies the site. The probability distribution of point and pair clusters is described with the help of two correlation functions³ as follows

$$P_i = \frac{1}{2} (1 + i\xi_1) \quad (3)$$

$$P_{ij} = \frac{1}{2^2} (1 + (i+j)\xi_1 + ij\xi_2) \quad (4)$$

while for the square cluster five correlation functions (CF) are needed:

$$P_{ijkl}^{\text{sq}} = \frac{1}{2^4} (1 + (i+j+k+l)\xi_1 + (ij+jk+kl+li)\xi_2 + (il+kj)\xi_{2\text{sq}} + (ijk+jkl+kli+lji)\xi_{3\text{sq}} + ijkl\xi_{4\text{sq}}) \quad (5)$$

The description can be further extended to clusters composed of a larger number of points, however, the number of CF rapidly increases with the cluster size. In fact, one has to assign CF to all topologically distinct subclusters³ of a given cluster and then to determine their equilibrium values by minimizing Eq. 1 with respect to the full set of CF. The difficulty of this procedure increases with the number of CF.

Much effort has been put into developing simplified versions of the CVM where the main requirement was the reduction of the number of the independent variables. One approach^{4,5} treats the basic cluster configurations as different molecules in a quasi-chemical equilibrium with a gas phase of A and B particles. Such a treatment becomes possible when the energy of the total configuration is expressed as an additive sum of the cluster energies (the clusters do not overlap, or overlap through point subclusters). The probabilities of cluster configurations can be then written as functions of "chemical potentials" of A and B in the gas phase, the configuration energy and the temperature. The number of the independent variables becomes equal to the number of point correlation functions.

Another approach^{6,7} consists in equilibrating the basic cluster with a subcluster assuming that the subcluster probability distribution (PD) is fixed. Such a treatment is advantageous when the energy of the cluster is expressed as an additive sum of the subcluster energies. The equilibrium between the basic cluster and the subcluster is then defined by the

maximum entropy of the basic cluster at the fixed subcluster PD. In this case the basic cluster probabilities can be found as functions of the subcluster PD. For example, when the range of interactions is limited to first neighbors, the probability of a square cluster can be found as a function of the *nn*-pair probabilities. The number of the independent variables then reduces to the number of the pair CF.

The present paper describes a method of constructing the basic cluster PD in an equilibrium with a given subcluster PD. The construction scheme is fully based on the so-called superposition operation which is explained in the next paragraph. The basic cluster PD will be calculated in two stages. At first we will calculate an initial basic cluster PD which is not constrained by the condition of the maximum entropy. Later we will introduce a sequence of the superposition operations, namely a stochastic irreversible algorithm which converts the initial cluster PD into the maximum entropy PD. The irreversible algorithm will be then used to construct a series of CVM approximations of increased accuracy for the Ising square lattice model.

SUPERPOSITION OPERATION

The superposition operation, illustrated in Fig. 1, enables one to write the probability of a configuration of a cluster C as a combination of the probabilities of configurations of smaller clusters A1 and A2

$$P(C) = P(A1)P(A2)/P(B) \quad (6)$$

Here $P(B)$ is the probability of subcluster B, which is common to A1 and A2. Eq. 6 can be easily derived⁸ from Bayes formula for the probability of a complex event. It is important to realize that Eq. 6 is only valid (the probability of the cluster C is normalized to 1) when the probability distribution of the subcluster B is exactly the same in A1 and A2. Therefore, when deciding whether two given clusters can be combined into a bigger one, one must be sure that this condition is fulfilled.

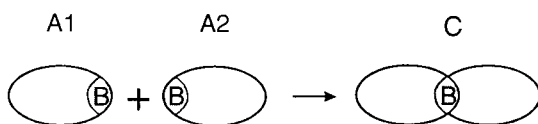


Figure 1. Superposition operation on cluster probabilities. When the clusters A1 and A2 have a common subcluster B the cluster probabilities can be combined according to Eq. 6 to obtain the probability distribution of the supercluster C.

Evidently, the distribution of the subcluster B will be the same in A1 and A2 if these clusters intersect through a single point or a single pair (we assume that the point and pair distribution is fixed, i.e. the same in all the clusters) or when A1 and A2 are symmetrical images of each other and B lies in the plane of symmetry. Figure 2 shows examples of the superposition operations. A chain fragment *ijk* can be constructed from pair clusters *ij* and *jk* connected through the common point *j*.

$$P_{ijk} = P_{ij}P_{jk} / P_j \quad (7)$$

The square cluster probability can be then constructed from probabilities of symmetrically related *ijk* and *ilk* chain fragments

$$P_{ijkl}^{sq} = P_{ijk}P_{ilk} / P_{i,k} \quad (8)$$

The probability of the common subcluster $i.k$ is given as follows

$$P_{i.k} = \sum_j P_{ijk} = \sum_l P_{ilk} \quad (9)$$

The procedure of the derivation of the cluster entropy can be easily generalized for the case of a nonzero long-range ordering (LRO). To introduce the LRO one has to specify two different point probabilities

$$P_{i\alpha} = \frac{1}{2}(1 + i\xi_{1\alpha}) \quad (10)$$

$$P_{i\beta} = \frac{1}{2}(1 + i\xi_{1\beta}) \quad (11)$$

and rewrite the Eq. 4 as follows

$$P_{i\alpha j\beta} = \frac{1}{2^2}(1 + i\xi_{1\alpha} + j\xi_{1\beta} + ij\xi_2) \quad (12)$$

The superposition operation must be then applied to the pair probabilities defined by Eq. 12.

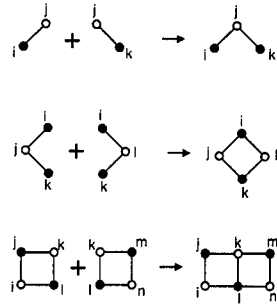


Figure 2. Examples of the superposition operation on different clusters. Black and white points show A-rich and B-rich sublattices.

The superposition operation (Eq. 6) can be also applied to clusters larger than pairs. For example, one can easily construct probability distributions of various fragments of chains of squares as shown in Fig. 3. Then by applying the superposition to the chain fragments one can arrive at clusters of various shape. Using the same principle one can construct various three-dimensional clusters^{7,8}.

It is important to note that the probability distributions of all the clusters shown in Fig. 2 and Fig. 3 are the functions of the same set of $\xi_{1\alpha}$, $\xi_{1\beta}$ and ξ_2 parameters.

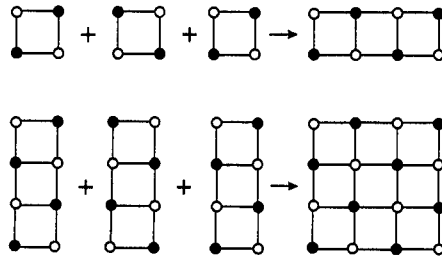


Figure 3. Construction of the initial probability distribution of a 16-point cluster through a sequence of superposition operations.

CALCULATION OF THE TOTAL ENTROPY

The superposition operation, or rather its extension to an infinitely long chain of superposed clusters, plays the central role in the derivation of CVM equations for the total lattice entropy. In the thermodynamic limit Eq. 1 can be written⁹ as follows

$$F = E - kT \ln(1/P_{\text{typ}}) \quad (13)$$

where P_{typ} is the probability of a typical configuration constrained by the energy E . In the one-dimensional case the lattice can be considered as an infinite chain of superposed pairs. Noting that Eq. 7 can be generalized for longer chain fragments

$$P_{ijkl} = P_{ij} P_{jk} P_{kl} / P_j P_k \quad (14)$$

and that the numbers of P_{ij} and P_j multipliers become equal in the limit $N \sim N_A$

$$P_{\text{typ}}^{1D} = \prod_{i,j} (P_{ij} / P_j)^{NP_j} \quad (15)$$

one finds the entropy of the chain of N pairs as follows

$$S_{1D} = k \ln(1/P_{\text{typ}}^{1D}) = kN \sum_j P_j \ln P_j - kN \sum_{i,j} P_{ij} \ln P_{ij} = S_{\text{pair}} - S_{\text{point}} \quad (16)$$

In analogous way the entropy of the chain of N squares (the ladder cluster) is written

$$S_{\text{ladder}} = kN \sum_{k,l} P_{kl} \ln P_{kl} - kN \sum_{i,j,k,l} P_{ijkl}^{\text{sq}} \ln P_{ijkl}^{\text{sq}} = S_{\text{square}} - S_{\text{pair}} \quad (17)$$

The important similarity of Eqs. 16 and 17 is that the overlapped chain elements (points in the 1D chain and pairs in the ladder) give negative contribution to the total chain entropy. Following this rule, one can consider the square lattice as an infinite chain of ladders¹⁰ overlapped through single chains, and write its entropy as follows

$$S_{\text{sq-lat}}^{\text{"4"}} = S_{\text{ladder}} - S_{1D} = S_{\text{square}} - 2S_{\text{pair}} + S_{\text{point}} \quad (18)$$

Following the same procedure, we have derived entropy equations for higher order approximations for the square lattice. For example, starting from a 9-point (four squares) basic cluster one can construct a chain composed of 9-point squares overlapped through 6-point clusters. At the same time, one notes that two such chains in the square lattice overlap through a ladder cluster which, in turn, can be constructed as a chain of 6-point clusters overlapped through square clusters. The obvious result is

$$S_{\text{sq-lat}}^{\text{"9"}} = S_{9\text{-point}} - 2S_{6\text{-point}} + S_{\text{square}} \quad (19)$$

The combinatorial factors of the considered approximations are given schematically in Fig. 4. Logarithms of the terms in curly brackets are proportional to the cluster entropies.

$\frac{\{\square\} \{\leftrightarrow\}}{\{\leftrightarrow\}^2}$ <p>1.069</p>	$\frac{\{\square\square\} \{\leftrightarrow\leftrightarrow\}}{\{\square\} \{\leftrightarrow\leftrightarrow\}}$ <p>1.061</p>	$\frac{\{\square\square\square\} \{\leftrightarrow\leftrightarrow\leftrightarrow\}}{\{\square\square\} \{\leftrightarrow\leftrightarrow\leftrightarrow\}}$ <p>1.059</p>
$\frac{\{\square\square\square\} \{\square\}}{\{\square\square\}^2}$ <p>1.020</p>	$\frac{\{\square\square\square\square\} \{\square\square\}}{\{\square\square\} \{\square\square\square\}}$ <p>1.010</p>	$\frac{\{\square\square\square\square\square\} \{\square\square\square\}}{\{\square\square\square\} \{\square\square\square\square\}}$ <p>1.009</p>
$\frac{\{\square\square\square\square\} \{\square\square\}}{\{\square\square\square\}^2}$ <p>0.989 "16A"</p>	$\frac{\{\square\square\square\square\square\} \{\square\square\}}{\{\square\square\} \{\square\square\square\square\}}$ <p>1.023</p>	
$\frac{\{\square\square\square\square\square\} \{\square\square\}}{\{\square\square\square\} \{\square\square\square\}}$ <p>1.009 "16B"</p>	$\frac{\{\square\square\square\square\square\square\} \{\square\}}{\{\square\} \{\square\square\square\square\}}$ <p>1.029</p>	

Figure 4. Combinatorial factors of CVM approximations considered in this study. The numbers below each factor show the critical temperatures calculated for the square-lattice Ising model scaled to Onsager's result ($4kT/J = 2.26919$). The numbers for the critical temperatures are precise within 0.1%. For the sake of simplicity, the combinatorial factors are shown for the disordered phase. In the ordered case more cluster terms are needed to account for cluster asymmetry due to ordering.

One can note that in the case of large clusters there is a different possibility in choosing the range of the cluster overlap in the cluster chains. We will discuss this subject later. It is important to note, however, that so far as the superposition operation lay in the basis of the derived approximations, the overlapped clusters which appear in these formulas are considered as subclusters of the basic clusters. The probabilities of the overlapped elements must be then calculated from the probabilities of the basic clusters through the summations over the missing indexes. For example, the probability distribution of a 6-point subcluster is derived from the probability of a 9-point basic cluster as follows

$$P_{ijklmn} = \sum_{q,p,r} P_{ijklmnqpr} \quad (20)$$

It is important to mention that Eq. 18 (as well as Eq. 19) implies an approximation because the S_{1D} term is not constructed as a subcluster of the ladder cluster. Accurate derivation of the S_{1D} term would require summation over the indexes of one "string" of the ladder.

Eqs. 18 and 19 are valid for the disordered phase. In the ordered case there could appear basic clusters or their subclusters with different types of ordering schemes. For example there exist two different types of ordered 9-point basic cluster (Fig. 5).

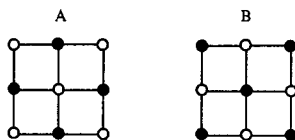


Figure 5. Ordered 9-point clusters of different types.

The equation for the lattice entropy must be modified accordingly

$$S_{\text{sq-lat}}^{\text{"9",lro}} = \frac{1}{2} (S_{9\text{-point A}} - 2S_{6\text{-point A}} + S_{\text{square A}}) + \frac{1}{2} (S_{9\text{-point B}} - 2S_{6\text{-point B}} + S_{\text{square B}}) \quad (21)$$

where probabilities (and the entropies) of different 6-point and 4-point subclusters are calculated from probabilities of different basic clusters.

ASYMMETRY PROBLEM

We have discussed so far the superposition operation and how it is used to calculate basic cluster probabilities. We have also discussed the algorithm of derivation of an equation for the lattice entropy from the basic cluster entropy. But we did not mention one important problem: the basic cluster probabilities resulting from the superposition operation are not yet suitable for the substitution into the lattice entropy equation. The problem is that the superposition operation does not necessarily result in the maximum entropy probability distribution of the supercluster C. For example, the superposition (Eq. 8) constrains only the nn pair probabilities in the square cluster to be the same as in the parent clusters A1 and A2, while probabilities of higher order neighbor pairs are not constrained to be the same. In fact, the second neighbor pairs ik and jl in the square cluster $ijkl$ are created by different superposition operations (Fig. 2) and their probability distributions are different. Because of the asymmetry of higher order correlations, the basic cluster entropy does not reach its maximum.

At the same time, the typical configuration must be characterized by the maximum entropy. Intuitively, one would expect that the best result would be obtained when the typical configuration is constructed from basic clusters having maximum symmetry and maximum entropy. Although this assumption is not generally true (see the Discussion), it enables one, as we will show, to construct remarkably accurate CVM approximations.

ANNEALING ALGORITHM

The aim of the "annealing" algorithm is to convert the basic cluster probability distribution resulting from a single "superposition" operation into the maximum entropy distribution. The annealing algorithm is defined as a sequence of decomposition, superposition and rotation operations applied to the same basic cluster probability distribution. Before the application of the next superposition operation, the basic cluster C is decomposed into subclusters A1, A2 and B according to a certain rule. The superposition operation (Eq. 6) is used then to restore the cluster to the previous shape. After that the cluster probability distribution is "rotated" (this is performed with the help of a circular shift of the indexes) and the sequence of decomposition and superposition operations is repeated. Each annealing step irreversibly modifies the cluster probability distribution.

The remarkable result of the annealing algorithm is a rapid "equilibration" of all high order correlations within the basic cluster, while all the nn pair correlations remain the same. The cluster probability distribution becomes more and more symmetric with each annealing step and its entropy rapidly reaches the maximum. This effect has been already

demonstrated⁷ for clusters of high symmetry such as square, hexagon, cube and octahedron. However, the described annealing algorithm⁷ was not applicable to less symmetric clusters. Here we describe a "general" annealing algorithm (Fig. 6) which can be applied to clusters of any topology.

The algorithm consists of the following cycle.

For the cluster points i from 1 to n :

- 1) Define the current point i plus all its nearest neighbors as a subcluster A1. Define the subcluster A2 as all the points of C excluding the current point. Define the subcluster B as all the points of A1 excluding the current point. Note that B is a common subcluster to A1 and A2.
- 2) Calculate the probability distributions of A1, A2 and B by taking sums over the points of C not included in A1, A2 and B respectively.
- 3) Calculate the new probability distribution of the cluster C using Eq. 6.

$i=i+1$.

Repeat the whole cycle several times.

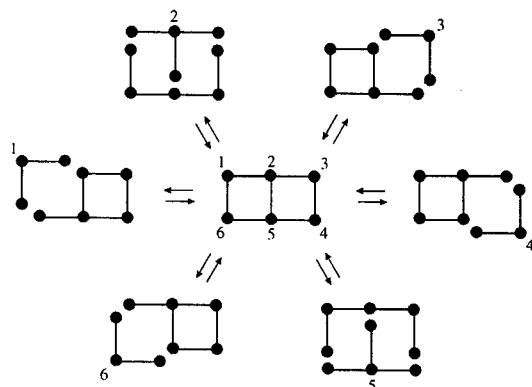


Figure 6. Annealing algorithm applied to a 6-point cluster. At each annealing step the cluster is destroyed into its subclusters A1 and A2 and then restored to the previous shape.

The annealing algorithm can be understood as an irreversible stochastic process similar to a Markov chain. The sequence of operations is irreversible because it involves the summation operation (step 2) during which certain correlations between the points of the cluster C are being lost. These correlations are then restored during the step 3 but in a more random way, because they are now mediated by the cluster B. One can also explain the entropy increase referring to the second law of thermodynamics.

An important feature of the algorithm is that the correlations between the nearest neighbors remain unchanged. This happens because each nn pair of the cluster C is being included into A1, or into A2, or into the both subclusters and thus is not modified. The final distribution of the cluster C is thus constrained by the same set of the correlation functions which have been used in the initial construction of the cluster.

The probability distribution of the cluster C remains correctly normalized in the course of the algorithm, because the superposition operation (Eq. 6) is always correctly defined (A1 and A2 are derived from the same cluster C and, therefore, subcluster B is bound to have the same probability distribution in A1 and A2).

The described algorithm can be applied to clusters of any topology and size. The only cluster-specific information required (in addition to the initial cluster PD) is a connectivity matrix. This is a matrix of n^2 integers (0's and 1's) where nonzero elements correspond to pairs of nearest-neighbor points within the cluster. Figure 6 illustrates the algorithm for a 6-point cluster.

The algorithm also works well for clusters that contain equilateral triangles (e.g. an octahedron) or tetrahedra as subclusters. In the course of the algorithm PD of these subclusters remains unchanged. But it is important to note that the probabilities of these subclusters cannot be constructed from pair probabilities and thus must be initially specified by full sets of the correlation functions. For example, to evaluate the PD of an octahedron, one would need to specify three correlation functions ξ_1 , ξ_2 and $\xi_{3\text{tri}}$ of the triangle. On the contrary, the evaluation of PD of square and cubic clusters (in the absence of LRO) requires only ξ_1 and ξ_2 .

The speed of conversion to an equilibrium distribution depends on the cluster size and on values of the pair correlation functions. When these values approach the state of complete disorder, the convergence requires very few annealing cycles. Naturally, it takes longer to anneal large clusters. But even for 16-point clusters the procedure requires only a few seconds on a regular workstation. A FORTRAN code of the general annealing algorithm is available from the authors.

RESULTS

We have used the described algorithm to maximize entropies of various clusters of a square net under the constraint of fixed pair CF. The maximum entropy probability distributions of these clusters were then substituted into CVM free energy equations corresponding to a set of approximations and the free energies were minimized with the respect to the pair CF. The combinatorial factors of these approximations together with the calculated temperatures of the order-disorder transitions scaled to the exact result of Onsager¹ are given in Fig. 4. Figure 7 plots the equilibrium temperature dependence of the long-range order parameter Q

$$Q = (P_{A\alpha} - P_{A\beta}) / (P_{A\alpha} + P_{A\beta}) \quad (22)$$

for a selected list of approximations. Figure 8 plots the equilibrium entropy resulting from two different 16-point approximations. In these calculations the step in the reduced temperature (kT/J) was 0.001. Thus the presently calculated values of the critical temperatures are precise within 0.1%.

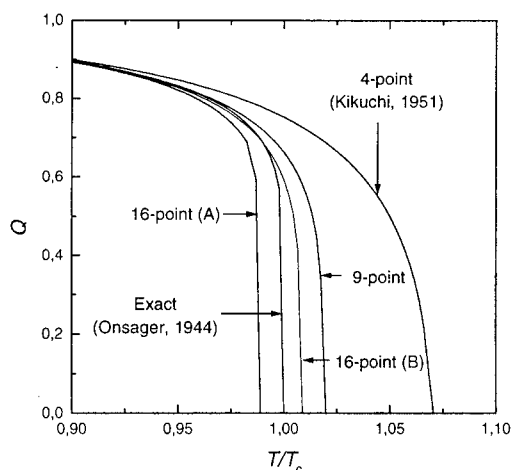


Figure 7. Temperature dependence of the long-range order parameter in the square lattice model according to a selected set of approximations and to the exact result. The temperature values are scaled to Onsager's result.

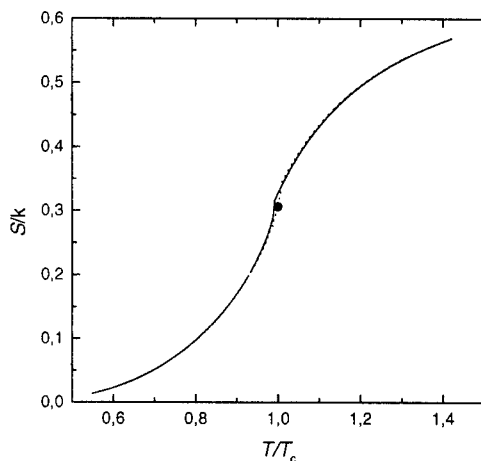


Figure 8. Temperature dependence of the entropy in the square lattice model according to "16A" (solid line) and "16B" (dotted line) approximations. The solid dot shows the exact entropy at the critical temperature.

DISCUSSION

The advantage of using the annealing algorithm consists in the fact that the number of the necessary independent parameters reduces to the set of the nn pair CF even when the basic cluster contains as many as 16 points. This greatly simplifies the free energy minimization procedure and facilitates the use of large basic clusters. As it could be expected, the degree of accuracy increases with the cluster size. The series of approximations for the square lattice entropy based on isometric 4-, 9- and 16-point clusters tends to approach the exact result (Fig. 4).

For the single square approximation the present method gives the same result ($4kT_c/J = 2.426$) as the traditional CVM², however, in the case of higher order approximations the two methods are not fully comparable. The traditional CVM performs the minimization of the total free energy, which is equivalent to the maximization of the *total* lattice entropy at the constraint of fixed pair probabilities. But the present method maximizes only the basic cluster entropy at the constraint of fixed pair probabilities. These two conditions are not the same when basic clusters overlap through elements larger than pairs. Evidently, the maximum of the total entropy requires certain balance between the entropy of the basic cluster and the entropy of the overlapped elements. This balance is achieved when the basic cluster entropy is not at the maximum.

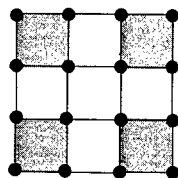


Figure 9. Schematic illustration of the "surface effect". The entropies of the square subclusters in the annealed 16-point cluster decrease in the succession dark-gray, gray and white. The entropy of the central (white) subcluster approaches the entropy which would have been observed if the given subcluster was located in an infinite lattice.

Nevertheless, the present method allows us to achieve a very high accuracy with respect to the exact result. This apparently happens due to a cancellation of errors. In the present approach we construct the typical configuration from *isolated* basic clusters. The maximum entropy of an isolated cluster is certainly higher than the entropy of a cluster of the same shape located in a continuous lattice. One can show that the "partial" entropies of the square subclusters of an annealed isolated 16-point basic cluster (Fig. 9) are not all the same and that the subclusters located closer to the cluster periphery have higher entropies. This "surface effect" is caused by the fact that atoms at the cluster boundary have more degrees of freedom. Thus one would expect that the construction using isolated annealed clusters would overestimate the total entropy. On the contrary, the total entropy is usually underestimated in our approach and the transition temperature is overestimated. This happens because the overlapped elements give negative contributions to the total entropy and these overlapped elements are represented by the subclusters which have high partial entropy. This effect tends to outweigh the positive "excess" entropy of basic clusters.

Our results show that the fortuitous compensation of the errors in positive and negative terms occurs when the overlapped regions are maximized. We observe that in the series of approximations based on the 12- and 15-point clusters the result gradually improves and the critical temperature approaches the correct result from above when the area of the overlap increases. The 16-point approximation series shows that the maximum overlap in fact overcorrects the negative term and causes overshooting of the critical temperature (16A approximation). Nevertheless, this approximation is still one of the best in regard to the minimum absolute error in the critical temperature.

The present results suggest that a successful approximation may not necessarily describe correctly the statistical properties of a given cluster in a given lattice. The most important is a good balance between the positive and negative entropy terms, while both terms could be inaccurate. Obviously, the safest strategy to achieve such a balance is to increase the cluster size. With an increase of the size of the basic cluster there appear more possibilities for compensating the errors. Moreover, with an increase of the cluster size the "surface effect" decreases and the entropy of an isolated cluster approaches the "correct" entropy of the cluster in a continuous lattice.

To minimize the "surface effect", it appears necessary to increase the cluster size in two directions. In the one-dimensional series (based on squares) the "surface effect" is apparently not minimized and the series converges to a result which is only slightly better than the original single square approximation. On the contrary, in the traditional method (total entropy maximization) the surface effect can be minimized via an optimal interplay of all the correlation functions. It appears that using the traditional method one can approach the exact result even by increasing the basic cluster in one direction only¹¹. According to the comment of Kikuchi and Brush¹¹, an infinite chain will correspond to Onsager's method¹. Apparently, the traditional CVM approach is more flexible in the search for the optimal compensation of the positive and negative terms.

However, this advantage of the traditional method remains illusive, because even for one-dimensional clusters, one would have to introduce a lot of variables which will eventually require to limit the cluster size. The increase of the cluster size in the present method is much less costly because mathematical complexity remains the same, only the computation time increases. We have demonstrated that with the present method one can easily achieve a degree of accuracy (1% error) that improves the best achievements of the traditional method.

In this paper we limited the discussion to the nearest-neighbor Ising model. However, the annealing algorithm may also be used when the range of interactions exceeds the nearest-neighbors. In such cases one has to construct the initial cluster PD starting from a subcluster which includes all the interactions. For example, the 9-point cluster in the BCC lattice must be constructed from "asymmetric triangles" and these triangles must be

described by the full set of triangle CF. The annealing algorithm must be modified in the way that the second-neighbor bonds are treated on equal basis with the first-neighbor ones.

We conclude that the present method is a reliable technique for modeling Ising-type systems with a limited interaction range.

ACKNOWLEDGEMENTS

The work benefited from daily discussions on the subject with R. J. Harrison. We acknowledge financial support from the Deutsche Forschungsgemeinschaft (Grant Pu 153/1-4).

REFERENCES

1. L. Onsager. Crystal statistics. I. A two-dimensional model with an order-disorder transition. *Phys. Rev.* 65: 117 (1944).
2. R. A. Kikuchi. Theory of cooperative phenomena. *Phys. Rev.* 81: 988 (1951).
3. J. M Sanchez and D. de Fontaine. The fcc Ising model in the cluster variation approximation. *Phys. Rev. B*, 17: 2926 (1978).
4. W.A. Oates, F. Zhang, S-L. Chen and Y.A. Chang. Improved cluster-site approximation for the entropy of mixing in multicomponent solid solutions. *Phys. Rev. B*, 59: 11222 (1999).
5. V.G. Vaks and G.D. Samoluyk. On accuracy of different cluster models in describing phase transitions in fcc alloys. *JETP*, 88: 89 (1999).
6. A.G. Schlijper and J. Westerhof. Improved cluster variation approximations by extension of local thermodynamic states. *Phys. Rev. B*, 36: 5458 (1987).
7. V. L. Vinograd, S. K. Saxena and A. Putnis. Calculation of the probability distribution of basic clusters involved in cluster variation approximations to the Ising model. *Phys. Rev. B*, 56: 11493 (1997).
8. V. L. Vinograd and A. Putnis. The description of Al,Si ordering in aluminosilicates using the cluster variation method. *Amer. Mineral.* 84: 311 (1999).
9. Z. Alexadrowicz. Stochastic models for the statistical description of lattice systems. *J. Chem. Phys.* 55: 2765 (1971).
10. D.de Fontaine. Configurational thermodynamics of solid solutions. *Solid State Phys.* 34: 73 (1979).
11. R. A. Kikuchi and S. G. Brush. Improvement of the cluster-variation method. *J. Chem. Phys.* 47: 195 (1967).

CVM CALCULATION OF THE SOLID-STATE EQUILIBRIA IN THE Fe-Co PHASE DIAGRAM

C. Colinet and A. Antoni-Zdziobek

Laboratoire de Thermodynamique et Physico-Chimie Métallurgiques
UMR, CNRS 5614/INPG/UJF
B.P. 75
F-38402 Saint Martin d'Hères Cedex

ABSTRACT

Solid-state phase equilibria in the Fe-Co system are investigated using the Cluster Variation Method (CVM) in the irregular tetrahedron approximation in the bcc lattice and in the regular tetrahedron approximation in the fcc lattice. Calculations are performed in the quaternary Fe+ Fe- Co+ Co- by considering both chemical and magnetic interactions. The A2/B2 order/disorder transition and the α/γ transition agree well with the experimental data in the literature. The composition dependence of the Curie temperatures for bcc and fcc alloys as predicted here are also presented.

INTRODUCTION

The binary Fe-Co phase diagram¹ presents a large domain of γ (fcc) solid solution extending from pure iron to pure cobalt for temperatures above 1258 K. The limit between the α (bcc) phase and the γ phase presents a maximum for a temperature of 1258 K and a iron composition of 0.55. Below this temperature the α domain extends in a large range of composition between pure iron and around 80 at. % of cobalt. The α phase is ordered as a B2 phase at temperatures below 1000 K for equiatomic composition. The magnetic transition intercepts the α/γ phase boundary for compositions around 27 at.% Fe and 75 at.% Fe in the cobalt rich domain and in the iron rich domain respectively. The Curie temperature is then higher than the order-disorder temperature and is also higher than the α/γ transition temperature.

The cluster variation method (CVM) allows to take into account both short range order and long range order in the phase diagram determination. It is well adapted to the study of the solid phase equilibria in the Fe-Co system. As the γ and α phases are ferromagnetic in the investigated temperature range, the considered system in the CVM is a four component system Fe+ Fe- Co+ Co-.

THE CLUSTER VARIATION METHOD

The cluster variation method has been used in the regular tetrahedron approximation in the face centered cubic solid solution (fcc) and in the irregular tetrahedron approximation in the body cubic centered (bcc) solid solution. In the fcc solid solution the maximum cluster which takes into account the first nearest neighbor pair interactions is a regular tetrahedron. In the bcc solid solution the irregular tetrahedron takes into account the first and second nearest neighbor pair interactions. The configuration energy referred to the pure elements in the same structure is written as function of the tetrahedron energies $\Delta\epsilon_{ijkl}$ in the $\{ijkl\}$ configuration :

$$U_{fcc} - U_{fcc}^0 = 2N \sum_{i,j,k,l=1}^4 \Delta\epsilon_{ijkl} z_{ijkl} \quad (1)$$

$$U_{bcc} - U_{bcc}^0 = 6N \sum_{i,j,k,l=1}^4 \Delta\epsilon_{ijkl} z_{ijkl} \quad (2)$$

z_{ijkl} is the tetrahedron probability in the $\{ijkl\}$ configuration. The configuration entropy is written as the function of the tetrahedron probabilities and the sub cluster probabilities^{2,3} :

$$S_{fcc} = Nk[-2 \sum_{i,j,k,l=1}^4 L(z_{ijkl}) + 6 \sum_{i,j=1}^4 L(y_{ij}^{(1)}) - 5 \sum_{i=1}^4 L(x_i)] \quad (3)$$

$$S_{bcc} = Nk[-6 \sum_{i,j,k,l=1}^4 L(z_{ijkl}) + 12 \sum_{i,j,k=1}^4 L(t_{ijk}) - 3 \sum_{i,j=1}^4 L(y_{ij}^{(2)}) - 4 \sum_{i,k=1}^4 L(y_{ik}^{(1)}) + \sum_{i=1}^4 L(x_i)] \quad (4)$$

z_{ijkl} , t_{ijk} , $y_{ij}^{(2)}$, $y_{ij}^{(1)}$ and x_i are respectively the tetrahedron, triangle, first nearest neighbor pair, second nearest neighbor pair and point probabilities. $L(x)$ is equal to $x \ln x$. The equilibrium of the system is obtained by minimizing the grand potential with respect to the cluster probabilities at constant effective chemical potential. The grand potential of the fcc solid solution referred to the pure fcc elements is defined by :

$$\Omega_{fcc}^* = U_{fcc} - U_{fcc}^0 - TS_{fcc} - N \sum_{i=1}^4 x_i \mu_{i,fcc}^* \quad (5)$$

where the $\mu_{i,fcc}^*$ are the effective chemical potential of species i referred to pure fcc constituents. In the same way the grand potential of the bcc solid solution referred to the pure bcc elements is defined by :

$$\Omega_{bcc}^* = U_{bcc} - U_{bcc}^0 - TS_{bcc} - N \sum_{i=1}^4 x_i \mu_{i,bcc}^* \quad (6)$$

where the $\mu_{i,bcc}^*$ are the effective chemical potential of species i referred to pure bcc constituents.

In this work we will also treat the equilibrium between two phases having different structures, let say fcc and bcc. In this case a common reference state R of the chemical potential, of the effective chemical potential and of the grand potentials must be chosen. In the fcc phase the effective chemical potential referred to R is :

$$\mu_{i,fcc/R}^* = \mu_{i,fcc}^* + (\mu_{i,fcc}^0 - \mu_{i,R}^0) - \frac{1}{4} \sum_{i=1}^4 (\mu_{i,fcc}^0 - \mu_{i,R}^0) \quad (7)$$

The grand potential referred to R is :

$$\Omega_{fcc/R}^* = \Omega_{fcc}^* + \frac{1}{4} \sum_{i=1}^4 (\mu_{i,fcc}^0 - \mu_{i,R}^0) \quad (8)$$

In the bcc phase, the connecting relations are :

$$\mu_{i,bcc/R}^* = \mu_{i,bcc}^* + (\mu_{i,bcc}^0 - \mu_{i,R}^0) - \frac{1}{4} \sum_{i=1}^4 (\mu_{i,bcc}^0 - \mu_{i,R}^0) \quad (9)$$

$$\Omega_{bcc/R}^* = \Omega_{bcc}^* + \frac{1}{4} \sum_{i=1}^4 (\mu_{i,bcc}^0 - \mu_{i,R}^0) \quad (10)$$

The terms written as μ_i^0 are the chemical potentials. The differences $\mu_{i,fcc}^0 - \mu_{i,R}^0$, $\mu_{i,bcc}^0 - \mu_{i,R}^0$ are the so-called lattice stabilities.

The tetrahedron energies can be written as a sum of pair interactions. However if these interactions are independent of the composition the thermodynamic data of mixing will be symmetric with respect to the 0.5 composition. To break the symmetry, either composition dependent interchange energies or many-body interactions must be introduced. This last scheme, suggested by Kikuchi et al.³ is adopted in the present work. The tetrahedron energies obtained by the sum of the pair interactions are multiplied by the proper enhancement factor α_{ijkl} . The tetrahedron energies are expressed as function of the effective pair interactions ($\Delta\epsilon_{ij} = \epsilon_{ij} - (\epsilon_{ii} + \epsilon_{jj})/2$) by the following relations :

$$\Delta\epsilon_{ijkl}^{fcc} = \frac{1}{2} (\Delta\epsilon_{ij} + \Delta\epsilon_{ik} + \Delta\epsilon_{il} + \Delta\epsilon_{jk} + \Delta\epsilon_{jl} + \Delta\epsilon_{kl}) (1 + \alpha_{ijkl}) \quad (11)$$

$$\Delta\epsilon_{ijkl}^{bcc} = \left[\frac{1}{6} (\Delta\epsilon_{ik}^{(1)} + \Delta\epsilon_{il}^{(1)} + \Delta\epsilon_{jk}^{(1)} + \Delta\epsilon_{jl}^{(1)}) + \frac{1}{4} (\Delta\epsilon_{ij}^{(2)} + \Delta\epsilon_{kl}^{(2)}) \right] (1 + \alpha_{ijkl}) \quad (12)$$

In the Fe-Co system, the magnetic interactions cannot be neglected. γ iron is antiferromagnetic at low temperature ($T_{Neel}=67K$) and the α iron is ferromagnetic ($T_{Curie}=1043K$). The cobalt is ferromagnetic in the γ structure ($T_{Curie}=1396K$) and in the metastable α structure ($T_{Curie}=1450K$). In the binary Fe-Co the α phase is strongly stabilized by the magnetic interactions. It is not the case in the γ phase. Therefore a magnetic interaction has to be included which will be done in the way outlined in⁴ :

$$\epsilon_{ij}^{(k)} = V_{ij}^{(k)} - J_{ij}^{(k)} \sigma_i \sigma_j \quad (13)$$

$V_{ij}^{(k)}$ is a non magnetic interaction energy and $J_{ij}^{(k)}$ is the magnetic interaction energy (proportional to the exchange integral). The parameter σ_i takes the values ± 1 in a spin $\frac{1}{2}$ treatment which will be used here. Two species $i\uparrow$ and $i\downarrow$ have been introduced for each element. Therefore the system which is treated with the CVM contains four species Fe+ Fe- Co+ Co-. Let us remark that the chemical potentials of the two species $i\uparrow$ and $i\downarrow$ are equal.

For the treatment of the equilibrium between α and γ phases one needs to choose a common reference state to compare the grand potentials. Therefore it is necessary to introduce the lattice stabilities of iron and cobalt. For a magnetic component the lattice stability contains a structural contribution and a magnetic contribution. In the CVM treatment with magnetic species the magnetic contribution is included in the calculation of the thermodynamic data, then only the structural contribution has to be introduced by changing the reference state. In order to estimate this structural contribution, the magnetic contribution for the pure elements has been calculated using the CVM and has been deduced from the Gibbs energy of the lattice stability proposed by SGTE⁵. It has been verified that the obtained values lead to the correct transition temperatures of iron ($T_{\alpha \rightarrow \gamma} = 1185$ K and $T_{\gamma \rightarrow \delta} = 1668$ K).

RESULTS AND DISCUSSION

The values of the parameters necessary for the calculations are reported in table 1.

Table 1. Chemical interchange energies $\Delta V_{ij} = V_{ij} - (V_{ii} + V_{jj})/2$, magnetic contributions (J_{ij}) and enhancement factors (in J)

Phase bcc		Phase fcc	
$\Delta V_{FeCo}^{(1),bcc} = -2178$	$J_{Fe^+Fe^+}^{(1),bcc} = 1342$	$\Delta V_{FeCo}^{(1),fcc} = -1358$	$J_{Fe^+Fe^+}^{(1),fcc} = -97$
$\Delta V_{FeCo}^{(2),bcc} = 0$	$J_{Co^+Co^+}^{(1),bcc} = 1855$		$J_{Co^+Co^+}^{(1),fcc} = 1160$
	$J_{Fe^+Co^+}^{(1),bcc} = 2029$		$J_{Fe^+Co^+}^{(1),fcc} = 1100$
Enhancement factors equal to 0.		$\alpha_{Co^+Co^+Co^+Fe^+} = -0.21$	
		$\alpha_{Fe^+Fe^+Fe^+Co^+} = -0.11$	
		$\alpha_{Co^+Co^+Co^-Fe^+} = -0.3$	
		Other enhancement factors equal to 0.	

In the α phase the parameters have been obtained previously⁴. The chemical interchange energy has been obtained from the B2 \rightarrow A2 order disorder temperature and from the mixing enthalpy. The values of the $J_{Fe+Fe+}^{(1),bcc}$ and $J_{Co+Co+}^{(1),fcc}$ terms are deduced from the Curie temperatures of pure iron (1043K) and pure cobalt (1396K). The values of $J_{Co+Co+}^{(1),bcc}$, $J_{Fe+Co+}^{(1),bcc}$ are obtained from the variation of the Curie temperature in the α phase as proposed by Inden and Meyer⁶. For the γ phase the value of $J_{Fe+Fe+}^{(1),fcc}$ is the one proposed by Lawrence and Rossiter⁷ to take into account the antiferromagnetic character of γ iron. The value of $J_{Fe+Co+}^{(1),fcc}$ is fitted from the experimental values of the Curie temperature in the Co rich domain. The value of the chemical interchange energy in the γ phase has been obtained

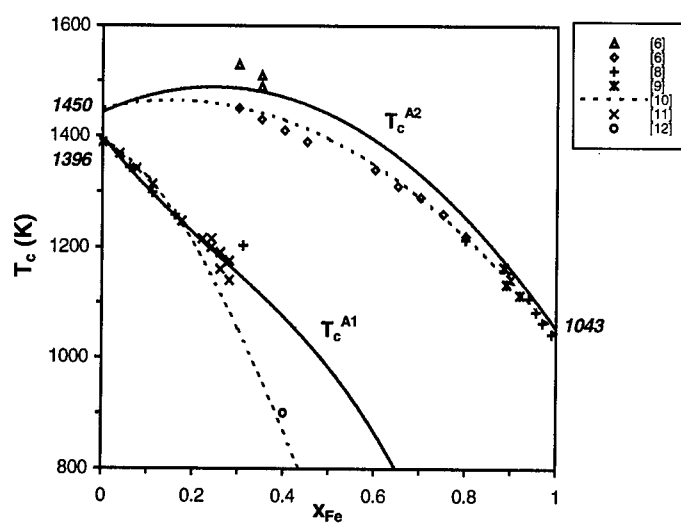


Figure 1. Curie temperatures in the fcc and bcc solid solutions.

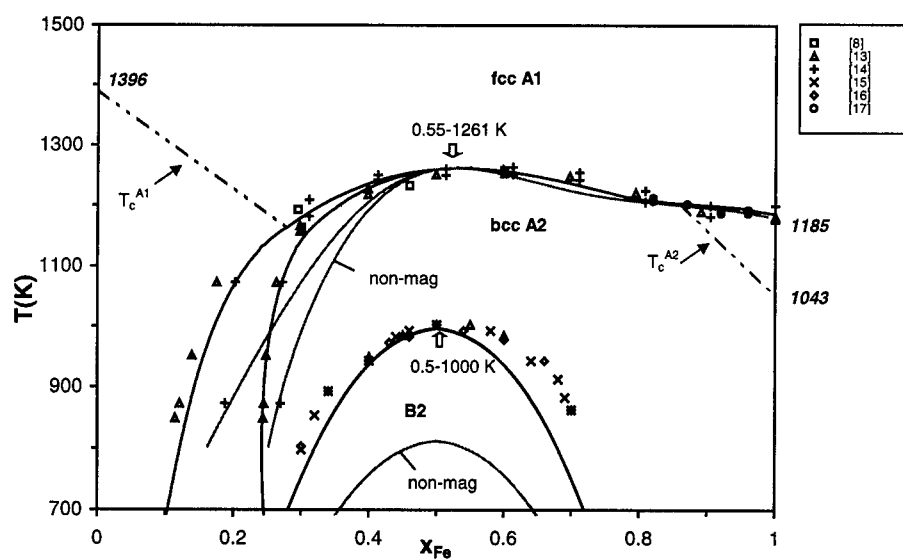


Figure 2. Experimental and calculated Fe-Co phase diagram.

from the maximum value of the α/γ phase boundary (experimental data 1258 K for 54 at.% Fe calculated value 1261 K for 55 at.% Fe). The values of the enhancement factors have been introduced to fit more precisely the α/γ phase boundary in the iron and cobalt rich domains.

The variations of the Curie temperatures in the bcc and fcc phases calculated with the model are presented in figure 1. The results are in good agreement with the experimental results found in the literature.

The order-disorder temperature as well as the α/γ phase boundary obtained in the present work are reported in figure 2. The results obtained without taking into account the magnetic interactions are also reported in this figure. The introduction of the magnetic interactions increases the order-disorder temperature. This introduction allows also a better representation of the α/γ phase boundary, more particularly it gives a good agreement with the phase boundary obtained by Ellis et al.¹³ where the two-phase domain is relatively large.

Previous studies⁴ had shown the interest of introducing both the chemical and magnetic interactions in the treatment of the bcc phase in ferromagnetic bcc Fe-Co alloys. The present study shows that it is possible to treat the equilibrium between α and γ phases in Fe-Co system using the CVM. The treatment by introducing the magnetic interactions leads to a good representation of the phase boundaries.

REFERENCES

1. T. Nishizawa and K. Ishida, Co-Fe, in: *Phase Diagrams of Binary Iron Alloys*, A.S.M. Int., USA (1993).
2. H. Ackermann, G. Inden, and R. Kikuchi, Tetrahedron approximation of the cluster variation method for bcc alloys, *Acta Metall.*, 37:1 (1989).
3. R. Kikuchi, D. De Fontaine, M. Murakami, and T. Nakamura, Ternary phase diagram calculations – II Examples of clustering and ordering systems, *Acta Metall.*, 25:207 (1977).
4. C. Colinet, G. Inden, and R. Kikuchi, CVM calculation of the phase diagram of bccFe-Co-Al, *Acta Metall. Mater.*, 41:1109 (1993).
5. A.T. Dinsdale, SGTE data for pure elements, *Calphad*, 15, 4:317, (1991).
6. G. Inden and W.O. Meyer, Approximate determination of the Curie temperatures of bcc Fe-Co alloys, *Z. Metall.*, 66:725 (1975).
7. P.J. Lawrence and P.L. Rossiter, Chemical and magnetic interactions in fcc Fe-Ni alloys using the cluster variation method, *J. Phys. F: Met. Phys.*, 16:543 (1986).
8. A.S. Normanton, P.E. Bloomfield, F.R. Sale, and B.B. Argent, A calorimetric study of iron-cobalt alloys, *Met. Sci.*, 9:510 (1975).
9. H. Stuart and N. Ridley, Lattice parameters and Curie-point anomalies of iron-cobalt alloys, *Brit. J. Appl. Phys.*, 2:485 (1969).
10. A.F. Guillermet, Critical evaluation of the thermodynamic properties of the iron-cobalt system, *High Temp.- High Press.*, 19:477 (1987).
11. H. Masumoto, On a new transformation of cobalt and the equilibrium diagrams of nickel-cobalt and iron-cobalt, *Tohoku Imperial University Science Report*, 1st ser., 15:450 (1926).
12. Y. Nakamura, M. Shiga, and S. Santa, Invar behavior of face-centered cubic FeCo alloys precipitated from copper, *J. Phys. Soc. Jpn.*, 26:210 (1969).
13. W.C. Ellis and E.S. Greiner, Equilibrium relations in the solid state of the iron-cobalt system, *Trans. A.S.M.*, 29:415 (1941).
14. J.H. Andrews and C.G. Nicholson, The iron-cobalt system, First Report of the Alloy Steels Research Committee, (1936).
15. H. Asano, Y. Bando, N. Nakanishi, and S. Kachi, Order-disorder transformation of Fe-Co alloys in fine particles, *Trans. Jpn. Inst. Met.*, 8:180 (1967).
16. J.A. Oyedele and M.F. Collins, Composition dependence of the order-disorder transition in iron-cobalt alloys, *Phys. Rev. B*, 16:3208 (1977).
17. W.A. Fisher, K. Lorenz, H. Fabritius, and D. Schlegel, Examination of the alpha-gamma transformation in very pure binary alloys of iron with molybdenum, vanadium, tungsten, niobium, tantalum, zirconium and cobalt, *Arch. Eisenhüttenwes.*, 41:489 (1970).

THE ONSAGER CAVITY FIELD IN FCC ALLOYS

S. Shallcross⁽¹⁾ and Györfy, B. L. ⁽²⁾

⁽¹⁾*H. H. Wills Physics Laboratory, University of Bristol
Royal Fort, Tyndall Avenue, Bristol BS8 1TL, U.K. and
Department of Physics, University of Liverpool
s.shallcross@bris.ac.uk*

⁽²⁾*H. H. Wills Physics Laboratory, University of Bristol
Royal Fort, Tyndall Avenue, Bristol BS8 1TL, UK
b.l.gyorffy@bris.ac.uk*

ABSTRACT

We discuss phase diagrams and concentration variations near surfaces of fcc alloys on the basis of replacing the Weiss field, in the Bragg-Williams approximation, by the Onsager Cavity field. We argue that this scheme is as tractable as the Mean Field Approximation for complex problems and provides an adequate account of correlations even in frustrated systems.

INTRODUCTION

Below some temperature T_0 all alloys will either order or phase separate. On the surface of alloys more complicated things will happen. One may see enrichment of one species in the surface region, the order of the phase transition may be different from that in the bulk and indeed it may order before the bulk does (Surface Induced Ordering, SIO) or remain disordered below the bulk transition (Surface Induced Disorder-ing, SID). On vicinal surfaces there are additional structural transitions,

between double and single step height structures for example. In short there is an enormous richness of surface behaviour in alloys, and of course this is the case with other defects such as antiphase boundaries and vacancies. This is not only scientifically interesting but technologically relevant as an understanding of these phenomena would make the task of manipulating catalysis on surfaces a great deal easier. Until recently experimental techniques could only probe, with certainty, the topmost few layers of alloy surfaces. Many of the phenomena described above as theoretical ideas without experimental verification. This has now changed and a new tool, X-ray grazing incidence, provides information for the *surface region* not just at the surface, for example Dosch et al. [1], [2] have studied Cu_3Au and found SID transition at the surface as the bulk undergoes a 1st order transition.

MODEL AND APPROXIMATIONS

One approach to the phenomena above is the Ising Hamiltonian on an assumed lattice

$$H = 1/2 \sum_{NN} v_{ij}^{(2)} \xi_i \xi_j + \sum_i v_i^{(1)} \xi_i + v_0.$$

where $\xi_i = 1$ if A atom is at site i and $\xi_i = 0$ if a B atom is at site i . As is well known.

$v_{ij}^{(2)} < 0$ implies segregation

and
 $v_{ij}^{(2)} > 0$ ordering.

Alloy problems can be investigated by solving the statistical mechanics for this model in some approximation. The usual methods are:

- Bragg-Williams mean field theory
- Cluster variation method
- Series expansions
- Monte Carlo

Down the list the methods are of increasing accuracy though increasingly more difficult to implement. Because of its simplicity the Bragg-Williams mean field (BWMF) can be solved for complex situations. In many cases it serves as a tractable 1st order approximation, although in some systems, particularly frustrated ones, for example spin glasses, it is a disaster. Further, and from a material specific point of view perhaps more importantly, only the BWMF can be deployed in a fully electronic (first principles) model [3].

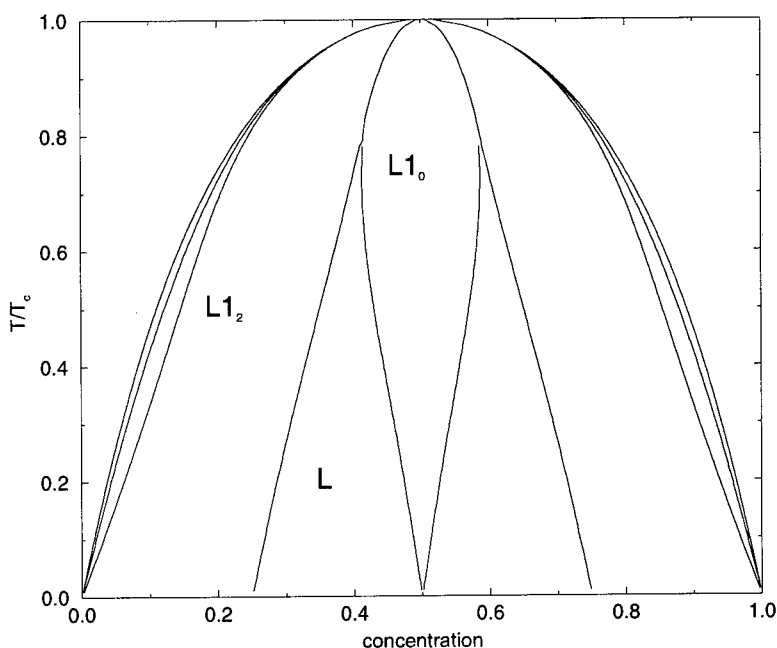


Figure 1 Bulk phase diagram in MWMF solution.

FACE CENTRED CUBIC LATTICE WITH ORDERING POTENTIALS, BWMF SOLUTION

The bulk phase diagram, a famous disaster, was first worked out by Shockley in 1937 [4]. It's clear that the extension of all phases to a multicritical point is wrong when one considers that the lattice is most frustrated *right between* the stoichiometries of the $L1_2$ and $L1_0$ phases. The ground state manifestation of this is that there are superdegenerate points at $c = 3/8$ and $c = 5/8$. The argument is that correlations will make the solid solution more stable than the ordered structures, and that this effect will be greatest in the most frustrated regions. Thus one would expect a lowering of the phase boundary between the stoichiometries of $L1_2$ and $L1_0$, and so a three peaked structure. The BWMF completely misses this as the only contribution to correlation energy is from long range order. With the more sophisticated approximations mentioned above, CVM and MC, the correlation energy is better handled and a three peaked structure is seen [8], [9]. On the other hand the virtues of the BWMF are particularly evident when one solves not the bulk but a surface problem. For example it renders the asymptotic phenomena on a (100) surface tractable, whilst it is difficult to treat with the more accurate approximations [5]. The main point of this report is to argue that the Onsager Cavity Field Approximation (OCFA) is as tractable as the BWMF for complex problems, and, furthermore, it provides an

adequate account of correlations even in frustrated systems, unlike the BWMF.

THE IDEA OF THE OCFA

Onsager's original paper, in 1936, was on dielectric materials [7] and his ideas were adopted by Brout and Thomas [6] for the Ising model of magnetism in 1967. Reformulating their ideas for the Ising model of alloys is straightforward. The mean field argument is that the occupation of a site is determined by an average of the surrounding medium, acting as a local molecular potential at that site. Onsager's observation is that the occupation of that site will clearly cause changes in the surrounding local environment. More precisely if one calculated the molecular potential with an A atom or B atom fixed at the site, the two potentials would be different, and one has the picture of the molecular potential being split into a part which depends on the occupation and a part which doesn't. Onsager's argument is that it is only the part that is independent of site occupation, the so-called cavity potential, which represents an effective medium. Thus the mean-field chemical potential can be written as a sum of this and a part that represents the coupling between the single-site and the effective medium, the so-called reaction potential.

$$\nu_i^{BWMF} = \nu_i^{Cavity} + \nu_i^{Reaction}$$

Following Brout we write

$$\nu_i^{Reaction} = -\Lambda_i(c_i - 1/2)$$

where the Onsager co-efficient, Λ_i can be shown to be related to the pair-potentials $v_{ij}^{(2)}$:

$$\Lambda_i = 1/\beta c_i(1 - c_i) \sum_j v_{ij}^{(2)} \alpha_{ij} \quad (1)$$

and the correlation functions, given by

$$\alpha_{ij} = \beta(\langle \xi_i \xi_j \rangle - c_i c_j).$$

The equation of state for this new approximation is, not suprisingly, just the old BWMF equation of state corrected by subtracting the reaction potential

$$\sum_j v_{ij}^{(2)} c_j + v_i^{(1)} + k_b T \ln \frac{c_i}{1 - c_i} - \nu_i - \Lambda_i(c_i - 1/2) = 0. \quad (2)$$

Clearly, the concentrations are now coupled to the correlation functions $\{\alpha_{ij}\}$. Differentiating the equation of state with respect to ν_j one has a closed set of equations for correlation functions in terms of the Onsager co-efficients

$$\alpha_{ij} = \beta c_i(1 - c_i)(\delta_{ij} - \sum_l v_{il}^{(2)} \alpha_{lj} + \Lambda_i \alpha_{ij})$$

and one has a set of coupled equations to be solved for $\{\alpha_{ij}\}$ and $\{\Lambda_i\}$ for a specified concentration configuration and temperature.

$$\alpha_{ij} = \beta c_i(1 - c_i)(\delta_{ij} - \sum_l v_{il}^{(2)} \alpha_{lj} + \Lambda_i \alpha_{ij}) \quad (3)$$

$$\Lambda_i = 1/\beta c_i(1 - c_i) \sum_j v_{ij}^{(2)} \alpha_{ij} \quad (4)$$

For 2nd order transitions it is easy to find transition temperature. The temperature at which the solid solution becomes unstable with respect to a concentration wave generated by reciprocal lattice vector \vec{q} is given by the much quoted formula

$$k_b T_c = -\frac{1}{4} (V_{BZ}^{-1} \int \frac{d^3 \vec{q}}{v^{(2)}(\vec{q}) - v^{(2)}(\vec{q})})^{-1}$$

An example is segregation on fcc lattice at a concentration of 0.5. Significantly, the transition temperature is an improvement on the BWMF solution. $(k_b T_c)_{BestMC} = 0.816(k_b T_c)_{BWMF}$ and $(k_b T_c)_{OCFA} = 0.75(k_b T_c)_{BWMF}$. However for 1st order transitions the equation of state has many symmetry breaking solutions at low temperatures and so one needs the free energy to determine the equilibrium state. It is this lack of a free energy to complete the theory that has hampered progress of the OCFA in alloy problems. In the next section we will show how to find this free energy. For the record we note that this has in fact been done, though from a rather different (and rather more formal) perspective. In a paper which to these authors seems much less well known than it deserves to be, Tokar et al. [11] have developed a free energy expression for their γ -*expansion*, better known in applications to short-range order. They show that even in lowest order this greatly improves the topology of the phase diagram for the fcc lattice. It turns out that the OCFA is equivalent to this lowest order approximation.

FREE ENERGY IN OCFA

The first point to make is that the BWMF equations are a trivial limit, $\{\Lambda_i\} \rightarrow 0$ of the OCFA. This suggests the form of the OCFA

free energy will be equal to the BWMF free energy with a correction due to correlations. That this limit exists serves to emphasise that the OCFA is an improved single site theory, in CVM for example the two-point (quasi-chemical) approximation does not contain the BWMF as a limiting case. Without any formal basis for an approach we proceed ad-hoc and 'integrate-up' equation (2) by guessing what this correction will be. In preparation for doing this we note that by substituting in the expression for correlation functions into equation (1) and re-arranging it, one is led to

$$1/2 \sum_i c_i(1 - c_i)\Lambda_i = 1/2 \sum_{ij} v_{ij}^{(2)} \langle \xi_i \xi_j \rangle - 1/2 \sum_{ij} v_{ij}^{(2)} c_i c_j. \quad (5)$$

Evidently the right hand side of this expression is the correlation energy, namely the internal energy minus the uncorrelated BWMF internal energy. This is clearly a formal improvement on the BWMF as there is now an expression for correlation energy for an *arbitrary* concentration configuration $\{c_i\}$. That is, there will be contributions to the correlation energy from both long range and short range order. It might be suspected that equation (5) forms the internal energy component of the free energy correction to BWMF theory that is required. On this basis one can proceed to guess the entropy component for various phases, so that the equation of state is reproduced by differentiating the free energy. To this end one notes that the appropriate representation for equations (3) and (4) is a basis of fourier transforms (for the solid solution phase), or partial fourier transforms (for the partially ordered structures $L1_0$ and $L1_2$), of the pair correlation functions and pair potentials. In figure 2 is shown these structures and the appropriate Brillouin zones for the inverse fourier transforms.

SOLID SOLUTION

As all sites are equivalent there will be only one Onsager co-efficient and so a state is described by $(\beta, \bar{c}, \Lambda)$. In the fourier transform basis the sets of equations (3) and (4) become

$$\begin{aligned} \Sigma &= \frac{1}{\beta \bar{c}(1 - \bar{c})} (1 - \Omega_{SS}^{-1} \int d^3 q v^{(2)}(q) \alpha(q)) \\ \alpha(q) &= (\Sigma + v^{(2)}(q))^{-1} \end{aligned}$$

where $\Sigma = 1/\beta \bar{c}(1 - \bar{c}) - \Lambda$. For each (β, \bar{c}) there are two coupled equations to solve for the two unknowns Λ and $\alpha(q)$. The correlation energy is given by $1/2 N c(1 - c)\Lambda$, and the entropy correction, chosen to

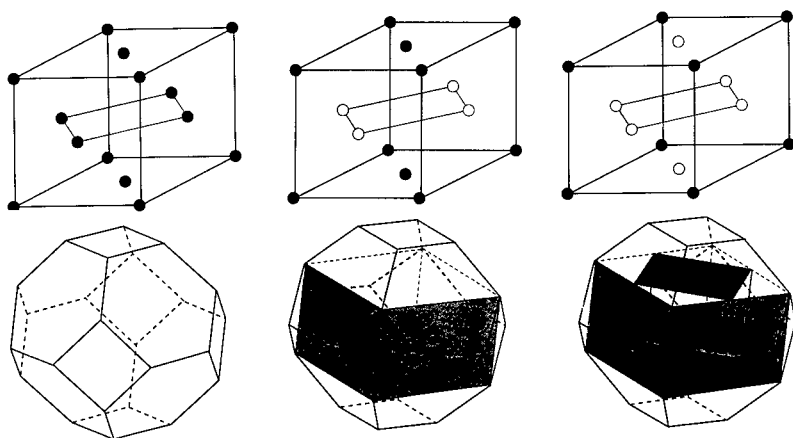


Figure 2 Brillouin zones for the solid solution, cuboid sublattice and cube sublattice.

reproduce the equation of state on setting $\frac{\partial \Omega}{\partial c} = 0$, gives

$$\begin{aligned}
 A/N &= 6v^{(2)}\bar{c}^2 + v^{(1)}\bar{c} + k_b T [\bar{c} \ln \bar{c} + (1 - \bar{c}) \ln (1 - \bar{c})] \\
 &- \nu(\bar{c} - 1/2) + 1/2\bar{c}(1 - \bar{c})\Lambda \\
 &+ k_b T/2 [-\Omega_{SS}^{-1} \int d^3 q \ln \alpha(q) + \ln \beta \bar{c}(1 - \bar{c})]
 \end{aligned}$$

where the Brillouin zone is that shown in figure 2(a).

L1₀ PHASE

There are two inequivalent sites in this structure and so a state is described by $(\beta, c_1, c_2, \Lambda_1, \Lambda_2)$. As one can see in figure 3 two pairs of sublattices can be joined to form two interpenetrating cuboid lattices. The unit cell is now a cuboid containing 1 site from each sublattice. By taking partial fourier transforms between sublattices the set of equations (3) becomes

$$\begin{pmatrix} \alpha^{11}(q) & \alpha^{12}(q) \\ \alpha^{21}(q) & \alpha^{22}(q) \end{pmatrix} = \begin{pmatrix} v^{11}(q) + \Sigma_1 & v^{12}(q) \\ v^{21}(q) & v^{22}(q) + \Sigma_2 \end{pmatrix}^{-1}$$

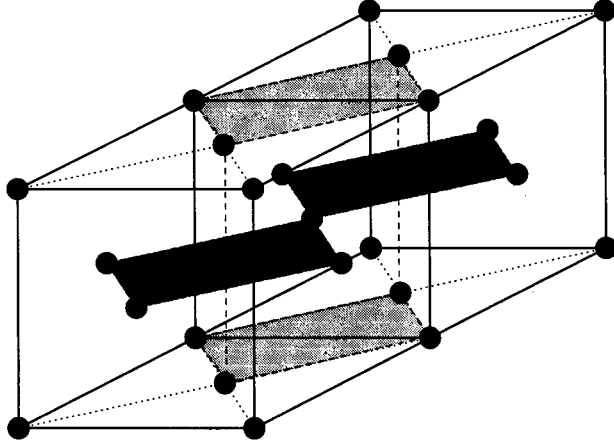


Figure 3 Two sublattices of the $L1_0$ structure.

where $\Sigma_1 = 1/\alpha_{11} - \Lambda_I$ and $\Sigma_2 = 1/\alpha_{22} - \Lambda_{II}$. The diagonal elements of the matrix are fourier transforms on the same sublattice, the off-diagonal elements are fourier transforms between sublattices. Inverting the above matrix one can find the α^{nm} 's in terms of v^{nm} 's and Σ_n 's. Defining

$$\begin{aligned}\alpha^1(q) &= \alpha^{11}(q) + \alpha^{12}(q) \\ \alpha^2(q) &= \alpha^{21}(q) + \alpha^{22}(q)\end{aligned}$$

one finds

$$\begin{aligned}\alpha^1(q) &= \frac{\Sigma_2 + v^{11}(q) - v^{12}(q)}{(v^{11}(q) + \Sigma_1)(v^{22}(q) + \Sigma_2) - v^{12}(q)v^{21}(q)} \\ \alpha^2(q) &= \frac{\Sigma_1 + v^{22}(q) - v^{21}(q)}{(v^{11}(q) + \Sigma_1)(v^{22}(q) + \Sigma_2) - v^{12}(q)v^{21}(q)}\end{aligned}$$

Finally one can show by Dirac construction, that the set of equations (4) becomes

$$\begin{aligned}\Sigma_1 &= \frac{1}{\beta c^1(1 - c^1)} (1 - \Omega_{SS}^{-1} \int d^3q v^{(2)}(q) \alpha^1(q)) \\ \Sigma_2 &= \frac{1}{\beta c^2(1 - c^2)} (1 - \Omega_{SS}^{-1} \int d^3q v^{(2)}(q) \alpha^2(q))\end{aligned}$$

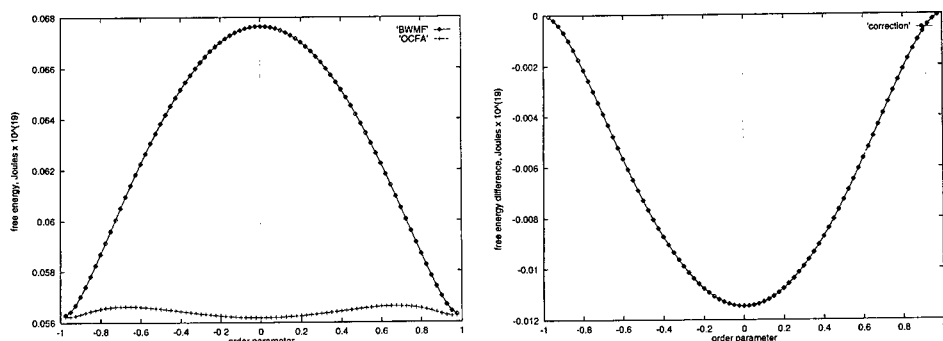


Figure 4 BWMP and OCFA free energies at the $A1 - L1_0$ transition in the OCFA solution.

Thus there are 4 equations to solve for the two unknown numbers Λ_1, Λ_2 , and the two unknown functions $\alpha^1(q)$ and $\alpha^2(q)$. The correlation energy is $1/2(1/2c^1(1 - c^1)\Lambda_1 + 1/2c^2(1 - c^2)\Lambda_2)$, and the entropy correction simply turns out to be the matrix analogue of solid solution equation.

$$\begin{aligned}
 A/N = & 6v^{(2)}c^2 - 1/2\eta^2 + v^{(1)}c - \nu(c - 1/2) \\
 & + k_bT/2[c^1 \ln c^1 + (1 - c^1) \ln(1 - c^1) \\
 & + c^2 \ln c^2 + (1 - c^2) \ln(1 - c^2)] \\
 & + 1/2(1/2c^1(1 - c^1)\Lambda_1 + 1/2c^2(1 - c^2)\Lambda_2) \\
 & + k_bT/2[-\Omega_{cuboid}^{-1}/2 \int d^3q \ln \|\alpha(q)\| \\
 & + 1/2 \ln \alpha_{11} + 1/2 \ln \alpha_{22}]
 \end{aligned}$$

where $\eta = c^1 - c^2$ and is the order parameter. In figure 4 we plotted the free energies, and the free energy correction due to correlations, at the stoichiometric composition of $L1_0$. The free energy correction is negative and greatest for the solid solution. It is this that causes the solid solution to become more stable than the $L1_0$ phase, and thus there is a lowering of the transition temperature.

$L1_2$ PHASE

As in the $L1_0$ phase there are two inequivalent sites and so a state is described by $(\beta, c_1, c_2, \Lambda_1, \Lambda_2)$. In this case though the simplest division is into the 4 cubic sublattices, 3 of which will be related by translation. The unit cell is now the standard unit cell which contains 1 site from each of the 4 cubic sublattices. Taking partial fourier transforms as before one is led to

$$\begin{pmatrix} \alpha^{11} & \alpha^{12} & \alpha^{13} & \alpha^{14} \\ \alpha^{21} & \alpha^{22} & \alpha^{23} & \alpha^{24} \\ \alpha^{31} & \alpha^{32} & \alpha^{33} & \alpha^{34} \\ \alpha^{41} & \alpha^{42} & \alpha^{43} & \alpha^{44} \end{pmatrix} = \begin{pmatrix} v^{11} + \Sigma_1 & v^{12} & v^{13} & v^{14} \\ v^{21} & v^{22} + \Sigma_2 & v^{23} & v^{24} \\ v^{31} & v^{32} & v^{33} + \Sigma_2 & v^{34} \\ v^{41} & v^{42} & v^{43} & v^{44} + \Sigma_2 \end{pmatrix}^{-1}$$

Proceeding as before we define

$$\begin{aligned} \alpha^1(q) &= \alpha^{11}(q) + \alpha^{12}(q) + \alpha^{13}(q) + \alpha^{14}(q) \\ \alpha^2(q) &= \alpha^{21}(q) + \alpha^{22}(q) + \alpha^{23}(q) + \alpha^{24}(q) \end{aligned}$$

and arrive at a (more complicated) set of 4 coupled equations to solve for the 4 unknowns $\Lambda_1, \Lambda_2, \alpha^1(q)$ and $\alpha^2(q)$.

$$\alpha^1 = \frac{\Sigma_2^2(v^{(2)}_{xy} + v^{(2)}_{yz} + v^{(2)}_{zx} - \Sigma_2) + F_1^{(1)}\Sigma_2 + F_2^{(1)}}{-\Sigma_1\Sigma_2^3 + G_1(\Sigma_2^2 + \Sigma_1\Sigma_2) - G_2(\Sigma_1 + 3\Sigma_2) - G_3}$$

$$\alpha^2 = \frac{\Sigma_2(v^{(2)}_{xy} - \Sigma_1)(\Sigma_2 - v^{(2)}_{yz} - v^{(2)}_{zx}) + F_1^{(2)}\Sigma_2 + F_2^{(2)}\Sigma_1 - F_3^{(2)}}{-\Sigma_1\Sigma_2^3 + G_1(\Sigma_2^2 + \Sigma_1\Sigma_2) - G_2(\Sigma_1 + 3\Sigma_2) - G_3}$$

$$\Sigma_1 = \frac{1}{\beta c^1(1 - c^1)}(1 - V_{BZ}^{-1} \int d^3q v^{(2)}(q) \alpha^1(q))$$

$$\Sigma_2 = \frac{1}{\beta c^2(1 - c^2)}(1 - V_{BZ}^{-1} \int d^3q v^{(2)}(q) \alpha^2(q))$$

where G_i and $F_i^{(j)}$ are the q dependent functions

$$\begin{aligned} G_1 &= (v^{(2)}_{xy})^2 + v^{(2)}_{yz})^2 + v^{(2)}_{zx})^2 \\ G_2 &= 2v^{(2)}_{xy}v^{(2)}_{yz}v^{(2)}_{zx} \\ G_3 &= v^{(2)}_{xy})^4 + v^{(2)}_{yz})^4 + v^{(2)}_{zx})^4 - 2v^{(2)}_{xy})^2 v^{(2)}_{yz})^2 - 2v^{(2)}_{yz})^2 v^{(2)}_{zx})^2 - 2v^{(2)}_{zx})^2 v^{(2)}_{xy})^2 \\ F_1^{(1)} &= v^{(2)}_{xy})^2 + v^{(2)}_{yz})^2 + v^{(2)}_{zx})^2 - 2v^{(2)}_{xy})^2 v^{(2)}_{yz})^2 - 2v^{(2)}_{yz})^2 v^{(2)}_{zx})^2 - 2v^{(2)}_{zx})^2 v^{(2)}_{xy})^2 \\ F_2^{(1)} &= v^{(2)}_{xy})^3 + v^{(2)}_{yz})^3 + v^{(2)}_{zx})^3 + 2v^{(2)}_{xy}v^{(2)}_{yz}v^{(2)}_{zx} \end{aligned}$$

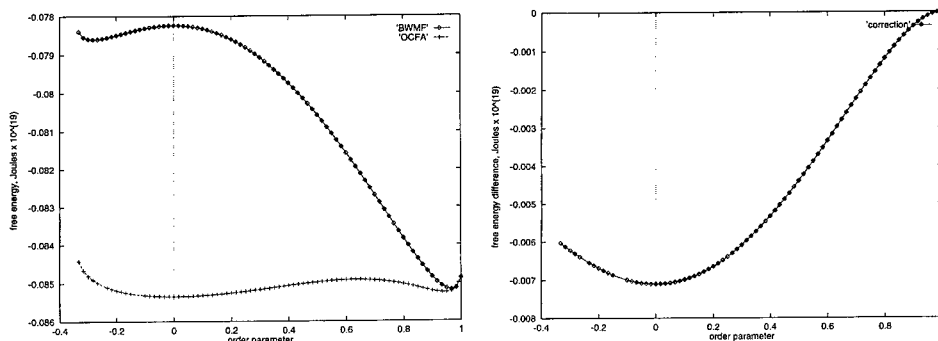


Figure 5 BWMF and OCFA free energies at the $A1 - L1_2$ transition in the OCFA solution.

$$\begin{aligned}
 & -v_{xy}^{(2)2}(v_{yz}^{(2)} + v_{zx}^{(2)}) - v_{yz}^{(2)2}(v_{zx}^{(2)} + v_{xy}^{(2)}) - v_{zx}^{(2)2}(v_{xy}^{(2)} + v_{yz}^{(2)}) \\
 F_1^{(2)} &= v_{yz}^{(2)} + v_{zx}^{(2)} \\
 F_2^{(2)} &= v_{xy}^{(2)}(v_{xy}^{(2)} - v_{yz}^{(2)} - v_{zx}^{(2)}) \\
 F_3^{(2)} &= F_2^{(1)}
 \end{aligned}$$

Where $\eta = c^I - c^{II}$, and the Brillouin zone is shown in figure 2(c). In figure 5 is plotted the free energies, and the free energy correction due to correlations, at the stoichiometric composition of $L1_2$. One finds a similar picture as in the $L1_0$ case, that is a lowering of the transition temperature.

BULK PHASE DIAGRAM FOR ORDERING POTENTIALS ON FCC LATTICE

A calculation of the bulk phase diagram shows that the lowering of the phase boundary is greatest in the most frustrated regions between the stoichiometries of $L1_2$ and $L1_0$ phases, and one has the 3 peaked structure seen in MC simulation and CVM calculations. The agreement between MC and the OCFA is quite good, the phase diagram from reference [9] is shown plotted on the same scale in figure 6. The phase transitions are now strongly first order at both the $L1_2$ and $L1_0$ stoichiometries, again in agreement with MC simulations. The TO-CVM, OCFA, and MC transition temperatures at $L1_2$ and $L1_0$ stoichiometries are shown below.

Method	$L1_0$ transition temp.	$L1_2$ transition temp.
TO-CVM	1.89	1.88
OCFA	1.748	1.826
MC	1.75	1.80

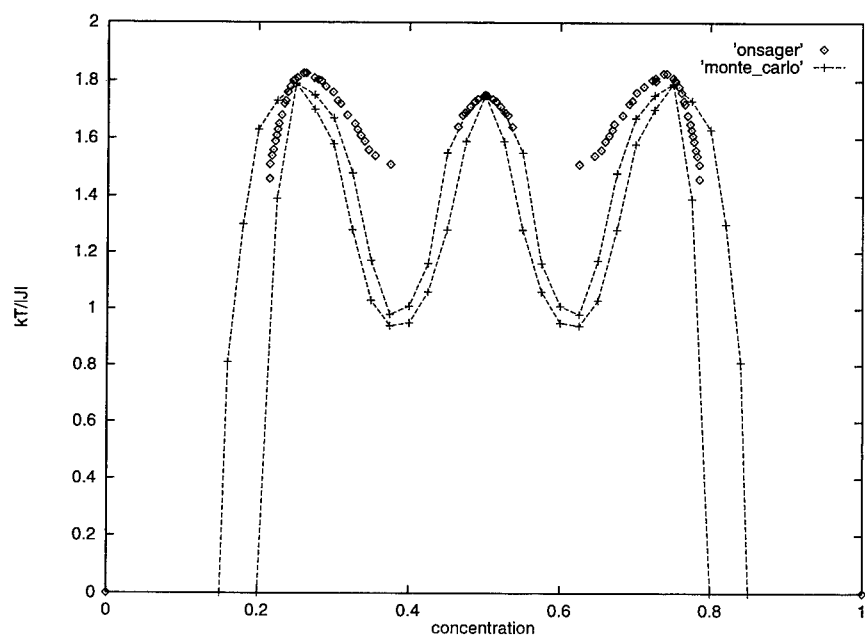


Figure 6 Bulk phase diagram in OCFA.

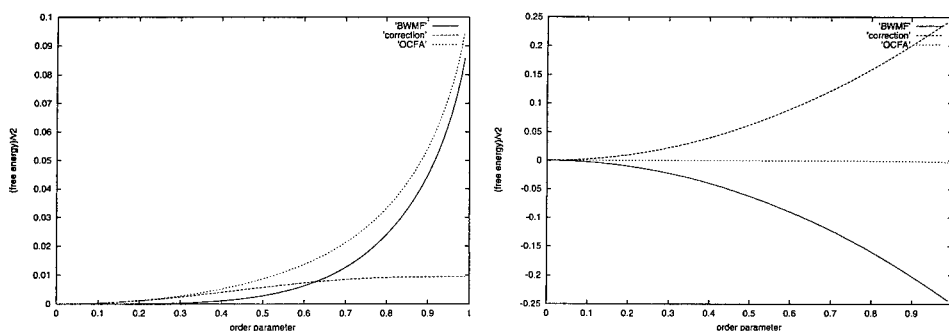


Figure 7 Free energy for 1d Ising model at $t=0.5$ and $t=0.001$.

SOME FURTHER OBSERVATIONS

LIMIT OF INFINITE INTERACTION RANGE

A question one would naturally ask is, what does the OCFA do in the regime where the BWMF theory is exact, that is when the interaction range (and so the number of nearest neighbours) becomes infinite. In the solid solution case, for example, one can see the answer clearly by noting that

$$v^{(2)}(q) = \sum_j v_{0j}^{(2)} e^{iq \cdot r_{0j}} = \frac{2v^{(2)}}{N} \sum_{n=1}^N \cos(nqa).$$

and so as N becomes large $v^{(2)}(q)$ will become zero and so also, from equation (5), will Onsager co-efficient Λ . The limit $\Lambda = 0$ is just the BWMF limit of the OCFA, and thus for infinite interaction range the OCFA reduces to the BWMF theory.

HIGH TEMPERATURE EXPANSION

It is interesting to do a high temperature expansion of the theory to first order in β . The correlation free energy becomes

$$\Omega^{cor} = -\frac{\beta}{4} \sum_{ij} v_{ij}^{(2)2} c(1-c)c(1-c) + ..$$

In fact this is just the first term of a high temperature renormalised perturbation series, which shows in a formal way that the OCFA is in general improving on the BWMF theory.

LOWER DIMENSIONS

Phase behaviour in lower dimensions is of some interest when one considers how the OCFA treats fluctuations. It is easy to show that the solid solution is stable at $T=0$ in both 1D and 2D, and indeed this

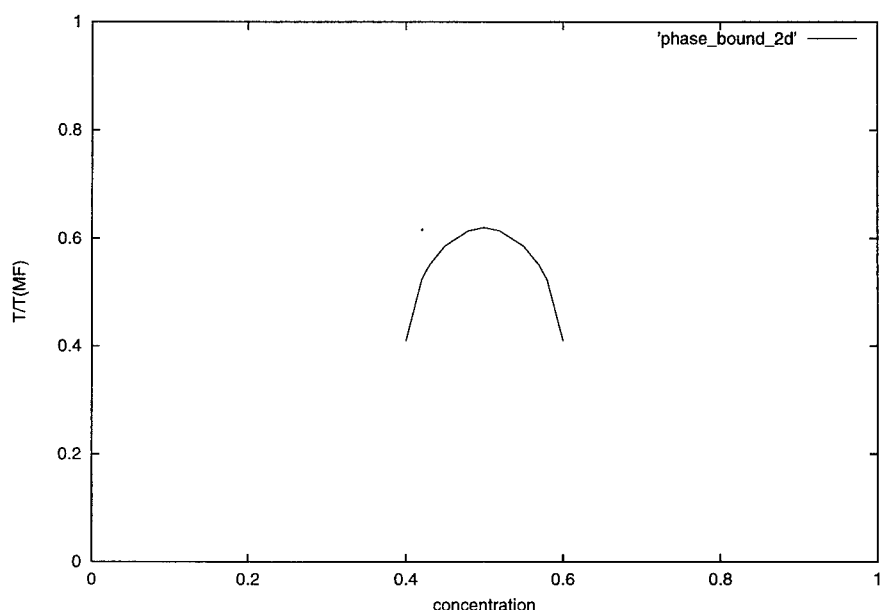


Figure 8 Phase diagram for 2d square lattice, nearest neighbour interactions only.

is true of all ordering vectors in the first Brillouin zones. In figure 7 is plotted the OCFA free energy at the value of the BWMF transition temperature and at $T \rightarrow 0$. There is no transition. However, for the 2D square lattice there is, though it is everywhere a 1st order transition. As one can see from the phase diagram in figure 8, though the order of the phase transition is badly wrong the phase boundary and transition temperature at $\bar{c} = \frac{1}{2}$ are reasonable.

Method	T_0 at $\bar{c} = \frac{1}{2}$	order of transition
Exact result	0.5673	2 nd
BWMF	1.0	2 nd
OCFA	0.62	1 st
CVM (square approx.)	0.6075	2 nd

ONSAGER CAVITY FIELD FOR SURFACES

In this section we present the OCFA equations for various surfaces and sketch the approach by which they may be solved.

PRINCIPLE (100) SURFACE, ONE ORDER PARAMETER PER LAYER

A surface problem is investigated by calculating a N_l layer film and making N_l large enough so that the surfaces are non-interacting. For the simplest case of one concentration per layer the system will be specified

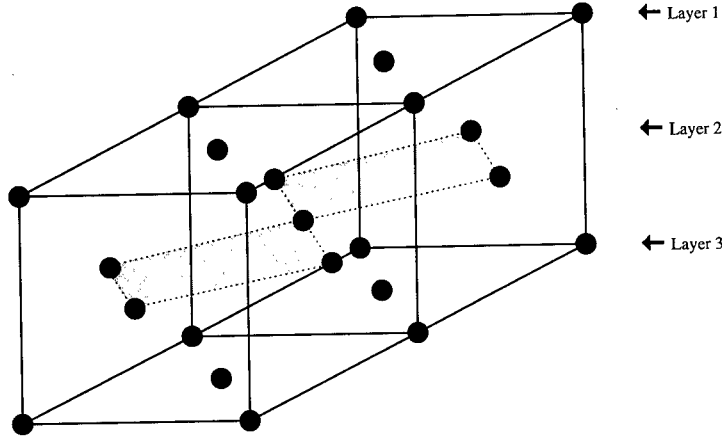


Figure 9 fcc alloy film with two order parameters per layer.

by $2N_l + 1$ variables, namely β and the sets $\{c_i\}$ and $\{\Lambda_i\}$. The subscript refers to the layer index. The appropriate basis for the set of equations (3), as one would expect by an analogy with the bulk case, is now a basis of partial fourier transforms between the layers of the film. In this representation one finds, with $N_l = 3$ for ease of presentation,

$$\begin{pmatrix} \alpha_{11} & \alpha_{12} & \alpha_{13} \\ \alpha_{21} & \alpha_{22} & \alpha_{23} \\ \alpha_{31} & \alpha_{32} & \alpha_{33} \end{pmatrix} = \begin{pmatrix} \Sigma_1 & v_{12}^{(2)} & v_{13}^{(2)} \\ v_{11}^{(2)} & \Sigma_2 & v_{23}^{(2)} \\ v_{31}^{(2)} & v_{32}^{(2)} & \Sigma_3 \end{pmatrix}^{-1} \quad (6)$$

With this matrix $\alpha(q)$ in terms of known functions one can write down a correction to the BWMF free energy

$$\begin{aligned} A^{correction}/N &= 1/2 \sum_{i=1}^{N_l} c_i(1 - c_i)\Lambda_i \\ &+ k_b T/2 [-\Omega_{layer}^{-1} \int d^3q \ln \|\alpha(q)\| + 1/2 \sum_{i=1}^3 \ln \alpha_{ii}] \end{aligned}$$

Proceeding as in the bulk cases by fourier transforming the set of equations (4), there would be $2N_l + 1$ coupled equations to solve.

PRINCIPLE (100) SURFACE, MORE THAN ONE ORDER PARAMETER PER LAYER

For N_s concentrations per layer a state will be specified by $N_s N_l + 1$ variables, β and the sets $\{c_i^j\}$ and $\{\Lambda_i^j\}$. Here we use the notation that the subscript refers to the layer index and the superscript to the layer sublattice index. In this case one now also has partial fourier transforms

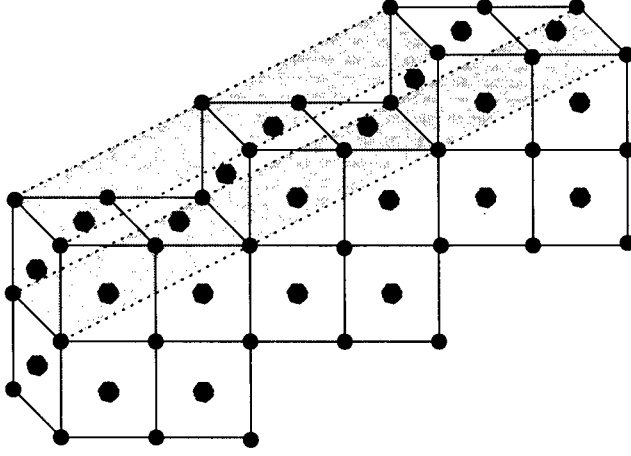


Figure 10 (100) vicinal surface with $h=1$ and $l=2$.

between the sub-lattices of the layers, as well as between the layers themselves. This has the effect that an element of the matrix in (6) is replaced by an N_s^2 elements as indicated below for the case $N_s = 2$

$$\alpha_{ij} \rightarrow \begin{pmatrix} \alpha_{ij}^{11} & \alpha_{ij}^{12} \\ \alpha_{ij}^{21} & \alpha_{ij}^{22} \end{pmatrix}$$

$$\begin{pmatrix} \alpha_{11}^{11} & \alpha_{11}^{12} & \alpha_{12}^{11} & \alpha_{12}^{12} \\ \alpha_{21}^{11} & \alpha_{21}^{12} & \alpha_{22}^{11} & \alpha_{22}^{12} \\ \alpha_{11}^{21} & \alpha_{11}^{22} & \alpha_{12}^{21} & \alpha_{12}^{22} \\ \alpha_{21}^{21} & \alpha_{21}^{22} & \alpha_{22}^{21} & \alpha_{22}^{22} \end{pmatrix} = \begin{pmatrix} \Sigma_1^1 & v_{11}^{(2)12}(q) & v_{12}^{(2)11} & v_{12}^{(2)12} \\ v_{11}^{(2)21} & \Sigma_1^2 & v_{12}^{(2)21} & v_{12}^{(2)22} \\ v_{21}^{(2)11} & v_{21}^{(2)12} & \Sigma_2^1 & v_{22}^{(2)12} \\ v_{21}^{(2)21} & v_{21}^{(2)22} & v_{22}^{(2)21} & \Sigma_2^2 \end{pmatrix}^{-1}$$

where we now show the formulae for $N_l = 2$. The free energy correction is

$$A^{correction}/N = 1/2 \sum_{i=1, j=1}^{N_l, N_s} c_i^j (1 - c_i^j) \Lambda_i^j + k_b T / 2 \left[-\frac{\Omega_{layer}}{2} \int d^2 q \ln \|\alpha(q)\| + 1/2 \sum_{i=1, j=1}^{N_l, N_s} \ln \alpha_{ii}^{jj} \right]$$

VICINAL (100) SURFACE

The geometry of a vicinal surface can be defined by the step height h and the terrace length l . The layers of symmetry related sites are now at

some angle $\tan^{-1} \frac{l}{h}$ to the [100] direction, and predictably partial fourier transforms between these layers form the convenient basis for the OCFA to be written down in. In this way one can see that there will in fact be no formal difference between the OCFA for principal or vicinal surfaces.

OUTLOOK AND CONCLUSIONS

The OCFA solves the BWMF problem of the fcc phase diagram for ordering potentials. It seems that the OCFA is a good approximation for frustrated systems. However, the MC and CVM methods both solve the same problem. The point we would like to make is that it is easy to write down equations to solve for various complex situations, particularly vicinal surfaces, in the OCFA which would be in the least extremely tedious with CVM and certainly extremely difficult with MC. In short, it is easier to write down the appropriate matrix of correlation functions than it is to do cluster algebra. Also, as the OCFA is a single site theory it can be implemented in a fully (first principles) electronic theory. This has been done for the solid solution case, see for example [10]. It is now *in principle* possible to do this for partially ordered structures, and with the free energies to calculate the phase diagram. One could then see the interplay between the frustration and the electronic effects. On the other hand there is no such thing as a free lunch, and it is probably true that the OCFA equations are more difficult to solve than the CVM equations once both are written down. On top of this it remains to be seen how good an approximation it really is, and one bulk calculation doesn't provide a conclusive answer to this question. A further test is of course surface calculations which we plan to do. It might be the case that the OCFA completely distorts the true surface behaviour, in which case it's usefulness is severely curtailed. However, in view of it's success in the bulk phase diagram and it's ease of implimentation one might, taking a pragmatic view, expect it to be some sort of half way house between BWMF and the CVM and MC calculations, so that one could perhaps use it to explore complex (and interesting) problems in the cases where the BWMF fails disasterously, and the generally better approximations like CVM and MC are difficult to implement.

ACKNOWLEDGEMENTS

SS would like to acknowledge the funding support of the EPSRC during this work. BLG would like to thank the Erwin Schroedinger Institute for Mathematical Physics, Vienna for hospitality during the preparation of this manuscript.

REFERENCES

- [1] H. Dosch et al. *Experimental evidence for an interface delocalisation transition in Cu₃Au* Phys. Rev. Lett. **60** 2382 (1988).
- [2] H. Reichert et al. *Thermodynamics of surface segregation profiles at Cu₃Au (001) resolved by X-ray scattering* Phys. Rev. Lett. **74** 2006 (1995).
- [3] B. L. Gyorffy, M. Stocks *Concentration waves and Fermi surfaces in random metallic alloys* Phys. Rev. Lett. **50** 374 (1983).
- [4] Shockley *Theory of order for the copper gold system* J. Chem. Phys. **6** 130 (1937).
- [5] W. Schweika et al. *Surface induced ordering and disordering in fcc alloys: a monte carlo study* Phys. Rev. B **53** 14 8937 (1996).
- [6] R. Brout and H. Thomas *Onsager cavity field approximation applied to magnetic systems* Physics **3** 6 317 (1967)
- [7] Lars Onsager *Electric moments of molecules in liquids* J. Am. Chem. Soc. **58** 1486 (1936).
- [8] A. Finel and F. Ducastelle *On the phase diagram of the face centred cubic Ising model with anti-ferromagnetic first-neighbour interactions* Europhysics Letters **1** 135 (1986).
- [9] H.T. Diep et al. *Phase diagrams in f.c.c. binary alloys: frustration effects* Europhysics Letters **2** 603 (1986).
- [10] J.B. Staunton *Compositional short range ordering in metallic alloys: band filling, charge transfer and size effects from a first-principles all-electron, Landau-type theory* Phys. Rev B (1994)
- [11] V.I. Tokar et al. *Phase Diagram of face centred cubic Ising model with anti-ferromagnetic nearest neighbour interactions: a novel approach* Comp. Mat. Science **8** 8 (1997)

IN-SITU CHEMICAL DYNAMICS AND PHASE MAPPING UNDER STEEP THERMAL GRADIENTS USING TIME-RESOLVED AND SPATIALLY RESOLVED X-RAY DIFFRACTION

Joe Wong¹, E.M. Larson², J.B. Holt³, T. Ressler⁴ and J. W. Elmer

¹Lawrence Livermore National Laboratory, University of California,
P.O. Box 808, Livermore, CA 94551, USA

²Grand Canyon University, College of Science, 3300 W. Camelback Rd, Phoenix, AZ 85107

³3908 Freed Ave, San Jose CA 95117

⁴Fritz-Haber-Institute of the Max-Planck-Society, Department of Inorganic Chemistry
Faradayweg 4-6, D-14195 Berlin, Germany

ABSTRACT

Time-resolved and spatially-resolved diffraction techniques have been developed recently to perform materials dynamics study in-situ extending into the time and spatial domain in high temperature processes. The applications of these methods to investigate the chemical dynamics of solid combustion reactions and to map phases and their transformation in fusion welds are exemplified in this paper.

INTRODUCTION

Real-time studies of dynamical processes in-situ under severe temperature or pressure conditions often pose a challenge for experimentalists. In materials synthesis such as combustion synthesis and materials joining processes such as welding, high intensity heat sources are used to create steep thermal gradients that rapidly heat and cool materials to and from their melting point. This rapid thermal cycling induces solid state reactions and/or phase transformations both on heating and on cooling, and causes melting and solidification in regions of the material where the liquidus temperature has been exceeded. Composition and/or structure fluctuations are expected to occur along thermal gradients, and microstructural discontinuities exist at (or near) the location of each phase transformation isotherm.

Combustion synthesis is a relatively novel mode of preparing high temperature materials via solid-state reactions. These reactions are universally accompanied by the release of a large amount of heat. Once ignited with an external heat source, these solid combustion synthesis (SCS) reactions become self-sustained and propagate to completion within seconds. Also known as self-propagating high temperature synthesis (SHS) reactions, these processes are characterized by a fast-moving combustion front (1 to 100 mm/s) and a self-generated temperature varying from 1000 to 4000K. A number of ceramic, intermetallic and composite materials have been synthesized by this method^{1,2}, including high temperature superconducting oxides^{3,4}.

Although the basic concepts of this method of materials synthesis are relatively easy to apply in principle, there remains a number of basic questions concerning the physical and chemical nature as well as the dynamics of phase transformation within the moving combustion front. The situation is true even with the most simple $A + B \rightarrow AB$ combustion reactions. Until recently⁵⁻⁷, it has been difficult to investigate these reactions because of the speed and extreme thermal conditions. Examinations of reactant and product phases and their microstructures are possible with x-ray diffraction and a variety of optical and electron microscopies. However, the high temperature and fast rates of combustion preclude any in-situ investigation of structural changes and chemical dynamics in the combustion zone in real time with most conventional techniques.

Material systems where thermally induced phase transformations play a significant role include allotropic elements such as pure titanium (hcp_bcc); two-phase alloys such as stainless steels (fcc_bcc); martensitic alloys such as iron-based steel alloys (fcc_bct); and dispersion-strengthened alloys. Most of the phase transformations of interest will involve deviations from equilibrium microstructures, resulting in partial transformations and/or the creation of metastable phases. These types of phase transformations have aroused a lot of interest in recent years in welding research development and in the metallurgical community⁸.

From a practical standpoint, solid state phase transformations and their kinetics play an important role in understanding various problems associated with thermal processing of materials such as sub-solidus cracking, cold cracking and distortion caused by residual stresses^{9,10}. Solution to these problems will greatly be facilitated by the development of novel experimental methods for determining phase transformation behavior in the steep thermal gradients and at the high cooling rates. Until more recently^{11,12}, no direct method existed for investigating solid state phase transformations that take place. Conventional methods for studying general phase transformation behavior are most *indirect* and of a *post-mortem* nature. Moreover, these methods only provide data for low heating and cooling rates on the order of ~ 1 K/s, which is much less than those of arc welds ($10 - 10^3$ K/s), and laser and electron beam welds ($10^2 - 10^4$ K/s).

We describe recently developed synchrotron techniques and their applications (a) to follow the course of reaction of a carefully chosen $Ta + C \rightarrow TaC$ solid combustion system with a time resolution of 50 ms by recording the time-resolved x-ray diffraction (TRXRD) patterns in situ and at high temperature and (b) to probe the phases and map their locations in steep thermal gradients (~ 100 K/mm) down to 200 μm in spatial extent in a Ti fusion weld by recording the spatially-resolved x-ray diffraction (SRXRD) patterns *in-situ* during the welding process.

The choice of the Ta-C combustion system is two-fold. Firstly, the combustion synthesis of both TaC and Ta₂C from Ta and C is atypical of many other combustion reactions because the adiabatic temperatures (2438 °C and 2360 °C for TaC and Ta₂C respectively) are below the melting temperatures of tantalum, carbon, the carbides and known eutectic compositions¹³. Therefore, these combustion reactions must occur in the solid state with no participation of a liquid phase. In fact, it has been suggested that the rate-controlling step in the combustion reactions of Ta and C is the diffusion of carbon into the tantalum particles¹⁴⁻¹⁶. Secondly, Ta and its compounds are strong x-ray scatterers which enable a short scan time for each diffraction pattern (tens of milliseconds with good signal-to-noise ratios)¹⁷.

To illustrate its novelty, we apply the SRXRD technique¹⁸ to map completely the phases and their solid-state transformations in titanium fusion welds. In a fusion weld, two distinct microstructural regions are formed: (i) the *fusion zone*, FZ, in which melting, solidification and solid state phase transformation have taken place, and (ii) the *heat affected zone*, HAZ, in which only solid state phase transformations have taken place. In each zone, metastable microstructures may be created that can enhance or degrade the quality of the weld, depending on the materials and processing parameters. Profile analyses of the diffraction data were used to elucidate the evolution of various types of high temperature microstructures in the vicinity of the HAZ around the liquid weld. The observed phase boundaries are compared with calculations from a heat flow model¹⁹.

EXPERIMENTAL METHODS

Time-resolved diffraction measurements

The diffraction-reaction chamber, and detectors are shown schematically in Figure 1. A detailed description of the apparatus has been given elsewhere^{6,20}. This apparatus was designed to accept a synchrotron beam incident at an angle of $\sim 20^\circ$ on a combustion specimen. The detectors are silicon position-sensitive photodiode arrays manufactured by Princeton Instruments, NJ. Each array is 25 mm long containing 1024 pixels, and is capable of recording a full scan of 1024 pixels in 4 ms. Diffraction experiments were performed at Brookhaven National Synchrotron Light Source (NSLS) on beamline X-11A using a focused beam monochromatized with a double Si(111) crystal at 8048.0 eV ($\lambda = 1.5406 \text{ \AA}$). The detectors each spanning $6^\circ 2\theta$ were centered at 36.5° and 72° (where θ is the Bragg angle for a given reflection) to collect the Ta (110) and (211) diffraction peaks at the start of the reaction as well the major diffraction peaks of both TaC and Ta₂C products in these 2θ windows. The vertical hutch slit was adjusted to a height of 0.46 mm for the Ta + C reaction (I) and 0.25 mm for the faster 2Ta + C reaction (II). These produced an x-ray beam of 1.1 mm and 0.6 mm long respectively along the length of the sample at a θ angle of 25° .

Diffraction patterns were collected and stored at constant time intervals from the initiation of the reaction through completion with a total collection time ranging from 15 to 50 seconds. A typical TRXRD experiment might consist of 500 scans each collected at 100 ms. Scan times of both 50 and 100 ms time frames were used for both reactions I and II. Data sets were collected during the burns of several samples of each mixture. Some expansion of the material was expected and took place during the reaction causing slight shifts in the peak positions to a higher 2θ value. Prior to ignition, the room temperature diffraction pattern of each specimen was routinely recorded to optimize sample position, choice of 2θ -window and S/N ratios with scan time. Diffraction scans were also taken of the cooled product 5-10 minutes after completion of the reaction. Conventional powder diffraction patterns from the surface as well as the interior of each reacted samples were later collected in the laboratory to verify the product phase using a conventional x-ray tube.

Preparation of combustion synthesis specimens

Stoichiometric mixtures of metal and carbon powders (1:1 and 2:1) respectively for reaction I: Ta + C = TaC and reaction II: 2Ta + C = Ta₂C were weighed and mechanically mixed in a SPEX mixer for 10-30 min. The combustion specimens were pressed cylindrical pellets, 19 mm in diameter and about 25 mm long with a green density of $\sim 55\%$. The pressed samples were ignited at one end by a resistively heated tungsten coil. After ignition, the burn became self-sustaining due

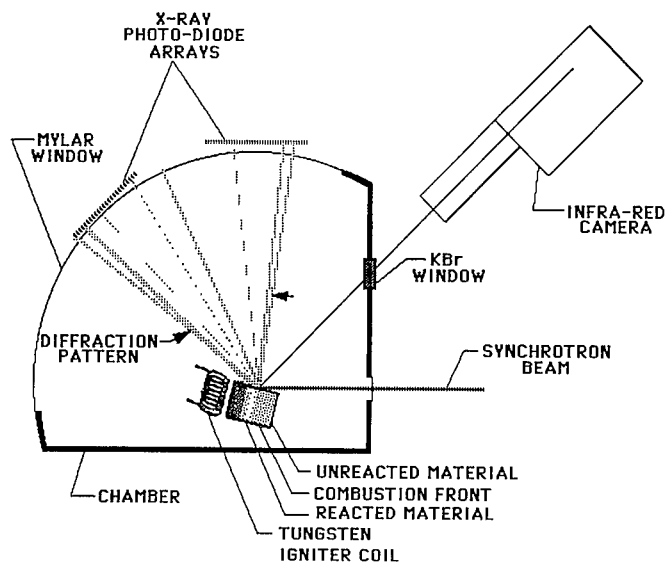


Figure 1. Schematic diagram showing the TRXRD diffractometer reaction chamber at NSLS Beamline X-11^{17,20}.

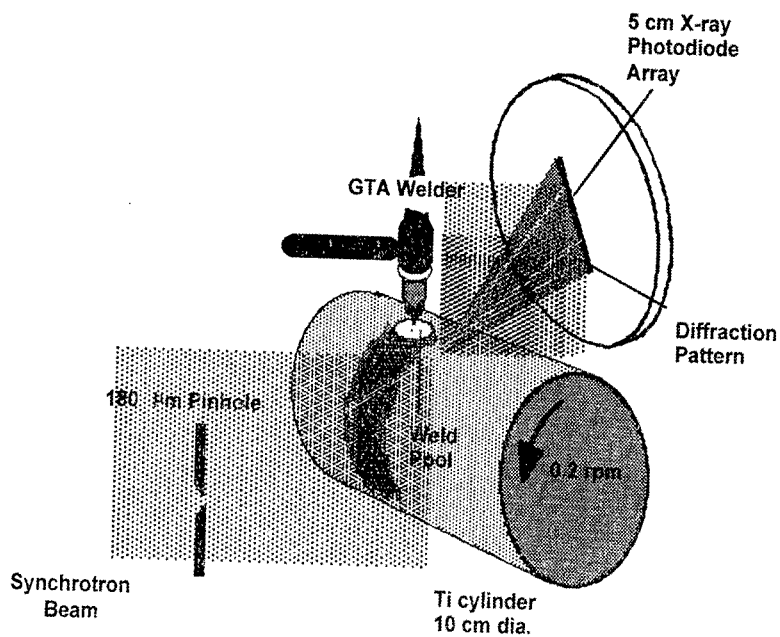


Figure 2. Schematics of the SRXRD setup used for in-situ phase mapping and real-time observation of microstructure evolution in fusion welds¹².

to the high exothermicity of the reaction. All Ta + C and 2Ta + C reactions reported here were performed in helium at a pressure of 1 atm or slightly less to obviate oxidation and to minimize air attenuation of the diffracted signals.

Spatially resolved x-ray diffraction (SRXRD) measurements

SRXRD experiments were performed on the 31-pole-wiggler beam line 10-2¹ at Stanford Synchrotron Radiation Laboratory (SSRL) with the storage ring operating at an energy of 3.0 GeV and injection current of ~100 mA. Details of the SRXRD instrument can be found elsewhere^{11,12}. A schematic representation of the experimental set-up is shown in Figure 2.

XRD measurements were made using a monochromatic x-ray beam with a photon energy of 8.5 keV (wavelength $\lambda = 1.4586$ Å). A Si(111) double crystal monochromator was used preceded by a toroidal mirror in a 1:1 focusing geometry. The spatial resolution of the experiment was determined by a 180 μm pinhole placed 30 cm in front of the weld. A photon flux of about $2 \cdot 10^9$ photons per second was determined using an ionization chamber situated between pinhole and weld. From photographic paper measurements the beam size on the titanium bar was estimated to be ~200 μm . X-ray diffraction patterns from the titanium bar were recorded on a 5 cm long water-cooled 2048-element position sensitive photodiode array detector. The detector, similar to those described in the TRXRD experiments, but upgraded to 50 mm long to contain 2048 pixels, was placed 9.5 cm from the weld at an angle of 30° with respect to the primary synchrotron beam covering a 2 θ range from 30° to 60°. The detector and associated *ST/21* data acquisition system were manufactured by Princeton Instruments²². The latter was used to store and display the x-ray diffraction data in real time.

SRXRD patterns were measured during welding by positioning the beam at a pre-determined location with respect to the welding electrode. A single diffraction pattern at each location was collected for 6 s while the bar rotated under the torch at a constant speed of 0.2 rpm. By incrementally jogging the weld to new locations in 200 μm intervals, a series of spatially-resolved x-ray diffraction patterns was collected along a lineal scan direction perpendicular to and away from the centerline of the weld. For example, a typical run consisted of gathering 40 x-ray diffraction patterns spanning a range of 8 mm through the HAZ. A schematic representation of the mapping procedure is presented in Figure 3. The dimension of the liquid weld pool was determined from the experiment, whereas the dimension of the heat affected zone was estimated from a heat-flow model¹⁹. Each dotted line represents a single experimental SRXRD run, and each dot denotes an x-ray diffraction pattern collected at this location with respect to the center of the weld. After completing a run, the weld was allowed to cool to room temperature and the electrode was repositioned to a new starting location with respect to the x-ray beam prior to taking the next series of data. As can be seen from Figure 3, by symmetry only one half the weld was mapped experimentally. In the following analysis, only the top half of the entire weld will be displayed for simplicity.

Titanium samples for welding

Cylindrical welding samples were machined from as received grade 2 commercially pure titanium measuring 10.2 cm in diameter and 12.7 cm length. These samples had a surface finish of 1.6 μm RMS and were round to within 10 μm on the diameter. Chemical analysis was performed using combustion analysis for O, C, N, and H, and inductively coupled plasma analysis for the remaining elements. The results show the following impurity content (wt %): 0.14 % Fe, 0.17 % O, 0.03 % Al, 0.02 % Cr, 0.008% C, 0.001 % H, 0.014 % N, 0.02 % Ni, 0.005 % V, 0.004 % Si. The final cylindrical samples were then vacuum annealed for 30 min at 400 °C to partially recover the cold work that was introduced during machining.

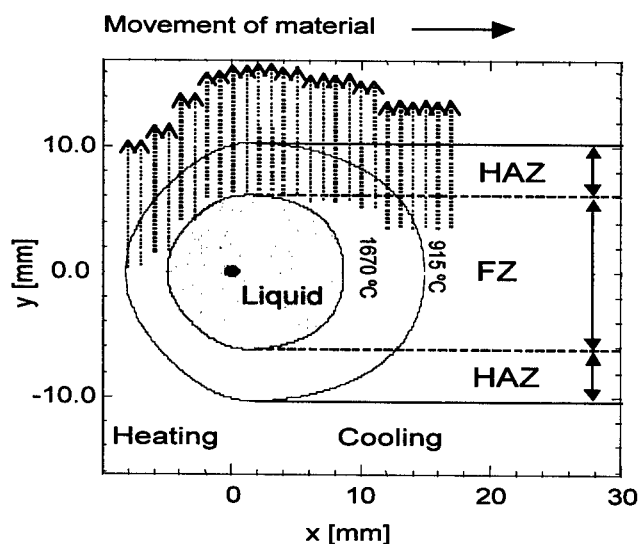


Figure 3. Schematic representation of the SRXRD procedure used. Indicated are HAZ (delimited by 915 °C isotherm) and FZ (limited by 1670 °C isotherm) as determined from heat-flow model calculations¹⁹, and the direction of movement of the titanium material underneath the tungsten electrode (black dot at $x = 0.0$ mm and $y = 0.0$ mm). Each dotted arrow represents a single experimental SRXRD run, and each dot denotes an x-ray diffraction pattern measured at this location. Heating and cooling side of the moving weld are indicated.

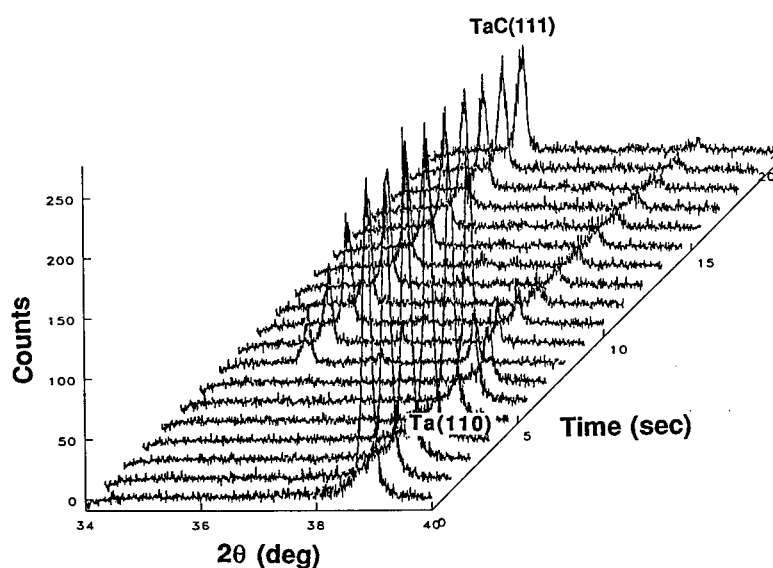


Figure 4. A 3-dimensional plot of the time-resolved diffraction patterns for the combustion reaction: $\text{Ta} + \text{C} \rightarrow \text{TaC}$ collected at 100 ms/scan. Only every 10th scan was plotted for visual clarity. $t = 0.0$ s corresponds to triggering of the detectors. Beyond 20s the TRXRD patterns remained unchanged.

Welding setup and procedure

Gas tungsten arc welds were made on the titanium bars using a 150 A direct current welding power supply with the electrode held at negative polarity. A new welding electrode made of W-2 % Th, 4.7 mm in diameter, was used for each weld. The power was maintained constant at 1.9 kW (100 A, 19 ± 0.5 V) for all welds, and helium was used as both a welding and shielding gas. The titanium bar was rotated at a constant speed of 0.20 rpm below the fixed electrode, which corresponds to a surface welding speed of 1.1 mm/s, and resulted in an 11 to 12 mm wide fusion zone on the surface of the titanium bar. All welding was performed inside a chamber purged with ultra high purity helium (99.999 %) to minimize oxidation of the titanium that had occurred¹². The He gas was also passed through the torch during welding to further prevent oxidation in the weld region and to cool the torch. The welding assembly was integrally mounted to a translation stage driven by a stepper motor with 10 μ m precision. Spatial mapping of the phases in the various regions of the HAZ was performed by using the translation stage to manipulate the weld (welding torch and workpiece) with respect to the fixed x-ray beam in order to sample discrete regions around the weld. Movements perpendicular to the centerline of the weld were controlled by a computer and were performed by direct translation of the workpiece with respect to the x-ray beam. An in-house designed software package was developed on a personal computer using LabView software v4.0 to control the position of the weld with respect to the x-ray beam, to control the bar rotational speed (welding speed), and to trigger the data acquisition system in a second computer.

RESULTS

Time-resolved diffraction data

The synthesis of TaC. Figure 4 shows a series of typical time-resolved diffraction patterns for the synthesis of TaC from a stoichiometric mixture of its constituent elements. In this TRXRD experiment, the detector counting time per diffraction pattern (scan) was 100 ms, and 500 such scans were recorded to yield a total measurement time of 50 s. In this 3-D plot, only every 10th scan was plotted to ease visual representation of the course of reaction with time. $t = 0$ corresponds to triggering of the detector to initiate collection of diffraction patterns of the reactant mixture prior to arrival of combustion front at the area of the sample illuminated by the synchrotron beam.

Examination of such a time series of TRXRD diffraction scans shows that the sequence of chemical events in the combustion zone may be represented by a subset of selected scans as plotted in Figure 5. Two tantalum metal peaks are prominent until 5.6 s have passed when the Debye-Waller effect diminishes their intensities due to arrival of the high temperature combustion front. The Ta (110) peak splits at 6.7 s and another peak is observed at $35^\circ 2\theta$. The Ta (211) has almost disappeared and only a hint of scattering is observed in the center of the second detector at high angle. At 7.5 s both TaC and Ta₂C peaks are clearly registered in both detectors. Considering the combustion front velocity (~ 2.0 mm/s) and beam width of 1.1 mm along the direction of combustion front, the combustion front would pass through the x-ray spot in ~ 0.55 s. After 30 seconds, most of the scattering from Ta₂C has disappeared leaving only TaC peaks prominent in the patterns, which shifted to higher 2θ values indicative of lattice contraction upon cooling. Laboratory XRD patterns showed only trace amounts of subcarbide in the interior as well as on the surface of reacted samples.

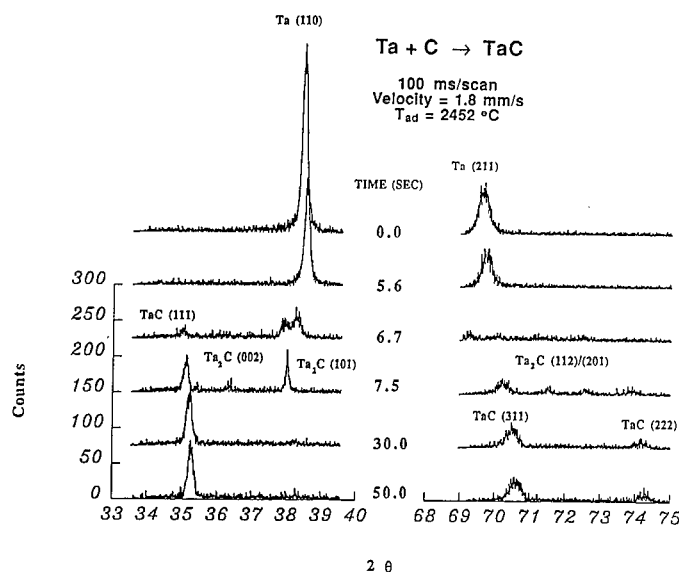


Figure 5. Selected TRXRD patterns collected at 100 ms/scan for the $\text{Ta} + \text{C} \rightarrow \text{TaC}$ combustion reaction, showing critical events in the course of the reaction. Time = 0.0 seconds corresponds to triggering of the detectors.

The Synthesis of Ta_2C . The $2\text{Ta} + \text{C} \rightarrow \text{Ta}_2\text{C}$ reaction was also monitored at both 100 ms and 50 ms time scale and the corresponding TRXRD scans are shown in Figure 6. Only 50 ms (one TRXRD frame) elapses from the time the Ta peaks begin to decrease at $t = 1.60$ s and the major Ta_2C peaks appear at $t = 1.65$ s. By the next frame, all the subcarbide peaks are evident with no indication of any other species present. Since this reaction was faster than the $\text{Ta} + \text{C}$ reaction and to test spatial resolution of the diffraction peaks, the hutch slit was adjusted to 0.25 mm. At a velocity of 5 mm/s, the burn front would pass through the 0.6 mm long x-ray beam spot in 0.12 s or 120 ms. The same scenario is replayed in all of the TRXRD data recorded for this reaction. However, there is no indication of an intermediate carbide phase. In post diffraction scans, Ta_2C is the only tantalum-containing phase present on the surface and in the interior of the combusted sample.

Spatially resolved x-ray diffraction data: Phase mapping in the HAZ of Ti fusion welds

Pure titanium exhibits two phase transitions: an $\alpha \rightarrow \beta$ phase transformation in the solid state at 882°C and melting at 1668°C ²³. In commercially pure grade 2 titanium employed in this work, the allotropic transformation from a hcp α -phase to a bcc β -phase occurs at $\sim 915^\circ\text{C}$ due to the presence of iron, oxygen, and other impurities²³. During the welding process, these phase transitions give rise to two distinct microstructural regions: a fusion zone (FZ) in which melting upon heating and solidification on cooling occur and a heat-affected zone (HAZ), in which the $\alpha \rightarrow \beta$ solid-state phase transformation and other microstructural changes take place. A typical series of SRXRD patterns measured across the $\alpha \rightarrow \beta$ phase transformation isotherm is shown in Figure 7. The starting position and scan direction of the SRXRD run with respect to the center of the weld are shown by the dotted arrow in the inset. A transition from a β -Ti bcc pattern at high temperature inside the HAZ, to a $\alpha + \beta$ -mixed zone, and eventually back to the α -Ti hcp pattern can be seen. In addition to phase transformations, the material undergoes annealing and

recrystallization in the cooler region and outside of the HAZ. SRXRD data obtained from different starting positions with respect to the weld center may be classified into five principal diffraction patterns. These patterns are labeled as α for the base hcp metal, α_{AR} for the annealed and partially re-crystallized hcp phase, α_{RG} for the re-crystallized and grain growth in the hcp phase, β for the fully transformed high temperature bcc phase and α_{BT} for the back transformed hcp phase. Examples for each of the principal patterns are displayed in Figure 8 together with one for the α - β -coexistence region. It should be noted that all principal diffraction patterns belong to either the α -Ti or the β -Ti phase, but indicate differences in texture, degree of re-crystallization or annealing, or phase concentration. These principal diffraction patterns and the associated microstructures are described in detail in the following section.

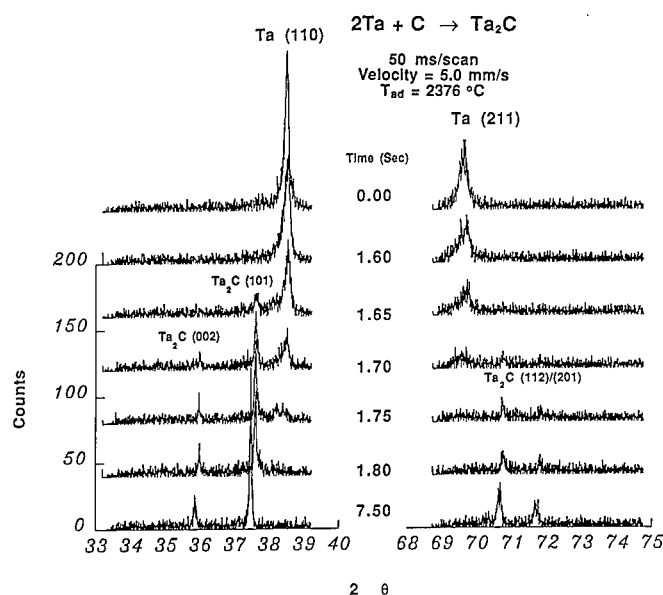


Figure 6. Selected TRXRD patterns collected at 50 ms/scan for the $2\text{Ta} + \text{C} \rightarrow \text{Ta}_2\text{C}$ combustion reaction, showing critical events in the course of the reaction. Time = 0.0 seconds corresponds to triggering of the detectors.

DISCUSSION

Chemical dynamics of the Ta-C combustion synthesis

Quantitative determinations of component concentrations in the TaC-Ta₂C system using intensities of diffraction peaks have been reported²⁴. In the present work, the concentration of the Ta reactant, Ta₂C and TaC final product at a given instant of time in the course of the reaction is assumed to be directly proportional to the intensities of all observed diffraction lines for the respective phase as shown in the TRXRD patterns given in Figs. 4-6. The summation of intensity over all lines eliminates effects of preferred orientation in the "powder" patterns observed using the present diffraction geometry. The intensity sum for each phase is then normalized to its maximum value and plotted as a function of time to yield a set of normalized concentration profiles vs. time. These profiles are shown in Figures 9 and 10 for reaction I and reaction II respectively.

Consider first the Ta + C reaction. In Figure 9, it is seen that the reduction in intensity of the Ta metal peak due to the Debye-Waller effect from pre-heating of the sample is responsible for the slope of the metal concentration between 2.0 - 5.5 s. Note that the Ta concentration profile intersects first with that of the Ta₂C intermediate, and that the TaC concentration has not reached its maximum until the Ta₂C concentration has grown and then diminished. Also, the chemical reaction is not confined to a narrow zone at the combustion front but continues after the passage of the front. The reaction temperature remains above 1200 °C for approximately 4 seconds since the average combustion front velocity is ~2 mm/s¹⁷. The normalized intensity plot of Figure 9 clearly shows that it takes 3-4 seconds for the growth of the TaC phase. This clearly substantiates the premise that the combustion synthesis reaction for TaC continues for several seconds and that an equilibrium is not reached until well after the passage of the burn front.

In solid state chemical reactions the interfacial area between reactants may influence the overall rate. If transport of atoms to the interface becomes too slow then the interfacial reaction becomes rate controlling. With most combustion reactions for metal carbides syntheses the melting point of the metal reactant is low enough that it melts at the combustion front and by capillary action surrounds the carbon particles. The occurrence maximizes the interfacial area. Furthermore, it seems unlikely that at 1700 °C the vapor pressure of Ta²⁵ is high enough to influence the overall rate of reaction by a vapor transport mechanism.

Thus, the experimental findings are consistent with a purely solid state mechanism. It is not unexpected that Ta₂C was observed first before the formation of TaC in reaction. Both self

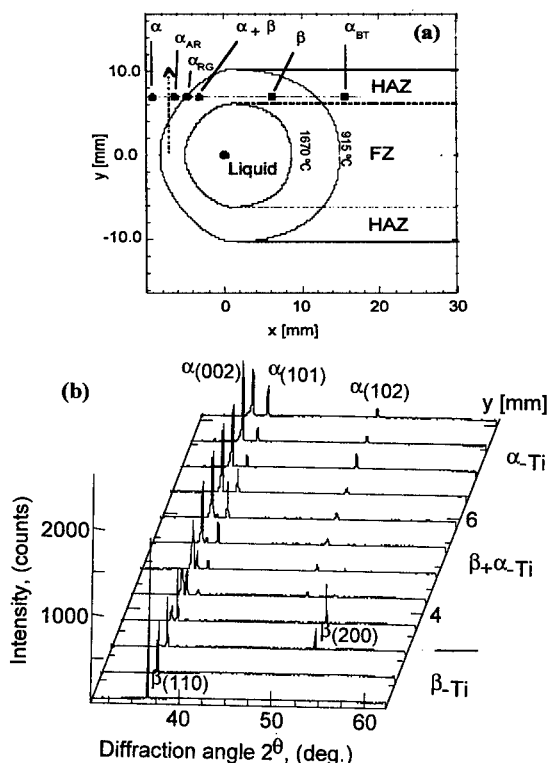


Figure 7. A series of SRXRD patterns measured across the $\alpha \rightarrow \beta$ phase transformation isotherm ($T = 915\text{ }^{\circ}\text{C}$) in the y -direction along the negative temperature gradient at a position $x = -6\text{ mm}$ ahead of the center of the weld (*dotted arrow in inset*) showing the β -Ti, $\alpha + \beta$ coexistence, and α -Ti zones.

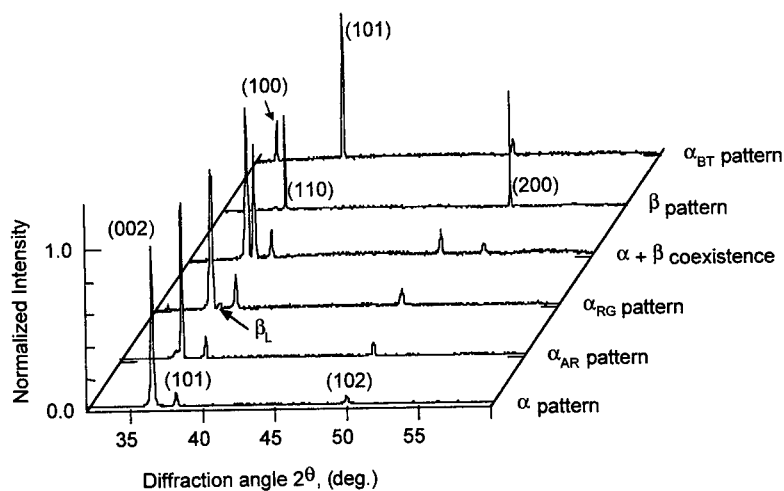


Figure 8. Principal diffraction patterns obtained from the current SRXRD measurement on titanium fusion welds. (○) represent the base metal hcp α -Ti phase. (α_{AR}) is for the annealed and recrystallized α -Ti. (α_{RG}) denotes a recrystallized α -Ti phase exhibiting large diffraction domains (grain growth). (α_{BT}) is for the back transformed α -Ti that forms from the region of the HAZ that once contained β -Ti. (○) is for the β -Ti phase and (β_L) is for the β -Ti that coexists with α -Ti in low amounts predominantly together with α_{BT} . The z-axis in the plot represents a line, $y = 7$ mm parallel to the centerline of the weld as shown in Fig. 5 inset, that would yield this series of six SRXRD patterns. Data were normalized to unity for the highest peak in each pattern.

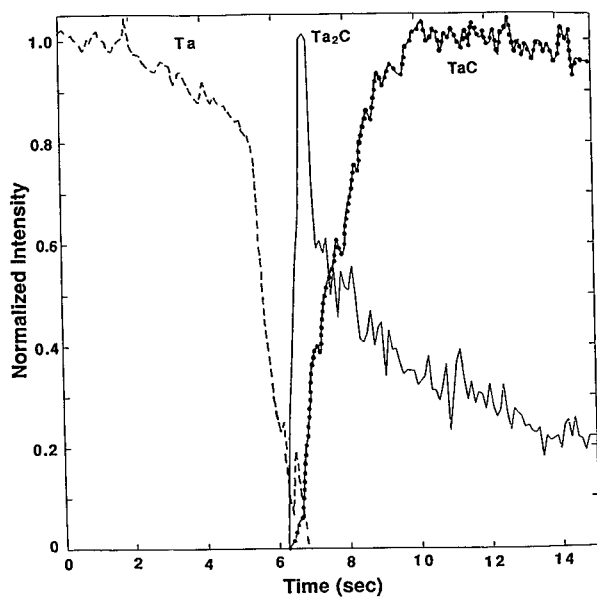


Figure 9. Normalized integrated intensities plotted as a function of time for Ta(110), Ta_2C (101) and TaC(111) diffraction peaks, showing the chemical changes in the course of the Ta + C reaction.

diffusion and chemical diffusion coefficients have been measured in TaC²⁶. These measurements indicate that in the temperature range of interest (1700-2000 °C) the carbon atom diffuses several orders of magnitude faster than the Ta atom in TaC. Therefore, as carbon diffuses into the Ta lattice, a dilute solid solution is formed. As more carbon diffuses into the Ta the concentration level of C is raised high enough for the formation of Ta₂C. In the Ta₂C structure (P6₃/mmc) there are two octahedral interstices on either side of a hexagonal layer. These are located directly above one another, and only one of these can be occupied. That is, only one-half of the octahedral interstices in Ta₂C is filled²⁷. Further, carbon diffused into the subcarbide lattice would have to be accommodated by a hexagonal-to-cubic transformation to the TaC phase, in which all octahedral sites can now be occupied. However, if there were just enough carbon to form the subcarbide as in reaction II, the final product would just be Ta₂C as was observed in reaction II.

Within the time resolution of our synchrotron diffraction experiments no intermediate phase is observed in the 2Ta + C reaction. The direct conversion of the stoichiometric powder mixture to Ta₂C is consistent with the phase diagram which shows only the two compounds. The formation of Ta₂C proceeds by a factor of ~2 faster than for the formation of TaC, as indicated by the steeper slopes of the Ta₂C concentration profiles (Figs. 9 and 10) as compared with that for the TaC formation (Figure 9). This suggests that the diffusion rate of carbon to the Ta metal lattice to form the Ta₂C hexagonal phase is a factor of two faster than the rate of carbon diffusion in the Ta₂C lattice in transforming to the final TaC product. It is challenging to elucidate the mechanism of each of these reactions to further our understanding of the observed reaction times.

Phase distribution in the Heat-affected zone of Ti fusion welds

In the following, the five principal diffraction patterns will be discussed in light of the associated microstructure at various locations in the HAZ and its vicinity *during the welding process*.

The α_{AR} pattern: location and associated microstructure. The locations at which the α_{AR} pattern was observed are plotted in Figure 11a. The corresponding diffraction pattern is shown in Figure 11b. Profile analysis revealed that the peak width of the α_{AR} patterns appearing at the end of each of the SRXRD scans was narrower than the room temperature base metal peak width. This implies that none of the SRXRD scans were measured far enough out to reach the unaffected titanium base metal.

Polycrystalline titanium base metal starts with small diffraction domains and grains that exhibit a high degree of disorder and internal stress due to the extrusion and machining process. Stresses and disorder result in broad single peaks originating from diffraction domains with sizes in the order of 20 nm. Domain sizes were obtained from the Scherrer formula²⁸ ($t = 0.9\lambda / (v_{hkl} \cos(\Theta_{hkl}))$), with t the thickness of a diffraction domain, λ the wavelength, and v_{hkl} and Θ_{hkl} the peak width (in radian) and Bragg angle of the (hkl) line, respectively. Thus, diffraction domain sizes were calculated to compare different phases and evaluate relative microstructural changes, but not to obtain absolute values.

Moving towards the center of the weld in x and y , annealing of the base metal takes place with increasing temperature. Defects and stress in the grains are being reduced and small diffraction domains grow to form larger, more perfect domains. This results in a progressive narrowing of diffraction peaks along the positive temperature gradient. Figure 12 shows the variation of the α -Ti (002) peak width for two experimental runs ahead of the weld center at position $x = -8$ and -7 mm.

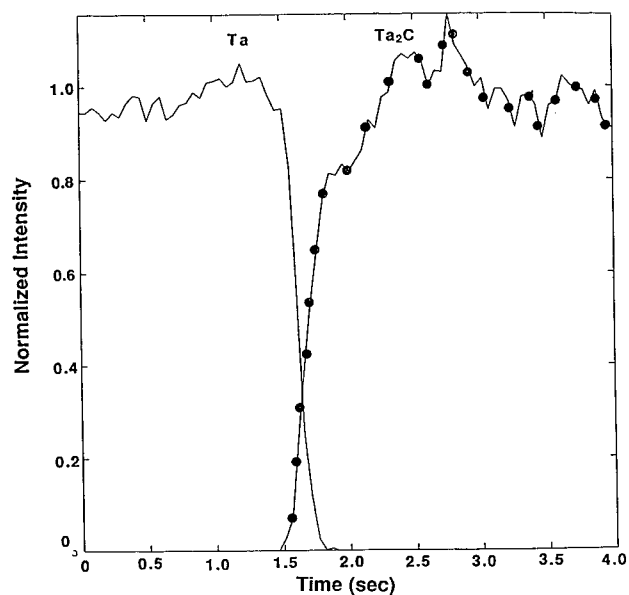


Figure 10. Normalized integrated intensities plotted as a function of time for Ta(110) and Ta₂C diffraction peaks, showing the chemical changes in the course of the 2Ta + C reaction.

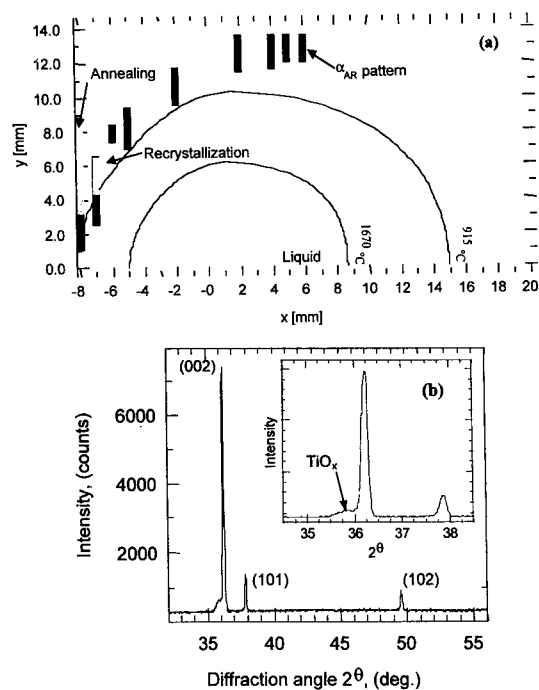


Figure 11. (a) SRXRD map highlighting the locations at which the α_{AR} pattern was observed in the vicinity of the HAZ during welding. Locations in the weld where annealing and recrystallization of the base material can be observed are indicated. (b) The corresponding diffraction pattern. Arrow in the inset indicates a low angle shoulder due to presence of a hexagonal TiO_x phase (see text).

The y scales of these two SRXRD runs were combined employing the simplified heat-flow model¹⁹. Peak width narrowing is given as difference between the α -Ti (002) peak width of the base metal at room temperature and the α_{AR} (002) peak width at temperature. As can be seen from Figure 12, the variation of the (002) peak width as a function of y -coordinates along a positive thermal gradient towards the weld center proceeds via a minimum in domain size. This suggests a three step mechanism, where the following three steps can be distinguished: (i) an initial annealing of defects and stress in the base metal and growth of diffraction domains resulting in a peak narrowing, (ii) a recrystallization process that yields smaller yet more perfect domains and leads to a broadening of diffraction peaks, (iii) subsequently a growth of diffraction domains which results in a narrowing of peaks eventually towards the α_{RG} phase. These three regions are indicated in Figure 11 by different shadings. The observed behavior is in good agreement with the conventional picture of annealing phenomena in metals which is believed to proceed via initial reduction of stress and number of defects, recrystallization, and grain growth. All these step are evident in the measured diffraction patterns at temperature.

Anisotropy in the thermal expansion coefficients of hcp α -titanium can be found in different peak shifts of the α -Ti (101), (002), and (101) diffraction lines. α -Ti is known to exhibit a larger thermal expansion in the c direction perpendicular to the basal plane of the hexagonal lattice²⁹ than in the a direction. For the α -Ti (002) peak, for instance, a temperature difference of about 200 K should result in a peak shift of about 0.06 degrees in 2θ for the scattering geometry used (thermal expansion coefficient $C_a = 7.5 \cdot 10^{-6} \text{ K}^{-1}$ in the a direction and $C_c = 1.1 \cdot 10^{-5} \text{ K}^{-1}$ in the c direction³¹ yield $C_{(002)} = 3.0 \cdot 10^{-4} \text{ }^\circ(2\theta)/\text{K}$ for (002) line). Calculation of relative diffraction plane d spacing expansion for the three α -Ti (101, 002, 102) peaks seen in the SRXRD data yields the largest effect on the (102) diffraction peak ($C_{(101)} < C_{(002)} < C_{(102)}$; with $C_{(102)}$ being $\sim 20 \%$ more than $C_{(002)}$ and $\sim 30 \%$ more than $C_{(101)}$). Figure 13 shows the peak shift of the three (hkl) α -Ti peaks with temperature for an experimental SRXRD run at a position of $x = -2$ with respect to the weld center. (hkl) peak positions were determined from a least-squares fit of a Gaussian profile function to the individual diffraction peaks. Temperature data were taken from the simplified heat flow model. For clarification, the difference of (hkl) peak positions at elevated temperature and at room temperature is displayed. Different expansion coefficients $C_{(hkl)}$ for different directions in the α -Ti lattice (Figure 18) can be seen from different slopes of the corresponding curves. A linear fit to each curve in Figure 13 yields expansion coefficients in terms of diffraction angle 2θ of $C_{(002)} = 2.0 \cdot 10^{-3} \text{ }^\circ(2\theta)/\text{K}$, $C_{(101)} = 1.5 \cdot 10^{-3} \text{ }^\circ(2\theta)/\text{K}$, and $C_{(102)} = 2.5 \cdot 10^{-3} \text{ }^\circ(2\theta)/\text{K}$. The qualitative difference between the $C_{(hkl)}$ expansion coefficients is in agreement with the above-mentioned considerations ($C_{(101)} < C_{(002)} < C_{(102)}$), with the ratio between $C_{(101)}$ and $C_{(102)}$ of 0.6 being slightly higher than the calculated difference of $\sim 30\%$. Furthermore, the experimental absolute values exceed the expected ones by one order of magnitude. This might be due to an additional peak shift caused by a slight wobbling motion of the titanium bar during the experiment.

The α_{RG} pattern: location and associated microstructure. The locations at which the α_{RG} pattern was observed are plotted in Figure 14a. The corresponding diffraction pattern is shown in Figure 14b. Further annealing and growth of α -Ti diffraction domains are expected with increasing temperature towards the weld center. The process can indeed be observed in a continuous decrease in diffraction peak width, which eventually leads to a transition from α_{AR} to α_{RG} patterns. α -Ti diffraction patterns from inside the HAZ (915 $^\circ\text{C}$ isotherm) correspond to $\alpha + \beta$ coexistence regions. Different kinetic mechanisms that govern $\alpha \rightarrow \beta$ and $\beta \rightarrow \alpha$ phase transformation ahead and behind the center of the weld, respectively, are responsible for the occurrence of α -Ti beyond the phase transformation isotherm on the heating side of the weld¹⁹.

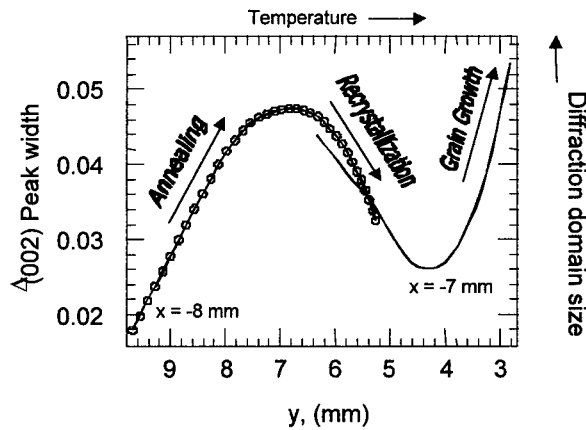


Figure 12. Variation of (002) α -Ti peak width as a function of y -coordinates along a positive thermal gradient obtained from two runs ahead of the weld at positions $x = -8$ and -7 mm. Plotted is the difference $\Delta(002)$ between α -Ti base metal (002) peak width at 20 °C and α_{AR} (002) peak width at temperature where an increasing $\Delta(002)$ reflects an increasing diffraction domain size.

Similar to the α_{AR} pattern, the observed α_{RG} pattern also exhibits a strong (002) intensity due to texture of the base metal, and a low angle shoulder due to contribution of TiO_x phases. However, the integrated intensity of the TiO_x peak seems to be larger for α_{RG} patterns compared to the base metal. Two reasons can account for this observation. Firstly, diffusion and segregation of oxygen into the existing TiO_x layer and annealing of the same, might result in an increase of TiO_x peak intensity. Secondly, in the coexistence region with β -Ti (Figure 14b), oxygen from titanium particles that already have been transformed to β -Ti diffuses to the remaining α -Ti, which has a higher oxygen solubility, resulting in an increase of the TiO_x contribution to the α -Ti diffraction

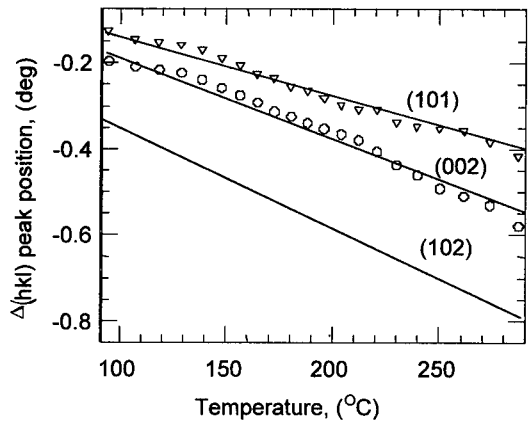


Figure 13. Evolution of α -Ti diffraction peak positions with temperature measured at a position of $x = 2$ mm with respect to the weld (squares: (102), circles: (002), triangles: (101)). Plotted is the difference $\Delta(hkl)$ between the α_{AR} (hkl) peak position at temperature and the α -Ti base metal (hkl) peak position at room temperature. Temperature information were extracted from the simplified heat flow model.

peaks. Additionally, a distinction of TiO_{x1} and TiO_{x2} diffraction peaks (Figure 15) as previously reported¹² is possible at this state of annealing and grain growth of α -Ti. An α_{RG} diffraction domain thickness of about 300 nm was estimated from single 'spike' width obtained from a least-squares fit of several Gaussian function to one Bragg peak (Figure 15). Due to the limited number of data points, peak widths (5 in number) were refined to vary the same plus two extra peaks for TiO_{x1} and TiO_{x2} shoulders.

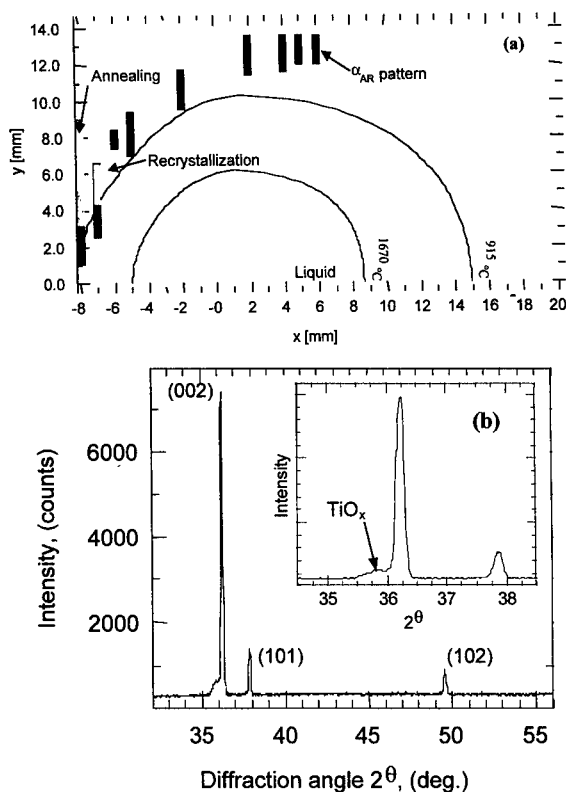


Figure 14. (a) SRXRD map highlighting the locations at which the α_{RG} pattern was observed in the vicinity of the HAZ during welding. Black bars inside the HAZ denotes regions of $\alpha + \beta$ coexistence. Dotted line indicates α_{RG} and α_{BT} coexistence zone (see text). (b) The corresponding diffraction pattern. Inset shows an enhanced TiO_x shoulder together with a β_{L} (110) peak due to contribution of β -Ti.

The β and β_{L} patterns: location and associated microstructure. The locations at which the β and β_{L} pattern were observed are plotted in Figure 16a. The corresponding diffraction pattern is shown in Figure 16b. At temperatures above the 915 °C $\alpha \rightarrow \beta$ phase transformation isotherm β -Ti becomes the thermodynamically more stable titanium phase. In the vicinity ~2.0 mm of the liquid weld pool and on the backside (cooler end) of the HAZ, 'pure' β -Ti diffraction patterns are observed (Figure 16). Further out in the cooler region but still in the HAZ, a large

$\alpha + \beta$ coexistence region can be found ahead of the liquid weld pool, whereas this region appears to narrow with increasing x . The transformation kinetics (hence mechanism) on the leading side of the liquid pool with thermal gradients ~ 100 K/mm may be very different from that of the cooler edge which may have a lower thermal gradient. Such difference in kinetics is largely responsible for the variation in spatial extent of the $\alpha + \beta$ coexistence regions in the HAZ¹⁹.

Large, well crystallized β -Ti domains in the hot region of the HAZ lead to strong and very narrow diffraction peaks (Figure 16b). Splitting within a given diffraction peak similar to those discussed for the α_{RG} pattern is observed. Since the β -Ti grains seem to grow larger than α -Ti grains particularly in the hot region of the HAZ near the weld pool, generally only one or two 'spikes' can be observed with occasional disappearance of all diffraction peaks. Similar to the base metal α -Ti patterns, the β -Ti patterns also show a preferred orientation in the diffraction patterns. On the average, most patterns showing a strong (110) peak and only a weak or no (200) peak can be found in the experimental data. This might be inherited from the preferred orientation of the α -Ti phase in (002) direction. In the $\alpha \rightarrow \beta$ phase transformation the most densely packed hcp layer (basal plane (002)) in α titanium becomes the most densely packed layer in the β titanium bcc structure leading to a preferred orientation of large β grains in the (110) direction of the cubic β -Ti lattice. Furthermore, the size of β diffraction domains in the cooler part of the HAZ following the phase transformation amounts to ca. 300 nm as calculated from diffraction peak width obtained from profile refinement to a multiplet (200) peak. This value is in good agreement with the diffraction domain size of α_{RG} -Ti prior to phase transformation, and gives credence to the supposition that the entire α -Ti grain transforms to β -Ti and retains its grain size upon phase transformation. This corroborates the idea of maintaining the most dense layer in hcp α -Ti and bcc β -Ti upon transformation as cause for the observed texture in β -Ti.

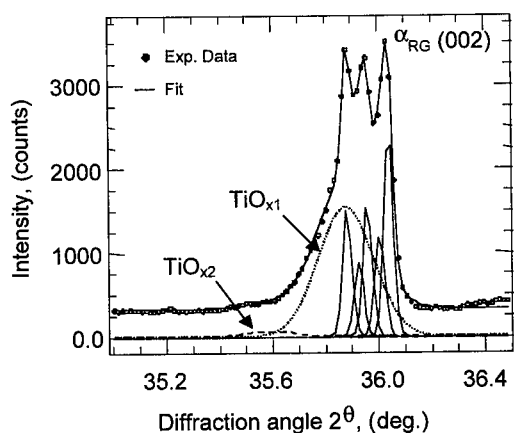


Figure 15. Profile refinement of α -Ti (002) peak in an α_{RG} diffraction pattern. Splitting of a single (002) Bragg peak is due to the scattering geometry used. Additional contribution of two different TiO_x phases to a low angle shoulder is indicated. The five narrow peaks (with same refined peak width) are attributed to at least five large domains in α -Ti diffracting into the photodiode.

In addition to diffraction patterns that exhibit strong β -Ti peaks, a low intensity (110) β_L peak is also observed, usually in coexistence with the α_{RG} pattern (Figure 14). The β_L pattern extends over a considerably long range in the y direction. The underlying microstructures that belong to locations on the map showing β_L diffraction patterns have to be divided into two different phases. Diffraction data taken below a straight line drawn from the maximum of the 915 °C isotherm in y parallel to x (Figure 16) belong to residual β -Ti that was not completely back transformed to α -Ti. This residual β -Ti stems from region in the HAZ where the phase transformation temperature was exceeded. The ratio of integrated intensities of (110) β_L peak and (002) α_{BT} peak amounts to ca. 0.1. In contrast, (110) β_L peaks measured above the maximum of the 915 °C isotherm in y correspond to α -Ti that had already started but did not completely transform to β -Ti. The early onset of the transformation can be explained by a slightly lowered $\alpha \rightarrow \beta$ transformation temperature in the vicinity of bcc nucleation sites within the material or due to impurities in the titanium¹⁹.

The α_{BT} pattern: location and associated microstructure. The locations at which the α_{BT} pattern was observed are plotted in Figure 17(a). The corresponding diffraction pattern is shown in Figure 17(b). This new α_{BT} pattern is found behind the “ β -pattern” region and outside the HAZ, and is associated with a new microstructure of α -Ti. This pattern corresponds to α -Ti that has been back transformed from β -Ti formed in the HAZ around the weld. Compared to the α_{RG} and the β pattern, the α_{BT} pattern shows no multiple diffraction line and the line width is in the same range as the α_{AR} pattern. The size of α_{BT} phase diffraction domains amounts to about 100 nm as obtained from the Scherrer formula. Since the α_{BT} phase stems from large β grains in the HAZ, it implies that the size of the β -Ti diffraction domains is *not* retained upon back transformation to α -Ti. This in turn suggests that large β domains break up into smaller α -Ti domains during the back transformation.

Another characteristic of the α_{BT} pattern is the absence of a distinct low angle shoulder due to contributions of TiO_x . This corroborates the assumption that TiO_x diffraction peaks originated from surface oxidized base metal or oxygen impurities rather than oxidation of the metal during welding. The $\alpha \rightarrow \beta$ phase transformation results in oxygen diffusion from the forming β -Ti grains to remaining α -Ti base metal grains owing to a higher solubility of oxygen in α -Ti. Therefore, $\beta \rightarrow \alpha$ back transformation affords low oxygen α -Ti that shows no distinct contribution of TiO_x . This region stems from the $\alpha + \beta$ coexistence region in the HAZ ($y = 9$ to 10 mm) that results in a mixed zone upon $\beta \rightarrow \alpha$ back transformation containing α -Ti that has never been transformed to β -Ti and back transformed α -Ti. Diffraction patterns belonging to this coexistence region can be identified by the occurrence of a low angle TiO_x shoulder together with a distinct (101) preferred orientation and the presence of (100) and (110) α -Ti peaks. Figure 18 shows a comparison of a α_{BT} diffraction pattern and a coexistence pattern. A low angle shoulder can be seen at the (002) peak of the coexistence pattern, whereas the strong (101) peak in both the coexistence and the α_{BT} pattern exhibits a symmetric profile without a low angle shoulder. Additionally, the α_{BT} pattern exhibits low β (110) peak due to residual amounts of β -Ti behind the HAZ of the weld.

CONCLUDING REMARKS

We have described synchrotron techniques that extend our experimental capability to probe materials processing in both the time domain and spatial regime. In the case of solid combustion syntheses of TaC and Ta₂C, the chemical dynamics of the combustion front has been elucidated with a time-resolution of 50 ms time frames by monitoring x-ray diffraction patterns of the reactants and products with synchrotron radiation. The synthesis of TaC from a stoichiometric

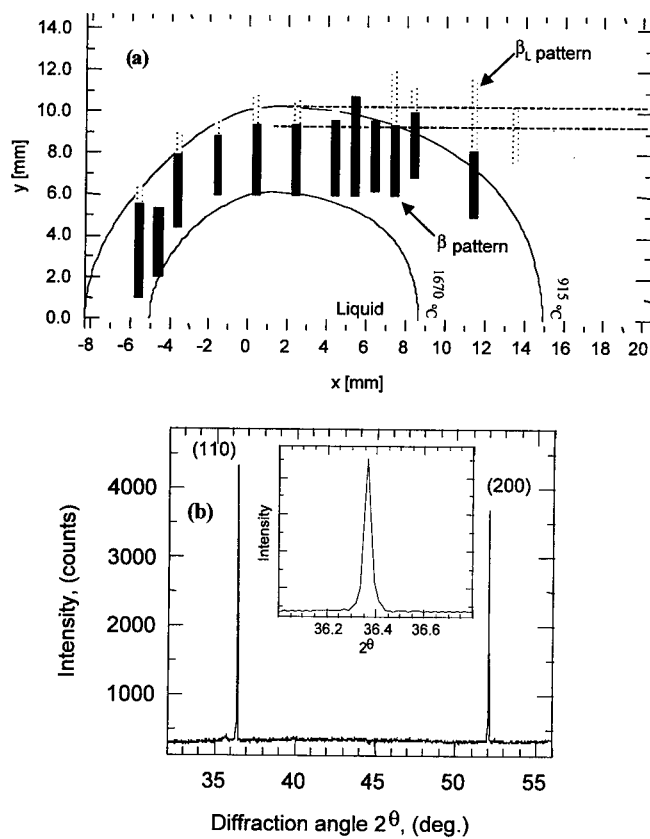


Figure 16. (a) SRXRD map highlighting the locations at which the β and β_L pattern was observed in the vicinity of the HAZ during welding. (b) The corresponding β -Ti diffraction pattern.

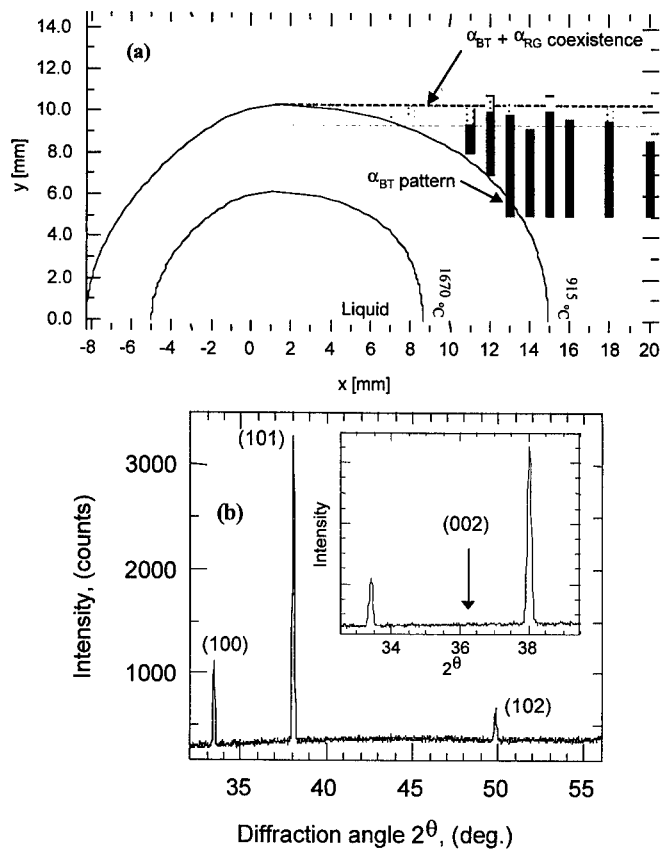


Figure 17. (a) SRXRD map highlighting the locations at which the α_{BT} pattern was observed in the vicinity of the HAZ during welding. (b) The corresponding diffraction pattern. Arrow in inset indicates absence of α -Ti (002) peak in this pattern.

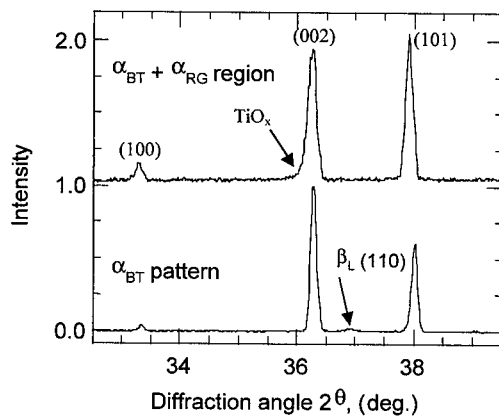


Figure 18. Comparison of α_{BT} pattern from α -Ti back transformed from HAZ β -Ti and a pattern from the boundary between α_{BT} + α_{RG} regions. Indicated by arrows are residual amounts of β -Ti (β_L (110)) in the α_{BT} pattern and a low angle shoulder due to TiO_x contribution to α_{RG} pattern.

1:1 mixture of Ta and C is preceded by the formation of Ta₂C, the concentration of which decreases with time as the diffusion controlled process proceeds to completion. Formation of Ta₂C from a 2:1 mixture of Ta and C occurs almost immediately with no indication of any other products. These results clearly demonstrate the usefulness of the TRXRD technique using intense synchrotron radiation to monitor phase transformation and high temperature solid state processes down to the milliseconds time regime not readily possible with conventional means.

The SRXRD results for Ti fusion welds illustrate the ability to map solid-state phases and their boundaries with sub-millimeter spatial resolution (~200 μ m) during materials processing *at temperature and in real time*. Spatially resolved and dynamic structural information of this sort, not readily obtainable with either conventional structural techniques (due to their ex-situ and post-mortem nature) or simple heat flow calculations^{11,19}, must be taken into account for qualitative understanding and quantitative modeling of phase transformation kinetics and microstructural evolution in systems under highly non-isothermal conditions³⁰. Improved methods such as a smaller beam spot emitted from 3rd generation synchrotron sources, better mechanical stability (tighter scattering geometry) and use of an areal detector would enable more quantitative structural information for future materials dynamic studies.

ACKNOWLEDGMENT

Work performed under the auspices of the US Department of Energy (DOE), Lawrence Livermore National Laboratory, under contract W-7405-ENG-48. We would like to thank P. A. Waide for technical assistance in the reaction chamber design and fabrication. The synchrotron experiments were carried out at both the National Synchrotron Light Source at Brookhaven and Stanford Synchrotron Radiation Laboratory supported by DOE, Division of Chemical Sciences.

REFERENCES

1. (a) Z.A. Munir, *Review of Self-propagating High Temperature Synthesis Reactions*, Ceramic Bulletin, 67: 342 (1988); (b) Z.A. Munir and U. Anselmi Tamburini, Mater. Sc. Rept. 3, 277 (1989).
2. A. G. Merzhanov, in "Combustion and Plasma Synthesis of High-Temperature Materials", Z. A. Munir and J. B. Holt eds., (1990) pp 1-53.
3. A.G. Merzhanov, *Macrokinetics of Self-propagating High Temperature Synthesis* Ceram. Trans. 13: 519 (1990).
4. J.-P. Lebrat and A. Varma, *SHS Synthesis of high temperature superconductors*, Physica C 184: 220 (1991).
5. V.V. Boldyrev and V. Aleksandrov, *Kinetics of the Ni-Al Combustion Synthesis Reaction*, Dok. Akad. Nauk. SSSR 259: 1127 (1981).
6. Joe Wong, E. M. Larson, J. B. Holt, P. Waide, B. Rupp and R. Frahm, *Time-resolved Diffraction Study of Solid Combustion Reaction*, Science 249: 1406 (1990).
7. R. Frahm, Joe Wong, J.B. Holt, E.M. Larson, B. Rupp and P.A. Waide, *Real time Probe of Reaction Centers in solid Combustion by QEXAFS Spectroscopy*, Phys. Rev. B46: 9205 (1992).
8. S.A David and J.M. Vitek eds., *International Trends in Welding Science and Technology*, ASM Intern. (1993).
9. B.K. Damkroger, G.R. Edwards, and B.B. Rath, *Crack Growth in Welded Ti Alloys*, Welding Journal, 68, 290 (1989).
10. M.C. McGuire, M.L. Santella and B.K. Damkroger, Ductility in welded intermetallic alloys, in: *The Science of Metal Joining*, M. H., Cieslak, J. Perepezko, S. Kang and M.E. Glicksman, eds. TMS (1992), 41.
11. J.W. Elmer, Joe Wong, M. Froeba, P.A. Waide and E.M. Larson, *Analysis of HAZ Phase Transformation using In-situ SRXRD*, Met. Mat. Trans. 27A, 775 (1996).
12. Joe Wong, E. M. Larson, J.B. Holt, P.A. Waide, B. Rupp and R. Frahm, *Time-resolved Diffraction Study of Solid Combustion Reactions*, Science 249, 1406 (1990).
13. T.B. Massalski, J.L. Muray, L.H. Bennett and H. Baker, eds., *Binary Alloy Phase Diagrams*, ASM, Vol. 1 (1986).
14. V. M. Shkiro, G. A. Nersisyan and I. P. Borovinskaya, *Phase equilibrium in the Ta-C system*, Fiz. Goreniya Vzryva, 14, 58, (1978).
15. V. M. Shkiro, G. A. Nersisyan, I. P. Borovinskaya, A. G. Merzhanev and V. Sh. Shokhtman, *Diffusion of C in the Ta-C System*, Poroshkovaya Metallurgiya, 4, 14, (1979).
16. V. M. Shkiro and G. A. Nersisyan, *Combustion Synthesis of TaC*, Fiz. Goreniya Vzryva, 14, 149, (1978).
17. E.M. Larson, Joe Wong, J.B. Holt, P.A. Waide, B. Rupp and L.J. Terminello, *A Time-resolved Diffraction study of the Ta-C Combustion Synthesis*, J. Mat. Res. 8, 133 (1993).

-
18. T. Ressler, Joe Wong and J.W. Elmer, *Investigation of Real time Microstructure Evolution in Steep Thermal Gradients*, J. Phys. Chem. B. **102**(52), 10724 (1998).
 19. J.W. Elmer, Joe Wong and T. Ressler, *SRXRD Phase Mapping in the HAZ of Pure Ti Arc Welds*, Met. Mater. Trans. **29A**, 2761 (1998).
 20. E. M. Larson, P. A. Waide and Joe Wong, *High Speed Diffractometer-Reaction Chamber using Synchrotron Radiation*, Rev. Sci. Instrum., **62**(1), 53-7, (1991).
 21. V. Karpenko, J.H. Kinney, S. Kulkarni, K. Neufeld, C. Poppe, K.G. Tirsell, Joe Wong, J. Cerino, T. Troxel, J. Yang, E. Hoyer, M. Green, D. Humpries, S. Marks and D. Plate, *A New Wiggler x-ray Beamline at SSRL*, Rev. Sci. Instrum., **60**, 1451 (1989).
 22. E.M. Larson, P.A Waide and Joe Wong, *High Speed Diffractometer-Reaction Chamber using Synchrotron Radiation*, Rev. Sci. Instrum., **62**, 53 (1991).
 23. M. Donachie, *Titanium A Technical Guide*, ASM International, 1989.
 24. A. A. Gavrish, M. P. Glazunov, Yu. M. Korolev, V. I. Spitsyn and G. K. Fedoseev, *Diffraction Intensities of the TaC and Ta₂C*, Russ. J. Inorg. Chem., **20**, 1269, (1975).
 25. R.E. Bolz and G.L. Ture, *Handbook of Tables for Appl. Eng. Sc.*, The Chemical Rubber Co., (1970) p. D-173
 26. I. I. Spivak and V. V. Klimenko, *Self Diffusion in TaC*, Fiz. Metal. Metalloved. **32**, 314, (1971).
 27. A.F. Wells, *Structural Inorganic Chemistry*, Oxford Univ. Press, 4th Ed. (1975), p. 760.
 28. D. Cullity, *Elements of x-ray diffraction*, 3rd ed.; Addison and Wesley, New York, 1967.
 29. N. Schmitz-Pranghe and P. Duenner, *High Temperature X-ray Diffraction Study of Ti and V*, Z. Metallkde, **59**, 377 (1968).
 30. Z. Yang, J.W. Elmer, Joe Wong and T. DebRoy, *Modeling of Phase Transformation and Grain Growth in the HAZ of Pure Ti Arc Welds*, The Welding Journal, (1999), in press.

DEVELOPMENT AND PROPERTIES OF ϵ -MARTENSITE IN Co-Cr-Mo ALLOYS FOR BIOMATERIALS APPLICATIONS

Hugo F. López, Armando Saldívar, and P. Huang
Materials Department, University of Wisconsin-Milwaukee
P.O. Box 784, Milwaukee, WI 53201

ABSTRACT

This work is related to the FCC \rightarrow HCP transformation exhibited by Co-base alloys. In particular it is known that the transformation occurs martensitically by either; (a) athermal, (b) isothermal, or (c) a strain induced transformation. The mechanisms involved are not exactly the same in each case, and the formation of ϵ -martensite can develop various morphologies. Nevertheless, in all of the modes of transformation, the nucleation stage seems to control the FCC \rightarrow HCP transformation rates.

INTRODUCTION

Human hip joints consist essentially of a ball and a socket coupling, with the socket (or acetabulum) being located on the pelvis and the ball (or head of the femur) being connected to the femur. Typical joint failures are often due to accidents, which are very common in elders, or to degenerative processes such as osteoarthritis or rheumatoid arthritis. In these cases, both joint components must be replaced. There are two main types of total hip prostheses; (i) both components are made of a metallic alloy, and (ii) the acetabular component is made up of ultrahigh molecular weight polyethylene (UHMWPE), with the femoral component being a metallic alloy. (1)

Cobalt base (Co-Cr-Mo-C) alloys have been widely used in the manufacture of these orthopedic implants, owing to their excellent biocompatibility, mechanical properties, and wear and corrosion resistance (2-4). However, it has been found that the wear debris produced at the wearing interfaces often leads to a substantial reduction in the mechanical stability of prostheses, and to the eventual failure of the inserted implants. (5). It is known that the mechanical properties of wrought forms of Co-based alloys are significantly superior to the same alloys in the as-cast condition (6, 7). In addition, in both types of metallurgical conditions, the alloy properties are further improved through appropriate heat treatments (8). Nevertheless, the

tribological properties of hip implants are directly related to the microstructural features of the contacting surfaces (5,9).

In as-cast alloys, carbide particles can cause acceleration of the rate of wear of the UHMWPE acetabular cup. Moreover, the wear rates of both, the acetabular cup and the metallic femur can be enhanced by a three-body wear process caused by the separation of carbide particles from the metallic matrix. (10). In an attempt to improve the wear properties of cobalt, Buckley and Johnson, (11) investigated the tribological behavior of single-crystal metals using metal-on-metal wear tests. Their results indicated that hexagonal close packed (HCP) crystal structures give rise to relatively low friction coefficients and reduced wear rates when compared with face centered cubic (FCC) metals. (12).

Co-Cr-Mo-C alloys, exhibit two allotropic forms, the HCP phase which is thermodynamically stable at room or human temperature and the FCC phase, which becomes stable at elevated temperatures. However, the HCP form is difficult to generate under normal cooling conditions, and in most Co-based alloys the FCC structure is retained at room temperature (8,13). Accordingly, the FCC \rightarrow HCP phase transformation is sluggish due to the limited chemical driving forces available at the transformation temperature. In pure Co the transformation takes place at 417°C by a diffusionless, martensitic transformation (14), but in the Co-27Cr-5Mo-0.05C wrought alloy, the Cr and Mo expand the HCP field, and the transformation temperature increases to near 970°C (15).

The HCP phase resulting from this martensitic reaction is known as ϵ -martensite. The metastable FCC phase can transform to HCP by plastic deformation (strain induced transformation, SIT). However the transformation does not exceed 80-90% due to premature fracture (10, 12). The amount of HCP formed during quenching from temperatures above the equilibrium temperature (athermal mechanism) is usually <25% (8,15,16). Recent experimental results have shown that the metastable FCC phase can fully transform through isothermal aging at temperatures between 650 and 950°C. (15,16). In the present work, the various modes of FCC \rightarrow HCP martensitic transformation (athermal, isothermal and strain induced) exhibited by a wrought Co-27Cr-5Mo-0.05C FCC \Rightarrow HCP were investigated.

EXPERIMENTAL PROCEDURE

A commercially available wrought low carbon Co-Cr-Mo alloy bar (equivalent to ASTM F-799) of 0.625 inches in diameter was used in this work. The chemical composition of the alloy (wt. %) as determined by spark emission spectroscopy is given in Table I.

Table 1 . Chemical composition of cobalt alloy (wt.%)

Cr	Mo	Ni	C	Mn	Si	Fe	Co
28.90	5.60	0.21	0.05	0.79	0.49	0.17	Balance

Athermal transformation

Small samples of the as-received alloy were subjected to solution heat treatments at temperatures ranging from 1000 to 1250°C. The samples were water quenched at 1 hour intervals. Heat treatments were performed using a high temperature tubular furnace and an inert Ar gas atmosphere (sequence I-II-IIIb, Figure 1).

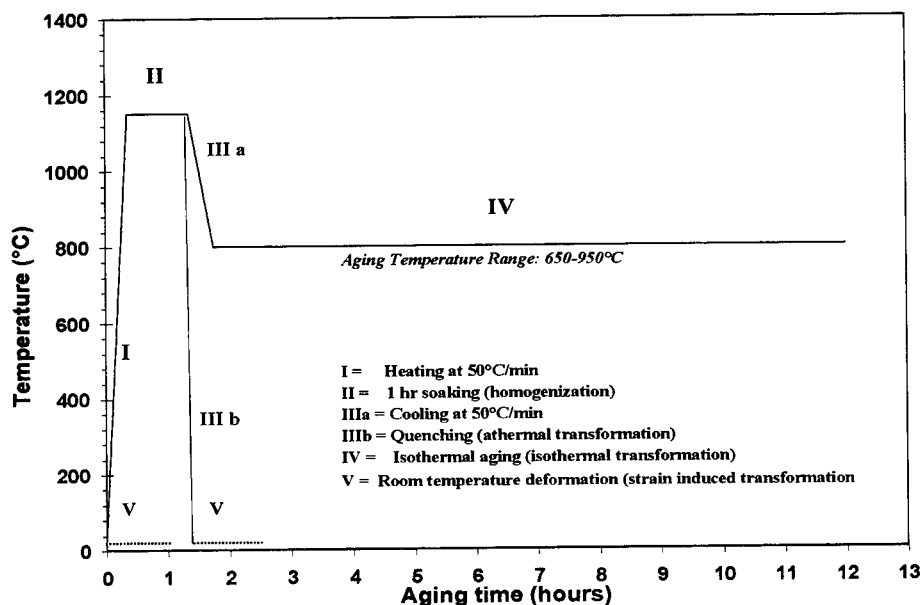


Figure 1. Schematic representation of the thermal cycles employed in the present work to study the FCC → HCP phase transformation in a Co-27Cr-5Mo-0.05C alloy.

Isothermal transformation

The kinetics of the isothermal martensitic transformation was followed *in-situ*, as shown schematically in the thermal cycle of Figure 1, sequences I-II-IIIa-IV. The experiments were carried out, using 0.5 mm-thick samples, inside an Anton Paar high temperature chamber adapted to a PHILIPS X-Ray diffractometer.¹ The specimen and the Pt heating element were protected against oxidation using an Ar gas inert atmosphere inside the high-temperature chamber. The Pt heating element also acted as the specimen holder during the X-ray diffraction measurements. The temperature was measured and controlled within $\pm 2^\circ\text{C}$ using a Pt/Pt-10Rh thermocouple spot welded to the back of the filament. The thermal cycle consisted of (1) heating to 1150°C at a rate of 50°C/min, (2) soaking for 1 hour at 1150°C, (3) cooling at 50°C/min to aging temperatures in the range of 650 to 950°C and (4) isothermal aging. The microstructural changes that occurred in each sample were followed *in-situ* using X-ray diffraction patterns as a function of time, during isothermal aging (up to 24 hours). This was followed by rapid alloy cooling to room temperature.

Strain-induced transformation

Compression and hardness tests (Rockwell C) were carried out in both as received and heat treated specimens. (dotted line in Figure 1). A Satec universal testing machine was

¹ PHILIPS is a trademark of Philips Instruments Corp., Mahwah, NJ.

employed for compression testing of 10 mm diameter specimens with an aspect ratio of 1:5. The extents of plastic deformation were systematically varied for specimens of a given grain size. Engineering strains of 0.0, 0.095, 0.251 and 0.295 corresponding to no deformation, yielding, fracture yielding and post fracture respectively, were externally implemented in the as received alloy.

Microstructural characterization

The main microstructural change detected by X-ray diffraction was the allotropic FCC(metastable) \rightarrow HCP transformation. The relative amounts of transformed HCP (f^{HCP}) and untransformed FCC (f^{FCC}) phases were estimated by measuring the integrated intensities of the (200)FCC and (1011)HCP X-ray diffraction peaks (I^{FCC}_{200} and I^{HCP}_{1011} , respectively). The weight fraction of the HCP phase was calculated using the expression, developed by Sage and Gillaud:(17)

$$f^{\text{hcp}} (\text{wt. pct}) = \frac{I_{1011}^{\text{hcp}}}{I_{1011}^{\text{hcp}} + 1.5I_{200}^{\text{fcc}}} \quad (1)$$

The specimen surfaces were prepared metallographically and X-ray diffraction patterns were measured using $\text{CuK}\alpha$ radiation ($\lambda = 1.54184 \text{ \AA}$). Scans (2θ) were carried out between 40 and 55° (2θ), a range suitable for determining the integrated intensities of the diffraction peaks required by Sage and Gillaud method (17). The microstructure of the heat treated and deformed specimens was characterized using standard metallographic techniques on a reflected-light metallographic microscope and a 30-kV scanning electron microscope.

RESULTS AND DISCUSSION

Homogenization of the FCC structure

X-ray diffraction patterns of the Co-27Cr-5Mo-0.05C alloy before, and during the homogenization heat treatment are shown in Figure 2.

The diffraction pattern of the as-received alloy at room temperature indicates the presence of some residual HCP phase, with FCC as the predominant phase. Notice that at the homogenization temperature, the height of the FCC diffraction peaks increases during the heat treatment while the HCP peaks decrease in height. After 1 hour of treatment total extinction of HCP phase is achieved. Considering that the FCC phase is stable at 1150°C , the 1 hour soaking treatment is long enough to homogenize the structure. This treatment guaranteed that only the FCC phase is present before the athermal or isothermal transformation.

In the as received condition, the grain structure was equiaxed with an average grain size (d) of $3 \mu\text{m}$. The homogenization treatment promotes normal grain growth, and various grain sizes were obtained depending on the heat treatment conditions. As a result of increasing grain sizes the alloy hardness consistently decreases as shown in Figure 3.

Athermal martensitic transformation

The athermal transformation occurs when the material is quenched at room temperature after the homogenization heat treatment, (IIIb in Figure 1). The quenched samples exhibit an equiaxed grain structure with annealing twins. These samples are mostly FCC although they contain variable amounts of HCP phase.

When the samples were quenched from temperatures above 1125°C, the microstructure showed a series of bands composed of parallel arrangements of fine straight intragranular striations within the FCC grains as shown Figure 4. Yang and Wayman (18) found that the formation of these kinds of triangular arrays of striations (as in the present case) are typical laths of martensite with a (111) habit plane for the austenitic parent phase. Apparently, this martensite is often initiated along annealing twin boundaries, as shown in Figure 4. Once the initial laths are developed, numerous fine parallel, secondary martensite units are found to nucleate along sides of the former ones.

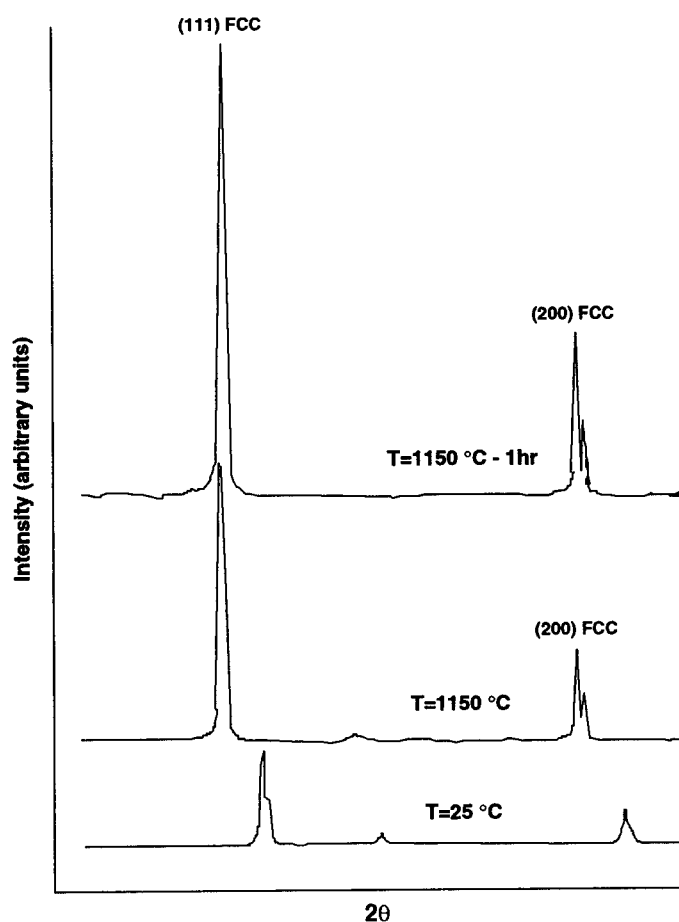


Figure 2. X-ray diffraction patterns showing the effect of the homogenization heat treatment on the structure of a Co-27Cr-5Mo-0.05C alloy.

Similar transformation markings were observed by Vander Sande et al. (8) in cast and wrought Co-28.5Cr-5.7Mo-2.2Ni-0.3C alloys, which were water quenched from 1230°C. The bands were characterized by TEM as heavily faulted martensitically transformed HCP. The origin of the intragranular striations was attributed to a diffusionless, martensitic phase transformation occurring as a result of quenching from temperatures within the FCC phase stability field.

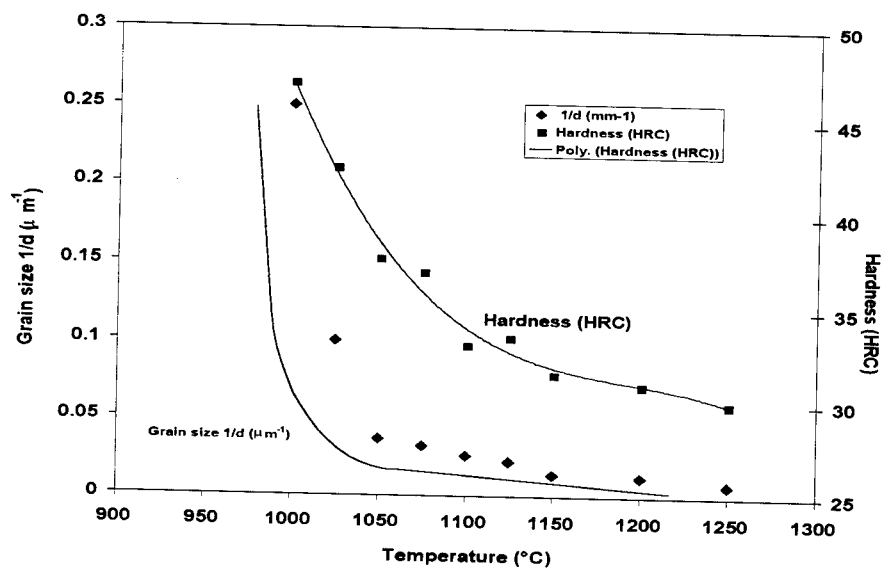


Figure 3. Relationship between grain size and hardness as a function of homogenization temperature. The soaking time was 1 hour at each temperature.

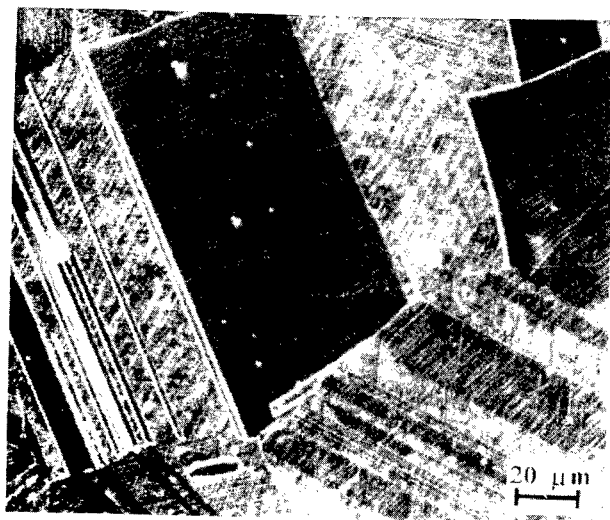


Figure 4. Photomicrograph showing the microstructure of a quenched specimen.

The HCP stacking sequence is produced by the generation of intrinsic stacking faults on each second (111) FCC plane. Due to the thermodynamic features of this transformation, the athermal transformation is incomplete, resulting in the retention of metastable FCC phase bands of few planes in thickness, inside the athermal HCP martensite. Olson and Cohen have suggested (19) that the local high energy of structural defects required for martensitic embryo formation can persist and even be created during high temperature annealing. Thus, increasing the solution temperature would increase the number of possible nucleation sites of the transformation of the FCC equilibrium phase before the material is quenched to room temperature. As a result, the amount of HCP phase formed during quenching would increase. Figure 5 shows that rising the solution temperature increases the amount of athermal martensite formed on quenching.

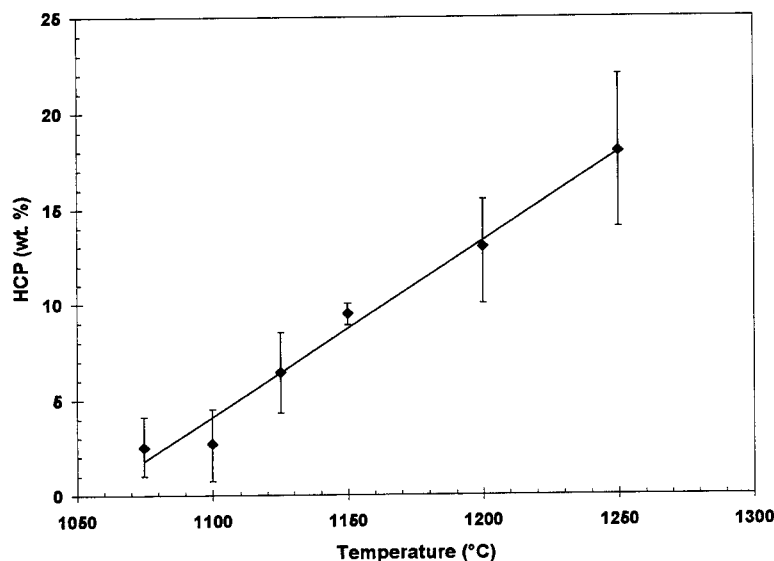


Figure 5. Effect of solution temperature on the amount of HCP athermal martensite formed in a quenched Co-27Cr-5Mo-0.05C alloy.

Strain induced HCP martensite

Systematic plastic straining of the as-received and heat treated alloys to various extents was followed by estimations of f_{HCP} martensite SIT ϵ -martensite for a given amount of plastic deformation. Accordingly, the f_{HCP} induced by the various grades of applied plastic straining and the effect of grain size are shown in Fig. 6a. and 6b. Moreover, Figure 7, shows the development of numerous parallel striations with various orientations intersecting stacking fault of anneal twin interfaces in the plastically deformed heat treated Co-alloy ($d=117 \mu\text{m}$). According to the literature, plastic straining of Co-alloys can result in significant work hardening through the development of twins or SIT ϵ -martensite (19-21).

The SIT mechanisms thus far proposed (19,22) suggest that the stacking fault intersections make the largest contribution to the exhibited work hardening behavior. These intersections have been considered as some kind of dislocation dipoles whose high strain fields impede the motion of slip dislocations (23). Shear band intersections have been established as

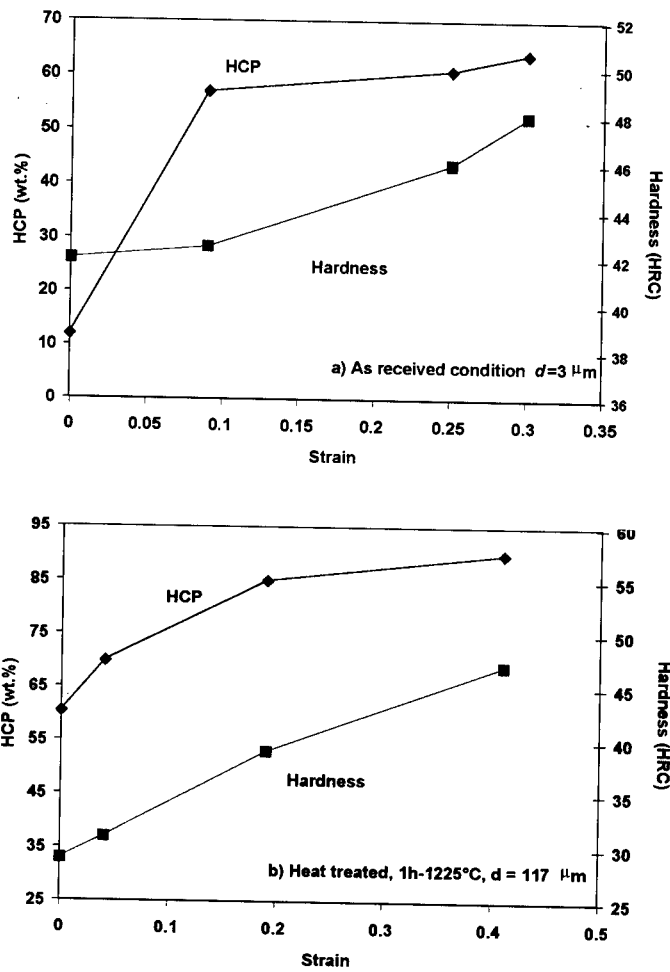


Figure 6. Volume fraction of HCP phase and alloy hardness in a) the as-received Co-alloy ($d=3 \mu\text{m}$), and b) heat treated Co-alloy ($d=117 \mu\text{m}$) as a function of applied plastic compressive strain.

the predominant sites for the strain induced nucleation of α -martensite (24). Among these works, a simplified expression (24) has been employed to explain the expected sigmoidal behavior or the volume fraction of SIT martensite f_{HCP} as a function of the amount of plastic straining.

$$f_{\text{HCP}} = 1 - \exp\{-ke^z\} \quad (2)$$

where e is the true plastic strain, k , z are experimentally determined material constants. Saldivar (15) and Salinas (10) found that the f_{HCP} values predicted by this equation during compressive plastic straining for the same Co-base alloy used in this work are in good agreement with the experimental f_{HCP} determinations. The values that Salinas found were $z = 2$ with k strongly dependent on grain size d (i.e., f_{HCP} is inversely related d for a fixed amount of plastic strain e).

Apparently, in fine grained alloys, relatively small amounts of plastic straining are able to trigger the formation of relatively large volume fractions of ϵ -martensite. Although it is not clear how this can be accomplished, it seems that the development of strain induced hcp-embryos is favored by the homogeneous nature of the deformation and the high level of alloy stressing.

The dynamic FCC to HCP transformation that occurs during plastic deformation significantly modifies the microstructural evolution and hence, the material flow and strain-hardening properties. From a microstructural viewpoint, the strain-induced phase transformation (SIT) found in the present alloy is characterized by the extensive development of intragranular striations. Salinas (10) found that the active micro-mechanisms during plastic deformation give rise to large strain hardening rates during tensile testing. As a result, the development of macroscopic flow instabilities, such as necking during tensile testing is delayed or inhibited and the material is capable of deforming uniformly up to the point of fracture.

Isothermal martensitic transformation

Figure 8 shows the X-ray diffraction patterns measured in-situ during isothermal aging of the Co-27Cr-5Mo-0.05C alloy cooled to 800°C at 50°C/min from 1150°C. Notice that the relative intensities of the (200) and (111) FCC diffraction peaks decrease as a function of time,



Figure 7. Optical micrograph of a heat treated Co-Cr-Mo -C alloy ($d=117 \mu\text{m}$) as a function of applied plastic compressive strain (0.195 plastic straining).

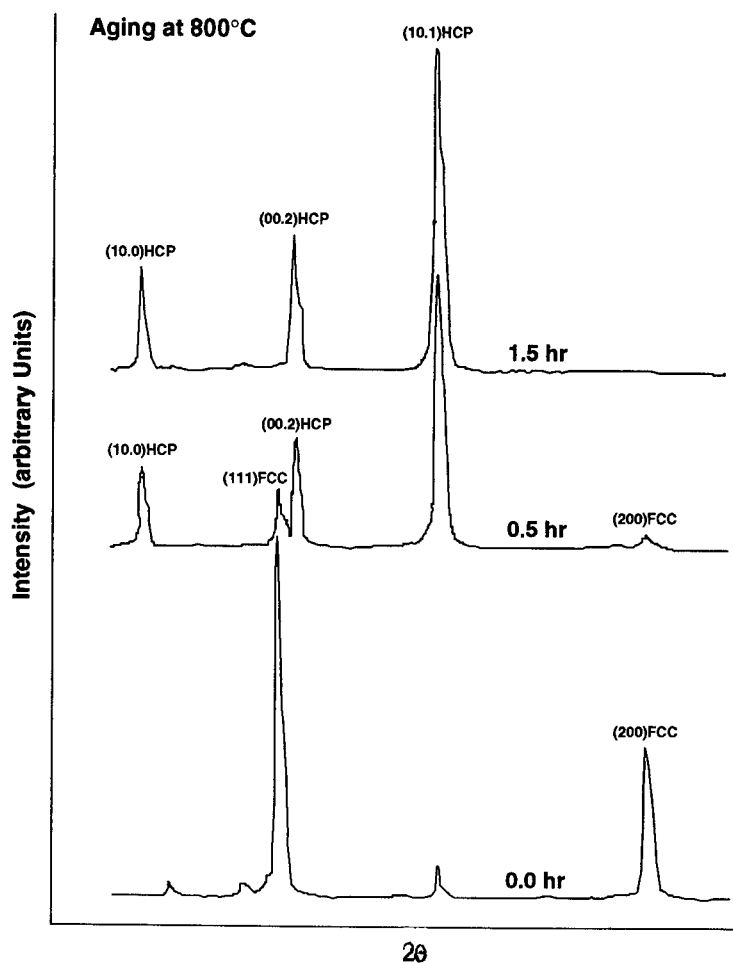


Figure 8. High temperature X-ray diffraction patterns measured *in-situ* during the isothermal aging of Co-27Cr-5Mo-0.05C heat treated during 1h at 1150°C and then cooled to 800°C.

concurrent with an increase in the relative intensities of the $(10\bar{1}0)$, (0002) and $(10\bar{1}1)$ HCP diffraction peaks. In particular, notice that cooling from 1150°C to 800°C causes a significant shift of the (111) and (200) FCC diffraction peaks to larger 2θ values. This in turn suggests that thermal contraction of the crystal lattice occurs normal to the reflecting planes as a result of cooling.

Figure 9 shows the transformation-time curves obtained for alloy aging in the range of 650 to 950°C. Notice that progress of the transformation follows a sigmoidal dependency, and this behavior is independent of temperature. The kinetic data for aging temperatures between 650 and 950°C is plotted in the form of an isothermal TTT diagram obtained from the transformation-time curves measured *in-situ* (see Figure 10). The start of the transformation requires only about 5 minutes at temperatures in the range of 800 to 850°C, completing the transformation in less than 1 hour. Aging treatments outside this temperature range cause a significant variation in the rates of transformation. These observations indicate that the main driving force for the isothermal martensitic transformation is the activation energy for martensite nucleation. In the isothermal martensitic transformation, the growth process is extremely fast, with each martensite plate reaching its final size in fractions of a second. The transformation continues to take place through the nucleation of new plates, and not through the growth of pre-existent nuclei. Accordingly, the reaction kinetics is controlled by the nucleation rates, and by the final size of the martensite plates.

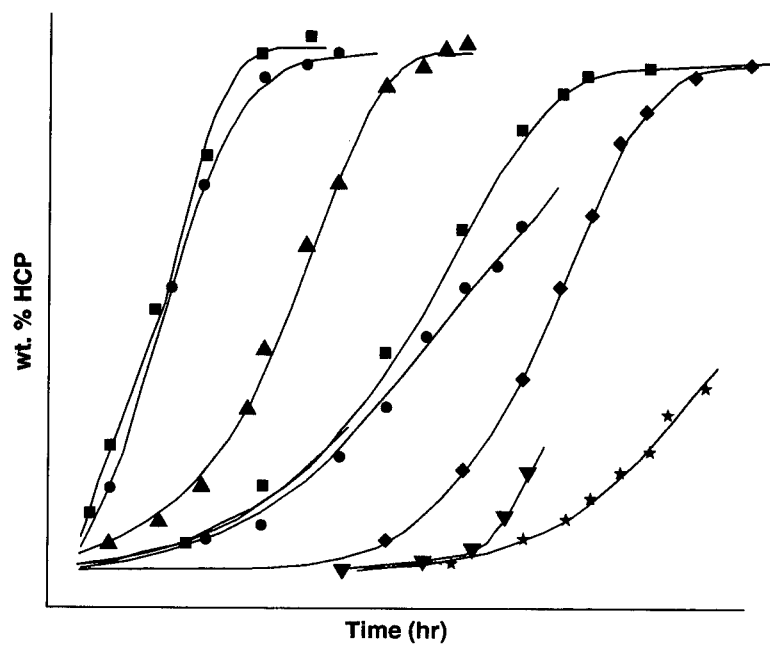


Figure 9. Transformation-time curves for the isothermal aging of Co-27Cr-5Mo-0.05C alloy, homogenized during 1h at 1150°C and aged at the indicated temperatures.

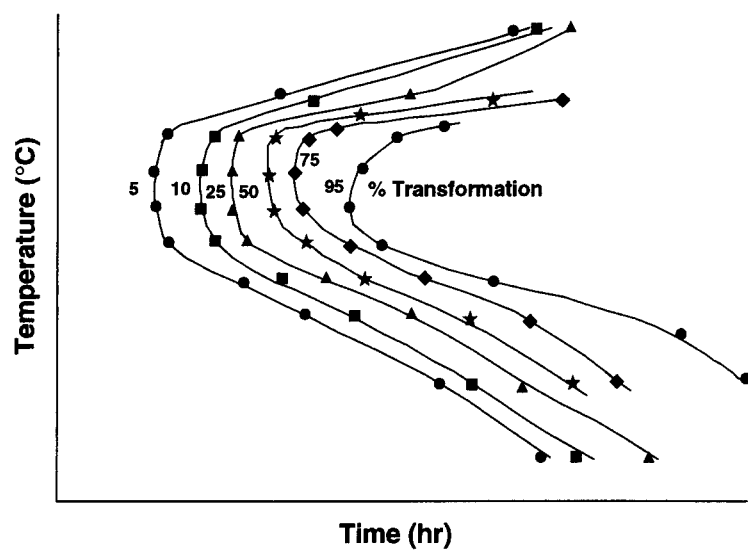


Figure 10. Transformation-temperature-time diagram for the isothermal FCC(metastable) → HCP transformation in Co-27Cr-5Mo-0.05C alloy, homogenized during 1h at 1150°C. Material directly cooled from 1150°C to the aging temperature. The amount of HCP phase was measured *in-situ* by high temperature X-ray diffraction.

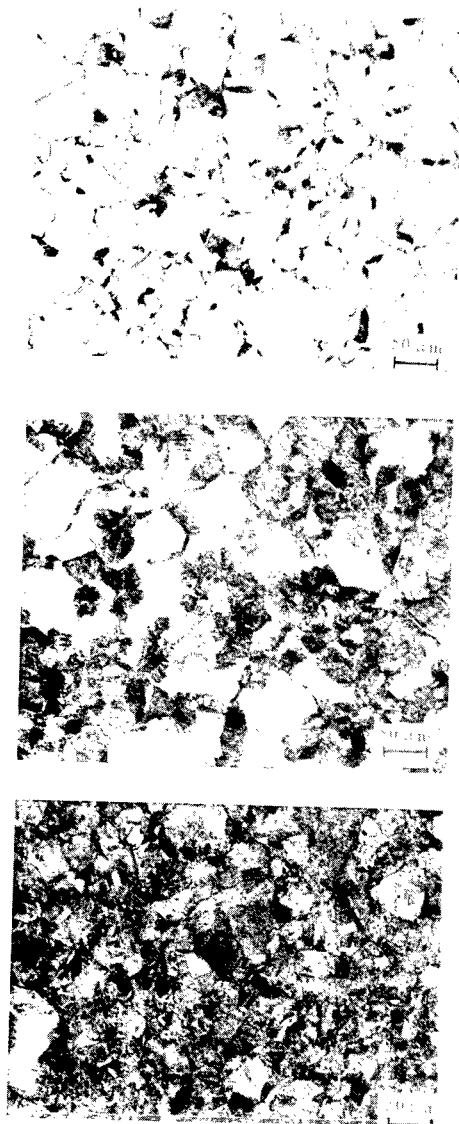


Figure 11. Effect of aging at 800°C on the microstructure of a Co-27Cr-5Mo-0.05C water quenched after 1h at 1150°C (optical photomicrographs): (a) 3h, (b) 10 h, and (c) 24 h.

The evolution of the microstructure, during isothermal aging at 800°C, for a series of samples homogenized at 1150°C is illustrated in Figure 11. Notice that isothermal aging causes the progressive formation on a new, two-phase microstructure. Figure 12 shows two SEM photomicrographs illustrating the morphology of the new microstructure, produced after isothermal aging at 800°C at 3, and 10 hours, respectively. The HCP product phase consists of colonies of very fine, uniformly oriented, discontinuous lamellae resembling a pearlitic-type microstructure.

Figure 12(a) shows that during the early stages of aging, the HCP phase formed at the FCC twin-grain boundary intersections. Figure 12(b) shows that a grain boundary-nucleated HCP phase does not continue to grow further with increasing aging time, so the transformation proceeds by continuous nucleation of HCP lamellae. At a first glance, the “pearlite-like” morphology of the HCP product phase and the sigmoidal kinetics suggest that the transformation follows the classical Cahn and Hagel model for austenite decomposition in steel (25). However, the microstructural evidence does not support this interpretation.

Instead, the model proposed by Cong Dahn et al. (26) to describe the kinetic behavior of the FCC→HCP transformation observed during isothermal aging of Co-27Cr-5Mo-0.25C alloy powders seems to be more appropriate. In their work, the sigmoidal shape of the transformation curves can be ascribed to the thermal activation nature of the martensitic nucleation. Under these conditions, the rate-limiting stage was assumed to be the thermally activated motion of Shockley partial dislocations and their interaction with solute clusters.

Thermodynamics and kinetics of the FCC→HCP isothermal transformation

The temperature dependance of the chemical free energy for the FCC→HCP transformation is given as

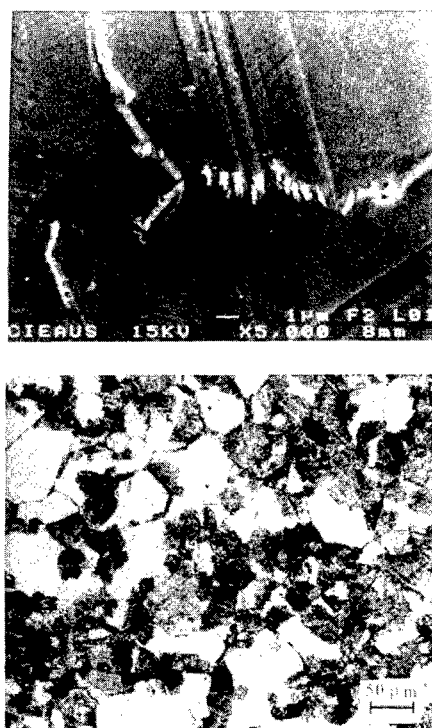


Figure 12. Effect of aging at 800°C on the microstructure of Co-27Cr-5Mo-0.05C water quenched after 1h at 1150°C (SEM photomicrographs): (a) 3h, (b) 24 h.

$$\Delta G^{FCC \rightarrow HCP} = \Delta H^{FCC \rightarrow HCP} - T \Delta S^{FCC \rightarrow HCP} \quad (3)$$

Free energy data for FCC \rightarrow HCP transformation in this alloy system is not readily available in the literature. Hence, Cong Dahn et al. estimated the equilibrium transformation temperature for a Co-27Cr-5Mo-0.25C alloy using the enthalpy, $\Delta H^{FCC \rightarrow HCP}$ for pure Co. Hence, in this work, the value of $\Delta H^{FCC \rightarrow HCP}$ used was estimated from the equilibrium temperature ($T = 970^\circ\text{C}$) determined by Saldivar (15). Moreover, the entropy change can be given by: (20,21)

$$\Delta S^{FCC \rightarrow HCP} = \frac{-\sqrt{3}}{8} N_A a^2 \frac{dy}{dT} \quad (4)$$

where:

- 1) $\frac{dy}{dT}$ = temperature derivative of the stacking fault energy. This value was taken from Ericson's data (20) on the temperature dependence of stacking fault energy for FCC Co, $dy/dT = 0.27 \text{ egs/cm}^2\text{-K}$
- 2) a = FCC lattice parameter. This value was experimentally determined in the present work at 980°C , from *in-situ* X-ray diffraction studies. $a^{FCC}(980^\circ\text{C}) = 3.618 \text{ \AA}$.
- 3) N_A = Avogadro's number

Thus, the value of $\Delta S^{FCC \rightarrow HCP} = -0.11 \text{ cal/mol-K}$, and $\Delta H^{FCC \rightarrow HCP} = -136.73 \text{ cal/mol}$. Thus, the final expression for the Gibbs free enthalpy becomes:

$$\Delta G^{FCC \rightarrow HCP} = -136.73 + 0.11 T \quad (5)$$

Based on the work of Cong et al. (26) on isothermal transformations of Co-base powders, a similar procedure was applied here in order to estimate the activation energy and other kinetic parameters for the *in-situ* isothermal transformation study.

Pati (27) and Magee (28) found that the activation energy (Q) for isothermal martensitic nucleation is linearly related to the transformation free-energy (ΔG) according to the relation:

$$Q = A + B\Delta G \quad (6)$$

Where A and B are constants. If this linear relation of $Q(\Delta G)$ is obeyed, the transformation rate can be given by:

$$\frac{df}{dt} = nVv \exp\left(\frac{-Q}{RT}\right) \quad (7)$$

where:

- f = volume fraction of martensite
- n = density of nucleation sites (10^6 cm^{-3} taken from Magee, 28)
- v = nucleation attempt frequency (10^{11} s^{-1} taken from Magee, 28)
- R = universal gas constant
- T = absolute temperature
- V = instantaneous mean martensite plate volume.

The V value was calculated using Fullman's formulation (29). As shown in equation 8.

$$V = \frac{\pi^2 f}{8EN_A} \quad (8)$$

where:

- E = average of the reciprocal length of martensite plates as measured on a random cross-section.
- N_A = number of plates per unit area.

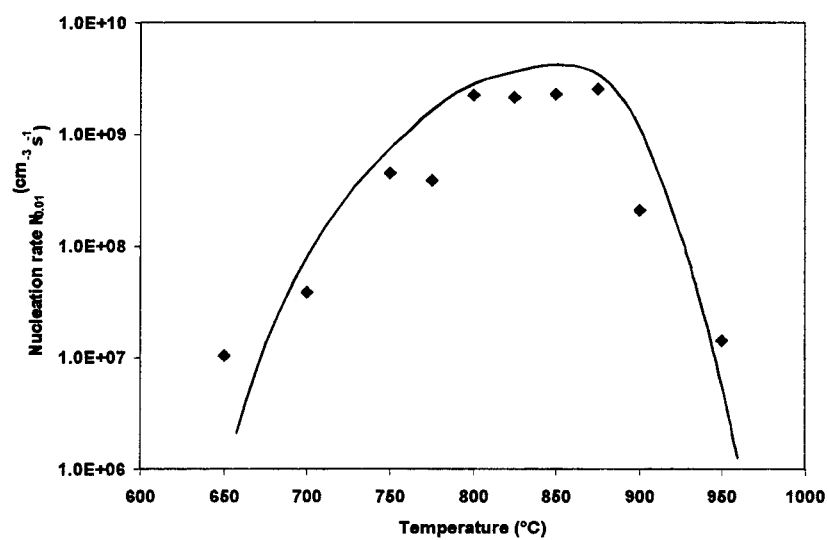


Figure 13. Nucleation rate as a function of temperature for the FCC \rightarrow HCP isothermal transformation in a Co-27Cr-5Mo-0.05C alloy.

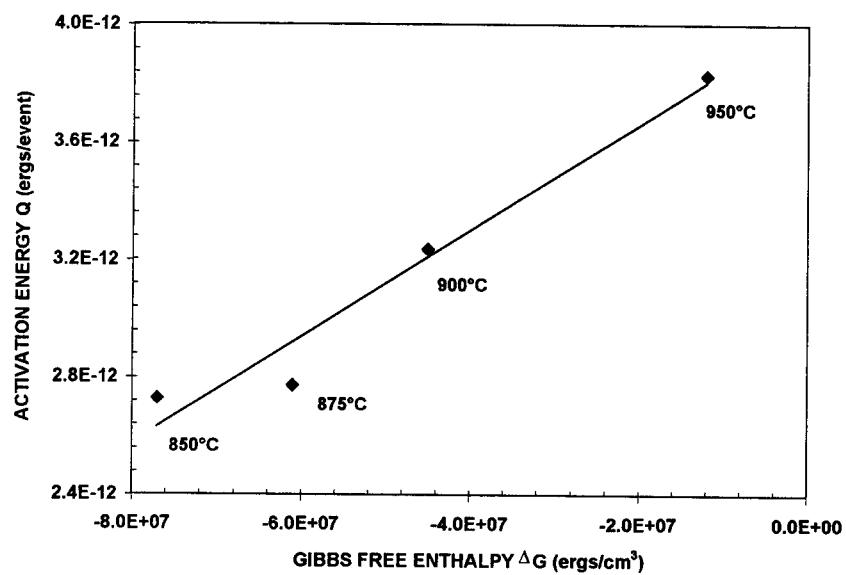


Figure 14. Linear dependence of the activation energy Q , experimentally estimated from the Gibbs free enthalpy change, during the FCC→HCP isothermal martensitic transformation in a Co-27Cr-5Mo-0.05C alloy.

Based on this equation the nucleation rate per unit volume is given as

$$N_{0.01} = \frac{N_v}{t_{0.01}} = \frac{8(EN_A)}{\pi^2 t_{0.01}} \quad (9)$$

where:

- 1) N_v = number of martensite plates per unit volume. It was established from metallographic evaluations in the SEM that in samples with <5% HCP phase there are 9.375×10^6 plates/cm²
- 2) E = average of the reciprocal length of the martensite plates as measured on a random cross-section. This value was measured in the same way as N_v . = $12,422 \text{ cm}^{-1}$
- 3) $t_{0.01}$ = time to produce 1% martensite. This value was obtained from the temperature-time-transformation results, as those shown in Figure 9.

The experimental values of $N_{0.01}$ for various temperatures are plotted in Figure 13. A C-curve kinetic behavior is observed with a maximum nucleation rate in the temperature range of 840 to 870°C. This figure shows that the nucleation rate increases from zero to a maximum value and then decreases with temperature. At higher temperatures, the critical embryo sizes for stable configuration become too large, and few can be formed, even when the atomic mobility is relatively high. Lowering the temperatures, results in a size reduction for the critical nuclei, but the atomic displacements are also reduced. At low undercoolings, the decreasing critical nuclei sizes combined with the increasing driving force easily offset the reduced atomic mobility, leading to increasing nucleation rates.

Assuming a constant nucleation rate up to $f=0.01$, and knowing the values of $N_{0.01}$, the activation energy may be calculated from the relation:

$$Q = -RT \ln \left(\frac{N_{0.01}}{nv} \right) \quad (10)$$

In the study of Adler and Olson (30), on the FCC → HCP transformation exhibited in Pu-Ga and Pu-Al, the Olson-Cohen (24) model was employed. It was found that the relation Q vs. ΔG follows a linear behavior only in the temperature range where corresponding to the maximum value of the kinetic curve, (nose of the C-curve) to the equilibrium temperature. In the present case, from 850 to near 970°C, as is shown (Figure 14) that the experimental results adjust to a linear relation, with the equation constants given by $A = 4.039 \times 10^{-12}$ ergs and $B = 1.824 \times 10^{-20} \text{ cm}^3$.

Cong et al (26) demonstrated the applicability of the model proposed by Olson-Cohen (24) for the isothermal martensitic transformation. An important aspect of their model is the formation of a martensitic embryo by a faulting process derived from a group of already existing dislocations which happen to be properly spaced. It is suggested that the critical condition for the spontaneous formation of an embryo occurs when the fault energy is close to zero. The very low stacking fault energy in the present alloy system lends some physical support to the concept of a HCP embryo, as the probability of the formation of a HCP nucleus increases as the fault energy decreases. Olson and Cohen assumed that the thermally activated motion of the partial dislocations bounding the fault is rate limiting, giving rise to the following expression for $Q(\Delta G)$:

$$Q = Q_0 + \left(\delta + \frac{\ddot{A}n\ddot{n}_A}{b} E^{str} + \frac{2\delta\ddot{A}n}{nb} \right) v^* + \left(\frac{\ddot{A}n\ddot{n}_A}{b} v^* \right) \ddot{A}G^{chem} \quad (11)$$

where:

ρ_A = density of atoms in a closed packed plane, (111)FCC of (0001)HCP.

This value was calculated in $2.9717 \times 10^9 \text{ mol/cm}^2$

E^{str} = coherency strain energy. = 42 J/mol 9 (taken from Olson-Cohen, 24)
 b = Burgers vector (1/6 <112> type) = 1.463 Å.
 σ = FCC/HCP interfacial energy. = 10 erg/ cm² (from Lecroisey and Pineau, 31)
 Δn = number of planes transformed per dislocation, $\Delta n = 2$ in FCC → HCP
 τ = athermal resistance to dislocation motion. $\tau = 0$ in heat treated alloys. (26)
 n = number of transformed compact planes in a formed by dislocations embryo.
 Rajan found that this value is $n = 10$. (23)
 v^* = activation volume for the motion of partial dislocations
 Q_0 = activation energy for dislocation motion in the absence of and applied strain.

Notice that equation. 11 is a straight line equation, and is equivalent to Eq. 6. Hence, from the knowledge of A and B constants, and the values of the parameters of Eq. 11, it is possible to estimate the values of v^* and Q_0 :

$$v^* = 6.32 \times 10^{-21} \text{ cm}^3 = 537 \Omega$$

$$Q_0 = 1.233 \times 10^{-12} \text{ erg} = 0.77 \text{ eV}$$

The Q_0 value found is consistent with that reported by Cong, Morphy and Rajan (26), (0.6 eV). This Q_0 is a measure of the activation energy needed for the motion of partial dislocations. The activation energy for dislocation motion is ≈ 1 eV; which is close to the Q_0 value estimated in this work of 0.77 eV. This in turn indicates that the thermally activated motion of partial dislocations bounding the fault embryo is indeed the rate limiting step. In fact as supported by TEM observations of Rajan, the slow growth of stacking faults and hence the motion of Shockley partials is rate limiting.

The value of the activation volume (v^*) is closely related to the nature of dislocation-obstacle interactions. As noted by Magee (28) a larger activation volume indicates a mechanism of long range interactions. The activation volume (v^*) calculated by Cong, Morphy and Rajan (26) was $v^* = 48 \Omega$, which corresponds to a short range interactions mechanism. At first sight, the value of $v^* = 537 \Omega$, seems too large and should be related to long range interactions. However, Sato et. al., in a study on the FCC → HCP transformation in stainless steel, suggested that values of activation energy as high as 500Ω, may be ascribed to short range interactions. Sato et. al., suggested that the transformation rate of the FCC → HCP transformation is controlled by the interaction between Shockley partials and short range obstacles. Alternatively, Cong, Morphy and Rajan (26) argue that partial dislocations experiment short range interactions mainly with stacking fault intersections and solute clusters.

REFERENCES

1. E. Smethurst and R.B. Waterhouse, *Causes of Failure in Total Hip Prostheses*, Journal of Materials Science, Vol. 12, (1977) pp. 1781-1792
2. R.M. Rose, *Materials for internal prostheses* in 1974 Yearbook of Science and Technology, McGraw Hill, New York.
3. D.C. Mears; Int. Met. Rev., Vol. 22, (1977), pp. 119-155.
4. H.S. Dobbs and Robertson, *Heat treatment of cast Co-Cr-Mo for orthopedic implant use*, Journal of Materials Science, 18, (1983), pp. 391-401.
5. C. Clarke, P. Campbell and N. Kossovsky; in *Particulate Debris from Medical Implants: Mechanisms of Formation and Biological Consequences*, K.R. St. John (ed.), ASTM STP 1144, American Society for Testing Materials, Philadelphia, (1992), pp. 7-26.
6. T.M Devine and J. Wulff, *Cast Vs. Wrought Cobalt-chromium surgical implant alloys* Journal of Biomedical Materials Research, Vol. 9, (1975), pp 151-167.
7. R.T Holt and W. Wallace; Mech. Eng. Report, MS-143, National Research Council Canada, Ottawa, 1980.
8. J.B. Vander Sande, J.R. Coke and J. Wulff, *A transmission electron microscopy study of the mechanisms of strengthening in heat-treated Co-Cr-Mo-C alloys*, Metallurgical Transactions A, Vol. 7A, (1976), pp. 389-397.
9. D. H. Buckley and R.L Johnson; Trans. ASLE, 8, (1965), 123, cited in "Crystal structure", Ch. 17 in *Wear of Metals*, A.D. Sarker (ed.), Pergamon Press, New York, (1976), pp. 93-95.
10. A. Salinas-Rodriguez and J.L. Rodriguez *Deformation behavior of low-carbon Co-Cr-Mo alloys* Journal of Biomedical Materials Research, Vol. 31, (1996), pp. 409-419.

11. D.H. Buckley; Cobalt, Vol. 38, 20, (1968) cited in "Crystal structure", Ch. 17 in Wear of Metals, A.D. Sarker (ed.), Pergamon Press, New York, (1976), pp. 93-95.
12. P. Huang *Martensitic transformation and its role on the tribological behavior of a CoCrMo implant alloy* Doctoral Thesis; University of Wisconsin-Milwaukee, U.S.A. (1997).
13. F. Sebilliau and H. Bibring *The allotropic transformation of Cobalt*, Rev. Met. 1642, (1955), pp. 209-217.
14. R. Adams and C. Altstetter; Transactions of the Metallurgical Society of AIME, Vol. 242, January 1968, pp. 139-143.
15. A.J. Saldívar García Doctoral Thesis, *Estudio por difracción de rayos-X In-situ de la transformación martensítica isotérmica en la aleación Co-27Cr-5Mo-0.05C*; CINVESTAV-IPN Unidad Saltillo, Mexico (1998).
16. A.J. Saldívar García, A. Maní M. and A. Salinas Rodríguez *Formation of HCP martensite during the isothermal aging of an FCC Co-27Cr-5Mo-0.05C orthopedic implant alloy* Metallurgical and Materials Transactions A; Vol. 30A, (May 1999), pp.1177-1184.
17. M. Sage and C. Gillaud *Méthode d'analyse quantitative des variétés allotropiques du cobalt par les rayons X*, Rev. Met. (1950), Vol. 49, pp. 139-145.
18. D.Z. Yang and C.M. Wayman *Slow growth of isothermal lath martensite in an Fe-21Ni-4Mn alloy*, Acta Metallurgica, Vol. 32, No. 6, pp. 949-954 (1984).
19. G.B. Olson and M. Cohen, *A general mechanism of martensitic nucleation: Part III Kinetics of martensitic nucleation*, Metallurgical Transactions A, 7A, (Dec. 1976), pp. 1915-1923.
20. T. Ericsson; Acta Metallurgica, Vol. 14, (1966), pp. 853,
21. L. Remy, A. Pineau, *Twinning of strain-induced FCC-HCP transformation on the mechanical properties of Co-Ni-Cr-Mo alloys*, Mater. Sci. Eng. 26, (1976), pp 123.
22. M. Cohen and C.M. Wayman, *Fundamentals of martensitic reactions*, Metallurgical Treatises in J.K. Tien, J.F. Elliot (Eds.), Conf. Proceedings Beijing China, (1981), p. 445.
23. K. Rajan, J.B. Vander Sande, *Room temperature strengthening mechanisms in a Co-Cr-Mo-C*, Alloy Journal of Materials Science, Vol. 17, (1982), pp. 769-778.
24. G.B. Olson and M. Cohen, *Kinetics of strain-induced martensitic nucleation*, Metallurgical Transactions A, 6A, (April 1975), pp. 791-795.
25. J. Cahn and W. Hagel *Decomposition of Austenite by Diffusional Processes*, V. Zackay and H. Aaronson, eds. Intersciences Publishers, Inc., New York, N.Y., (1962), p. 134.
26. N. Cong Dahn, D. Morphy and K. Rajan, *Kinetics of the martensitic FCC-HCP transformation in Co-Cr-Mo alloy powders*, Acta Metallurgica., Vol. 32, No. 9, (1984), pp.1317-1322.
27. S.R. Pati and M. Cohen, Acta Metallurgica. Vol.17, (1969), p.189.
28. C.L. Magee, Metallurgical Transactions, Vol.2, (1971), p. 2409.
29. R.L. Fullman, Trans. Am. Inst. Min. Engrs., Vol. 197, (1953), p. 447.
30. P.H. Adler and G.B. Olson, *Thermodynamics and kinetics of δ - α martensitic transformation in Pu-alloys*; Metallurgical Transactions A, Vol. 19A, (1988), pp. 2705-2711.
31. F. Lacroissey and A. Pineau, *Martensitic transformations induced by plastic deformation in the Fe-Ni-Cr-C System*, Metallurgical Transactions A, Vol. 3A, (1972), pp. 387-395.

MAGNETIC PROPERTIES

DIFFUSE SCATTERING OF Cu_3Au : DISPLACEMENTS AND FERMI SURFACE EFFECTS

W. Schweika

Institut für Festkörperforschung
Forschungszentrum Jülich, 52425 Jülich, Germany

G.E. Ice, J.L. Robertson, C.J. Sparks, and J. Bai

Oak Ridge National Laboratory
Oak Ridge, Tennessee 37830, U.S.A.

Abstract

The diffuse x-ray scattering of Cu_3Au has been studied utilizing contrast variation by resonant scattering. The data has been analyzed in view of separating (i) individual atomic pair-displacements and (ii) to distinguish mere size-effects from those due to charge transfer. A particularly interesting aspect of the latter approach is that higher order correlations related to charge transfer such as Fermi-surface effects can also be revealed in the pattern of displacement scattering.

INTRODUCTION

During the past decades many extensive diffuse scattering studies have been performed to reveal the short-range order in binary alloys, and quite a few of them are particularly related to the local order in disordered Cu-Au alloys [1]-[6]. Several methods to analyze the diffuse scattering data have been developed, essentially based on a Fourier-analysis of scattering data from a large volume in reciprocal space [7]-[12]. While lattice symmetry properties immediately separate short-range order correlation (i.e. correlations in occupational fluctuations) from static displacement scattering (correlations that involve static positional fluctuations) the individual species dependent pair displacements can only be determined separately by a variation of the scattering contrast between the alloying elements. In principle, for x-rays this can be achieved just by the atomic form factor dependence on the scattering vector, whereas in practice an additional contrast variation by using x-rays and neutrons or utilizing the resonant scattering near absorption edges is advantageous if not necessary. Among those few elaborate studies that aimed to resolve such individual pair displacements, there are

special important results (for instance for a better understanding of the interplay between displacements and magnetism in Invar alloys [13, 14]) and a few typical trends – oscillating displacements in ordering alloys, unlike pairs often have the shortest distance, – although a better general understanding of configurational statistics of alloys including the displacements is a still demanding problem, and it is a goal of today's first-principles alloy theories.

Here we discuss new diffuse scattering data from Cu_3Au , using a single crystal measured in-situ at $T=723$ K. Instead of applying for instance the straightforward 3- λ method [13, 14], the separation here is supported and checked by model calculations of the second order scattering terms, which are related to static and dynamic displacements. Further on, this will help to discuss true size effects and displacements that stem from charge transfer. Further details of the formalism are described in [16]. One reason for using the present approach is that the 3- λ method is rather demanding in the accuracy of a sufficiently large 3-dimensional data basis. Recall that one has to analyze the differences of differences of weak diffuse intensities to separate individual pair displacements. It has also to be admitted that the present database is not as complete as the ones that have been used previously for this separation technique. New experimental studies on Cu_3Au and CuAu are already in progress [15], and may allow a determination of short-range order parameters and displacement parameters with better precision than is possible with the present data. Nonetheless, it will be shown that there is sufficient information to obtain in particular the individual nearest neighbor displacements. From previous x-ray diffuse scattering investigations, Butler and Cohen [6] reported the doubtful result that the distances between neighboring copper atoms are larger than those between gold pairs. However, the recent extended x-ray absorption fine structure (EXAFS) measurements by Frenkel *et al* [17] yield the expected opposite result. In view of the simplicity of EXAFS measurements, it is worth pointing out the principal strength and the potentially extreme sensitivity of diffuse scattering experiments to both short-range order and displacements.

While it is well known that the Fermi surface maybe imaged from the short-range order scattering – this is typical for those nearly frustrated fcc alloys that are energetically nearly degenerate and form long period ordered structures (CuAu II , Cu_3Pd , ...) – there is no report of any influence on the displacements. It is a further aim of this study to see whether or not one can detect such Fermi-surface effects.

EXPERIMENT

The diffuse x-ray scattering measurements were performed at beam-line X-14 at the National Synchrotron Light Source, Brookhaven National Laboratory. The sample was a Cu_3Au single crystal with a surface cut of (421) and a composition of 25.3 at% Au. During the experiment the sample was kept in an evacuated furnace under a Be-dome mostly at a temperature of 723 K, and some data along main symmetry directions have been taken also at 773 K. Three different x-ray energies were chosen, 11909 eV (near Au L-edge at 11919 eV), 10500 eV and 8959 eV (near Cu-K edge at 8979 eV), to achieve a favorable scattering contrast by anomalous scattering. In addition to calculated anomalous scattering factors [18], EXAFS-measurements were made near the Au L-edge and Cu K-edge for a precise determination of changes in the real part $f'(E)$ using the Kramers-Kronig relation, as shown in Fig. 1.

The incident beam flux is monitored before and after the incident beam slits. To analyze the scattered beam a mosaic, sagittal-focusing graphite (002) crystal was used, which allows the separation of the elastic signal from the resonant Raman scattering

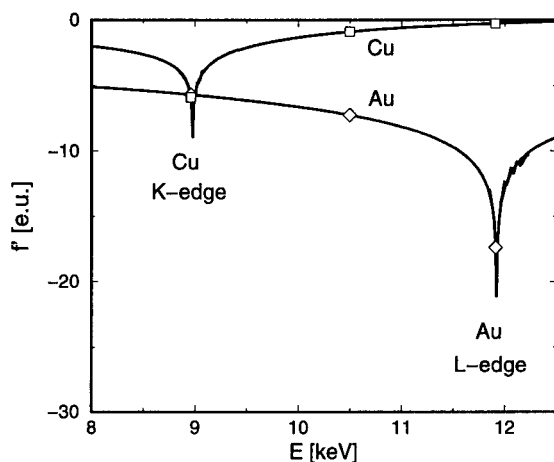


Figure 1. Anomalous variation of the real part of the scattering amplitudes of Cu and Au for the three energies used.

by distributing the intensity on a linear position-sensitive proportional counter[19, 20]. This energy analysis also reveals the Compton scattering that is removed, although it is almost negligibly small in the present case. The HWHM resolution of the experimental setup is better than 0.04 reciprocal lattice units (r.l.u.). The data were taken in the usual reflection mode on a four-circle diffractometer. For calibration the intensities have been compared to the integrated Bragg reflections of a Ni-powder reference standard.

Then, including corrections for absorption, surface roughness and taking into account an averaged Debye-Waller factor for Cu and Au, $\langle u^2 \rangle = 0.021 \text{ \AA}^2$ at 723 K[21], the intensities were converted into Laue units, $I_{Laue} = c^{Cu} c^{Au} |f_Q^{Au} - f_Q^{Cu}|^2$, where c^{Cu} (c^{Au}) is the atomic fraction of Cu (Au) and f_Q^{Cu} (f_Q^{Au}) the complex x-ray atomic scattering factor of Cu (Au).

RESULTS AND DISCUSSION

In the following only the intensities measured along high symmetry directions are considered. Therefore, the database to determine short-range order parameters and lattice displacement parameters is restricted. Contrary to any previous work, rigorous model calculations were performed to check the steps in the data analysis of these parameters. The more interesting and important aspect is the deeper insight and understanding of the experimental results that will be fruitful in future diffuse scattering investigations.

Intensities along main symmetry directions

Figure 2 displays the x-ray diffuse intensities in electron units as measured in the [h00] direction showing that the particular choice of the x-ray energies yielded a sufficiently strong scattering contrast. Note that the resolution is sufficient so that the high intensities seen near the fundamental Bragg peaks (200) and (400) are still free from Bragg scattering and have their origin in the local disorder. Near the zone boundaries at (100) and (300), there are short-range order peaks. A closer look reveals

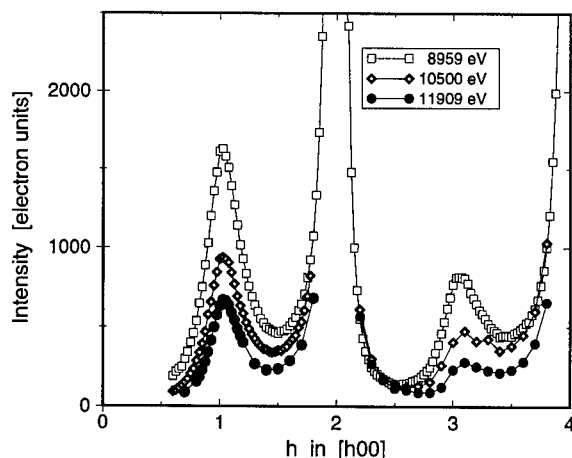


Figure 2. Diffuse x-ray intensities in the $[h00]$ direction measured at three different energies and normalized to electron units showing the effect of the contrast variation by anomalous scattering near the Cu-K edge and Au-L edge. (Lines are only guides for the eye.)

that the short-range order peaks are strongly asymmetric which is indicative of strong displacements in this alloy.

Thermal Diffuse Scattering

Near the fundamental Bragg peaks there are large intensities that stem from thermal diffuse scattering (TDS). Within the 3- λ method one uses a data set with the least scattering contrast $f_B - f_A$ to eliminate this TDS contribution as well as other second order displacement terms proportional to $\langle f \rangle^2$. Here the TDS is calculated in first order approximation from experimental phonon frequencies. The phonon properties were established from a weighted average (by the root of masses) of the phonon frequencies for pure Cu[22] and Au[23]. These are found to be in agreement with the phonon measurements of Katano *et al*[24] performed on disordered Cu_3Au . The phonon peaks are rather broad and this damping has been related mainly to the large mass disorder[24].

One may note that the TDS, as can be seen in Fig. 3, is not the main contribution near the Bragg peaks. This additional scattering arises from static displacements.

Static Displacement Fields

The local microscopic details of displacements in alloys which we wish to analyze from the x-ray data are unknown. They depend on different atomic sizes, charge transfer and interference with short-range order, at least in the macroscopic limit. Scattering near the Bragg peaks is well-defined within the elastic theory by macroscopic properties, *i. e.* the bulk modulus and the change of the lattice parameter with composition[25]. Considering only size effects due to near neighbor forces and neglecting for instance further possible Coulomb interactions due to charge transfer, the local displacements in diluted alloys can be determined from the asymptotic decay of displacement fields around single defects as it is the intriguing idea of the Kanzaki force model[26]. Here one determines the entire static long-range displacement field in linear response of short-

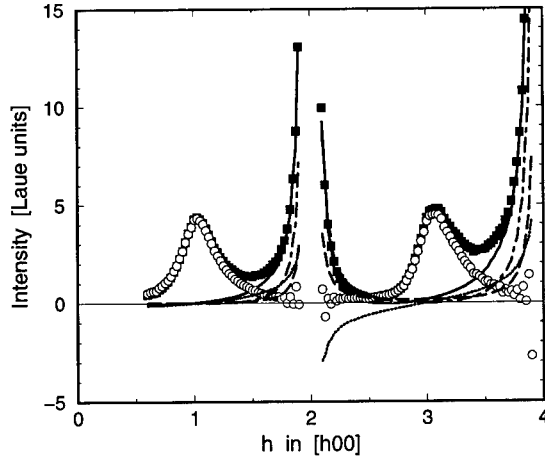


Figure 3. Illustration of the separation of the X-ray diffuse intensities in the [h00] direction. Data (*solid squares*) are normalized to Laue units and calculated scattering contributions are subtracted (*open circles*). Calculated intensities are thermal diffuse scattering (*long dashed line*), asymptotic static displacement scattering to second order (Huang scattering) (*dotted-dashed line*), and to 1st order (asymmetric part of Huang scattering) (*dotted line*), and the sum of these calculated intensities (*solid line*).

range forces for a given dynamical matrix (as has been used for the TDS calculation). Fourier transforms are deconvoluted according to

$$\mathbf{u}_{\mathbf{q}} = \Phi_{\mathbf{q}}^{-1} \mathbf{F}_{\mathbf{q}}. \quad (1)$$

For concentrated alloys it does not make sense to distinguish between defect and host atoms but forces due to say Cu or Au are proportional to the occupational fluctuation $\Delta c_{\mathbf{R}} = c_{\mathbf{R}}^{(i)} - c^{(i)}$ (— equals to c^{Au} (c^{Cu}) if site \mathbf{R} is occupied with a Cu (Au) atom —) and likewise the displacements around the site \mathbf{R} .

With the constraint of the macroscopic limit there is no free parameter within the nearest neighbor force model. The relaxation volume $V_R = 3\Omega(\partial a/a\partial c^{Au})$ can be used to estimate the nearest neighbor force \mathbf{F} from the fact that the asymptotic form of the force field in the macroscopic limit has to obey $\sum_l \mathbf{R}_l \cdot \mathbf{F}_l = 3B V_R$ (where B is the bulk modulus).

The approximate description of the diffuse scattering intensity (per atom) to first and second order given by [16, 27]:

$$I_{\mathbf{Q}} = c^{Cu} c^{Au} \alpha_{\mathbf{q}} |\Delta f_{\mathbf{Q}} + \langle f_{\mathbf{Q}} \rangle i \mathbf{Q} \cdot \mathbf{u}_{\mathbf{q}}|^2, \quad (2)$$

is rather appropriate for a force model which makes use of Eq. 1. Here $\alpha_{\mathbf{q}}$ denotes the Fourier transform of the usual Cowley-Warren short-range order parameter, $\Delta f_{\mathbf{Q}}$ and $\langle f_{\mathbf{Q}} \rangle$ represent the difference and the average of the \mathbf{Q} -dependent atomic form factors respectively, \mathbf{Q} the scattering vector, and \mathbf{q} the reduced scattering vector. Both $\alpha_{\mathbf{q}}$ and the Fourier transform of the displacements $\mathbf{u}_{\mathbf{q}}$ are periodic in reciprocal space. In Eq. 2 one assumes the linear superposition of the displacement fields. The short-range order itself and its effects on the arrangements of the displacements are taken into account. However, the local variation of the scattering factors and off-diagonal displacement

terms are neglected but could be included in a straightforward manner in a computer modeling of the local (dis-)order. In a first attempt to separate the large contribution near the Bragg peaks, it is sufficient to use the extrapolated short-range order intensity for $\mathbf{Q} = (2\pi/a)\mathbf{h} \rightarrow 0$. We used an estimate of $\alpha_{q \rightarrow 0} = 0.25$. Although there are in principle no more unknown parameters, because of their uncertainties we would obtain only a rough estimate. Therefore, a refinement of a single parameter (for all three x-ray energies and lattice directions) yields in [100] direction for instance:

$$i \mathbf{u}_{\mathbf{q} \rightarrow 0} = -\frac{\mathbf{q}}{q^2} \frac{3 \partial a}{a \partial c^{Au}} \frac{c_{11} + 2 c_{12}}{c_{11}} = -0.47 \frac{\mathbf{q}}{q^2}$$

Figure 3 shows a typical separation of the intensity contributions. One may note the remarkable agreement between measured intensity and the calculated total intensity.

This first approach gives a particular noteworthy result for the separated linear displacement scattering in the [100] direction. The short-range order intensity is nicely described by a simple Lorentzian – as related to exponentially decaying correlations. One recognizes that, if we take out the trivial h -dependence, the displacement intensity is well described by a simple analogous function, the sinus-Fourier transform of exponentially decaying displacements with a correlation length that is *identical* with the one for the short-range order, see Fig. 4. To show the reproducibility of the separation for

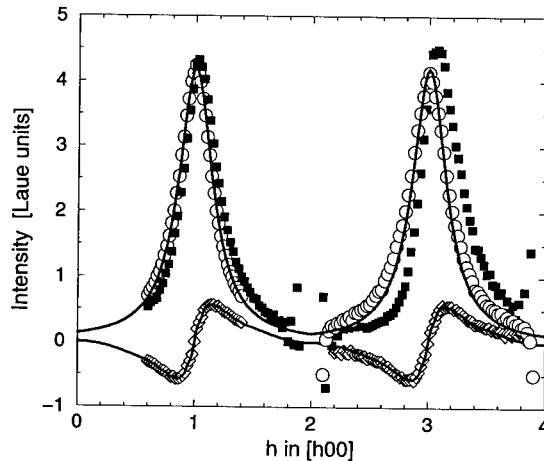


Figure 4. The remaining diffuse intensity due to local disorder (*solid squares*, see also Fig. 3) is separated in parts due to symmetrical short-range order (*open circles*) and asymmetric 1st order local displacement term (*open diamonds*). The reproducibility of the periodic patterns of the displacement term is best shown after removal of the h dependence. The short-range order is well described by a Lorentzian, solid line. The sinus-Fourier transform of the exponential decay that is found for the short-range order describes the local displacement term (solid line).

\mathbf{h} between the (200) and (400), we have used the lattice Fourier transform, rather than the simple analytic expression for the continuum $const (h'/\kappa) \mathcal{L}(h')$, where $\mathcal{L}(h')$ is the Lorentzian, with $h' = h - h_c$ centered at $h_c = (1, 0, 0)$, and κ is the inverse correlation length of the short-range order.

This indicates that in addition to the $1/r^2$ -dependence of the tails of the displacement fields due to elastic properties there is an essential local part that is ruled by

short-range order. In case of only mere size effects (due to nearest neighbor forces) this convolution with short-range order explains the typical spatial oscillations that have been found in real space displacement parameters for many alloys. However, two reasons exist for the exponentially decaying contribution, 1) the short-range ordering of mere size effects as included in the above model or 2) additional displacements due to charge transfer and its spatial modulations that should follow the short-range order as well. So far it is not possible to discriminate between these two contributions since Eq. 2 is only an approximation (where the actual scattering amplitude of the displaced atom is substituted by the average scattering factor). With respect to the different Q -dependence of the x-ray atomic form factors, to first order this affects only the magnitude of the separated displacement scattering and not its shape.

However, for a separation of the displacement scattering into species dependent displacements, one has to turn back to the contrast variation. Here the question of the validity of the approximation discussed before is irrelevant for the removal of the essential second order displacement scattering terms. Particularly, for data scans along high symmetry lines, the model calculation are simple to perform, and also in view of an analysis that aims primarily at the separation of say individual nearest neighbor displacements, such a database should provide a reasonable first estimate.

Short-Range Order

The short-range order parameters have been obtained by a linear least squares fit (based on singular value decomposition) from the separated short-range order intensities of 168 data points along [100], [110], [111], and [1h0]. The best results have been obtained from the data measured at an energy just below the Cu K-edge having the largest scattering contrast Δf_Q . The result is shown in Fig. 5 in comparison with

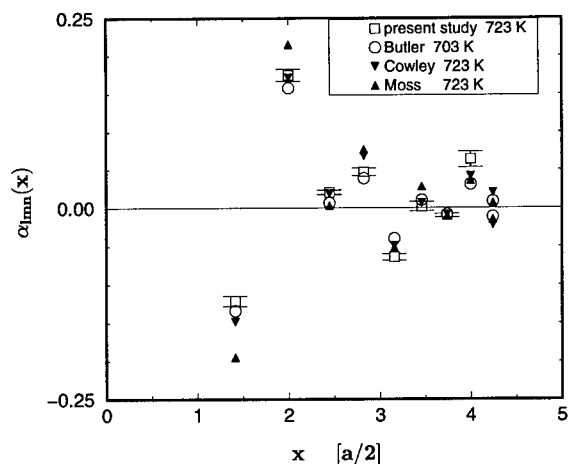


Figure 5. Comparisons of our analysis with other's short-range order parameters for disordered Cu_3Au near $T = 723 \text{ K}$.

reported values for disordered Cu_3Au at or near $T = 723 \text{ K}$. The results were obtained including a fit of $\alpha_{000} = 1.004 \pm 0.020$ (only statistical errors are given). An inclusion of parameters beyond α_{400} destabilizes the results. Of course in view of the small database,

no claim can be made with respect to an improved accuracy. Future work is still desirable for instance to determine the long-range part of the effective pair-interactions for a better understanding of the peak splitting and the Fermi-surface effects that will be discussed below.

Species Dependent Displacements

With respect to the mean lattice there are only two independent linear displacement parameters, and two data sets with different scattering contrast are sufficient to determine the individual displacements between Cu-Cu, Cu-Au and Au-Au pairs. As expected the combination with the largest change in contrast (data taken near the Au L-edge and Cu K-edge) give the most reliable parameters (Table 1), while the other two combinations gave consistent results with only larger errors. Significant displacements were found particularly for the first and second nearest neighbor pairs. The relative statistical errors are about 10%. As expected the largest displacements are found between Au-Au nearest neighbors. Their larger positive displacements means that the average distance between nearest Au-Au pairs is greater than the average lattice ($a_0/\sqrt{2}$) by 0.165 Å. The different signs between nearest and second nearest neighbor displacements can be understood from the chemical short-range order in the alloy. Given in Fig 6. is a drawing of the L1₂ structure of ordered Cu₃Au. With reference to Fig 6, the inter-

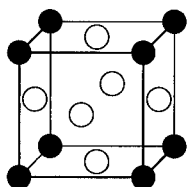


Figure 6. L1₂ structure of ordered Cu₃Au.

mediate four nearest neighbors sites between second neighbor pairs are occupied with higher probability by the smaller Cu atoms in the case of Au-Au and Cu-Au second neighbor pairs, and by the larger Au atoms in the case of Cu-Cu second neighbor pairs.

Table 1 Individual pair-displacements for nearest and second nearest neighbors in Cu₃Au at 723 K. The relative statistical errors are about 10 %

lmn	u_{lmn}^{Cu-Cu}	u_{lmn}^{Cu-Au}	u_{lmn}^{Au-Au}
110	-0.024 Å	0.014 Å	0.165 Å
200	0.023 Å	-0.021 Å	-0.037 Å

It is interesting to compare the present results with those from other experimental investigations and theoretical calculations. In a previous x-ray study of disordered Cu₃Au, Butler and Cohen[6] analyzed their x-ray data (measured with a single energy, Co-K_α) in view of species dependent displacements using a method[10] that is based on the differences in the Q-dependences of the atomic form factors. According to their

results, the largest distances between nearest neighbors occurred for Au-Cu pairs and the shortest distances between Au-Au pairs in contradiction to the present results and the usual expectation that Au is 'larger' than Cu.

Recently, Frenkel *et al* [17] performed an EXAFS-study of quenched Cu-Au alloys and obtained results with similar accuracy to those reported here that are very consistent with the present ones.

Theoretical attempts to calculate these displacements and mean bond distances have been made by various groups and a few results are available for CuAu alloys and Cu₃Au in particular. Mousseau *et al* [28] calculated displacements in Cu-Au alloys based on a nearest neighbor central force model (CFM) and the embedded atom method (EAM). While the CFM gives the result of $u_{110}^{Cu-Cu} < u_{110}^{Cu-Au} < u_{110}^{Au-Au}$ for all compositions – as expected when considering only size effects –, the EAM indicates a crossing of $u(CuCu)$ and $u(CuAu)$ for large Au concentrations. In computer model calculations relaxing the resimulated SRO configuration based on Lennard Jones potentials, Horiuchi *et al* [29] obtained the relative bond distances 0.994, 1.005, 1.026 for CuCu, CuAu, AuAu pairs respectively, which are in better agreement with the present result. More recently, Wolverton *et al* [30] performed a calculation within the local density approximation for a small cell of 8 atoms for random Cu-Au configurations. Their results for Cu₃Au (for an average bond length of 2.6492 Å for this special, fairly random configuration) gave $u_{110}^{Cu-Cu} = -0.059$ Å, $u_{110}^{Cu-Au} = 0.036$ Å, $u_{110}^{Au-Au} = 0.076$ Å, which are in qualitative agreement with the present results. However, one may note that different 'bond lengths' are to be expected for random and SRO configurations.

If one neglects SRO effects on the nearest neighbor displacements, one might distinguish their 'size' and 'charge' related origins. In the case where charge transfer effects dominate the ions hard core repulsion (size effect) one expects that unlike neighbors are closer than like neighbor pairs. Assuming that

$$\langle u^{ij} \rangle_{lmn} \approx \langle u_0^i \rangle_{lmn} + \langle u_0^j \rangle_{lmn} + \langle \delta u^{ij} \rangle_{lmn} ,$$

one obtains the contribution due to size, $\langle u_0^{Au} \rangle_{110} = 0.05$ Å and second contribution due to charge, $\langle \delta u^{Au-Au} \rangle_{110} = -3 \langle \delta u^{Au-Cu} \rangle_{110} = 9 \langle \delta u^{Cu-Cu} \rangle_{110} = 0.064$ Å. In an early study of the de Haas van Alphen effect [31] in diluted CuAu alloys, a charge transfer of $\Delta z_{Au} = -0.32$ has been reported. This is also indicated by the Pauling electronegativities of 1.9 and 2.54 for Cu and Au, respectively, while the sign of the charge transfer cannot be obtained from the displacements. Obviously, charge transfer leads to even larger Au-Au distances than those expected from mere size effects and explains why Cu-Au and Cu-Cu distances are more similar.

The superposition of displacements following the chemical short-range order and displacements due to charge transfer are higher order correlation functions, 3-point and 4-point correlations respectively, as has been discussed in more appropriate scattering expressions [16]. For a separation without the approximations made above, the local structure needs to be simulated in a computer model. Furthermore, in view of a more appropriate treatment of the configurational thermodynamics of alloys including charge and size effects, such simulations can be based on the 'compressible Ising model' as proposed by B. Chakraborty [32]. Plans are to use this model in future inverse Monte Carlo simulations to determine – in addition to the effective interaction energies – the gradient of the effective pair potential that is related to properties like the charge transfer. Therefore, the information that can be obtained from diffuse scattering experiments should provide an unique and sound basis.

Fermi-surface effects

In some alloys like Cu-Au, one observes a fine structure in the x-ray diffuse scattering around the short-range order peaks, namely a fourfold splitting of the intensity, which is commonly attributed to the Fermi-surface effect and is supposed to arise from the weak (log) singularity in the dielectric response. Recently, Reichert *et al*[33] reported an anomalous behavior of such a splitting for Cu₃Au, since the wave vector was found to shift with temperature. This observation was surprising at first sight and gave rise to a controversial debate about its origin.[34, 35] In a subsequent study of disordered CuAu[36], which also exhibits a splitting of the short-range order maxima, the peak positions, however, shifted less significantly than in Cu₃Au. The splitting related to the nesting condition is schematically shown in Fig. 7, and its observation requires a sufficiently good resolution.

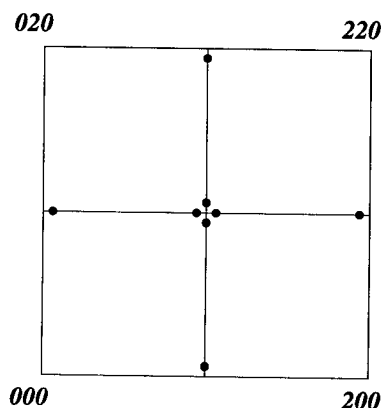


Figure 7. Scheme of the fourfold short-range order peak splitting in the scattering plane ($h,k,0$) as observed for Cu₃Au.

Because of the large displacements in Cu₃Au, the actual intensity is affected by large asymmetric contributions and the fourfold splitting of the SRO intensity is not readily visible around the (110). However, both the SRO peak splitting and the influences of the Fermi surface on the static displacements are revealed by the present separation of the data. For comparison, note that in a previous investigation[33] of the SRO peak splitting such complications have been avoided by measuring perpendicular to the direction [100] at the equivalent (100) peak.

Fig. 8 displays the data measured along the [110] direction and the calculated intensity contributions. Again the model calculations discussed above were used to remove the intensities due to the related second order displacements. A separation of the remaining symmetric and antisymmetric part of the intensity gives the short-range order and the linear displacement contribution. The SRO intensity is compared to a Lorentzian which emphasises the little extra intensities which are related to the $2k_f$ screening mechanism. The convolution of short-range order and displacements according to Eq. 2 within the nearest neighbor force model yields the intensity, see Fig. 8, that is expected from size effects only. The interesting feature is the remaining difference in the separated data related to displacements and the model calculation. The

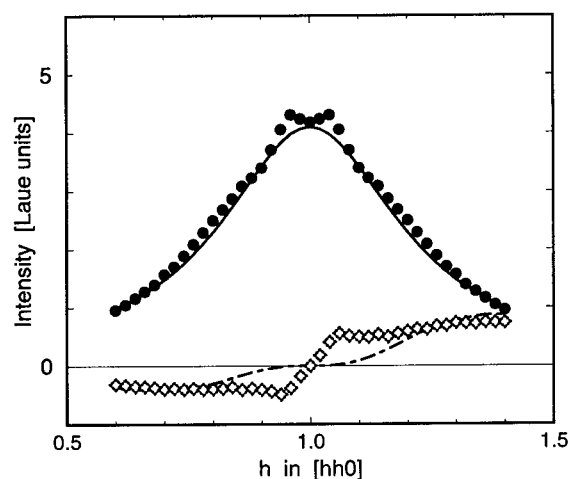


Figure 8. Diffuse scattering of disordered Cu_3Au in $[110]$ direction. Model calculations (dot-dashed line) of the size effect scattering (open diamonds) including its interference with short-range order reveal a residual intensity contribution that can be related to a Fermi surface effect on the displacement pattern in analogy to the observed features in the short-range order intensity (filled circles). A Lorentzian (solid line) is shown for comparison indicating that the Fermi surface effect on the short-range order intensity is rather subtle.

remaining intensity peaks in an asymmetric fashion where the short-range order split peaks occur. The splitting of the short-range order is consistent with the observation by Reichert *et al.*[33]. Surprisingly, a Fermi surface effect appear even more obviously in the displacement scattering rather than in the short-range order intensity. Similar results are obtained for data taken at higher temperatures where the wave vector of the asymmetric peaks do not shift significantly with temperature and agrees with the extrapolated high temperature peak position of the short-range order maxima.

SUMMARY AND CONCLUDING REMARKS

Contrary to previous investigations of local order in Cu_3Au , the resonant (or anomalous) scattering variation near the absorption edges was used to separate individual pair displacements. The model calculations have successfully separated in a controlled manner and within a good approximation the second order displacement scattering terms. In addition, they have yielded a deeper insight into displacement patterns in alloys. This includes for instance the typical asymmetry of the diffuse peaks, *e. g.* at (100), due to displacements, which is of course bound in an asymmetrical way to the shape of short-range order itself, and should be observed in studies of other alloys. With regard to the fine structure of the diffuse scattering near the (110), in addition to the well-known short-range order peak splitting, a particular observation has been the finger print left by the Fermi surface on the displacement scattering. In view of previous puzzling results on the individual pair displacements, the present data settles this dispute and confirms that Au-Au neighbor pairs have the largest mean distance. Although the displacements have been determined rather precisely for Cu_3Au , future experimental work for a more complete data set of different compositions combined

with the usual $3\text{-}\lambda$ separation technique is certainly still desirable to obtain more accurate short-range order and displacement parameters for this important, much studied model system. As discussed above, qualitative agreement is found with results of recent theoretical calculations, and possible improvements in first-principles calculations may be expected for sufficiently larger model systems to account for the short-range order effects on displacements. Further development in the treatment of the configurational thermodynamics of alloys should be based on extended Ising models[32] that account explicitly for both (hard-core) size and charge related displacements that can be obtained from diffuse scattering experiments.

References

- [1] J.M. Cowley, J. Appl. Phys. **21**, 24 (1950).
- [2] B.W. Roberts, Acta Metall. **2**, 597 (1954).
- [3] S.C. Moss, J. Appl. Phys. **35**, 3547 (1964).
- [4] P. Bardhan and J.B. Cohen, Acta Cryst. **A32**, 597 (1976).
- [5] F. Livet and M. Bessiere, J. Physique **48**, 1703-8 (1987).
- [6] B. D. Butler and J. B. Cohen, J. Appl. Phys. **65**, 2214 (1989).
- [7] C.J. Sparks, B. Borie, *Local atomic arrangements studied by x-ray diffraction*, pp 5-46, Gordon & Breach, New York (1966).
- [8] B. Borie, C.J. Sparks, Acta Cryst. **A27**, 198 (1971).
- [9] R.O. Williams, Metall. Trans. **5**, 1843 (1974).
- [10] P. Georgopoulos and J.B. Cohen, J. Phys. (Paris) Colloq. **33**, C7-191 (1977); P. Georgopoulos, J.B. Cohen, Acta Metall. **29**, 1535 (1981).
- [11] L. Schwartz and J.B. Cohen. *Diffraction from Materials*, Academic Press, New York (1977).
- [12] G.E. Ice, J.L. Robertson, and C.J. Sparks, in *Methods in Materials Research: A Current Protocols Publication*, Elton N. Kaufmann, Alan Goldman (Eds.), John Wiley & Sons, New York (1998).
- [13] G.E. Ice, C.J. Sparks, A. Habenschuss, L.B. Shaffer, Phys. Rev. Lett. **68**, 863 (1992).
- [14] J.L. Robertson, G.E. Ice, C.J. Sparks, X. Jiang, P. Zschack, F. Bley, S. Lefebvre, and M. Bessiere,
- [15] C.J. Sparks, private communication. Phys. Rev. Lett. **82**, 2911 (1999).
- [16] W. Schweika, *Disordered Alloys, Diffuse Scattering and Monte Carlo Simulations*, Springer Tracts in Modern Physics Vol. **141**, G. Höhler (Ed.), Springer, Heidelberg (1998).
- [17] A.I. Frenkel, E.A. Stern, A. Rubshtein, A. Voronel, and Yu. Rosenberg, J. Phys. IV France **7** (1997)

- [18] D.T. Cromer and D. Liberman, J. Chem. Phys. **53**, 1891 (1970); Acta Cryst. **A37**, 267 (1981).
- [19] G.E. Ice, C.J. Sparks, and L.B. Shaffer, in *Resonant Anomalous X-Ray Scattering, Theory and Applications*, G. Materlik, C.J. Sparks, and K. Fischer (Eds.), 1994 Elsevier Science B. V., pp. 265-294.
- [20] X. Jiang, G.E. Ice, C.J. Sparks, J.L. Robertson, and P. Zschack, Phys. Rev. B **54**, 3211 (1996).
- [21] Separate Debye Waller factors for Cu and Au are easily introduced, although for the relatively small scattering vectors considered here this seems to be of minor importance.
- [22] E.C. Svensson, B.N. Brockhouse, J.M. Rowe, Phys. Rev. **155**, 619 (1967).
- [23] J.W. Lynn, H.G. Smith, R.M. Nicklow, Phys. Rev. B **8**, 3493 (1973).
- [24] S. Katano, M. Iizumi, and Y. Noda, J. Phys. F: Met. Phys. **18**, 2195 (1988).
- [25] H. Trinkaus, Phys. Stat. Sol. B **51**, 307 (1972); P. Dederichs, J. Phys. F **3**, 471 (1973).
- [26] H. Kanzaki, J. Phys. Chem. Solids **2**, 24 (1957); H. Kanzaki, J. Phys. Chem. Solids **2**, 107 (1957).
- [27] M.A. Krivoglaz, *Diffuse Scattering of X-Rays and Neutrons by Fluctuations*, Springer, Berlin (1996).
- [28] Normann Mousseau and M.F. Thorpe, Phys. Rev. B **45**, 2015 (1992).
- [29] T. Horiuchi, S. Takizawa, T. Suzuki, and Tetsuo Mohri, Metall. Mater. Trans. **26A**, 11 (1994)
- [30] C. Wolverton, V. Ozolins, and Alex Zunger, Phys. Rev. B **57**, 4332 (1998).
- [31] R.G. Poulsen, D.L. Randles, M. Springford, J. Phys. F: Metal Phys. **4**, 981 (1974).
- [32] B. Chakraborty, Europhys. Lett. **30**, 531 (1995).
- [33] H. Reichert, S.C. Moss, and K.S. Liang, Phys. Rev. Lett. **77**, 4382 (1996).
- [34] V. Ozolins, C. Wolverton, and Alex Zunger, Phys. Rev. Lett. **79**, 955 (1997).
- [35] H. Reichert, S.C. Moss, and K.S. Liang, Phys. Rev. Lett. **79**, 956 (1997).
- [36] O. Malis, K.F. Jr. Ludwig, W. Schweika, G.E. Ice, and C.J. Sparks, Phys. Rev. B **59**, 11105 (1999).

AB INITIO THEORY OF PERPENDICULAR TRANSPORT IN METALLIC MAGNETIC MULTILAYERS

Josef Kudrnovský⁽¹⁾, Václav Drchal⁽¹⁾, Claudia Blaas⁽²⁾,
Peter Weinberger⁽²⁾, Ilja Turek⁽³⁾, and Patrick Bruno⁽⁴⁾

⁽¹⁾*Institute of Physics, Academy of Sciences of the Czech Republic*

Na Slovance 2, CZ-182 21 Prague 8, Czech Republic

kudrnov@fzu.cz

⁽²⁾*Center for Computational Materials Science, Technical University of Vienna*

Getreidemarkt 9/158, A-1060 Vienna, Austria

cb@cms.tuwien.ac.at

⁽³⁾*Institute of Physics of Materials, Academy of Sciences of the Czech Republic*

Žitkova 22, CZ-616 62 Brno, Czech Republic

turek@ipm.cz

⁽⁴⁾*Max-Planck-Institut für Mikrostrukturphysik*

Weinberg 2, D-06120 Halle, Germany

bruno@mpi-halle.de

ABSTRACT

The current-perpendicular-to-plane (CPP) magnetoconductance of a sample sandwiched by two ideal non-magnetic leads is described at an *ab initio* level. The so-called 'active' part of the system is a trilayer consisting of two magnetic slabs of finite thickness separated by a non-magnetic spacer. We use a transmission matrix formulation of the conductance based on surface Green functions as formulated by means of the tight-binding linear muffin-tin orbital method. An equivalent and computationally more efficient formulation of the problem based on reflection matrices is also presented. The formalism is extended to the case of lateral supercells with random arrangements of atoms which in turn allows to deal with ballistic and diffusive transport on equal footing. Applications refer to fcc-based Co/Cu/Co(001) trilayers.

INTRODUCTION

Transport in layered materials is subject of intensive theoretical investigations, in particular in view of the discovery of the giant magnetoconductance (GMC) in metallic multilayers [1, 2]. Various theoretical treatments have been proposed, based on the semiclassical Boltzmann equation or, alternatively, on a Kubo-Greenwood type formulation within a free-electron model with random point scatterers, for the Kronig-Penney model, or within a single-band tight-binding model. A description of experimental and theoretical results can be found in a recent review article [3]. Up to now the GMC effect has been observed mostly in the diffusive transport regime in which the mean free path is much smaller than the dimension of the so-called 'active' part of the multilayer system, i.e., the whole system with exception of the leads. Most of measurements up to date were performed in the current-in-plane (CIP) geometry [1], the current-perpendicular-to-plane (CPP) geometry [2] seems to be experimentally more demanding. From a theoretical standpoint of view CPP transport is interesting because of an obvious role played by interfaces, its close relation to tunneling across an insulator or vacuum, and because of its relation to a semi-classical view of ballistic transport [4]. The present theoretical understanding of the CPP transport has been reviewed in a recent paper [5], including the transport in the ballistic regime. In this regime, in contrast to the diffusive regime, the mean free path is larger than the dimension of the 'active' part of the multilayer system. The spin-dependent scattering at ideal interfaces between magnetic and non-magnetic metals which form a multilayer, the so-called intrinsic potential scattering, is usually said to be the origin of the GMC in the ballistic regime [4]. In the diffusive regime the GMC is thought to originate from spin-dependent scattering off impurities in the bulk and/or at interfaces between the magnetic slabs and the spacer (extrinsic defects). It should be noted that in real multilayers also dislocations or stacking faults occur, and magnons and phonons can cause dynamical perturbations. While in the limiting cases of the strong diffusive regime and the ballistic regime simplifications can be made, a real multilayer system usually represents a mixture of both intrinsic and extrinsic defects.

Ab initio calculations of the GMC are still rather rare. We mention a Boltzmann-type approach developed for multilayer systems within the relaxation-time approximation, which is limited to either weak scattering or very low-concentration [6] limits. Typically, the electronic structure of a three-dimensional periodic (infinite) multilayer system is determined (velocities and the Fermi surface) and, in separate calculations, the spin-

dependent relaxation time of bulk impurities is found and used to solve the (classical) Boltzmann equation. Clearly, the change of the superlattice bandstructure due to impurities is neglected, hence the above mentioned limitation of the method. A solution of the Boltzmann equation for layered systems without the relaxation-time approximation has also been suggested [7]. Recently *ab initio* calculations using a Kubo-Greenwood approach generalized to layered systems [8, 9] have appeared in which (substitutional) disorder is included within an inhomogeneous coherent potential approximation (CPA). This is an appropriate approach to deal with the influence of imperfections and to treat intrinsic and extrinsic scattering on equal footing. However, up to now in there the so-called vertex corrections with respect to the configurational average of the products of two single particle Green functions are neglected. The above mentioned approaches can in principle be used for both the CIP and CPP geometry.

An alternative theoretical approach based on non-equilibrium Green functions or on a transmission matrix formalism (Landauer-type approach) can be used for the CPP transport. A useful review of these techniques can be found in a recent monograph [10].

It is the aim of this paper to formulate a surface Green function (SGF) approach to CPP transport in magnetic multilayers within the tight-binding linear muffin-tin orbital (TB-LMTO) method [11]. Related formulations based on empirical tight-binding (TB) models have appeared recently [13, 14, 15, 16]. The present formulation is then extended to the case of lateral two-dimensional supercells with random occupation of lattice sites by two kinds of atoms, whereby the stacking of such random layers in the growth direction can be arbitrary. The usefulness of such an approach has recently been illustrated for the case of a single-band TB model [17]. In particular it has been shown that current fluctuations due to different configurations are small for metallic multilayers if the size of the supercells is large enough. It should be mentioned, however, that in the case of tunneling through an amorphous spacer such fluctuations can be quite large [18]. We shall present an *ab initio* application of such an approach for the case of Co/Cu/Co(001)-based trilayers.

THEORY

Suppose the magnetic multilayer system consists of a semi-infinite left (\mathcal{L}) and a semi-infinite right (\mathcal{R}) non-magnetic lead sandwiching a trilayer consisting of a left and a right magnetic slab of varying thickness separated by a non-magnetic spacer again of varying thickness. The sequence of planes of atoms (layers) in the growth direction of the trilayer

is assumed to be arbitrary. In principle, atomic layers can be viewed in terms of $n \times n$ supercells ($n \times n$ two-dimensional complex lattice). In order to describe disorder (substitutional binary alloys) it is then necessary to average over different sizes n of supercells, and for each n over different occupations of the sites within the supercell by the two constituents involved. Quite clearly such an approach applies to disordered spacers and/or magnetic slabs as well as to disordered interfaces. In the following we neglect possible layer and lattice relaxations in the system; all formulations and calculations are based on a fcc Co(001) parent lattice.

ELECTRONIC STRUCTURE

The electronic structure of the system is described in terms of the following TB-LMTO Hamiltonian,

$$H_{\mathbf{R}L, \mathbf{R}'L'}^{\gamma, \sigma} = C_{\mathbf{R}L}^{\sigma} \delta_{\mathbf{R}, \mathbf{R}'} \delta_{L, L'} + (\Delta_{\mathbf{R}L}^{\sigma})^{1/2} \left\{ S^{\beta} \left(1 - (\gamma^{\sigma} - \beta) S^{\beta} \right)^{-1} \right\}_{\mathbf{R}L, \mathbf{R}'L'} (\Delta_{\mathbf{R}'L'}^{\sigma})^{1/2}, \quad (1)$$

where \mathbf{R} is the site index, σ is the spin index, and the potential parameters $C_{\mathbf{R}L}^{\sigma}$, $\Delta_{\mathbf{R}L}^{\sigma}$, and $\gamma_{\mathbf{R}L}^{\sigma}$ are diagonal matrices with respect to the angular momentum $L = (\ell m)$. The non-random screened structure constants matrix $S_{\mathbf{R}L, \mathbf{R}'L'}^{\beta}$, and the site-diagonal screening matrix $\beta_{\mathbf{R}, LL'} = \beta_L \delta_{L, L'}$ are spin-independent. Assuming one and the same two-dimensional translational symmetry in each atomic layer p , $\mathbf{k}_{||}$ -projections can be defined, where $\mathbf{k}_{||}$ is a vector from the corresponding surface Brillouin zone (SBZ). In a principal layer formalism [11], the screened structure constants $S_{p,q}^{\beta}$ are of block tridiagonal form. Neglecting layer relaxations they are given by

$$S_{p,p}^{\beta}(\mathbf{k}_{||}) = S_{0,0}^{\beta}(\mathbf{k}_{||}), \quad S_{p,q}^{\beta}(\mathbf{k}_{||}) = S_{0,1}^{\beta}(\mathbf{k}_{||}) \delta_{p+1,q} + S_{1,0}^{\beta}(\mathbf{k}_{||}) \delta_{p-1,q}. \quad (2)$$

The properties of individual atoms occupying lattice sites are characterized by potential function matrices,

$$P_{\mathbf{R}}^{\beta, \sigma}(z) = \frac{z - C_{\mathbf{R}}^{\sigma}}{\Delta_{\mathbf{R}}^{\sigma} + (\gamma_{\mathbf{R}}^{\sigma} - \beta)(z - C_{\mathbf{R}}^{\sigma})}, \quad (3)$$

which are diagonal with respect to L and are obtained by solving the corresponding Kohn-Sham equations. The potential functions assume the same value $P_p^{\beta, \sigma}(z)$ for each site within a given atomic layer p for

1×1 -supercells, and, in principle, n^2 different values $P_{p,i}^{\beta,\sigma}(z)$ for $n \times n$ -supercells. Finally, we define the infinite (screened) Green function matrix $g^{\beta,\sigma}(z)$ in the TB-LMTO method as

$$\left(g^{\beta,\sigma}(\mathbf{k}_{\parallel}, z)\right)_{p,q}^{-1} = P_p^{\beta,\sigma}(z) \delta_{p,q} - S_{p,q}^{\beta}(\mathbf{k}_{\parallel}). \quad (4)$$

Assuming that the ‘active’ part of the multilayer system consists of N layers and that the physical properties of all lead layers are identical, we can characterize these layers by so-called embedding potentials $\Gamma_p^{\beta,\sigma}$ [11], which for $p = 1$ and $p = N$ are given by

$$\begin{aligned} \Gamma_1^{\beta,\sigma}(\mathbf{k}_{\parallel}, z) &= S_{1,0}^{\beta}(\mathbf{k}_{\parallel}) \mathcal{G}_{\mathcal{L}}^{\beta,\sigma}(\mathbf{k}_{\parallel}, z) S_{0,1}^{\beta}(\mathbf{k}_{\parallel}), \\ \Gamma_N^{\beta,\sigma}(\mathbf{k}_{\parallel}, z) &= S_{0,1}^{\beta}(\mathbf{k}_{\parallel}) \mathcal{G}_{\mathcal{R}}^{\beta,\sigma}(\mathbf{k}_{\parallel}, z) S_{1,0}^{\beta}(\mathbf{k}_{\parallel}), \end{aligned} \quad (5)$$

and which are zero otherwise. The quantities $\mathcal{G}_{\mathcal{X}}^{\beta,\sigma}$, $\mathcal{X} = \mathcal{L}, \mathcal{R}$, are the corresponding SGFs of the ideal left and right leads.

The layer-diagonal blocks of the inverse of the Green function matrix can then be written as

$$\begin{aligned} \left(g^{\beta,\sigma}(\mathbf{k}_{\parallel}, z)\right)_{p,p}^{-1} &= P_1^{\beta}(z) - S_{0,0}^{\beta,\sigma}(\mathbf{k}_{\parallel}) - \Gamma_1^{\beta,\sigma}(\mathbf{k}_{\parallel}, z) \quad \text{for } p = 1, \\ \left(g^{\beta,\sigma}(\mathbf{k}_{\parallel}, z)\right)_{p,p}^{-1} &= P_p^{\beta}(z) - S_{0,0}^{\beta,\sigma}(\mathbf{k}_{\parallel}) \quad \text{for } 1 < p < N, \\ \left(g^{(0,\sigma)}(\mathbf{k}_{\parallel}, z)\right)_{p,p}^{-1} &= P_N^{\beta}(z) - S_{0,0}^{\beta,\sigma}(\mathbf{k}_{\parallel}) - \Gamma_N^{\beta,\sigma}(\mathbf{k}_{\parallel}, z) \quad \text{for } p = N, \end{aligned} \quad (6)$$

while its off-diagonal blocks are given by

$$\left(g^{\beta,\sigma}(\mathbf{k}_{\parallel}, z)\right)_{p,q}^{-1} = -S_{0,1}^{\beta}(\mathbf{k}_{\parallel}) \delta_{p+1,q} - S_{1,0}^{\beta}(\mathbf{k}_{\parallel}) \delta_{p-1,q}. \quad (7)$$

It should be noted that Eqs. (4–7) only apply in the case of an infinite parent lattice (no layer relaxations). In this way the originally infinite matrix can easily be reduced to a finite matrix with the embedding potentials acting as boundary conditions. The block-tridiagonal form in Eq. (7) of the inverse of the Green function allows to use efficient methods [11, 12] to determine any non-vanishing block of $g_{p,q}^{\beta,\sigma}(\mathbf{k}_{\parallel}, z)$. In particular, this applies to the blocks $g_{1,N}^{\beta,\sigma}(z)$, $g_{N,1}^{\beta,\sigma}(z)$, and/or $g_{N,N}^{\beta,\sigma}(z)$ which are needed for the evaluation of the GMC described in the next subsection. We refer the reader to a recent book [11] for further details concerning the TB-LMTO method for layered systems.

In the case of two-dimensional $n \times n$ (lateral) supercells the above expressions remain formally the same, however, each quantity is now

replaced by a supermatrix labelled by the positions of the sites within a given supercell. In the case of binary substitutional alloys the corresponding potential functions are assumed to have only two different values for the two constituents involved, i.e., we neglect possible local environment effects and short-range order within a given supercell. It should be noted that, in principle, for each chosen supercell all inequivalent potential functions have to be determined selfconsistently.

MAGNETOCONDUCTANCE

Our derivation of the conductance \mathcal{C}_M follows that given in [13]. Its details will be published elsewhere. In the following a subscript $M=F$ (AF) denotes the ferromagnetic (antiferromagnetic) configuration of the magnetizations in the magnetic slabs, respectively.

The resulting expression for the conductance per interface atom is given by

$$\mathcal{C}_M = \sum_{\sigma} \mathcal{C}_M^{\sigma}, \quad \mathcal{C}_M^{\sigma} = \frac{e^2}{h} \frac{1}{N_{\parallel}} \sum_{\mathbf{k}_{\parallel}} T_M^{\sigma}(\mathbf{k}_{\parallel}, E_F), \quad (8)$$

where N_{\parallel} is the number of \mathbf{k}_{\parallel} -points in the SBZ and E_F is the Fermi energy. Suppressing the subscript M the transmission coefficient $T^{\sigma}(\mathbf{k}_{\parallel}, E)$ can be expressed as

$$T^{\sigma}(\mathbf{k}_{\parallel}, E) = \lim_{|\delta| \rightarrow 0} \text{tr} \{ B_1^{\beta, \sigma}(\mathbf{k}_{\parallel}, E) g_{1,N}^{\beta, \sigma}(\mathbf{k}_{\parallel}, z_+) \\ \times B_N^{\beta, \sigma}(\mathbf{k}_{\parallel}, E) g_{N,1}^{\beta, \sigma}(\mathbf{k}_{\parallel}, z_-) \}, \quad (9)$$

where tr denotes the trace over angular momenta,

$$B_1^{\sigma}(\mathbf{k}_{\parallel}, E) = i \left(\Gamma_1^{\beta, \sigma}(\mathbf{k}_{\parallel}, z_+) - \Gamma_1^{\beta, \sigma}(\mathbf{k}_{\parallel}, z_-) \right), \\ B_N^{\sigma}(\mathbf{k}_{\parallel}, E) = i \left(\Gamma_N^{\beta, \sigma}(\mathbf{k}_{\parallel}, z_+) - \Gamma_N^{\beta, \sigma}(\mathbf{k}_{\parallel}, z_-) \right), \quad (10)$$

and $z_{\pm} = E \pm i\delta$. In this formulation we have assumed a collinear spin structure and that the spin σ is a good quantum number. This assumption is valid only for collinear spin structures if the spin-orbit interaction is neglected. The magnetoconductance ratio is then defined as

$$GMC = (\mathcal{C}_F^{\uparrow} + \mathcal{C}_F^{\downarrow}) / (\mathcal{C}_{AF}^{\uparrow} + \mathcal{C}_{AF}^{\downarrow}) - 1. \quad (11)$$

The reflection and transmission coefficients are related by

$$R^{\sigma}(\mathbf{k}_{\parallel}, E) = 1 - T^{\sigma}(\mathbf{k}_{\parallel}, E), \quad (12)$$

and can be expressed as (I is the unit matrix)

$$R^\sigma(\mathbf{k}_\parallel, E) = \lim_{|\delta| \rightarrow 0} \text{tr} \left\{ \left[B_N^\sigma(\mathbf{k}_\parallel, E) g_{N,N}^{\beta,\sigma}(\mathbf{k}_\parallel, z_+) + i I \right] \right. \\ \left. \times \left[B_N^\sigma(\mathbf{k}_\parallel, E) g_{N,N}^{\beta,\sigma}(\mathbf{k}_\parallel, z_-) - i I \right] \right\}, \quad (13)$$

such that the magnetoconductance can be evaluated using the layer-diagonal blocks of the Green function matrix $g^{\beta,\sigma}(z)$ rather than the layer off-diagonal blocks as in the case of the transmission coefficient [13].

There exists, however, a direct way of expressing the transmission coefficient $T^\sigma(\mathbf{k}_\parallel, E)$ in terms of the layer-diagonal blocks of the system Green function $g^{\beta,\sigma}(z)$, namely,

$$T^\sigma(\mathbf{k}_\parallel, E) = \lim_{|\delta| \rightarrow 0} \text{tr} \left\{ \tilde{B}_N^\sigma(\mathbf{k}_\parallel, E) g_{N,N}^{\beta,\sigma}(\mathbf{k}_\parallel, z_+) \right. \\ \left. \times B_N^\sigma(\mathbf{k}_\parallel, E) g_{N,N}^{\beta,\sigma}(\mathbf{k}_\parallel, z_-) \right\}, \quad (14)$$

where B_N^σ is defined in Eq. (10), and \tilde{B}_N^σ is given by

$$\tilde{B}_N^\sigma(\mathbf{k}_\parallel, E) = i \left(\tilde{\Gamma}_N^{\beta,\sigma}(\mathbf{k}_\parallel, z_+) - \tilde{\Gamma}_N^{\beta,\sigma}(\mathbf{k}_\parallel, z_-) \right), \quad (15)$$

where $\tilde{\Gamma}_N^{\beta,\sigma}$ is the embedding potential of the semi-infinite 'fragment' to the left of the last layer in the trilayer system.

The generalization of the formalism to the supercell case proceeds similarly to the previous section: the corresponding matrices are substituted by supermatrices labelled by individual atoms within a supercell and the \mathbf{k}_\parallel -integration is confined to the (n^2 -times smaller) SBZ corresponding to the supercell. However, the computational effort within the present SGF technique can significantly be reduced by using the fact that the SGFs are independent of the choice of a supercell, since the atomic position vectors within a given supercell are nothing but lattice vectors of the two-dimensional lattice that corresponds to the parent lattice (1×1 -supercell) of the leads. One can express the supercell (sc) SGF therefore in terms of the SGF of the original lattice as follows

$$\mathcal{G}_{K,K'}^{sc}(\mathbf{q}_\parallel, z) = \sum_{\mathcal{R}_K} e^{-i \mathbf{q}_\parallel (\mathcal{R}_K - \mathcal{R}_{K'})} \mathcal{G}_{\mathcal{R}_K, \mathcal{R}_{K'}}^{sc}(z), \\ \mathcal{G}_{\mathcal{R}_K, \mathcal{R}_{K'}}^{sc}(z) = \frac{1}{N_\parallel} \sum_{\mathbf{k}_\parallel}^{\text{SBZ}} e^{i \mathbf{k}_\parallel (\mathcal{R}_K - \mathcal{R}_{K'})} \mathcal{G}(\mathbf{k}_\parallel, z), \quad (16)$$

where \mathbf{k}_\parallel and \mathbf{q}_\parallel denote vectors in the SBZ of the original lattice and in the supercell SBZ, respectively, and the \mathcal{R}_K refer to atomic positions within the supercell.

The computational scheme described above can be used also for supercell studies based on a single-band TB model. Assuming a nearest-neighbor hopping parameter t and identical left and right leads, we obtain [17]

$$T^\sigma(\mathbf{k}_\parallel, E) = t^2 |A^\sigma(\mathbf{k}_\parallel, E) g_{1,N}^\sigma(\mathbf{k}_\parallel, z_+)|^2, \quad (17)$$

where

$$A^\sigma(\mathbf{k}_\parallel, E) = -\frac{1}{\pi} \text{Im } \mathcal{G}^\sigma(\mathbf{k}_\parallel, E + i\delta) \quad (18)$$

are the Bloch spectral functions of the corresponding SGF $\mathcal{G}^\sigma(\mathbf{k}_\parallel, z)$ for the leads.

RESULTS AND DISCUSSION

We have performed calculations for the following formal multilayer system:

$$\begin{array}{c} \text{Cu(001)} \\ \text{semi-infinite} \\ \text{lead} \end{array} \parallel \begin{array}{c} \text{M}_m \\ \text{magnetic} \\ \text{slab} \end{array} \left| \begin{array}{c} \text{S}_s \\ \text{spacer} \end{array} \right| \begin{array}{c} \text{M}_m \\ \text{magnetic} \\ \text{slab} \end{array} \parallel \begin{array}{c} \text{Cu(001)} \\ \text{semi-infinite} \\ \text{lead} \end{array} \quad (19)$$

where $N = 2m + s$. For $\text{Co}_m/\text{Cu}_s/\text{Co}_m$ trilayers we have studied: (i) the dependence of the GMC on the thickness of magnetic slabs m and (ii) the oscillatory behavior of the GMC as a function of the spacer thickness s . Furthermore, we have studied (iii) the oscillatory behavior of the GMC as a function of the spacer thickness for a (CuPd) superstructure spacer, namely, $\text{Co}_m/(\text{CuPd})_r/\text{Co}_m$ trilayers, where r is the number of repetitions. If s is an even number then the superstructure is terminated by a Pd layer, if s is odd the terminating layer is formed by Cu atoms. The combined effect of intrinsic and extrinsic defects will be demonstrated for Co/Cu/Co-based trilayers on the following cases: (i) interdiffused interfaces; (ii) a random spacer sandwiched by ideal magnetic slabs; (iii) an ideal Cu spacer sandwiched by disordered magnetic slabs; and (iv) a case with combined disorders of types (ii) and (iii).

NUMERICAL IMPLEMENTATION

Random substitutional alloys A_{1-x}B_x are simulated by random supercells with the same average composition. Random configurations were generated using the RM48 random number generator [19] and the binary correlation function was evaluated to test the 'randomness' of each configuration. For the single-band TB model we have tested $n \times n$ random supercells ($n=5, 7, 10$) corresponding roughly to a $\text{A}_{85}\text{B}_{15}$ random substitutional alloy, namely, 21 A atoms and 4 B atoms for the 5×5 -supercell and 41 A atoms and 8 B atoms for the 7×7 -supercell randomly

distributed over the sites within the supercell. In the case of the TB-LMTO model we have tested only 5×5 - and 7×7 -supercells. In all cases (typically an average over 5 configurations for a 5×5 -supercell and an average over 3 configurations for a 7×7 -supercell were calculated) the results for the partial currents agreed within 1–3%, the agreement being better for larger supercells. The same random supercells were used for both the single-band model and the TB-LMTO studies.

In principle, one should use selfconsistent potential parameters corresponding to a given random supercell, however, such an approach is numerically prohibitive for 5×5 - or 7×7 -supercells. For the case of a 2×2 -supercell and $A_{75}B_{25}$ alloys we found that the fluctuations of the calculated potential parameters for A and B atoms for different random configurations from those obtained selfconsistently using the CPA are quite small (of the order of a few per cent). We have thus used the selfconsistent CPA potential parameters determined for a given alloy composition [11] also in the present supercell calculations. It should be noted that the same parameters were employed for various random configurations as well as for different supercell sizes. We have thus neglected all possible fluctuations of the potential parameters due to a variation of the local environment and assumed that the potential parameters take only two values the same for any A and B atom within a supercell. The potential parameters used are those of the corresponding A/B interface (ideal or random) where A(B) corresponds to atoms forming magnetic (spacer) layers. We have also neglected the layer dependence of the potential parameters and chosen their bulk-like values.

The k_{\parallel} -integration covers 10000 points in the full fcc(001)-SBZ (400 (196) points in the corresponding 5×5 - (7×7)-supercell SBZ). In some cases, in particular in the ballistic regime a much higher number of k_{\parallel} -points was used to obtain well converged results. In all cases we have employed $|Imz_{\pm}| = 10^{-7}$ Ry. It should be noted that for a 1×1 -supercell one can integrate over the irreducible part of the SBZ while for the random supercell the k_{\parallel} -integration is confined to the full supercell SBZ (or, more precisely, over a half of the supercell SBZ due to time-reversal symmetry).

BALLISTIC TRANSPORT

We shall start our discussion by a remark concerning some general features of the electronic structure of Cu bands and of Co spin-up (\uparrow) and Co spin-down (\downarrow) bands at the Fermi energy of Cu leads. It should be noted that by 'bands' we mean the bands of the three-dimensional periodic bulk systems fcc Cu and fcc Co (at the Fermi energy of Cu).

The Cu- and Co \uparrow -bands are very similar representing only a very weak intrinsic scattering potential at the Cu/Co interface. Consequently, the transmission of \uparrow -electrons for a ferromagnetic alignment of the magnetizations (and hence also their conductance as given by Eq. (8)) through the Co/Cu interfaces is large. On the contrary, the large difference between the Cu- and Co \downarrow -bands acts as an effective potential barrier at the interface for \downarrow -electrons and, hence, gives rise to much smaller F \downarrow - and AF-conductances. It should be also noted that in this paper we will study only symmetrical trilayers, i.e., the case of identical left and right magnetic slabs for which spin-up and spin-down conductances for the AF alignments coincide.

The dependence of the GMC of ideal Co $_m$ /Cu $_5$ /Co $_m$ trilayers on the thickness of the magnetic slabs m is presented in Fig. 1. The most remarkable feature is a strong suppression of the GMC (Fig. 1a) for small thicknesses of the magnetic slabs and a saturation of about 100% at large thicknesses. This result can be understood by plotting partial conductances, namely the F \uparrow - and F \downarrow -conductances for the ferromagnetic alignment of the magnetizations in the left and the right magnetic slabs and that for the antiferromagnetic alignment (AF-conductances). The suppression of the GMC is quite likely due to an effective potential barrier in the $d\downarrow$ -channel because of the above mentioned large difference between the Cu- and Co \downarrow -bands. Hence, a narrower magnetic slab allows for a larger transmission of electrons, in particular for the F \downarrow -conductance and both AF-conductances. As a result, the total AF-conductance increases faster than the total F-conductance and hence the GMC ratio drops (see also [16]). The oscillatory behavior of the conductances can be related to the oscillatory behavior of the F \downarrow -conductances of a single Co slab of varying thickness embedded into the Cu host (Fig. 1b, empty symbols). Quite clearly such oscillations can be ascribed to multiple scattering effects of \downarrow -electrons at the interfaces. The GMC of finite Co slabs never reaches the limit of semi-infinite Co slabs because of different ballistic conductances of Cu leads for the case of finite Co slabs and those of Co leads in the case of semi-infinite Co leads.

The effect of quantum current oscillations was first studied by Mathon [14] using an empirical multiband TB-model within a Kubo-Landauer type approach by considering the dependence of the GMC on the thickness of the spacer. In Fig. 2 we present such calculations for Co $_5$ /Cu $_s$ /Co $_5$ trilayers with varying thickness of the spacer s . We clearly observe pronounced GMC oscillations (Fig. 2a) around a value of about 115% which are damped with increasing spacer thickness. It should be noted that in order to obtain converged results for the present case it is necessary to use a much finer sampling of the irreducible SBZ than mentioned above, namely 30000 k_{\parallel} -points in the irreducible SBZ. A clearer picture is obtained by looking at the partial conductances, Fig. 2b. The

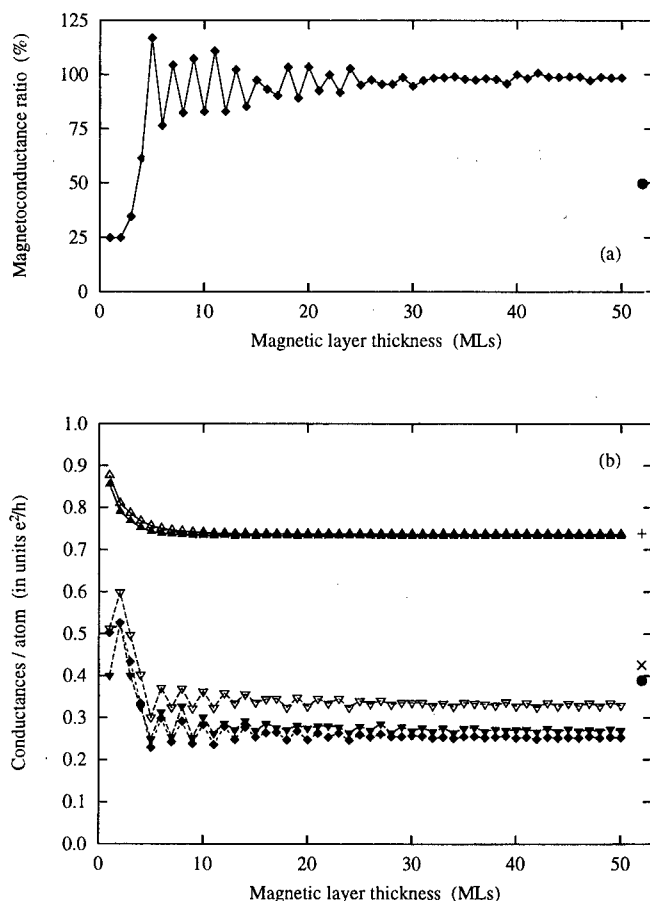


Figure 1 Ideal $\text{Co}_m/\text{Cu}_5/\text{Co}_m$ trilayers sandwiched by semi-infinite Cu leads as a function of the thickness of the magnetic slabs m : (a) magnetoconductance ratio (diamonds) and the limit of semi-infinite Co slabs (heavy dot); (b) conductances per atom for the ferromagnetic \uparrow -spin (up-triangles), ferromagnetic \downarrow -spin (down-triangles), and antiferromagnetic configuration (diamonds). Empty symbols (up- and down-triangles) refer to the ferromagnetic \uparrow - and \downarrow -spin conductances of a single Co slab of varying thickness embedded into a Cu host. For semi-infinite Co slabs the ferromagnetic \uparrow - (+), \downarrow - (\times), and antiferromagnetic (heavy dot) conductances are shown, respectively.

oscillatory behavior originates mostly from the $\text{F}\downarrow$ -conductances whose amplitudes are much larger than those of the AF-conductances while the $\text{F}\uparrow$ -conductances are essentially thickness independent. We observe oscillations with a period of about 5–6 MLs in both the $\text{F}\downarrow$ - and AF-conductances while some admixture of short-period oscillations with a period of about 2.5 MLs is seen in the $\text{F}\downarrow$ -conductances. We note that these values correlate reasonably well with similar values obtained for the interlayer exchange coupling using the same electronic structure model

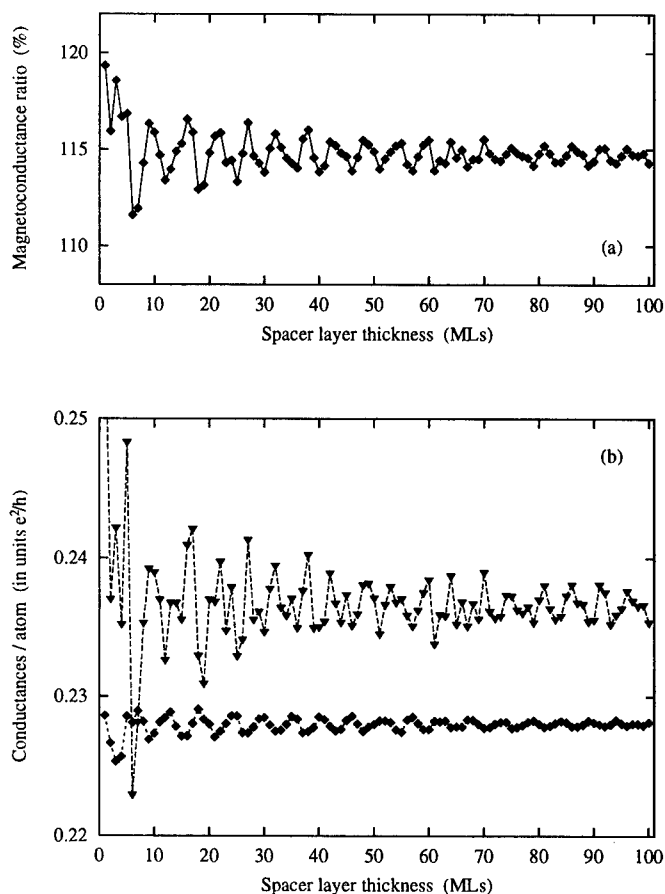


Figure 2 Ideal $\text{Co}_5/\text{Cu}_s/\text{Co}_5$ trilayers sandwiched by semi-infinite Cu leads as a function of the spacer thickness s : (a) magnetoconductance ratio (diamonds); (b) conductances per atom for the ferromagnetic \downarrow -spin (down-triangles) and antiferromagnetic configuration (diamonds). Note the reduced scale of y-axis.

(see, e.g., [21]). The amplitudes are roughly damped as s^{-1} , where s is the spacer thickness [14].

The oscillations of the GMC with respect to the spacer thickness s may also have an extrinsic origin rather than the intrinsic origin described above. In Fig. 3 we plot the dependence of the GMC as a function of the thickness of (CuPd) bilayers again sandwiched by Co slabs each 5 MLs thick. We have thus a superstructure in the spacer. The characteristic zig-zag shape of the GMC (Fig. 3a) is due to alternating Cu and Pd layers. By using this superstructure spacer we have combined magnetic (Co/Cu, for even numbers of spacer layers also Co/Pd) and non-magnetic (Cu/Pd) scattering at interfaces. The higher (smaller) values of the GMC correspond to the case of odd (even) numbers of spacer layers. The oscillations are clearly related to oscillations in the $F\uparrow$ - and $F\downarrow$ -conductances (Fig. 3b) which oscillate in phase giving rise

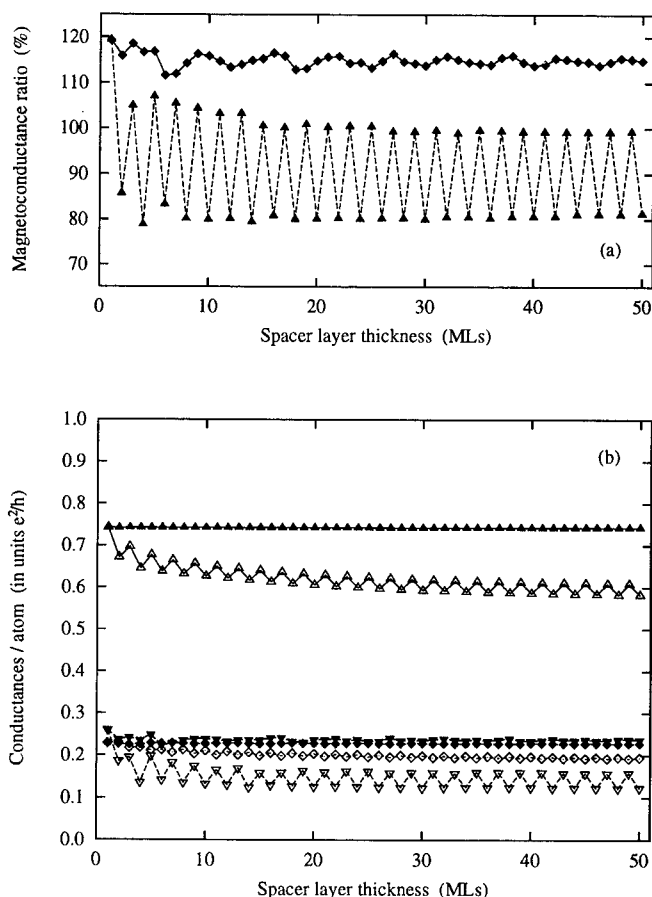


Figure 3 $\text{Co}_5/(\text{CuPd})_r/\text{Co}_5$ and ideal $\text{Co}_5/\text{Cu}_s/\text{Co}_5$ trilayers sandwiched by semi-infinite Cu leads as a function of the spacer thicknesses s ($r = s/2$): (a) magnetoconductance ratio (diamonds, Cu spacer; triangles, (CuPd) spacer); (b) conductances per atom for the ferromagnetic \uparrow -spin (up-triangles), ferromagnetic \downarrow -spin (down-triangles), and antiferromagnetic configuration (diamonds). Full symbols refer to a Cu spacer, empty symbols to a (CuPd) spacer.

to an enhancement of oscillation amplitudes. It should be noted that as compared to the ideal trilayer the $F\uparrow$ - and $F\downarrow$ -conductances are reduced by the same amount. This fact indicates that the oscillations are now due to (dominating) non-magnetic scattering at the Cu/Pd interfaces rather than due to magnetic scattering at the Cu/Co interfaces as before (see Fig. 2b). The drop of the F- and AF-conductances can be understood in analogy to the interpretation given for Fig. 1b: the reason is a formation of an additional potential barrier in the d -channel due to a mismatch of Cu- and Pd-bands at the Fermi energy.

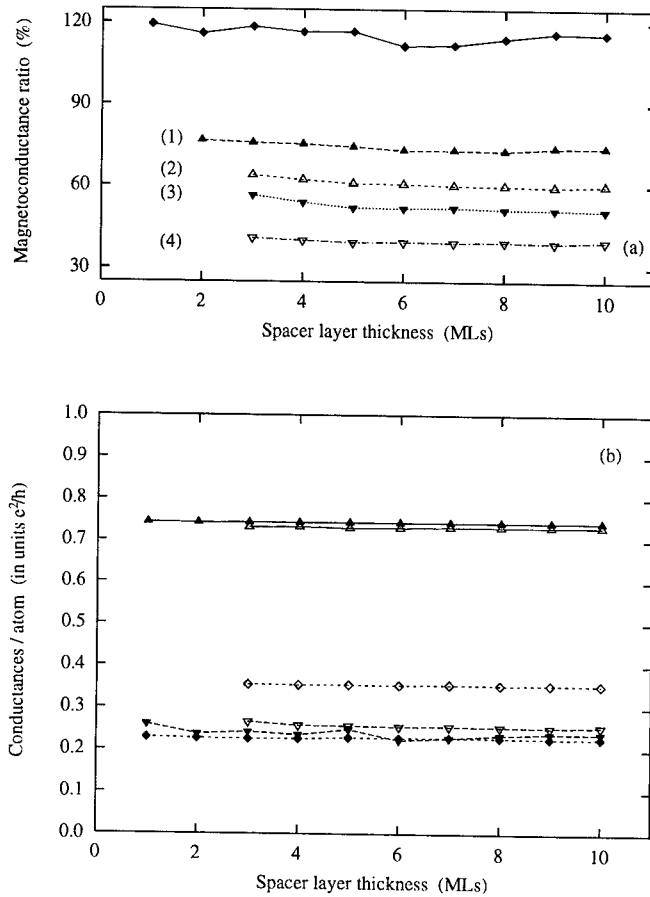


Figure 4 Trilayers with 15%-interdiffused interfaces and ideal $\text{Co}_5/\text{Cu}_s/\text{Co}_5$ trilayers sandwiched by semi-infinite Cu leads as a function of the spacer thickness s : (a) magnetoconductance ratio (diamonds, ideal trilayer; up-triangles-(1), one of the inner interfaces is interdiffused; empty up-triangles-(2), both inner interfaces are interdiffused; down-triangles-(3), two inner and one of outer interfaces are interdiffused; empty down-triangles-(4), all four interfaces are interdiffused); (b) conductances per atom for the ferromagnetic \uparrow -spin (up-triangles), ferromagnetic \downarrow -spin (down-triangles), and antiferromagnetic configuration (diamonds). Full symbols refer to an ideal trilayer, empty symbols to a trilayer with all interfaces interdiffused.

COMBINED BALLISTIC AND DIFFUSIVE TRANSPORT

In general, in addition to scattering at intrinsic defects (system interfaces) there is scattering at extrinsic defects, namely at impurities, stacking faults, dislocations, and there are even dynamical effects like scattering of electrons with phonons or magnons. Here we assume substitutional impurities in the spacer, magnetic slabs, and at their interfaces in a reference system which consists of the left and right semi-infinite Cu leads sandwiching two Co slabs, each 5 MLs thick, and separated by a Cu spacer of varying thickness (1-10 MLs).

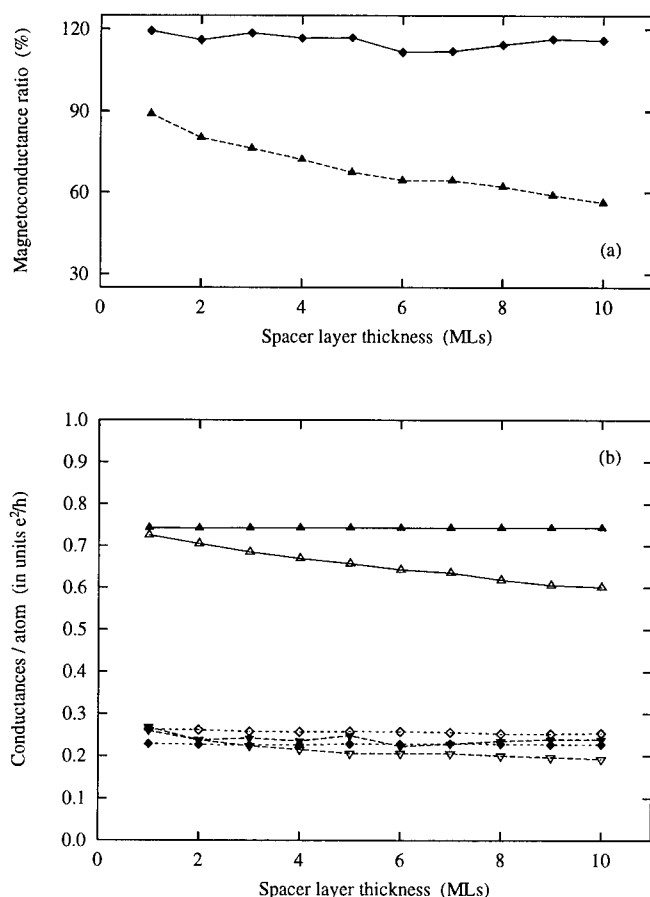


Figure 5 $\text{Co}_5/(\text{Cu}_{85}\text{Ni}_{15})_s/\text{Co}_5$ trilayers with alloyed spacer and ideal $\text{Co}_5/\text{Cu}_s/\text{Co}_5$ trilayers sandwiched by semi-infinite Cu leads as a function of the spacer thickness s : (a) magnetoconductance ratio (diamonds, ideal trilayer; triangles, alloyed spacer); (b) conductances per atom for the ferromagnetic \uparrow -spin (up-triangles), ferromagnetic \downarrow -spin (down-triangles), and antiferromagnetic configuration (diamonds). Full symbols refer to an ideal trilayer, empty symbols to a trilayer with alloyed spacer.

The effect of disorder at the Co/Cu interfaces is shown in Fig. 4. The interdiffused interface consists of two disordered interface layers with compositions $\text{Co}_{85}\text{Cu}_{15}$ (the Co side) and $\text{Co}_{15}\text{Cu}_{85}$ (the Cu side). The GMC decreases monotonically with the number of disordered interfaces, and disorder suppresses the oscillations present for an ideal interface. Disorder influences the $F\uparrow$ -conductances very weakly because of the similarity of the Cu- and the $\text{Co}\uparrow$ -bands. The AF-conductances, however, are much larger as compared to an ideal trilayer and their increase results in a decrease of the GMC. This behavior seems to contradict a common (but incorrect) belief that disorder always reduces the conductance. In fact, the effect of disorder is fourfold: (i) it increases the overall amount of scattering which contributes to the reduction of the transmis-

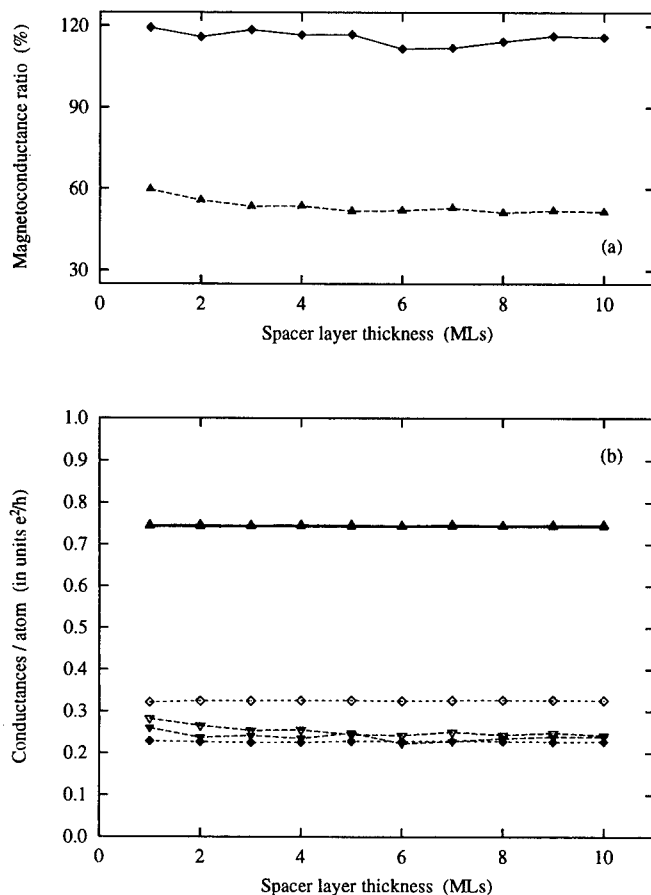


Figure 6 $(\text{Co}_{85}\text{Ni}_{15})_5/\text{Cu}_s/(\text{Co}_{85}\text{Ni}_{15})_5$ trilayers with alloyed magnetic slabs and ideal $\text{Co}_5/\text{Cu}_s/\text{Co}_5$ trilayers sandwiched by semi-infinite Cu leads as a function of the spacer thickness s : (a) magnetoconductance ratio (diamonds, ideal trilayer; triangles, alloyed magnetic slabs); (b) conductances per atom for the ferromagnetic \uparrow -spin (up-triangles), ferromagnetic \downarrow -spin (down-triangles), and antiferromagnetic configuration (diamonds). Full symbols refer to an ideal trilayer, empty symbols to a trilayer with alloyed magnetic layers.

sion probability and, hence, the conductance; (ii) the relaxation of a strict conservation of \mathbf{k}_{\parallel} in disordered systems opens up new transmission channels which contribute to an increase of the conductance; (iii) interdiffusion smoothes the abrupt potential barrier of the ideal trilayer which in turn also leads to an increased transmission coefficient; and (iv) the alloying in magnetic layers can increase (decrease) the effective barrier for \uparrow - and/or \downarrow -electrons at the Co/Cu interface and thus decrease (increase) the conductance in this channel. Therefore, the net influence of disorder on the conductance results from a competition between these effects and may lead to an increase or decrease of the conductance, depending on the system under consideration (see also [20]).

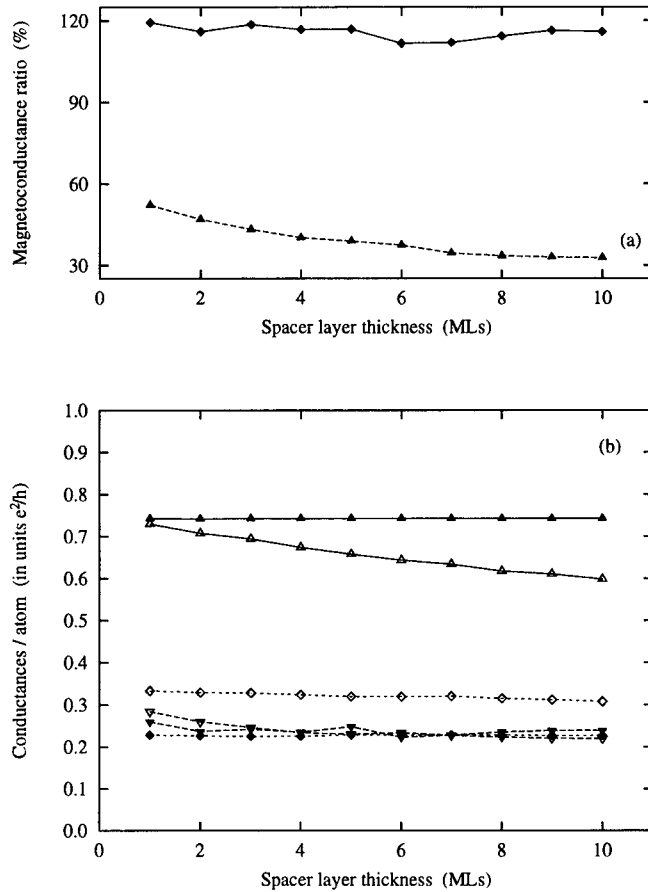


Figure 7 $(\text{Co}_{85}\text{Ni}_{15})_5/(\text{Cu}_{85}\text{Ni}_{15})_s/(\text{Co}_{85}\text{Ni}_{15})_5$ trilayers with combined alloying in both the spacer and magnetic slabs and ideal $\text{Co}_5/\text{Cu}_s/\text{Co}_5$ trilayers sandwiched by semi-infinite Cu leads as a function of the spacer thickness s : (a) magnetoconductance ratio (diamonds, ideal layer; triangles, alloyed magnetic slabs and spacer); (b) conductances per atom for the ferromagnetic \uparrow -spin (up-triangles), ferromagnetic \downarrow -spin (down-triangles), and antiferromagnetic configuration (diamonds). Full symbols refer to an ideal trilayer, empty symbols to an alloyed trilayer.

The effect of alloying in the non-magnetic spacer ($\text{Cu}_{85}\text{Ni}_{15}$) on the magnetoconductance is presented in Fig. 5. We observe a monotonic decrease of the GMC ratio as a function of the spacer thickness (Fig. 5a). The origin of this decrease can be traced from Fig. 5b. Disorder in CuNi alloys strongly depends on the concentration but for the Cu-rich alloys the states at the Fermi energy are influenced only weakly by disorder [22]. Therefore, the $F\downarrow$ - and AF-conductances are only slightly smaller than those of an ideal trilayer. Consequently, the effect of extrinsic potential scattering for the $F\downarrow$ - and AF-conductances is rather small as compared to the strong intrinsic scattering at the interfaces. On the other hand, the effect of extrinsic defects dominates the $F\uparrow$ -conductances where intrinsic scattering is negligibly small. In fact it is the $F\uparrow$ -channel

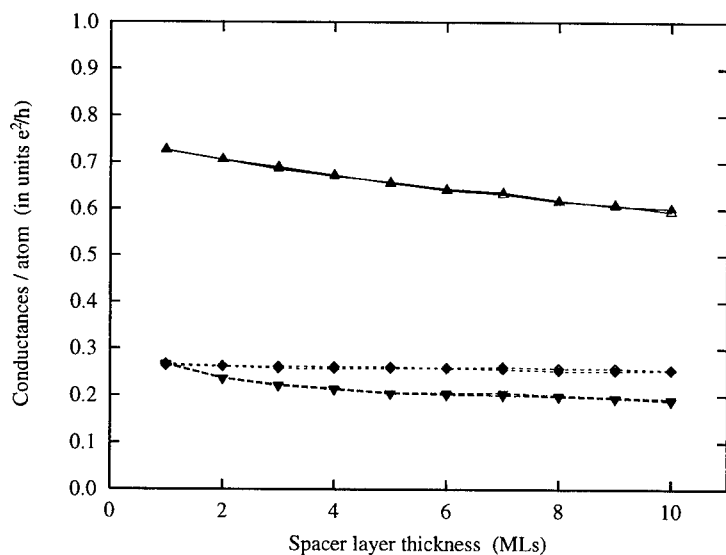


Figure 8 $\text{Co}_5/(\text{Cu}_{85}\text{Ni}_{15})_s/\text{Co}_5$ trilayers with alloyed spacer sandwiched by semi-infinite Cu leads as a function of the spacer thickness s : conductances per atom for the ferromagnetic \uparrow -spin (up-triangles), ferromagnetic \downarrow -spin (down-triangles), and antiferromagnetic configuration (diamonds). Full symbols refer to 5×5 -supercell calculations, empty symbols to 7×7 -supercell calculations.

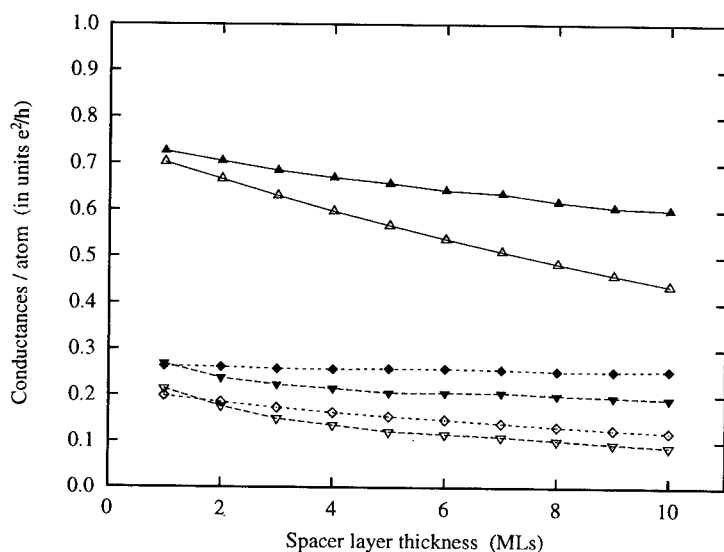


Figure 9 $\text{Co}_5/(\text{Cu}_{85}\text{Ni}_{15})_s/\text{Co}_5$ trilayers with alloyed spacer sandwiched by semi-infinite Cu leads as a function of the spacer thickness s : conductances per atom for the ferromagnetic \uparrow -spin (up-triangles), ferromagnetic \downarrow -spin (down-triangles), and antiferromagnetic configuration (diamonds). Full symbols refer to 5×5 -supercell calculations, empty symbols to CPA calculations neglecting vertex corrections.

which is mostly responsible for the decrease of the GMC ratio with increasing spacer thickness.

The effect of alloying in the magnetic slabs ($\text{Co}_{85}\text{Ni}_{15}$) on the magnetoconductance is presented in Fig. 6. Contrary to the case of disorder in the spacer the GMC ratio quickly saturates to approximately half of the value for an ideal trilayer. The behavior of the partial conductances is similar to that for an interdiffused interface. The $F\uparrow$ -conductances are nearly the same as for the ideal trilayer due to the similarity of the $\text{Co}\uparrow$ - and the $\text{Ni}\uparrow$ -bands at the Fermi energy. Since the $\text{Co}\downarrow$ -bands are higher in energy as compared to the $\text{Ni}\downarrow$ -bands, alloying of Co with Ni decreases effectively the potential barrier height resulting thus into a larger transmission coefficient (conductance) as compared to the ideal trilayer. Consequently, the AF-conductances of the alloyed magnetic layers are larger than those of an ideal trilayer. The effect is the same for the $F\downarrow$ -conductances but much weaker, indicating dominating intrinsic scattering at interfaces for this channel.

The results of the study of combined disorder in both the spacer ($\text{Cu}_{85}\text{Ni}_{15}$) and the magnetic layers ($\text{Co}_{85}\text{Ni}_{15}$) are presented in Fig. 7. They are qualitatively similar to those for a random spacer but the GMC already starts at a value of about 60%, the value of disordered magnetic layers separated by an ideal Cu spacer (see Fig. 6). The decrease of the GMC is due to a corresponding decrease of the $F\uparrow$ -conductances resulting from alloying in the spacer.

Fig. 8 illustrates (for the case of partial conductances) the robustness of supercell calculations with respect to the supercell size and the configurational average (5×5 -supercell averaged over five configurations versus 7×7 -supercell averaged over three configurations). Illustrated here is the case of alloying in the spacer (in other cases the agreement is equally good). The good agreement between both calculations (number of atoms for the larger supercell increases two times) is obvious.

Finally, in Fig. 9, for the trilayer $\text{Co}_5/(\text{Cu}_{85}\text{Ni}_{15})_s/\text{Co}_5$ we compare the results of the supercell calculations with CPA-type transport calculations neglecting vertex corrections. In this limit we can still use the expression given by Eq. (8) but now specified to the 1×1 -supercell case and with $g_{1,N}^{\beta,\sigma}(z)$ and $g_{N,1}^{\beta,\sigma}(z)$ substituted by $\langle g_{1,N}^{\beta,\sigma}(z) \rangle$ and $\langle g_{N,1}^{\beta,\sigma}(z) \rangle$, where $\langle \dots \rangle$ denotes the CPA configurational averaging. The essence of the approximation thus consists in an independent configurational average of two Green functions keeping in mind that quantities $B_1^{\sigma}(E)$ and $B_N^{\sigma}(E)$ are related to non-random leads. The results now also depend on the choice of layers 1 and N between which we determine the conductance, i.e., the results neglecting vertex corrections which are based on Eqs. (8) and (13) are no longer identical. The CPA results are qualitatively similar to those obtained from the supercell calculations although

the CPA conductances are somewhat smaller, indicating perhaps that using a CPA-type approach vertex corrections ought to be included for CPP transport.

CONCLUSIONS AND OUTLOOK

We have presented an *ab initio* formulation of CPP transport in magnetic trilayers (spin valves). The approach is formulated within the framework of the TB-LMTO method and surface Green functions and can easily be generalized to lateral supercells, in particular since the lead supercell surface Green functions can be obtained from the surface Green function of the original two-dimensional lattice by means of a lattice Fourier transformation.

We have considered a number of interesting geometrical arrangements for both the ballistic and diffusive transport and discussed the results of the numerical calculations in terms of partial conductances of the \uparrow - and \downarrow -channels in the F and AF alignments. Although all calculations were done for the reference Co/Cu/Co(001) trilayer the present results have a broader validity because in quite a few binary magnetic systems the scattering in one spin channel can be significantly larger than in the other channel. We also discussed the effect of quantum oscillations of the magnetocurrent. Extensive numerical tests seem to indicate that already 5×5 -supercells containing 25 atoms averaged over a limited number of random configurations (typically a configurational average over 5 different configurations was employed) give representative results for the CPP magnetoconductance. The present approach can also be generalized to the case of transport across a barrier (semiconductor or transition-metal oxide spacer or vacuum) as well as to the case of superconductor-metal interfaces.

Acknowledgments

Financial support for this work was provided by the Grant Agency of the Czech Republic (Project No. 202/97/0598), the Grant Agency of the Academy of Sciences of the Czech Republic (Project A1010829), the Center for Computational Materials Science in Vienna (GZ 45.442 and GZ 45.420), the Austrian Science Foundation (FWF P11626-PHY), the MŠMT of the Czech Republic (COST P3.70), the Austrian BMWV and the MŠMT of the Czech Republic (AKTION WTZ I.23), and the TMR Network 'Interface Magnetism' of the European Commission (Contract No. EMRX-CT96-0089).

REFERENCES

- [1] M.N. Baibich, J.M. Broto, A. Fert, F. Nguyen Van Dau, F. Petroff, P. Etienne, G. Creuzet, A. Friedrich, and J. Chazelas, *Giant Magnetoresistance of (001)Fe/(001)Cr Magnetic Superlattices* Phys. Rev. Lett. **61**, 2472 (1988); G. Binasch, P. Grünberg, F. Saurenbach, and W. Zinn, *Enhanced Magnetoresistance in Layered Magnetic-Structures With Antiferromagnetic Interlayer Exchange* Phys. Rev. B **39**, 4828 (1989).

- [2] W.P. Pratt Jr., S.-F. Lee, J.M. Slaughter, R. Loloee, P.A. Schroeder, and J. Bass, *Perpendicular Giant Magnetoresistances of Ag/Co Multilayers* Phys. Rev. Lett. **66**, 3060 (1991).
- [3] P.M. Levy, Solid State Phys. **47**, 367 (1994).
- [4] K.M. Schep, P.J. Kelly, and G.E.W. Bauer, *Ballistic transport and electronic structure* Phys. Rev. B **57**, 8907 (1998).
- [5] M.A.M. Gijs and G.E.W. Bauer, *Perpendicular giant magnetoresistance of magnetic multilayers* Adv. Phys. **46**, 285 (1997).
- [6] P. Zahn, I. Mertig, M. Richter, and H. Eschrig, *Ab-Initio Calculations of the Giant Magnetoresistance* Phys. Rev. Lett. **75**, 3216 (1995).
- [7] D.R. Penn and M.D. Stiles, *Solution of the Boltzmann equation without the relaxation-time approximation* Phys. Rev. B **59**, 13338 (1999).
- [8] W.H. Butler, X.-G. Zhang, D.M.C. Nicholson, and J.M. Mac Laren, *First-Principles Calculations of Electrical-Conductivity and Giant Magnetoresistance of Co-Vertical-Bar-Cu-Vertical-Bar-Co Spin Valves* Phys. Rev. B **52**, 13399 (1995).
- [9] P. Weinberger, P.M. Levy, J. Banhart, L. Szunyogh, and B. Újfalussy, *'Band structure' and electrical conductivity of disordered layered systems* J. Phys.: Condens. Matter **8**, 7677 (1996); C. Blaas, P. Weinberger, L. Szunyogh, P.M. Levy, and C.B. Sommers, *Ab initio calculations of magnetotransport for magnetic multilayers* Phys. Rev. B **60**, 492 (1999).
- [10] S. Datta, *Electronic Transport in Mesoscopic Systems* (Cambridge University Press, Cambridge, 1995).
- [11] I. Turek, V. Drchal, J. Kudrnovský, M. Šob, and P. Weinberger, *Electronic Structure of Disordered Alloys, Surfaces and Interfaces* (Kluwer, Boston-London-Dordrecht, 1997).
- [12] V. Drchal, J. Kudrnovský, and I. Turek, *Ab-initio calculations of the electronic and atomic structure of solids and their surfaces* Comput. Phys. Commun. **97**, 111 (1996).
- [13] J.A. Stovneng and P. Lipavský, *Multiband Tight-Binding Approach to Tunneling in Semiconductor Heterostructures - Application to Gamma-X Transfer in GaAs* Phys. Rev. B **49**, 16494 (1994).
- [14] J. Mathon, A. Umerski, and M. Villeret, *Oscillations with Co and Cu thickness of the current- perpendicular-to-plane giant magnetoresistance of a Co/Cu/Co(001) trilayer* Phys. Rev. B **55**, 14378 (1997).
- [15] J. Cerdá, M.A. Van Hove, P. Sautet, and M. Salmeron, *Efficient method for the simulation of STM images. I. Generalized Green-function formalism* Phys. Rev. B **56**, 15885 (1997).
- [16] S. Sanvito, C.J. Lambert, J.H. Jefferson, and A.M. Bratkovsky, *General Green's-function formalism for transport calculations with spd Hamiltonians and giant magnetoresistance in Co- and Ni-based magnetic multilayers* Phys. Rev. B **59**, 11936 (1999).
- [17] P. Bruno, H. Itoh, J. Inoue, and S. Nonoyama, *Influence of disorder on the perpendicular magnetoresistance of magnetic multilayers* J. Mag. Mag. Mat. **198-199**, 46 (1999).
- [18] E.Yu. Tsymbal and D.G. Pettifor, *Spin-polarized electron tunneling across a disordered insulator* Phys. Rev. B **58**, 432 (1998).

-
- [19] F. James, *A Review of Pseudorandom Number Generators* Comput. Phys. Commun. **60**, 329 (1990).
 - [20] S. Zhang and P. Levy, *Interplay of the specular and diffuse scattering at interfaces of magnetic multilayers* Phys. Rev. B **57**, 5336 (1998).
 - [21] V. Drchal, J. Kudrnovský, I. Turek, and P. Weinberger, *Interlayer magnetic coupling: The torque method* Phys. Rev. B **53**, 15036 (1996).
 - [22] B.L. Gyorffy and G.M. Stocks, in *Electrons in Disordered Metals and at Metallic Surfaces*, eds. P. Phariseau, B.L. Gyorffy, and L. Scheire (NATO ASI Series, Plenum Press, New York, 1979).

THE FERM SURFACES OF METALLIC ALLOYS AND THE OSCILLATORY MAGNETIC COUPLING BETWEEN MAGNETIC LAYERS SEPARATED BY SUCH ALLOY SPACERS

Györffy, B. L.⁽¹⁾ and Lathiotakis, N. N.⁽²⁾

H. H. Wills Physics Laboratory, University of Bristol

Royal Fort, Tyndall Avenue, Bristol BS8 1TL, U.K.

⁽¹⁾b.l.gyorffy@bristol.ac.uk

⁽²⁾n.lathiotakis@bristol.ac.uk

ABSTRACT

We review the theory of oscillatory magnetic coupling in metallic multilayers across alloy spacers. We illustrate the relationship between the frequencies of the oscillations and the extremal caliper vectors of the Fermi surface of the spacer by explicit calculations for $\text{Cu}_{(1-x)}\text{Ni}_x$, $\text{Cr}_{(1-x)}\text{V}_x$ and $\text{Cr}_{(1-x)}\text{Mo}_x$ alloys. We argue the measurement of the frequencies of such oscillations can be an extremely useful and cheap probe of the Fermi surface of random alloys.

INTRODUCTION

Many random alloys such as $\text{Cu}_{(1-x)}\text{Ni}_x$, $\text{Cu}_{(1-x)}\text{Au}_x$ are metals and therefore have Fermi surfaces in a well defined sense [1]. Moreover, these Fermi surfaces determine many of the properties of these scientifically interesting and technologically important class of materials. Thus, it would be useful to know what these Fermi surfaces are like and how they evolve with changing concentration. Unfortunately the classic probes of the Fermi surface such as the measurement of the de Haas van Alphen (dHvA) oscillations [2, 3] work only if the quasi-particles can complete

a cycle along the Landau orbit between two scattering events associated by deviations of the crystal potential from periodicity. As it happens this physical requirement of long quasi-particle life times translates into very small, \sim ppm, concentration of impurities and hence no dHvA signal is expected for the concentrated alloys of interest. This leaves, until recently, two dimensional Angular Correlation of (Positron) Annihilation Radiation (2d ACAR) and Compton Scattering (SC) studies, which do not require long quasi-particle life times, as the only source of reasonably direct quantitative information about the Fermi Surfaces of Random Alloys [4]. Our aim here is to argue that measurements of the oscillatory coupling between magnetic layers across random alloy spacers can also provide such information.

In short, what one measures is the exchange coupling $J_{12}(L)$ between magnetic layers 1 and 2 separated by a non magnetic spacer layer of thickness L made of a random metallic alloy. A schematic picture of the experiment configuration is shown in Fig. 1 and the exchange interaction J_{12} is defined in terms of the magnetic interaction energy $\delta E_{12}(L)$:

$$\delta E_{12}(L) = J_{12}(L) \mathbf{M}_1 \mathbf{M}_2, \quad (1)$$

where $\mathbf{M}_1, \mathbf{M}_2$ are the average magnetization of magnetic layers 1 and 2 respectively. As was discovered by Parkin *et al* [5], and has been observed for a vast variety of systems [6], $J_{12}(L)$ oscillates between being Ferromagnetic, $J_{12} < 0$ and Antiferromagnetic, $J_{12} > 0$ as a function of the separation L . In fact most experiments seem to be consistent with the formula [7, 8]

$$J_{12}(L) = -\frac{1}{L^2} \sum_{\nu} A_{\nu} \cos(Q_{\nu} L + \phi_{\nu}) e^{-L/\Lambda_{\nu}}, \quad (2)$$

where each contribution $\nu = 1, 2, \dots$ is characterized by the period $P_{\nu} = 2\pi/Q_{\nu}$, amplitude A_{ν} , phase ϕ_{ν} and coherence length Λ_{ν} which is infinite for pure metal spacer but is finite if the spacer is a random metallic alloy. Our discussion will focus on the astonishing fact that Q_{ν} is a quantitative measure of a geometrical feature of the Fermi surface of the infinite (bulk) spacer metal. In fact, most theories predict the form in eq. (1) asymptotically for large L and Q_{ν} turns out to be an extremal caliper vector, connecting two opposite points on the Fermi surface, in the direction perpendicular to the plane of the magnetic layers, that is to say in the growth direction of the multilayer system [7, 8, 9, 10]. This result is well confirmed for a large number of pure metal spacers. In the next two sections we review the agreement between the predicted and measured evolution of Q_{ν} with concentration x for random metallic alloys. In section 5 we will discuss the exponential damping factor and

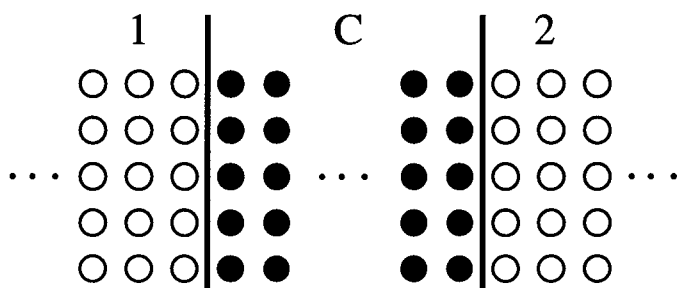


Figure 1 Schematic view of a sandwich structure of 1 and 2 magnetic layers separated by a non magnetic spacer layer C which could be disordered in general.

in section 6 we present an asymptotic theory for the amplitudes and the phases Q_ν .

The interest in the above interlayer magnetic coupling has arisen in the wake of its discovery, because of its connection with the technologically very important Giant Magneto-resistance (GMR) phenomenon. From this point of view the problem is largely solved. The physical mechanism is understood to be the planar defect analogue of the RKKY interaction between point like magnetic defects in metals, enhanced by confinement [7]. In this contribution we wish to emphasize another aspect of the problem. Namely, we shall explore the possibility of using the oscillatory coupling phenomenon as a new probe of the Fermi surface in transition metal alloys. Clearly, compared with 2d-ACAR the measurement of these oscillations is simple and cheap and hence the prospects of such a project are bright. However, before the full power of the method can be assessed, both the experimental technique and the theoretical framework used to interpret the data will require further scrutiny. In what follows we will present a few initial steps in the direction of the latter.

EVOLUTION OF THE FERMI SURFACE OF $\text{Cu}_{(1-x)}\text{Ni}_x$ ALLOYS WITH CONCENTRATION

The FCC $\text{Cu}_{(1-x)}\text{Ni}_x$ alloys are one of the best known examples for which the rigid band model completely misconstrues the nature of the changes in the electronic structure on alloying [11, 12]. Thus a direct experimental study of the Fermi surface is of fundamental interest from the point of view of the electronic structure of metallic alloys.

Oscillations for this alloy systems have been observed in three separate experiments. Parkin *et al.* [13] and Bobo *et al.* [14] studied a Co/ $\text{Cu}_{(1-x)}\text{Ni}_x$ /Co system with (111) growth direction, while Okuno *et*

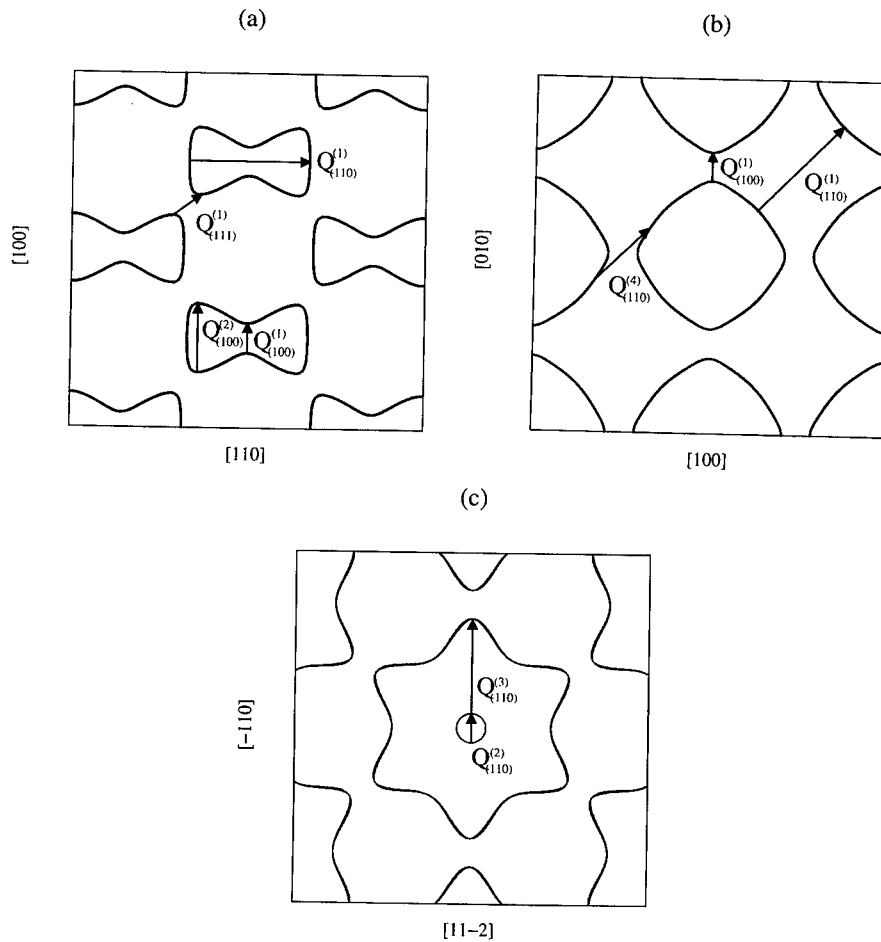


Figure 2 Three different cross sections of the Cu Fermi surface in the repeated zone scheme with all the extremal vectors: (a) perpendicular to the $[1-10]$ direction at distance $\Delta k=0$ to the Γ point, (b) perpendicular to the $[001]$ at distance $\Delta k=0$ and (c) perpendicular to the $[111]$ at $\Delta k=\sqrt{3}/2$.

al.[15] studied the same system for the (110) orientation. The relatively long oscillation period ($\sim 10\text{\AA}$) observed in all of these experiments is believed to correspond to neck caliper vectors of the Cu-like Fermi surface of $\text{Cu}_{(1-x)}\text{Ni}_x$ alloys for $x \leq 0.4$. In particular in the case of (110) direction, the caliper vector is the diameter of the neck itself, while in the case of (111) orientation it spans the neck in an angle of 19.47° with respect to the neck plane. In fig. 2 all the extremal vectors for the (100) , (110) and (111) directions are shown. The ones we already mentioned for the (110) and (111) directions are the $Q_{(110)}^{(2)}$ and $Q_{(111)}^{(1)}$

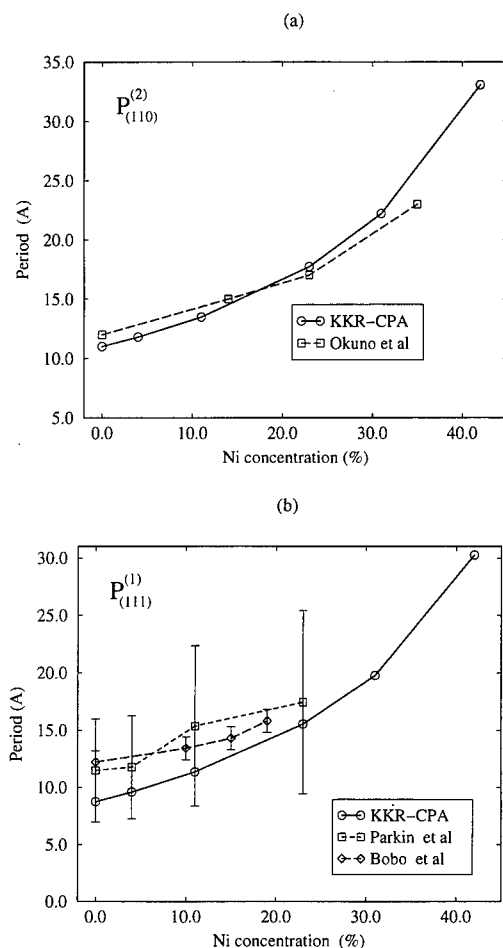


Figure 3 Comparison of the calculated large periods as functions of Ni concentration with the experiments of Bobo et al [14] and Parkin et al [13] for the period $P_{(111)}^{(1)} = 2\pi[Q_{(111)}^{(1)}]^{-1}$ (a) and Okuno et al [15] for the period $P_{(110)}^{(2)} = 2\pi[Q_{(110)}^{(2)}]^{-1}$ (b).

respectively. In the refs. [10, 16] we have calculated the concentration dependence of these extremal vectors using the KKR-CPA electronic structure method [11, 17] and have compared the predicted oscillation periods with the experimental ones. We present that result also in fig. 3 for both the (110) and (111) orientations.

The decrease with concentration of the neck diameter, resulting in an increase of the oscillation period, is in qualitative agreement with the Rigid Band Model. Indeed, that decrease comes from the fact that an electron-like neck of the Fermi surface such as the one we are looking for is expected to shrink when electrons are removed from the system (for instance by increasing the Ni concentration) but the calculated as well as the observed shrinkage is more gentle than the predicted from

the Rigid Band Model. The excellent agreement between our calculation and the experiment as illustrated in fig. 3 is one more striking example of the success of the CPA theory in binary alloy systems. The relatively simple Fermi surface of the $\text{Cu}_{(1-x)}\text{Ni}_x$ binary alloy system ($x < 0.5$) makes it easy to examine whether the evolution of the Fermi surface with alloying is in agreement with OMC measurements, and as is illustrated in fig. 3 that agreement is excellent. In the next section a binary alloy system with much more complicated Fermi surface is examined, namely the $\text{Cr}_{1-x}\text{V}_x$ binary alloy.

WHICH PIECE OF THE FERMI SURFACE DRIVES THE LONG PERIOD OSCILLATIONS ACROSS $\text{Cr}_{(1-x)}\text{V}_x$ SPACERS?

Although the long period ($\sim 18 \text{ \AA}$) oscillation for Fe/Cr/Fe was the first example in which Oscillatory coupling was discovered [5], until recently the origin of the long period oscillation was the subject of an open debate [9, 18, 19, 20, 21, 22, 23]. In the literature, the most popular caliper vectors for being relevant are those spanning the electron-like lenses of the Fermi surface and the hole-like ellipsoidal pockets centered at the N points. A further point of interest is that the long period oscillation appears to be unaffected by the orientation of the specimen, at least for the (100), (110) and (211) directions, leading to the conclusion that the coupling comes from a fairly isotropic region of the Fermi surface [24]. The extra complication that makes it extremely difficult to associate the oscillation period with a specific piece of the Fermi surface comes from the fact that the Cr Fermi surface is fairly complicated with high degree of nesting features arising from the d-states. It is rather difficult even to enumerate all the extremal vectors of the Fermi surface and of course the procedure of just comparing the experimental periods with the frequencies of the Fourier transform of a total energy calculation totally fails in this case. Of course the panacea would be to calculate the amplitudes of the individual oscillatory terms and reveal which terms are dominant. Such calculations have been done using semi-empirical Tight Binding methods [9, 23], and although the size of the associated period is significantly smaller than the observed, they conclude that the origin of the oscillation is the N hole-like pocket for both the (100) and (110) orientations. Unfortunately, other authors are drawing different conclusions [19, 24].

In ref. [25] we suggested that the evolution of the Fermi surface with alloying in the Cr spacer could give conclusive answer to the debate. Indeed, there are experiments on the OMC across $\text{Cr}_{(1-x)}\text{V}_x$ as well as $\text{Cr}_{(1-x)}\text{Mn}_x$ spacers for poly-crystalline samples with (110) predominant orientation [26]. The idea is that if the origin of the oscillation is an

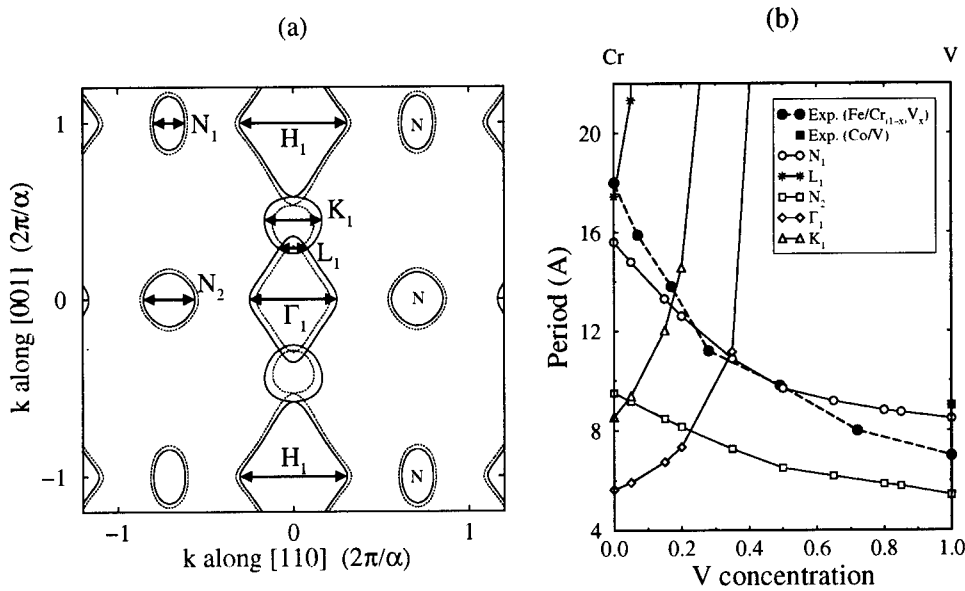


Figure 4 (a) Cross sections of the pure Cr (solid) and of $\text{Cr}_{0.85}\text{V}_{0.15}$ (dotted) Fermi surfaces, perpendicular to $[1-1\ 0]$ direction through Γ point. (b) The dependence of the oscillation periods (corresponding to the extremal vectors shown in (a)) with V concentration. Experimental data from ref. [26] for $\text{Fe/Cr}_{(1-x)}\text{V}_x$ and ref. [30] for Co/V sandwiches are also included in (b) for comparison.

electron-pocket then that pocket should shrink as V is added enhancing the size of the oscillation period. If on the other hand, the origin is a hole-like pocket the period should decrease when electrons are taken out by replacing Cr atoms by V impurities. The opposite apply in the case of alloying with Mn. What the experiment shows is a monotonic decreases of the period with V concentration and increase with Mn concentration, which is consistent with the source of oscillation being a hole-like pocket. Of course the RBM is not quantitatively correct in general, but it serves as a good qualitative picture. Of course, our calculation is based on the KKR-CPA method and so one expects the agreement to be better than merely qualitative level. In fig. 4 the experimental period is shown as a function of the V concentration along with the theoretical (KKR-CPA) periods predicted from various extremal vectors of the alloy Fermi surface. As we see the period predicted from the N-hole-like pocket is the only one which agrees quantitatively with experiment. Thus, our results strongly suggest that the source of the oscillations for both pure Cr as well as $\text{Cr}_{(1-x)}\text{V}_x$ spacers is the N-hole-like pocket of the Fermi surface [25]. For this particular case the rigid band model seem to agree quantitatively with the more accurate CPA result, as has been shown by Koelling [27] who used that model to draw similar conclusion to ours for the Cr spacer long period oscillation.

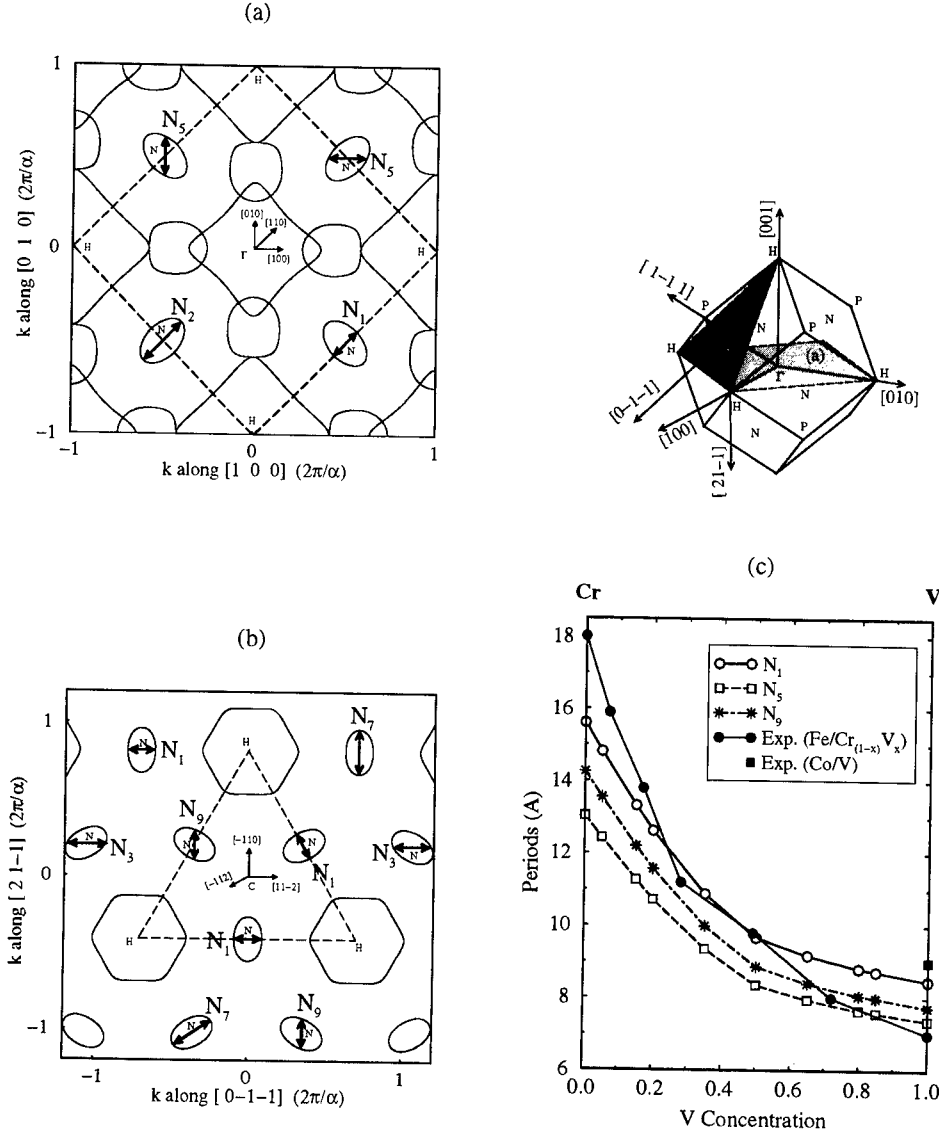


Figure 5 (a),(b) The Brillouin zone of BCC lattice with cross sections of the Fermi volume by the two planes shown in the inset. N_1, N_2, N_3 are the extremal vectors for the (110) direction, while N_4, N_5 are those for the (100) and N_6, N_7, N_8, N_9 for the (211). The N_4 (not shown in (a) and (b) cuts) is the ellipsoid principal axis along the NP direction. N_6 and N_8 also are not shown in these cross sections. (c) The largest oscillation periods for each of the (110), (100) and (211) directions corresponding to the N_1, N_5 and N_9 extremal vectors respectively as functions of V concentration. The dependence of the periods corresponding to the rest of the extremal vectors is similar but the sizes of these periods are significantly smaller than the ones plotted. The experimental data of Parkin for Fe/Cr_(1-x)V_x [26] and Co/V [30] sandwiches are also included in (c) and refer to the (110) direction.

The lattice mismatch at the interfaces of the sandwich structures, is one of the factors that could affect the agreement between theory and experiment in comparing the sizes of the oscillation periods to the sizes of the extremal vectors of the bulk Fermi surface [28]. In the case of Cr as well as $\text{Cr}_{(1-x)}\text{V}_x$ spacers, that lattice mismatch is not important since the lattice constants of Cr, V, and Fe are very close to each other, but in other cases like for example Fe/Mo/Fe or Fe/ $\text{Cr}_{1-x}\text{Mo}_x$ /Fe alloy spacers the effect of lattice mismatch might be large enough to be ignored. Thus, for instance, in ref. [28], we argue that it could be the explanation for the dramatic discrepancy between the Rigid Band idea and the significant decrease with concentration been observed experimentally for Fe/ $\text{Cr}_{1-x}\text{Mo}_x$ /Fe systems. The point is that since Cr and Mo are isoelectronic, according to the Rigid Band Model no change in the Fermi surface, and therefore in the period of the oscillation, is expected with alloying. We argue in ref. [28] that the size of the effect of lattice mismatch may be enough to resolve the dilemma. However, one needs to know more about the exact geometry of the sandwich structure before drawing definite conclusion.

Having established the relation of the N-hole pocket and the OMC across Cr and $\text{Cr}_{(1-x)}\text{V}_x$ spacers the OMC can become a powerful experimental technique for studying the geometry of that pocket and how it evolves with concentration. In particular the N-hole pocket ellipsoid appears to grow isotropically with V concentration as is shown in fig. 5. In that figure the periods predicted from the 3 smallest N pocket extremal vectors for the (100), (110) and (211) directions are shown as functions of V concentration. That does not appear to be the case in recent 2d-ACAR experiments [29] where a rotation of the N-hole pocket is observed with increasing concentration of Vanadium. The only experimental technique apart from 2-d ACAR which could resolve this extremely delicate feature of the Fermi surface appears to be the OMC.

Finally, it is of some interest to note that the long period oscillation across $\text{Cr}_{(1-x)}\text{V}_x$ spacers is an example in which the alloy theory gives a conclusive answer, by continuity, to an outstanding problem concerning the pure metal spacer system.

THE EXPONENTIAL DAMPING DUE TO DISORDER SCATTERING

As we have already mentioned an exponential damping of the OMC is inevitably present in the case of disordered binary alloy spacers. The characteristic length of the damping, *i.e.* the quantity Λ_d in the eq. (2) is related to the coherence length of the quasi-particle states at the end-points of the extremal vector, which is a measure of the mean free path for these states. A convenient quantity to describe the electronic structure of substitutionally disordered systems such as the random binary

alloys is the so called Bloch Spectral Function (BSF) $A_B(\mathbf{k}, E)$ which is the number of states per Energy and wave length [11]. In the case of pure metals, that function is simply a sum of delta functions either as function of E at a constant wavevector \mathbf{k} , or as a function of the wavevector \mathbf{k} for constant value of the energy. For constant $E = E_f$, where E_f is the Fermi energy, the positions of the peaks in \mathbf{k} -space define the Fermi surface of the metal. The \mathbf{k} -space representation is still a good description of the electronic structure of the alloy although strictly speaking there is periodicity only on the average. In terms of the BSF, the fundamental difference between a pure metal and a disordered alloy is the lowering of the height and broadening of the δ -function peaks of the pure metal. Thus, a Fermi surface for the alloy is still defined through the position of the peaks but these peaks have a finite width, the inverse of which defines the coherence lengths we mentioned above. In a simple theory for the OMC for disordered spacer, we showed in ref [10] that

$$\frac{1}{\Lambda_\nu} = \Gamma_\nu^{(+)} - \Gamma_\nu^{(-)}, \quad (3)$$

where $\Gamma^{(+)}$, $\Gamma^{(-)}$ are the widths of the BSF peaks along the direction of the extremal vector with (+) and (−) labeling the two peaks at the end-points of the extremal vector. Of course the Fermi surface is well defined if the size of $\Gamma_\nu^{(+)}$ and $\Gamma_\nu^{(-)}$ is small compared to Q_ν , *i.e.* the size of the extremal vector itself. In that case of course, Λ_ν is large compared to the oscillation period P_ν , *i.e.* no damping is observed within the first few oscillation periods.

In the light of the above discussion, the obvious question is how broad are the spectral functions for the cases of extremal vectors we considered above for the $\text{Cu}_{(1-x)}\text{Ni}_x$ and $\text{Cr}_{(1-x)}\text{V}_x$ Fermi surfaces? In fig 6 we show the BSF along these extremal vectors. We see that for $\text{Cu}_{(1-x)}\text{Ni}_x$ at concentrations of the order $x \approx 0.5$, where an electronic topological transition (ETT) takes place [31], the widths become comparable with the size of the extremal vectors. On the other hand for $\text{Cr}_{(1-x)}\text{V}_x$ the extremal wave vector size is always very large compared to the width of the peaks. The BSF peaks for the N-hole pocket appear to be the sharpest for the whole Fermi surface. Although ETT occurs in other parts of the Fermi surface, the N-hole pockets are robust in alloying, with only its total volume increased as more V is added. Thus, in both $\text{Cu}_{(1-x)}\text{Ni}_x$ ($x \leq 0.4$) and $\text{Cr}_{(1-x)}\text{V}_x$ for the whole range of V concentration, no significant damping is expected in agreement with the experiments on these two systems [13, 14, 15, 26].

It would be interesting if an alloy spacer system was found with a topological transition (ETT) taking place near the extremal vector at some value of the concentration x_o . The exponential damping of the OMC for values of x close to x_o could be measured and the dramatic

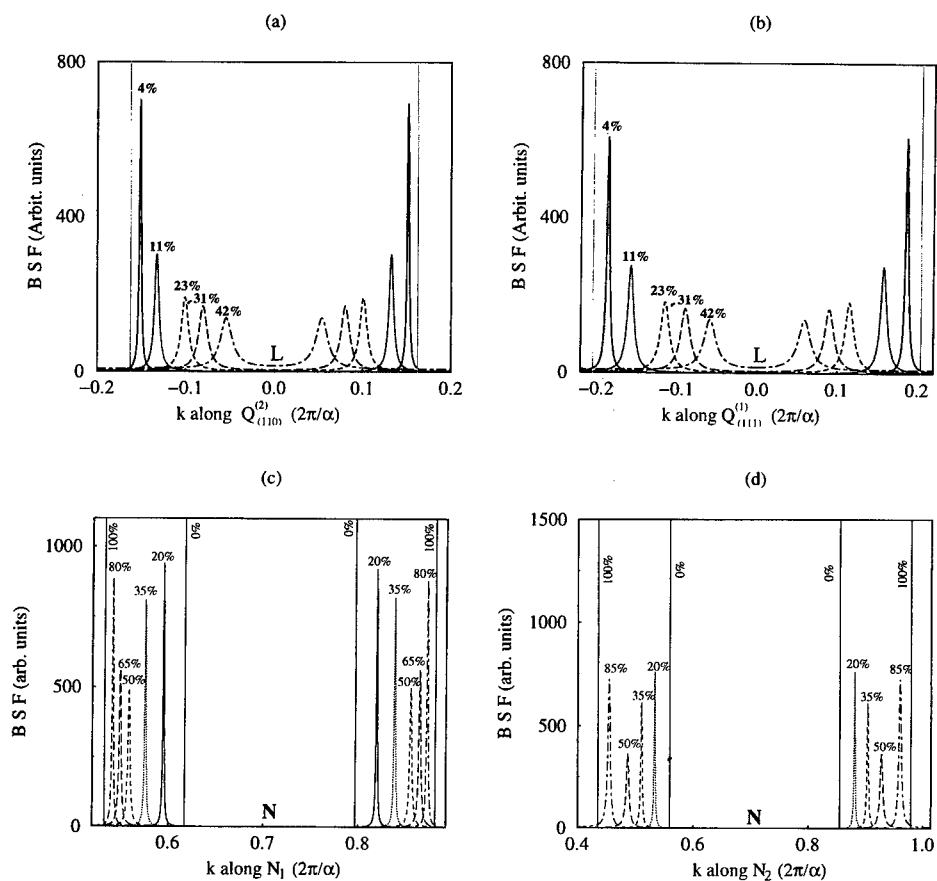


Figure 6 The Bloch Spectral Function along the direction of the extremal vectors $Q_{110}^{(2)}$ (a) and $Q_{111}^{(1)}$ (b) for $\text{Cu}_{(1-x)}\text{Ni}_x$ and N_1 (c) and N_2 (d) for $\text{Cr}_{(1-x)}\text{V}_x$ for various concentrations.

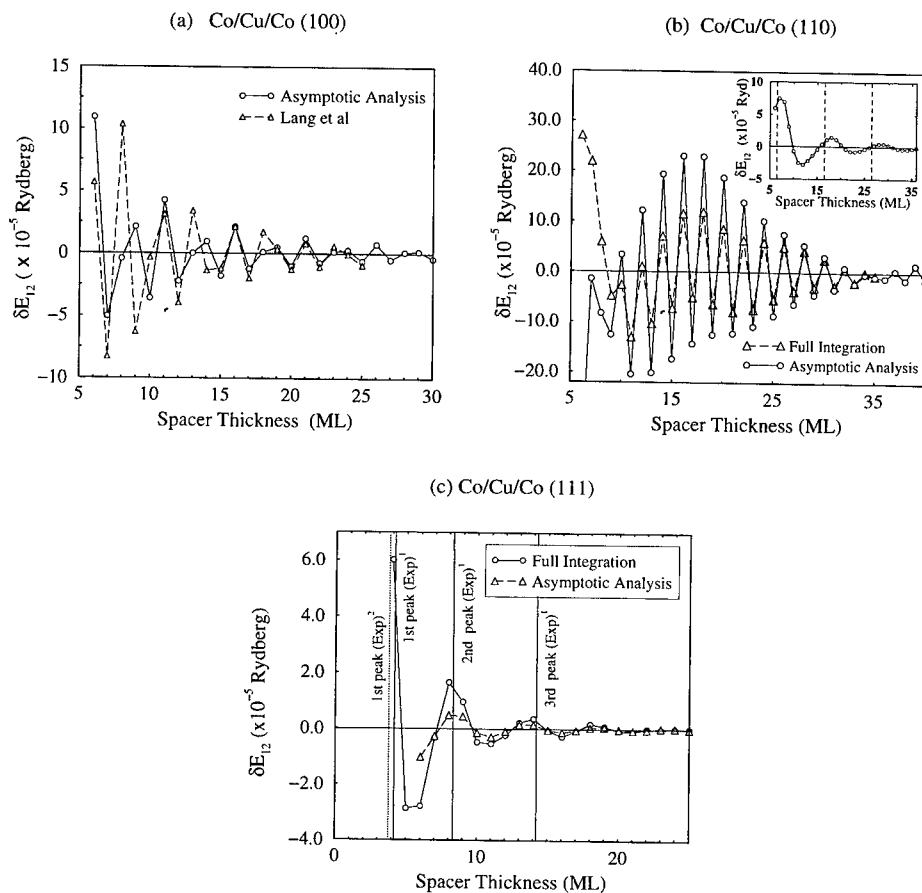


Figure 7 The calculated OMC for the Co/Cu/Co structure as function of the spacer thickness: (a) The asymptotic analysis result for the (100) orientation (solid line), compared with the total energy calculation result of Lang et al [34]. (b) The OMC for (110) for both asymptotic analysis (sum of two contributions, originating from $Q_{(110)}^{(1)}$ and $Q_{(110)}^{(2)}$ in fig. 2) and full integration calculation for the (110) orientation. In the inset the contribution of the large period oscillation (originating from $Q_{(110)}^{(2)}$) is plotted with the vertical lines indicating the positions of the AF peaks found in experiment [35]. (c) The OMC for both full integration and asymptotic analysis calculations for the (111) orientation. The vertical lines again indicate the positions of the AF peaks as found in the experiments of Johnson et al [35] (Exp)¹ and Parkin et al [36] (Exp)².

prediction of the theory is that no oscillation would be observed for the concentration where the ETT occurs. Such an experiment would be a direct observation of the ETT. Moreover, the characteristic length of the damping for x close to but not equal to x_0 would be a direct measurement of the coherence length at particular points of the Fermi surface, *i.e.* the endpoints of the extremal vector. Of course such measurements require further refinement of the experimental techniques used for measuring the OMC.

CALCULATIONS OF THE AMPLITUDES A AND PHASES ϕ

The asymptotic analysis leading to a theory of the amplitudes A_ν and the phases ϕ_ν has been carried out within a number of approaches to the problem of calculating the distortions in the electronic structure of the spacer by the magnetic layers [32]. In particular, it was carried out for the powerful, fully first principles screened KKR method [33]. Quantitative calculation of the asymptotic formulas are compared with the results of full total energy calculations and experiments in fig. 7. Similar calculations for alloy spacers are in progress.

As can be seen in fig. 7 the agreement between our calculated amplitudes and phases with both theoretical [34] and experimental results [35, 36] for the OMC across Co/Cu/Co is remarkable for all the orientations. In particular there is very good quantitative agreement between our results and Lang *et al.* [34] in the amplitudes as seen in fig. 7a for the (100) orientation. Furthermore, there is excellent agreement with the experiments of refs. [35, 36] concerning the phases and periods, *i.e.* the positions of AF peaks, as seen in the inset of fig. 7b and in fig. 7c. There is only agreement in the order of magnitude with experiments concerning the size of the interaction. For example, for the (100) orientation Johnson *et al.* [35] have measured 0.4 mJ/m^2 for an average Cu thickness of 6.7 ML, while we find 3.3 mJ/m^2 and -1.0 mJ/m^2 for 6 and 7 ML respectively. For the (111) Johnson *et al.* [35] measured 1.1 mJ/m^2 for 4 ML of Cu thickness, while our calculated value for the same thickness is 2.1 mJ/m^2 . The agreement with experiments with regard to the amplitudes, although it is restricted to the order of magnitude so far, is at least convincing evidence that our models describe the effect which is also seen by experiments. In conclusion, we note that the asymptotic formulas such as the one we derived in [32] may play a role in interpreting OMC experiments similar to that of the Lifshitz-Kosevich semi-classical formula [37], used to deducing the Fermi surface geometry from the measurement of the de Haas van Alphen oscillations.

References

- [1] B. L. Györfy, B. Ginatempo, D. D. Johnson, D. M. Nicholson, F. J. Pinski, J. B. Staunton and H. Winter, *Phil. Trans. R. Soc. London A* **334** 515-526 (1991).
- [2] M. Springford (Ed) "*Electrons at the Fermi Surface*", Cambridge University Press, (1980).
- [3] P. T. Coleridge in "*Electrons at the Fermi Surface*", Ed. M. Springford, Cambridge University Press, (1980).
- [4] S. Berko, *Proc. NATO ASI on the Electorns in Disordered Metals and at Metallic Surfaces*, ed. P. Phariseau, B. L. Györfy and L. Scheire (New York:Plenum), p 239-91 (1979); S. Berko, it proc. "Enrico Fermi" Course LXXXIII, Varena, Positron Solid State Physics, ed. W. Brandt, North Holland Pub. Co. (1983).
- [5] S. S. P. Parkin, N. More, K. P. Roche, *Phys. Rev. Lett.* **64**, 2304 (1990).
- [6] B. Heinrich, J. A. C. Bland (Eds.), *Ultrathin Magnetic Structures II*, Springer-Verlag (1994).
- [7] P. Bruno, C. Chappert, *Phys. Rev. Lett.* **67**, 1602 (1991).
- [8] D. M. Edwards, J. Mathon, R. B. Muniz and M. S. Phan, *Phys. Rev. Lett.* **67**, 493 (1991); *J. Phys.: Cond. Matt.*, **3**, 4941 (1991).
- [9] M.D. Stiles., *Phys. Rev. B*, **48**, 7238 (1993).
- [10] N. N. Lathiotakis, B. L. Györfy, Újfalussy B and J. Staunton (1998) *J. Mag. Mag. Matt.*, **185** 293 (1998).
- [11] B. L. Györfy, and G. M. Stocks, '*Electrons in Disordered Metals and at Metallic Surfaces*', Ed. P. Phariseau, B. Györfy and L. Scheire, NATO ASI Series, Plenum Press, New York (1979).
- [12] J. S. Faulkner, *Progress in Matt. Sc.*, **27**, 1-87 (1982).
- [13] S.S.P. Parkin, C. Chappert, F. Herman, *Europhys. Lett.* **24**, p 71 (1993).
- [14] Bobo F-J., Hennen L., Piecuch M. and Hubsch J., *Europhys. Lett.* **24**, pp. 139-144 (1993); *ibid. J.Phys.: Condens. Matter* **6** 2689 (1994).
- [15] S.N. Okuno, K. Inomata, *Phys. Rev. Lett.* **70**, 1711 (1993); *ibid. J. Mag. Mag. Matt.* **126**, 403 (1993).
- [16] N. N. Lathiotakis, B. L. Györfy, J. B. Staunton, *J. Phys.: Condens. Matter* **10**, 10357 (1998).
- [17] E. Bruno, B. Ginatempo, *Phys. Rev. B* **55**, 12946 (1997); E. Bruno, G. M. Florio, B. Ginatempo, E. S. Giuliano, *J. Comp. Phys.* **111**, 248 (1994).
- [18] M. van Schilfgaarde, W. A. Harrison, *Phys. Rev. Lett.* **71**, 3870 (1993).
- [19] D. D. Koelling., *Phys. Rev. B* **50**, 273 (1994).
- [20] D. Li, J. Pearson, S. D. Bader, E. Vescovo, D.-J. Huang, P. D. Johnson, B. Heinrich, *Phys. Rev. Lett.* **78**, 1154 (1997).
- [21] S. Mirbt, A. M. N. Niklasson, B. Johansson, H.L. Sriver, *Phys. Rev. B* **54**, 6382 (1996); S. Mirbt, B. Johansson *Phys. Rev. B* **56**, 287 (1997).
- [22] M. D. Stiles, *Phys. Rev.* **54**, 14679 (1996).
- [23] L. Tsetseris, B. Lee, Y-C. Chang, *Phys Rev. B* **55**, 11586 (1997).

- [24] E. E. Fullerton, M. J. Conover, J. E. Mattson, C. H. Sowers, S. D. Bader, *Oscillatory Interlayer Coupling and Giant Magnetoresistance in epitaxial Fe/Cr(211) and (100) superlattices*, Phys. Rev. B, **48**, 15755 (1993); *ibid* *Orientationally independent Antiferromagnetic Coupling in epitaxial Fe/Cr (211) and (100) superlattices*, J. App. Phys., **75**, 6461 (1994).
- [25] N. N. Lathiotakis, B. L. Györffy, E. Bruno, B. Ginatempo and S. S. P. Parkin, *Oscillatory Exchange Coupling across Cr_(1-x)V_x alloy spacers*, Phys. Rev. Lett. **83**, 215 (1999).
- [26] M. van Schilfgaarde, F. Herman, S. S. P. Parkin, and J. Kudrnovský, *Theory of Oscillatory Exchange Coupling in Fe/(V,Cr) and Fe/(Cr,Mn)*, Phys. Rev. Lett., **74**, 4063 (1995).
- [27] D. D. Koelling, *Long-period oscillation in the magnetic coupling through chromium in a magnetic multilayer: Bulk issues* Phys. Rev. B **59**, 6351 (1999).
- [28] N. N. Lathiotakis, B. L. Györffy, B. Ginatempo, E. Bruno, *The dilemma of the rigid band model arising from measurements of the Oscillatory Exchange Coupling across Cr(1-x)Mox alloy spacers*, J. Mag. Mag. Mat., **198**, 447 (1999).
- [29] A. Alam, private communication.
- [30] S. S. P. Parkin, *Systematic variation of the strength and oscillation period of indirect Magnetic Exchange Coupling through the 3d, 4d, and 5d transition-metals*, Phys. Rev. Lett. **67**, 3598 (1991).
- [31] E. Bruno, B. Ginatempo, E.S. Giuliano, A.V. Ruban, Y. Vekilov, *Fermi Surfaces and Electronic Topological Transitions in metallic solid-solutions*, Phys. Rep., **249**, 353 (1994).
- [32] B. Újfalussy, N. N. Lathiotakis, B. L. Györffy, J. B. Staunton, *Asymptotic behaviour of the Oscillatory Exchange Coupling across alloy spacers: a first-principles approach*, Phil. Mag. B **78**, 577 (1998); N.N. Lathiotakis, B. L. Györffy and B. Újfalussy, *First-principles asymptotics for the Oscillatory Exchange Coupling in Co/Cu/Co of (100), (110), and (111) orientations*, Phys. Rev. B, **61**, 6854 (2000).
- [33] L. Szunyogh, B. Újfalussy, P. Weinberger, J. Kollár, *Self-consistent localized KKR scheme for surfaces and interfaces*, Phys. Rev. B, **49**, 2721 (1994).
- [34] L. Nordström, P. Lang, R. Zeller and P. H. Dederichs, *Influence of the magnetic-layer thickness on the Interlayer Exchange Coupling - Competition between oscillation periods*, Phys. Rev. B **50**, 13058 (1994).
- [35] M. T. Johnson, R. Coehoorn, J. J. de Vries, N. W. E. McGee, J. aan de Stegge, P. J. H. Bloemen, *Orientational dependence of the Oscillatory Exchange Interaction in Co/Cu/Co*, Phys. Rev. Lett. **69**, 969 (1992).
- [36] S. S. P. Parkin, R. F. Marks, R. F. C. Farrow, G. R. Harp, Q. H. Lam, and R. J. Savoy, *Giant Magnetoresistance and enhanced Antiferromagnetic Coupling in highly oriented Co/Cu (111) superlattices*, Phys. Rev. B **46**, 9262 (1992).
- [37] E. M. Lifshitz, L. P. Pitaevskii, Statistical Physics, Part 2, Landau and Lifshitz Course of Theoretical Physics, Vol. 9, Pergamon Press (1980).

ON ELEMENT-SPECIFIC MAGNETOMETRY WITH LINEAR DICHROISM IN PHOTOEMISSION

F.O. Schumann¹, R.F. Willis¹, K.W. Goodman², and J.G. Tobin²

¹The Pennsylvania State University, Department of Physics
University Park, PA 16802

²Department of Chemistry and Material Science, Lawrence Livermore National
Laboratory, Livermore, CA 94550

ABSTRACT

In this paper, we investigate the magnetic linear dichroism in the core-level photoemission spectra of the binary alloys $\text{Co}_x\text{Ni}_{1-x}$ and $\text{Fe}_x\text{Ni}_{1-x}/\text{Cu}(100)$. These epitaxial films have fcc structures, but very different magnetic behaviors. We show that the x-ray magnetic linear dichroism in photoemission (XMLD) signal tracks the magnetization in these alloys. Comparison with recent SQUID data provides a quantitative check and endorses the view that XMLD monitors the element-specific magnetometry.

INTRODUCTION

Magnetic dichroism in absorption and core-level photoemission has emerged as new tool for probing magnetic properties. Core-level spectroscopy is inherently element-specific and offers the possibility to investigate element-specific magnetic properties. In particular, it has been shown that changes in the magnetization can be tracked element-specifically [1, 2].

However, a lack of consensus on what constitutes the spectroscopic multiplet structure raises questions concerning the applicability of this method. In this paper, we present results which show that the dichroism of the spectral lineshape track the changing magnetization in these alloys. Specifically, we report on the concentration dependence of the magnetic dichroism for fcc $\text{Co}_x\text{Ni}_{1-x}$ and $\text{Fe}_x\text{Ni}_{1-x}$ ultrathin alloy films of the 3p core levels in photoemission with linearly polarized light (XMLD). In the case of $\text{Co}_x\text{Ni}_{1-x}$ alloys we have also compared the dichroism obtained in absorption

with circular polarization and in photoemission with linearly polarized light, and observed essentially the same trends in behavior using both methods[3].

EXPERIMENTAL METHODS

We have chosen fcc $\text{Co}_x\text{Ni}_{1-x}$ and $\text{Fe}_x\text{Ni}_{1-x}$ binary alloys because of their very different behaviors in the bulk. $\text{Co}_x\text{Ni}_{1-x}$ is structurally and magnetically well-behaved: in particular the magnetic moment varies linearly as a function of concentration [4]. This is in sharp contrast to fcc $\text{Fe}_x\text{Ni}_{1-x}$ which displays a magnetic instability at ~65% Fe content [5]. An extended regime of fcc stability is possible via epitaxy on Cu(100) [6-8]. If XMLD is indeed a sensitive probe of the element-specific magnetization, we should expect very different behavior for this latter alloy. This has been observed and will be discussed in the following.

Growth and structural aspects of $\text{Co}_x\text{Ni}_{1-x}$ and $\text{Fe}_x\text{Ni}_{1-x}/\text{Cu}(100)$ have been thoroughly studied and we found for both systems good pseudomorphically epitaxial growth in the fcc structure[7, 8]. The photoemission dichroism experiments were performed at the SpectroMicroscopy Facility on Beamline 7 at the Advanced Light Source, Berkeley [9]. For photoemission of the 3p core levels we utilized 190 eV photons (p-polarized) and collected electrons in normal emission with an angular resolution of 2° . The angle of incidence of the photon beam was 60° with respect to the surface normal and the magnetization was in the 'transverse' geometry [8]. A field pulse from a coil near the sample magnetized the sample along the {001} direction.

RESULTS

First we display the concentration dependent 3p magnetic dichroism asymmetry for ~6 ML $\text{Co}_x\text{Ni}_{1-x}/\text{Cu}(100)$ in Figure 1 [10]. For the Co 3p level we find a constant asymmetry of ~10% which agrees with previous work by Kuch et al.[11], who investigated Co/Cu(100). For the Ni 3p level we observe a small value of ~2%. The results of the XMLD measurement suggest that the magnetic states of the Co and Ni atoms are not changing, since their asymmetry remains constant as the stoichiometry is changed. From the bulk we also know that the moments are concentration independent [4]. This might be regarded as evidence that the XMLD asymmetry is tracking a quantity closely related to the element-specific magnetic moment [2].

In Figure 2 we show the magnetic dichroism asymmetry for the Fe and Ni 3p levels. We notice a high asymmetry for the Fe 3p level at low Fe concentrations which is strongly reduced at high Fe concentrations. As explained previously [8] we can identify three regimes (I-III) on the basis of the variation of the atomic volume and the Fe magnetic asymmetry[8]. Clearly the concentration dependence is now distinctively different in the $\text{Fe}_x\text{Ni}_{1-x}$ alloy. (In our figures, we have added lines as guides to the eye.)

DISCUSSION

We want to discuss now to what extent XMLD can be used for elemental magnetometry of alloys. We were encouraged to pursue this aspect of our work by the results of Sirotti et al. on Fe bulk samples [2]. They compared the low-temperature dependence of the Fe 3p linear dichroism and asymmetry in the spin-polarization of secondary electrons. The latter is now very well established to be proportional to the magnetization [12]. Sirotti et al. observed that both techniques gave identical results and they concluded that the XMLD asymmetry is indeed proportional to the overall magnetization in the single element systems.

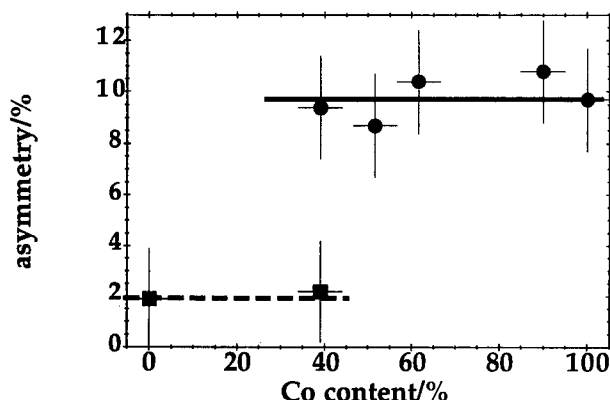


Figure 1: Concentration dependence of the Co (points) and Ni (squares) 3p asymmetry for 6 ML thick films at 300 K.

As shown in Figure 1, the element-specific magnetic properties of Co and Ni in $\text{Co}_x\text{Ni}_{1-x}$ remain constant. From these data, we find that the average dichroism asymmetry for Co and Ni is 9.8% and 2%, respectively.

We can replot the data of fig.1 by 'calibrating' the average asymmetries in the following way: (i) 9.8 % asymmetry equals $1.7 m_B$ for Co and (ii) 2 % asymmetry equals $0.6 m_B$ for Ni. (Here, m_B stands for Bohr Magnetons.) These are the known magnetic moments for bulk Co and Ni[4, 13]. Now we are able to calculate the average moment as a function of concentration for each data point. First we convert the dichroism asymmetry for Co and Ni into an element-specific moment. Secondly, as a test, we calculate the average moment using the following stoichiometric equation:

$$\mu = x \cdot \mu_{\text{Co/Fe}}(x) + (1 - x) \cdot \mu_{\text{Ni}}(x)$$

If we replace the actual data points with the averaged dichroism asymmetry for Co and Ni, the solid line results, plotted in Figure 3. The error bars reflect the uncertainties of the original data in Figure 1.

We can repeat this procedure for $\text{Fe}_x\text{Ni}_{1-x}$ alloys, for which we use the following "calibration": (i) 8.5 % asymmetry equals $2.5 m_B$ for Fe and (ii) 2% asymmetry equals $0.6 m_B$ for Ni. In Figure 2 we have shown that the phase diagram of $\text{Fe}_x\text{Ni}_{1-x}$ alloys can be divided into 3 regimes. We concluded that Fe is in a high-spin (HS) state for concentrations up to ~65%. Following the work of Abrikosov et al. [14] we associate this state with an atomic magnetic moment of $2.5 m_B$; for Ni we have used the bulk value [14]. Again we can calculate the average moment using equation (1). The solid line in Figure 4 is the result if we replace the actual data points by the fitted curve in Figure 2.

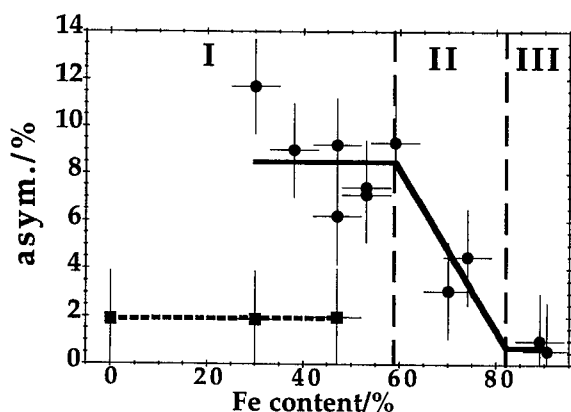


Figure 2. Concentration dependence of the Fe 3p (solid circles) and Ni 3p (solid squares) asymmetry at ~300 K, the film thickness was 5.5 -9.0 ML. Solid line is a fit as explained in [8].

Clearly in order to endorse XMLD as an element-specific magnetometer we need a comparison to results using an absolute magnetometer. Recently Freeland et al. provided results to this effect on ultrathin $\text{Fe}_x\text{Ni}_{1-x}$ alloys [15]. They investigated 4 ML thick $\text{Fe}_x\text{Ni}_{1-x}$ multilayers grown mainly on a Cu (111) substrate. Using SQUID magnetometry they have determined absolute values of the average moment. We show their results together with our replotted data from figs. 3 and 4, in Figure 5. We have also included a data point for 6 ML Fe/Cu (100) from a previous publication of the same group [16]. This clearly shows an almost linear increase for Fe concentrations up to ~65%. Extrapolation of this part of the curve to 100% Fe gives rise to a value of over $2.5 m_B$, close to that of fcc Fe in its HS state (about $2.9 m_B$.) Further evidence that the Fe moment stays constant in a HS state up to 65% Fe has been provided by Mössbauer

spectroscopy [15]. This work confirms our conclusions based on the high value of the Fe asymmetry up to ~65% Fe content as discussed previously [8].

Going beyond 65% Fe content, Freeland et al. observe a strong reduction of the magnetic moment towards smaller values. For pure Fe they find a magnetic moment of ~1 m_B. In this Fe-rich regime, their data show a considerable scatter of values, presumably due to different amounts of strain. This is particularly true for the (100) oriented thin films. These show a consistently smaller value of the moment than those in the (111) orientation.

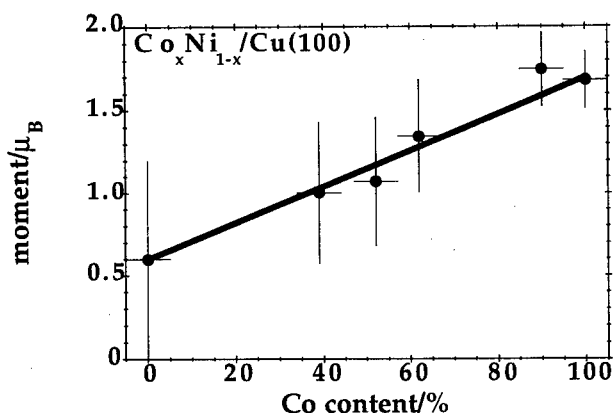


Figure 3. Average moment of $\text{Co}_x\text{Ni}_{1-x}/\text{Cu}(100)$ alloy films using the 'calibration' as explained in the text.

The apparent discrepancy between the previous experimental data points and our work (full line) in Figure 5 can be explained as follows. The difference between the 2 data points from samples with the (100) orientation is due to the thickness. Increasing the thickness obviously reduces the average moment due to the relief of volumetric strain, which is consistent with the Mössbauer experiments on Fe/Cu(100) [17]. Thickness dependent magnetic and structural properties are known to exist in the thickness regime 4-7 ML [17-20]. This is also true for $\text{Fe}_x\text{Ni}_{1-x}/\text{Cu}(100)$ alloy films, as previously reported [8]. We suspect that the $\text{Fe}_x\text{Ni}_{1-x}(111)$ films investigated by Freeland et al. have not the same atomic volume as our films for Fe concentrations larger than 65%. Either the films in the (111) direction have not fully relaxed or there is real difference in the volume instability. As it turns out there is evidence for the latter. The structure of Fe/Cu(111) has been carefully determined by means of LEED I-V [21]. In accord with earlier reports [22], it is found that for thicknesses up to 5 ML a fcc phase exists and we derive an atomic volume of 11.68 Å³ for 5 ML. This value is almost exactly in between 11.4 and 12.1 Å³, which are representative for 2 different magnetic

phases in the case of Fe/Cu(100) [20]. We have essentially derived the same values via an extrapolation [8]. Following the work of Keavney et al. we associate an atomic volume of 11.4 \AA^3 with an average Fe moment of 0.3 m_B . On the other hand an average moment of $\sim 2 \text{ m}_B$ has been observed for the HS state [16, 17]. Making the reasonable assumption that the moment is a linear function of the atomic volume [16] we determine an average moment of $\sim 1 \text{ m}_B$ for fcc Fe/Cu (111). This is in good agreement with the results of Freeland et al.[15].

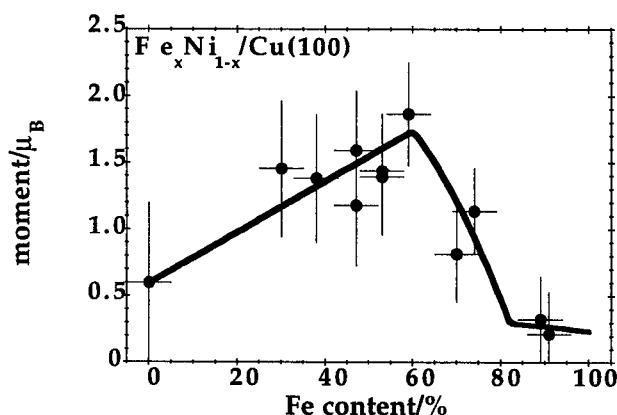


Figure 4. Average moment of $\text{Fe}_x\text{Ni}_{1-x}/\text{Cu}(100)$ alloy films using the 'calibration' as explained in the text.

It is also important to note that Tian et al. do not observe extra spots in the fcc phase, contrary to the observation for fcc Fe/Cu(100) [18, 20, 23]. Obviously, the structural instabilities and therefore magnetic states do not manifest themselves as clearly for pure Fe/Cu (111) as compared to Fe/Cu(100). Our work and the results of Freeland et al. agree that for up to $\sim 65\%$ Fe content Fe is in a HS state. Beyond this concentration the behavior of the atomic volume for $\text{Fe}_x\text{Ni}_{1-x}$ in the (100) and (111) orientation is different.

So far we have discussed our results in terms of ground state properties. However our measurements have been performed at temperatures in the range 250-300 K. We will show that any effect of temperature is rather minimal and not significant in the present context. The variation of the magnetization for bulk Ni is given in reduced temperature units T/T_c in Kittel [13]: e.g., for $T/T_c=0.7$ the magnetization is still 80 % of $M(0 \text{ K})$. As an example, we investigated $\sim 6 \text{ ML}$ thick Ni/Cu(100) with XMLD and we know that $T_c \sim 400 \text{ K}$ [24]. This means that 300 K is equal to 0.75 in reduced units. Consequently the error associated with the measurement at 'high' temperatures is much smaller than the error bar for the Ni XMLD asymmetry (see Figure 4). It is the latter

which results in the rather large error bar of our average moment plot in figs. 3 and 4. Alloying Ni with Co pushes the $T_c(d)$ dependence quickly up [7]. We find for 6 ML $\text{Co}_{10}\text{Ni}_{90}$ that 300 K is equivalent to ~ 0.65 in reduced units. Now the magnetization has only decreased by $\sim 10\%$. This trend of a decreasing deviation of the magnetization continues if the Co content is increased. Therefore we conclude that the error due to thermal excitations can be neglected and is at all times smaller than the error bar of the average moment (see Figure 3). We can now apply the same reasoning for $\text{Fe}_x\text{Ni}_{1-x}$ alloy films. For concentrations up to $\sim 65\%$ Fe the thermal excitations account for only $\sim 10\%$ decrease in $M(0\text{ K})$.

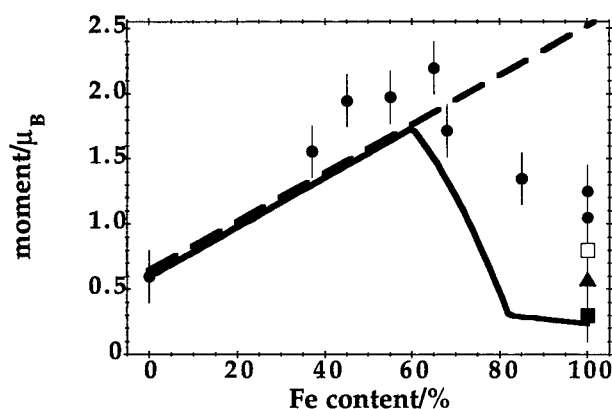


Figure 5. Comparison of the calibration curve of Figure 4 and the results of Freeland et al. (points/open squares are for (111)/(100) orientation) [15]. Included is also a data point from Keavney et al. (square)[16]. Triangle follows from Kümmerle et al. on Fe/Cu(111) [22].

For concentrations beyond 65% Fe we have to assume a larger deviation. As shown in a previous publication [7] $\text{Fe}_{75}\text{Ni}_{25}/\text{Cu}(100)$ alloys show only weak thickness dependence of T_c in the thickness interval ~ 4 -10 ML. The value is around 300 K, which is not much higher than 250 K, the temperature during thickness dependent measurements [8]. We now estimate that the magnetization has decreased by 40 %. Therefore we should replace the value of 0.3 m_B for pure Fe with 0.5 m_B . This is still significantly too small when compared with the data of Freeland et al. for the (111) orientation. Therefore the remaining differences are mainly due to the different volume instability for $\text{Fe}_x\text{Ni}_{1-x}/\text{Cu}(111)$.

SUMMARY

We have systematically investigated element-specific magnetic properties with XMLD for two different binary alloys. These results endorse the use of XMLD in

photoemission as an element-specific technique for studying ferromagnetism in metastable, binary-alloy, pseudomorphically epitaxial films. The difference in the spectral lineshapes when the direction of the magnetization is switched reflects the magnitude of the magnetization. This is clearly reflected in the contrasting behavior of the $\text{Co}_x\text{Ni}_{1-x}$ and $\text{Fe}_x\text{Ni}_{1-x}$ alloys with changing stoichiometry. The observed behavior of the ferromagnetic response suggests a simple summing of the magnetic moments, depending on the alloy composition. This in turn further underlines the magnetometry deduced from the XMLD signals.

ACKNOWLEDGMENTS

Funding was provided via NSF grant DMR-95-21126. This work was also performed under the auspices of the U.S. Department of Energy by LLNL under contract No. W-7405-ENG-48. We would like to acknowledge support with the ALS measurements from Drs. J. Denlinger, E. Rotenberg and A. Warwick.

REFERENCES

1. D. Schmitz, O. Rader, C. Carbone and W. Eberhardt, Temperature dependence of the magnetic circular dichroism of the $c(2\times 2)$ Mn/Ni(100) surface alloy, *Phys. Rev. B* 54:15352 (1996).
2. F. Sirotti, G. Panaccione and G. Rossi, Atom-specific surface magnetometry, *Phys. Rev. B* 52: R17063 (1995).
3. S.Z. Wu, F.O. Schumann, R.F. Willis, K.W. Goodman, J.G. Tobin and R. Carr, Magnetic dichroism effect of binary alloys using a circularly polarized x ray, *J. Vac. Sci. Technol.* A15:2287 (1997).
4. M.F. Collins and D.A. Wheeler, Magnetic Moments and the Degree of Order in Cobalt-Nickel Alloys *Proc. Phys. Soc. Lond.* 82:633 (1963).
5. E.F. Wassermann, The Invar problem, *J. Mag. Magn. Mat.* 100:346 (1991).
6. J. Dresselhaus M. Moller, T. Kleemann and E. Kisker, Spin-resolved temperature-dependent photoemission from ultrathin FENI alloy-films, *J. Mag. Magn. Mat.* 148:172 (1995).
7. F.O. Schumann, S.Z. Wu, G.J. Mankey and R.F. Willis, Growth and magnetic properties of $\text{Co}_x\text{Ni}_{1-x}$ and $\text{Fe}_x\text{Ni}_{1-x}$ ultrathin films on Cu(100), *Phys. Rev. B* 56:2668 (1997).
8. F.O. Schumann, R.F. Willis, K. G. Goodman and J. G. Tobin, Magnetic instability of ultrathin fcc $\text{Fe}_x\text{Ni}_{1-x}$ films, *Phys. Rev. Lett.* 79: 5166 (1997).
9. J.G. Tobin, K.W. Goodman, G.J. Mankey, R.F. Willis, J.D. Denlinger, E. Rotenberg and A. Warwick, Magnetic x-ray linear dichroism in the photoelectron spectroscopy of ultrathin magnetic alloy films *J. Appl. Phys.* 79:5626 (1996).
10. The element-specific asymmetry is calculated as the ratio of the difference spectrum over twice the mean peak height. We cannot use the expression $I(\text{up})-I(\text{down})/I(\text{up})+I(\text{down})$ due to the concentration dependence of the 3p peak heights.
11. W. Kuch, M.T. Lin, K. Meinel, C.M. Schneider, J. Noffke and J. Kirschner, Spin-resolved substrate band mapping in Fe/Cu(100) - application of the spin-filter effect, *Phys. Rev. B* 51:609 (1995).
12. H.C. Siegmann, Surface and 2d-magnetism, *J. Phys.: Condens. Matter* . 4:8395 (1992).
13. C. Kittel, *Introduction to Solid State Physics*. (John Wiley & Sons, Inc., New York, 1991).
14. I.A. Abrikosov, O. Eriksson, P. Soderlind, H.L. Skriver and B. Johansson, Theoretical aspects of the FeNi_{1-x}C Invar alloy, *Phys. Rev. B* 51:1058 (1995).

15. J.W. Freeland, I.L. Grigorov and J.C. Walker, Magnetic phase transition in epitaxial Ni_{1-x}Fe_x alloy thin films, *Phys. Rev. B* . 57:80 (1998).
16. D.J. Keavney, D.F. Storm, J.W. Freeland, I.L. Grigorov and J.C. Walker, Site-specific Mossbauer evidence of structure-induced magnetic phase-transition in FCC Fe(100) thin-films, *Phys. Rev. Lett.* 74:4531 (1995).
17. R.D. Ellerbrock, A. Fuest, A. Schatz, W. Keune and R.A. Brand, Mossbauer-effect study of magnetism and structure of FCC-like Fe(001) films on Cu(001), *Phys. Rev. Lett.* 74:3053 (1995).
18. J. Thomassen, F. May, B. Feldmann, M. Wuttig and H. Ibach, *Phys. Rev. Lett.* 69:3831 (1992).
19. M. Zharnikov, A. Dittschar, W. Kuch, C.M. Schneider and J. Kirschner Magnetic order-disorder transition mediated by a temperature-driven structural transformation, *Phys. Rev. Lett.* 76:4620 (1996).
20. S. Müller, P. Bayer, C. Reischl, K. Heinz, B. Feldmann, H. Zillgen and M. Wuttig, Structural instability of ferromagnetic FCC Fe films on Cu(100), *Phys. Rev. Lett.* 74:765 (1995).
21. D. Tian, F. Jona and P.M. Marcus, Structure of ultrathin films of Fe on Cu (111) and Cu (110), *Phys. Rev. B* . 45:11216 (1992).
22. W. Kümmerle and U. Gradmann, Ferromagnetism in gamma-iron, *Solid State Comms.* 24:33 (1977).
23. J. Thomassen, B. Feldmann and M. Wuttig, Growth, structure and morphology of ultrathin iron films on Cu(100) *Surf.Sci.* 264:406 (1992).
24. F. Huang, M.T. Kief, G.J. Mankey, R.F. Willis, Magnetism in the few-monolayers limit - A surface magnetooptic Kerr-effect study of the magnetic-behavior of ultrathin films of Co, Ni, and Co-Ni alloys on Cu(100) and Cu(111), *Phys. Rev. B* 49:3962 (1994).

ELASTIC PROPERTIES

DEFORMATION AND FRACTURE OF TiC/Mo(Nb) IN-SITU COMPOSITES

Shuji Hanada, Naoyuki Nomura, and Kyosuke Yoshimi

Institute for Materials Research
Tohoku University, Sendai 980-8577, Japan

INTRODUCTION

TiC having high melting temperature (3340 K) and relatively low density ($4.9 \text{ Mg} \cdot \text{m}^{-3}$) is considered to be promising as structural material at very high temperatures above 1500 K. Industrial applications of TiC have been limited, however, only to hard materials or cutting tools because of its low fracture toughness at ambient temperature. To improve the fracture toughness is essential to develop TiC as a structural material. Many studies have addressed the improvement of fracture toughness in ceramics by incorporating a second phase¹. Among them, some as-synthesized ex-situ (artificial) composites reinforced by a second phase were found to possess fracture toughness of an acceptable value for industrial material. However, the ex-situ composites consisting of non-equilibrated constituents were degraded in fracture toughness as well as high temperature strength during exposure to high temperature owing to the formation of brittle phase(s) at the interface. These results suggest that a second phase which can be equilibrated with a ceramic should be incorporated to improve the mechanical properties of ceramics at ambient and elevated temperatures.

Refractory metals such as Nb and Mo will be attractive second phases to introduce into TiC, since they can create in-situ composites with TiC, and in-situ composites to be developed are necessary to have melting temperature much higher than 1500 K. Moreover, according to the ternary phase diagrams of Nb-Ti-C and Mo-Ti-C systems^{2,3}, Nb and Mo are equilibrated with TiC in a relatively wide composition range at high temperature. This means that in-situ composites can be fabricated with a wide variety of volume fractions of the ductile phase. In-situ composites for high temperature applications are of great advantage with respect to thermodynamically stable interface between two phases, as compared with ex-situ composites. In this paper, in order to evaluate the potential of TiC/Mo(Nb) in-situ composites as structural material, high temperature strength and ambient temperature fracture toughness were examined in relation to microstructure.

EXPERIMENTAL PROCEDURE

Referring to the pseudo binary Mo-TiC phase diagram in Fig.1⁴, nominal compositions were selected with Nb-40mol%TiC, Nb-20mol%Mo-40mol%TiC, Nb-40mol%Mo-40mol%TiC, Mo-40mol%TiC and Mo-23.5mol%TiC (eutectic composition). These alloys will be hereafter abbreviated

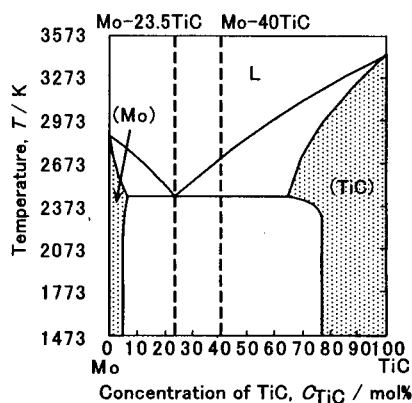


Figure 1. Pseudo binary phase diagram of Mo-TiC⁴.

as Nb-40TiC, Nb-20Mo-40TiC, Nb-40Mo-40TiC, Mo-40TiC and Mo-23.5TiC, respectively. 99.6 mass%Nb, 99.98 mass%Mo and 99.4 mass%TiC powders were blended by a cross rotary mixer and arc-melted in an Ar atmosphere. The arc-melted buttons were annealed to examine the stability of microstructures. Microstructures were observed in an optical microscope and a scanning electron microscope (SEM). Existing phases were identified by an X-ray diffractometer (XRD), an electron probe micro analyzer (EPMA) and a transmission electron microscope equipped with energy dispersive X-ray spectroscopy (TEM-EDX). Compression tests were carried out at temperatures from 1473 K to 1873 K in an Ar atmosphere at a strain rate of $1.6 \times 10^{-4} \text{ s}^{-1}$ on an Instron 8562-type machine. Resistivity of a ductile phase to cracking due to indentation was investigated by using a Vickers hardness tester at room temperature. Fracture toughness at room temperature was evaluated using arc-melted Mo-23.5TiC and Mo-40TiC with different volume fractions of constituent phases. After arc-melting (AM) both alloys were hot-isostatically pressed in an Ar atmosphere at 190 MPa and 2073 K for 2 h to minimize cavities. In order to investigate the effect of microstructure on fracture toughness, two other fabrication processes of directional solidification (DS) and hot-pressing via powder metallurgy (HP) were employed for different microstructures, since it was difficult to change the microstructure only by heat treatment. This experiment was carried out only for Mo-40TiC, because high-temperature strength is much higher at this composition than at eutectic Mo-23.5TiC. DS process by the floating zone method in an induction furnace was performed in a He atmosphere at a traveling speed of 30 mm/h. Blended powders of Nb, Mo and TiC were hot-pressed at 2073 K and 70 MPa for 2 h to facilitate sintering and annealed at 2073 K for 24 h to homogenize chemical composition and stabilize microstructure. To evaluate the fracture toughness of these composites three-point bending test was carried out at a cross head speed of $8.3 \times 10^{-6} \text{ m} \cdot \text{s}^{-1}$ using bend samples of 3 mm (thickness) \times 6 mm (width) \times 30 mm (length) with a span length of 24 mm. The single-edge notched beam (SENB) method was used owing to the difficulty of introducing a sharp pre-crack with fatigue test. A notch with a notch length to width ratio of 0.5 was introduced by electro-discharge machining with a thin wire of 100 μm in diameter. The direction of the notch was perpendicular to the growth direction for DS sample. The surfaces of bend samples were chemically polished with a colloidal solution consisting of Si dioxide. The bending test was performed at ambient temperature in air.

RESULTS AND DISCUSSION

Figure 2 shows optical micrographs of as-cast composites. Primary phase particles and eutectic lamellae are observed in Mo-40TiC. The primary phase was identified as TiC by EPMA. No discernible precipitate was seen in TiC except for Nb-40TiC. After annealing at 1873 K for 24 h, fine precipitates were observed in the primary TiC phase. The size of these precipitates increased with increasing Nb concentration. Since no phase was detected by XRD except A2 and B1 phases, the precipitates in TiC were regarded as an A2 (bcc) phase. Substitution behavior of Mo and Nb in the composites was analyzed by EPMA and TEM-EDX. It was found that Nb substitutes for Ti in TiC more preferentially than Mo does. TiC and NbC have B1 structure and form a complete solid solution

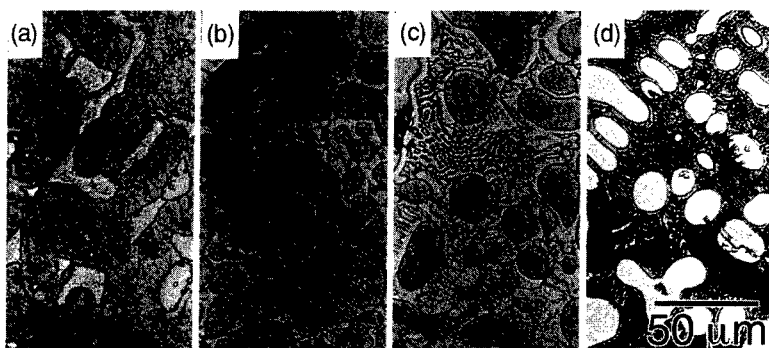


Figure 2. Optical micrographs of Nb-Mo-TiC as-cast composites: (a) Nb-40TiC, (b) Nb-20Mo-40TiC, (c) Nb-40Mo-40TiC, and (d) Mo-40TiC.

at 1873 K. In Mo-C binary system, a MoC has B1 structure above 2233 K. In Mo-Ti-C ternary system, TiC and MoC do not form a solid solution below 2273 K. Accordingly, the substitution of Nb for Ti in TiC at 1873 K is more preferential than that of Mo. Figure 3 shows the temperature dependence of compressive yield stress of TiC/Mo(Nb) in-situ composites in the temperature range from 1273 to 1873 K. It is evident that yield stress tends to increase by alloying with Mo and Nb-40Mo-40TiC shows the highest yield stress above 1673 K. It should be noted that yield stresses of Nb-40Mo-40TiC and Mo-40TiC are higher than those of monolithic TiC above 1473 K. It is generally accepted that yield stress of a composite is controlled by the rule of mixture. And high temperature strength of a ductile bcc phase-toughened ceramic is known to degrade by the bcc phase. Since both Nb and Mo are soluble in TiC as described above, TiC seems to be significantly solid solution strengthened by Mo. Indeed, the present EPMA result indicated that Mo content in TiC increases with increasing Mo content in TiC/Mo(Nb) composite. Monolithic TiC has been reported to be strengthened more significantly by Mo than by Nb⁵. On the other hand, Mo has been found to be solid solution strengthened by alloying with Nb⁶. Eventually the highest yield stress of Nb-40Mo-40TiC above 1673 K will be interpreted in terms of the rule of mixture.

Figure 4 shows the SEM micrographs indicating cracks introduced by indentation tests for Nb-20Mo-40TiC. While cracks propagate almost straight to a long distance in TiC of as-cast sample as shown in Fig.4(a), the length of cracks is distinctly reduced in annealed sample as shown in Fig.4(b). Vickers hardness and crack length measured by the indentation tests are summarized in Table 1, where crack length was measured from the corner of an indentation trace to the tip of a crack. The hardness values would be apparent because of extensive cracking around the indentation trace depending on composition and heat treatment. The average crack length of composites is smaller than that of monolithic TiC, and the crack length of annealed samples is less than half the length of as-cast samples.

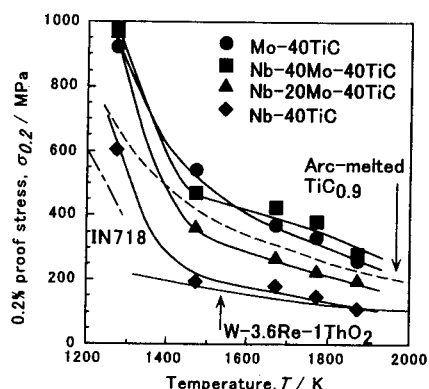


Figure 3. Temperature dependence of 0.2% proof stress of TiC/Mo(Nb) at $1.6 \times 10^{-4} \text{ s}^{-1}$.

Table 1. Vickers hardness and crack length measured by indentation tests

Sample	Hv (2.9N)	Crack length (μm)
TiC (monolithic)	2479	11
Nb-40TiC (as-cast)	971	4.6
Nb-40TiC (annealed)	1116	1.5
Nb-20Mo-40TiC (as-cast)	1823	7.5
Nb-20Mo-40TiC (annealed)	1213	2.4
Nb-40Mo-40TiC (as-cast)	1730	9.7
Nb-40Mo-40TiC (annealed)	1368	4.1
Mo-40TiC (as-cast)	1777	-
Mo-40TiC (annealed)	1636	7.8

This result indicates clearly that crack propagation is restrained by bcc precipitates in TiC. Furthermore, the average crack length increases as Mo concentration increases. This change of the average crack length with Mo content is attributable to the particle size of bcc precipitates, because the volume fraction of bcc precipitates is almost the same in each composite. It has been reported that the ductile phase toughening is effective when the particle size of a ductile phase is larger than the process zone at a crack tip⁷. In the present composites, however, the size of bcc precipitates is less than $1\ \mu\text{m}$ as shown in Fig.4. This particle size will be too small to act effectively as a ductile phase.

Fracture toughness was evaluated, therefore, by three point bending test using AM-, DS- and HP-processed Mo-40TiC with different thickness of Mo phase. X-ray diffraction analysis has revealed that Mo-40TiC in-situ composites prepared by AM, DS and HP processes are composed of TiC and Mo, indicating that TiC and Mo phases are thermally stable at the final annealing temperature, 2073 K. In arc-melted and annealed in-situ composites, fine eutectic microstructures are observed for Mo-23.5TiC and Mo-40TiC, as shown in Fig.5(a) and (b), respectively. TiC particles corresponding to dark areas were surrounded by continuous Mo phase in gray areas. The eutectic microstructure in Mo-23.5TiC appears to consist of colonies. On the other hand, large primary TiC particles can be observed in Mo-40TiC. It should be noted, however, that the thickness of Mo phase between TiC particles is similar for Mo-23.5TiC and Mo-40TiC, although the microstructures are quite different from each other. Fig.5(c) shows the microstructure of DS-processed Mo-40TiC, indicating that coarsening occurs during the processing. The thickness of Mo phase between TiC particles is found to increase by about 4 times through DS-processing. It was unsuccessful to create elongated microstructure along the growth direction at this DS condition. The reason is uncertain at present, but controlling of thermal gradient and growth speed (G/R) ratio and/or chemical composition will be needed to obtain the elongated microstructure. The microstructure of HP-processed Mo-40TiC is different from the melt-processed one, as shown in Fig.5(d). It is evident that nearly equiaxed Mo particles with sizes of about $10\text{--}20\ \mu\text{m}$ are distributed together with TiC particles. Some spherical pores are observed in TiC phase. It has been reported that the generation of pores originates from gas contamination³. Oxygen adsorbed on powder may react with carbon in TiC to liberate CO gas during hot pressing. If the gas is enclosed in TiC grains, pores will be generated. A density of TiC single phase was reported to be 92 %

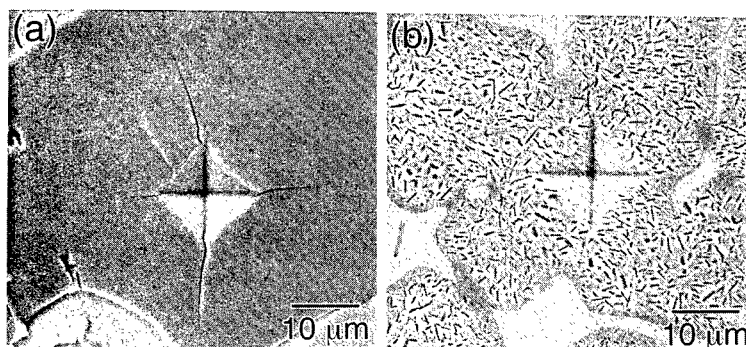


Figure 4. Microstructures after indentation test of (a) as-cast and (b) annealed Nb-20Mo-40TiC.

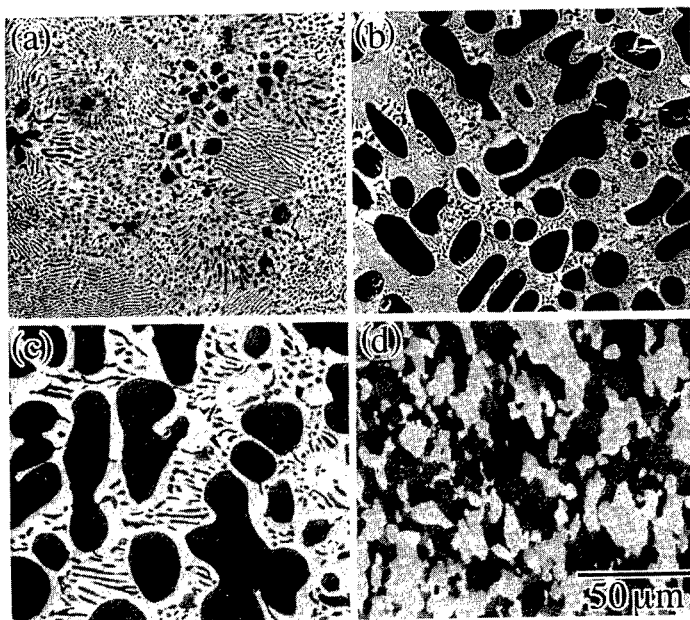


Figure 5. SEM micrographs of (a) AM Mo-23.5TiC, (b) AM Mo-40TiC, (c) DS Mo-40TiC and (d) HP Mo-40TiC.

on sintering in an induction furnace⁹. However, a density of HP-processed composite was found to be 98.1 % in this study, suggesting that HP processing enhances densification because of deformability of TiC at high temperature. It is interesting to note that Mo-40TiC subjected to different processes has almost the same volume fraction of Mo phase, but different features of microstructure.

Figure 6 shows the load-displacement (L-D curves) by SENB tests for (a) AM Mo-23.5TiC, (b) AM Mo-40TiC, (c) DS Mo-40TiC and (d) HP Mo-40TiC. Deviation from elastic deformation is seen in the L-D curves except HP Mo-40TiC. DS Mo-40TiC exhibits appreciable plastic deformation and yields the highest load (P_q). On the other hand, the values of peak load and displacement in AM Mo-40TiC are lower than those of DS Mo-40TiC. HP Mo-40TiC fractures during elastic deformation at a low load value. In order to investigate the difference of the L-D curves, fractography was examined for HP Mo-40TiC. Figure 7 shows SEM micrographs indicating (a) crack propagation and (b) fracture surface of HP Mo-40TiC. It is clearly seen that the crack in Fig.7(a) propagates in a zigzag

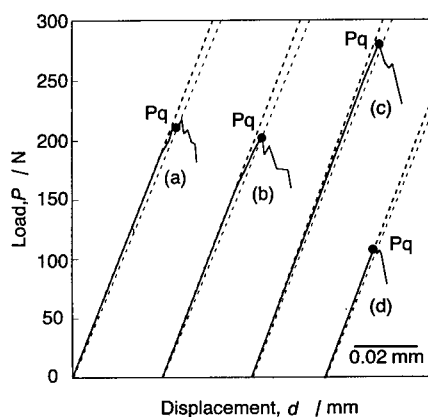


Figure 6. Load-displacement curves by SENB tests for (a) AM Mo-23.5TiC, (b) AM Mo-40TiC, (c) DS Mo-40TiC and (d) HP Mo-40TiC.

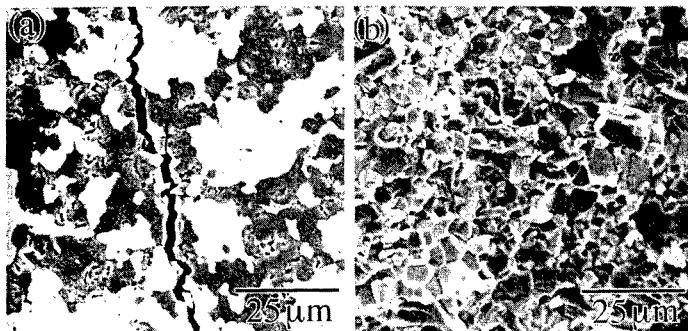


Figure 7. SEM micrographs indicating (a) crack propagation and (b) fracture surface of HP Mo-40TiC.

way and goes throughout TiC grains or boundaries of two phases, and no Mo particles show ductile fracture or crack bridging. Intergranular fracture is dominantly observed, although transgranular fracture is partially seen in TiC particles including pores, as shown in Fig.7(b). In ex-situ composites, a crack often initiates at a reaction phase between constituent phases, because the phase is mostly very brittle. By contrast, no reacted phase other than TiC and Mo is generated in the present in-situ composites. There could be other reason(s) for brittle behavior of Mo particles in the composite. Impurities in Mo such as oxygen have been reported to cause embrittlement in Mo¹⁰. Oxygen would be readily introduced during powder processing. In addition, pores generated by CO gas could be also an origin of fracture. At present it is difficult to identify the dominant source of fracture in HP composite, but it is suggested that oxygen plays an important role for the fracture. If this is the case, the fracture toughness of HP composite will be improved by developing powder metallurgy processes to eliminate or alleviate oxygen contamination.

Figure 8 shows the effect of volume fraction of Mo phase on fracture toughness evaluated by three point bend test as a function of thickness (λ) of Mo phase between TiC particles for various composites. It is clear that fracture toughness of TiC is increased from $3 \text{ MPa} \cdot \text{m}^{1/2}$ for monolithic TiC to a value over $10 \text{ MPa} \cdot \text{m}^{1/2}$ by controlling microstructure. From comparison of Mo-40TiC with Mo-23.5TiC, fracture toughness is not necessarily increased by increasing volume fraction of Mo phase. On the contrary, although Mo-40TiC in-situ composite subjected to various processes has almost the same volume fraction of Mo, fracture toughness varies significantly. This means that fracture toughness is improved by changing microstructure rather than increasing volume fraction of Mo. It should be noted that fracture toughness tends to increase with increasing thickness of Mo phase between TiC particles. This result is consistent with observations on WC/Co hard materials, where

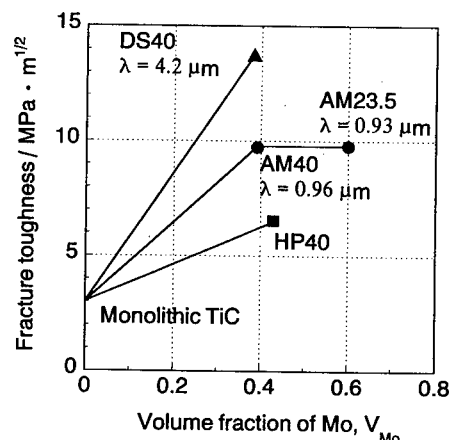


Figure 8. Effect of volume fraction of Mo phase on fracture toughness.

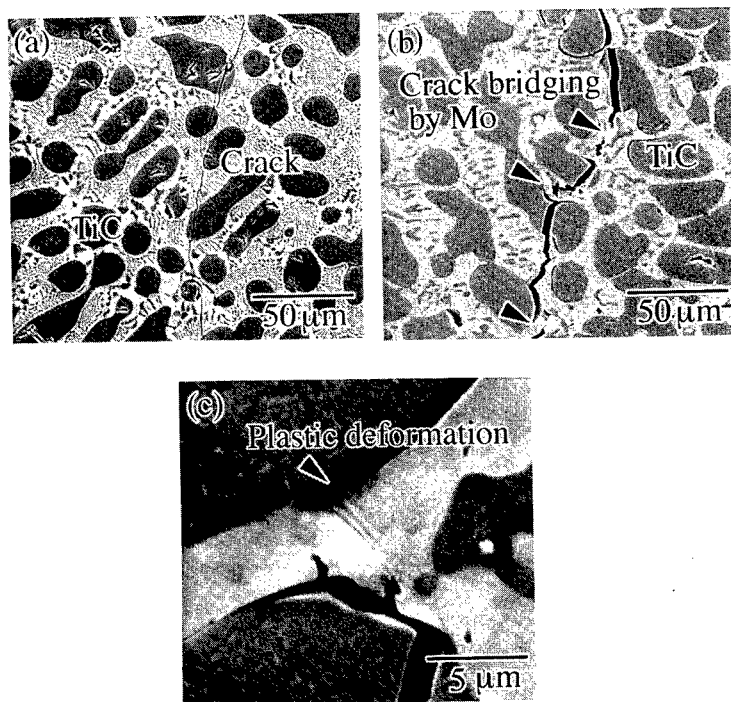


Figure 9. SEM micrographs indicating crack propagation in (a) AM Mo-40TiC, (b) DS Mo-40TiC and (c) DS Mo-40TiC at a higher magnification.

fracture toughness of WC/Co composites containing high volume fraction of Co depends on thickness of Co phase¹¹. Also, fracture toughness of laminated Al/Al₂O₃ composites has been reported to be proportional to the square root of thickness of Al phase¹².

Figure 9 shows SEM micrographs indicating crack propagation in (a) AM Mo-40TiC, (b) DS Mo-40TiC and (c) DS Mo-40TiC at a higher magnification. A crack propagates almost straight in fine eutectic regions, as shown in Fig.9(a). It appears that thin Mo layers between TiC particles are not resistant to crack propagation. In contrast, in Fig.9(b), thick Mo regions seem to work as bridges or ligaments on crack propagation. Evidently, Mo between TiC particles is heavily deformed, as shown in Fig.9(c). This is a clear evidence for high fracture toughness of DS Mo-40TiC. The crack also propagates at an interface between the two phases, which may be related to weak bonding of the interface. Since the coefficient of thermal expansion for TiC is higher than that of Mo, stress fields are generated around the interface on cooling after annealing. These stress fields will provide partial cracking at the interface. Many cracks are actually observed at boundaries between the two phases.

SUMMARY

Microstructures of fully annealed TiC/Mo(Nb) in-situ composites consist of TiC and Mo(Nb), and they are very stable at elevated temperature. Both Nb and Mo are soluble in TiC. Compressive yield strength above 1473 K of TiC/Mo(Nb) in-situ composites, Mo-40TiC and Nb-40Mo-40TiC, is higher than that of monolithic TiC. This is because the constituent phases, TiC and Mo, are significantly solid solution strengthened. Mo-40TiC fabricated by directional solidification shows the highest fracture toughness value of about 13 MPa · m^{1/2} among the composites investigated. Fracture toughness of melt-processed TiC/Mo in-situ composites does not necessarily depend on volume fraction of Mo, but depends on thickness of Mo phase between TiC particles. Crack propagation is accompanied with bridging and ligament formation due to the Mo phase, thereby increasing fracture toughness. To increase fracture toughness of powder metallurgy-processed Mo-TiC in-situ composites, contamination by gas impurities should be avoided.

ACKNOWLEDGEMENTS

The authors thank Mr. S. Watanabe and Mr. T. Sugawara for sample preparation. This work was supported by Research Fellowships of Japan Society for Promotion of Science for Young Scientist and Postdoctoral Fellowships for Research Abroad from Japan Society for the Promotion of Science.

REFERENCES

1. K.M.Prewo: *High Temperature/High Performance Composites*, ed. F.D.Lemkey et al., MRS Symp. Proc., Vol. 120, Pittsburgh, MRS, 1988, p. 145.
2. K.Ono and J. Moriyama: *Handbook of Ternary Alloy Phase Diagrams* Vol.6, ed. P.Villars, A.Prince and H.Okamoto, Materials Park, ASM, 1995, p.7200.
3. H.Holleck: *Handbook of Ternary Alloy Phase Diagrams* Vol.6, ed. P.Villars, A.Prince and H.Okamoto, Materials Park, ASM, 1995, p.7089.
4. V.N.Eremenko and T.Ya: *Poroshkovaya Met.*, 5: 3(1963).
5. S.Tsurekawa, M.Nakajima and H.Yoshinaga: *J.Japan Inst. Metals*, 58: 994(1994).
6. R.Jackson, H.J.Carvalhinsons and B.B.Argent: *J. Inst. Metals*, 96: 2469(1968).
7. D.L.Anton and D.M.Shah: *Intermetallic Matrix Composites*, ed. D.L.Anton et al., MRS Symp. Proc., vol.194, Pittsburgh, MRS, 1990, p. 45.
8. K.Tokumoto, H.Shinoaki, T.Kitada and S.Sakaguchi: *J. Japan Soc. Powder Metallurgy*, 41: 27(1994).
9. K.Hara, H.Yoshinaga and S.Morozumi: *J. Japan Inst. Metals*, 42: 1039(1978).
10. A. Kumar and B. L. Eyre: *Proc. R. Soc. Lond.*, A 370: 431(1980).
11. J. R. Pickens and J. Gurland: *Mat. Sci. Eng.*, 33: 135(1978).
12. M. C. Shaw, D. B. Marchall, M. S. Dadkhah and A. G. Evans: *Acta metall. mater.*, 41: 3311(1993).

DOUBLED FATIGUE STRENGTH OF BOX WELDS BY USING LOW TRANSFORMATION TEMPERATURE WELDING MATERIAL

Akihiko OHTA, Naoyuki SUZUKI, and Yoshio MAEDA

National Research Institute for Metals
1-2-1 Sengen, Tsukuba-shi, Ibaraki 305-0047, Japan

ABSTRACT

The low transformation temperature welding material is developed to improve the fatigue strength by introducing compressive residual stress around weld. The developed welding material which contains 10% chromium and 10% nickel, begins to transform from austenite to martensite at about 180°C and finishes it at room temperature. During the transformation, the weld metal expands. This expansion induces the compressive residual stress around the welded part of 20 mm thick JIS SM490 steel plate. The magnitude of welding residual stress is estimated to be about -100 MPa for the developed joint, while that is about 500 MPa for the conventional one. The stress ratio effect due to the compressive residual stress makes the fatigue strength doubled. The fatigue limit for conventional box welds is 65 MPa, while that for developed one is about 130 MPa.

INTRODUCTION

Fatigue fracture causes more than seventy percent of accidental failures. The large structures are made by welding. The welded part has very low fatigue strength as compared to the base plate. This low fatigue strength of the welded part is due to stress concentration¹⁾ and high tensile residual stress^{2,3)}.

Some methods have been proposed to improve the fatigue strength of welded joints by inducing the compressive residual stress at the fatigue critical zone⁴⁻⁶⁾. However, these methods require additional process after welding.

In this paper, it is shown that the fatigue strength of welded joints is improved by inducing compressive residual stress around the weld toe using welding wire developed for these experiments which expands near room temperature due to the transformation from austenite to martensite.

EXPERIMENTAL DETAILS

The material used in this experiment is 20 mm thick JIS SM490 steel plate. The chemical composition and mechanical properties of this steel and the welding wires are shown in Tables 1 and 2, respectively.

Table 1. Chemical composition of materials

Material		Chemical composition (wt %)							
		C	Si	Mn	Ni	Cr	Mo	V	Fe
Welding material	10Cr-10Ni	0.025	0.32	0.70	10.0	10.0	0.13		Remainder
	MIX50	0.10	0.39	0.90					Remainder
	KC60	0.07	0.49	0.96			0.42		Remainder
	KM80	0.06	0.20	1.21	2.66	0.80	0.48		Remainder
Base Material	SM490	0.16	0.43	1.40					Remainder
	HT580	0.14	0.31	1.41	0.05	0.04	<0.01		Remainder
	HT780	0.10	0.17	0.85	1.25	0.48	0.50	0.035	Remainder

Table 2. Mechanical properties and transformation properties of materials

Material		Mechanical properties				Transformation properties	
		Yield Strength (Mpa)	Tensile Strength (Mpa)	Elongation (%)	Impact value (J/C)	Temperature Ms(°C)	Strain eff(%)
Welding Material	10Cr-10Ni	*763	*868	*21	30/-20	180	-0.55
	MIX50	440	540	32	160/-20	590	0.67
	KC60	579	661	27	114/-5	450	0.23
	KM80	760	810	25	70/-40	330	-0.02
Base Material	SM490	366	538	30	221/0	550	0.29
	HT580	497	605	34	302/-5	460	0.33
	HT780	821	859	31	246/-5	440	0.05

* Obtained from ingot.

The developed 1.2 mm dia. welding wire which contains 10% chromium and 10% nickel has a special transformation property as shown in Fig. 1. The beginning temperature of transformation from austenite to martensite is 180°C while that of SM490 is about 500°C. This expansion induces compressive residual stress due to the constraints of the surrounding base metal.

The relationship between stress and temperature by allowing the strain of welding wire to be zero during cooling is shown in Fig. 2. It is clear that compressive stress is induced at room temperature in the case of developed welding wire. In contrast, tensile stress is induced in the conventional welding wire as shown in a broken line of Fig. 2. The box welded specimens of Fig.3 were made by gas metal arc welding. The shielding gas contains 80% argon and 20% CO₂. The welding voltage, welding current, welding speed and heat input were 30V, 220A, 30cm/min and 1.3MJ/m, respectively. The pass sequence is shown in Fig. 4.

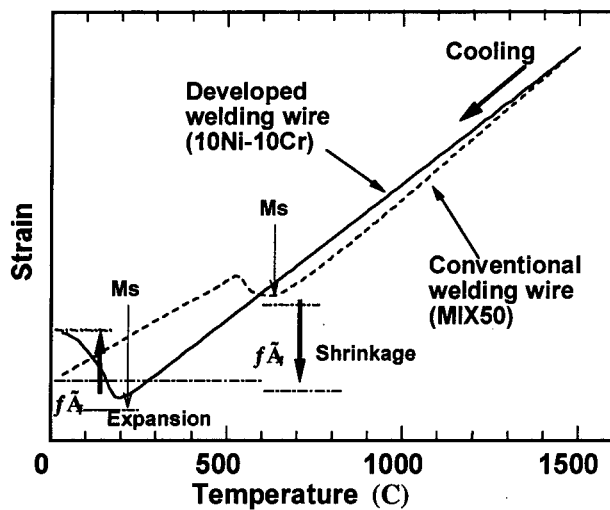


Figure 1. Variation of strain with cooling in constraint free condition.

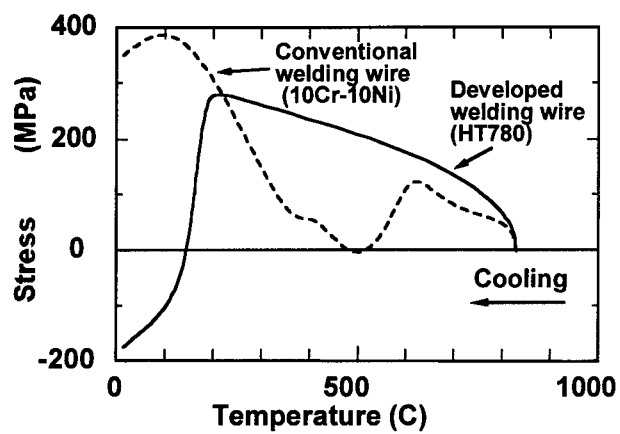


Figure 2. Variation of stress with cooling in zero strain controlled condition.

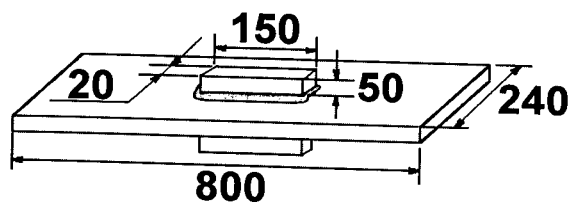


Figure 3. Fatigue specimen.

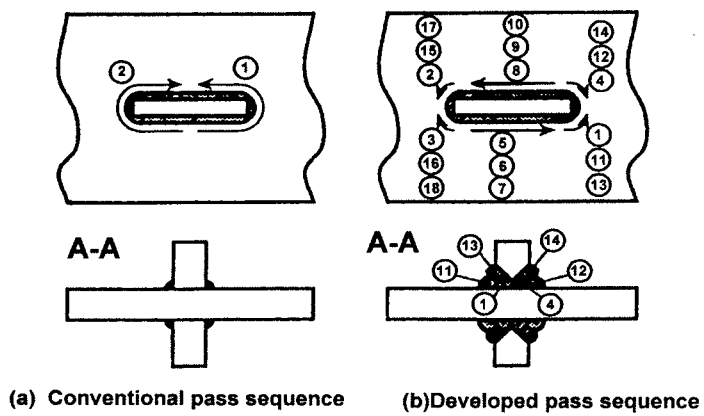


Figure 4. Edge preparation and pass sequence.

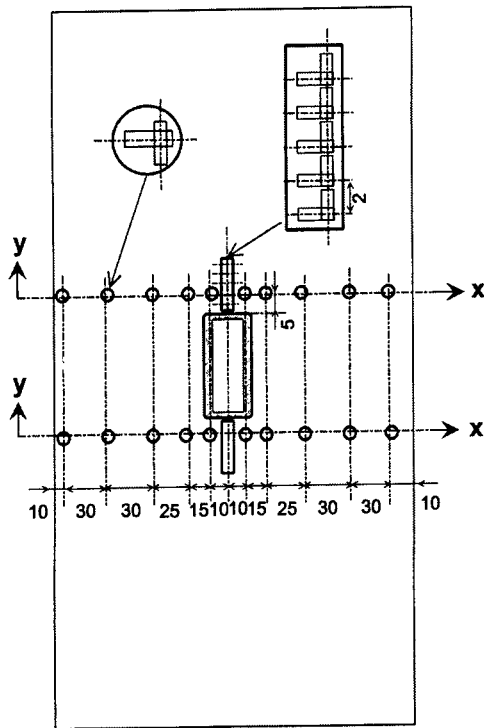


Figure 5. Position of strain gages to measure residual stresses.

This was determined by considering the difference of temperature rise between base plate and stiffener. That is, the volume of stiffener is small as compared with the base plate, and the temperature of stiffener tends to become higher. Therefore, if the longitudinal ends of stiffener were not welded by the welded passes of 1 to 4 prior to the longitudinal weld passes of 5 to 10, the expansion of stiffener became large as compare with the expansion of base plate. This difference in expansion between base plate and stiffener introduces tensile residual stress in the box welds after the cooling down to room temperature. The welding passes of 1 to 4 prevented this kind of residual stress, because both of the length between base plate and stiffener were the same before the temperature rise. The edge preparation and three passes were made to increase the volume of weld metal which is the driving element of residual stress. The residual stress distribution was measured by using rosette type strain gages and cutting around them. The position of strain gages bonded on specimen is shown in Fig.5. The fatigue tests were conducted on electrohydraulic machines in an ambient air. The stress ratio was 0. The test frequency varied from 2 to 50 Hz corresponding to the stress range.

RESULTS AND DISCUSSION

Fig. 6 shows the macroscopic appearance of welded part. The frank angle of weld toe made by the new wire is steep as compared with the conventional one. Fig. 7 shows the residual stress distribution. The distribution along the width of specimen at the cross section of the distant of 5 mm from weld toe shows the tensile residual stress around the middle of plate. In the cases of conventional wires, the distribution pattern is similar. So, the curve for SM490 with MIX50 is shown in Fig. 7 as an example. The intensity for conventional wire is large as compared with new wire.

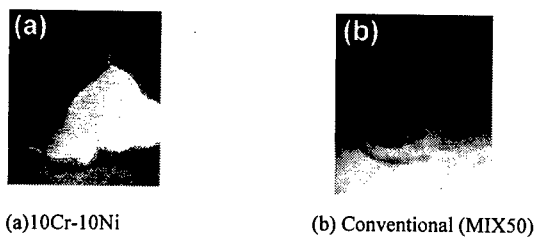


Figure 6. Macroscopic view of welded cross section at the end of attachment.

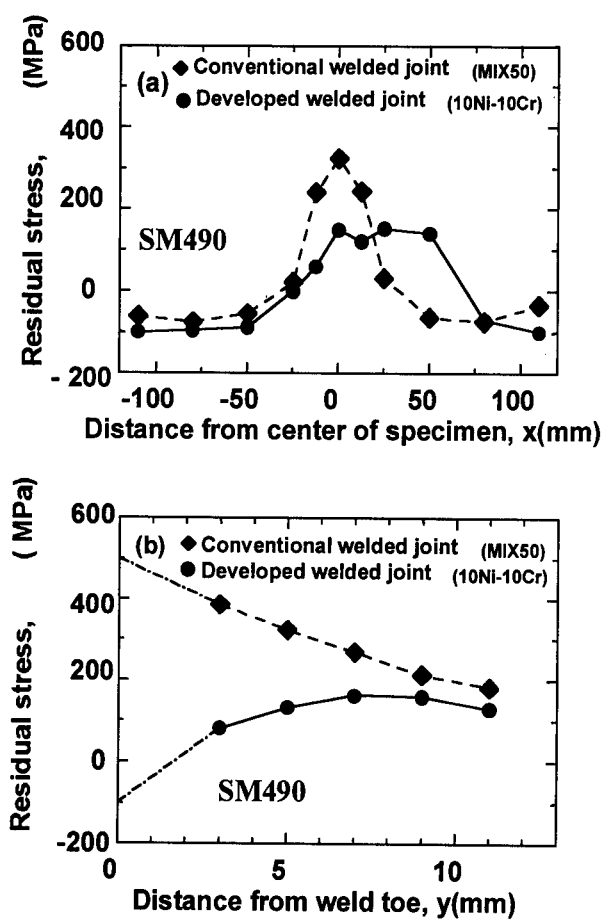


Figure 7. Residual stress distribution. (a) Width direction. (b) Parallel to loading direction

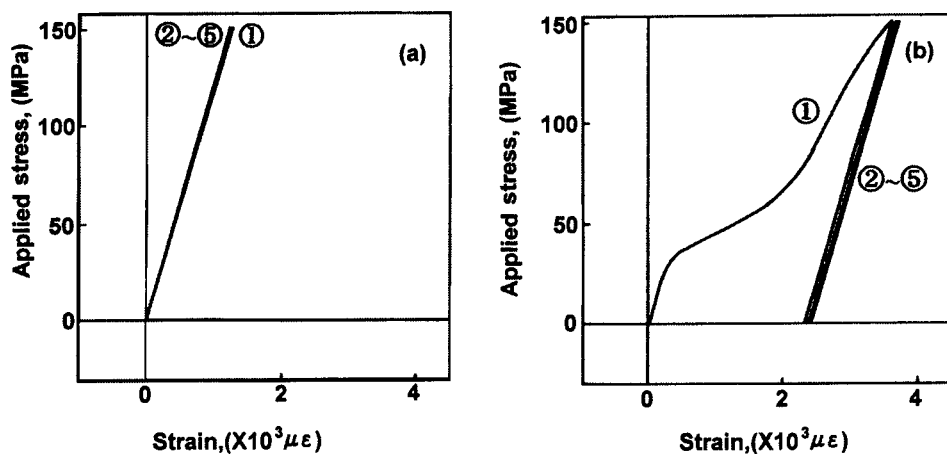


Figure 8. Variation of strain near weld toe with cycling. (a) 10%Cr-10%Ni. (b) Conventional (MIX50)

The trends along the axis parallel to loading direction are quite different between conventional and new wires. In the case of conventional wire, the residual stress increases monotonously with approaching weld toe. The magnitude of tensile residual stress at the weld toe exceeds the yield strength of material. In the case of a new wire, the residual stress distribution has a peak. The extrapolation of this trends suggests that the residual stress at the weld toe is compressive. The variation of strain at 5 mm distant from weld toe with cycling at the beginning period of fatigue test is shown in Fig. 8. The number in circle represents the repeating cycles in this figure. The plastic strain was observed in conventional joint, because the tensile residual stress near the weld toe is added to the applied stress. While in new joint, the elastic behavior is observed, because the compressive residual stress is subtracted from the applied stress.

Fig. 9 shows the fractured specimen. The fatigue crack initiated from blowhole in the weld metal made by new wire on the low stress range condition, while it initiated at the weld toe in the case of conventional wire under all stress range conditions. Fig. 10 shows the S-N diagram. The fatigue strengths for the conventional box welds are similar in spite of the variation of strength of steel and welding wire. The fatigue strength at 10^7 cycles is 65 MPa for the conventional wires. In the case of new wire, the fatigue strength is improved about 2 times at 10^7 cycles. The improved ratio decreases with the increase of stress range. This occurs from the increase of real stress ratio which is obtained from the sum of the residual stress and applied stress. That is, the compressive residual stress becomes effective in the lower stress range.



Figure 9. Fractured specimen.

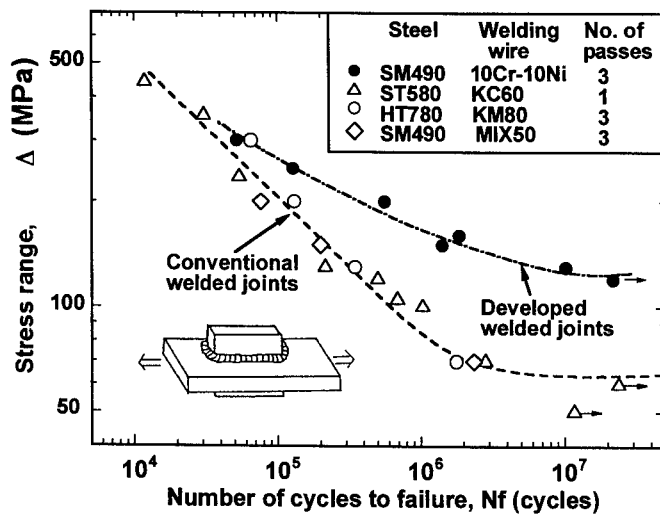


Figure 10. S-N curves.

CONCLUSIONS

The fatigue strength at 10^7 cycles of SM490 steel box welds as welded condition was improved about two times of conventional ones by using in the low transformation temperature welding wire which contains 10% Cr and 10% Ni. This improvement was realized by the compressive residual stress induced by expansion of the weld metal from austenite to martensite in the final part of cooling process.

REFERENCES

1. W.W.Sanders, A.T.Derecho, and W.H.Munse, Effect of External Geometry on Fatigue Behavior of Welded Joints, *Welding Journal* 44:49s(1965).
2. J.W.Fisher, Fatigue Strength of Welded A514 Steel Beams, Proc. Conf. Fatigue Welded Structures I, The Welding Institute, Abington, 135(1971).
3. A.Ohta, N.Suzuki, and Y.Maeda, Effect of Residual Stresses on Fatigue of Weldments, International Conference on Performance of Dynamically loaded Welded Structures, Welding Research Council, New York, 108(1997).
4. I.J.Polmear, Effect of Peening on the Fatigue Performance of Aluminum Alloy Fillet Welds, *Mat. Forum* 2:20(1979).
5. A.Ohta, Y.Maeda, and M.Kanao, Significance of Residual Stress on Fatigue Properties of Welded Pipes, *Int. J. Press. Vessels & Piping* 15:229(1984).
6. V.L.Trufiakov, P.P.Mikheev, Yu.F.Kudravstev and E.S.Stanukov, Ultrasonic Impact Treatment of Welded Joints, IIW Doc. XIII-1609-95, 1(1995).

THE EVALUATION OF THE FRACTURE STRAIN OF ITO FILMS ON POLYMERIC SUBSTRATES

Z. Chen, W. Wang, and B. Cotterell

*Institute of Materials and Research, 10 Kent Ridge Crescent
The Republic of Singapore 119260*

ABSTRACT

One of the mechanical issues concerning flexible organic light emitting device (OLED) is the flexibility, which is controlled by the fracture strength of the brittle films in the device. For example, the integrity of the anode material, the ITO film in the device directly controls the functioning of the device. Understanding the behaviour of these films under flexed condition will help maximize the flexibility of the device. Experiments have been devised to achieve this goal by bending the films of interests to gradually increased curvature over the point of film cracking, both under tension and compression. Fracture mechanisms under tension is found to be parallel channelling crack. Under compression the film fails by tunnelled buckling delamination prior to film cracking, which superficially looks very similar to the tensile cracking if observed under an optical microscope or lower-resolution SEM. Based on the understanding of the thin film mechanics on the above phenomena, we are able to calculate the fracture toughness of the ITO film, as well as to have an estimation of the film adhesion toughness. These parameters serve as the design values for flexible devices. Ways to improve the flexibility are also discussed from device design point of view.

INTRODUCTION

There is a general category of thin, layered device that has thin film electrical components inside, such as the liquid crystal display, organic solar cell and organic light emitting displays (OLED). Advantage is gained by making them flexible. The OLED has a promising future in panel display industry not only because it can be made flexible, but also because it possesses other unique properties, such as light-weight, wide display angle, high resolution, etc [1-3]. Our motivation comes from the device structural design that requires to know the limit of flexing of the device. In this type of device, the anode materials are usually made of transparent conducting oxide (TCO) such as Indium-Tin Oxide (ITO). These materials are ceramic and are brittle by nature, which has become one of the key factors that limit the flexibility. Of course depending on the

design and materials selection, there might be other brittle components in the device but the use of TCO is inevitable. Our priority is to study the failure strain of this type of material under flexed condition.

An important issue about brittle thin film system is that the film cracking is often the reason behind the failure. The fracture toughness will therefore be used as a general, scalable parameter for the design. It should also be pointed out that the fracture toughness of thin film is usually different, if not at all unavailable, from the values measured in the bulk material. Adhesion between the film and its substrate is another important issue and is often not straight forward to measure. We will in this paper attempt to evaluate both the fracture toughness and the adhesion strength of the ITO film through our novel testing scheme. Obviously this has to be done based on the understanding of the failure mechanisms.

EXPERIMENTAL DETAILS AND INTERPRETATION

Buckling type of test seems to be most appropriate for thin-sheet, layered structure in that large curvature, and thus large strain can be easily achieved (see Figure 1). When the films are clamped at both ends, the curvature will be even higher than the simple support for a same amount of displacement. Thus depending on the flexibility of the specimen the most suitable way of clamping can be selected accordingly.

Commercially available ITO-on-polymer substrates have been tested. A typical ITO coated polymer sheet has a total thickness of about 0.18 ~ 0.20 mm, while the ITO's thickness is around 100 nm. This paper will only demonstrate the methodology through the results of one particular product. The plane strain modulus of the ITO film and the polymer substrate materials are 250 GPa and 4 GPa, respectively. These values are measured by nano-indentation method.

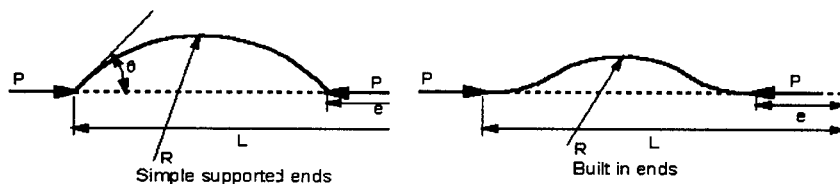


Figure 1. Buckling test. Left: simple support ends; right: built-in ends.

Fixtures that can do both type of gripping were home-made and the tests were carried out in an Instron machine, where the load and the displacement were recorded. Since the film is conducting while the substrate is non-conducting, an ohm-meter was used to monitor the resistance variation in the film along the loading direction. Generally it was observed that the resistance was very sensitive to the film integrity, which is understandable because the measured value is virtually the sheet resistance which is heavily influenced by

any sectioning through the film thickness. When the ITO film was under compression, the resistance might not change significantly when the film started to crack since at the compressive state the cracked parts would remain in contact with each other. We therefore had to return the displacement to the original position (zero displacement) and to record both values before and after the return. This was done for only limited number of times for each specimen therefore there will be no worries about the effect of fatigue.

The testing scheme in Figure 1 can be analysed as a plane strain beam loaded along its axis. Large deformation buckling theory of beams gives [4]:

$$\lambda = 2 \left[1 - \frac{E(k)}{K(k)} \right]; \quad \frac{l}{R} = 4K(k)k \quad (1)$$

where $K(k)$ and $E(k)$ are complete elliptic integrals of the first and second, $k = \sin(\theta/2)$, L is the original length of the beam, R the radius of curvature and $\lambda = e/L$ is the contraction ratio. For the two schemes in Figure 1, $l = L$ for simple support and $l = L/2$ for built-in ends. Therefore purely from geometric argument we will be able to calculate the radius of the bending from measuring the shortening of the beam, e . The strain at the outmost layer of the film is:

$$\varepsilon = \frac{y_f}{R} \quad (2)$$

where y_f is the distance from the film to the neutral axis of the composite sheet material, see Figure 2. Under the elastic regime mechanics of materials gives this distance as

$$y_f = \frac{(h_f + h_s) \left[\frac{\bar{E}_f}{\bar{E}_s} \left(\frac{h_f}{h_s} \right)^2 + 2 \frac{h_f}{h_s} + 1 \right]}{2 \left(1 + \frac{h_f}{h_s} \right) \left(1 + \frac{\bar{E}_f}{\bar{E}_s} \frac{h_f}{h_s} \right)} \quad (3)$$

in which h is the thickness of individual layer and the modulus $\bar{E} = E$ for plane stress and $\bar{E}' = E/(1 - \nu^2)$ for plane strain condition (in our case plane strain modulus will be used). The subscripts f and s are for the film and the substrate respectively. When $\frac{h_s}{h_f} \gg 1$, the position of the neutral axis can be quite accurately estimated by

$$y_f \approx \frac{h_f + h_s}{2} \quad (4)$$

which is the basis of the famous Stoney formula. On other situations Equation 3 has to be applied to enable an accurate solution. Equation 4 can also be applied to the other extreme when the film is much thicker than the substrate. Since in our case the ITO film is very thin, the applied strain on the film through the whole thickness is practically constant and can be given through the bent radius of curvature, R , as

$$\varepsilon = \frac{(h_f + h_s)}{2R} \quad (5)$$

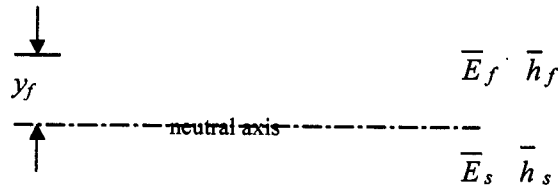


Figure 2. Neutral axis of the composite film of two materials.

Samples are tested with the ITO film placed on both tension side and compression side. Resistance-strain curves were recorded. It was found that the test generated very consistent results so that for each condition three to four samples would suffice. SEM observation was made on the tested samples afterwards.

RESULTS AND ANALYSIS

Figure 3a shows the results of normalized resistance by the value at the flat state versus the strain on the ITO film when the ITO is in tension. Figure 3b did the same for ITO in compression. On both plots a sudden increase of the resistance can be clearly identified which suggest that the film has been broken at that particular point of applied strain. We take the value at the point before the sudden rise as the critical strain. Clearly the critical strain under compressive loading is higher than under tension (1.7% versus 1.1%) for our tested samples. Therefore the device designer should take the tension results as the safety limit. The reason for higher compressive limit in this case should be clear after further analysis. Notice that these values are for the particular thickness of the film only. A more general parameter that can scale with the size of the film has to be found out after the mechanisms of the failure is understood.

Microscopic observation shows that the fracture pattern on ITO under tension is parallel channelling crack, see Figure 4a. Channelling crack of this kind has been studied by Beuth [5], Hutchinson [6], Hutchinson and Suo [7]. For film channelling crack, steady-state propagation establishes quickly after the crack advances for a few film thickness. It has been shown that for an existing partially-through defect in a stiff film on a compliant substrate it is energetically

favourable for the crack to run through the whole thickness once the initiation starts [5]. How the crack is initiated in the first place is not important since we put our conservative design point as the one to guard against crack propagation as outline by Hutchinson's [6] *fail safe* method. The essence of this approach is to design to prevent the steady-state crack propagation rather than crack initiation.

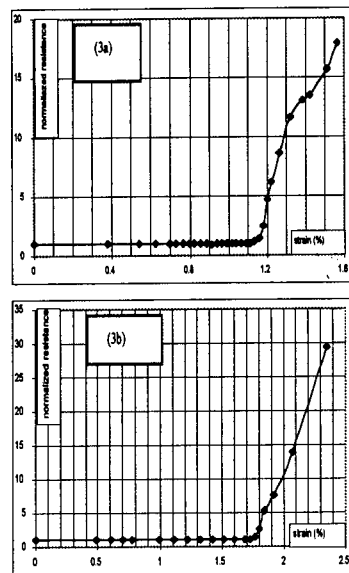


Figure 3. Typical measurements of the critical strain. 3a): ITO in tension; 3b): ITO in compression.

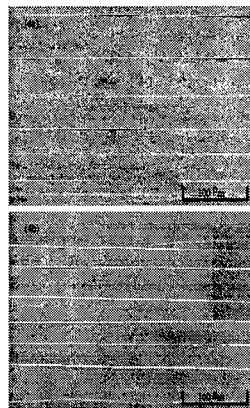


Figure 4. a) Microscopic graph of cracked ITO film in tension. b) ITO film in compression.

In the experiments it was observed that once a channelling crack forms, it and many others will propagate for large distance across the specimen leading to parallel multiple cracks. These cracks will not interfere with others until the spacing becomes very close (8 times the film thickness for the case studied by Thouless [8]). The steady state fracture toughness, G_{ss} is given as [5, 6]

$$G_{ss} = \frac{1}{2} \frac{\sigma^2 \pi h_f}{\bar{E}_f} g(\alpha, \beta) \quad (6)$$

The factor $g(\alpha, \beta)$ is a function of the Dundurs' parameter, α and β , which for plane strain condition are given by

$$\alpha = \frac{\bar{E}_f - \bar{E}_s}{\bar{E}_f + \bar{E}_s}; \quad \beta = \frac{\bar{E}_f \left(\frac{1-2\nu_s}{1-\nu_s} \right) - \bar{E}_s \left(\frac{1-2\nu_f}{1-\nu_f} \right)}{2(\bar{E}_f + \bar{E}_s)} \quad (7)$$

Of these two parameters α is much more important. The value of the g factor can be computed by finite element method as in [5]. For our ITO-polymer combination, $\alpha=0.968$ and $\beta=0.158$, assuming typical Possion's ratios for ceramic and polymer as $\nu_f=0.2$ and $\nu_s=0.4$, respectively. From Equation 6 we have the value of G_{ss} to be about 62 J/m^2 . This has provided a defects-tolerant design parameter for deposited ITO film.

Compressive cracking of the ITO films shows similar parallel patterns, as shown in Figure 4b. However when we employed a high resolution scanning electron microscope to observe the details of the cracking, it was revealed that the failure mechanism in this case is that the film delaminates and buckles, closely followed by film cracking. Details were reported elsewhere [9]. Plus the knowledge from Figure 4b, we conclude that the failure in this case is by steady-state tunnelled buckling delamination and film cracking. Again as in the tensile cracking, it is not possible to study the growth of the delamination at the tip of the failed film. Rather we study the steady state propagation by looking at the difference in the stored energies well beyond and far behind the crack tip. For film delamination and cracking, the total energy release rate is given by

$$G_t = G_d + \left(\frac{h_f}{2b} \right) G_c \quad (8)$$

where G_d and G_c are for the energies released by delamination and film cracking respectively and $2b$ is the delamination width.

The mechanics that describe stiff film on compliant film buckling has to take into consideration of the compliance from the substrate, which has not been done before. This piece of work has been summarised for publication by the authors [10] and the essence of this study will be highlighted here. For a stiff film on compliant substrate combination, Hutchinson's limiting solution [7] may not give correct value of delamination toughness in our particular case. For example, for the tested results in Figure 3b, buckling without considering the effects from the substrate gives the delamination toughness about 4.9 J/m^2 for a film thickness to delaminated width ratio of about 1:20. This ratio was measured from SEM and AFM pictures. It has to be emphasised that the delamination toughness is not very sensitive to the ratio around this region. Our new analysis takes into account the effect from the compliant substrate and has found out that the contribution to the energy release rate from the substrate can be significantly higher than from the film alone. Therefore ignoring the substrate's effect will

lead to a serious underestimation when the film is stiffer than the substrate. However when the film's modulus is no less than the substrate, Hutchinson's solution [6] is accurate enough by assuming a rigid substrate.

Based on the new analysis, the delamination toughness is estimated to be about 35 J/m^2 . Other interesting results are that when the delaminated width increases the mode mixity angle increases much slower than Hutchinson's results [7] towards mode II and the average energy release rate has a maximum. These results may explain why the delamination has a fixed width rather than spreading sideways without limit.

DISCUSSION

It has been shown that a brittle stiff film on a soft compliant substrate breaks under both tension and compression. Under tension the failure is by channelled cracking of the film while in compression it is tunnelled delamination and cracking. The fracture toughness and the delamination toughness derived from the tests will provide vital information for the device designer.

In our particular case, the critical strain under tension is less than the one under compression. However there is no reason that the compressive failure strain should always be higher than the tensile one. Clearly when the adhesion between the film and the substrate is weak, the delamination may happen under lower strain. The ratio of the film cracking toughness to the one of delamination could decide which mode is more critical. Knowing the tensile cracking toughness, G_c^{cri} , and the adhesion toughness, G_d^{cri} , the criterion is that when the ratio of delamination toughness to the cracking toughness is larger than the one of their energy release rates, i.e. when $\frac{G_d^{cri}}{G_c^{cri}} > \frac{G_d}{G_c}$, tension is more critical for

the same amount of strain. For the tested ITO on polymer, G_d/G_c is about 0.30 [9], which is less than the toughness ratio, 0.56, obtained in this study. Therefore it confirms our observation that ITO in tension is more critical. If the adhesion is weakened somehow in this materials combination to be lower than 20 J/m^2 , compressive crack could happen at lower strain than in tension.

From design point of view, it is always possible to maximize the flexibility by placing the most critical component near the neutral axis. There will be inevitably other laminated layers other than the two we have studied in a device. Therefore chances exist to achieve this by varying the thickness and the modulus of individual layers in the design. Take a simple example as in the ITO/polymer system: we can choose the layer on the other side of the ITO film as such that the new neutral axis is pushed closer to the film. Let's set the target to be the centre of the ITO film so that half of the film was above the neutral axis and half below. In this case the influence of the ITO film to the shift of the neutral axis is none and that the calculation can be done as if there were only two layers: the substrate and the "capping" layer. By substituting the film layer by the cap layer and equating $y_f = h_f$ in Equation 3, we have

$$\frac{\bar{E}_c}{E_s} = \left(\frac{h_s}{h_c} \right)^2 \quad (9)$$

where the subscripts c stands for the cap layer. By manipulating either the thickness or the modulus, extremely small radius of curvature can be achieved while not straining the ITO much. Of course we have not taken into account of the mechanical limit of the other "less dangerous" layers, which now may be more critical than the brittle film [11]. The same principle applies to any number of layers.

Another advantage of sandwich the brittle film, when the above centralisation is impossible (e.g. multiple brittle layers), is that the energy release rate will be lower than the one shown in Figure 2 under the same film stress, provided that the adhesion between layers is perfect. Therefore the allowed bending will be higher. The amount of improvement depends on the thickness and the modulus of the substrates. The upper limit will be about 58% in strain [9]. We wish to discuss this issue further in the future.

ACKNOWLEDGEMENTS

The authors would like to thank Dr. K. Y. Zeng in IMRE for the measurement of the Young's modulus of the ITO film and the polymer substrate by nano-indentation method. Mr. S. Y. Siew from Singapore Polytechnic has helped some of the tests during his industrial attachment to IMRE. Helpful discussion with Dr. Tsai and his colleagues in Instron Singapore Pte Ltd are gratefully acknowledged.

REFERENCES

- [1] G. Gu, Z. Shen, P. E. Burrows and S. R. Forrest, Transparent Flexible Organic Light-Emitting Devices, *Advanced Materials*, Vol. 9, 1997, pp. 725-728
- [2] G. Gu, P. E. Burrows, S. Venkatesh, S. R. Forrest and M. E. Thompson, Vacuum-Deposited, Nonpolymeric Flexible Organic Light-Emitting Devices, *Optics Letters*, Vol. 22, 1997, pp. 172-174
- [3] P. E. Burrows, G. Gu, V. Bulovic, Z. Shen, S. R. Forrest and M. E. Thompson, Achieving Full-Color Organic Light-Emitting Devices for Lightweight, Flat-Panel Displays, *IEEE Transactions on Electron Devices*, Vol. 44, 1997, pp. 1188-1203
- [4] S. J. Britvec, *The Stability of Elastic Systems*, Pergamon Press, NY, 1973
- [5] J. L. Beuth, Jr, Cracking of Thin Bonded Films in Residual Tension, *International Journal of Solids and Structures*, Vol. 29, 1992, pp 1657-1675
- [6] J. W. Hutchinson, *Mechanics of Thin Films and Multilayers*, Technical University of Denmark, 1996
- [7] J. W. Hutchinson and Z. Suo, Mixed Mode Cracking in Layered Materials, *Advances in Applied Mechanics*, Vol. 29, 1992, pp. 63-191
- [8] M. D. Thouless, Crack Spacing in Brittle Films on Elastic Substrates, *Journal of American Ceramic Society*, Vol. 73, 1990, pp. 2144-2146
- [9] Z. Chen, B. Cotterell et al, Foldability and Reliability Assessment of Flexible Opto-electronics, to be submitted
- [10] B. Cotterell and Z. Chen, Buckling and Cracking of Thin Films on Compliant Substrate under Compression, submitted to *International Journal of Fracture*, 1999
- [11] B. Cotterell and Z. Chen, *Mechanical Limits of OLED Devices*, IMRE Internal Report, 1998

AB INITIO STUDY OF STRUCTURE AND COMPRESSIBILITY OF GARNETS

V. Milman¹, R. H. Nobes², E. V. Akhmatkaya²,
B. Winkler³, C. J. Pickard³, J. A. White¹

¹MSI, The Quorum, Barnwell Rd, Cambridge CB5 8RE, UK

²FECIT, 2 Longwalk Road, Stockley Park, Uxbridge UB11 1AB, UK

³Institut für Geowissenschaften, Mineralogie/Kristallographie
Olshausenstr 40, D 24098 Kiel, Germany

ABSTRACT

The structure and properties of anhydrous end-members of the garnet family (ugrandite and pyrospite garnets) have been investigated as a function of applied pressure. We also calculated properties of hydrogrossular and hydropyrope at ambient and high pressure and explained the experimentally observed difference in the stability of the hydrogarnet substitution in grossular and pyrope. The study has been performed with the density-functional theory code CASTEP that uses pseudopotentials and plane-wave basis set.

The geometrical parameters of the unit cells containing in excess of 80 atoms have been fully optimised. The calculated static geometry, bulk modulus and its pressure derivative are in good agreement with the available experimental data. It is shown that the framework distortion achieved through the bending of the angle between the octahedra and tetrahedra is the main compression mechanism for all garnets studied.

INTRODUCTION

Garnets are abundant in the Earth's crust and upper mantle, and have therefore been the subject of numerous experimental studies aimed at elucidating their structure, stability, and the relationship between composition, structure and properties (Geller 1967; Meagher 1982; Geiger 1996). The

general chemical formula of a garnet can be written as $X_3Y_2Z_3O_{12}$. The common silicate garnets with $Z=Si$ are conventionally divided into two groups, pyrospites ($Y=Al$) and ugrandites ($X=Ca$). The members of the first group are pyrope ($Mg_3Al_2Si_3O_{12}$), almandine ($Fe_3Al_2Si_3O_{12}$) and spessartine ($Mn_3Al_2Si_3O_{12}$), while the ugrandites include uvarovite ($Ca_3Cr_2Si_3O_{12}$), grossular ($Ca_3Al_2Si_3O_{12}$), and andradite ($Ca_3Fe_2Si_3O_{12}$). All these garnets crystallise in the body-centred cubic space group $Ia\bar{3}d$ with eight formula units per unit cell.

The garnet structure can be described as chains of alternating corner-sharing ZO_4 tetrahedra and YO_6 octahedra, while divalent X cations occupy large dodecahedral cavities and are eight-fold coordinated. The unit cell of an anhydrous garnet contains 160 atoms which makes quantum mechanical studies of these systems extremely demanding. However, experimental data on high-pressure behaviour of rock-forming garnets are extremely scarce (Hazen and Finger 1989; Leger *et al.* 1990; Olijnyk *et al.* 1991; Lager and Von Dreele 1996; Zhang *et al.* 1998; Conrad *et al.* 1999) and often inaccurate as will be discussed below. First principles modelling offers therefore the best chance of predicting the behaviour of garnets under the extreme conditions found in the crust and upper mantle, thereby allowing a deeper understanding of the response of the garnet structure to increasing pressure.

The goal of the present work is to shed some light on compressibility mechanism of end-member anhydrous garnets, as well as to study the stability of hydrous garnets.

A previous study of aluminosilicate garnets (Akhmatskaya *et al.* 1999) showed that the density functional formalism provides a reliable theoretical framework for describing fine details of the effect of pressure on the garnet structure. The present systematic investigation of the family of silicate garnets shows that the use of parameter-free quantum mechanical calculations is going to have a significant impact on the future of the structural studies of complex inorganic compounds.

COMPUTATIONAL DETAILS

The quantum-mechanical calculations performed here are based on density functional theory, DFT (Hohenberg and Kohn 1964, Kohn and Sham 1965). Exchange–correlation effects were taken into account using the generalised gradient approximation, GGA (Perdew and Wang 1992), as implemented by White and Bird (1994). A spin-polarised version of this exchange–correlation functional was applied for almandine, spessartine, andradite and uvarovite, the garnets that contain $3d$ transition elements (Fe, Mn, or Cr). The total energy code CASTEP (MSI 1998) was used, which utilises pseudopotentials to describe electron–ion interactions and represents electronic wavefunctions using a plane wave basis set (Payne *et al.* 1992). We used ultrasoft pseudopotentials (Vanderbilt 1990) which require significantly less computational resources than norm-conserving potentials (Lin *et al.* 1993). The density mixing scheme as described by Kresse and Furthmüller (1996) was used for self-consistent solution of the density functional equations. An energy cut-off of 380 eV and a single Γ point sampling of the Brillouin zone were found to be sufficient to

obtain well converged structural properties. All calculations were performed on a Fujitsu VX vector processor.

Full geometry optimisations were performed. Calculations were considered converged when the maximum force on atoms was below 0.01 eV/Å. The calculated pressures were used to construct the equation of state, which was fitted to a third-order Birch–Murnaghan equation to obtain the bulk modulus, B , and its pressure derivative, B' . We used only the data for pressures below 30 GPa in order to use a procedure which is similar to that used in the data analysis of the experimental studies (Hazen and Finger 1989; Leger *et al.* 1990; Olijnyk *et al.* 1991; Lager and Von Dreele 1996; Zhang *et al.* 1998; Conrad *et al.* 1999).

RESULTS AND DISCUSSION

Equation of state for andradite and uvarovite

We present the results for these two garnets in more detail; our theoretical findings for aluminosilicate garnets (pyrope, grossular, almandine, and spessartine) have been presented elsewhere (Akhmatskaya *et al.* 1999). The calculated equation of state up to 100 GPa is compared with the experimental data for andradite and uvarovite in Figs. 1 and 2, respectively. A high-pressure single-crystal study of andradite (Hazen and Finger 1989) presents a rare source of experimental information on the compression mechanism of the garnet structure. One should bear in mind, however, that the highest pressure results from that study are likely to have been collected under nonhydrostatic conditions. It has been shown recently (Sinogeikin and Bass 1999) that even slight deviations from hydrostatic conditions can lead to an error of about 2% in the estimated bulk modulus. The presence of the uniaxial stress components has been also observed in the experimental investigation of uvarovite (Leger *et al.* 1990) so that the measured data above 10 GPa are not entirely reliable as is illustrated by a significant scatter of experimental points in Fig. 2.

The calculated equations of state for andradite and uvarovite agree well with the experiment, especially in the low pressure region where the measured data are more reliable. The equilibrium lattice constants, bulk moduli and their pressure derivatives for these and other garnets are compared to experiment in Table 1.

It is well known that the density functional results for lattice parameters of solids can be in error of 1–2%, and it is thus interesting to observe that the typical accuracy for silicate garnets is significantly better, of the order of 0.1%. The difference between calculated and measured cell parameters in these systems is comparable to discrepancies between different experimental results and is on the same scale as the variations caused by thermal effects or by impurities. The accuracy of the calculated bulk moduli is also very high, typically of the order of 1–2%, and only results for uvarovite exhibit a 12% error.

The compressibility data for uvarovite merits further discussion. Experimental results obtained by Leger *et al.* (1990) and shown in Fig. 2 can be divided into two pressure regions. The high-pressure data were obtained in a solidified pressure-transmitting medium, which caused significant

nonhydrostatic effects and resulted in large data scatter. The low-pressure data agrees very well with the calculated equation of state. A third-order Birch–Murnaghan equation fitted to the low-pressure subset of the experimental measurements gives $B=144\pm 8$ GPa (with B' fixed to 4.7) which is in perfect agreement with the theoretical value, see Table 1.

Table 1 shows that the density functional approach describes the compressibility of silicate garnets very accurately. Furthermore, even the “soft”

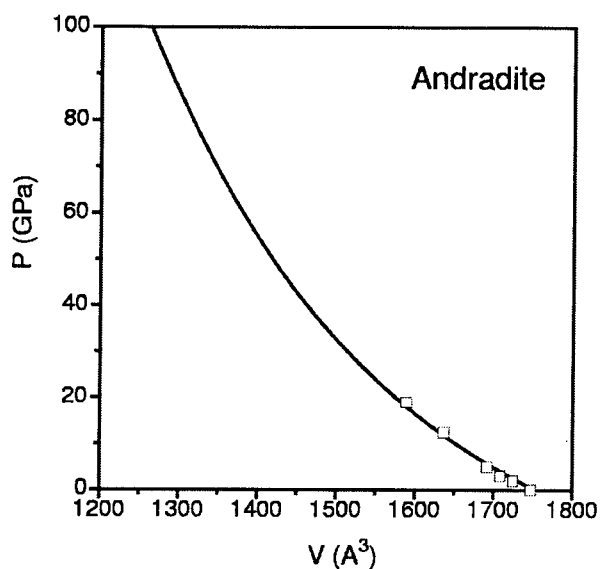


Figure 1. Equation of state for andradite. Present results are shown with the solid line, squares - experimental data (Hazen and Finger 1989).

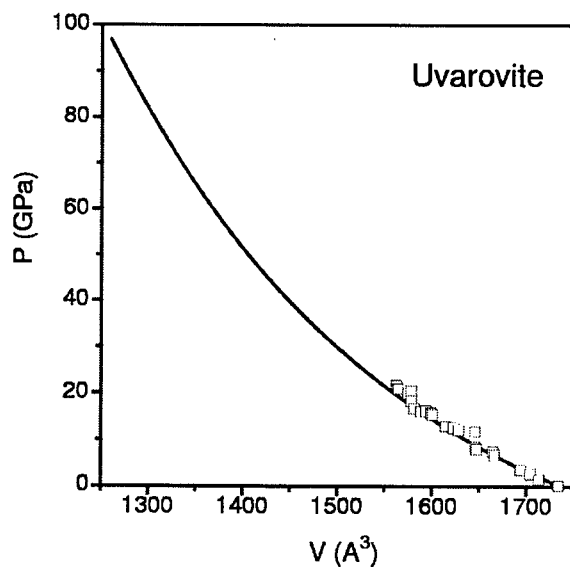


Figure 2. Equation of state for uvarovite. Present results are shown with the solid line, squares - experimental data (Leger *et al.* 1990).

hydrogrossular structure that is obtained as a result of the complete hydrogarnet substitution, $\text{Si} \leftrightarrow (\text{OH})_4$, is characterised equally well. The biggest discrepancies are observed for the garnets containing 3d-elements, and the reason might be related to the role of magnetic effects at low temperature. It is known that almandine orders antiferromagnetically on cooling to 7.5 K (Prandl 1971) and it has been suggested that the actual magnetic structure involves non-collinear arrangement of spins (Oliveira *et al.* 1989). An antiferromagnetic ordering has also been observed in andradite at 11.5 K (Murad 1984), and it is likely that both spessartine and uvarovite also exhibit magnetic ordering at low temperatures. All calculated results in this paper refer to the ferromagnetic ordering which was found to be stable at the GGA level of theory, while all experimental compressibilities refer to the paramagnetic structure that is stable at room temperature.

Table 1. Calculated and measured equation of state parameters for garnets.

		a, Å	B, GPa	B'
Pyrope	theory	11.428	170	4.3
	exp	11.439 ^a	171 ^a	4.4 ^a
Grossular	theory	11.857	166	4.3
	exp	11.837 ^b	165.7 ^c	5.5 ^c ; 4.2 ^d
Almandine	theory	11.509	176	4.2
	exp	11.507 ^e	175 ^f	3.0 ^g
Spessartine	theory	11.616	183	3.6
	exp	11.606 ^b	179 ^d	7.0 ^h
Andradite	theory	12.058	147	4.4
	exp	12.051 ⁱ	158 ^c	5.9 ^c
Uvarovite	theory	12.021	143	4.7
	exp	12.024 ^j	162 ^k	4.7 ^l
Hydrogrossular	theory	12.640	56	3.6
	exp	12.570 ^m	52 ^m ; 66 ⁿ	4.0 ^m ; 4.1 ⁿ

a) Zhang *et al.* (1998)

b) Geiger and Ambruster (1997)

c) Conrad *et al.* (1999)

d) Weaver *et al.* (1976)

e) Prandl (1971)

f) Sato *et al.* (1978)

g) Takahashi and Liu (1970)

h) Babuska *et al.* (1978)

i) Armbruster and Geiger (1993)

j) Carda *et al.* (1994)

k) Bass (1986)

l) Leger *et al.* (1990)

m) Lager and Von Dreele (1996)

n) Olijnyk *et al.* (1991)

The accuracy and reliability of the theoretical results appears to be at least as good as that of experimental data obtained from single crystal diffraction experiments at high pressure. In fact, in some cases experimental results are pronouncedly less reliable than the theoretical ones. One obvious reason is the difficulty of creating hydrostatic conditions at high pressure as discussed above. Fig. 3 illustrates the effect of experimental errors on the pressure dependence of

bond lengths in andradite. There are altogether five experimental points at nonzero pressures. Hazen and Finger (1989) have described the point at 2 GPa as unreliable, and indeed it does not follow a generally smooth pressure dependence of Ca–O and Fe–O bond lengths. The points at 12.5 and 19 GPa correspond to nonhydrostatic conditions, and Hazen and Finger (1989) noted that they observed significant distortions from cubic symmetry in these measurements. The remaining data do not provide sufficient information to study the compression mechanism of garnets.

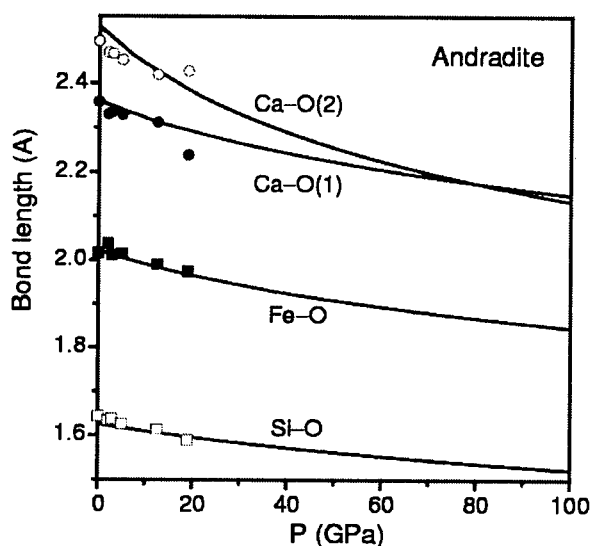


Figure 3. Pressure dependence of the bond lengths in andradite: solid lines - present results, symbols - experiment (Hazen and Finger 1989)

Polyhedral distortion under pressure

It is useful to introduce a quantitative measure of the polyhedral distortion and to analyse the compression mechanism in terms of the distortion indices. We characterised the garnet structure using the following indices: the bond length distortion, BLD, of the XO_8 dodecahedron; the edge length distortion, ELD, of the YO_6 octahedron; and the angular distortion, AD, of the YO_6 octahedron and of the SiO_4 tetrahedron (Baur 1974; Renner and Lehmann 1986; Akhmatkaya *et al.* 1999). The pressure dependence of these indices in andradite is illustrated in Fig. 4. The results for uvarovite are very similar. All polyhedra in these two garnets become more regular at pressures up to 30–35 GPa. Further compression changes the sense of the distortion of the YO_6 octahedra, see Fig. 4, i.e., they become irregular again.

These data together with the previous results for aluminosilicate garnets (Akhmatkaya *et al.* 1999) show that the trend for the SiO_4 tetrahedron and for the XO_8 dodecahedron to become more regular on compression is a general one. The only reliable set of experimental data is available for pyrope (Zhang *et al.* 1998) and it agrees with the theoretical observations. It appears that the

qualitative difference between the garnets studied here is in the response of the YO_6 octahedra to pressure. The results for spessartine are similar to those for andradite and uvarovite, i.e., the octahedra attain a regular shape at a moderate pressure and become distorted on further compression. The octahedra in pyrope and almandine become more distorted under pressure, and grossular is the only garnet where the octahedra get more regular in the whole pressure range studied.

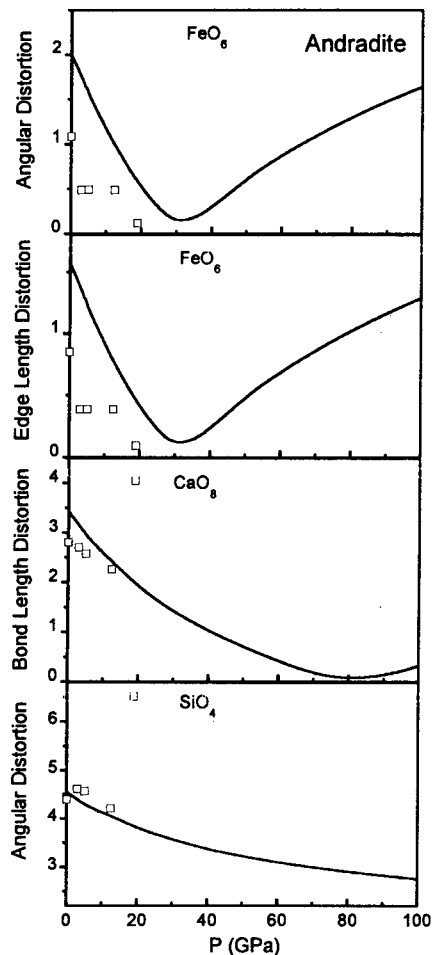


Figure 4. Pressure dependence of polyhedral distortions in andradite. Experimental data (squares) are from Hazen and Finger (1989).

The data presented above can be used to analyse the compression mechanism of garnets. We have shown before that the change of the Si–O–Al angle is responsible for the compression of the framework in aluminosilicate garnets (Akhmatskaya *et al.* 1999). The main fingerprint of this mechanism was found in the linear correlation between the relative change of the Si–O–Al angle and the relative change of all the distortion indices studied. We illustrate this in Fig.

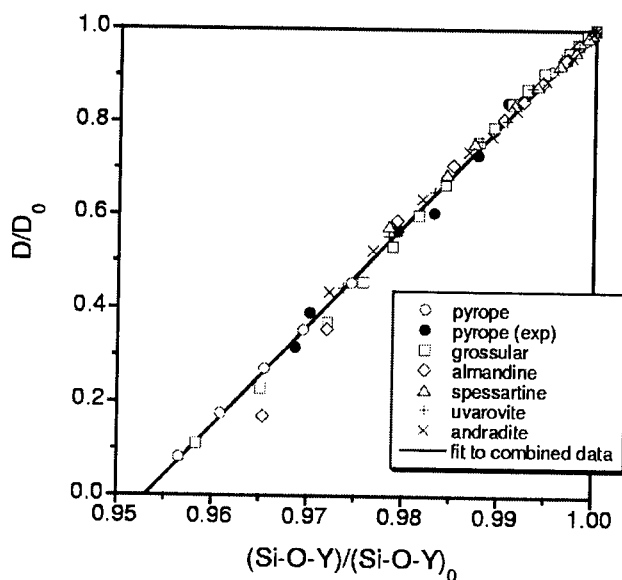


Figure 5. Linear correlation of the normalised BLD parameters (D/D_0) for XO_8 polyhedra with the relative change of the Si–O–Y angle. Experimental data for pyrope (Zhang *et al.* 1998) and calculated values for six garnets are described by the same linear fit.

5 that contains the combined data for six garnets including the experimental results for pyrope. The slope of the linear fit through all the data is 21.4, which coincides within the statistical error with the slope of 21.5 previously obtained for the aluminosilicate garnets only (Akhmatskaya *et al.* 1999).

Energetics of the hydrogarnet substitution

The changes of the structure and physical properties of nominally anhydrous minerals due to the incorporation of hydrogen are of great technological relevance. They are also of considerable interest in the Earth sciences in connection with the introduction of significant amounts of ‘water’ into the Earth’s mantle, which would significantly change its physical properties (O’Neil *et al.* 1993). Due to their abundance, stability and chemical variability, the garnet family is one of the most interesting mineral groups that may represent a possible storage medium for hydrogen in the Earth’s mantle. In grossular all the SiO_4 -tetrahedra can be replaced by O_4H_4 complexes and hence it has been possible to determine accurately the structure and equation of state of hydrogrossular (katoite), $Ca_3Al_2(O_4H_4)_3$. However, in contrast to grossular, it has not yet been possible to introduce substantial amounts of hydrogen into garnets belonging to the pyrope group (Wilkins and Sabine 1973; Aines and Rossman 1984). Infrared spectroscopic studies show that there are several sites that hydrogen can occupy in pyrope garnets, and the hydrogarnet substitution is probably only one possible mechanism for hydrogen incorporation. It would therefore be of interest to establish why the hydrogarnet substitution in pyrope is energetically less favourable than in grossular.

The accuracy of the theoretical description of the hydrogrossular structure is illustrated by the data in Table 1. As a next step we carried out a geometry optimisation of the hypothetical hydropyrope to compare its structure and energetics with that of katoite in order to shed light on the relative stability of these two hydrogarnets.

The hydrogarnet substitution in pyrope is found to have a smaller effect on the lattice parameter than in grossular: the corresponding differences are 0.615 Å and 0.788 Å, respectively, when compared with theoretical lattice parameters of anhydrous minerals. This means that the volume effect of the hydrogarnet substitution is roughly 21% in grossular and only 17% in pyrope. This is the expected behaviour since on the basis of ionic radii Mg is generally considered to be 'too small' to occupy the large dodecahedra even in anhydrous pyrope. Any further expansion of the pyrope structure caused by the hydrogarnet substitution is thus energetically unfavourable if it involves an increase of the size of the dodecahedron. This constraint means that the OH groups in hydropyrope have to be closer to each other than in hydrogrossular, so that hydrogen bonding between these groups can develop even at ambient pressure. The balance between the related energy gain and the elastic strain involved in the expansion of polyhedra would determine the relative stability of hydropyrope and hydrogrossular.

The quantitative measure of the relative stability of these two hydrogarnets is determined by E_{rel} :

$$E_{\text{rel}} = [E(\text{grossular}) - E(\text{hydrogrossular})] - [E(\text{pyrope}) - E(\text{hydropyrope})].$$

This quantity conveniently can be determined without resorting to the formation energies of each garnet and it is not affected by, e.g., thermal corrections. We obtained $E_{\text{rel}} = 1.93$ eV, or 186 kJ/mol, which confirms that hydrogrossular is significantly more stable than the hypothetical hydropyrope.

It is more difficult to evaluate the absolute formation energy of hydrogarnets with respect to anhydrous garnets since this comparison has to include the enthalpy of SiO_2 and of liquid water. A rough estimate suggests that this value is close to zero for hydrogrossular, and is consequently equal to ~ -180 kJ/mol for hydropyrope. These results show that the expansion of the dodecahedral site due to the hydrogarnet substitution can only be sustained when the anhydrous structure contains a big divalent cation (e.g., Ca). This suggests that a further study of hydrous uvarovite and andradite can provide additional insight into the problem of water incorporation into the garnet structure.

CONCLUSIONS

We have shown that state-of-the-art quantum mechanical methods as implemented on high-performance vector processors are sufficiently robust and accurate to be used for predictive studies of complex systems with approximately 100 atoms in the unit cell. The results presented provide better

insight into properties and structures of garnets at ambient conditions and under pressure. In particular, we have demonstrated that the kinking of the angle between SiO_4 tetrahedra and YO_6 octahedra is the major compression mechanism in end-member pyrope and ugrandite garnets.

The hydrogarnet substitution is found to be energetically less favourable in hydropyrope than in hydrogrossular, which is consistent with experimental findings that only small amounts of hydrogen can be incorporated into the former.

REFERENCES

- Aines, R.D., and Rossman, G.R. (1984). *Water in Minerals - a Peak in the Infrared*, J. Geophys. Res. **89** 4059-4071.
- Akhmatskaya, E.V., Nobes, R.H., Milman, V., and Winkler, B. (1999) Z. Kristallogr. (in press).
- Armbruster, T., and Geiger, C.A. (1993) Eur. J. Mineral. **5** 59-71.
- Babuska, V., Fiala, J., Kumazawa, M., Ohno, I., and Sumino, Y. (1978) *Elastic Properties of Garnet Solid-Solution Series*, Phys. Earth Planet. Inter. **16** 157-176.
- Bass, J.D. (1986) *Elasticity of Uvarovite and Andradite Garnets*, J. Geophys. Res. **91** 7505-7516.
- Baur, W.H. (1974) *Geometry of Polyhedral Distortions - Predictive Relationships For Phosphate Group*, Acta Crystallogr. B **30** 1195-1215.
- Carda, J., Tena, M.A., Monros, G., Esteve, V., Reventos, M.M., and Amigo, J.M. (1994) *A Rietveld Study of the Cation Substitution Between Uvarovite and Yttrium-Aluminum Synthetic Garnets, Obtained By Sol-Gel Method*, Cryst. Res. Technol. **29** 387-391.
- Conrad, P.G., Zha, C.-S., Mao, H.-K., and Hemley, R.J. (1999) *The high-pressure, single-crystal elasticity of pyrope, grossular, and andradite*, Amer. Mineralogist **84** 374-383.
- Geiger, C. A. (1996) *An investigation of the microscopic structural and the macroscopic physicochemical properties of aluminosilicate garnets and their relationships*. Habilitationsschrift, Kiel University.
- Geiger, C.A., and Armbruster, T. (1997) $\text{Mn}_3\text{Al}_2\text{Si}_3\text{O}_{12}$ spessartine and $\text{Ca}_3\text{Al}_2\text{Si}_3\text{O}_{12}$ grossular garnet: Structural dynamic and thermodynamic properties, Amer. Mineralogist **82** 740-747.
- Geller, S. (1967) Z. Kristallogr. **125** (1967) 1-47.
- Hazen, R.M., and Finger, L.W. (1989) *High-Pressure Crystal-Chemistry of Andradite and Pyrope - Revised Procedures For High-Pressure Diffraction Experiments*, Amer. Mineralogist **74** 352-359.
- Hohenberg, P., and Kohn, W. (1964) Phys. Rev. **136** 864-871.
- Kohn, W. and Sham, L.J. (1965) Phys. Rev. **A140** 1133-1138.
- Kresse, G., and Furthmüller, J. (1996) *Efficient iterative schemes for ab initio total-energy calculations using a plane-wave basis set*, Phys. Rev. **B54** 11169-11186.
- Lager, G.A., and Von Dreele, R.B. (1996) *Neutron powder diffraction study of hydrogarnet to 9.0 Gpa*, Amer. Mineralogist **81** 1097-1104.
- Leger, J. M., Redon, A.M., and Chateau, C. (1990) *Compressions of Synthetic Pyrope, Spessartine and Uvarovite Garnets Up to 25-Gpa*, Phys. Chem. Minerals **17** 161-167.
- Lin, J.S., Qteish, A., Payne, M.C., and Heine, V. (1993) *Optimized and Transferable Nonlocal Separable Abinitio Pseudopotentials*, Phys. Rev. **B47** 4174-4180.
- Meagher, E. P. (1982) Silicate garnets. In: *Orthosilicates*, ed. by Ribbe, P.H., 25-66.
- MSI (1998) CASTEP User Guide. Molecular Simulations Inc., San Diego, CA.
- Murad, E. (1984) *Magnetic-Ordering in Andradite*, Amer. Mineralogist **69** 722-724.
- Olijnyk, H., Paris, E., Geiger, C.A., and Lager, G.A. (1991) *Compressional Study of Katoite [$\text{Ca}_3\text{Al}_2(\text{O}_4\text{H})_3$] and Grossular Garnet*, J. Geophys. Res. **96** 14313-14318.
- Oliveira, J. C. P. de, Costa, M. I. da, Schreiner, W. H., and Vasquez, A. (1989) *Magnetic-Properties of the Natural Pyrope Almandine Garnets*, J. Magnet. Mater. **79** 1-7.
- O'Neill, B., Bass, J.D., and Rossman, G.R. (1993). *Elastic Properties of Hydrogrossular Garnet and Implications for Water in the Upper-Mantle*, J. Geophys. Res. **98** 20031-20037.

- Payne, M.C., Teter, M.P., Allan, D.C., Arias, T.A., and Joannopoulos, J.D. (1992) *Iterative Minimization Techniques For Abinitio Total-Energy Calculations - Molecular-Dynamics and Conjugate Gradients*, Rev. Mod. Phys. **64** 1045–1097.
- Perdew, J.P., and Wang, Y. (1992) *Accurate and Simple Analytic Representation of the Electron-Gas Correlation-Energy*, Phys. Rev. **B45** 13244–13249.
- Prandl, W. (1971) *Z. Kristallogr.* **134** 333–343.
- Renner, B., and Lehmann, G. (1986) *Correlation of Angular and Bond Length Distortions in To4 Units in Crystals*, *Z. Kristallogr.* **175** 43–59.
- Sato, Y., Akaogi, M., and Akimoto, S. I. (1978) *Hydrostatic Compression of Synthetic Garnets Pyrope and Almandine*, *J. Geophys. Res.* **83** 335–338.
- Sinogeikin, S.V., and Bass, J.D. (1999) *Single-crystal elasticity of MgO at high pressure*, Phys. Rev. **B59** 14141–14144.
- Takahashi, T., and Liu, L. (1970). *J. Geophys. Res.* **75** 5757–5766.
- Vanderbilt, D. (1990) *Soft Self-Consistent Pseudopotentials in a Generalized Eigenvalue Formalism*, Phys. Rev. **B41** 7892–7895.
- Weaver, J. S., Takahashi, T. and Bass, J. (1976) *Isothermal Compression of Grossular Garnets to 250 Kbar and Effect of Calcium On Bulk Modulus*, *J. Geophys. Res.* **81** 2475–2482.
- White, J.A., and Bird, D.M. (1994) *Implementation of Gradient-Corrected Exchange-Correlation Potentials in Car-Parrinello Total-Energy Calculations*, Phys. Rev. **B50** 4954–4957.
- Wilkins, R.W.T., and Sabine, W. (1973) *Amer. Mineralogist* **58** 508–516.
- Zhang, L., Ahsbahs, H., and Kutoglu, A. (1998) *Hydrostatic compression and crystal structure of pyrope to 33 Gpa*, Phys. Chem. Miner. **25** 301–307.

SHORT-RANGE ORDERING KINETICS AND MICROSTRUCTURAL DEVELOPMENT DURING POST-DEFORMATION ANNEALING

M. SPANL, P. ROSENKRANZ, A. KORNER, W. PÜSCHL,
AND W. PFEILER

Institut für Materialphysik, University of Vienna, Strudlhofgasse 4, A-1090 Vienna, Austria

ABSTRACT

After plastic deformation the initial degree of short-range order (SRO), the contribution of point defects on ordering kinetics and the development of SRO in a defected structure were studied. In the present work the results of three different binary alloys (α -AuFe, α -AgZn, α -CuAl) are compared and discussed. Measurements of resistivity, differential scanning calorimetry (DSC) and microhardness were used to study short-range order kinetics within a defected microstructure. It was possible to separate resistivity changes caused by pure SRO changes from resistivity changes only due to defect annealing. Isothermal studies on the recrystallized alloy systems yield information on ordering kinetics. With a simple model for isothermal SRO-kinetics the separated data were fitted and the formation enthalpy, migration enthalpy and dislocation density for the deformed state were obtained. Differences in the annealing behaviour of the deformed microstructure between α -AgZn and α -CuAl as obtained by transmission electron microscopy (TEM) and light microscopy are discussed briefly.

INTRODUCTION

Interaction between the atoms in a binary solution usually causes them to be distributed over the lattice positions in a non-random way. Short-range ordering (SRO) results if unlike neighbours are preferred. Most investigations of SRO have been done in the fully recrystallized state.

Due to the technical application of such materials it is important to study their physical properties in the more realistic state of a certain degree of deformation. An obvious point of interest is the interaction between deformation induced defect structures and ordering kinetics. During post-deformation annealing many processes take place simultaneously affecting each other in some way: a) development of SRO over a broad temperature interval depending on the alloy system; b) processes of defect annealing (recovery, recrystallization) which occur in different stages [1,2]; c) these various

processes are influenced by the continuous change of concentration of thermal and deformation-induced vacancies.

Studying changes of electrical resistivity after adequate temperature treatment is a sensitive tool for the investigation of changes in SRO [3]. The establishment of SRO and most processes of defect annealing are brought about by formation, migration and annihilation of point defects. Whereas the point defects themselves due to their very small resistivity contribution are not registered, one observes the defect mediated changes of SRO (SRO-amplifier). To get a picture of the interaction between development of SRO and defect structure it was tried to characterise the different annealing stages which occur during isochronal annealing. Measurements of microhardness, resistivity and differential scanning calorimetry (DSC) were well suited for this purpose. During annealing in the recrystallized state only SRO-induced resistivity changes are present, whereas in the deformed state a contribution by defect annealing is superposed. It is therefore necessary to separate both contributions if we want to compare the pure SRO-induced resistivity changes in the deformed and recrystallized state.

In this paper former results on α -AgZn and α -AuFe [4-6] are compared with newer ones of α -CuAl. The following aspects are discussed in this paper: (i) the microstructural development during post deformation annealing, (ii) the development of SRO in a deformed structure, (iii) the initial degree of SRO in the as-deformed state, (iv) the contribution of quenched-in surplus vacancies on ordering kinetics.

EXPERIMENTAL PROCEDURE

Polycrystalline samples of Cu-15at.%Al, Ag-21at.%Zn and Au14at.%Fe were deformed by cold rolling at room temperature (60% and 80% reduction in thickness). Resistivity measurement was done by the potentiometric method in liquid N₂ relative to a dummy specimen (accuracy $\pm 3 \times 10^{-4}$). DSC-measurements were performed in a Perkin Elmer DSC-7, and investigations of microhardness were done with a Paar MTH-4 microhardness tester. Meander shape resistivity samples were cut out by spark erosion whereas disc-shape samples (3mm in diameter) for DSC and microhardness studies were mechanically punched out. Temperature annealing was carried out in a standard resistance furnace under purified Argon atmosphere. For details about experimental procedures see [4,6].

RESULTS AND DISCUSSION

Defect annealing

In Fig. 1 the development of microhardness versus temperature during post deformation annealing for all investigated alloys is shown. The different stages of defect annealing are clearly resolvable and the onset of massive defect annealing is indicated for each material. From common interpretation of microhardness isochrones it is known that SRO (SRO hardening) and annealing

of point defects cause only small mechanical changes, whereas recovery and recrystallization processes are connected with rearrangement and massive loss of dislocations which causes a considerable decrease in microhardness. The following characterisation of the stages was made [7,8].

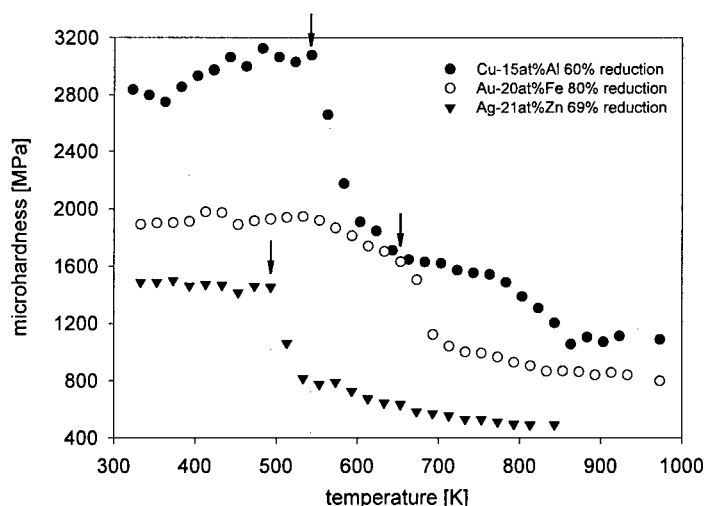


Figure 1. Microhardness versus isochronal annealing temperature of deformed Au14at.%Fe, cold rolled to 80% thickness reduction (○), Ag-21at.%Zn 69% reduction (▼) and Cu-15at.%Al, 60% reduction (●). Arrows and dotted lines mark the onset of massive dislocation loss.

Stage one is mainly related to recovery processes with minor rearrangement of dislocations and some SRO-hardening effects. It was determined by TEM [8,9] that nucleation of dislocation cells and subgrains starts in this range. This is followed by recrystallization processes in the second stage. The third stage is mostly related to grain growth.

A detailed study by TEM and light microscopy of the microstructural changes during post-deformation annealing in α -AgZn and α -CuAl showed two main differences when comparing the annealing behaviour of these two alloys. Whereas in α -AgZn the formation of cell structure is visible in the beginning of the annealing stage II it is assumed that in the case of α -CuAl cell structures were already formed during the early stages of the iterative rolling procedure. In spite of the high degree of deformation some of these cell structures remain and act as nuclei for the subsequent recovery process. The difference in cell formation could not be explained by the relevant dissociation width $G \cdot b / \gamma_{SFE}$ (G -shear modulus, γ_{SFE} -stacking fault energy, b -Burgers vector) of dislocations of these two alloys because there are hardly differences. It is known, however, that planar slip behaviour is connected with the presence of well established SRO in solid solutions [10,11]. Formation of dislocation cells is hindered by inhomogeneous dislocation movement (planar slip). This may be

the origin of the observed difference because the initial degree of SRO after similar deformation is lower in α -CuAl compared to α -AgZn (see next section Fig. 4 and Fig. 5). This way dislocation movement may be less hindered in α -CuAl and the formation of cell structure may occur during deformation already. Further, the growth process of the subgrains in α -CuAl seems to proceed independently of their local environment, whereas in α -AgZn it was found that growth stops at a size of about 5-7 μm in stage II until the whole sample volume is filled by these subgrains. Mobilisation of grain boundaries during subsequent annealing in stage III initiates a continuous growth process of the grains.

Fig. 2 shows the result of the DSC measurements of Cu-15at.%Al during heating with a rate of 10K/min. In the first run (deformed state) a step-like decrease in heat flow (exothermic reaction) occurs which is interpreted as the development of SRO and minor defect annealing processes, respectively. This is followed by a pronounced increase starting at about 550K resulting in a peak at about 580K. This onset of endothermic heat flow is in very good

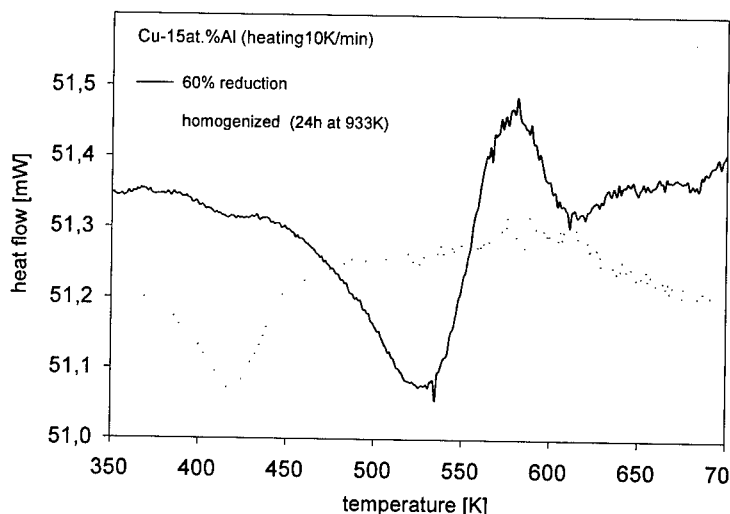


Figure 2. Heat-flow against temperature during DSC-runs on deformed (60% reduction in thickness (full line) and recrystallized (dotted-line) samples of Cu-15at.%Al. Heating rate: 10 K/min.

correspondence with the onset of massive defect annealing at 545K obtained from microhardness measurements. The endothermic peak nearly vanishes in the recrystallized state (quenched from 820K); only the smaller exothermic contribution due to the establishment of SRO is observed. DSC runs performed on the other systems yielded no significant results.

SRO-kinetics in the deformed state

To study SRO kinetics in deformed samples by resistivity measurement it is necessary to separate resistivity changes caused by defect annealing from those due to pure SRO which occur simultaneously. The separation procedure is based on isochronal measurements of as-rolled α -AuFe (microhardness (\circ) in Fig.1 and resistivity (\square) in Fig.3), which showed that relevant defect annealing occurred only above 650K. It was concluded that resistivity measurements during isochronal annealing of α -AuFe in the deformed state (∇ and \square in Fig.3) up to 650K reflect SRO-induced resistivity changes only because the same SRO-equilibrium curve was reached as in the recrystallized state. That this behaviour should also be followed by the other alloys was one of the assumptions of the separation procedure [6,9]. The supposition of undisturbed equilibrium values is supported by model calculations of SRO kinetics [8].

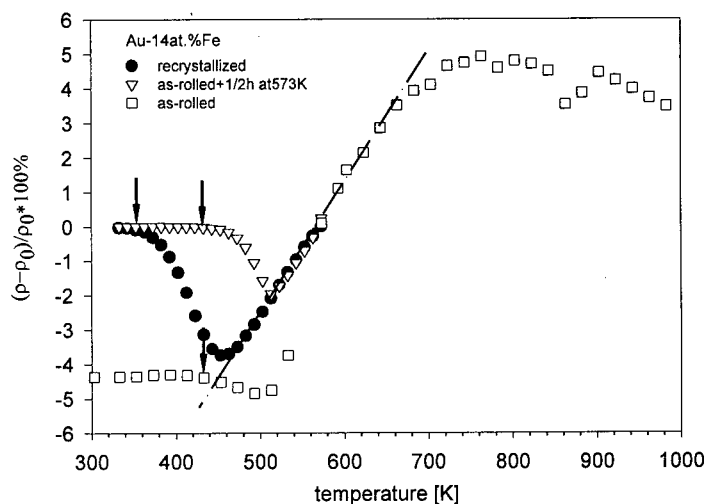


Figure 3: As-measured SRO-induced resistivity changes versus isochronal annealing temperature of Au-14at.%Fe, (\bullet) recrystallized (8h annealing at 1073K+1/2h at 573K), (\square) as-rolled (80%), (∇) as-rolled + 1/2h at 573K. Arrows mark onset temperatures of SRO-change; dotted lines mark starting level of isochronal annealing treatment; dashed-dotted line represents SRO equilibrium curve.

From the microhardness isochrones of Fig. 1 and the corresponding resistivity isochrones of the recrystallized state (\bullet in Figures 4 and 5) it is observed that for α -AgZn and α -CuAl a separation of effects due to defect annealing and SRO-processes is necessary because they take place in the same temperature range. With certain assumptions corresponding to common ordering behaviour the SRO-processes were separated [6,9] and are plotted in Fig. 4 and Fig. 5. In correspondence with the usual interpretation the isochrones

of Figs. 3-5 can be explained as follows. Depending on the alloy system at a certain temperature excess and thermal vacancies become mobile and a step-like decrease in resistivity is observed which is connected with an increase in the degree of SRO in these alloys. With increasing temperature the resistivity of all samples reaches a minimum. Subsequently, the system is able to establish SRO equilibrium states within the time interval of an isochronal step.

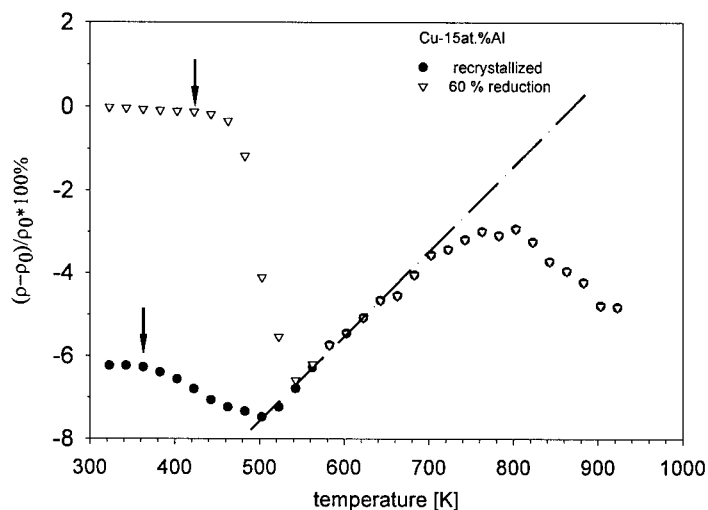


Figure 4. SRO-induced resistivity changes versus isochronal annealing temperature of Cu-15at.%Al, (●) recrystallized, (▽) as-rolled (60% reduction). Arrows mark onset temperatures of SRO-change; dotted lines mark starting level of isochronal annealing treatment; dashed-dotted line represents SRO equilibrium curve.

For a further increase of temperature resistivity follows the equilibrium line of SRO where the degree of SRO changes reversibly (dash-dotted line in Figs. 3-5). At high temperatures the isochrone bends away from the equilibrium line due to quenching effects (see e.g. Fig. 3 and 5). Analysis of the SRO induced isochrones yields the following results:

(a) The development of SRO in a deformed structure: In α -AuFe (well separated temperature ranges of SRO-change and defect annealing) the SRO equilibrium state is observed to be independent of deformation. We hold this to be valid also for the other alloys α -CuAl and α -AgZn with good justification.

(b) The degree of SRO in the as-deformed state: Assuming a one to one correspondence between electrical resistivity and the degree of SRO, the initial degree of SRO before isochronal annealing treatment can be estimated from the intersection of the horizontal line through the starting value of the isochrone (dotted line in Fig. 3-5) with the equilibrium-line of SRO (dash-dotted line in Fig. 3-5). From the dependence of resistivity on SRO it can be concluded that

the initial degree of SRO in the as-deformed state is *lower* in the case of α -CuAl and α -AgZn (higher initial resistivity value than for the recrystallized state) which is the expected behaviour if moving dislocations reduce the degree of order. In α -AuFe, however, the initial degree of SRO after plastic deformation is found to be *higher* compared to the recrystallized state. This unexpected behaviour may be due to a transient high concentration of deformation induced vacancies produced during cold rolling which leads to re-ordering of the material behind the moving dislocations.

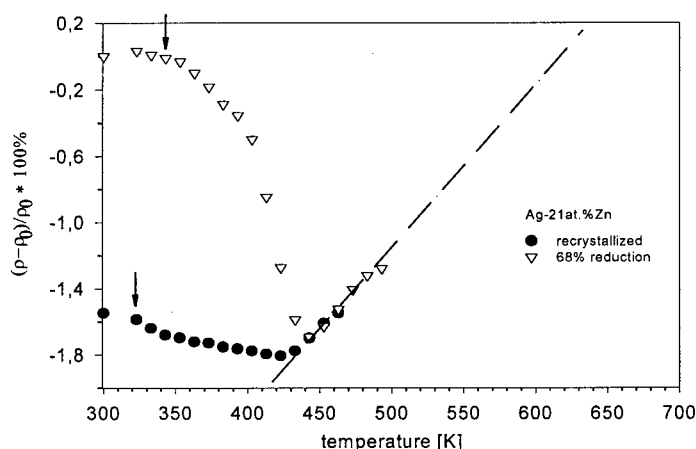


Figure 5. SRO-induced resistivity changes versus isochronal annealing temperature of Ag-21at.%Zn, (●) recrystallized, (▽) as-rolled (68% reduction). Arrows mark onset temperatures of SRO-change; dotted lines mark starting level of isochronal annealing treatment; dashed-dotted line represents SRO equilibrium curve.

(c) The contribution of quenched-in surplus vacancies on ordering kinetics:

SRO relaxation times are significantly influenced by pre-deformation. In all three alloy systems the evolution of SRO is considerably retarded in the as-rolled state in comparison to the recrystallized state. Obviously because of high dislocation density a big amount of point defects annihilates before contributing to ordering kinetics which is not the case for the recrystallized samples. This behaviour becomes very clear for α -AuFe (Fig.3) where the recrystallized state and the state as-rolled+1/2h at 573K start at the same initial degree of SRO. When the equilibrium-line is reached both states behave equally with respect to ordering. Starting from a considerably higher degree of SRO (see above) the sample in the *as-rolled* state shows the very same onset of atomic migration (arrows in Fig.3) as the state as-rolled+1/2h at 573K. This result is due to the unchanged defect structure in both states.

A simple model for SRO-relaxation [12] was fitted to the separated isochrones of pure SRO-induced resistivity changes in the deformed and recrystallized state. Migration and formation enthalpies as well as dislocation

densities where obtained from these fits which are listed in Table 1. The data in Table 1 are more or less equal in the deformed and the recrystallized state; it can therefore be concluded that the vacancy parameters are independent of the degree of deformation.

Table 1. Vacancy parameters as obtained from fitting a simple model for SRO kinetics to the separated pure SRO-induced resistivity isochrones

sample	formation enthalpy H_f [eV] $\pm 5\%$	migration enthalpy H_m [eV] $\pm 5\%$	dislocation density [cm ⁻²] $\pm 30\%$	pre-exp. factor τ_0 [min ⁻¹] $\pm 30\%$
Ag-21at.%Zn				
as-rolled (68%)	0.57	0.93	6×10^{12}	1×10^{15}
recrystallized	0.56	0.82	6×10^8	1×10^{15}
Au-14at.%Fe				
as-rolled (80%)	0.81	0.90	5×10^{13}	1×10^{16}
recrystallized	0.79	0.90	5×10^6	1×10^{16}
Cu-15at.%Al				
as-rolled (60%)	0.75	0.71	2×10^{12}	9×10^{12}
recrystallized	0.79	0.66	9×10^5	5×10^{12}

ACKNOWLEDGEMENT

Financial support by the Austrian 'Fonds zur Förderung der wissenschaftlichen Forschung' and the 'Hochschuljubiläumsstiftung der Gemeinde Wien' is gratefully acknowledged. A. K. wishes to acknowledge the financial support from the „Jubiläumsfonds der österreichischen Nationalbank“.

REFERENCES

1. Humphreys F.J. and Hatherly M., 1995, *Recrystallization and Related Annealing Phenomena*, Pergamon, Oxford.
2. Cahn R.W., 1983, Recovery and recrystallization, in: *Physical Metallurgy*, Cahn R.W., Haasen P., ed., North Holland Physics Publishing, Amsterdam.
3. Pfeiler W., *Investigation of short-range order by electrical resistivity measurement*, Acta Met. 36:2417 (1988).
4. Migschitz M., Garlipp W. and Pfeiler W., *Short-range order kinetics in α -AgZn for various states of post-deformation annealing after cold-rolling*, Acta Mater. 44:2831 (1996).
5. Migschitz M., Garlipp W. and Pfeiler W., *Resistometric study of short-range order kinetics in α -AgZn*, Mat. Sci. Eng. A214:17 (1996).
6. Migschitz M. and Pfeiler W., *Vacancy activation enthalpies of Au-Fe alloys determined from SRO-induced resistivity changes*, Mat. Sci. Eng. A206:155 (1996).
7. Spanl M., Rosenkranz P. and Pfeiler W., *Interaction of deformation and short-range order during post-deformation annealing in α -CuAl*, Mat. Sci. Eng. A234-236:541 (1997).
8. Migschitz M., Korner A., Garlipp W., Pfeiler W., *Changes of microstructure in α -AgZn during post-deformation annealing after cold rolling*, Acta Mater. 44:2821 (1996).

9. Spanl M., Korner A., Pfeiler W., *Changes of microstructure during post-deformation annealing in α -CuAl*, Scripta Mat. 41:505 (1999).
10. Gerold V. and Karnthaler H.P., *On the origin of planar slip in f.c.c. alloys*, Acta Metall. 37:2177 (1988).
11. Schwander P., Schönfeld B. and Kosterz G., *Configurational energy change caused by slip in short-range ordered Ni-Mo*, Phys. Stat. Sol. (b) 172: 73 (1992).
12. Schulze A. and Lücke K., *The influence of vacancies on short-range order formation in Au-Ag alloys*, Acta Metall. 20:529 (1972).

POINT DEFECTS IN NIAL ALLOYS UNDER PRESSURE

Alexander Y. Lozovoi⁽¹⁾, Ali Alavi⁽¹⁾, Pavel A. Korzhavyi⁽²⁾,
and Michael W. Finnis⁽¹⁾

⁽¹⁾ Atomistic Simulation Group, School of Mathematics and Physics
The Queen's University of Belfast, Belfast BT7 1NN
Northern Ireland, United Kingdom

⁽²⁾ Condensed Matter Theory Group, Physics Department
Uppsala University, SE-751 21 Uppsala, Sweden

ABSTRACT

We investigate the effect of elevated pressures on the point defect thermodynamics in NiAl alloys. A particular motivation for this study is due to the expected elimination of structural vacancies on the Al-rich side at high pressure. We employ the density functional theory to compute point defect energies as a function of pressure, which are in turn used as input to the Wagner-Schottky model. We find that at about 200 kbar a change in the constitutional defect from V_{Ni} to Al_{Ni} does take place. The extension of the Wagner-Schottky model by introducing elastic interactions between defects leads to the prediction of a qualitatively new phenomenon in the system, namely the appearance of an isostructural phase transition terminated at a critical point. Similar behaviour is expected in some other ordered off-stoichiometric compounds.

INTRODUCTION

Intermetallic B2 compound NiAl exists as a homogeneous phase over the wide composition range of 45 to almost 60 at.% Ni. It is highly ordered and practically does not disorder up to the melting point ($T_m = 1911$ K for the stoichiometric composition $Ni_{0.5}Al_{0.5}$). There are numer-

ous applications of NiAl alloys in industry; it is also a well-known model system for studying physical properties of ordered compounds (see [1] for a review).

In 1937 Bradley and Taylor have discovered [2] that off-stoichiometric NiAl alloys demonstrate a peculiar crystal structure: on the Ni-rich side excess Ni atoms substitute Al atoms on their sublattice (substitutional solid solution), whereas when Al atoms are in excess they remain on their own sublattice creating therefore vacancies on the Ni sublattice (subtractional solid solution). Since that time many other similar systems have been found. Such binary compounds, with substitutional defects on one side of stoichiometry and vacancies on the other, have been called "triple-defect compounds" [3], which is slightly misleading [4]; NiAl at elevated pressure turns out to be a good example to demonstrate that (see below).

Surprisingly, only little is known about NiAl at high pressure. Experimental information is rather poor: in this connection we can mention the study by Taylor and Doyle [5], in which the authors looked for β -manganese or γ -brass type structures in the Al-rich region of NiAl at temperatures 1000 – 1500°C and pressure up to 78 kbar: No change in the crystal structure was found, instead the authors reported that they observed the "partial filling" of structural vacancies. The B2 structure remained stable in a more recent investigation of stoichiometric NiAl compound up to a maximum pressure of 250 kbar by Otto, Vassiliou, and Frommeyer [6]. However, as argued in ref. [7], one can expect the change of the ground state crystal structure on the Al-rich side from subtractional to substitutional solid solution at high pressure due to the larger formation volume of Ni vacancies compared to Al antisites.

We report below the results of the first systematic study of point defect statistics in NiAl alloys at high pressure. We work within *ab initio* supercell density functional theory, in the local density approximation (LDA), in conjunction with simple thermodynamic models. A preliminary account of the present investigation has been published elsewhere [8] and should be viewed as complementary to the current paper.

NON-INTERACTING POINT DEFECTS IN ORDERED COMPOUNDS AT FINITE PRESSURE

We consider here an ordered alloy $A_{1-x}B_x$, which assumes that each of the alloy components (A or B) has its own well defined sublattice. Deviation from stoichiometry is accommodated by point defects, which are conventionally called *constitutional* defects. At any finite temperature

some *thermal* point defects are additionally generated: constitutional and thermal defects exist in equilibrium in the crystal with concentrations which minimize the Gibbs free energy G of the system at given temperature T and pressure p .

Variables

There are four possible types of point defects in an ordered crystal, namely the vacancies and antistructural atoms on the two sublattices; the possibility of any interstitial defects is neglected here. Following the notation introduced in ref. [9], we characterize the state of the crystal by six concentrations c_{ij} having a meaning of a concentration *per sublattice site* of the species i (atom A, atom B, or a vacancy V) on the sublattice j (A or B), e.g. c_{aa} , c_{vb} , etc. All the concentrations should be non-negative and are subject to the following constraints:

$$c_{aa} + c_{ba} + c_{va} = 1, \quad (1)$$

$$c_{ab} + c_{bb} + c_{vb} = 1, \quad (2)$$

and there is also a fixed number of atoms n_j of each kind ($j = a, b$):

$$N(c_{aa} + c_{ab}) = n_a, \quad (3)$$

$$N(c_{ba} + c_{bb}) = n_b, \quad (4)$$

where N denotes the number of sites per sublattice. Since there are 7 variables (c_{ij} and N) and 4 constraints Eqs. (1)–(4)), the number of independent variables is reduced to 3.

Thermodynamic potentials

Let us further assume that point defects do not interact and are randomly distributed over the crystal. These two assumptions form a basis for the Wagner-Schottky (WS) model (a gas of non-interacting point defects on well defined sublattices), in which the enthalpy of the crystal H is a linear function of defect concentrations.

In this case, at given external pressure p and some set of species concentrations characterized by the vector \mathbf{c} [10]:

$$\mathbf{c} = \{c_{ij}; i = a, b, v; j = a, b\},$$

the enthalpy of the system can be written as:

$$H(p, \mathbf{c}, N) = N \sum_{i,j} c_{ij} h_{ij}(p) = N \mathbf{c} \cdot \mathbf{h}(p), \quad (5)$$

where $\mathbf{h}(p)$ is a vector with partial species enthalpies $\{h_{ij}; i = a, b, v; j = a, b\}$ as the components. The partial enthalpies are considered as the

parameters of the WS model and could be extracted, for example, from *ab initio* supercell calculations.

Here we neglect any explicit temperature dependence of the enthalpy. We do not consider vibrational contribution to the entropy of the crystal either, assuming that the entropy of the system is purely the configurational entropy, which in the mean-field approximation depends only on the species concentration:

$$S(\mathbf{c}, N) = -k_B N \sum_{i,j} c_{ij} \log c_{ij} = -k_B N \mathbf{c} \cdot \log \mathbf{c} , \quad (6)$$

where k_B is Boltzmann's constant and in which we define $\log \mathbf{c}$ as a vector with components $\log c_{ij}$. Hence we arrive at the Gibbs free energy in the form:

$$G(p, T, \mathbf{c}, N) = H(p, \mathbf{c}, N) - TS(\mathbf{c}, N) = N \mathbf{c} \cdot (\mathbf{h}(p) + k_B T \log \mathbf{c}) . \quad (7)$$

The rest of the procedure is completely analogous to the case of zero pressure [11]: the equilibrium state of the alloy as a function of the temperature and pressure ($\mathbf{c}^{eq}(p, T)$ and $N^{eq}(p, T)$) should be found by minimizing the Gibbs free energy (7) with respect to species concentrations \mathbf{c} and the number of sublattice sites N , subject to constraints (1)–(4). As a result, one arrives at a set of the “mass-action” type equations (e.g., Eq. (11) in ref. [11]) which can be solved numerically or analytically at each value of the temperature and pressure. The only difference with respect to a zero pressure case is that in the corresponding expressions of ref. [11] the partial energies e_{ij} are replaced by the partial enthalpies h_{ij} . For example, chemical potentials are connected to the equilibrium concentrations as follows:

$$\begin{aligned} \mu_a(p, T) &= h_{aa}(p) - h_{va}(p) + k_B T \log [c_{aa}^{eq}(p, T)/c_{va}^{eq}(p, T)] , \\ \mu_b(p, T) &= h_{bb}(p) - h_{vb}(p) + k_B T \log [c_{bb}^{eq}(p, T)/c_{vb}^{eq}(p, T)] . \end{aligned}$$

After equilibrium concentrations $\mathbf{c}^{eq}(p, T)$ and the number of sites per sublattice $N^{eq}(p, T)$ are found, one can substitute them into Eqs. (5)–(7) to obtain the actual enthalpy, entropy, and Gibbs free energy of the system. The remaining thermodynamic functions can be then calculated using standard definitions. In particular, it is straightforward to show that the volume of the system V , defined as the partial derivative of G with respect to p , also depends on defect concentrations linearly:

$$V(p, \mathbf{c}^{eq}(p, T), N^{eq}(p, T)) = N^{eq}(p, T) \mathbf{c}^{eq}(p, T) \cdot \mathbf{v}(p) , \quad (8)$$

where $\mathbf{v}(p)$ is the vector of partial species volumes v_{ij} which are defined as

$$v_{ij}(p) = \frac{dh_{ij}(p)}{dp} .$$

The total energy E can be then found using the Legendre transformation as $E = H - pV$ and therefore is again a linear function of c^{eq} .

Constitutional and thermal defects

The division of point defects into constitutional and thermal looks rather artificial, as they are physically the same objects. The convenience of the division consists in the following. Let us write the equilibrium defect concentration c (hereafter we drop the superscript "eq" implying that all considered concentrations correspond to equilibrium) as a sum of the concentration of constitutional defects c^0 and thermal defects c^t :

$$c(p, T) = c^0(p) + c^t(p, T) . \quad (9)$$

Due to their definition, constitutional defects are independent of temperature. As in the $T \rightarrow 0$ limit one can neglect the entropy contribution, their concentration is defined by the minimum of the enthalpy H , which is a linear function of defect concentrations; therefore there is only one kind of point defect which enters c^0 . The magnitude of the concentration c^0 is defined by the deviation from the stoichiometry x and also by the particular type of point defect chosen by the system to be a constitutional one (for given x , the necessary concentration of vacancies should be about twice as large as the corresponding concentration of antistructural atoms). c^0 depends on pressure in the sense that there may be an abrupt change in the preferred constitutional defect as the pressure is varied.

As the composition of the alloy is fixed, thermal defects should always appear in a balanced manner on the both sublattices (see, e.g., ref. [12]). The simplest examples are a pair of vacancies, one on each sublattice (assumed not to be a bound divacancy), an exchange defect (a pair of antistructural atoms, one on each sublattice), and a triple defect (an antistructural atom on one sublattice and two vacancies on the other). Therefore the concentration of thermal defects c^t can be considered as a sum of concentrations of different composition-conserving defect combinations (CDs), which play the role of elementary thermal excitations in the defect structure of the system. Furthermore, since the concentration depends on temperature exponentially, there is usually only one CD (namely the lowest in enthalpy) which determines the concentration of each type of point defect.

More extensive discussion of the CDs in ordered compounds can be found in refs. [7, 13], see also the paper by Korzhavyi *et al.* in the current volume [4]. We just note here that even the change of the constitutional defect type can be conveniently described in terms of CDs: the substi-

Table 1 The simplest composition conserving defect combinations (CDs) and their formation enthalpies h_{CD} related to the partial species enthalpies h_{ij} in an ordered $A_{1-x}B_x$ compound (note, that only three CDs are independent). The last 3 columns contain the calculated formation enthalpies in NiAl ($A = \text{Ni}$, $B = \text{Al}$) at different external pressure: 0, $p_{cross} \simeq 192$ kbar, and 300 kbar respectively. The reverse interbranch defects IA- and IB- (not listed) are opposite in sign to IA+ and IB+ defects respectively; their enthalpies $h_{IA-} = -h_{IA+}$ and $h_{IB-} = -h_{IB+}$. The change of the sign of an interbranch defect enthalpy with pressure (IB \pm in case of NiAl) means the switch of the type of constitutional defects.

Defect combination	Notation	Constitution	$h_{CD} = f(h_{ij})$	h_{CD} (eV) in NiAl		
				0	p_{cross}	300 kbar
Triple-A defect	TA	$2 V_A + A_B$	$h_{TA} = h_{ab} + 2h_{va} - h_{aa}$	1.58	2.99	3.63
Divacancy	D	$V_A + V_B$	$h_D = h_{va} + h_{vb}$	2.18	3.69	4.37
Exchange defect	X	$B_A + A_B$	$h_X = h_{ba} + h_{ab} - h_{bb} - h_{aa}$	2.65	2.99	3.10
Triple-B defect	TB	$2 V_B + B_A$	$h_{TB} = h_{ba} + 2h_{vb} - h_{bb}$	5.44	7.38	8.21
Inter-branch-A+	IA+	$2 V_B - A_B$	$h_{IA+} = -h_{ab} + 2h_{vb} + h_{aa}$	2.78	4.39	5.11
Inter-branch-B+	IB+	$2 V_A - B_A$	$h_{IB+} = -h_{ba} + 2h_{va} + h_{bb}$	- 1.07	0	0.53
A-vacancy jump	JA	$V_B + B_A - V_A$	$h_{JA} = h_{ba} + h_{vb} - h_{va} - h_{bb}$	3.25	3.69	3.84
B-vacancy jump	JB	$V_A + A_B - V_B$	$h_{JB} = h_{ab} + h_{va} - h_{vb} - h_{aa}$	- 0.60	- 0.70	- 0.74

tution of a constitutional defect of one type by another corresponds to a so-called interbranch CD. Basically, the knowledge of the formation enthalpy of CDs h_{CD} , which are the corresponding sum of the CD constituents is enough for the exact description of point defect statistics within the WS model. We list for convenience in Table 1 the explicit expressions for h_{CD} of some useful defect combinations (note again that only 3 of them are independent).

SUPERCCELL CALCULATIONS

The defect enthalpies as a function of pressure were obtained within the finite-temperature density functional formalism [14] employing su-

percell geometry. Each type of defect was set up in a supercell, containing 48 lattice sites and having hexagonal symmetry. The total energy of the supercells was calculated at a number of different volumes (about ten). At each volume the positions of the atoms were relaxed until the maximal force component dropped below 1 mH/a.u. For each of the supercells, the obtained energy-volume dependence was interpolated in polynomial form and converted to the enthalpy as a function of pressure, which in turn was used as an input for the WS model or extended WS model, described in Sec. *Isostructural phase transition* and also in ref. [8].

Calculations were performed within the plane-wave pseudopotential approach. For the integration over the Brillouin zone we used 11 k -points in its 1/12 irreducible part. Al and Ni atoms were represented by the norm-conserving Troullier-Martins pseudopotentials, and the energy of 80 Ry was used as a cutoff for the plane-wave representation of the wave functions.

The calculated lattice parameter (2.897 Å), bulk modulus (1.69 Mbar), and formation enthalpy of stoichiometric NiAl (− 0.69 eV/atom) at zero pressure are in good agreement with the most recent experiments (2.886 Å [6], 1.56 ± 0.03 Mbar [6], and − 0.68 eV/atom [15], respectively). In addition, the calculated pressure-volume curve for stoichiometric NiAl is close to the experimental equation of states obtained in ref. [6]. This appears to be an example of the LDA error being compensated by errors in the pseudopotentials, since one expects the atomic volume to be underestimated in an all-electron LDA calculation.

RESULTS AND DISCUSSION

We discuss below the behaviour of point defects in $\text{Ni}_{1-x}\text{Al}_x$ with increasing pressure, as given by the WS model. In the notation we use in the paper, "A" means "Ni" and "B" means "Al".

Calculated CD formation enthalpies at zero pressure, crossover pressure p_{cross} , and 300 kbar are listed in Table 1. We are aware of only two articles, in which the experimental energy of triple defect in NiAl is reported. Henig and Lukas [16] give the value of 1.87 eV, and Bai and Collins [17] suggest the interval 1.65–1.83 eV (all energies refer to zero pressure). In recent measurements by Schaefer, Frenner, and Würschum [18], the vacancy formation enthalpy of 1.5 ± 0.25 eV in $\text{Ni}_{0.47}\text{Al}_{0.53}$ at high temperature (above 1000 K) has been found; we calculated the enthalpy in this region numerically using our CD energies and arrived at the effective vacancy formation enthalpy as large as 1.61 eV.

The good agreement of our results with experiment should be interpreted with caution. From a theoretical point of view and the results of extensive tests we have noted a significant dependency of the numerical results on the particular pseudopotential used for Al, and we do not believe our Al-pseudopotential gives an especially good representation of the very best all electron LDA results, represented by ref. [12], even though it may give better agreement with experimental results. Even this agreement is debatable in the case of experiments on point defects, which are subject to considerable uncertainty, but a full assessment of the situation is beyond the scope of this paper.

Constitutional defects in NiAl

At zero pressure, antistructural Ni atoms (Ni_{Al}) and vacancies on the Ni sublattice (V_{Ni}) are found to be the constitutional defects on Ni-rich and Al-rich sides respectively, which is in agreement with experimental observation [2]. With pressure increasing, $h_{\text{IA}+}$ remains positive and grows, therefore no change in the constitutional defect type is expected on the Ni-rich side. On the other hand, $h_{\text{IB}-}$ changes sign at the pressure $p_{\text{cross}} = 192$ kbar which indicates that at this crossover pressure antistructural Al atoms (Al_{Ni}) become more favorable than V_{Ni} , consequently the subtractional solid solution should be replaced by the substitutional one. A similar value for the crossover pressure (175 kbar) was predicted in ref. [7]. No experimental verification of the change in the ground state of the compound is yet known to the authors.

Thermal defects in NiAl

Once the constitutional defect type is determined, the CD that corresponds to a dominant thermal excitation can be easily found, at least in the low temperature limit. The straightforward way to do so is to calculate its *effective* formation enthalpy h^{eff} from the slope of an Arrhenius plot. It has been shown in ref. [7] that the effective formation enthalpy of a particular CD $h_{\text{CD}}^{\text{eff}}$ defined in this way, is just the formation enthalpy of the CD h_{CD} divided by the number of its constituents, excluding defects which coincide with the constitutional defects. For example, if the triple-Ni (TA) defect is the dominant thermal excitation, its effective formation enthalpy $h_{\text{TA}}^{\text{eff}}$ would be:
 $h_{\text{TA}}/1$ in Al-rich NiAl (subtractional solid solution),
 $h_{\text{TA}}/2$ in Ni-rich NiAl, and
 $h_{\text{TA}}/3$ in the stoichiometric NiAl and in Al-rich NiAl (substitutional solid solution),

where h_{TA} is the formation enthalpy of the TA defect. Comparing the effective enthalpies of possible CDs, one can identify the lowest one.

The condition of $T \rightarrow 0$ is not as strict as it looks. In most cases the concentration of point defects in NiAl as a function of temperature is close to a straight line in Arrhenius coordinates up to the melting point. That means that the slope at zero and high temperature is the same and thus the above consideration works rather well. Basically, it does not work in cases when the difference between the effective enthalpies of two different CDs creating the same point defect is of order of $k_B T$, where T is the temperature under consideration (as in case of a stoichiometric FeAl compound in which triple-Fe and exchange CDs are very close [19]).

We plot the effective formation enthalpies of the simplest defect combinations as a function of pressure on Fig. 1, assuming for each CD in turn that it is the lowest one. Based on these plots, one can conclude that in the whole pressure range under investigation the TA defect dominates at stoichiometry and in Ni-rich NiAl alloys, and the IB- defect is the lowest one in subtractional Al-rich alloys for $0 \leq p \leq p_{cross}$ [20]. For zero pressure, this agrees with existing first-principles calculations of point defect energies in NiAl [7, 12, 21]. We also obtain that the IB+ defect provides the lowest effective formation enthalpy in substitutional Al-rich alloys.

We draw attention to the fact that above the crossover pressure on both sides of stoichiometry NiAl alloys exist as substitutional solid solutions whereas the dominant excitation in stoichiometric NiAl is still a triple defect. As mentioned in the Introduction, there is no clear distinction in the literature between compounds demonstrating antistructural defects and vacancies on either sides of stoichiometry and those having a triple defect as a dominant thermal excitation at the stoichiometric composition (see ref. [22] for a recent review). However, as shown in ref. [4], these two features are not equivalent: neither the first follows from the second, nor the the second from the first. Up to now no compounds were known to the authors, which would fall in one of the respective area of the structure maps of ref. [4] to prove this statement *de facto*: NiAl above the crossover pressure seems to be such a case [23].

This is clearly seen on Fig. 2 (the figure is Fig. 3 from [4], adapted for the case of equiatomic compounds, on which we additionally plot the trajectory QR of NiAl compound with pressure increasing). Indeed, above some pressure the QR curve crosses the LP line on Fig. 2(a) and enters the (B_A, A_B) area, which means that NiAl becomes a compound with antistructural constitutional defects on both sides of stoichiometry. Meanwhile, on Fig. 2(b) the QR curve remains entirely within the (TA) region, therefore the triple-Ni defect dominates in stoichiometric

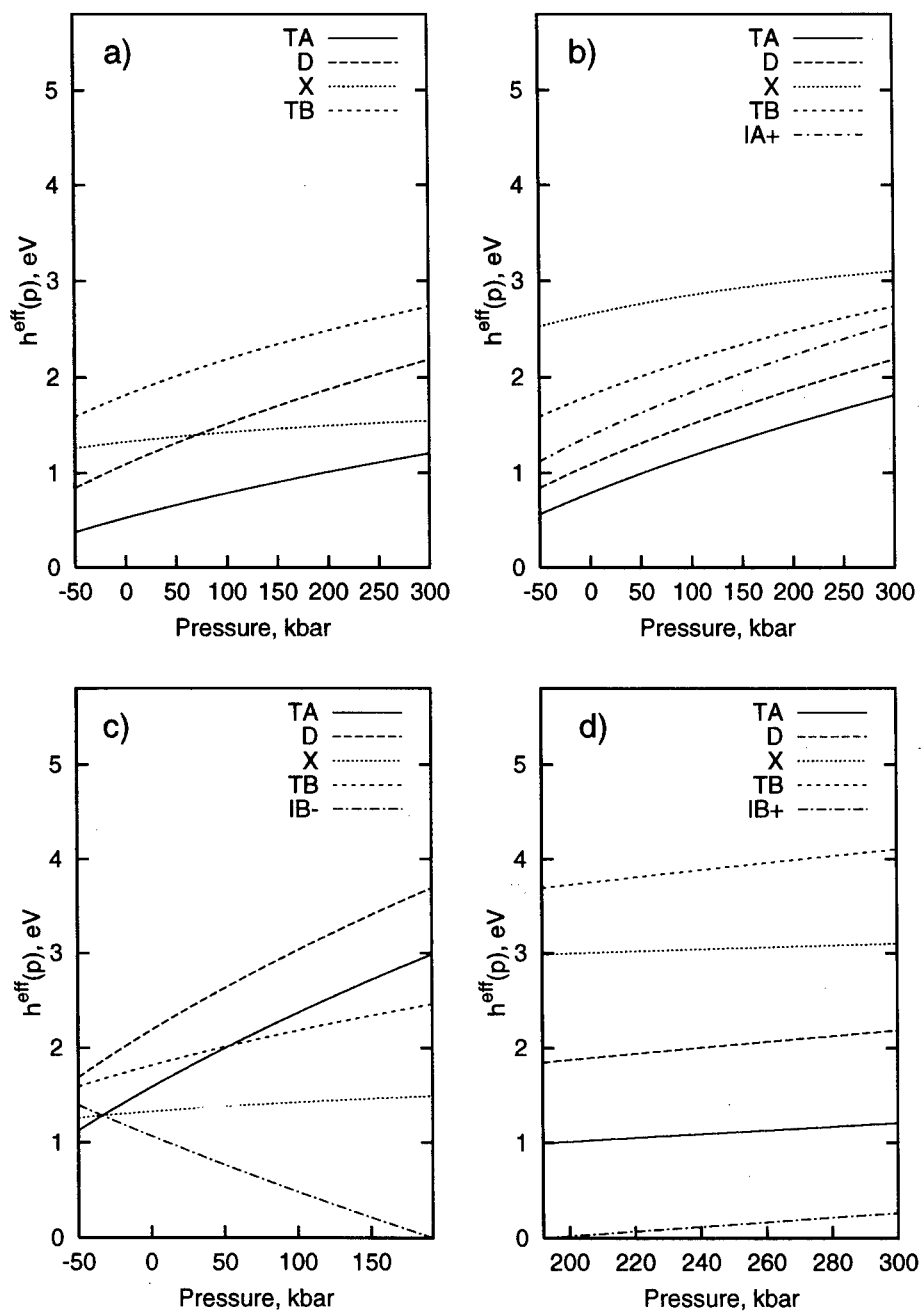


Figure 1 Pressure dependence of the effective formation enthalpies $h^{eff}(p)$ of the simplest CDs in the zero temperature limit: a) in stoichiometric NiAl compound; b) in Ni-rich NiAl alloys; c) in Al-rich NiAl alloys (subtractional solid solution); and d) in Al-rich NiAl alloys (substitutional solid solution) as given by the WS model.

NiAl. Interestingly enough, on figures Fig. 2(b-d) the QR curve always points toward the LK_iN triangle where the exchange defect X has the lowest effective formation enthalpy. This agrees with "common sense" expectations: at high enough pressure a system would prefer to avoid creating vacancies. If one tries to extrapolate the curves on Fig. 1(a) to higher pressure, the enthalpies of X and TA may cross each other at about 550-600 kbar: this is the pressure at which curve QR would intersect line LK on Fig. 2(b) – after that NiAl becomes an "anti-structure defect" compound in all senses. Much higher pressure is required to make the curve cross the LK_1 line on Fig. 2(c) (Ni-rich alloys), and it is impossible to say whether the curve ever enters the LK_3N triangle on Fig. 2(d) (Al-rich alloys) at all. The moving of the point representing NiAl along the QR line slows down noticeably as the pressure becomes higher and higher. The trajectory is very unlikely to reach the LN line: this line represents the case when the exchange defect has zero formation enthalpy, which is hard to imagine at whatever high applied pressure.

The NiAl trajectory intersects the dashed line on Fig. 2(d) at the same pressure, as it crosses line LP on Fig. 2(a): the change of the solid solution type on the Al-rich side occurs simultaneously with the change of sign of the IB_{\pm} complex defect within the WS model. Another event which Fig. 2(d) demonstrates is the crossing of the QR and LK_4 lines. The crossing point corresponds to the intersection of IB_{-} and TA curves on Fig. 1(c) at approximately -30 kbar and means that at such a negative pressure the triple-Ni defect starts to dominate also in Al-rich alloys.

Concluding this section, we would like to emphasize that all the above considerations rely only on h_{CD} enthalpies as functions of pressure, i.e. without performing actual calculations of defect concentrations. The latter, of course, could also be done, however we preferred a qualitative analysis for understanding the broad picture. It also demonstrates the strong points of the WS approach to large extent. A quantitative calculation at high temperature should also take account of formation entropies and the temperature dependence of the formation enthalpies [11].

ISOSTRUCTURAL PHASE TRANSITION

The WS model is often a good tool to bridge the gap between microscopic *ab initio* calculation and point defect statistics in a macroscopic system. In many cases it gives defect concentrations with a high degree of confidence, given the underlying point defect formation energies. Nevertheless, it does not work in cases where defect-defect interactions become important. In particular, there is no point in trying to use the

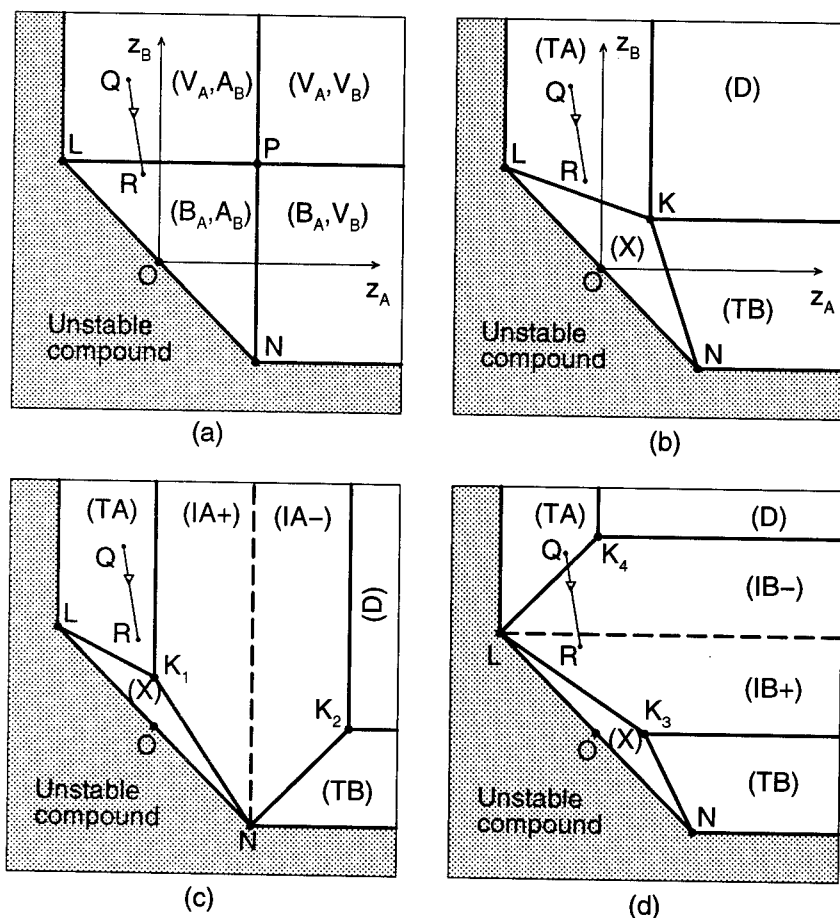


Figure 2 Position of NiAl on the point defect structure maps [4] denoting the constitutional defects (a); and the dominant thermal defects in the low temperature limit for stoichiometric (b), Ni-rich (c), and Al-rich (d) alloys. The maps correspond to the equiatomic binary compound case, $z_A = h_{JA}/h_D$, $z_B = h_{JB}/h_D$. The coordinates of points (z_A, z_B) are: O(0,0); L(-1,1); N(1,-1); P(1,1); K(1/2,1/2); K₁(0,1/2); K₂(1,0); K₃(1/2,0); and K₄(0,1) (more details about the maps can be found in ref. [4] in the present volume). The position of NiAl alloys (A=Ni, B=Al) with pressure changing is marked with curve QR: point Q corresponds to $p = -50$ kbar, point R to $p = 300$ kbar; the position at zero pressure is marked with the triangle.

WS model if any cooperative phenomena involving defect structures take place. The next question we address, namely, whether any phase transition occurs in the crystal at $p = p_{cross}$, requires extending the WS model by including interactions between defects.

Even if "chemical" defect-defect interactions are weak and short-ranged as required by the WS model, there are still long-ranged elastic interactions which arise due to lattice distortion introduced by point defects.

Let us map a crystal with randomly distributed point defects onto a conglomerate of supercells containing one point defect each. Within the WS model defects exist independently, therefore the volume of each supercell at given external pressure is defined by its energy-volume curve as given by *ab initio* calculations. The total volume of the crystal in this case depends linearly on the number of each type of defects, which is reflected by Eq. (8).

In general, at some arbitrary external pressure the volume of supercells containing different types of point defects is different. Being placed in the same crystal, such supercells encounter certain mismatch at the boundary and have to align their lattice parameters. This picture provides a simple way to introduce elastic interactions between defects: let us assume from the beginning that the average volume of each supercell corresponds to the average volume of the crystal at given c . The resulting equation together with the appropriately modified Eq. (5) forms a basis for the extended Wagner-Schottky (EWS) model, which is described in ref. [8].

In the EWS model the enthalpy of the crystal becomes non-linear with respect to defect concentrations, which means that defects now "see" each other via the averaged crystal volume, i.e. due to interaction of the elastic type. It can be shown either by the second-order Taylor expansion of the enthalpy in powers of defect concentrations [8], or using classical elasticity theory [25], that the defect *mixing* enthalpy can be defined and that it is positive. The latter means that the change of the constitutional defect type should be the first-order phase transition (FOPT).

As long as defects are assumed to be randomly distributed, the change of the constitutional defects does not change the symmetry of the system. Consequently, the FOPT is an isostructural phase transition in which the phase-coexistence line is terminated with a critical point. Our calculations show that in Al-rich NiAl the position of the critical point strongly depends on the alloy composition: the larger the deviation from stoichiometry, the higher are the critical pressure and critical temperature.

Let us now take a more general view, and consider some ordered off-stoichiometric compound. Due to the presence of at least 2 sublattices, there are several ways for a compound to accommodate the deviation from stoichiometry by creating constitutional point defects (vacancies and antisites, for example): the choice of the particular type of the defects depends on their formation enthalpy. If now the external conditions (pressure in our case) are changed so that another point defect type becomes favorable, the system can undergo an isostructural FOPT of the type described. The magnitude of the associated volume change is proportional to the constitutional defect concentration (typically, several percent) and the formation volume of corresponding defect substitution (interbranch CD): if vacancies are involved, the formation volume should be of order one atomic volume. That suggests a class of systems in which to look for an isostructural phase transition in solids.

SUMMARY

We investigate the thermodynamics of point defects in NiAl alloys at pressures up to 300 kbar on the basis of *ab initio* plane-wave pseudopotential supercell calculations in conjunction with simple thermodynamic models of the Wagner-Schottky type:

- 1) The change of the constitutional defect type in Al-rich alloys takes place at a crossover pressure of 192 kbar from V_{Ni} to Al_{Ni} ; the type of solid solution on the Al-rich side is correspondingly changed from subtractive to substitutional.
- 2) Up to 300 kbar, the dominant thermal excitation in stoichiometric NiAl compounds is still a triple-Ni complex defect: the switch to an exchange defect may take place at much higher pressure.
- 3) No variations either in constitutional defects or in the dominant type of thermal defects are expected on the Ni-rich side.
- 4) The change in the type of solid solution on the Al-rich side turns out to be an isostructural phase transition terminated by a critical point; we suggest that such a phenomenon should be typical for ordered compounds with constitutional defects.

Acknowledgments

We thank the EPSRC for provision of computer time on the Cray T3E-1200E via the UKCP consortium (Grant M01753), and for other resources (Grant L08380), and we acknowledge the Centre for Supercomputing in Ireland for computer resources on the IBM SP2.

REFERENCES

- [1] R. D. Noebe, R. R. Bowman, and M. V. Nathal. Physical and Mechanical Properties of the B2 Compound NiAl. *Int. Mater. Rev.* **38**, 193 (1993).
- [2] A. J. Bradley and A. Taylor. An X-Ray Analysis of the Nickel-Aluminium System. *Proc. R. Soc. A* **159**, 56 (1937).
- [3] R. J. Wasilewski. Structure Defects in CsCl Intermetallic Compounds – I. Theory. *J. Phys. Chem. Solids* **29**, 39 (1968); Structure Defects in CsCl Intermetallic Compounds – II. Experimental. *J. Phys. Chem. Solids* **29**, 51 (1968).
- [4] See the paper P. A. Korzhavyi, I. A. Abrikosov, and B. Johansson. *Ab Initio* Study of Vacancies in Metals and Compounds. in the current volume.
- [5] A. Taylor and N. J. Doyle. Further Studies on the Nickel-Aluminium System. II. Vacancy Filling in β and δ -Phase Alloys by Compression at High Temperatures. *J. Appl. Crystallogr.* **5**, 210 (1972).
- [6] J. W. Otto, J. K. Vassiliou, and G. Frommeyer. Equation of state of polycrystalline Ni₅₀Al₅₀. *J. Mater. Res.* **12**, 3106 (1997).
- [7] P. A. Korzhavyi, A. V. Ruban, A. Y. Lozovoi, Yu. Kh. Vekilov, I. A. Abrikosov, and B. Johansson. Constitutional and Thermal Point Defects in B2–NiAl. *Phys. Rev. B* **61**, 6003 (2000).
- [8] A. Alavi, A. Y. Lozovoi, and M. W. Finnis. Pressure-Induced Isostructural Phase Transition in Al-Rich NiAl Alloys. *Phys. Rev. Lett.* **83**, 979 (1999).
- [9] M. W. Finnis. Calculating Grain Boundary Energies and Other Defect Energies in Ordered Alloys. in: *Properties of Complex Inorganic Solids*, Proc. 1st Int. Alloy Conference, Athens, Greece, 17–21 June 1996, Eds. A. Gonis, A. Meike, and P. E. A. Turchi, Plenum Press, New York, 339 (1997).
- [10] The term “vector” is introduced to shorten the notations without assigning any special meaning to this object.
- [11] M. Hagen and M. W. Finnis. Point Defects and Chemical Potentials in Ordered Alloys. *Phil. Mag. A* **77**, 447 (1998).
- [12] B. Meyer and M. Fähnle. Atomic Defects in the Ordered Compound B2–NiAl: A Combination of *Ab Initio* Electron Theory and Statistical Mechanics. *Phys. Rev. B* **59**, 6072 (1999); Correction. *Phys. Rev. B* **60**, 717 (1999).
- [13] P. A. Korzhavyi, I. A. Abrikosov, and B. Johansson. Constitutional and Thermal Defects in Nickel Aluminides. in *High-Temperature Ordered Intermetallic Alloys VIII*, edited by E. P. George, M. Yamaguchi, and M. J. Mills (Mater. Res. Soc. Proc. **552**, Pittsburgh, PA, 1999), in press.
- [14] A. Alavi, J. Kohanoff, M. Parrinello, and D. Frenkel, *Ab Initio* Molecular Dynamics with Excited Electrons. *Phys. Rev. Lett.* **73**, 2599 (1994).
- [15] K. Rzyman, Z. Moser, R. E. Watson, and M. Weinert. Enthalpies of Formation of AlNi: Experiment versus Theory. *Journal of Phase Equilibria* **19**, 106 (1998).
- [16] E.-T. Henig and H. L. Lukas, Kalorimetrische Bestimmung der Bildungsenthalpie und die Beschreibung der Fehlordnung der geordneten β -Phase (Ni,Cu)_{1-x}Al_x. *Z. Metallkde.* **66**, 98 (1975).
- [17] B. Bai and G. S. Collins. Equilibrium Defects and Concentrations in Nickel Aluminide. in *High-Temperature Ordered Intermetallic Alloys VIII*, edited by

-
- E. P. George, M. Yamaguchi, and M. J. Mills (Mat. Res. Soc. Symp. Proc. **552**, Pittsburgh, 1999), in press.
- [18] H.-E. Schaefer, K. Frenner, and R. Würschum. Time-Differential Length Change Measurements for Thermal Defect Investigations: Intermetallic B2-FeAl and B2-NiAl Compounds, a Case Study. *Phys. Rev. Lett.* **82**, 948 (1999).
- [19] M. Fähnle, J. Mayer, and B. Meyer. Theory of Atomic Defects and Diffusion in Ordered Compounds, and Application to B2-FeAl. *Intermetallics* **7**, 315 (1999).
- [20] At high temperature, however, the triple-Ni defect should dominate in Al-rich alloys at zero pressure [7, 12, 13]
- [21] C. L. Fu, Y.-Y. Ye, M. H. Yoo, and K. M. Ho. Equilibrium-Point Defects in Intermetallics with the B2 Structure – NiAl and FeAl. *Phys. Rev. B* **48**, 6712 (1993).
- [22] M. Kogachi, T. Haraguchi, and S. M. Kim. Point Defect Behavior in High Temperature Region in the B2-Type Intermetallic Compound FeAl. *Intermetallics* **6**, 499 (1998).
- [23] According to some recent research, [19, 22], the FeAl compound at zero pressure turns out to be almost a border case: constitutional defects there are antistructural atoms on both sides of stoichiometry [19, 22], whereas at the equiatomic composition the triple-Fe defect is just slightly higher in energy, than the exchange defect [19]. A so-called “hybrid” behaviour of the compound is also pointed out in ref. [24].
- [24] R. Krachler, H. Ipser, B. Sepior, and G. Vogl. Diffusion Mechanism and Defect Concentrations in β' -FeAl, an Intermetallic Compound with B2 Structure. *Intermetallics* **3**, 83 (1995).
- [25] A. Y. Lozovoi, A. Alavi, P. A. Korzhavyi, and M. W. Finnis. Thermodynamics of Point Defects in NiAl Alloys at Finite Pressure., to be published.

MICROSTRUCTURAL CHARACTERISTICS OF MIXED III-V LAYERS

S. Mahajan

Department of Chemical and Materials Engineering
Center for Solid State Electronic Research
Arizona State University
Tempe, AZ 85287-6006

ABSTRACT

We have shown that atomic species in mixed III-V layers, differing in their covalent tetrahedral radii, are not distributed at random on their respective sublattices. Two types of deviations from randomness are observed: (1) phase separation, and (2) atomic ordering. We have highlighted the microstructural characteristics of phase separated and phase separated/ordered layers and have discussed their origins. We have also briefly considered the influence of these features on electronic properties and device performance.

INTRODUCTION

The binary III-V compound semiconductors have specific band gaps. In principle, we can produce materials having intermediate values of band gaps by mixing appropriate amounts of suitable binaries. The resulting ternaries and quaternaries, such as *InGaP*, *InGaAs*, *InGaN*, *AlGaN*, and *InGaAsP*, form a basis of a number of electronic devices and systems.

The mixed III-V compounds containing *P*, *As*, and *Sb* crystallize in the zinc-blende structure, whereas group III nitrides grown at high temperatures exhibit the wurtzite structure. These two structures consist of two interpenetrating FCC sublattices. One of the sublattices is occupied by group III atoms, whereas group V atoms reside on the second sublattice. An interesting question is whether or not the atomic species in mixed III-V layers are distributed at random on their respective sublattices?

A number of studies have shown that atomic species in mixed layers, differing in their covalent tetrahedral radii, are not distributed at random on their respective

sublattices. Two types of deviations from randomness are observed: (1) phase separation, and (2) atomic ordering. Recently, Zunger and Mahajan [1] reviewed the published literature, and the reader is referred to this article for details.

In this paper, we briefly highlight the microstructural characteristics of mixed III-V layers and discuss their origins. We also consider the influence of these features on electronic properties and device reliability.

PHASE SEPARATION

The small scale contrast fluctuations, referred to as lateral phase separation, were first seen in *InGaAsP* layers by Henoc et al. [2] using transmission electron microscopy. Subsequently, Mahajan et al. [3], Norman and Booker [4], Chu et al. [5], McDevitt et al. [6] and Lee et al. [7] investigated this phenomenon in detail. Figure 1 taken from the study of McDevitt et al. [6] shows the contrast behavior of microstructures observed in an *InGaAsP* layer, grown on a (001) *InP* substrate by liquid phase epitaxy, under various reflections. The layer is lattice matched to the substrate, and emits at 1.33 μm . The micrographs in Fig. 1 exhibit two prominent features: (1) fine scale speckle structure, and (2) basket-weave pattern. Both of these features are aligned along the [100] and [010]

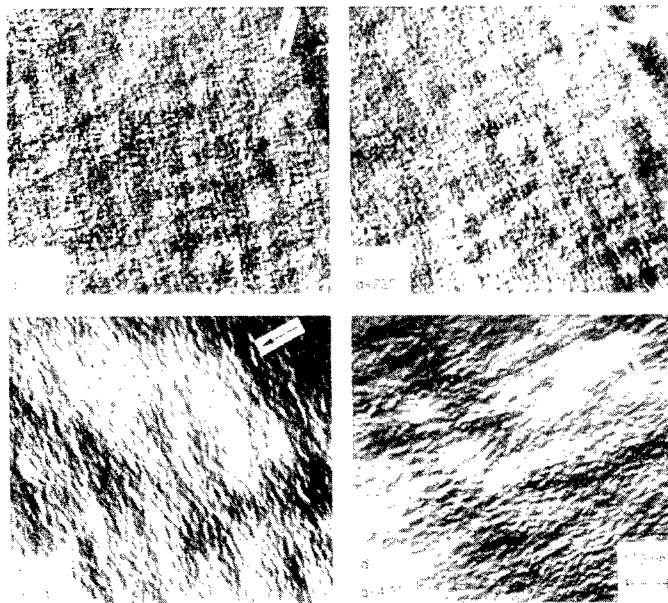


Figure 1. Dark-field electron micrographs obtained from a (001) *InGaAsP* layer grown on an *InP* substrate by liquid phase epitaxy. The operating reflections in (a), (b), (c), and (d) are $\bar{2}20$, 220 , 040 , and $\bar{4}00$. After McDevitt et al. [6].

directions, and their respective wavelengths are ~ 10 and 100 nm. It can also be deduced from Fig. 1 that the speckle structure produces strains along the $[100]$ and $[010]$ directions.

When the layer in Fig. 1 was examined in cross-section using the 004 reflection, the speckle contrast was not observed [6]. This implies that phase separation does not occur along the growth direction and is two-dimensional in nature. To further confirm this assessment, McDevitt et al. [6] investigated *InGaAsP* layers grown on (110) , $(\bar{1}\bar{1}\bar{1})_s$, and (123) *InP* substrates. In each case the observed microstructure reflected the crystallography of the growth surface, and in no case was phase separation seen along the growth direction. Furthermore, phase separation occurred along soft directions lying in each growth surface.

The presence of phase separated microstructures is not consistent with the bulk thermodynamic calculations of Stringfellow [8] and Onabe [9], who predicted low critical temperatures for decomposition because of the strain energy considerations. If we invoke that the speckle structure in Fig. 1 represents *In*-rich and *Ga*-rich regions, we can rationalize as follows the discrepancy between the theory and the experiments. We envisage that the speckle structure evolves at the surface while the layer is growing. Since the covalent tetrahedral radius of *In* atoms is larger than that of *Ga* atoms, the volumes of *In*-centered tetrahedra in mixed III-V layers will be larger than those of *Ga*-centered tetrahedra. It is conceivable that the system may have lower strain energy when the two types of tetrahedra are separately clustered, resulting in *In*-rich and *Ga*-rich regions at the surface. These regions are subsequently incorporated into the layer during additional growth because of kinetic constraints. This implies that phase-separated microstructures observed in mixed layers [1-7] are non-equilibrium in nature.

The non-equilibrium nature of phase separation was borne out by the study of Lee et al. [7]. These authors diffused zinc at 390°C for 20 hours into phase-separated *InGaAs* layers grown at 485°C because the in-diffusion of *Zn* would tend to mix atoms on the group III sublattice. Their results are reproduced as Fig. 2, where three different regions are apparent. Near the surface, i.e., the top region, the microstructure is more or less homogeneous. In the region defined by the arrows, the fine scale speckle structure has been eliminated by the in-diffusion of zinc, whereas the less distinct coarse modulations are still present. Both the speckle structure and the coarse modulations are observed near the layer-substrate interface, i.e., the lower region. The preceding results indicate that the phase-separated microstructure observed in *InGaAs* layers is non-equilibrium in nature in the bulk, and are consistent with the calculations of Stringfellow [8] and Onabe [9] that are based on bulk thermodynamics.

An interesting question is whether or not the concept of self-organization of atomic species in mixed layers, proposed by Glas and co-workers [10-12], can explain the origins of the speckle structure seen in Fig. 1. Based on their arguments, it is difficult to comprehend the two-dimensional nature of phase-separated microstructures [5,6] and the presence of satellites in electron diffraction patterns obtained from phase-separated layers [6].

The fine scale speckle structure was observed in mixed layers grown by equilibrium and non-equilibrium growth techniques [3,7]. McDevitt et al. [6] showed that wavelengths of the speckle structure were affected by the growth temperature as well as the growth technique. They attributed these effects to changes in surface diffusion characteristics.



Figure 2. Cross-section electron micrograph obtained from an *InGaAs* layer grown at 480°C in which *Zn* was diffused at 390°C for 50 hours. Note the presence of three regions: (1) near the surface, the microstructure is more or less homogeneous, (2) in the region bounded by the arrows the fine scale modulations have been eliminated by the in-diffusion of zinc, whereas the less distinct coarse modulations are still present, and (3) near the layer/substrate interface both the coarse and fine modulations are still present. After Lee et al. [7].

The basket weave pattern observed in Fig. 1 is sometimes referred to as coarse contrast modulations in the literature, and has been seen by a number of investigators [2-7, 13-15]. Two explanations have been proposed for their formation. According to Henoc et al. [2], they represent composition modulations and evolve by surface spinodal decomposition. The major difficulty with this idea is that the observed wavelength of the modulations is too long for them to evolve by surface diffusion during the time it takes to deposit a bilayer.

Alternatively, Mahajan and co-workers [3, 6, 7, 14] have suggested that the coarse modulations form to accommodate the two-dimensional strains associated with the fine scale speckle structure. Let us consider the situation in Fig. 1 where the speckle structure develops along the [100] and [010] directions lying in the (001) growth surface. As indicated earlier, the formation of the fine scale structure results in biaxial strains or stresses along the [100] and [010] directions. Instead of having the layer uniformly strained across the layer/substrate interface, the system may lower its energy by dividing

the surface into tension and compression regions. We envisage that this feature is responsible for coarse contrast modulations. Furthermore, the higher the interfacial strains resulting from the speckle structure, the smaller the wavelength of the coarse contrast modulations.

The above assessment is borne out by the study of Lee et al. [15], where they grew *InGaAs* layers of the same composition on (001) *InP* substrates at different temperatures by liquid phase epitaxy. Their results are reproduced as Fig. 3. The coarse contrast modulations are only seen in a layer grown at 480°C, i.e., Fig. 3(a), where the compositional difference between the phase-separated regions is larger and thus the two-dimensional strains are higher.

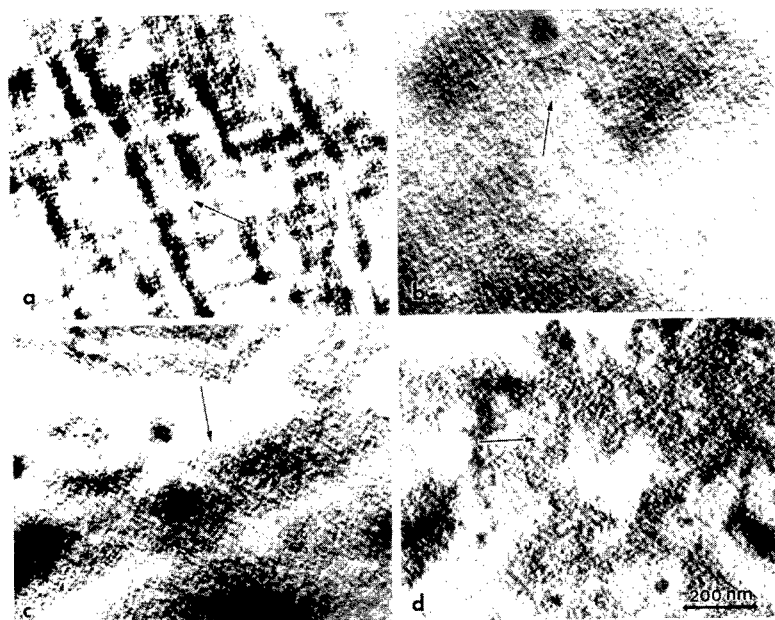


Figure 3. Dark-field micrographs obtained from (001) *InGaAs* layers grown at (a) 480, (b) 540, (c) 600, and (d) 640°C. The operating reflection in each case is 220 and is indicated by an arrow. After Lee et al. [15].

A related form of lateral phase separation is observed in short period superlattices [16]. Figure 4 taken from the study of Cheng et al. [16] showed, using a variety of characterization techniques, the presence of unintentional lateral composition modulations along the $[1\bar{1}0]$ direction in which the *In* composition was found to vary smoothly from 42 to 56%, while the complementary *Ga* composition varied between 58 and 44%.

We can rationalize the above observations on lateral composition modulations in short period superlattices in terms of the conceptual framework used to explain the origin of coarse contrast modulations. Assuming that the short period superlattice is not lattice-

matched to the underlying substrate, undulations comprising tension and compression regions may develop at the growing surface. Since the covalent tetrahedral radius of *In* atoms is larger than that of *Ga* atoms, the *In* and *Ga* atoms are incorporated preferentially into the tension and compressive regions, respectively, resulting in lateral composition modulations. Again, the period of the modulations will depend on interfacial strains. The larger the strains, the shorter the period. Furthermore, the modulations in Fig. 4 are not driven by a thermodynamic instability, but by the presence of stresses that lead to segregation. Therefore, it would be more appropriate to refer to them as stress-induced composition fluctuations.

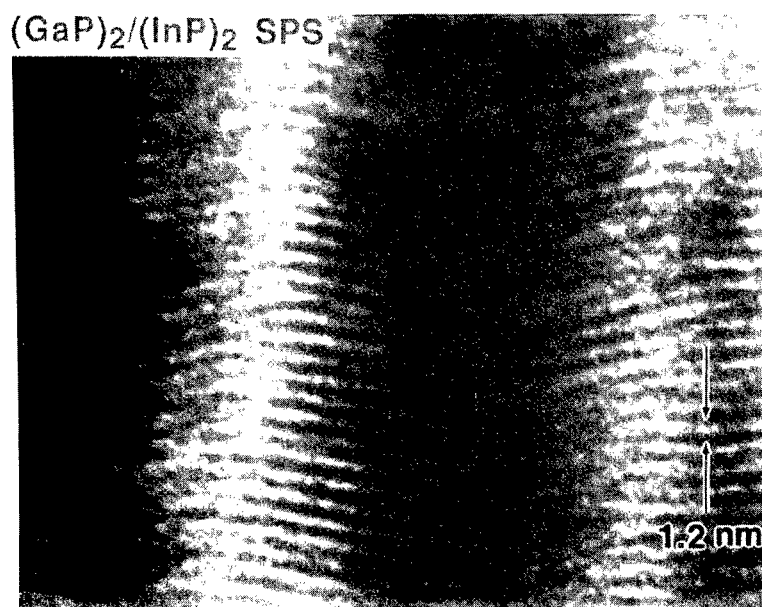


Figure 4. Dark-field TEM image of the $(\text{GaP})_2/(\text{InP})_2$ superlattices showing lateral phase separation. After Cheng et al. [16].

Naturally-occurring, vertical phase separation has been observed in lattice-mismatched, mixed III-V layers grown on (001) substrates [17]. The study of Ferguson et al. [17] showed that the vertical phase separation in *InAsSb* layers only occurred when the growth temperature was below 430°C. Above this temperature, homogeneous solid solution was obtained. Figure 5 shows an example of vertical phase separation in an *InAsSb* layer deposited on a (001) *GaAs* substrate [17]. It is clear that the layer has vertically separated into two phases; their compositions as determined by photoluminescence are $\text{InAs}_{0.69}\text{Sb}_{0.31}$ and $\text{InAs}_{0.37}\text{Sb}_{0.63}$ [17].

The origin of vertical phase separation is not well understood. A plausible explanation in the case of *InAsSb* layers could be as follows. It appears from the work of Ferguson et al. [17] that the critical temperature for phase separation is below 430°C. If

we invoke that the lower growth temperatures lie within the surface spinodal region, then layers can decompose in two ways: (1) lateral phase separation, and (2) vertical phase separation. If the *InAsSb* layer were to laterally phase separate into *As*-rich and *Sb*-rich regions, the interfacial strain energy would be high because the respective mismatches with the underlying substrate would be 7.45 and 10.6%. This calculation assumes that Vegards Law is obeyed. On the other hand, if the layer were to vertically phase separate so that the *As*-rich layer is contiguous to the substrate, then the mismatch would be ~7.45%, energetically less unfavorable situation. We therefore infer that vertical phase separation may be preferred over lateral phase separation in *InAsSb* layers.

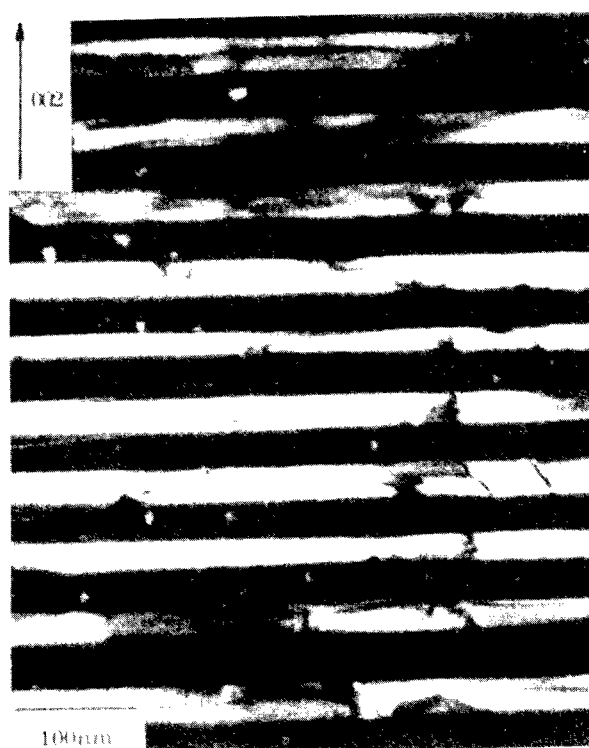


Figure 5. Cross-sectional dark-field electron micrograph obtained from an *InAsSb* layer grown by molecular beam epitaxy at 340°C that shows vertical phase separation. After Ferguson et al. [17].

We envisage that lattice-mismatched, mixed layers will decompose via vertical phase separation. This suggestion is consistent with the recent study of Neubauer et al. [18] on $Al_{0.25}Ga_{0.75}N$ layers grown (0001) sapphire by plasma-induced molecular beam epitaxy. One of their results is reproduced as Fig. 6(a), and the corresponding diffractogram is shown in Fig. 6(b). The presence of darker and lighter regions is clearly evident in Fig. 6(a). The digital analysis of these lattice images indicates that the *AlGa*N layer decomposes into one monolayer containing 89% *Al* and about 3 monolayers with 4% *Al*. The four monolayer periodicity is consistent with the diffractogram shown in Fig. 6(b), where the observed periodicity is $4 \times d_{(0002)}$, $d_{(0002)}$ being the lattice spacing of (0002)

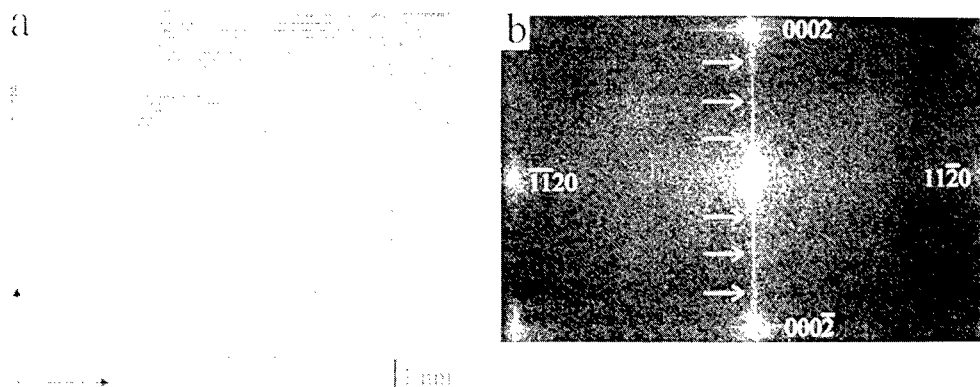


Figure 6. (a) Cross-sectional high resolution transmission electron micrograph obtained from an $Al_{0.35}Ga_{0.65}N$ layer, and (b) diffractogram obtained from the enclosed region in (a). After Neubauer et al. [18].

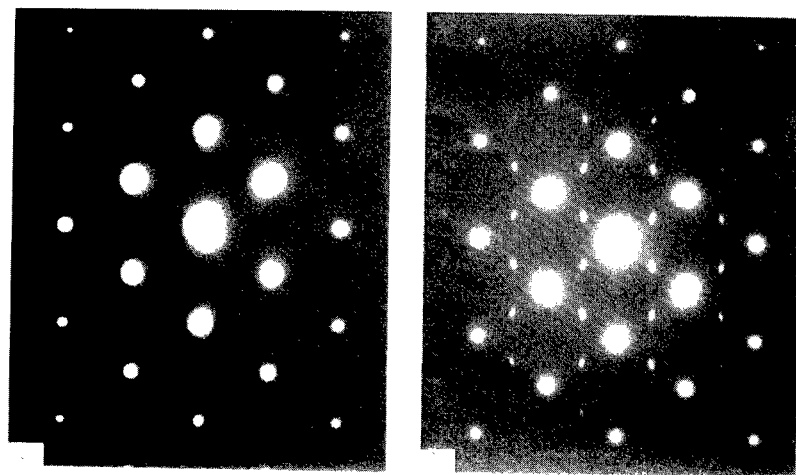


Figure 7. Electron diffraction patterns obtained from an ordered $InGaP$ layer grown by organometallic vapor phase epitaxy on a (001) $GaAs$ substrate at $650^{\circ}C$: (a) pattern observed from the $[1\bar{1}0]$ zone axis; only reflections belonging to the zinc-blende structure are present, and (b) pattern observed from the $[110]$ zone axis; superlattice reflections are present at $\frac{1}{2}[111]$ and $\frac{1}{2}[\bar{1}\bar{1}\bar{1}]$ and equivalent positions. After Philips et al. [23].

planes. Furthermore, they observed that the periodicity of naturally occurring short period superlattices depended on the layer composition.

Recently, Ruterano and Deniel [19] observed 0001, 0003, ... superlattice spots from *InGaN* layers, and attributed them to atomic ordering. Could they be due to vertical phase separation induced short period superlattices consisting of *In*-rich and *Ga*-rich monolayers? This is an interesting question because *InGaN* layers are a prime candidate to exhibit phase separation since the tetrahedral radii difference between the *In* and *Ga* atoms is substantial.

ATOMIC ORDERING

In (001) mixed III-V layers grown by a variety of vapor phase techniques, atomic ordering co-exists with phase separation [1]. However, ordering is absent in layers deposited by liquid phase epitaxy [1-4, 6, 7]. As a result of ordering, double and triple period superlattices evolve spontaneously on two of the four {111} planes [1, 20-24].

Figures 7(a) and 7(b) shows $[\bar{1}10]$ and $[110]$ electron diffraction patterns obtained from a lattice-matched *InGaP* layer grown by organometallic vapor phase epitaxy on (001) *GaAs* at 650°C [23]. The $[\bar{1}10]$ zone axis pattern in Fig. 7(a) shows only the fundamental zinc-blende reflections, whereas, in addition to the fundamental reflections, $\frac{1}{2} [\bar{1}11]$ and $\frac{1}{2} [1\bar{1}\bar{1}]$ superlattice spots and their equivalents are observed in Fig. 7(b). This implies that real space periodicities along the $[\bar{1}11]$ and $[1\bar{1}\bar{1}]$ directions are doubled. Since the atomic arrangement of {111} planes in a random III-V alloy crystallizing in the zinc-blende structure is $A(III)a(V)B(III)b(V)C(III)c(V)A(III)a(V)\dots$, the preceding observations suggest that following atomic arrangement on $(\bar{1}11)$ and $(1\bar{1}\bar{1})$ planes in an ordered *InGaP* layer: $A(In)a(P)B(Ga)b(P)C(In)c(P)A(Ga)a(P)B(In)b(P)C(Ga)c(P)A(In)a(P)\dots$ resulting in double period superlattices. Furthermore, these ordered variants are referred to as $\{111\}_B$ or $CuPt_B$ because the line of intersections of the $(\bar{1}11)$ and $(1\bar{1}\bar{1})$ planes with the (001) surface is parallel to that of the $\{111\}_B$ planes in which the group V atoms are uppermost.

Murgatroyd et al. [25] and Chen et al. [26] investigated atomic ordering in (001) *GaAsSb* and *GaAsP* layers in which atomic substitutions occurred on the group V sublattice. They showed that ordering occurs on the $(\bar{1}11)_B$ and $(1\bar{1}\bar{1})_B$ planes in these layers. Combining these results with those on the mixed group III sublattice, it is inferred that the pair of {111} planes on which ordering occurs is independent of the sublattice on which the atomic substitutions are effected.

Since $CuPt_B$ ordering is observed on only two of the four {111} planes, it is likely not to be a bulk phenomenon and may occur close to the surface. A number of investigators [22-25] invoked that the occurrence of (2 x 4) surface reconstruction on group V terminated (001) surfaces was responsible for atomic ordering. As illustrated in Fig. 8, the occurrence of surface reconstruction produces subsurface stresses. The stresses are compressive in nature beneath the dimers, whereas they are tensile in character between the dimers. The existence of these stresses will bias the occupation of subsurface sites by atomic species differing in their covalent tetrahedral radii. The valence force field calculations of Philips et al. [27] indicated that it is energetically more favorable for larger size atoms to occupy $[110]$ rows between the dimers, whereas small size atoms lie

along $[110]$ rows underneath the dimers. As a result, $[110]$ rows will alternate in composition along the $[\bar{1}\bar{1}0]$ direction. For example, $[110]$ rows of *In* and *Ga* atoms will be located between the dimers and underneath the dimers in an ordered *InGaP* layer. In the presence of surface steps, the rows shift laterally during growth, leading to the development of *CuPt*-type order [22-25]. Furthermore, an ordered variant can be selectively chosen by tilting the (001) substrate around the $[110]$ axis [23, 26]. Philips et al. [23] attributed this to biasing the direction of dimerization, i.e., $[\bar{1}\bar{1}0]$ or $[\bar{1}10]$.

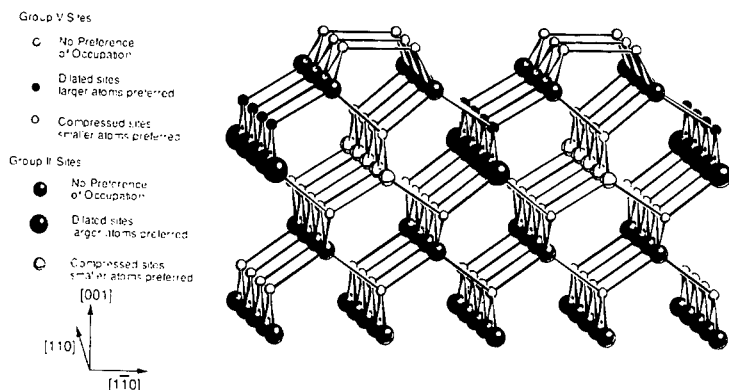


Figure 8. Preferential subsurface site occupation by atomic species differing in covalent tetrahedral radii as a result of dimerization induced subsurface strains. After Philips et al. [23].

McFadden investigated in detail the domain structure in *InGaP* layers grown on (001) vicinal *GaAs* substrates by organometallic vapor phase epitaxy [27]. Some of the results of his study are highlighted in Figs. 9 and 10. Figure 9 was obtained from a region close to the layer/substrate interface, whereas Fig. 10 came from a region that was close to the surface. The average domain size is fairly small near the substrate, and the domains coarsen substantially as the layer thickens. Furthermore, the domain walls are faceted.

Two explanations were proposed to rationalize the above observations. First, the existence of ordering in subsurface layers will tend to dimerize the growing surface in such a way that the two features are commensurate with each other. As a result, the existing order will be propagated into the growing layer. Second, the occurrence of step flow during the layer growth could cause the coalescence of the domains.

That atomic ordering is surface-reconstruction driven is supported by the studies of Gomyo et al. [28] and Philips et al. [29]. They showed that in the presence of a (2×3) surface reconstruction, triple-period superlattices developed only on $(111)_A$ and $(\bar{1}\bar{1}\bar{1})_A$ planes. Figure 11(a) shows a $[\bar{1}\bar{1}0]$ diffraction pattern obtained from an *InGaAs* layer grown by molecular epitaxy on a (2×3) reconstructed (001) surface; the indexed pattern is shown in Fig. 11(b). The superlattice spots are observed at $\frac{1}{3}[111]$, $\frac{2}{3}[111]$ and $\frac{1}{3}[\bar{1}\bar{1}\bar{1}]$, $\frac{2}{3}[\bar{1}\bar{1}\bar{1}]$ and equivalent positions. Diffuse intensity spikes are attributed to the presence of a large number of domain boundaries and shallowly inclined interfaces in *as*-grown layers [30].

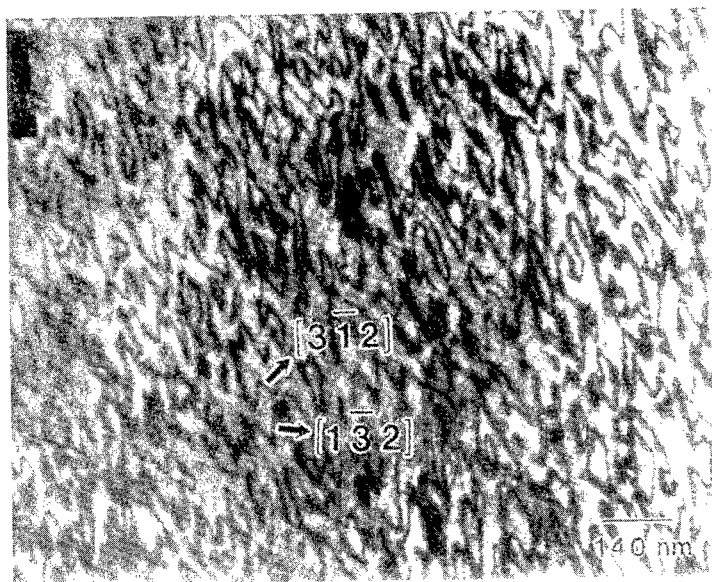


Figure 9. Dark-field, plan view image of single ordered variant *InGaP* layer, grown by organometallic vapor phase epitaxy, showing faceted domain boundaries. The micrograph was obtained from a portion of the layer that was close to the substrate. After McFadden [27].

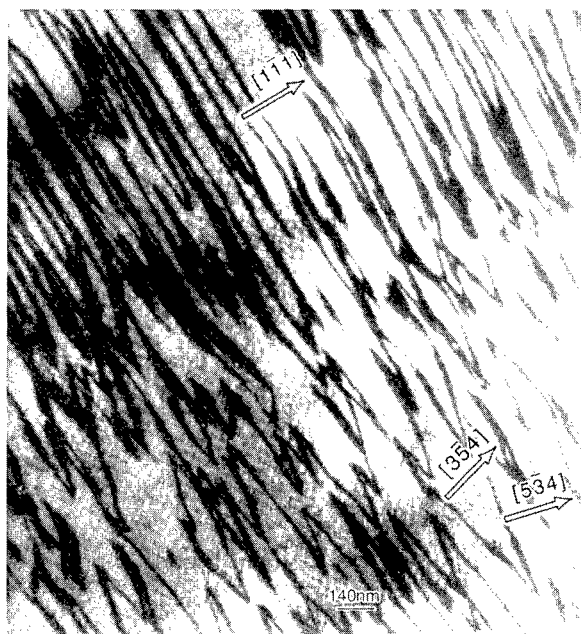


Figure 10. Dark-field, plan view image of single ordered variant *InGaP* showing faceted domain boundaries. The micrograph was obtained from a portion of the layer that was close to the surface. After McFadden [27].

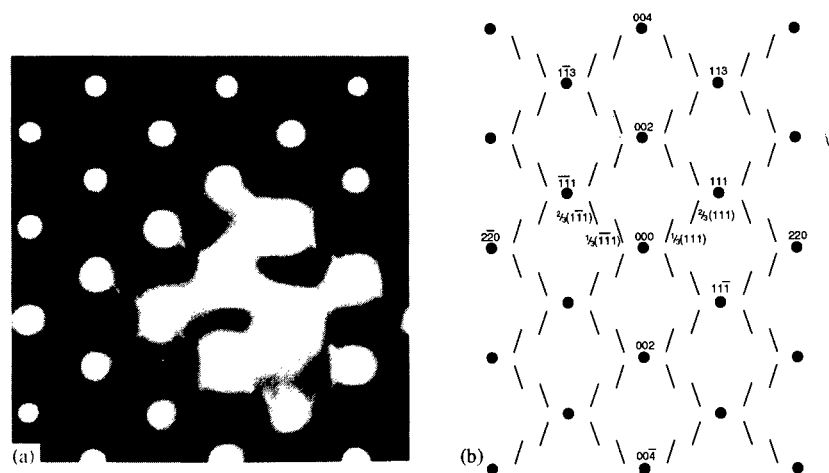


Figure 11. (a) $[1\bar{1}0]$ electron diffraction pattern obtained from an *InGaAs* layer grown by molecular beam epitaxy on a (2×3) reconstructed (001) surface, and (b) the indexed pattern. The presence of superlattice spots at $\frac{1}{3}[111]$, $\frac{2}{3}[111]$, and $\frac{1}{3}[1\bar{1}1]$, $\frac{2}{3}[1\bar{1}1]$ and equivalent positions are clearly evident. After Philips et al. [29].

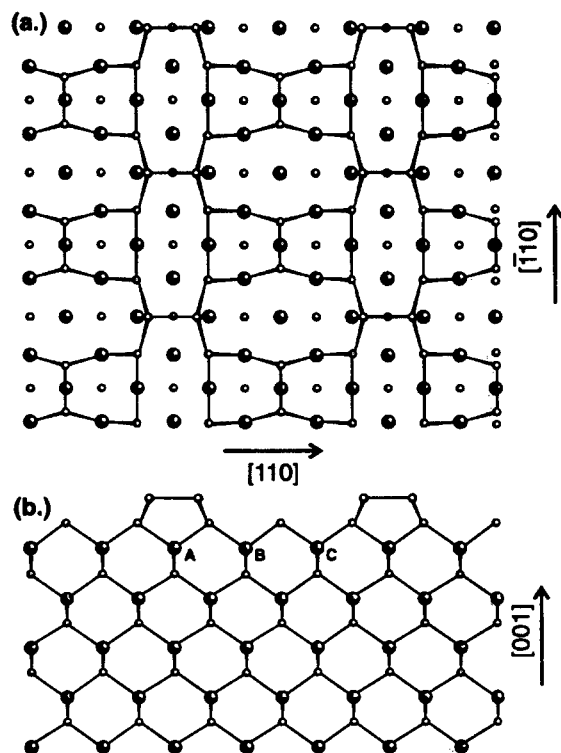


Figure 12. (a) $[1\bar{1}0]$ cross-section of a (2×3) reconstructed (001) surface, and (b) atomic arrangement resulting from intraplanar and interplanar ordering. After Philips [30].

The above observations can be rationalized by referring to Figs. 12(a) and 12(b). Figure 12(a) shows the $[\bar{1}\bar{1}0]$ section of a (001) surface that has undergone (2×3) reconstruction. It is clear from this figure that preferential occupation of subsurface rows by atomic species differing in tetrahedral radii would occur along the $[\bar{1}10]$ direction. In the case of an *InGaAs* layer, *Ga* atoms would tend to segregate to the row marked A in Fig. 12(a), whereas *In* atoms would prefer rows B and C. Since these two rows are equivalent insofar as lattice distortion is concerned, the average atomic concentrations along these two rows should be the same. As a result of the preferential site occupation, the triple-period superlattice may evolve as schematically illustrated in Fig. 12(b).

Since phase separation co-exists with atomic ordering in mixed III-V layers grown by vapor phase techniques, an interesting question is whether or not phase separation precedes ordering or vice versa? As indicated earlier, McDevitt et al. [6] demonstrated that phase separation occurred on the surface while the layer is growing. For ordering to evolve, the phase-separated microstructure must undergo atomic rearrangement in subsurface layers. Since bulk diffusion is extremely slow in III-V materials, the ordered arrangement could not develop by subsurface diffusion. It is likely that the required atomic rearrangement occurs at step edges because of the prevailing stress state [23]. To effect this rearrangement the stress state must change from tensile to compressive and back to tensile as the step propagates a distance of $\frac{a}{2\sqrt{2}}$, where a is the lattice parameter of the material.

McFadden measured the dependence of order parameter on growth conditions in *InGaP* layers [27]. The highest value of the order parameter obtained in his study was 0.5. This observation is consistent with the above discussion that phase separation precedes atomic ordering, and the phase-separated microstructure is not fully converted into an ordered arrangement because of the kinetic constraints.

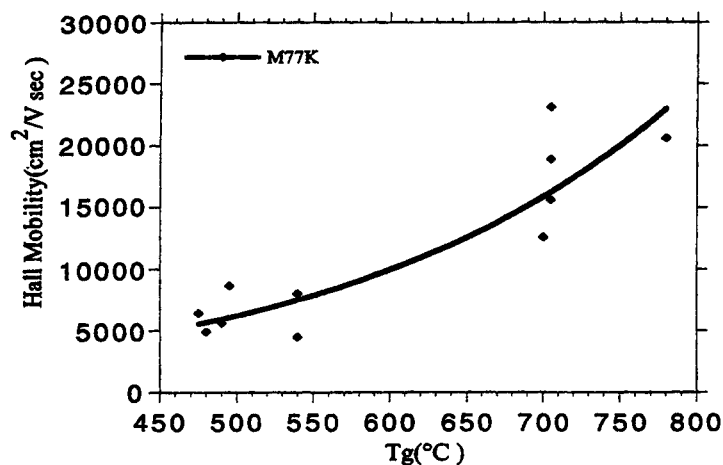


Figure 13. Plot showing the variations in 77K carrier mobility of *InGaAs* layers as a function of growth temperature. After Lee et al [15].

INFLUENCE OF PHASE SEPARATION AND ATOMIC ORDERING ON ELECTRONIC PROPERTIES AND DEVICE BEHAVIOR

The presence of phase separation reduces carrier mobility [14, 15, 31, 32]. This effect is shown in Fig. 13, where the carrier mobilities of *InGaAs* layers at 77K are plotted as a function of growth temperatures. It is clear that the mobility increases with the growth temperature. As discussed earlier, the higher the growth temperature, the smaller the compositional difference between the phase-separated regions and vice versa. Since different compositions will have different band gaps, microband offsets will develop at interfaces between the phase separated regions. For carriers to move through the layer, they must overcome these band offsets. At a low growth temperature, the band offset is larger because of the larger compositional difference between the phase separated regions. As a result, the carrier mobility in the layer is low.

McDevitt [31] showed that the carrier mobility of phase separated *InGaAsP* layers was increased by annealing them at high temperatures for extended periods. He attributed the increase to the reversion of phase separation.

In principle, the presence of atomic ordering should reduce carrier scattering, and thus enhance mobility. This is not generally achieved in mixed layers [1]. This effect is caused by the scattering of carriers from domain boundaries. Furthermore, ordering reduces band gaps [1] because of the changes in lattice periodicity.

The presence of phase separation and atomic ordering in mixed III-V layers has ramifications in device performance and reliability. Consider a situation where a phase separated *InGaAs* layer is being used as an active layer in a high electron mobility transistor. If we could eliminate phase separation in the layer, we can further enhance its mobility, suggesting that phase separation may have deleterious effects on device performance. On the other hand, Mahajan [33] argued that the occurrence of phase separation and atomic ordering in active, mixed III-V layers of light emitting devices enhanced their degradation resistance. This occurred because non-radiative recombination-enhanced glide and climb of dislocations that led to degradation was difficult in the presence of these microstructural features. The preceding discussion suggests that the microstructure of an active layer in a device must be tailored for optimal performance.

An interesting question is how to tailor microstructures of mixed III-V layers? Since only phase separation is observed in layers grown by liquid phase epitaxy [1-4, 6, 7], it is then feasible to exclude ordering from these layers. Another approach for eliminating ordering would be to substantially misorient underlying substrates so that the length of terraces is considerably reduced. This situation may not be conducive to surface reconstruction, thus eliminating the source of ordering. Both phase separation and ordering may also be eliminated from layers by the in-diffusion of dopants that cause mixing of atomic species [17]. However, this may increase carrier concentration in layers, leading to lower mobilities.

SUMMARY

We have shown that atomic species in mixed III-V layers, differing in their tetrahedral radii, are not distributed at random on their respective sublattices. Two types of deviations from randomness are observed: (1) phase separation, and (2) atomic ordering. The highlights of these microstructural features are as follows:

Phase Separation

- In nearly lattice-matched layers, lateral phase separation occurs on the surface while the layer is growing.
- The coarse modulations evolve to accommodate the two-dimensional strains associated with lateral phase separation.
- The composition modulations observed in $(GaP)_2(InP)_2$ short period superlattices may be due to stress-induced segregation.
- In lattice-mismatched systems, vertical phase separation may be energetically less unfavorable than lateral phase separation.

Atomic Ordering

- Atomic ordering is effected by subsurface stresses caused by surface reconstruction. The period of ordering-induced superlattices on $\{111\}$ planes can be changed from double to triple by replacing (2×4) surface reconstruction with (2×3) .
- Ordered regions grow in size with layer thickness.

Both of these microstructural features affect electronic properties, and the microstructure of an active layer needs to be tailored for optimal device performance.

ACKNOWLEDGMENTS

The author gratefully acknowledges the support of his research through grants from the Department of Defense (DOD-MURI Grant F49620-95-1-0447) and the National Science Foundation (MRSEC Grant DMR-9632635), and the fruitful discussion with his colleagues.

REFERENCES

1. A. Zunger and S. Mahajan, "Atomic Ordering and Phase Separation in Epitaxial III-V Alloys" Handbook on Semiconductors, edited by S. Mahajan, vol. 3, North-Holland, Amsterdam, p. 1399-1514 (1994).
2. P. Henoc, A. Izrael, M. Quillec, and H. Launois, "Composition Modulation in Liquid Phase Epitaxial $In_xGa_{1-x}As_yP_{1-y}$ Layers Lattice Matched to InP Substrates," *Appl. Phys. Lett.* 40, 963-65 (1982)
3. S. Mahajan, B.V. Dutt, H. Temkin, R.J. Cava, and W.A. Bonner, "Spinodal Decomposition in InGaAsP Epitaxial Layers," *J. Cryst. Growth* 68, 589-95 (1984).
4. A.G. Norman and G.R. Booker, "Transmission Electron Microscopes and Transmission Electron Diffraction Observations of Alloy Clustering in Liquid Phase Epitaxial (001) GaInAsP Layers," *J. Appl. Phys.* 57, 4715-20 (1985).
5. S.N.G. Chu, S. Nakahara, K.E. Strege, and W.D. Johnston, Jr., "Surface Layer Spinodal Decomposition in $In_{1-x}Ga_xAs_yP_{1-y}$ and $In_{1-x}Ga_xAs$ Grown by Hydride Transport Vapor-Phase Epitaxy," *J. Appl. Phys.* 57, 4610-15 (1985).
6. T.L. McDevitt, S. Mahajan, D.E. Laughlin, W.A. Bonner, and V.G. Keramidas, "Two-Dimensional Phase Separation in $In_{1-x}Ga_xAs_yP_{1-y}$ Epitaxial Layers," *Phys. Rev. B* 45, 6614-22 (1992).

7. K. Lee, S. Mahajan, and W.C. Johnson, "Stability of Phase Separated Microstructure in LPE-Grown InGaAs Epitaxial Layers," *Mats. Sci. Eng. B* 28, 209-13 (1994).
8. G.B. Stringfellow, "Miscibility Gaps in Quarternary III-V Alloys," *J. Cryst. Growth* 58, 194-202 (1982).
9. K. Onabe, "Calculation of Miscibility Gap in Quarternary InGaPSa with Strictly Regular Solution Approximation," *Jpn. J. Appl. Phys.* 21, 797-98 (1982).
10. F. Glas, "Elastic State and Thermodynamic Properties of Inhomogeneous Epitaxial Layers: Application to Immisible Alloys," *J. Appl. Phys.* 62, 3201-08 (1987).
11. F. Glas and P. Henoc, "Study of Static Atomic Displacements by Channelled-Electron-Beam-Induced X-ray Emission: Application to InGaAs Alloy," *Phil. Mag. A*, 56, 311-28 (1987).
12. F. Glas, C. Gors, and P. Henoc, "Diffuse Scattering, Size Effect, and Alloy Disorders in Ternary and Quarternary III-V Compounds," *Phil. Mag. B*, 62, 373-94 (1990).
13. M.M.J. Treacy, J.M. Gibson, and A. Howie, "On Elastic Relaxation and Long Wavelength Microstructures in Spinodally Decomposed InGaAsP Epitaxial Layers," *Phil. Mag. A*, 51, 380-417 (1985).
14. S. Mahajan, "The Current Understanding of Phase Separation and Atomic Ordering in Mixed Layers," *Inst. Phys. Conf. Ser.* 160, 367-76 (1997).
15. K. Lee, W.C. Johnson, and S. Mahajan, "Origins of Coarse Contrast Modulations in InGaAs Layers," *Inst. Phys. Conf. Ser.* 146, 235-40 (1995).
16. K.Y. Cheng, K.-C. Hsieh, and J.N. Baillargeon, "Formation of Lateral Quantum Wells in Vertical Short-Period Superlattices by Strain-Induced Layer-Ordering Process," *Appl. Phys. Lett.* 60, 2892-94 (1992).
17. I.T. Ferguson, A.G. Norman, B.A. Joyce, T.Y. Seong, G.R. Booker, R.H. Thomas, C.C. Philips, and R.A. Stradling, "Molecular Beam Epitaxial Growth of InAsSb Strained Layer Superlattices. Can Nature do it Better?" *Appl. Phys. Lett.* 59, 3324 -26(1991).
18. B. Neubauer, A. Rosenauer, D. Gerthsen, O. Ambacher, M. Stutzmann, M. Albrecht, and H.P. Strunk, "Analysis of Composition Fluctuations in $\text{Al}_x\text{Ga}_{1-x}\text{N}$," *Mats. Sci. Eng. B* 59, 182-85 (1999).
19. P. Ruterana and F. Deniel, "Observations of Ordering and Phase Separation in $\text{In}_x\text{Ga}_{1-x}\text{N}$ Layers," *Mats. Sci., Eng. B* 59, 186-190 (1999).
20. M.A. Shahid, S. Mahajan, D.E. Laughlin, and H.M. Cox, "Atomic Ordering in $\text{Ga}_{0.47}\text{In}_{0.53}\text{As}$ and $\text{In}_{1-x}\text{Ga}_x\text{As}_y\text{P}_{1-y}$ Alloy Semiconductors," *Phys. Rev. Lett.* 58, 2567-70 (1987).
21. M.A. Shahid and S. Mahajan, "Long-Range Atomic Order in $\text{Ga}_x\text{In}_{1-x}\text{As}_y\text{P}_{1-y}$ Epitaxial Layers," *Phys. Rev. B* 38, 1344-50 (1988).
22. T. Suzuki, A. Gomyo, and S. Iijima, "Strong Ordering on GaInP Alloy Semiconductors: Formation Mechanism for the Ordered Phase," *J. Crystal Growth*, 93, 396-405 (1988).
23. B.A. Philips, A.G. Norman, T.Y. Seong, S. Mahajan, G.R. Booker, M. Skowronski, J.P. Harbison, and V.G. Keramidas, "Mechanism of CuPt-Type Ordering in Mixed III-V Epitaxial Layers," *J. Cryst. Growth* 140, 249-63 (1994).
24. S. Mahajan, "Two-Dimensional Phase Separation and Surface-Reconstruction Driven Atomic Ordering in Mixed III-V Alloys," *Mats. Sci. Eng. B* 30, 187-196 (1995).

25. I.J. Murgatroyd, A.G. Norman, and G.R. Booker, "Observation of {111} Ordering and [110] Composition Modulation in Epitaxial GaAsSb Layers," *J. Appl. Phys.* 67, 2310-19 (1990).
26. G.S. Chen, D.H. Jaw, and G.B. Stringfellow, "Effects of Substrate Misorientation on Ordering in GaAs_{0.5}P_{0.5} Grown by Organometallic Vapor Phase Epitaxy," *Appl. Phys. Lett.* 53, 2475-77 (1990).
27. R.S. McFadden, "Ordering Defects on InGaAs and InGaP Epitaxial Layers," Ph.D. Dissertation, Carnegie Mellon University (1995).
28. A. Gomyo, K. Makita, I. Hino, and T. Suzuki, "Observation of a New Ordered Phase in Al_xIn_{1-x}As Alloy and Relation Between Ordering and Surface Reconstruction during MBE Growth," *Phys. Rev. Lett.* 72, 673-75 (1994).
29. B.A. Philips, A. Kamiya, I. Hingerl, L.T. Florez, D.E. Aspnes, and J.P. Harbison, "Real-Time Observation of Atomic Ordering in InGaAs Epitaxial Layers," *Phys. Rev. Lett.* 74, 3640-43 (1995).
30. B.A. Philips, "Role of Surface Reconstruction in Atomic Ordering in (001) Mixed III-V Epitaxial Layers," Ph.D. Dissertation, Carnegie Mellon University (1995).
31. T.L. McDevitt, "Phase Separation in In_{1-x}Ga_xAs and InGaAsP Epitaxial Films," Ph.D. Dissertation, Carnegie Mellon University (1990).
32. K. Lee, "Phase Separation in In_{1-x}Ga_xAs and Zn Te_xSe_{1-x} Epitaxial Films," Ph.D. Dissertation, Carnegie Mellon University (1994).
33. S. Mahajan, "Growth- and Processing Induced Defects in Semiconductors," *Progress in Mats. Sci.* 33, 1-84 (1989).

DYNAMICAL LATTICE INSTABILITIES IN ALLOY PHASE DIAGRAMS

Göran Grimvall

Theoretical Physics, Department of Physics
Royal Institute of Technology
SE-100 44 Stockholm, Sweden

INTRODUCTION

Ab initio electron structure calculations can accurately give total energies of solids in assumed atomic configurations for which there are no experimental data. As an example, one may calculate the total energy of silicon and germanium not only in the observed and stable diamond-type lattice structure but also in body centred cubic, face centred cubic, hexagonal close packed and other structures.¹ Similarly the difference in cohesive energy between bcc, fcc and hcp lattice structures can be obtained across a transition-metal row in the Periodic Table.² As another example, one may find the vacancy formation energy in 3d-, 4d- and 5d-transition metals when they are assumed to have a bcc structure and compare that with the results in an assumed fcc structure.³ In all such calculations, the atomic positions are kept fixed in a certain lattice structure, i.e. bcc, fcc, hcp etc. However many of these structures, for a given chemical composition, are dynamically unstable. The well-known conditions for elastic stability under shear, in a lattice of cubic symmetry, are⁴

$$c_{44} > 0; \quad C' = (c_{11} - c_{12})/2 > 0 \quad (1)$$

where c_{ij} are single-crystal elastic constants. Even if these inequalities referring to long-wavelength deformations are fulfilled, there may be instabilities under a lattice modulation of short wavelength. To ensure stability of a lattice for any small displacement of the atoms

from their assumed equilibrium positions, all phonon frequencies $\omega(\mathbf{q},s)$ of wavevectors \mathbf{q} and mode indices s must be real, i.e.,

$$\omega^2(\mathbf{q},s) > 0 \quad (2)$$

DYNAMICAL INSTABILITY IS A COMMON PHENOMENON

Not until recently has it been realised how common it is that structures previously assumed to be metastable structures (i.e. structures with an energy higher than that of the observed ground state) are in fact dynamically unstable; cf., e.g., Wills et al.⁵, Craievich et al.^{6,7}, Grimvall.^{4,8} and further references in Table 1. In earlier calculations, when one obtained vibrational modes (\mathbf{q},s) with $\omega^2(\mathbf{q},s) < 0$, this was often assumed to be due to deficiencies in the theoretical description of the interaction between the atoms. Furthermore, for a long time the existence of lattice instabilities was the (unknown) reason why *ab initio* calculations of total energies of elements in bcc, fcc and hcp structures sometimes came out to be very different from what one inferred from a semiempirical analysis of experimental binary alloy phase diagrams using the Calphad method. The two views have now been reconciled.⁸

Table 1 gives some examples of dynamical instabilities, as obtained in *ab initio* calculations. The list is far from complete and only serves the purpose of showing how common and varied the instabilities are. Many further examples of instabilities in the long-wavelength limit, i.e. elastic constants violating one of the inequalities in eq. (1), are found in Wills et al.⁵ and Craievich et al.⁷ Such *ab initio* electronic structure calculations, giving the total energy of the static lattice along so called Bain paths for lattice deformations, are now common practice. In order to be accurate they should allow the crystal volume to vary along the Bain path, so as to give the energy minimum.

Table 1. The observed structure (at room temperature and normal pressure) of some materials, and examples of structures that have been found to be dynamically unstable.

Material	Observed structure	Unstable structure	Reference
Cu	fcc	bcc	Kraft et al. ⁹
Ni	fcc	bcc	Craievich and Sanchez ¹⁰
Os	fcc	bcc	Wills et al. ⁵
Mg	hcp	bcc	Moriarty and Althoff ¹¹
Re	hcp	bcc	Persson et al. ¹²
Cr	bcc	fcc	Craievich and Sanchez ¹⁰
W	bcc	fcc	Einarsdotter et al. ¹³
GaAs	diamond	NaCl	Ozoliņš and Zunger ¹⁴

It is clear from Table 1 that a material which is stable in the close packed fcc or hcp lattices may be dynamically unstable in the bcc lattice, and vice versa. However, we also

note that both the close packed and the bcc structures may be dynamically stable at all temperatures below the melting temperature, as is the case for iron. Titanium, zirconium and hafnium exemplify that the hcp and the bcc structures are dynamically stable at high temperatures, while the bcc phase appears to be dynamically unstable at low temperatures.¹⁵

APPROACHING A LATTICE INSTABILITY IN AN ALLOY

As an illustration consider a binary alloy $A_{1-c}B_c$ at 0 K, where the element A is observed in the fcc lattice structure and has a dynamically unstable bcc lattice, while element B is stable in the bcc and unstable in the fcc phase. One example¹⁶ is $A = \text{Pt}$, $B = \text{W}$, and another¹⁰ is $A = \text{Ni}$, $B = \text{Cr}$. Let the concentration c increase from $c = 0$ to the critical concentration c^* beyond which $\omega^2(\mathbf{q},s)$ is no longer positive for all modes (\mathbf{q},s) . Since a phase diagram is determined by a comparison of Gibbs energies $G = H - TS$ of competing phases, it is interesting to investigate $G(T;c)$ as c approaches c^* from the stable region.

The essential physics can be described by harmonic lattice vibrations. We therefore assume that the phonon spectrum is independent of the temperature T , and ignore the anharmonic corrections that certainly are present close to c^* . Furthermore we focus on the high-temperature region, $T > \theta_D$ where θ_D is a characteristic Debye temperature. Then, for a spectrum of harmonic vibrations and at pressure $p \approx 0$, the vibrational contribution to the Gibbs energy has the form (per atom)⁴

$$G_{\text{vib}} = H_{\text{vib}} - TS_{\text{vib}} \approx -3k_B T \ln(k_B T / h \omega_{\log}) = -3k_B T \{ 1/3 + \ln(T/\theta_D) \} \quad (3)$$

Here ω_{\log} is the logarithmic average of the phonon frequencies. The last equality refers to a phonon spectrum described by a Debye model. Then G_{vib} diverges towards $-\infty$ when $c \rightarrow c^*$ (i.e. when $\theta_D \rightarrow 0$), and the corresponding phase would be significantly stabilised at concentrations just before one reaches c^* . However, in a Debye model all the phonon frequencies simultaneously tend to 0 as $c \rightarrow c^*$. In a real system, on the other hand, there will one particular mode (\mathbf{q},s) for which $\omega(\mathbf{q},s)$ first becomes 0 when $c = c^*$, while other modes still have a finite ω . Therefore the singularity in S_{vib} is weak. In fact, S_{vib} has a finite limiting value when $c \rightarrow c^*$ in the model of harmonic vibrations.¹⁶

On the basis of eq. (3) we can understand some features in the phase diagram of a binary alloy with phases that are dynamically unstable for certain concentration ranges. The gradual softening of the phonon spectrum as the concentration approaches the stability limit (i.e. the lowering of ω_{\log}) tends to decrease G_{vib} , and thus tends to make the phase thermodynamically more stable in competition with other phases. Therefore the vibrational part of the Gibbs energy must be considered in a discussion of the phase diagram of such systems; cf. work on Ni-Cr¹⁰ and W-Re.^{12,17} However, we also noted above that the singularity in S_{vib} is weak. It therefore often happens that the experimentally determined phase diagram shows no particular feature that immediately reveals the existence of

dynamical instabilities. One such example is the Pt-W system.¹⁶ The fcc Pt-W solid solution becomes unstable in the W-rich end, but does so at Pt concentrations which are well within the two-phase field in the phase diagram; cf. Figure 1. Hence there is no conspicuous precursor effect in the fcc phase field related to the instability. A similar situation holds for the bcc phase field in the W-Re phase diagram¹⁷. Pure W has the bcc lattice structure, while pure bcc Re is dynamically unstable.

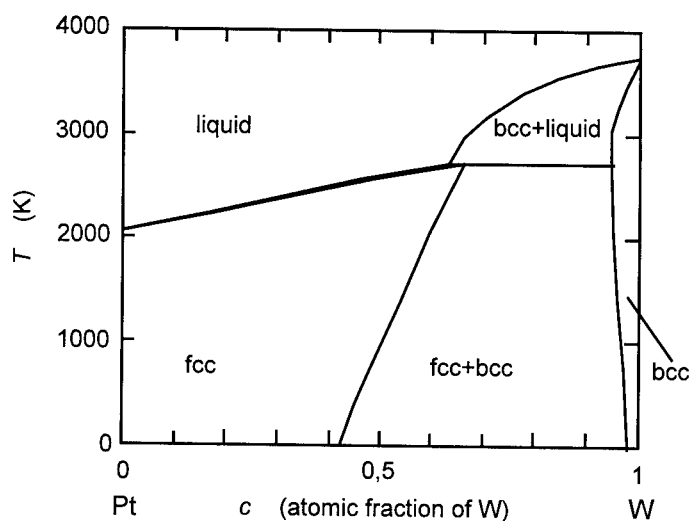


Figure 1. The essential features of the experimental Pt-W phase diagram.

Magnesium provides an interesting case of a lattice instability. At zero pressure Mg is stable in the hcp lattice. The high-pressure form of Mg has the bcc structure, but it becomes dynamically unstable at lower pressures ($p < p_c \approx 50$ MPa at low T). The temperature-pressure phase diagram of Mg has been obtained in *ab initio* calculations.¹¹ The phase diagram does show a precursor effect, in the form a tendency to a stabilisation of the high-pressure bcc structure for p just above the critical pressure p_c at which the bcc phase becomes dynamically unstable, Figure 2. Since the stabilising effect is due to the entropy term S_{vib} in the Gibbs energy $G = H - TS$, it is only seen at high temperatures T where TS_{vib} gives a significant contribution to G .

CONCLUSIONS

It is common to discuss properties of materials not only in that crystal structure which is observed in thermal equilibrium (e.g., bcc), but also in other structures (e.g., fcc and hcp). Not until recently has it been appreciated that these other structures may not be metastable phases but are in fact dynamically unstable and therefore have an undefined

entropy and Gibbs energy. The source of such information is usually some form of ab initio calculation of unstable phonon modes. This paper gives examples of materials showing lattice instabilities. In particular, the behavior of the Gibbs energy of binary alloys $A_{1-c}B_c$ and the consequences for the phase diagram are considered, as the concentration c approaches the limit of dynamical stability.

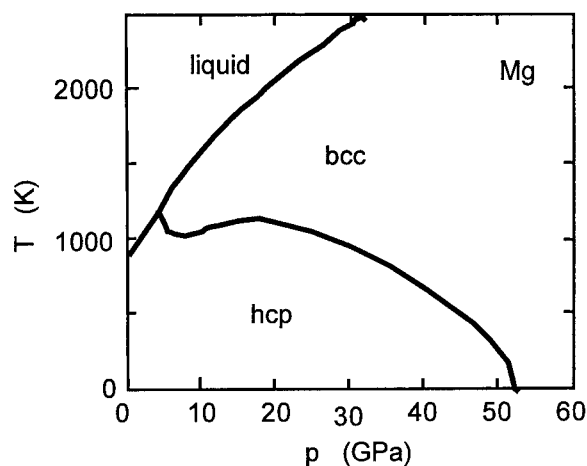


Figure 2. The temperature-pressure phase diagram of magnesium. Adopted from ab initio-type calculations by Moriarty and Althoff.¹¹

ACKNOWLEDGEMENT

I want to thank my present and previous graduate students Kristin Persson (*née* Einarsdotter), Mathias Ekman and Vidvuds Ozoliņš for many discussions. This work was supported by the Swedish Foundation for Strategic Research (SSF) under Materials Consortium 9.

REFERENCES

1. M.T. Yin and M.L. Cohen, *Theory of static structural properties, crystal stability, and phase transformations: Application to Si and Ge*, Phys. Rev. B 26:5668 (1982).
2. H. Skriver, *Crystal structure from one-electron theory*, Phys. Rev. B 31:1909 (1985).
3. P.A. Korzhavyi, I.A. Abrikosov, B. Johansson, A.V. Ruban, and H.L. Skriver, *First-principles calculations of the vacancy formation energy in transition and noble metals*, Phys. Rev. B 59:11693 (1999).

-
4. G. Grimvall, *Thermophysical Properties of Materials*, North-Holland, Amsterdam (1999).
 5. J.M. Wills, O. Eriksson, P. Söderlind, and A.M. Boring, *Trends of the elastic constants of cubic transition metals*, Phys. Rev. Lett. 68:2802 (1992).
 6. P.J. Craievich, M. Weinert, J.M. Sanchez, and R.E. Watson, *Local stability of non-equilibrium phases*, Phys. Rev. Lett. 72:3076 (1994).
 7. P.J. Craievich, J.M. Sanchez, R.E. Watson, and M. Weinert, *Structural instabilities of excited phases*, Phys. Rev. B 55:787 (1997).
 8. G. Grimvall, *Reconciling ab initio and semiempirical approaches to lattice stabilities*, Ber. Bunsenges. Phys. Chem. 102:1083 (1998).
 9. T. Kraft, P.M. Marcus, M. Methfessel, and M. Scheffler, *Elastic constants of Cu and the instability of its bcc structure*, Phys. Rev. B 48:5886 (1993).
 10. P.J. Craievich and J.M. Sanchez, *Vibrational free energy in the Ni-Cr system*, Comput. Mater. Sci. 8:92 (1997).
 11. J.A. Moriarty and J.D. Althoff, *First-principles temperature-pressure phase diagram of magnesium*, Phys. Rev. B 51:5609 (1995).
 12. K. Persson, M. Ekman, and G. Grimvall, *Dynamical and thermodynamical instabilities in the disordered rhenium-tungsten system*, Phys. Rev. B 60 (1999), in press.
 13. K. Einarsdotter, B. Sadigh, G. Grimvall, and V. Ozoliņš, *Phonon instabilities in fcc and bcc tungsten*, Phys. Rev. Lett. 79:2073 (1997).
 14. V. Ozoliņš, and A. Zunger, *Theory of systematic absence of NaCl-type (β -Sn-type) high pressure phases in covalent (ionic) semiconductors*, Phys. Rev. Lett. 82:767 (1999).
 15. K.-M. Ho, C.L. Fu, and B.N. Harmon, *Vibrational frequencies via total-energy calculations. Applications to transition metals*, Phys. Rev. B 29:1575 (1984).
 16. A. Fernández Guillermet, V. Ozoliņš, G. Grimvall, and M. Körling, *Phase stabilities in the Pt-W system: Thermodynamic and electronic-structure calculations*, Phys. Rev. B 51:10364 (1995).
 17. M. Ekman, K. Persson, and G. Grimvall, *Phase diagram and lattice instability in tungsten-rhenium alloys*, J. Nucl. Mater. (1999), in press.

BOND-ORDER POTENTIALS FOR TRANSITION METALS BASED BINARY ALLOYS: Ti-Al AND Mo-Si ALLOYS

S. Znam¹, D. Nguyen-Manh², D. G. Pettifor² and V. Vitek¹

¹Department of Materials Science and Engineering, University of Pennsylvania, Philadelphia, Pennsylvania, 19104-6272, U.S.A.

²Department of Materials, University of Oxford, Parks Road
Oxford OX1 3PH, UK

INTRODUCTION

Intermetallic compounds have been studied very extensively in the last two decades since they are considered excellent materials for high-temperature applications (for recent reviews see Liu et al. 1992; Westbrook and Fleischer 1995; Stoloff and Sika 1996). The main reasons are that they tend to be intrinsically very strong, possess high elastic moduli and have low self-diffusion coefficients and thus a high creep strength as well as corrosion resistance. The intermetallics that have been in use for a long time are alloys of Ni and Al, such as superalloys containing Ni₃Al particles (see, for example, Nabarro 1994; Stoloff and Liu 1996) and NiAl based alloys (see, for example, Darolia, et al. 1992; Noebe, et al. 1996) as well as Fe-Al alloys (Stoloff 1998). In recent years the development and investigation of new intermetallics that are believed to supersede the Ni-Al and Fe-Al based alloys has been pursued very actively. The most interesting are compounds with higher melting temperatures than Ni-Al alloys and with low density

combined with high strength and modulus that give rise to attractive specific properties (property divided by density).

At present one of the most promising new compounds is TiAl crystallizing in the $L1_0$ structure (Dimiduk 1999). This material has not only very attractive specific properties but also a relatively high toughness and ductility have been achieved by inventive metallurgical processing. Aluminium rich alloys have a single-phase $L1_0$ structure but stoichiometric and titanium rich alloys exhibit two-phase lamellar structure, consisting of layers of tetragonal, $L1_0$, TiAl and hexagonal, DO_{19} , Ti_3Al (for a review see Huang and Chestnutt 1995). Interestingly, the most ductile material is the two phase lamellar alloy although its components are quite brittle in single crystalline form (Yamaguchi, et al. 1996; Kim 1998).

A possible next generation of compounds that has invoked a wide-spread interest, are transition metal (TM) silicides formed from refractory metals of groups IVa - VIa (for reviews see Vasudevan, et al. 1999). Their melting temperature is appreciably higher than that of Ni or Ti based aluminides, comparable to silicon-based ceramics, but they are metallic materials and, consequently, possess relatively high thermal conductivity and are plastically deformable. Until now di-silicides have been the most investigated group of these materials, in particular $MoSi_2$ which crystallizes in the tetragonal $C11b$ structure (see, for example, Ito, et al. 1997, 1999; Mitchell and Misra 1999). However, more complex silicides, such as Mo_5Si_3 which crystallizes in the body-centered tetragonal $D8_m$ structure, are also strong candidates mainly because of their superior corrosion resistance and high creep strength (Chu, et al. 1999).

However, the above mentioned benefits of intermetallic compounds do not come without attendant drawbacks. The single largest impediment is their low ductility and/or toughness at ambient temperatures. In general, these properties tend to plummet as the crystal symmetry decreases and the covalency of bonding increases. Both TiAl based alloys and TM-silicides possess non-cubic crystal structures and their bonding has a significant covalent component (Siegl, et al. 1997; Tanaka, et al. 1999). The ductility of any crystalline material is controlled by the motion of dislocations and it is a common feature of complex structures that dislocations possess non-planar sessile cores and thus very high Peierls stresses (for reviews see Duesbery and Richardson 1991; Vitek 1992). This characteristic of the atomic structure of dislocations, which is further enhanced if the covalent component of bonding is significant, controls then to a great extent the mechanical behaviour of these materials. A fundamental understanding of these problems can be attained by atomistic modelling of dislocations, stacking-fault type defects and interfaces present in these materials. An appropriate description of atomic interactions is an essential precursor for physically meaningful studies of this type.

While LDA based ab initio calculations are at present the state of the art, they are severely limited by the number of independent atoms that can be treated in such studies and, for example, thousands of atoms need to be included in dislocation calculations. Simple alternatives, embedded-atom or Finnis-Sinclair type potentials (Daw and Baskes 1984; Finnis and Sinclair 1984), that proved very valuable in many metallic systems, are

central force schemes and not sufficient if the covalent component of bonding is significant. The semi-empirical method in which the required covalent character of bonding is included explicitly is the tight-binding method. In recent years this method has been reformulated in terms of Bond-order Potentials (BOP) (Pettifor 1989, 1995; Pettifor and Aoki 1991; Horsfield, et al. 1996a, b; Bowler, et al. 1997) using the orthogonal basis and two-centre bond (hopping) integrals. In this case a very important problem is the transferability of the bond integrals. This is particularly crucial when the method is to be used in studies of extended defects with structures very different from ideal lattices. This problem is thoroughly investigated in this paper by studying the environmental dependence of the bond integrals using the ab initio all electron TB-LMTO method (Andersen and Jepsen 1984; Skriver 1984; Andersen, et al. 1985). It is shown that in Ti-Al alloys the bond integrals are transferable and can be represented as functions of the separation of atoms. The BOP is then constructed for these alloys using the usual two-center bond integrals and testing of these potentials demonstrates their capability to describe atomic interactions in a broad variety of structures. On the other hand, in molybdenum silicides the transferability of the bond integrals is limited and it is proposed that an environmental dependence of the two-centre bond integrals needs to be introduced in order to overcome this problem when constructing BOP for these alloys.

DEFINITION OF BOND-ORDER POTENTIALS

The BOP method is a tight-binding scheme in which the computational effort scales linearly with the number of particles considered (Horsfield and Bratkovsky 1996; Horsfield, et al. 1996a, b; Bowler, et al. 1997; Nguyen-Manh, et al. 1998). The energy of a system of atoms is divided into three parts and can be written as

$$U = U_{\text{pair}} + U_{\text{bond}} + U_{\text{env}} \quad (1)$$

U_{pair} represents the electrostatic interaction between the atoms and the overlap repulsion between the valence d and p orbitals. It is principally repulsive and described by a pair-potential, the functional form of which has been taken as

$$V^{s_i, s_j}(R_{ij}) = \sum_{k=1}^6 A_k^{s_i, s_j} (R_k^{s_i, s_j} - R_{ij})^3 H(R_k^{s_i, s_j} - R_{ij}) \quad (2)$$

where $H(x)$ is the Heaviside step function, R_{ij} is the separation of interacting atoms i and j and s_i and s_j mark the type of species at the sites i and j , respectively. This is a sum of cubic splines that extends up to the cut-off $R_1^{s_i, s_j}$. The node points of the splines, $R_k^{s_i, s_j}$, and numerical coefficients, $A_k^{s_i, s_j}$, are used as fitting parameters as described below. This functional form assures that V^{s_i, s_j} and its first and second derivatives are

everywhere continuous and equal to zero at the cut-off; the same form was used in the construction of many-body central force potentials of the Finnis-Sinclair type (Ackland, et al. 1987).

U_{bond} is the bond energy arising from formation of the valence band that comprises terms dependent on bond angles; in Ti-Al alloys and transition metal silicides this contribution originates from d and p electrons and also includes their hybridization. Within the BOP it is written as

$$U_{\text{bond}} = \sum_{\substack{I, J \\ i \neq j}} H_{I, J} \Theta_{J, I} \quad (3)$$

where $H_{I, J}$ and $\Theta_{J, I}$ are the Hamiltonian and bond order matrix elements, respectively. The index $I \equiv [i, L_i, s_i]$, where i numbers the atomic sites in the system studied, $L_i = (\ell, m)_i$ where ℓ denotes the quantum orbital moment and m the quantum magnetic moment for spherical symmetry and s_i has the same meaning as in the case of the pair potential; analogously $J \equiv [j, L_j, s_j]$, $L_j = (\ell, m)_j$. Thus the bond energy associated with atom i , U_{bond}^i , is within the BOP method decomposed explicitly in terms of the contribution from individual bonds which atom i makes with the neighbouring atoms j (Pettifor 1995). The values of $H_{I, J}$ are ascertained on the basis of ab initio calculations and for $i \neq j$ the functional forms of $H_{I, J}$, called in the following the bond integrals, are also determined. This is discussed in the following section.

The bond-order matrix can be expressed for a given Hamiltonian in terms of the derivative of certain diagonal elements of the Green's function (Aoki 1993; Aoki and Pettifor 1993). These diagonal elements are evaluated using the recursion method of continued fractions (Haydock 1980) with the recursion coefficients determined by the Lanczos algorithm (Lanczos 1950). In order to damp down the long-range Friedel oscillations that are present in metallic materials, a fictitious finite temperature of the electrons is introduced in order to achieve rapid real-space convergence of the bond-order potentials. For this reason the free bond energy rather than the internal bond energy is used in the calculations (Horsfield and Bratkovsky 1996; Girshick, et al. 1998). The relatively complex procedures involved in evaluation of U_{bond} are all part of the suit of computer codes available as the Order N (OXON) package.

The environmentally dependent part of the energy, U_{env} , represents the s,p ion core repulsion (Pettifor 1978) and it is described by a repulsive central-force many body potential which was proposed to have the screened Yukawa form (Nguyen-Manh, et al. 1998)

$$U_{\text{env}} = \frac{1}{2} \sum_{\substack{i, j \\ i \neq j}} B^{s_i, s_j} \frac{\exp[-\frac{1}{2}(\lambda^{s_i} + \lambda^{s_j})(R_{ij} - 2R_c^{s_i, s_j})]}{R_{ij}} \quad (4.1)$$

with

$$\lambda^{s_i} = \lambda_0^{s_i} + \left[\sum_{k \neq i} C^{s_i} \exp(-v^{s_i} R_{ik}) \right]^{1/n^{s_i}} \quad (4.2)$$

where B^{s_i, s_j} , C^{s_i} , v^{s_i} , $\lambda_0^{s_i}$, $R_c^{s_i, s_j}$ and n^{s_i} are adjustable parameters, in general dependent on the type of species, s_i . This form was deduced in the framework of an investigation of the total energy contributions to the Cauchy pressures ($C_{12} - C_{66}$ and $C_{13} - C_{44}$ for the tetragonal symmetry). This contribution is particularly important when some of the Cauchy pressures are negative, which is the case in both TiAl (Tanaka, et al. 1996; Tanaka and Koiwa 1996) and MoSi₂ (Tanaka, et al. 1997). The reason is that for structures in equilibrium U_{pair} does not contribute to the Cauchy pressures (Sob and Vitek 1996; Girshick, et al. 1998) and the bond part alone also gives positive contributions (Nguyen-Manh, et al. 1998).

Atomistic simulations require not only evaluation of the energy but also its derivatives with respect to the positions of atoms, i. e. forces acting on individual atoms. The calculation of the derivatives of the pair and environmental parts of the energy is straightforward. The derivatives of the bond part can be found using the Hellmann-Feynman theorem (Hellmann 1937; Feynman 1939) provided the bond order is computed sufficiently accurately (Girshick, et al. 1998); evaluation of these derivatives is also part of the Order N (OXON) package.

BOND ENERGY: HAMILTONIAN MATRIX ELEMENTS AND THEIR TRANSFERABILITY

For $i \neq j$ the bond integrals $H_{i,j}$ are commonly determined within the orthogonal two-centre approximation. However, when a more general non-orthogonal basis set is introduced within the tight-binding method, the overlap matrix, $S_{i,j}$, and three-center integrals intersect an environmental dependence that is neglected in this approximation. Hence, the transferability of the bond integrals based on the orthogonal basis set to different environments may be limited and needs to be thoroughly investigated. This is particularly important when BOPs are to be used in studies of complex defects with structures very different from the ideal lattices and, in the case of alloys, for different compositions. This problem is addressed in this section.

However, the first important approximation is the limited set of orbitals used in the tight-binding scheme. Specifically, in the case of Ti-Al and Mo-Si alloys we have included d orbitals centred on Ti or Mo, respectively, and p-orbitals centred on Al or Si, respectively. Thus $H_{i,j} \neq 0$ in the following three cases: (i) $s_i = s_j = \text{Ti}(\text{Mo})$, $L_i = L_j$ and $\ell = 2$ (d-orbital); (ii) $s_i = s_j = \text{Al}(\text{Si})$, $L_i = L_j$ and $\ell = 1$ (p-orbital); (iii) $s_i = \text{Ti}(\text{Mo})$, $s_j = \text{Al}(\text{Si})$, $L_i = (2, m)_i$ (d-orbital) and $L_j = (1, m)_j$ (p-orbital), or vice versa. The validity of this

approximation was tested by comparing the electronic densities of states (DOS) calculated in this tight-binding p-d approximation with those evaluated using the ab-initio all electron tight-binding LMTO method (Andersen, et al. 1985). This test demonstrated that for both TiAl with the $L1_0$ structure and MoSi_2 with the $C11_b$ structure all the important features of the DOS are well reproduced within the p-d approximation (Nguyen-Manh, et al. 2000; Znam, et al. 2000). Note that in this approximation the species and the values of L_i are uniquely linked so that the species index, s_i , can be omitted from the index I used in marking the elements of the Hamiltonian matrix $H_{I,J}$.

In order to investigate the transferability of the bond integrals and to determine their functional forms, $H_{I,J}$ need to be evaluated as functions of the separation of atoms i and j for various structures using an ab-initio technique. Such technique must employ a small, single-electron basis of atom-centered, short-range orbitals and the Hamiltonian must have a simple analytical form that relates to a two-center, orthogonal tight-binding Hamiltonian so that a direct link with the tight-binding method can be established. The first-principles TB-LMTO (Andersen and Jepsen 1984; Andersen, et al. 1985) is such a method. In this approach the minimal basis of muffin-tin orbitals is transformed in the two-centre approximation exactly into a localized basis with at most one s-type, three p-type and five d-type orbitals per atom. The TB-LMTO Hamiltonian may be expressed in the orthonormal representation as a power series in the two-centre tight-binding Hamiltonian

$$H_{I,J}^\alpha \equiv (c_I^\alpha - E_v) \delta_{IJ} + \sqrt{d_I^\alpha} S_{I,J}^\alpha \sqrt{d_J^\alpha} \quad (5)$$

where the superscript α denotes that the Hamiltonian is constructed using the screened structure constants, $S_{I,J}^\alpha$. These are determined by the positions of the atoms in the system studied. They are given in terms of the conventional canonical structure constants $S_{I,J}^0$ by the matrix equation (Andersen, et al. 1985; Andersen, et al. 1994)

$$S^\alpha = S^0 (1 - \alpha S^0)^{-1} \quad (6)$$

where α is a diagonal matrix with elements $\alpha_{I,J} = \alpha_i \delta_{i,j} \delta_{L_i, L_j}$ that characterizes the corresponding LMTO representation (Andersen and Jepsen 1984; Andersen, et al. 1985). E_v are the energy expansion parameters taken at the center of the occupied part of the L_i projected valence density of states (Skriver 1984). Coefficients $(c_I^\alpha - E_v)$ and d_I^α can be obtained from the self-consistent LMTO potential parameters c_I^γ , d_I^γ and γ_I that are tabulated in (Andersen, et al. 1985) using the expression (Nowak, et al. 1991)

$$\frac{c_I^\alpha - E_v}{c_I^\gamma - E_v} = \left(\frac{d_I^\alpha}{d_I^\gamma} \right)^{1/2} = 1 + \frac{\alpha_I - \gamma_I}{d_I^\gamma} (c_I^\gamma - E_v) \quad (7)$$

The optimum values of α_i that yield the most localized orbitals are $\alpha_s = 0.3546$, $\alpha_n = 0.0530$ and $\alpha_d = 0.0170$ (Nowak, et al. 1991).

Owing to the short-range character of the screened structure constants the second term in equation (5) gives for $i \neq j$ the effective bond integrals. However, it should be noted that the reduction of S_{IJ}^α to axially symmetric two-centre integrals with σ , π and δ states (for the direction $R_i - R_j$ connecting the two atoms chosen as the z axis of the coordinate system) is no longer exact. The reason is that the screened structure matrix, unlike the canonical one, generally has lower than cylindrical symmetry because of its dependence on the local environment. Hence, the resulting bond integrals H_{IJ} are, in general, environmentally dependent.

While the on-site Hamiltonian elements do not enter directly into equation (3), they are needed when evaluating the bond order. They can be again determined using equations (5-7) and their values were calculated in this way for ideal structures such as $L1_0$ TiAl. However, they are adjusted self-consistently to maintain local charge neutrality with respect to each atom via the so-called promotion energy. This condition reflects the perfect screening properties of metallic materials (Pettifor 1995) and it is achieved efficiently within the BOP scheme as described in (Horsfield, et al. 1996a, b; Bowler, et al. 1997).

In order to investigate the bond integrals employed in BOP for Ti-Al alloys, their dependence on the separation of atoms was calculated using equations (5-7) for $L1_0$ TiAl and DO_{19} Ti_3Al as well as for pure Ti and Al. This was achieved by evaluating the integrals in each case for several volumes per atom. The employment of different structures and compositions allows us to investigate possible environmental dependence of these integrals. The results of these calculations, presented in Fig. 1, show an excellent transferability between different structures and compositions for all the bond integrals used: $dd\sigma$ and $dd\pi$ for Ti-Ti bonding ($dd\delta$ is not included in Fig. 1 but displays the same behaviour), $pp\sigma$ and $pp\pi$ for Al-Al bonding and $dp\sigma$ and $dp\pi$ for Ti-Al bonding. Detailed numerical values of these integrals will be presented in (Znam, et al. 2000). This finding confirms that the bond integrals can be represented as functions of the separation of the atoms and the corresponding analytical formulae used for these integrals in the framework of BOP are given in the next section.

A salient feature of the Ti-Al alloys, as well as of pure Ti and Al, is that their structures are close packed and thus the second nearest neighbour spacing is much larger than that of the first nearest neighbours. Hence, owing to the short-range nature of the screened structure matrix, all the bond integrals are negligible at second nearest neighbours.

The bond integrals for Mo-Mo ($dd\sigma$ and $dd\pi$; $\delta d\delta$ is again not presented), Si-Si ($pp\sigma$ and $pp\pi$) and Mo-Si ($dp\sigma$ and $dp\pi$), calculated using the same TB-LMTO scheme, are presented in Fig. 2. These calculations were performed for the experimentally observed structures $MoSi_2$ (C11b), Mo_5Si_3 (D8_m), Mo_3Si (A15) and pure Mo (bcc) and for MoSi and pure Si in hypothetical B2 and bcc structures, respectively. The situation

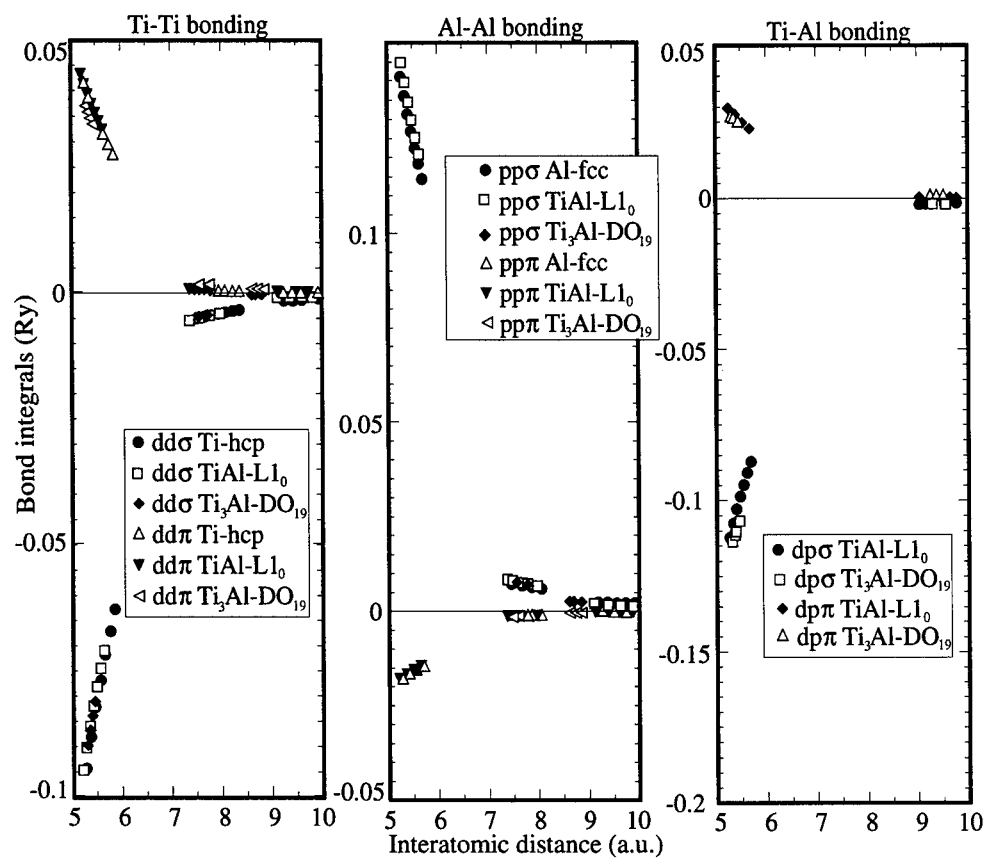


Figure 1. Bond integrals in Ti-Al alloys calculated using TB-LMTO as function of the separation of atoms.

regarding the transferability and dependence on the separation of atoms is now different. Some of the bond integrals display noticeably different values for the same atomic separation but different structures, as well as a discontinuity between the first and second nearest neighbours for the bcc-like structures. Unlike in close packed structures, in the bcc lattice the first and second neighbours are close to each other (14% difference in interatomic distances) and this results in different environmental screening for the two-centre bond integrals. This effect has also been found recently in the development of an empirical environmentally dependent spd-based tight binding model for molybdenum that contains fifty three adjustable parameters (Haas, et al. 1998a, b). However, in this study the discontinuous behaviour was found only for $ss\sigma$ and $sp\sigma$, whereas our present parameter-free calculations show this effect for all bond integrals and it is most pronounced for $dd\pi$, $pp\pi$ and $dp\pi$, as seen in Fig. 2.

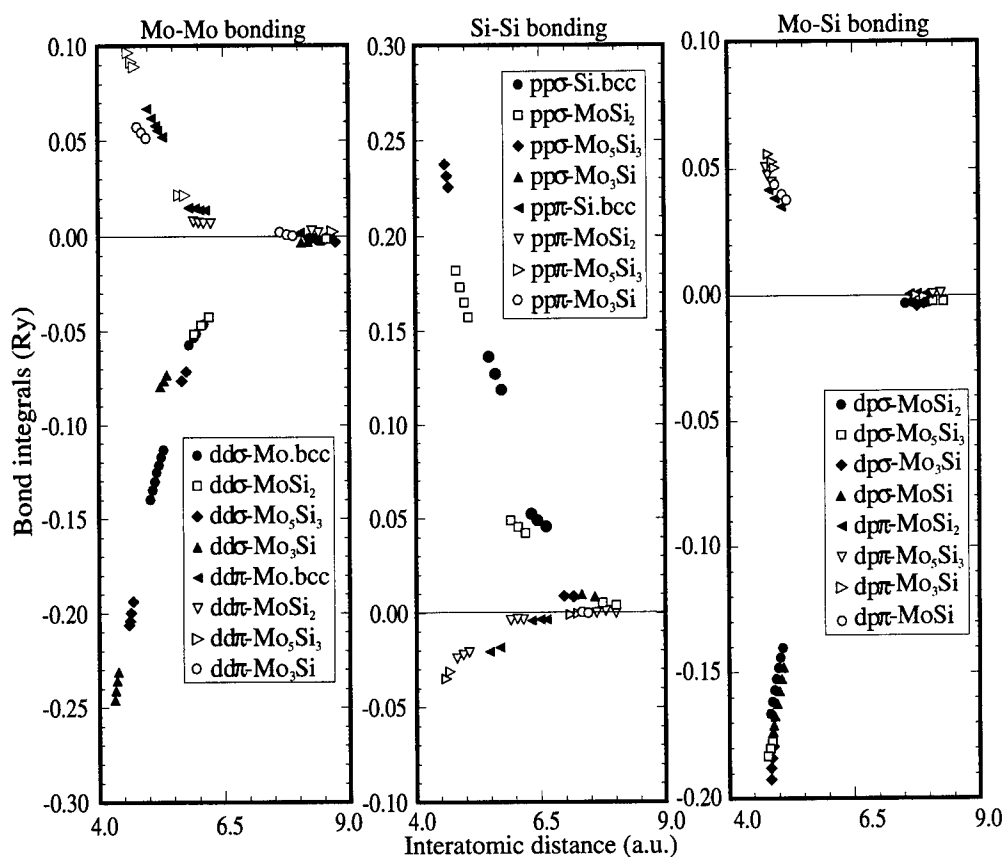


Figure 2. Bond integrals in Mo-Si alloys calculated using TB-LMTO as function of the separation of atoms.

BOND-ORDER POTENTIALS FOR TiAl

Construction of the potentials

Since BOP is a semi-empirical method of describing the atomic interactions, various equilibrium properties of pure titanium and TiAl are fitted during their construction. However, it is important to note that the number of empirical data fitted is quite small (nine for TiAl). The BOPs obtained describe the Ti-Ti, Al-Al and Ti-Al interactions in TiAl and, moreover, the part describing Ti-Ti interaction also represents BOP for pure Ti. But, the same is not true for Al as no properties of pure aluminium have been fitted when constructing the BOP for TiAl. We should note that the BOP for pure Ti developed in the present study is not the same as that advanced earlier (Girshick, et al. 1998) although the fitting procedure is similar, since the environment dependent term was not included in (Girshick, et al. 1998).

An important feature of the fitting procedure is that it is sequential. This means that first U_{bond} is constructed based solely on ab-initio calculated data with no empirical input, next U_{env} is obtained by fitting the Cauchy pressures and, finally, the pair potential is fitted so as to reproduce several equilibrium properties, namely, lattice parameters, remaining elastic moduli and cohesive energy. Starting with the bond energy, the most important quantities are the numbers of d and p electrons and the bond integrals. Furthermore, the number of levels included in the Lanczos algorithm for evaluation of the Green's functions and the effective electronic temperature, T_e , have to be chosen. These were taken as four, i. e. nine moments, and $k_B T_e = 0.3\text{eV}$, respectively. No empirical input has been used at this stage. The numbers of electrons have been chosen so as not to be far from the values found in ab initio calculations but were used as adjustable parameters as explained below. The bond integrals are represented analytically such as to reproduce the TB-LMTO calculations presented in Fig. 1. Since they can be regarded as functions of the separation of atoms they have been described by the functional form suggested by Goodwin, Skinner and Pettifor (1989).

$$H_{i\ell_i, j\ell_j, \mu} = H_{i\ell_i, j\ell_j, \mu}^0 \left(\frac{R_0^{\ell_i, \ell_j}}{R_{ij}} \right)^{n_a^{\ell_i, \ell_j}} \exp \left\{ n_a^{\ell_i, \ell_j} \left[\left(\frac{R_0^{\ell_i, \ell_j}}{R_c^{\ell_i, \ell_j}} \right)^{n_c^{\ell_i, \ell_j}} - \left(\frac{R_{ij}}{R_c^{\ell_i, \ell_j}} \right)^{n_c^{\ell_i, \ell_j}} \right] \right\} \quad (8)$$

where R_{ij} is the separation of atoms i and j , ℓ_i and ℓ_j are either 1 or 2, representing p or d states, and μ denotes σ , π or δ (quantum magnetic moment in cylindrical symmetry).

$H_{i\ell_i, j\ell_j, \mu}^0$ can then be written using the usual notation $dd\sigma$, $dd\pi$, ..., $pd\pi$ (for example $H_{11, 12, \sigma}^0 = pd\sigma$). The ratios of the bond integrals are not canonical but again determined on the basis of ab initio TB-LMTO calculations: $dd\sigma : dd\pi : dd\delta = -1.526 : 0.5284 :$

-0.0622, $pp\sigma : pp\pi = 1.8986 : -0.2255$ and $pd\sigma : pd\pi = -1.397 : 0.3748$. $R_0^{i,j}$, $R_c^{i,j}$, $n_a^{i,j}$ and $n_c^{i,j}$, together with the numbers of p and d electrons, are adjustable parameters used to fit the ab initio calculated bond integrals and assure correct order of energies of competing structures B2 (CsCl), B1 (NaCl) and B19 (hexagonal). The numbers of p and d electrons ascertained in this fitting process are 1.1 and 2.0, respectively.

The on-site elements $H_{11,11}$ and $H_{12,12}$ for Al and Ti, respectively, were evaluated using equations (5-7) for the ideal $L1_0$ TiAl and DO_{19} Ti_3Al . They were found to be very similar in both cases which demonstrates the perfect screening criterion for these intermetallic compounds. In the present study we used as the initial on-site elements entering the BOP scheme the TB-LMTO values for $L1_0$ TiAl averaged over different μ 's: $H_{11,11}(Al) = 0.279$ Ry and $H_{12,12}(Ti) = 0.110$ Ry. As mentioned earlier, they are then adjusted self-consistently to maintain local charge neutrality.

As the second step, the parameters B^{s_i,s_j} , C^{s_i} , v^{s_i} , $\lambda_0^{s_i}$, $R_c^{s_i,s_j}$ and n^{s_i} in equations (4.1) and (4.2) have been fitted to reproduce the Cauchy pressures. This fitting was first carried out for pure Ti so that the above parameters were determined for $s_i = s_j = Ti$. In this case the two Cauchy pressures are positive: $C_{12} - C_{66} = 0.261 \text{ eV}/\text{\AA}^3$ and $C_{13} - C_{44} = 0.109 \text{ eV}/\text{\AA}^3$. When fitting the Cauchy pressures for TiAl the above parameters were determined for $s_i = s_j = Al$ while we set $A^{TiAl} = \sqrt{A^{TiTi}A^{AlAl}}$ and $R_c^{TiAl} = 1/2(R_c^{TiTi} + R_c^{AlAl})$. In this case the two Cauchy pressures are negative: $C_{12} - C_{66} = -0.040 \text{ eV}/\text{\AA}^3$ and $C_{13} - C_{44} = -0.213 \text{ eV}/\text{\AA}^3$. It should be noted that the introduction of the repulsive environment dependent term allows us to reproduce both positive and negative Cauchy pressures on an equal footing.

Finally, the remaining elastic moduli (three for pure Ti and four for TiAl), lattice parameters (a and c) and cohesive energies have been reproduced by fitting the parameters entering equation (2) for the pair-potentials. The detailed numerical values of the fitted quantities and corresponding parameters in BOP will be presented in Ref. (Znam, et al. 2000).

Testing of the potentials

The first and most important requirement is that the fitted equilibrium $L1_0$ structure of TiAl is stable relative to possible alternative crystal structures with 1:1 ratio of Ti and Al, in particular B2 (CsCl), B1 (NaCl) and B19 (hexagonal). This, together with the correct order of energies of competing structures, has been assured when fitting the bond integrals (equation (8)). However, the magnitudes of the energy differences between alternative structures have not been fitted and thus an appropriate test of the ability of BOP to determine such differences is to compare ab initio and BOP calculated values. This is done in Table 1 where the energy differences between the above mentioned structures and the equilibrium $L1_0$ structure are summarized for BOP and ab initio calculations employing FP-LMTO (Nguyen-Manh, et al. 1995; Nguyen-Manh and

Pettifor 1999a). Obviously, the agreement between the BOP and ab initio calculated energy differences is very good.

Table 1. Energy differences between alternative crystal structures with 1:1 ratio of Ti and Al and the L1₀ structure calculated ab initio by FP-LMTO method and by using the constructed BOP

COMPARED STRUCTURES	BOP (meV/atom)	FP-LMTO (meV/atom)
B2 - L1 ₀	138	142
B1 - L1 ₀	699	667
B19 - L1 ₀	43	42

Since the potentials are intended for atomistic modeling of extended defects they have to be applicable when the atomic environment is considerably different from that in the ideal lattice. While this can never be fully tested as the variety of environments encountered in such defects is very rich, an assessment can be made by investigating the highly distorted structures encountered along certain transformation paths (Milstein, et al. 1994; Nguyen-Manh, et al. 1996; Sob, et al. 1997; Nguyen-Manh and Pettifor 1999b; Paidar, et al. 1999). Three distinct transformation paths have been investigated, tetragonal, trigonal and hexagonal, that connect highly symmetric structures that may be equilibrium crystal structures. Each of these paths can be characterized by a single parameter, p , and the variation of the total energy of the corresponding structures with the parameter p has been calculated using BOP and the full-potential linearized augmented plane waves (FP-LAPW) code described in (Blaha, et al. 1990). An analogous investigation of the applicability of the central-force Finnis-Sinclair type potentials for TiAl, constructed in (Vitek, et al. 1997a), has been made recently (Paidar, et al. 1999) and the FP-LAPW data used in Figs. 3-5 have been reproduced from this paper. Similarly, a detailed description of the three transformation paths can be found in (Paidar, et al. 1999) and here we only summarize the main features of these paths.

The tetragonal path, also called the Bain path, is the simplest continuous path between the bcc and fcc lattices in elemental solids and corresponds to a homogeneous straining. The parameter p is equal to the c/a ratio of the tetragonal structures encountered along the path and in the case of an elemental solid $p = 1$ for the bcc lattice and $p = \sqrt{2}$ for the fcc lattice. In the case of an ordered binary AB alloy, $p = 1$ corresponds to the B2 (CsCl) superlattice and $p = \sqrt{2}$ to the L1₀, fcc-based, superlattice. In fact, the symmetry of all the structures corresponding to $p > 1$ is L1₀. It should be emphasized here that $p = c/a$ characterizes distortions with respect to the B2 structure. When considering the fcc structure as a reference, the ratio of the corresponding tetragonal lattice parameters, c , and a , $c/a_t = p/\sqrt{2}$ and thus the fcc-based L1₀ superlattice formed for $p = \sqrt{2}$ corresponds to $c/a_t = 1$.

The trigonal path also corresponds to a homogeneous deformation but in the case of an elemental solid it connects three cubic structures, bcc, sc and fcc, and the transformation parameter p varies from 1 for bcc, through 2 for sc to 4 for fcc lattices. The corresponding ordered binary stoichiometric structures are B2, B1 and $L1_1$. All other structures encountered along this path also possess the $L1_1$ symmetry.

Finally, the hexagonal transformation path connects in the case of elemental solids the bcc and hcp lattices. However, it does not correspond to a homogeneous deformation. It is a combination of a homogeneous deformation that preserves the atomic volume with shuffling of alternative close packed atomic planes in opposite directions; the shuffling is linearly coupled to the magnitude of straining. In elemental solids $p = 0$ corresponds to the bcc lattice and $p = 1$ to the hcp lattice. All other structures encountered along this path are orthorhombic. In the case of an ordered binary AB alloy, $p = 0$ corresponds to the B2 superlattice and $p = 1$ to the B19 superlattice; the structure corresponding to $p \neq 1$ has the same B19 symmetry.

The dependence of the energy per atom on the parameter p is shown for the three transformation paths considered in Figs. 3, 4 and 5. The circles represent BOP and triangles ab initio calculations; the energy is always measured relative to the minimum for a given path. The agreement between BOP and ab initio calculations is certainly adequate for all three cases.

A similar comparison was also made for the central-force Finnis-Sinclair potentials by Paidar et al.(1999) and while the general shape of the calculated dependencies is reproduced in the central-force framework, the agreement with ab initio data is considerably less satisfactory.

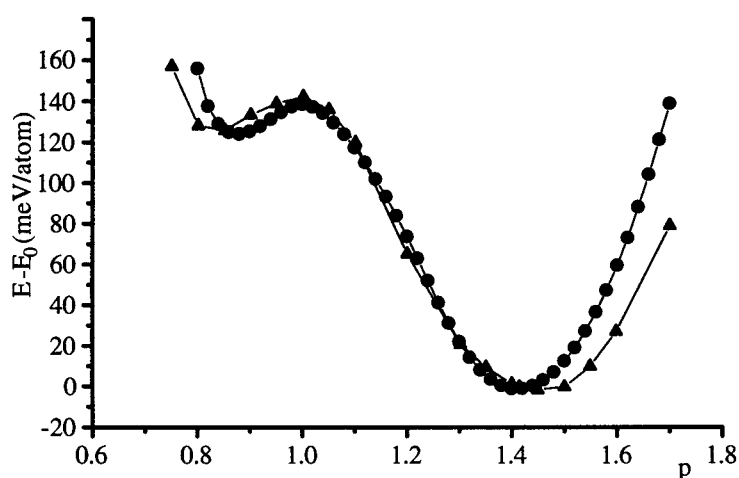


Figure 3. Tetragonal transformation. The circles represent BOP and triangles ab initio calculations.

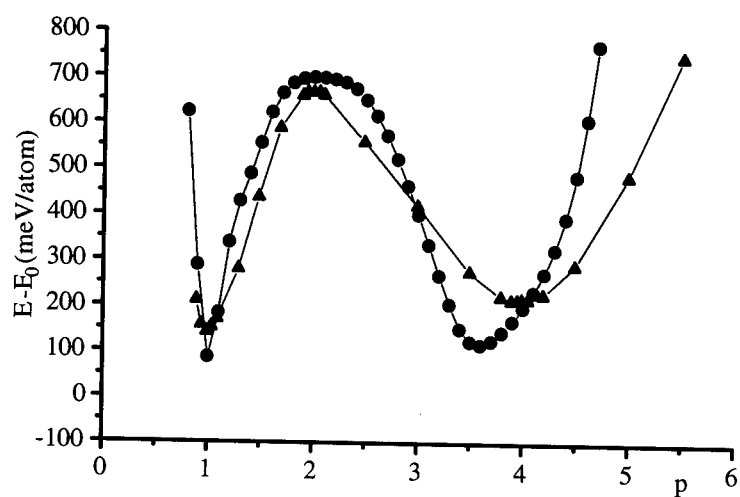


Figure 4. Trigonal transformation. The circles represent BOP and triangles *ab initio* calculations.

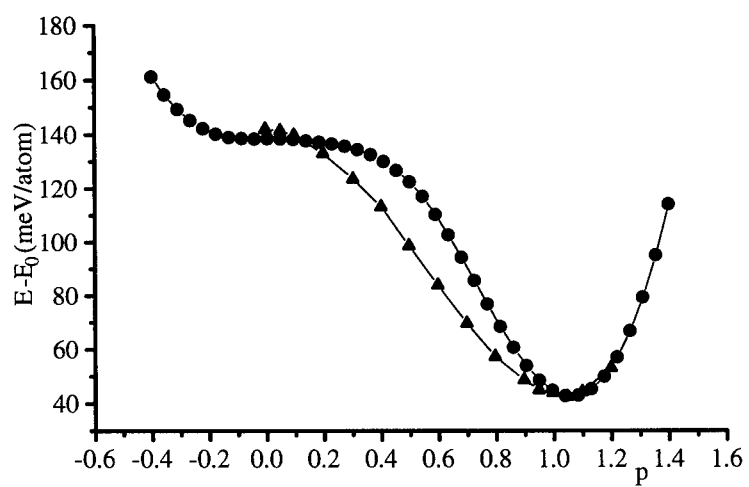


Figure 5. Hexagonal transformation. The circles represent BOP and triangles *ab initio* calculations.

For the tetragonal transformation (Fig. 3) it should be noted that the extremum for $p = 1$, corresponding to the B2 structure, is dictated by the symmetry and for TiAl it is a maximum for this path. The minimum is found for $p = 1.44$ which corresponds to the $L1_0$ structure with $c/a_t = 1.02$ which was fitted in the construction of both the BOP and Finnis-Sinclair potentials (Vitek, et al. 1997a). Near this minimum the agreement with ab initio data is very good for both BOP and central-force potentials (Paidar, et al. 1999) but for $0.8 < p < 1.1$, i. e. in the vicinity of the B2 structure, BOP reproduces the ab initio data appreciably more adequately.

For the trigonal transformation both BOP and Finnis-Sinclair potentials reproduce the ab initio data quite well (Paidar, et al. 1999). In particular, both duplicate correctly the position of the second minimum for $p \approx 4$ that is not dictated by the symmetry. The BOP results again show a better agreement in the vicinity of the B2 structure, i.e. for $p \approx 2$.

In the case of the hexagonal transformation, the results of BOP and Finnis-Sinclair potentials calculations follow similar curves but BOP results are in much better numerical agreement with ab initio data. The results of Finnis-Sinclair potentials are displaced by an almost constant shift towards lower values and for the structure corresponding to $p = \sqrt{2}$ the energy is almost the same as that of the $L1_0$ structure. The reason is that for this value of p the separations of the first and second neighbours are practically the same as in the $L1_0$ lattice and thus in any central-force model only more distant neighbours contribute significantly to this energy difference; this contribution is particularly small for the potentials used in (Paidar, et al. 1999). Consequently, a relatively high energy of the structure corresponding to $p = \sqrt{2}$ found in ab initio calculations must result from the non-central character of atomic interactions which is correctly captured by BOP.

Finally, the energies of the following stacking fault-like defects on the (111) planes in $L1_0$ TiAl were calculated: Anti-phase boundary (APB) with the displacement $\frac{1}{2}[\bar{1}01]$, complex stacking fault (CSF) with the displacement $\frac{1}{6}[\bar{2}11]$ and super lattice intrinsic stacking fault (SISF) with the displacement $\frac{1}{6}[11\bar{2}]$. The results are shown in Table 2 where the energies calculated using BOP are compared with those evaluated ab initio using FP-LAPW (Ehmann and Fähnle 1998) and FP-LMTO (Vitek, et al. 1997b) methods and the Finnis-Sinclair (FS) potential (Vitek, et al. 1997a). The agreement between BOP and the ab initio calculations is more than adequate. The most remarkable is that a relatively high energy of the SISF is correctly reproduced. In the case of the Finnis-Sinclair potential it is very low for the same reason as in the structure corresponding to $p = 1$ in the hexagonal transformation. While other central force potentials may lead to higher values of the SISF energy (Simmons, et al. 1997), energies

Table 2. Energies of stacking fault-like defects (in mJm⁻²) calculated using four different descriptions of atomic interactions

	APB	CSF	SISF
BOP	541	349	180
FP-LAPW	667	362	172
FP-LMTO	710	314	134
FS POTENTIALS	275	275	2.9

as high as those found *ab initio* cannot be reproduced. The reason is again that the magnitude of this energy is controlled by non-central interactions.

DISCUSSION

The bond-order potentials for Ti-Al alloys presented in this study are eminently suitable for atomistic studies of extended crystal defects in $L1_0$ TiAl. First, and most importantly, the bond integrals determining the bond part of the energy are transferable to various environments and can be regarded as functions of the separations of the corresponding pairs of atoms. This was established by the detailed *ab initio* calculations employing the all electron TB-LMTO method. The potentials then reproduce the equilibrium lattice parameters, cohesive energies and elastic moduli of TiAl and not only guarantee the stability of the $L1_0$ structure with respect to alternative structures with the same stoichiometry but give corresponding energy differences in agreement with values calculated *ab initio*.

A prominent value of these potentials is that they reproduce very adequately the variation of the energy for three transformation paths along which the structures sampled are very far from the ideal $L1_0$ lattice. This is very important because the significant application of these potentials is in studies of extended lattice defects such as dislocations and interfaces. Indeed, as shown in this paper, they give values of the energies of the three important planar defects, APB, CSF and SISF, in very good agreement with *ab initio* calculations. This is in contrast with central-force potentials, investigated in (Paidar, et al. 1999), that often lead to too low energies, in particular when the separations of the first nearest neighbours in the defective structure is almost the same as in the ideal $L1_0$ lattice. Such a situation is encountered most conspicuously in the SISF and for the hexagonal transformation. Evidently, the higher energies than what is found using central forces are a consequence of different bond angles present in these structures when compared with the $L1_0$ structure. This angular dependence of atomic interactions is correctly captured by the BOP. However, as pointed out in (Paidar, et al. 1999), the central-force potentials may be sufficient when investigating structural features of extended defects provided the configurations studied are associated with significant changes in separations of the first and second nearest neighbours.

Finally, the study of the transferability of the bond integrals established that they are transferable not only to different structures at a fixed stoichiometry but also to different stoichiometries. This suggests that the constructed BOPs can also be employed when investigating the variation of energies and structures of extended defects in TiAl with deviations away from stoichiometry as well as in studies of Ti-Al alloys with different structures and stoichiometries. For example, as shown in (Znam, et al. 2000), the same BOP can be used in studies of Ti_3Al crystallizing in the DO_{19} structure.

However, the situation is more complex in the case of molybdenum silicides. The limited transferability of the bond integrals, in particular for π -bonds that are crucial for Si-Si and Mo-Si bonding, represents a considerable challenge for the BOP formalism in

the framework of which one would like to construct transferable potentials applicable not only to one type of silicide, e. g. MoSi_2 , but to other silicides, such as Mo_5Si_3 .

Furthermore, the discontinuities of the bond integrals seen in Fig. 2 expose the fact that, unlike in Ti-Al alloys, a simple dependence on the separation of atoms is not adequate even for one particular silicide, such as MoSi_2 , and their environmental dependence must be considered.

In order to overcome this difficulty we have recently derived an analytical form of the environmental dependence of the two-centre bond integrals (Nguyen-Manh, et al. 2000). This new formalism is based on using the overlap matrix, neglected within the orthogonal tight-binding representation, to screen the two-centre bond integrals. An environmental dependence of the bond integrals has also been introduced in a recently developed spd-tight binding method (Haas, et al. 1998a, b) where it is modeled via an empirical function that has the same dependence on the separation of atoms irrespective of the angular dependence of the bond integral. In contrast, the new analytical form incorporating the environmental dependence of the bond integrals is angular dependent.

As an example of this approach Fig. 6 shows the dependence of the $\text{pp}\pi$ bond integral related to the Si-Si bonding in MoSi_2 on the separation of Si atoms. In this figure the ab initio calculated values of this bond integral clearly display a discontinuity

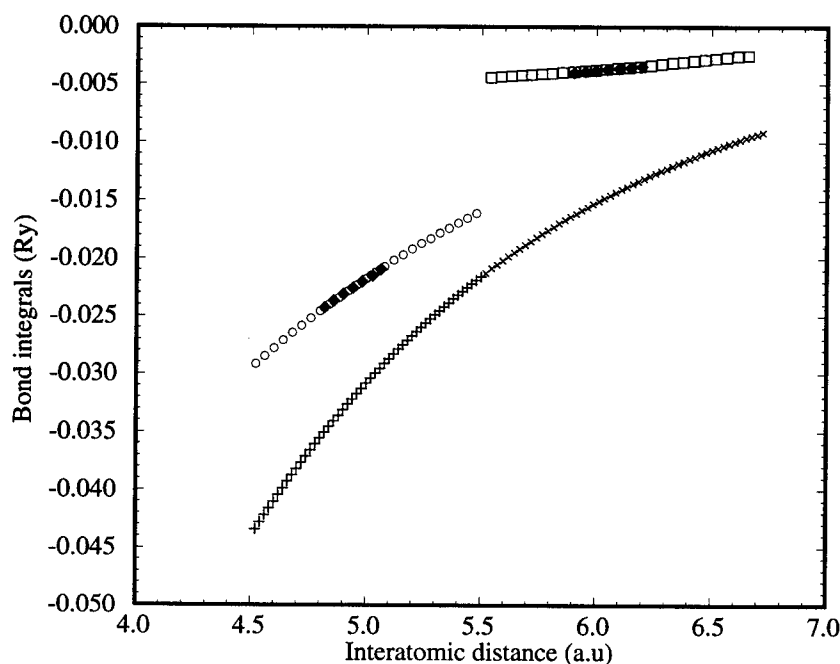


Figure 6. Dependence of the $\text{pp}\pi$ bond integral associated with the Si-Si bonding in MoSi_2 on the separation of Si atoms. The symbols \bullet represent values calculated ab initio, \circ and \square screened bond integrals in the vicinity of the first and second nearest neighbours, respectively, and $+$ and \times non-screened bond integrals in the vicinity of the first and second nearest neighbours, respectively.

between first and second neighbours. It is seen that this discontinuity is excellently reproduced by the screened, environmentally dependent, bond integrals. For comparison the non-screened bond integrals are also shown in this figure. They display a continuous transition from first to second nearest neighbours and do not follow the ab initio calculated values. A similar behaviour has been found for $dd\pi$ and $pp\pi$ bond integrals and it also applies in pure bcc molybdenum. Thus within this new formalism the transferability of bond integrals between bcc Mo and C11_6 , MoSi_2 and, presumably other silicides, is recovered. These environment dependent bond integrals can then be used in the construction of BOP for TM-silicides, analogously as the bond integrals dependent only on the separation of pairs of atoms have been used in the construction of BOP for TiAl.

ACKNOWLEDGMENTS

This research was supported in part by the U.S. Department of Energy, BES Grant. no. DE-FG02-98ER45702 (SZ, DNM, VV), NSF - Grant No. DMR96-15228 (SZ, VV) and by SANYO Electric Co. (DNM). DNM would like to thank Prof. O. K. Andersen for stimulating discussions on new developments of the TB-LMTO method. The computations were performed in part at the Materials Modelling Laboratory, Department of Materials, Oxford University on the HP EXEMPLAR computer that was funded jointly by Higher Education Funding Council of England and by Hewlett-Packard, and in part at the NCSA computing facility at Boston University under grant no. NSF30266.

REFERENCES

- Ackland, G. J., Tichy, G., Vitek, V. and Finnis, M. W., 1987, *Simple N-Body Potentials For the Noble-Metals and Nickel*, Philos. Mag. A **56**:735.
- Andersen, O. K. and Jepsen, O., 1984, *Explicit, 1st-Principles Tight-Binding Theory*, Phys. Rev. Lett. **53**:2571.
- Andersen, O. K., Jepsen, O. and Glötzel, D., 1985, in *Highlights of Condensed Matter Theory*, F. Bassani, F. Fumi and M. P. Tosi, ed., North Holland, Amsterdam, p. 59.
- Andersen, O. K., Jepsen, O. and Krier, G., 1994, in *Lectures on Methods of Electronic Structure Calculations*, V. Kumar et al., ed., World Scientific, Singapore, p. 63.
- Aoki, M., 1993, *Rapidly Convergent Bond Order Expansion For Atomistic Simulations*, Phys. Rev. Lett. **71**:3842.
- Aoki, M. and Pettifor, D. G., 1993, in *Physics of Transition Metals*, P. M. Oppeneer and J. Kübler, ed., World Scientific, Singapore, p. 299.
- Blaha, P., Schwartz, K., Sorantin, P. and Trickey, S. B., 1990, *Full-Potential, Linearized Augmented Plane-Wave Programs For Crystalline Systems*, Comp. Phys. Commun. **59**:399.
- Bowler, D. R., Aoki, M., Goringe, C. M., Horsfield, A. P. and Pettifor, D. G., 1997, *A comparison of linear scaling tight-binding methods*, Modelling and Simulation in Mat. Sci. Eng. **5**:199.
- Chu, F., Thoma, D. J., McClellan, K. J. and Peralta, P., 1999, *Mo_5Si_3 single crystals: physical properties and mechanical behavior*, Mat. Sci. Eng. A **261**:44.
- Darolia, R., Lahrman, D. F., Field, R. D., Dobbs, J. R., Chang, K. M., Goldman, E. H. and Konitzer, D. G., 1992, in *Ordered Intermetallics - Physical Metallurgy and Mechanical Behaviour*, C. T. Liu, R. W. Cahn and G. Sauthoff, ed., Kluwer Academic Publishers, Dordrecht, p. 679.
- Daw, M. S. and Baskes, M. I., 1984, *Embedded-Atom Method - Derivation and Application to Impurities, Surfaces, and Other Defects in Metals*, Phys. Rev. B **29**:6443.
- Dimiduk, D. M., 1999, *Gamma titanium aluminide alloys - an assessment within the competition of aerospace structural materials*, Mat. Sci. Eng. A **263**:281.
- Duesbery, M. S. and Richardson, G. Y., 1991, *CRC Critical Reviews in Solid State and Materials Science* **17**:1.
- Ehmann, J. and Fähnle, M., 1998, *Generalized stacking-fault energies for TiAl: mechanical instability of the (111) antiphase boundary*, Philos. Mag. A **77**:701.

- Feynman, R. P., 1939, *Phys. Rev.* **56**:340.
- Finnis, M. W. and Sinclair, J. E., 1984, *A Simple Empirical N-Body Potential For Transition-Metals*, *Philos. Mag. A* **50**:45.
- Girshick, A., Bratkovsky, A. M., Pettifor, D. G. and Vitek, V., 1998, *Philos. Mag. A* **77**:981.
- Goodwin, L., Skinner, A. J. and Pettifor, D. G., 1989, *Generating Transferable Tight-Binding Parameters - Application to Silicon*, *Europhys. Lett.* **9**:701.
- Haas, H., Wang, C. Z., Fähnle, M., Elsässer, C. and Ho, K. M., 1998a, in *Tight-Binding Approach to Computational Materials Science*, P. E. A. Turchi, A. Gonis and L. Colombo, ed., Vol. 491, Materials Research Society, Pittsburgh, p. 327.
- Haas, H., Wang, C. Z., Fähnle, M., Elsässer, C. and Ho, K. M., 1998b, *Environment-dependent tight-binding model for molybdenum*, *Phys. Rev. B* **57**:1461.
- Haydock, R., 1980, in *Solid State Physics*, H. Ehrenreich and D. Turnbull, ed., Vol. 35, Academic Press, New York, p. 216.
- Hellmann, H., 1937, *Einführung in die Quantenchemie*, Deuticke, Leipzig.
- Horsfield, A. P. and Bratkovsky, A. M., 1996, *O(N) tight-binding methods with finite electronic temperature*, *Phys. Rev. B* **53**:15381.
- Horsfield, A. P., Bratkovsky, A. M., Fearn, M., Pettifor, D. G. and Aoki, M., 1996a, *Bond-order potentials: Theory and implementation*, *Phys. Rev. B* **53**:12694.
- Horsfield, A. P., Bratkovsky, A. M., Pettifor, D. G. and Aoki, M., 1996b, *Bond-order potential and cluster recursion for the description of chemical bonds: Efficient real-space methods for tight-binding molecular dynamics*, *Phys. Rev. B* **53**:1656.
- Huang, S. C. and Chestnutt, J. C., 1995, in *Intermetallic Compounds-Principles and Practice*, J. H. Westbrook and R. L. Fleischer, ed., Vol. 2, John Wiley & Sons, New York, p. 73.
- Ito, K., Matsuda, K., Shirai, Y., Inui, H. and Yamaguchi, M., 1999, *Brittle-ductile behavior of single crystals of MoSi₂*, *Mat. Sci. Eng. A* **261**:99.
- Ito, K., Yano, T., Nakamoto, T., Moriwaki, M., Inui, H. and Yamaguchi, M., 1997, *Microstructure and mechanical properties of MoSi₂ single crystals and directionally solidified MoSi₂-based alloys*, *Prog. Mater. Sci.* **42**:193.
- Kim, Y. W., 1998, *Strength and ductility in TiAl alloys*, *Intermetallics* **6**:623.
- Liu, C.T., Cahn, R.W. and Sauthoff, G., ed., 1992, *Ordered Intermetallics - Physical Metallurgy and Mechanical Behaviour*, Kluwer Academic Publishers, Dordrecht.
- Lanczos, C., 1950, *J. Res. Natl. Bur. Stand.* **45**:225.
- Milstein, F., Fang, H. E. and Marschall, J., 1994, *Mechanics and Energetics of the Bain Transformation*, *Philos. Mag. A* **70**:621.
- Mitchell, T. E. and Misra, A., 1999, *Structure and mechanical properties of (Mo, Re)Si-2 alloys*, *Mat. Sci. Eng. A* **261**:106.
- Nabarro, F. R. N., 1994, *The Superiority of Superalloys*, *Mat. Sci. Eng. A* **184**:167.
- Nguyen-Manh, D., Bratkovsky, A. M. and Pettifor, D. G., 1995, *Quantum-Mechanical Predictions In Intermetallics Modeling*, *Phil. Trans. Roy. Soc. London A* **351**:529.
- Nguyen-Manh, D. and Pettifor, D. G., 1999a, *Electronic structure, phase stability and elastic moduli of AB transition metal aluminides*, *Intermetallics* **7**:1095.
- Nguyen-Manh D. and Pettifor D.G., 1999b, in *Gamma Titanium Aluminides 1999*, Kim, Y-W., Dimiduk, D.M. and Loretto, M.H., ed., TMS Publication, p. 175.
- Nguyen-Manh, D., Pettifor, D. G. and Vitek, V., 2000, to be published.
- Nguyen-Manh, D., Pettifor, D. G., Znam, S. and Vitek, V., 1998, in *Tight-Binding Approach to Computational Materials Science*, P. E. A. Turchi, A. Gonis and L. Colombo, ed., Vol. 491, Materials Research Society, Pittsburgh, p. 353.
- Nguyen-Manh, D., Pettifor, D. G., Shao, G., Miodownik, A. P. and Pasturel, A., 1996, *Metastability of the omega-phase in transition-metal aluminides: First-principles structural predictions*, *Philos. Mag. A* **74**:1385.
- Noebe, R. D., Bowman, R. R. and Nathal, M. V., 1996, in *Physical Metallurgy and Processing of Intermetallic Compounds*, N. S. Stoloff and V. K. Sikka, ed., Chapman & Hall, New York, p. 212.
- Nowak, H. J., Andersen, O. K., Fujiwara, T., Jepsen, O. and Vargas, P., 1991, *Electronic-Structure Calculations For Amorphous Solids Using the Recursion Method and Linear Muffin-Tin Orbitals - Application to Fe₃OB₂O*, *Phys. Rev. B* **44**:3577.
- Paidar, V., Wang, L. G., Sob, M. and Vitek, V., 1999, *A study of the applicability of many-body central force potentials in NiAl and TiAl*, *Modelling and Simulation in Mat. Sci. Eng.* **7**:369.
- Pettifor, D. G., 1978, *Theory of Energy-Bands and Related Properties of 4d Transition- Metals .3. S and D Contributions to Equation of State*, *J. Phys. F: Metal Phys.* **8**: 219.

- Pettifor, D. G., 1989, *New Many-Body Potential For the Bond Order* Phys. Rev. Lett. **63**:2480.
- Pettifor, D. G., 1995, *Bonding and Structure of Molecules and Solids*, Oxford University Press, Oxford.
- Pettifor, D. G. and Aoki, M., 1991, *Bonding and Structure of Intermetallics - a New Bond Order Potential*, Phil. Trans. Roy. Soc. London A **334**:439.
- Siegl, R., Vitek, V., Inui, H., Kishida, K. and Yamaguchi, M., 1997, *Directional bonding and asymmetry of interfacial structure in intermetallic TiAl: Combined theoretical and electron microscopy study*, Philos. Mag. A **75**:1447.
- Simmons, J. P., Rao, S. I. and Dimiduk, D. M., 1997, *Atomistics simulations of structures and properties of 1/2 <110> dislocations using three different embedded-atom method potentials fit to gamma-TiAl*, Philos. Mag. A **75**:1299.
- Skriver, H. L., 1984, *The LMTO method*, Springer, New York.
- Sob, M. and Vitek, V., 1996, in *Stability of Materials*, NATO Advanced Science Institute, Series B: Physics, Vol. 355, A. Gonis, P. E. A. Turchi and J. Kudrnovsky, ed., Plenum Press, New York, p. 449.
- Sob, M., Wang, L. G. and Vitek, V., 1997, *Local stability of higher-energy phases in metallic materials and its relation to the structure of extended defects*, Comp. Mat. Sci. **8**:100.
- Stoloff, N. S., 1998, *Iron aluminides: present status and future prospects*, Mat. Sci. Eng. A **258**:1.
- Stoloff, N. S. and Liu, C. T., 1996, in *Physical Metallurgy and Processing of Intermetallic Compounds*, N. S. Stoloff and V. K. Sikka, ed., Chapman & Hall, New York, p. 159.
- Stoloff, N. S. and Sikka, V. K., ed., 1996, *Physical Metallurgy and Processing of Intermetallic Compounds*, Chapman & Hall, New York.
- Tanaka, K., Ichitsubo, T., Inui, H., Yamaguchi, M. and Koiwa, M., 1996, *Single-crystal elastic constants of gamma-TiAl*, Philos. Mag. Lett. **73**:71.
- Tanaka, K., Inui, H., Yamaguchi, M. and Koiwa, M., 1999, *Directional atomic bonds in MoSi₂ and other transition-metal disilicides with the C11(b), C40 and C54 structures*, Mat. Sci. Eng. A **261**:158.
- Tanaka, K. and Koiwa, M., 1996, *Single-crystal elastic constants of intermetallic compounds* Intermetallics **4**:S29.
- Tanaka, K., Onome, H., Inui, H., Yamaguchi, M. and Koiwa, M., 1997, *Mat. Sci. Eng.* **240**: 188.
- Vasudevan, A. K., Petrovic, J. J., Fishman, S. G., Sorrell, C. A. and Nathal, M. V., ed., 1999, *Proceedings of the Engineering Foundation High Temperature Structural Silicides Conference*, Mat. Sci. Eng. A **261**.
- Vitek, V., 1992, *Structure of Dislocation Cores in Metallic Materials and Its Impact On Their Plastic Behavior*, Prog. Mater. Sci. **36**:1.
- Vitek, V., Girshick, A., Siegl, R., Inui, H. and Yamaguchi, M., 1997a, in *Properties of Complex Inorganic Solids*, A. Gonis, A. Meike and P. E. A. Turchi, ed., Plenum Press, New York, p. 355.
- Vitek, V., Ito, K., Siegl, R. and Znam, S., 1997b, *Structure of interfaces in the lamellar TiAl: effects of directional bonding and segregation*, Mat. Sci. Eng. A **240**:752.
- Westbrook, J.H. and Fleischer, R.L., ed., 1995, *Intermetallic Compounds-Principles and Practice*, John Wiley & Sons, New York.
- Yamaguchi, M., Inui, H., Yokoshima, S., Kishida, K. and Johnson, D. R., 1996, *Recent progress in our understanding of deformation and fracture of two-phase and single-phase TiAl alloys*, Mat. Sci. Eng. A **213**:25.
- Znam, S., Nguyen-Manh, D., Pettifor, D. G. and Vitek, V., 2000, to be published.

THE MAGNETITE (001) SURFACE: INSIGHTS FROM MOLECULAR DYNAMICS CALCULATIONS

James R. Rustad, Evgeny Wasserman, and Andrew R. Felmy

W. R. Wiley Environmental Molecular Science Laboratory
Pacific Northwest National Laboratory
Mail Stop K8-96, PO Box 999, Richland, WA 99352

ABSTRACT

A classical polarizable potential model is used in a molecular dynamics model of the magnetite (001) surface. The model, previously applied to the tetrahedral, or "A" termination of magnetite (001) is here applied to the octahedral or "B" termination, as well as to the hydroxylation of both the "A" and "B" termination. Surface relaxations for the "B" terminated surface are small, and consistent with the observed $(\sqrt{2} \times \sqrt{2})R45$ cell observed in LEED experiments. Additionally, it is shown that the relaxation of a tetrahedral defect on the "B" terminated surface does not give rise to the same relaxation mechanism as that calculated for the tetrahedral sites on the "A" surface. The lack of a "dimer" forming at the defect site is consistent with recent STM studies. Calculations on charge-ordered magnetite slabs indicate that, within the context of the ionic model used here, the surface energy of the "A" termination of magnetite is lower than that of the "B" termination over a wide range of oxygen fugacities. Hydroxylation has a negligible effect on the relative energies of the "A" and "B" surfaces, however, the large gain in energy associated with tetrahedral ion relaxation on the "A" surface could explain the lack of two high temperature peaks expected for successive removal of adsorbing waters from the same tetrahedral site.

INTRODUCTION

The magnetite (Fe_3O_4) 001 surface has been extensively studied using UHV techniques [1,2] (and references therein). These studies show the existence of at least two terminations for magnetite (001) depending on sample preparation and handling. In this paper, a classical "ionic" potential model is applied to calculate the structures and relative energies of two terminations of magnetite (001), as identified previously by other

investigators, which are believed to correspond to the two terminations observed in the UHV studies.

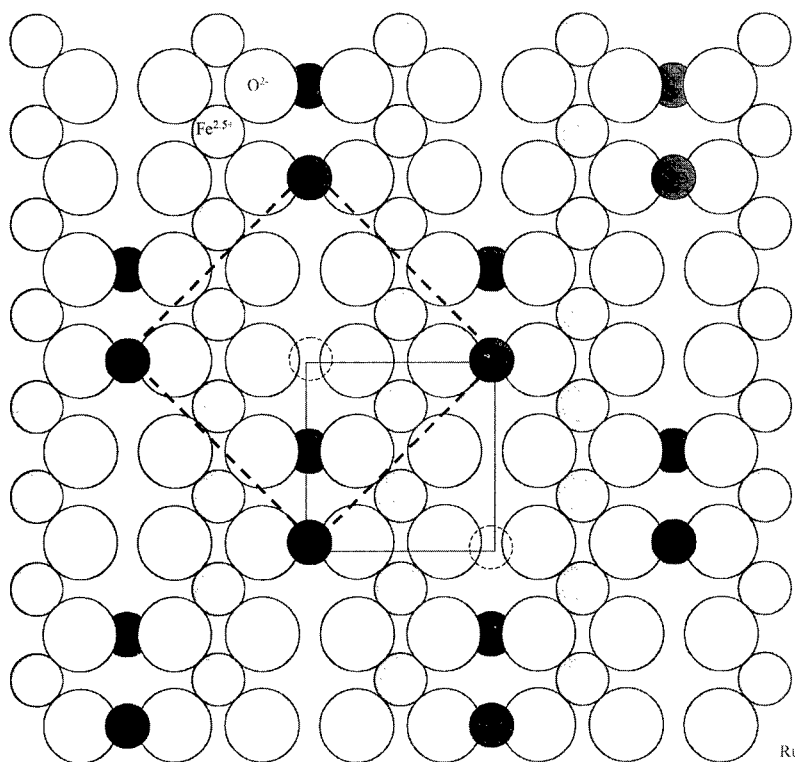


Figure 1. This neutral, stoichiometric layer may be stacked parallel to (001) (with a 90 degree rotation and a 1/4, 1/4 offset) to generate the magnetite structure. Dashed atoms represent iron ion positions in stacking units immediately above the one illustrated. Dashed unit cell is the $(\sqrt{2} \times \sqrt{2})R45$ unit cell characteristic of the surface and the solid unit cell is the bulk unit cell.

The spinel structure may be thought of as a sequence of neutral stacking units parallel to (001) as shown in Figure 1. This stacking sequence builds up the octahedral and tetrahedral sites characteristic of the spinel structure. The unit cell of the stacking layer is $(\sqrt{2} \times \sqrt{2})R45$ relative to the bulk. In the bulk, a tetrahedral atom, coming from the overlying stacking unit, is bonded to the oxygens at the center of the unit cell. This shrinks the cell by a factor of $1/\sqrt{2}$ and rotates the cell by 45 degrees. In magnetite, Fe^{3+} occupies the tetrahedral sites, while the octahedral sites are filled with an equal mixture of Fe^{2+} and Fe^{3+} . Above the Verwey temperature (119 K), the electrons in the rows of octahedral sites are delocalized; these sites may be thought of as being occupied by $\text{Fe}^{2.5+}$ ions. Termination of the stacking sequence in Figure 1 will result in a neutral, stoichiometric, autocompensated surface with two-fold coordinated Fe^{3+} and five-fold

coordinated $\text{Fe}^{2.5+}$ sites [3]. This surface is referred to as the tetrahedral or "A" termination. Of course, the Fe^{3+} are not tetrahedral at the surface; the two oxygen ions required to complete the tetrahedron belong to the overlying layer, which is absent at the surface. Similarly, the $\text{Fe}^{2.5+}$ sites are not octahedral at the surface because the oxygen ion required to complete the octahedron belongs to the overlying layer. Nevertheless, it will be convenient to speak of tetrahedral and octahedral surface sites with the understanding that some of the coordinating oxygen atoms may not be present.

The "B" or octahedral termination has been discussed in [2]. The simplest way to envision this termination is the following (see Figures 2 and 3 for the structures of the "A" and "B" terminated surfaces, respectively). Within each unit cell:

1. remove $1/2$ e from two of the $\text{Fe}^{2.5+}$ in the octahedral sites to give Fe^{3+} sites.
2. place the electron on the tetrahedral Fe^{3+} site to make an Fe^{2+} site.
3. remove FeO from the system by taking the tetrahedral Fe^{2+} site and creating an oxygen vacancy.

The surface is neutral; only FeO was removed. Because FeO was removed from the surface, the "B" termination is oxidized relative to Fe_3O_4 and the relative stabilities of the "A" and "B" terminations would be expected to depend on the oxygen fugacity in the system. Note that both surfaces maintain the $(\sqrt{2} \times \sqrt{2})R45$ unit cell characteristic of the neutral stacking units. This cell is in fact observed in LEED patterns taken of magnetite (001) for both terminations [1, 4].

POTENTIAL MODEL AND PREVIOUS WORK

The model employed here is basically an ionic model which was originally designed to calculate structures and energies for hydroxylated/hydrated ferric oxide surfaces. The O-H potential functions were taken from the polarizable, dissociating water model of Halley and co-workers [5], which is essentially a modification of the Stillinger-David model [6]. The Fe-O parameters, including a short-range repulsion and charge-dipole cutoff functions were fit to the Fe^{3+} - H_2O potential surface of Curtiss and co-workers [7]. This model has been used in a variety of applications including ion hydrolysis in solution [8], ferric oxide and oxyhydroxide crystal structures [9], the vacuum termination of hematite (001) [10], monolayers of water on hematite (012) [11, 12], and the surface charging behavior of goethite (FeOOH) and hematite [13, 14]. This model has a tendency to overestimate Fe-O bond distances. For example, the Fe-O distance in the hexaquo $\text{Fe}(\text{H}_2\text{O})_6^{3+}$ complex, as predicted by the model, is about 207 pm, whereas the experimental distance (known from ferric alum salts) is 199 pm [15]. Similarly overestimated Fe-O bond lengths (205-206 pm) have been observed in high-level quantum chemistry calculations [16]. It is important to emphasize that, because of the requirement that the O-O functions remain the same in the ferric oxide solid as in water, the potential cannot be "fixed" in a straightforward manner. If the Fe-O interaction is changed to make a shorter Fe-O bond, the octahedrally-coordinated crystals become unstable towards tetrahedral coordination.

More recently, the potentials were applied to magnetite [17]. In that work, it was shown that, at least in a structural sense, a reasonable model for magnetite and wustite could be obtained simply by changing the Fe charge to 2.5+ or 2+, keeping the same short-range repulsive and charge-dipole cutoff function parameters. As is the case for the ferric oxide structures, the Fe-O bond was found to be approximately 5 percent too large, for example, the Fe^{2+} -O distance in $\text{Fe}(\text{H}_2\text{O})_6^{2+}$ was predicted to be 221 pm, as opposed

to the experimental value of 215 pm. High-level quantum mechanical calculations give 219 pm [16]. It appears that going beyond our rather crude description of the Fe-O bond may be difficult for *ab initio* methods. Given our good agreement with experiment in areas outline above, and in view of the electronic structural complexity of magnetite (giving rise to formidable challenges in applying *ab initio* methods), it seems justifiable to continue to explore the predictions of this simple model.

RESULTS

Structure of the “A” terminated Surface

The relaxed structure for the “A” termination was calculated in a previous paper [17]. The surface is predicted to undergo significant surface relaxation involving the rotation of the two-fold coordinated irons into the adjacent octahedral vacancies exposed at the surface. At the same time the bulk tetrahedral ferric ions, which share a face with the surface half-octahedron newly occupied by the relaxing surface ferric irons, are themselves pushed to the surface, yielding a sequence of ferric “dimers” as shown in Figure 2. The relaxation can be viewed as an attempt to reestablish a Pauling bond order of 2.0 for the surface oxygens, some of which have become significantly over and undercoordinated at the unrelaxed surface. The relaxation energy associated with the reconstruction is approximately 0.72 J/m², which is quite significant given that the unrelaxed surface energy is about 2.3 J/m².

Structure of the “B” terminated Surface

The relaxed structure for the “B” termination is shown in Figure 3. If the “B” surface is generated from the “A” surface using the three-step recipe listed above, the octahedral sites are treated as a mixture of equal numbers of Fe^{2.5+} and Fe³⁺ sites, as shown in the Figure. Maintaining our policy, for the present, of keeping the electrons delocalized, this mixture of Fe^{2.5+} and Fe³⁺ sites is treated as if all surface irons have a charge of +2.75. Each of the three different possibilities for creation of the oxygen vacancy were tested. In the lowest energy structure, the oxygen atom adjacent to the vacancy moves into a bridging position with respect to the two Fe³⁺ irons at the surface. This small relaxation contributes less than 0.1 J/m² to the slab energy. The ($\sqrt{2} \times \sqrt{2}$)R45 symmetry is maintained during the surface relaxation.

STM images of what is believed to be the “B” termination reveal the presence of a small number of “defects” involving the presence of tetrahedral sites between the octahedral rows [4]. These defects appear as single dots in the STM images. This does not appear to be consistent with the mode of relaxation of the tetrahedral sites on the “A” surface as identified in [17]. If that mechanism were to hold, the tetrahedral sites should always occur in pairs. It must be kept in mind, however, that the “B” terminated surface is oxidized, and the presence of excess ferric ions on the surface could possibly inhibit the relaxation mechanism identified in [17], because of the excess positive charge. To address this issue, we have calculated the relaxation of a tetrahedral defect on the “B” termination. For this charge-delocalized model, the mechanism identified on the “A” surface indeed does not occur. Therefore the presence of single ion defects on tetrahedral sites on the “B” surface does not refute operation of the “A” relaxation mechanism as identified in [17].

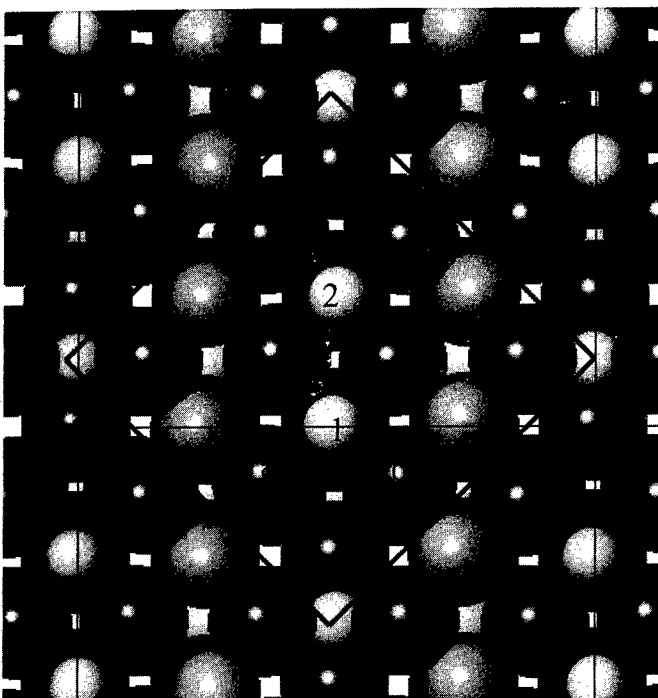


Figure 2. Structure of the relaxed “A” termination of magnetite (001). Large light atoms are $\text{Fe}^{2.5+}$ and small light atoms are Fe^{2+} . Large dark atoms are O. Tetrahedral Fe(1) has relaxed onto the surface plane from its initial twofold position above and between O(a) and O(b). Fe(2) was pushed up to the surface plane from below.

Relative Energetics of Vacuum “A” and “B” Terminations

A major objective of this paper is to assess the relative stabilities of the “A” and “B” terminations. As described below, it is necessary for this purpose to use a charge-ordered slab to model the surface, rather than using a non-integral charge on the octahedral sites. The model system described here therefore differs from that described in [17] in that the system is charge-ordered. The charge-ordering scheme, taken from Hamilton [18] is shown in Figure 4. In either the “A” or “B” terminations, the terminating surface could consist of either Fe^{2+} or Fe^{3+} ions. Because, within the context of our model, the Fe^{2+} ions prefer to be at the surface, we choose the former arrangement. For this arrangement, the relaxation of the surface tetrahedral iron atoms is the same as in the charge-delocalized arrangement as described in [17]. The structure of the “B” termination is also essentially unchanged from the charge-disordered case.

For non-stoichiometric systems, calculation of the surface energies cannot be carried out in the standard way, according to the formula $\gamma = 1/2A(E_{\text{slab}} - E_{\text{bulk}})$, where A is the area of the slab, E_{slab} is the energy of the slab and E_{bulk} is the bulk energy of an equivalent number of formula units in the bulk. The issue, of course, is that for the nonstoichiometric “B” surface, there is no “bulk” value against which to reference the slab energy. A similar problem was addressed by Wang and coworkers [19] in their study of nonstoichiometric terminations of hematite (001). Here, we take a similar approach, but need to overcome the constraints of using the ionic model: we cannot calculate energies for O_2 or metallic iron.

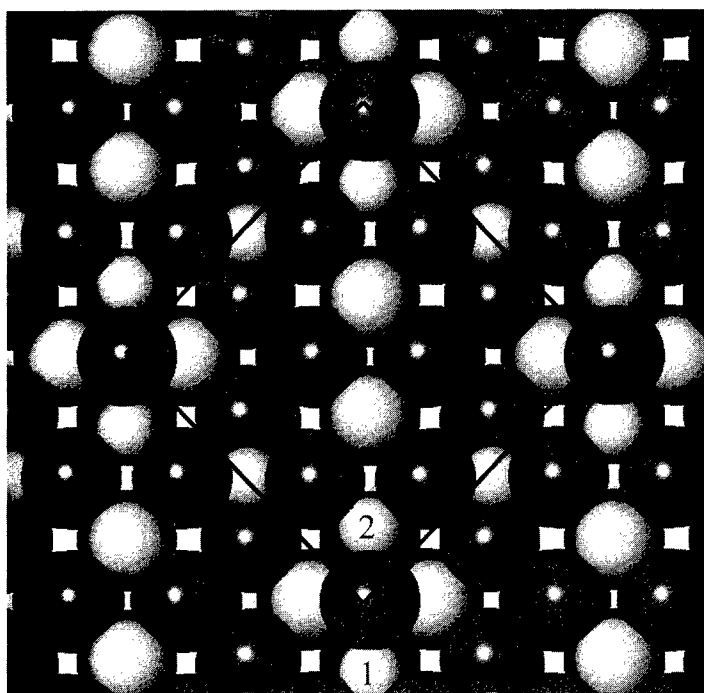


Figure 3. Structure of the relaxed "B" terminated surface of magnetite (001). Atoms are identified according to the protocol in Figure 2. The major structural feature is the bridging O between the Fe^{3+} ions.

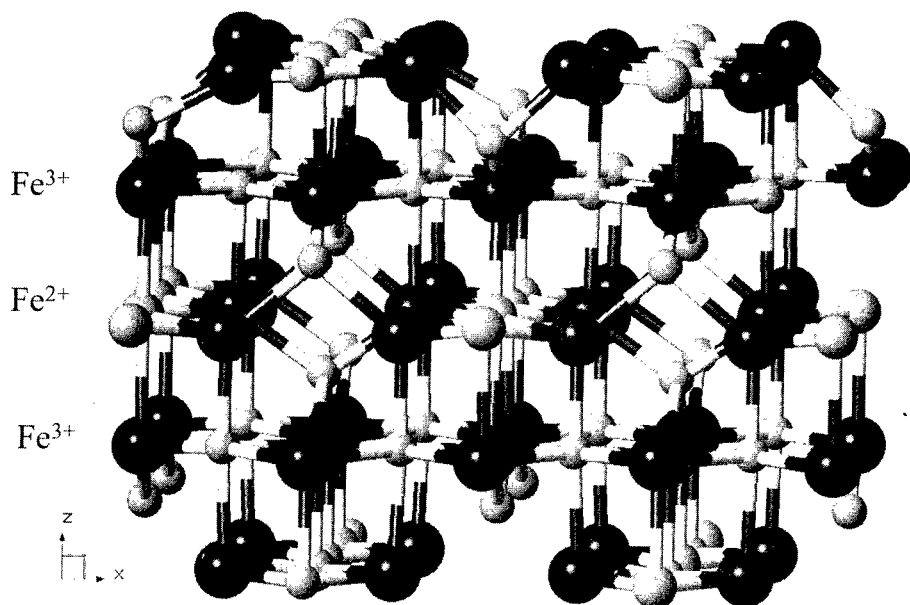


Figure 4. Charge ordering scheme used in the calculation of the relative energies of the "A" and "B" terminations. Atoms are identified according to the protocol in Figure 2. Fe^{2+} and Fe^{3+} are arranged in layers parallel to (001).

Following [19], we start with the equation giving the total energy of the slab in terms of the chemical potential of Fe and O, where we have assumed that pV and TS are small and/or constant from slab to slab:

$$\Omega_{\text{slab}} = E_{\text{slab}} - N_{\text{Fe}}\mu_{\text{Fe}} - N_{\text{O}}\mu_{\text{O}} \quad (1)$$

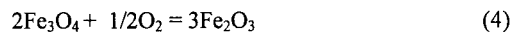
Because of the interdependence between the chemical potentials of magnetite, oxygen and iron:

$$\mu_{\text{Fe}} = 1/3 \mu_{\text{Fe}_3\text{O}_4} - 4/3 \mu_{\text{O}} \quad (2)$$

Equation (1) may therefore be rewritten:

$$\Omega_{\text{slab}} = E_{\text{slab}} - 1/3 N_{\text{Fe}} \mu_{\text{Fe}_3\text{O}_4} + (4/3 N_{\text{Fe}} - N_{\text{O}}) \mu_{\text{O}} \quad (3)$$

where the first two terms are just the standard definition of the energy of the slab relative to the bulk, and the third term accounts for stoichiometric deviations in terms of the chemical potential of oxygen (note that this term is zero for a stoichiometric slab as $4/3 N_{\text{Fe}} = N_{\text{O}}$). Of course, the chemical potential of oxygen cannot be calculated directly in the context of an ionic model. However, for the equilibrium between oxygen gas, magnetite and hematite, the chemical potential of oxygen gas is defined:



$$1/2\mu_{O_2} = 3\mu_{Fe_2O_3} - 2\mu_{Fe_3O_4} \quad (5)$$

Therefore, we can define an “energy” for the O_2 gas by evaluating the left side of equation 5 using the ionic model. Similarly, for the equilibrium between magnetite and wustite:

$$1/2\mu_{O_2} = \mu_{Fe_3O_4} - 3\mu_{FeO} \quad (6)$$

and wustite and hematite:

$$1/2\mu_{O_2} = \mu_{Fe_2O_3} - 2\mu_{FeO} \quad (7)$$

Because the oxygen pressures for each of these buffers are known [20] one can plot the calculated oxygen chemical potentials as a function of $\log P_{O_2}$. Equations (6) and (7) represent metastable equilibria, but, nevertheless, oxygen pressures for each of the reactions are known and can be used to establish the relationship between the calculated oxygen chemical potential and P_{O_2} . This allows the calculation of the surface energy of the model slab as a function of oxygen pressure in Equation (3). This relationship allows calculation of the relative energies of the “A” and “B” terminated slabs over the entire range of accessible conditions. As shown in Figure 5, the “A” termination is everywhere stable relative to the “B” termination. As a caveat, we remark that this calculation will depend to some extent on the possibility of rearranging charge in going from the “A” to the “B” termination. We have ignored this possibility.

It was mentioned above that estimation of the relative energies of the “A” and “B” terminations required charge-ordered slabs. This is because the energy of the charge-delocalized slab with $Fe^{2.5+}$ octahedral sites is significantly higher (2.4 eV/formula unit) than that of the charge-localized slab, because of both Madelung and polarization effects. The higher (less negative) coulomb energy would be offset in the delocalized system by a decrease in the kinetic energy of the electrons, which, of course, is not included in the ionic model. One must therefore use the charge-ordered magnetite to maintain consistency with the hematite and wustite energies, otherwise the energy of magnetite will be artificially raised above hematite and wustite due to the delocalized charge in magnetite.

Hydroxylated “A” and “B” terminations

Upon exposure to the atmosphere, water molecules will adsorb to undercoordinated iron ions at the surface to complete their coordination spheres. It may be fortuitous that the “B” terminated surface has been observed by a group working at Tulane University in the humid climate of Louisiana, U.S.A. [4], while the “A” terminated surface has been observed by workers at the W. R. Wiley Environmental Molecular Sciences Laboratory, a U.S. DOE user facility located in the arid climate at Richland, Washington, U.S.A. [1], but it does raise the reasonable question that water activity may have some role in promoting one surface over another. Of course there is plenty of water available even in the dry Richland air to cover the unsaturated surface sites, nevertheless, the issue warrants further investigation.

Calculations were carried out on three sets of hydroxylated slabs, including both the relaxed and unrelaxed “A” terminations, and the “B” termination. For the “A” sites four waters are added per unit cell to the octahedral sites and two waters per unit cell are added to the tetrahedral sites. Assuming each of the sites has at least one proton, there are $12!/(6! \times 6!) = 924$ possible tautomers for each unit cell. An exhaustive search through these possible tautomers yielded the structure shown in Figure 6a as the lowest-energy tautomer. An analogous investigation for the “B” terminated surface yielded the

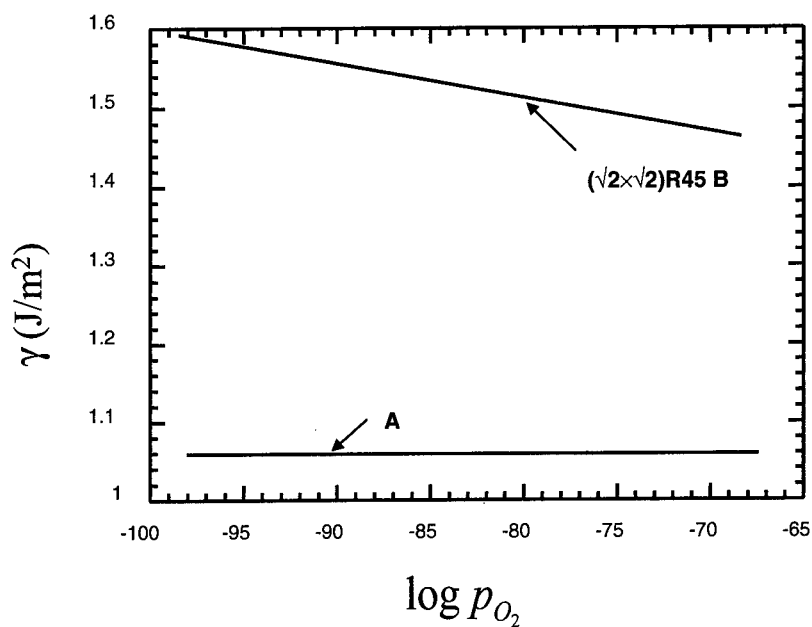


Figure 5. Relative energies of the "A" and "B" terminated surfaces using the charge ordering scheme in Figure 4.

structure shown in Figure 6b. Because of the large number of tautomers within the unit cell, it was not possible to examine arrangements outside the $k=0$ (all unit cells the same) approximation, as was done for hematite (012) [12]. Total water binding energies for both surfaces were about 2.32 J/m², indicating that the presence of water will have little effect, at least in a thermodynamic sense, on which surface is observed.

It is of interest that the unrelaxed "A" terminated surface is lower in energy than the relaxed "A" surface upon hydroxylation; the presence of water in the system should "undo" the surface relaxation predicted in [17]. This in fact explains an apparent paradox suggested by temperature-programmed desorption studies on magnetite (001) [21].

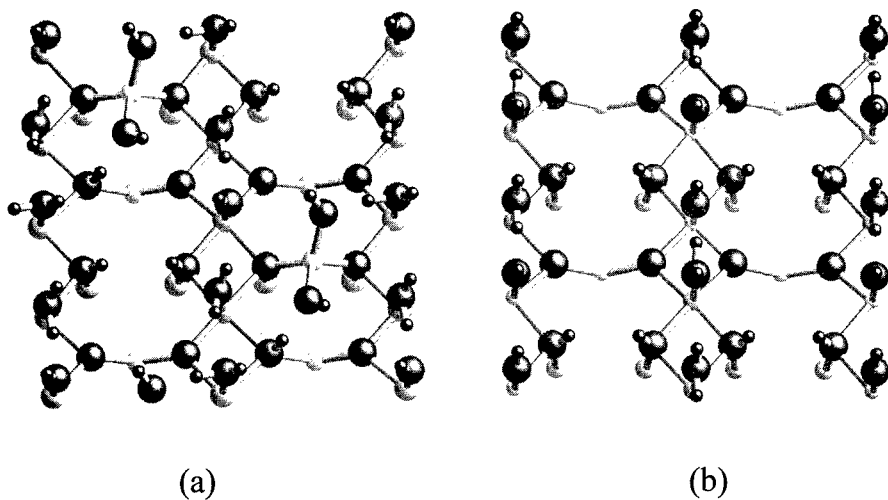


Figure 6. Minimum energy tautomeric forms for the hydroxylated "A" (a) and "B" (b) terminations. Note that in the minimum energy structure for "A", tetrahedral sites revert back to the unrelaxed configuration.

These investigators showed the existence of three peaks in the (001) TPD spectrum at 225, 260, and 325 K. Each peak contributes approximately equal amounts to the TPD spectrum. In one possible interpretation, the 225 and 260 K peaks are contributed by octahedral Fe^{2+} and Fe^{3+} sites, while the peak at 325 K is coming from the Fe^{3+} tetrahedral sites. An objection to this interpretation is that one would not expect the two waters on the tetrahedral sites to desorb at the same temperature. Once one of the waters has desorbed, the remaining water should be held significantly more tightly as the surface Fe^{3+} is now only threefold coordinated. It seems reasonable to expect two peaks at high temperature because the desorbing waters are coming from the same site.

This puzzling lack of two peaks at high temperatures can be rationalized by calling on the large surface relaxation energy to reduce the binding energy of the final water removed from the surface. Calculation of binding energies for each of the waters on the tetrahedral sites shows that the binding energy of the second water (43 kcal/mol) is in fact the same as that of the first (44 kcal/mol). The similarity in binding energies arises because the "A" surface relaxation mechanism is not accessible until the second water is removed from the surface. After this water is desorbed, the system gains 0.72 J/m^2 of surface energy in relaxation, thus decreasing the total binding energy of the second water to a value very close to that of the first water.

CONCLUSIONS

Classical ionic potential model was used to calculate the structure of the octahedral "B" termination of magnetite (001), and the relative energies of the tetrahedral "A" and octahedral "B" terminations of magnetite (001) both under vacuum and hydroxylated conditions. The conclusions resulting from the calculations presented here may be summarized as follows:

1. Surface relaxations for the "B" terminated surface are small, and consistent with the observed $(\sqrt{2} \times \sqrt{2})R45$ cell observed in LEED experiments.
2. The relaxation of a tetrahedral defect on the "B" terminated surface does not give rise to the same relaxation mechanism as that calculated for the "A" surface. This means that a "dimer" would not be observed at these defect sites, which is consistent with STM studies.
3. Within the context of the ionic model used here, the surface energy of the "A" termination of magnetite is lower than that of the "B" termination over a wide range of oxygen fugacities.
4. Hydroxylation has a negligible effect on the relative energies of the "A" and "B" surfaces.
5. The large gain in energy associated with tetrahedral ion relaxation on the "A" surface could explain the lack of two high temperature peaks expected for successive removal of adsorbing waters from the same tetrahedral site.

ACKNOWLEDGEMENT

This work was supported by the U.S. Department of Energy, Office of Basic Energy Sciences, Engineering and Geosciences Division, contract 18328. Pacific Northwest Laboratory is operated for the U.S. Department of Energy by Battelle Memorial Institute under Contract DE-AC06-76RL0 1830. We are grateful to the National Energy Research Supercomputing Center for a generous grant of computer time.

REFERENCES

- [1] S. A. Chambers and S. A. Joyce, "Growth of beta- MnO_2 films on $\text{TiO}_2(110)$ by oxygen plasma assisted molecular beam epitaxy" *Surface Science Letters* 420 (1999) 111.

- [2] F. C. Voogt, "NO₂-assisted molecular beam epitaxy of iron oxide films," Ph.D. Thesis, Groningen: Rijkuniversiteit Groningen, 1998, pp. 158.
- [3] Y. J. Kim, Y. Gao, and S. A. Chambers, Selective growth and characterization of pure, epitaxial alpha-Fe₂O₃(0001) and Fe₃O₄(001) films by plasma-assisted molecular beam epitaxy" *Surf. Sci.* 371 (1997) 358.
- [4] B. Stanka, W. Hebenstreit, U. Diebold, and S. A. Chambers, "Surface reconstruction of Fe₃O₄(001)" *Surf. Sci.* 448 (2000) 49.
- [5] J. W. Halley, J. R. Rustad, and A. Rahman, "A Polarizable, Dissociating Molecular-Dynamics Model for Liquid Water" *J. Chem. Phys.* 98 (1993) 4110.
- [6] F. H. Stillinger and C. W. David, *J. Chem. Phys.* 69 (1978) 1473.
- [7] L. A. Curtiss, J. W. Halley, J. Hautman, and A. Rahman, *J. Chem. Phys.* 86 (1987) 2319.
- [8] J. R. Rustad, B. P. Hay, and J. W. Halley, "Molecular-Dynamics Simulation Of Iron(III) And Its Hydrolysis Products In Aqueous-Solution" *J. Chem. Phys.* 102 (1995) 427.
- [9] J. R. Rustad, A. R. Felmy, and B. P. Hay, "Molecular statics calculations of proton binding to goethite surfaces: A new approach to estimation of stability constants for multisite surface complexation models" *Geochim. et Cosmochim. Acta* 60 (1996) 1553.
- [10] E. Wasserman, J. R. Rustad, A. R. Felmy, B. P. Hay, and J. W. Halley, "Ewald methods for polarizable surfaces with application to hydroxylation and hydrogen bonding on the (012) and (001)surfaces of alpha-Fe₂O₃" *Surface Science* 385 (1997) 217.
- [11] M. A. Henderson, S. A. Joyce, and J. R. Rustad, "Interaction of water with the (1x1) and (2x1) surfaces of alpha-Fe₂O₃(012)" *Surface Science* 417 (1998) 66.
- [12] J. R. Rustad, E. Wasserman, and A. R. Felmy, "Molecular modeling of the surface charging of hematite - II. Optimal proton distribution and simulation of surface charge versus pH relationships" *Surface Science* 424 (1999) 28.
- [13] J. R. Rustad, A. R. Felmy, and B. P. Hay, "Molecular statics calculations of proton binding to goethite surfaces: A new approach to estimation of stability constants for multisite surface complexation models: *Geochim. et Cosmochim. Acta* 60 (1996) 1563.
- [14] A. Felmy and J. Rustad, "Molecular statics calculations of proton binding to goethite surfaces: Thermodynamic modeling of the surface charging and protonation of goethite in aqueous solution" *Geochimica et Cosmochimica Acta* 62 (1998) 25.
- [15] J. K. Beattie, S. P. Best, B. W. Skelton, and A. H. White, "Structural Studies on the Cesium Alums, CSMIII[SO₄]₂12H₂O" *J. Chem. Soc. Dalton Transactions* (1981) 2105.
- [16] R. Akesson, L. G. M. Pettersson, M. Sandstrom, and U. Wahlgren, "Ligand-Field Effects in the Hydrated Divalent and Trivalent Metal-Ions of the First and 2nd Transition Periods" *J. Am. Chem. Soc.*, 116 (1994) 8691.
- [17] J. R. Rustad, E. Wasserman, and A. R. Felmy, "A molecular dynamics investigation of surface reconstruction on magnetite (001)" *Surface Science* 432 (1999) L583
- [18] W. C. Hamilton, *Physical Review* 110 (1958) 1050.
- [19] X.-G. Wang, W. Weiss, S. K. Shaikhutdinov, M. Ritter, M. Petersen, F. Wagner, R. Schlogl, and M. Scheffler, "The hematite (alpha-Fe₂O₃) (0001) surface: Evidence for domains of distinct chemistry" *Phys. Rev. Lett.* 81 (1998) 1038.
- [20] R. M. Garrels and C. L. Christ, *Minerals, Solutions, and Equilibria*. San Francisco: Freeman, Cooper & Company, 1965.
- [21] C. H. F. Peden, G. S. Herman, I. Z. Ismagilov, B. D. Kay, M. A. Henderson, Y. J. Kim, and S. A. Chambers, "Model catalyst studies with single crystals and epitaxial thin oxide films" *Catalysis Today* 51 (1999) 513.

Chairpersons/Organizers of IAC-2

A. Meike (USA)

Earth and Environmental Sciences
P.O. Box 808
Livermore, CA 94550
USA

A. Gonis (USA)

Chemistry and Materials Science
P.O. Box 808
Livermore, CA 94550
USA

P. E. A. Turchi (USA)

Chemistry and Materials Science
Lawrence Livermore National Laboratory
P.O. Box 808
Livermore, CA 94550
USA

K. Rajan (USA)

Department of Materials Science
and Engineering
Rensselaer Polytechnic Institute
110 Materials Research Center
Troy, NY 12180
USA





1. Chen 2. Yamaura 3. Grimvall 4. Vinograd 5. Mohri 6. Hanada 7. Colinet
8. Schultess 9. Gyorffy 10. Schweika 11. Rustad 12. Lodder 13. Klein
14. Papaconstantopoulos 15. Ruban 16. Salje 17. Milman 18. Glassley
19. Faulkner 20. Masuda-Jindo 21. Meike 22. Athenes 23. Lopez 24. Schmid
25. Gonis 26. Mahajan 27. Wuensch 28. Kudrnovsky 29. Shallcross 30. Watanabe
31. Kokowa 32. Spanl 33. Khorzavyi 34. Ohta 35. Pfeiler 36. Vaks 37. Lozovoi
38. Lang 39. Chepulski 40. Turchi 41. Butler 42. Fries 43. Wong 44. Hickernell

List of Participants IAC-2

Dr. M. Athenes

Commissariat a l'Energie Atomique
DECM/SRMP
91191 Gif-sur-Yvette Cedex
France
Tel: +33-1-6908-3769
Fax: +33-1-6908-6867
email: Manuel.Athenes@cea.fr

Dr. W. H. Butler

Metals and Ceramics
MS-6114
4500 South
Oak Ridge Nat. Lab.
Oak Ridge, TN 37831, USA
Tel: 423-574-4845
Fax: 423-574-7659
e-mail: bhb@ornl.gov

Dr. Z. Chen

Institute of Materials Research
Materials Engineering
Nanyang Technological University
Blk N2-1c-87, Singapore 639798
Tel: +65-790-4256
e-mail: aszchen@ntu.edu.sg

Dr. R. V. Chepulskyy

Department of Solid State Theory
Institute for Metal Physics
36, Academician Vernadsky Blvd.
UA-252680 Kyiv-142
Ukraine
Tel: (380) 44 4449513
Fax: (380) 44 4442561
e-mail: chep@imp.kiev.ua

Prof. C. Colinet

Laboratoire de Thermodynamique
et Physico-Chimie Métallurgiques
UMR, CNRS 5614/INPG/UJF
B.P. 75
F-38402 Saint Martin d'Hères Cedex
France
Tel: +33-4-7682-6514
Tel: +33-1-7682-6767
e-mail: catherine.colinet
@ltpcm.inpg.fr

Prof. J. S. Faulkner

Department of Physics
Florida Atlantic University
Boca Raton, FL 33431
USA
Tel: 561-297-3429
Fax: 561-297-2662
e-mail: faulkner@fau.edu

Dr. S. Fries

Access e.V., RWTH-Aachen
Intzestrasse 5
D-52072 Aachen
Germany
Fax: +46-241-38578
e-mail sufries@aldix.mpi-
stuttgart.mpg.de

Dr. W. E. Glassley

Lawrence Livermore Nat. Lab.
PO Box 808, L-202
Livermore, CA 94550, USA
Tel: 925-422-7150
Fax: 925-423-7040
e-mail: glassley@llnl.gov

Dr. A. Gonis

Lawrence Livermore Nat. Lab.
PO Box 808, L-353
Livermore, CA 94550, USA
Tel: 925-422-7150
Fax: 925-423-7040
e-mail: gonis1@llnl.gov

Prof. G. Grimvall

Theoretical Physics
Royal Institut of Technology
SE-100 44 Stockholm, Sweden
Tel: +46-8-790-7174
Fax: +46-8-104-879
e-mail: grimvall@theophys.kth.se

Prof. B. L. Györfy

H H Wills Physics Laboratory
Tyndall Avenue
Bristol BS8 1TL, UK
Tel: +44-117-928-8704
Fax: +44-117-925-5624

Dr. S. Hanada

Institute for Materials Science
Katahira 2-1-1, Aoba-ku
Sendai 980-8577
Japan
Tel: 81-22-215-2115
Fax: 81-22-215-2116
e-mail: hanada@imr.tohoku.jp

Dr. K. Masuda-Jindo

Dept. of Mat. Sci. and Eng.
Tokyo Institute of Technology
Nagatsuta, Midori-ku
Yokohama 226-0026, Japan
Tel +81-45-924-5636
Fax: +81-424-75-0650
e-mail: wmfjindo@din.or.jp

Prof. B. Klein

Vice Provost for Academic Personnel
University of California
One Shields Avenue
Davis, CA 95616, USA
Tel: 530-752-2072
Fax: 530-752-6359
e-mail: bmklein@ucdavis.edu

Prof. H. Kokawa

Department of Materials processing
Graduate School of Engineering
Tohoku University
Aoba-yama 02
Sendai 980-8579, Japan
Tel: +81-22-217-7351
Fax: same as Tel
e-mail: kokawa@
material.tohoku.ac.jp

Dr. P. A. Korzhavyi

Condensed Matter Theory Group
and Physics Department
Uppsala University
PO Box 530
Uppsala S-751 21, Sweden
Tel: +46-18-471-7308
Fax: +46-18-511-784
e-mail: kpa@fysik.uu.se

Dr. J. Kudrnovsky

Institute of Physics AS CR
Na Slovance 2,
CZ-182 21 Prague
Czech Republic
Tel: 420-2-6605-2905
Fax: 420-2-821-227
e-mail: kudrnov@fzu.cz

Mr. H. Lang

Institut für Materialphysik
Strudlhofgasse 4
A-1090 Vienna, Austria
Tel: +43-1-31367-3209
Fax: +43-1-3100-183

Dr. N. Lathiotakis

H H Wills Physics Laboratory
Tyndall Avenue
Bristol BS8 1TL, UK
Tel: +44-117-928-8704
Fax: +44-117-925-5624

Prof. A. Lodder

Vrije Universiteit
De Boelelaan 1081
1081 HV Amsterdam
The Netherlands
Fax: +31-20-444-7992
e-mail: alod@nat.vu.nl

Dr. Hugo F. Lopez
Materials Department
University of Wisconsin-Milwaukee
P.O. Box 784
Milwaukee WI 53201
email: hlopez@csd.uwm.edu

Dr. A. Lozovoi
Atomistic Simulation Group
School of Mathematics and Physics
The Queen's University of Belfast
Belfast BT7, 1NN, Northern Ireland
Tel: +44-1231-273-528
Fax: +44-1232-241-958
e-mail: s.lozovoi@pub.ac.uk

Prof. S. Mahajan
Department of Chemical, Biological
& Materials Eng
Arizona State University
Tempe, AZ 85287-9710
USA
Tel: 602-965-9710
Fax: 602-965-0037
e-mail: smahajan@asu.edu

K. Masuda-Jindo
Department of Materials
Science and Engineering,
Tokyo Institute of Technology,
Nagatsuta, Midori-ku,
Yokohama 226-8503
Japan
Fax: 81-424-75-0650
e-mail: wmfjindo@din.or.jp

Dr. V. Milman
MSJ, The Quorum
Barnwell Rd.
Cambridge CB5 8RE
UK
Tel: +44-1223-413-300
Fax: +44-1223-413-301
e-mail: vmilman@msi-eu.com

Dr. A. Meike
GGS, L-201
Lawrence Livermore Nat. Lab.
PO Box 808
Livermore, CA 94551
USA
Tel: 925-422-3735
Fax: 925-423-1057
e-mail: meike1@llnl.gov

Dr. M. Menon
Department of Physics
University of Kentucky
Lexington, KY 40506
USA
Tel: 606-257-8737
Fax: 606-323-1029
e-mail: super250@pop.uky.edu

Prof. T. Mohri
Division of Materials Science and
Engineering
Graduate School of Engineering
Hokkaido University
Kita-13 Nishi-8
Kita-Ku
Sapporo 060-8628
Japan
Tel: +81-11-706-6348
Fax: +81-11-706-7812
e-mail: tmohri@eng.hokudai.ac.jp

Dr. A. Ohta
National Research Institute
for Metals
1-2-1 Sengen,
Tsukuba-shi, Ibaraki 305-0047
Japan
Fax: +81-298-59-2201
e-mail: ohta-a@nrim.go.jp

Dr. D. Papaconstantopoulos
Naval Research Laboratory
Center for Computational
Materials Science, Code 6390
Washington DC 20375
Tel: 202-767-6886
Fax: 202-404-7546
e-mail: papacon@dave.nrl.navy.mil

Dr. W. Pfeiler

Institut für Materialphysik
Strudlhofgasse 4
A-1090 Vienna
Austria
Tel: +43-1-31367-3209
Fax: +43-1-4277-9513
e-mail: PFEILER@ap.univie.ac.at

Prof. S. K. Saxena

Department of Earth Science
PC344, University Park
Florida International University
Miami, Florida, USA
Tel: 305-348-3117
Fax: 305-348-3877
e-mail: saxenas@fiu.edu

Prof. K. Rajan

Rensselaer Polytechnic Inst.
School of Engineering
Materials Engineering Department
Troy, NY 12180-3590
USA
Tel: 518-276-6126
Fax: 518-276-8554
e-mail: rajan@rpi.edu

Dr. F. Schmid

Theoretische Physik
Fakultaet fr Physik
Universitaet Bielefeld
Universitaetsstrae 25
D-33615 Bielefeld, Germany
Tel: +49-521-106-6901
Fax: +49-521-106-6455
e-mail: schmid@Physik.Uni-Bielefeld.de

Dr. A. Ruban

CAMP, Physics Department
Technical University of Denmark
Bldg. 307
Lyngby 2800
Denmark
Tel: +45-4525-3234
Fax: +45-4593-2399
e-mail: ruban@fysik.dtu.dk

Dr. T. Schulthess

Oak Ridge National Laboratory
Metals and Ceramics
MS-6114, 4500 South
Oak Ridge TN 37831 USA
Tel: 423-574-4244
Fax: 423-574-7659
e-mail: schulthesstc@ornl.gov

Dr. J. Rustad

MS K8-96
Pacific Northwest Laboratory
PO Box 999,
Richland WA, 99352
USA
Tel: 509-376-3979
Fax: 509-376-3650
e-mail: James.Rustad@pnl.gov

Dr. W. Schweika

Institut für Streumethoden
IFF
Forschungszentrum Jülich
D-52425 Jülich
Germany
Tel: +49-2461-61-6650
Fax: +49-2461-61-2610
e-mail: w.schweika@fz-juelich.de

Prof. E. K. H. Salje

Dept. of Earth Sciences
University of Cambridge
Downing Street
Cambridge CB 2, 3EQ, UK
Tel: +44 1223 333481
Fax: +44 1223 333478
e-mail: es10002@esc.ac.uk

Mr. S. Shallcross

H H Wills Physics Laboratory
Tyndall Avenue
Bristol BS8 1TL
UK
Tel: +44-117-928-8704
Fax: +44-117-925-5624
S.Shallcross@bristol.ac.uk

Mr. M. Spanl
Institut für Materialphysik
Strudlhofgasse 4
A-1090 Vienna
Austria
Tel: +43-1-31367-3209
Fax: +43-1-3100-183
e-mail: spanl@ap.univie.ac.at

Dr. J. Tobin
Lawrence Livermore National Lab.,
PO Box 808, L-357
Livermore, CA 94550, USA
Tel: +925-422-7247
Fax: +925-423-7040
e-mail: tobin1@llnl.gov

Dr. P. E. A. Turchi
Lawrence Livermore Nat. Lab.
PO Box 808, L-353
Livermore, CA 94550, USA
Tel: +925-522-9925
Fax: +925-423-7040
e-mail: turchi1@llnl.gov

Dr. V. Vaks
RRC Kurchatov Institute
Moscow 123182, Russia
Tel: +7-095-196-9826
Fax: +7-095-882-5804
e-mail: vaks@mbslab.kiae.ru

Dr. V. Vinograd
Institut fuer Mineralogie,
Universitat Muenster,
Corrensstrasse 24, 48149
Muenster, Germany
e-mail: vinogra@uni-muenster.de

Dr. T. Watanabe
Prof. Tadao Watanabe
Laboratory of Materials Design and
Interface Engineering
Department of Machine Intelligence
and Systems Engineering
Faculty of Engineering, Tohoku
University, Sendai 980-8579, Japan
Tel: 81-22-217-6902
Fax: 81-22-217-6903
e-mail: watanabe@mdie.
mech.tohoku.ac.jp

Dr. J. Wong
Lawrence Livermore Nat. Lab.
PO Box 808, L-353
Livermore, CA 94551, USA
Tel: 925-423-6385
Fax: 925-424-4737
e-mail: wong10@llnl.gov

Prof B. Wuensch
Ceramics Division 13-4037
Massachusetts Institute of Technology
77 Massachusetts Avenue
Cambridge, MA 02139-4307
Tel: 617-253-6889
Fax: 617-253-5827
e-mail: wuensch@mit.edu

Mr. S. Znam
Department of Materials Science
and Engineering
University of Pennsylvania
Philadelphia, PA 19104, USA
Tel: +215-898-7883
Fax: +215-573-2128
e-mail: vitek@lrsm.upenn.edu

AUTHOR INDEX

- Abrikosov, 63-76
Akhmatskaya, 417-427
Alavi, 439-453
Aldivar, 301-320
Antoni-Zdziobek, 261-265
Athenes, 175-185
- Bai, 329-341
Becker, 249-259
Belashenko, 155-173
Bellon, 175-185
Binder, 77-87
Blaas, 343-363
Bruno, 343-363
Bucklen, 39-47
- Chen, Y.-C., 39-47
Chen, Z., 409-415
Charache, 39-47
Chepulsii, 89-99
Colinet, 261-265
Cotterell, 409-415
- Dekker, 49-59
Dobretsov, 155-173
Drchal, 343-363
Dubrovinsky, 221-233
- Eberman, 101-113
Elmer, 285-299
- Faulkner, 199-218
Felmy, 499-509
Finnis, 439-453
Freeman, 39-47
- Glassley, 141-153
- Goodman, 381-390
Grimvall, 473-477
Györfy, 267-283, 365-379
- Haas, 77-87
Hanada, 393-399
Holt, 285-299
Huang, 301-320
Hung, 235-247
- Ice, 329-341
Igarishi, 27-37
- Johansson, 63-76
- Khorzhavyi, 63-76
Kikuchi, 235-247
Kokawa, 17-25
Korner, 429-437
Korzhavyi, 439-453
Koyanagawa, 17-25
Kudrnovský, 343-363
Kuwana, 17-25
- Lang, 115-121
Larson, 285-299
Lathiotakis, 365-379
Lodder, 49-59
Lopez, 301-320
Lozovoi, 439-453
- Maeda, 401-407
Mahajan, 455-471
Martin, 175-185
Masuda-Jindo, 235-247
Meike, 141-153
Milman, 417-427
Moghadam, 199-218

Mohri, 123-138	Shallcross, 267-283
Ngyuen-Manh, 479-497	Shimada, 17-25
Nicols, 39-47	Spanl, 187-197, 429-437
Nobes, 417-427	Sparks, 329-341
Nomura, 393-399	Stocks, 199-218
	Suzuki, 401-407
Ohta, 401-407	Tobin, 381-390
Pankratov, 155-173	Tsurekawa, 27-37
Pettifor, 479-497	Turek, 343-363
Pfeiler, 115-121, 187-197, 429-437	Ujfalussy, 199-218
Pickard, 417-427	
Podloucky, 115-121, 187-197	Vaks, 155-173
Püschl, 187-197, 429-437	Vinograd, 249-259
Putnis, 249-259	Vitek, 479-497
Rajan, 39-47	Wang, C.A., 39-47
Ressler, 285-299	Wang, W., 409-415
Robertson, 329-341	Wang, Yang, 199-218
Rohrhofer, 115-121	Wasserman, 499-509
Rosenkranz, 429-437	Watanabe, 27-37
Rustad, 499-509	Weinberger, 343-363
	White, 417-427
Salje, 3-15	Willis, 381-390
Samolyuk, 155-173	Winkler, 417-427
Sanders, 39-47	Wong, 285-299
Sato, 17-25	Wuensch, 101-113
Saxena, 221-233	
Schmid, 77-87	Yamaura, 27-37
Schumann, 381-390	Yoshimi, 393-399
Schweiger, 187-197	
Schweika, 329-341	Znam, 479-497

SUBJECT INDEX

- Aging
 isothermal, 309, 315-319
- Al alloy *see* Aluminum alloy
- Alloy, *see also* entries under specific alloys
 semiconductor, 39
 solid solution, *see* Solid solution
- Almandine ($\text{Fe}_3\text{Al}_2\text{Si}_3\text{O}_{12}$), *see* Garnet, almandine
- Aluminum alloy
 Ni-Al, 440-451
 Cu-Al, 430-436
 Ti-Al, 482-485, 488-495
- Andradite ($\text{Ca}_3\text{Fe}_2\text{Si}_3\text{O}_{12}$), *see* Garnet, andradite
- Angular correlation positron annihilation
 2-dimensional (2d ACAR), 366, 373
- Annealing, 116-120, 296, 299, 310, 313
 defect, 430
- Annealing algorithm, 255
- Antiferromagnetic, 263, 366, 421
- Antiphase boundaries (APBs), 162-171, 493
- Antiphase ordered domains, (APDs), 163, 168
- Atomic mobility, 323; *see also* Diffusion and Ionic mobility
- Atomic scattering factor, 331
- Austenitic transformation *see* Phase transformation, austenitic
- bcc (body-centered cubic), 66, 78, 162, 176, 177, 221, 240, 242, 262-265, 372, 394, 395, 474-476
 $Ia3d$ space group, 418
- Binding energy, 507-508
- Bloch Spectral Function (BSF), 374, 375
- Bond energy, 482-483
- Bond order potential (BOP), 481, 485, 488-496
- Body-centered cubic, *see* bcc
- Bragg-Williams approximation, 11
- Bragg-Williams mean field (BWMF)
 theory, 268-272, 279-280
- Bravais lattice, 89-90
- Brioullin zone, 272, 273
- Buckle test, 410
- Central force model (CFM), 337
- Chemical potential, 262, 263, 505
- Cluster Variation Method (CVM) 125-
 128, 130-137, 157, 236, 242, 250, 251, 253-255, 258, 259, 262, 264, 266, 269, 277
 cluster field method (CFM), 157
 continuous displacement (CD)
 formulation, 236
 tetrahedron cluster field method (TCFM), 157
- Co, *see* Cobalt
- Co alloy, *see* Cobalt alloy
- Cobalt, 264
- Cobalt alloy
 Co-Cr-Mo, 308-322
 Co-Ni, 382
- Coherent potential approximation (CPA), 199-216, 345, 350, 360-362
 Korringa-Kohn-Rostoker CPA (KKR-CPA), 200, 204, 206, 208, 214-216, 369-371
 polymorphous CPA (PCPA), 205, 207, 209, 213-216
 screened CPA (S-CPA), 203, 204, 215

- Coherent potential approximation
(continued from previous page),
screened impurity model CPA (SIM-CPA), 203-205, 215
- Coincident site lattice (CSL), 22,24,29-32
- Composition-conserving defect
concentration (CD), 443-445
- Constitutional defect, 440; *see also* Point defect
- Copper alloys
Cu-Au, 245, 330-339
Cu-Pd, 168
Fe1.34at.%Cu, 179
- Cordierite, 6
- Corrosion
intergranular, 17-24
- Crack, 413
compressive, 414
propagation, 396, 413
- Cu alloys *see* Copper alloys
- Curie temperature, 263-266
- Current-in-plane (CIP), 345
- Current-perpendicular-to-plane (CPP), 344, 345, 362
- Defect, *see also* defect type
annealing, 430
formation energy, 190
migration energy, *see also* Diffusion, 190-193
structural, 313
- Density function theory (DFT), 418
and local density approximation (DFT-LDA), 200-201, 203-204, 209-210, 214-216
- dhcp (double hexagonal close-packed), 222, 226
- Diamond-anvil cell (DAC), 222, 223, 225, 230
- Diffraction
electron, 460, 462
Kikuchi pattern, 21
spatially resolved x-ray diffraction (SRXRD), 288-298
superlattice reflection, 226,227
time resolved x-ray diffraction (TRXRD), 287-293
x-ray, 228, 310, 396; *see also* X-ray
- Diffusion, 176-183
grain boundary, 148
oxygen, 148-150
twin boundary, 3-15
- Dimer, 178-182
- Direct valence, 56-57
- Dislocation, 319, 324
- Disorder, 359, 358, 357; *see also* Order kinetics, 133
order, 77-85
spinodal, 124-137
- Dynamical instability, 474
- Electromigration, 50-58
- Electron microprobe, 32; *see also* Electron probe microanalyzer
- Electron probe microanalyzer (EPMA), 394-395
- Electronic structure, 50-58
calculation of, 474
- Electronic topological transition (ETT), 374, 375, 377
- Embedded atom method (EAM), 337
- Embrittlement
oxidation, 29-36
- Entropy
calculation of, 253
correction, 272
- Fatigue, 401, 407
fracture, 401
strength, 408
- Face-centered, *see* fcc
- Failure strain, *see* Strain, failure
- fcc (face-centered cubic), 66, 159, 166, 221, 227, 229-230, 239-241, 262-265, 269, 277, 310-324, 346, 367, 386, 474
- Fe, *see* Iron
- Fe alloy, *see* Iron alloy
- Feldspar, 143, 147
- Fermi energy, 355, 359
- Fermi surface, 330, 338, 367-370
- Ferromagnetic, 263, 366
- Fourier transform, 272, 274, 281, 333-334, 370
- Fracture, *see also* Crack
fatigue, 401
toughness, 396, 410
- Garnet, 143, 147; *see also* mineral name
for formula
almandine, 418, 421-424
andradite, 418-424
grossular, 418, 421-424
hydrogrossular (katoite), 424
pyrope, 418, 421-424
spessartine, 418, 421-424
uvarovite, 418-424
- Giant magnetoconductance (GMC), 344-357

- Giant magnetoresistance (GMR), 367
- Gibbs free energy, 8, 9
- Goethite (FeOOH), 501
- Grain boundary, 17-24, 28-36, 432
 - character distribution of (GBCD), 31-35
 - electromigration, 54, 55
 - transport, 3-15
- Green's function, 345-349, 361
 - Korringa-Kohn-Rostoker (KKR), 53, 200, 204, 206, 208, 214-216
 - self-consistent (LSGF), 66, 205, 207, 209, 216
- Grossular ($\text{Ca}_3\text{Al}_2\text{Si}_3\text{O}_{12}$), *see* Garnet, grossular
- hcp, 226-228, 310-324, 474; *see also* dhcp
- Hematite, 505, 507
- Hip joint, 307
- Hydrogrossular ($\text{Ca}_3\text{Al}_2(\text{O}_4\text{H}_4)_3$), *see* Garnet, hydrogrossular
- Indium tin oxide (ITO) film, 410-416
- Infrared spectroscopy, 424
- Ionic mobility, 3; *see also* Diffusion and atomic mobility
- Ionic potential model, 508
- Instability
 - phase, 46
- Interphase boundary (IPB), 170
- Iron, 221-231, 264
 - melting curve, 230
- Iron alloy
 - Au-Fe, 430-436
 - austenite stainless steel, 19, 20
 - Fe-Al, 116-120, 163
 - Fe-Co, 263-266
 - Fe-Cu, 384-387
 - Fe-Ni, 382-384, 386
 - Fe-Si, 162
 - Ni4at%iron alloy, 29-35
 - SM 490 steel, 402, 408
- Kikuchi pattern, 21
- Kinetic cluster field approach (KCFA)
- Kinetics
 - ordering 116-120
 - phase transformation, 316, 319
- Kohn-Sham, 346
- Kolmogorov-Johnson-Mehl-Avrami (KJMA) law, 179
- Korringa-Kohn-Rostoker (KKR), 53, 200, 204, 206, 208, 214-216
- Krivoglaz-Clapp-Moss (KKM), 94
- Kubo-Greenwood, 344, 345
- Kubo-Landauer, 352
- Landau potential, 4
- Laser heating, 222-224
- Lattice gas model, 90
- Lattice instability, 476
- Linear muffin tin orbital (LMTO), 484
 - full potential (FP-LMTO), 489, 493
 - tight binding (TB-LMTO), 345-347, 351, 484-488
- Local density approximation, 445
- Locally self-consistent multiple scattering method (LSMS), 200, 202, 205, 207, 209, 213, 214
- Long range order, *see* Order, long-range
- Magnetic dichroism, 381
- Magnetite (Fe_3O_4), 143, 147, 499-505
- Magnetoconductance, 348; *see also* Giant magnetoconductance
- Markovian process, 176
- Martensite, 311, 313
- Martensitic transformation, *see* Phase transformation, martensitic
- Mean-field approximation (MFA), 94, 157
 - kinetic MFA (KMFA), 157
- Mean square relative displacement (MSRD), 246, 247
- Microstructure *see* microstructure type
- Modulated structure, 43-45
- Molecular dynamics calculation, 499
- Monomer, 177-180
- Monte Carlo (MC), 6, 10, 78-84, 196
- Multilayer, *see also* Semiconductor
 - metallic magnetic, 345; *see also* multilayer composition
 - Co/Cu/Co, 345, 350, 352, 356-362
 - Fe/Cr/Fe, 370-373
 - Cu/Ni/Cu, 367-369
- Neutron diffraction analysis, 105-107
- Ni alloy, *see* Nickel alloy
- Nickel alloy
 - Ni-Al, 68, 166, 190-196
 - Ni-V alloy, 95
- Onsager Cavity Field Approximation (OCFA), 270-272, 277-280
- Order, 421
 - cation and anion, 102-112
 - disorder, 77-85, 189,
 - kinetics of ordering, 116-120

Order (continued from previous page),
 Krivoglaz-Clapp-Moss, 94
 long-range (LRO), 116-120, 130-133,
 160-161, 195, 196, 252,
 257, 272
 order-disorder transition, 240, 264
 short-range, 89-95, 183, 271, 272,
 331-338, 429-436
 spinodal, 162
 and surfaces, 77-85
 Order parameter, 5-14, 80-84, 245, 247,
 275, 280, 281, 335
 Organic light emitting display (OLED),
 409
 Path probability method (PPM) 128-130
 Phase boundary
 phase diagram, 227
 phase separating curves, 240, 242
 Phase diagram
 computationally determined, 241,
 243, 271, 278
 experimentally determined, 227, 229
 phase boundary, 227
 phase separating curves, 240
 Phase separation, 456
 Phase transformation, 292, 296-302; *see*
also Transition
 allotropic, 310
 diffusionless, 311
 isothermal, 309, 316
 kinetics, 162-170, 301
 martensitic, 309, 311, 315, 316, 323
 order-disorder transformation, 242
 strain induced (SIT), 313-315
 Phase transition, *see* Transition, *see also*
 Phase transformation
 Planck radiation function, 224
 Plastic strain, *see* Strain, plastic
 Platinum
 alloy with tungsten, 476
 Point defect
 formation energy, 64, 68-72
 thermal, 441, 443
 Precipitate, 396; *see also* Symplectite
 Pressure, 445-448, 476
 extremes of, 231
 Probability distribution (PD), 250, 251,
 257, 259
 probability distribution function
 (PDF), 236
 Pt, *see* Platinum
 Pyrochlore, 102-112
 Pyrope ($\text{Mg}_3\text{Al}_2\text{Si}_3\text{O}_{12}$) *see* Garnet, pyrope
 Pyroxene, 143, 147
 Quartz, 143, 147
 Raman scattering, 330
 Reciprocal space, 333
 Relaxation time, 136
 Scanning electron microscope (SEM),
 319, 393-399
 Self-assembly, 46-48
 Self organization
 self organized compositional
 modulation (SOCM), 42-
 45
 Semiconductor, *see also* Alloy,
 semiconductor
 of binary III-V compounds, 455
 $\text{Ga}_{1-x}\text{In}_x\text{As}_y\text{Sb}_{1-y}$, 39-41
 InGaAsP, 456-468
 InAsSb layers in, 460, 461
 Shear band, 313
 Short range order, *see* Order, short-range
 Si alloy, *see* Silicon alloy
 Silicon alloy,
 Mo-Si, 483, 487, 493, 495
 Single edged notched beam (SENB) test,
 397
 Solid solution, 102-112; *see also* Alloy
 Spectroradiometry, 224
 Spessartine, ($\text{Mn}_3\text{Al}_2\text{Si}_3\text{O}_{12}$), *see* Garnet,
 spessartine
 Spinel structure, 500
 Spinodal disorder, 124-137
 Spinodal order, 162
 Stacking fault,
 complex stacking fault (CSF), 493
 superlattice intrinsic stacking fault
 (SISF), 493
 Stacking fault energy, 320, 323, 431
 Strain 403, 412, 414
 failure, 410
 plastic, 313-315
 Strain energy, 461
 Strain induced transformation (SIT), *see*
 Transformation, strain
 induced
 Stress, 403, 406
 Structural defect *see* Defect, structural
 Superlattice, 45, 46
 reflections of, *see also* Diffraction,
 226, 227
 Surface
 ordering, 77-85
 relaxation, 500-508
 Susceptibility, 134-136
 Symplectite, 143, 147
 Ta alloys, *see* Tantalum alloys

- Tantalum alloys
TaC alloys, 287, 291-297
- Temperature
extremes of, 231, 286
- Thermal diffuse scattering 332
- Ti, *see* Titanium
- Ti alloy, *see* Titanium alloy
- Tight binding linear muffin tin orbital (TB-LMTO), *see* Linear muffin tin orbital, tight binding
- Titanium, 289, 295-299
- Titanium alloy
Mo-Ti-C, 393-399
Nb-Ti-C, 393-399
- Transformation, *see* Phase transformation; *see also* Transition
- Transition, 271; *see also* Phase transformation
far-from-equilibrium, 128
first order phase transition (FOPT) 451, 452
isostructural, 449-451
near-equilibrium, 128
order-disorder, 240
temperature, 131, 275, 277, 280
- Transmission Electron Microscope (TEM), 20-22, 42-44, 149-150, 311, 324, 394, 431, 456-465
dark field, 459-461
- Transport, 344
ballistic, 356
diffusive, 356
- Tungsten
alloy with Pt, 476
WO_{3-x}, 3
- Twin walls, 4-14
- Uvarovite (Ca₃Cr₂Si₃O₁₂), *see* Garnet, uvarovite
- Vacancy, 117-119, 176-182, 189, 193, 441, 444
formation energy, 66-68, 193
migration energy, (*see also* Diffusion), 194
- Wagner-Schottky model, 69, 70, 441, 445, 449
- Weld, 401, 402
- Wind valence, 50-53
- W, *see* Tungsten
- X-ray, 222, 225; *see also* Diffraction, x-ray
absorption fine structure (EXAFS), 330
atomic scattering factor, 331
magnetic linear dichroism (XMLD), 382-384, 386
spatially resolved x-ray diffraction (SRXRD), 288-298
time resolved x-ray diffraction (TRXRD), 287-293
- X-ray absorption fine structure (EXAFS), 330
- X-ray magnetic linear dichroism (XMLD), 382-384, 386
- YBa₂CuO₇
on SrTiO₃ substrates, 6
- Zn alloy, *see* Zinc alloy
- Zinc alloy
Ag-Zn, 430-436